frontiers | Research Topics

Impact of ocean forcing on the coastal hydrology, environment and freshwater resources

Edited by
Tianyuan Zheng, Chengji Shen, Xiuyu Liang and Olaf Kolditz

Coordinated by
Guangquan Chen

Published in
Frontiers in Marine Science

ISSN 1664-8714
ISBN 978-2-8325-5598-9
DOI 10.3389/978-2-8325-5598-9

About Frontiers

Frontiers is more than just an open access publisher of scholarly articles: it is a pioneering approach to the world of academia, radically improving the way scholarly research is managed. The grand vision of Frontiers is a world where all people have an equal opportunity to seek, share and generate knowledge. Frontiers provides immediate and permanent online open access to all its publications, but this alone is not enough to realize our grand goals.

Frontiers journal series

The Frontiers journal series is a multi-tier and interdisciplinary set of open-access, online journals, promising a paradigm shift from the current review, selection and dissemination processes in academic publishing. All Frontiers journals are driven by researchers for researchers; therefore, they constitute a service to the scholarly community. At the same time, the *Frontiers journal series* operates on a revolutionary invention, the tiered publishing system, initially addressing specific communities of scholars, and gradually climbing up to broader public understanding, thus serving the interests of the lay society, too.

Dedication to quality

Each Frontiers article is a landmark of the highest quality, thanks to genuinely collaborative interactions between authors and review editors, who include some of the world's best academicians. Research must be certified by peers before entering a stream of knowledge that may eventually reach the public - and shape society; therefore, Frontiers only applies the most rigorous and unbiased reviews. Frontiers revolutionizes research publishing by freely delivering the most outstanding research, evaluated with no bias from both the academic and social point of view. By applying the most advanced information technologies, Frontiers is catapulting scholarly publishing into a new generation.

What are Frontiers Research Topics?

Frontiers Research Topics are very popular trademarks of the *Frontiers journals series*: they are collections of at least ten articles, all centered on a particular subject. With their unique mix of varied contributions from Original Research to Review Articles, Frontiers Research Topics unify the most influential researchers, the latest key findings and historical advances in a hot research area.

Find out more on how to host your own Frontiers Research Topic or contribute to one as an author by contacting the Frontiers editorial office: frontiersin.org/about/contact

Impact of ocean forcing on the coastal hydrology, environment and freshwater resources

Topic editors

Tianyuan Zheng — Ocean University of China, China
Chengji Shen — Hohai University, China
Xiuyu Liang — Southern University of Science and Technology, China
Olaf Kolditz — Helmholtz Centre for Environmental Research, Helmholtz Association of German Research Centres (HZ), Germany

Topic coordinator

Guangquan Chen — First Institute of Oceanography, Ministry of Natural Resources, China

Citation

Zheng, T., Shen, C., Liang, X., Kolditz, O., Chen, G., eds. (2024). *Impact of ocean forcing on the coastal hydrology, environment and freshwater resources*. Lausanne: Frontiers Media SA. doi: 10.3389/978-2-8325-5598-9

Table of contents

frontiers | Frontiers in Marine Science

TYPE Original Research
PUBLISHED 04 December 2023
DOI 10.3389/fmars.2023.1319751

OPEN ACCESS

EDITED BY
Olaf Kolditz,
Helmholtz Association of German Research Centres (HZ), Germany

REVIEWED BY
Peipeng Wu,
Jilin University, China
Jian Song,
Hohai University, China

*CORRESPONDENCE
Jiazhong Qian
qianjiazhong@hfut.edu.cn
Huan Wang
wanghuanformal@163.com

RECEIVED 11 October 2023
ACCEPTED 20 November 2023
PUBLISHED 04 December 2023

CITATION
Fang Y, Qian J, Ma L and Wang H (2023) Groundwater dynamics in intertidal zones of beach aquifers during salt-fingering flow.
Front. Mar. Sci. 10:1319751.
doi: 10.3389/fmars.2023.1319751

Groundwater dynamics in intertidal zones of beach aquifers during salt-fingering flow

Yunhai Fang[1], Jiazhong Qian[1]*, Lei Ma[1] and Huan Wang[2]*

[1]School of Resources and Environmental Engineering, Hefei University of Technology, Hefei, China, [2]College of Environmental Science and Engineering, Guilin University of Technology, Guilin, China

At aquifer-sea interfaces, submarine groundwater discharge (SGD) and related chemical loads are closely related to groundwater environment in the intertidal zone of coastal aquifers. Although unstable salinity distribution in the intertidal zone associated with salt-fingering flow has been known as a natural phenomenon for some coastal aquifers, a quantitative understanding of groundwater dynamics in the intertidal zone during salt-fingering flow is still lacking. This study investigated the movement features of salt fingers and the response laws of freshwater discharge zone (FDZ) in the intertidal zone, considering the fixed and seasonal inland conditions. The results revealed that during salt-fingering flow, the finger was repeatedly generated and detached from the intertidal zone. Horizontally, the finger moved toward the sea, and the finger speed first increased at the development stage, then remained unchanged at the separation stage, and finally decreased at the mergence stage. The movement speed of salt fingers was closely related to ambient freshwater flow in the FDZ. In the vertical direction, the finger first permeated downward with a decreasing speed, and then the upward discharge of fresh groundwater in the FDZ region with an increased flow velocity pushed the finger upwards with an increasing speed. In contrast to the results in a stable intertidal regime, the width of FDZ at the aquifer-sea interface fluctuated over time, and the variation trends possessed a well agreement with the flux of fresh groundwater discharge. This suggested that the width of FDZ at the aquifer-sea interface can be used as an indicator of fresh groundwater discharge, even in an unstable regime, to provide a basis for field monitoring. The intensity of salt-fingering flow varied over time under the condition of seasonal freshwater inflow. The mean duration of salt fingers decreased slightly with the increase of seasonal freshwater periods due to a decrease in the interface perturbation for the intertidal environment. These findings lay the foundation for gaining a better understanding of the potential implications of salt-fingering flow on SGD and related solute transports.

KEYWORDS

flow instability, submarine groundwater discharge, movement characteristics, tide, unconfined aquifer

1 Introduction

Water exchange across the aquifer-sea interface is the result of groundwater-seawater interactions. Generally, groundwater discharged from coastal aquifers into the ocean, termed as submarine groundwater discharge (SGD), is an important part of the global water cycle (Rodellas et al., 2015). It has been estimated that SGD fluxes may exceed river inflows on a global scale (Kwon et al., 2014). SGD has been identified as an important channel of widespread attention for terrestrial freshwater, nutrients, metals, and carbon to enter the ocean, affecting coastal water quality and ecosystems (Andrisoa et al., 2019; Starke et al., 2020; Kim et al., 2022). At the aquifer-sea interface, SGD fluxes, related chemical loads, and discharge locations are closely related to the groundwater environment in the intertidal zone of the aquifer (Robinson et al., 2018; Santos et al., 2021). Previous studies suggest that ocean forces (i.e., tides and waves) induce an upper saline plume (USP) in the intertidal zone, in addition to the known saltwater wedge (SW) formed by seawater intrusion in the lower aquifer (Figure 1A). Fresh groundwater bypasses the USP and carries inland solutes into the ocean, and the discharge hotspot is concentrated near the low-tide mark (Lebbe, 1981; Kuan et al., 2019). Moreover, the difference in the composition of freshwater and seawater generates geochemical (salinity, pH, and redox) gradients at the edge of the USP, which is an active reaction region and affects the fate of inland solutes and chemical loads discharged into the ocean (Heiss et al., 2017; Heiss et al., 2020). Therefore, it is essential to study groundwater dynamics in the intertidal zone for accurately estimating SGD and associated solute transports.

Groundwater dynamics in the intertidal zone are governed by the hydrodynamic conditions of coastal aquifers, e.g., head difference, salinity difference, temperature difference, tide, and wave (Lu and Werner, 2013; Nguyen et al., 2020; Wu et al., 2023). Previous studies have understood the salinity distribution in the intertidal zone as a layered and stable structure, with the USP, freshwater discharge zone (FDZ), and SW followed below the tidal flats (Heiss and Michael, 2014; Zheng et al., 2022). As the hydrodynamic conditions change, the USP expands or contracts in the intertidal zone with an approximate "U" shape (Yu et al., 2019). Thus, the USP morphology and the intertidal salinity distribution are stable (Figure 1B). Certainly, there are some conditions (e.g., a high fresh groundwater flux) where the USP may not form in the intertidal zone (Evans and Wilson, 2017). The saltwater in the USP region flows above fresh groundwater, generating a reverse salinity (density) gradient. Gravity causes this structure to tend to be unstable. Greskowiak (2014); Shen et al. (2019), and Geng et al. (2020) proposed and confirmed the phenomenon of unstable USP using numerical simulations, and found that in coastal aquifers with gentle beach slopes, the unstable USP continues to generate salt fingers that subsequently possess a finger-like vertical seepage, termed as salt-fingering flow (Figure 1C). Experimental studies of Fang et al. (2021, 2022a) and

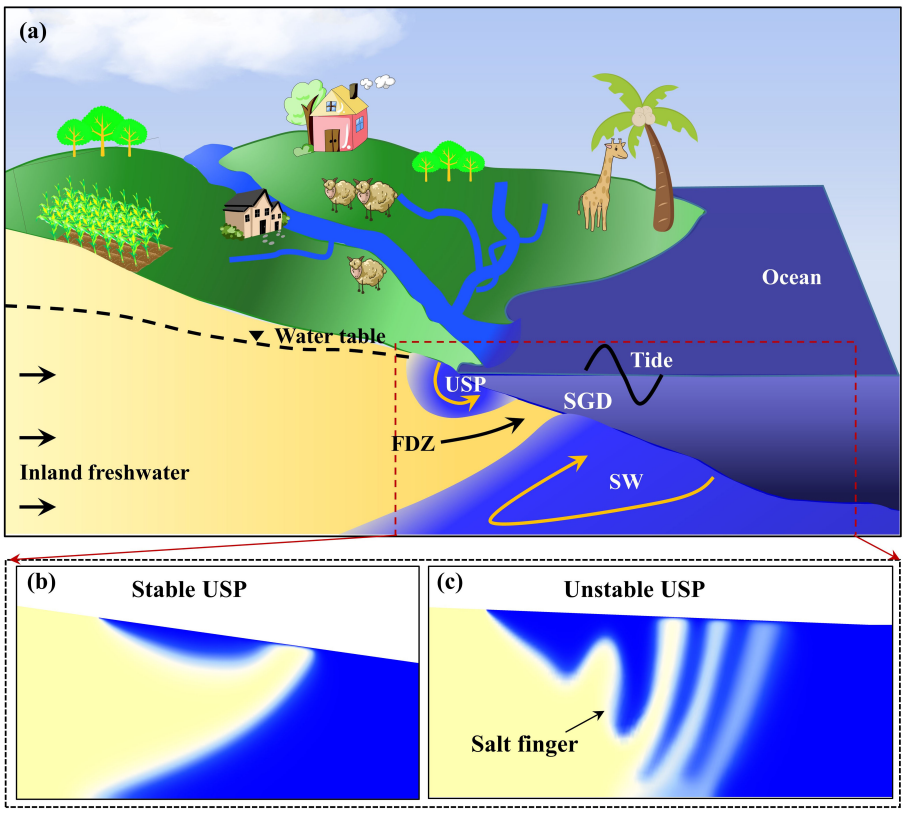

FIGURE 1
Schematic diagram of salinity distribution in a two-dimensional (2D) cross-shore profile of a coastal unconfined aquifer **(A)** with a stable **(B)** and unstable **(C)** intertidal regime. USP, upper saline plume; SW, saltwater wedge; FDZ, freshwater discharge zone.

Röper et al. (2015) also photographed the flow instability of salt fingers in the intertidal zone via a lab-scale sand tank. In the sandy tidal flat of Shilaoren, Jiaozhou Bay, Zhang Y. et al. (2021) and Xing et al. (2023) used electrical resistivity tomography and hydrological monitoring to successfully capture the process of unstable USP and subsequent salt-fingering flow. Therefore, the unstable USP associated with salt-fingering flow is a natural phenomenon for some coastal aquifers, which updates the conventional understanding of the salinity distribution in the intertidal zone.

Flow instability of salt fingers has a significant impact on SGD. During salt-fingering flow, the FDZ is separated by salt fingers, thus forming multiple freshwater discharge routes that changed over time. As a result, the discharge hotspot at the aquifer-sea interface is not limited to the low-tide mark (Zhang J. et al., 2021). Fang et al. (2021; 2022b) further demonstrated that the phase-averaged SGD fluxes fluctuated irregularly over time, and the fluctuation was positively correlated with the intensity of salt-fingering flow. These characteristics differ significantly from the results under the stable USP regime that the water exchanges across the aquifer-sea interface are constant with continuous tide cycles (Greskowiak, 2014). Although a growing number of studies have revealed the effect of unstable USP on the SGD fluxes, the current understanding of the movement of salt fingers remains at the stage of qualitative description and lacks quantitative characterization. Previous studies have qualitatively described the movement of salt fingers between the USP and the SW. There is little published data on the movement route and speed of salt fingers and the response of FDZ. In other words, a quantitative understanding of groundwater dynamics in the intertidal zone during salt-fingering flow is still lacking. While quantifying groundwater dynamics in the intertidal zone is a prerequisite for accurately predicting and explaining the spatiotemporal evolution of SGD fluxes. In addition, due to the timescale changes in external forcing conditions (e.g., seasonality in subsurface inflow or hydraulic gradient), the USP regime is not always stable or unstable, but experiences a dynamic transformation of stability over time (Fang et al., 2022a). However, under the dynamically stable-unstable regime, the quantitative characteristics of salt finger movement also remain unclear.

To address these issues, we conducted numerical simulations to investigate groundwater dynamics in the intertidal zone during salt-fingering flow. Specifically, the numerical model presented herein has been verified in our previous experimental study in a laboratory beach aquifer. Based on laboratory-scale simulation results, three key objectives were addressed in this study: (a) quantify the movement features of salt fingers and the response laws of FDZ; (b) examine the influence of fixed subsurface inflow with an unstable USP regime on the intertidal groundwater dynamics; and (c) reveal the influence of seasonal subsurface inflow with a dynamically stable-unstable regime on the intertidal groundwater dynamics.

2 Methodology

2.1 Laboratory beach aquifer

Our experimental studies of Fang et al. (2021; 2022a; 2022b) have successfully confirmed the stable, unstable, and dynamically stable-unstable USP phenomena in the intertidal zone of coastal aquifers. Laboratory experiments were conducted in a well-designed sand tank with a dimension of 172.9 cm (length) × 45.0 cm (height) × 8.0 cm (width) (Figure 2). The central chamber (gray section) was filled with white quartz sand, which represents a quasi two-dimensional profile of an unconfined aquifer with a beach slope of 1/10.5. After sieving, the particle size of the quartz sand was relatively uniform (d_{50} = 0.6 mm; d_{90}/d_{10} = 2.4), and the average hydraulic conductivity and porosity were 4.8×10^{-3} m/s and 0.4, respectively. The sea level fluctuated over time via a tidal generator (VHO) with a tidal amplitude of 2.2 cm and a period of 1 min. Artificial seawater was prepared by dissolving 34.5 g sodium chloride (NaCl, AR grade) and 1.5 g red food dye (Sinopharm Chemical Reagent, Co., Ltd) per liter of deionized water. Food dyes are often used in seawater tracing in the studies of groundwater-seawater interactions due to their inert relationship (adsorption and reaction) with quartz sand (Goswami and Clement, 2007).

2.2 Numerical simulations

In order to quantify groundwater dynamics in the intertidal zone, a density-dependent and variably saturated groundwater flow and solute transport program, FEFLOW, was used to numerically simulate the interactions of groundwater and seawater in the laboratory-scale aquifer. According to the setup of laboratory experiments, the following assumptions were adopted in the numerical model to simplify the problems: (a) the unconfined aquifer was homogeneous and isotropic; (b) both the fluid and the porous media were incompressible; and (c) the fluid density was only related to solute concentration. Based on these assumptions, we used the Richard's equation and the advection-diffusion equation to govern the processes of density-dependent and variably saturated groundwater flow and solute transport (Diersch, 2014). The relationship between relative permeability, phase saturation, and capillary pressure was defined by the following functions (Van Genuchten, 1980):

$$\begin{cases} s = s_r + (1 - s_r)\left[\frac{1}{1+|a\Psi|^n}\right]^{\left(\frac{n-1}{n}\right)} \\ k_r = s_w^{1/2}\left\{1 - \left[1 - s_w^{\left(\frac{n}{n-1}\right)}\right]^{\left(\frac{n-1}{n}\right)}\right\}^2 \\ s_w = \frac{s - s_r}{1 - s_r} \end{cases} \quad (1)$$

where s and s_r are the water saturation [-] and residual water saturation [-], respectively; a and n are the constants; Ψ is the capillary pressure head [L]; k_r is the relative hydraulic conductivity [-].

The domain of numerical model was designed based on the experiments, as highlighted by the gray section in Figure 2. The top and bottom boundaries of the numerical model were set to a no-flux condition. The freshwater boundary on the right was set to a given flux with the solute concentration of 0 g/L. The sea boundary on the left was defined as a tidal boundary that the sea level fluctuated over time obeying a sinusoidal function (Fang et al., 2022b). During tidal fluctuations, the model nodes above the sea level were set as a

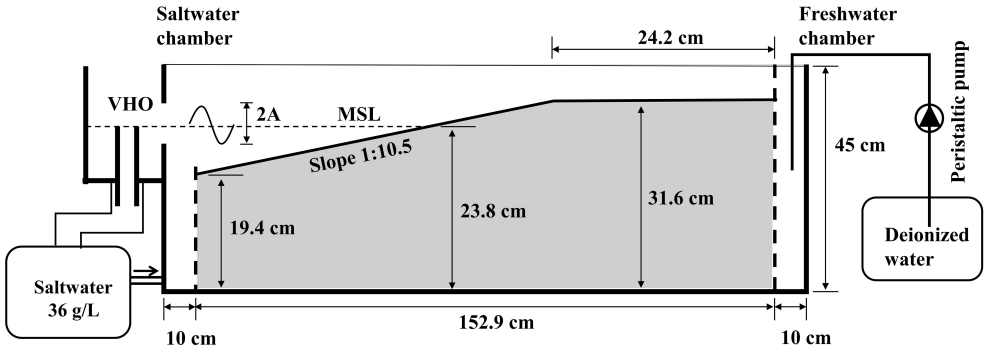

FIGURE 2
Schematic diagram of the experimental setup. The gray section is filled with quartz sand and represents the domain of the lab-scale numerical model. This figure is revised from Fang et al. (2022a). MSL, mean sea level.

seepage face that allowed groundwater to discharge into the ocean, and the nodes below the sea level were defined as a head condition that changed with the tidal stage (Xin et al., 2015). The salt concentration at the sea boundary was 36 g/L.

The hydrogeological parameters used in the numerical simulations were consistent with those determined in laboratory experiments (Table 1). We adopted the finite element method for spatial discretization and refined the mesh in the intertidal zone. The model domain was discretized into 398136 triangles with a total number of nodes of 200165. This meshing met the criteria proposed by Kooi et al. (2000), which dedicated to free convection in groundwater environment.

2.3 Simulated scenarios

The laboratory-scale numerical model has been verified in our previous study of Fang et al. (2022b) via a comparison of experimental and simulation results of salinity distribution under the stable, unstable, and dynamically stable-unstable regimes. In the present study, the verified model was used to quantify the characteristics of intertidal groundwater dynamics during salt-fingering flow. We first defined a base case (case F1) to reveal in detail the movement features of salt fingers and the response of FDZ and explain their internal mechanisms. The USP regime in case F1 was unstable by fixing a low freshwater influx of 0.271 m^3/d/m. Next, the fixed freshwater influx was increased to 0.296 m^3/d/m in case F2 under an unstable USP regime in order to examine the differences in the movement features of salt fingers. In the last trial, seasonal freshwater inflow with the same varying range of 0.323–0.271 m^3/d/m was considered to generate a dynamically stable-unstable intertidal environment. As field observations by Heiss and Michael (2014) and Zhang B. et al. (2021) suggested that the monthly variation of inland groundwater level was similar to a sine or cosine cycle with a period of one year, seasonal freshwater inflow in the present study was treated as a cosine function over time. The period of seasonal influx was preset to 365 min in case S1 where intertidal groundwater dynamics under a dynamically stable-unstable regime could be quantified. In cases S2 and S3, the periods of seasonal influx were increased to 548 and 730 min, respectively, investigating the influence of the period of seasonal freshwater inflow.

TABLE 1 Porous medium parameters used in the laboratory-scale numerical model.

Parameter	Unit	Value
Porosity	–	0.4
Hydraulic conductivity	m/s	4.8×10^{-3}
Longitudinal dispersivity	m	0.0025
Transverse dispersivity	m	0.00025
Molecular diffusion	m^2/s	1×10^{-9}
Residual water saturation	–	0.1
Constants *n* in the Van Genuchten functions	–	2.68
Constants *a* in the Van Genuchten functions	/m	7.8

2.4 Evaluation indexes

The movement of salt fingers in the intertidal zone was measured by tracking transient changes in the position of the tip and middle endpoints of target finger. The trial-and-error results indicated that laboratory-scale fingers could be clearly outlined by the 0.3 isohalines for external morphology and the 0.8 isohalines for internal morphology. The deepest fronts of the external and internal profiles were defined as the tip and middle endpoints of target finger, respectively. Thus the horizontal (V_x) and vertical (V_z) speed of the finger endpoints can be expressed as:

$$V = \frac{dF(x,z)}{dt} \quad (2)$$

where $F(x, z)$ is the coordinate of finger endpoint [L] and t is the time [T]. For ease of understanding, we specified that salt finger moved toward the sea in the horizontal direction and down in the vertical direction with a positive speed, and a negative value was defined in the opposite direction. The measurement of finger speeds at the tip endpoint (TV_x and TV_z) and the middle endpoint

(MV_x and MV_z) further investigated the speed differences at different positions during salt finger movement. The difference between the time when finger endpoints appeared and disappeared in the aquifer was defined as the duration time of a single salt finger. During salt-fingering flow, the salinity distribution in the intertidal zone would possess a responsive change. The change in the USP salt volume was measured by the USP salt mass, and the change in the FDZ was quantified by the indexes of the width of FDZ at the aquifer-sea interface and the flux of fresh groundwater discharge.

3 Results and discussion

3.1 Movement of salt fingers and response of FDZ

Numerical results of salinity distribution in case F1 with an unstable USP regime are shown in Figure 3A. The solid and dashed white lines represented the 0.3 and 0.8 isohalines, respectively, which clearly outlined the shape of the tip and middle of the salt finger. As observed in the study of Fang et al. (2021), salt fingers were repeatedly generated and detached from the USP region, which included the process of the development, separation, and mergence. Figure 3A shows a snippet of this cyclic process. Salt fingers occurred in the lower part of the USP, that is, between the mid-tide mark and the low-tide mark. To quantify the movement characteristics of salt fingers, a complete trajectory of the tip and middle endpoints of the finger is recorded in Figure 3B. The cross marks represented the position of the tip and middle endpoints of the salt finger at the moment of Figure 3A. A continuous animation of salt-fingering flow with slow motion is shown in Supplementary Material Video 1 as an auxiliary illustration. As shown in Figure 3B, salt finger movement was concentrated in the region between the mid-tide mark and the low-tide mark. The middle endpoints of the salt finger were closer to the low-tide mark at the same moment than the tip endpoints. The duration of a salt finger movement cycle was 28 min. The salt finger always moved horizontally toward the sea, but in the vertical direction, the salt finger first moved slightly downward and then continued upward. These caused the entire trajectory of the salt finger to move closer to the low-tide mark, and eventually the salt finger also disappeared near the low-tide mark. The reasons for the change in the movement direction of the salt finger were described in the next paragraph below.

The movement speed of the finger middle and tip endpoints, including the horizontal and vertical components, is shown in Figure 4. It should be noted that in this study we defined the salt fingers moving toward the sea and downward at a positive speed. The speed of the middle and tip of the salt finger possessed a similar trend. Horizontally, the finger speed was positive, indicating the movement toward the sea, and the speed value first increased, then remained unchanged, and finally decreased. In the vertical direction, the positive speed of salt finger decreased first, indicating the movement downward. The finger speed was then negative and the absolute value increased, which revealed the upward movement of the finger with an increasing speed. In addition to the influence of the gravity, the movement of salt fingers was also affected by ambient freshwater flow in the FDZ (Fang et al., 2021). Figure 5 shows the salinity distribution and groundwater flow field in the intertidal zone at different times of Figure 4. The middle and right panels indicate the scalar magnitude of the horizontal and vertical components of flow velocity, respectively. Driven by the inland hydraulic gradient, fresh groundwater in the FDZ was discharged toward the sea, but there was an upward component of flow velocity of freshwater near the lower part of the USP. In this study, salt fingers formed below the middle-tide mark, and the initial infiltration direction of gravity-induced finger flow was also downward, which has been widely confirmed in the Elder problem (Xie et al., 2011; Xie et al., 2012). Thus, the salt finger first penetrated downward in the vertical direction in Figures 3, 4. The upward discharge of fresh groundwater in the FDZ region then pushed the finger upwards.

The movement speed of salt fingers was closely related to the ambient flow of fresh groundwater. The middle panel of Figure 5 indicates the horizontal flow velocity of inland freshwater driving the movement of the salt finger, highlighted by the “A” marker. At 12 min, the horizontal velocity in region A` was fast with a value of 50 m/d, while at the time of 1 min and 22 min, the horizontal velocity in region A and A`` decreased to about 30 m/d. This explained the trend of horizontal movement speed of the salt finger in Figure 4 (first increasing, then constant, and finally decreasing). At the development stage of salt fingers (0–5 min), the horizontal

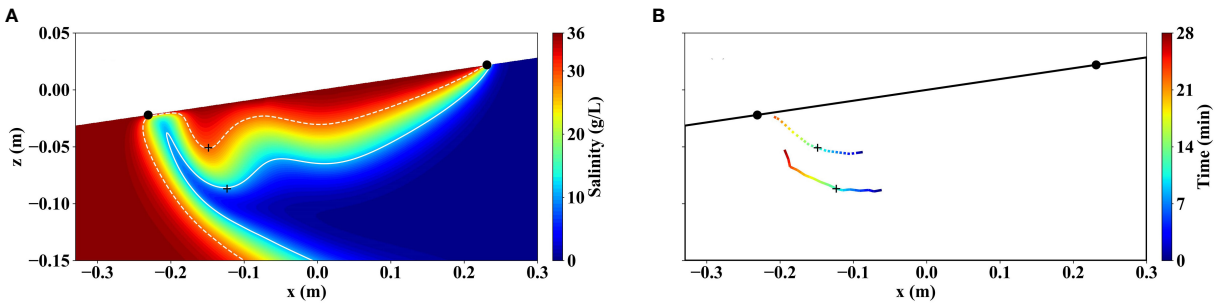

FIGURE 3
Simulated salinity distribution **(A)** and trajectory of salt finger movement **(B)** in case F1 with an unstable USP regime. The black circle indicates the range of the intertidal zone, and the plus sign represents the salt finger endpoint.

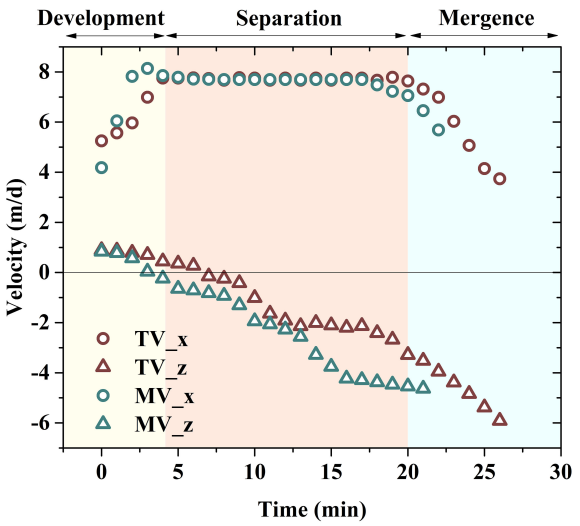

FIGURE 4
Movement speed of salt finger measured by the tip (TV) and middle (MV) endpoints, including the horizontal (x) and vertical (z) components. The movement process of salt finger consists of three stages: development, separation, and mergence.

flow velocity of freshwater in region A was low, and thus, a small driving force resulted in a slow movement of salt fingers in the horizontal direction. The horizontal velocity of freshwater in region A` was high at the separation stage (5–20 min), and the increased driving force induced a rapid horizonal movement of salt fingers. At the mergence stage (20–28 min), individual salt finger merged with the SW, and the horizontal velocity of freshwater in region A`` near the residual finger was relatively small, which caused a slow movement of the finger in the horizontal direction. The vertical flow velocity of groundwater in the intertidal region is presented in the right panel of Figure 5. The vertical flow velocity of freshwater in region A increased over time (Figures 5A3–C3), and the increased driving force led to an accelerated upward movement of salt fingers (Figure 4).

Figure 6 records the changes in the USP salt mass (including separated salt fingers), the width of FDZ at the aquifer-sea interface, and the flux of fresh groundwater discharge during salt-fingering flow. For convenience, the time in Figure 6 is the relative time with the simulated time T_1 as the reference. The shaded part is the corresponding time in Figures 3, 4. The width of FDZ and the flux of fresh groundwater discharge fluctuated over time, which was significantly different from the result (constant with continuous tidal cycles) in a stable USP regime (Kuan et al., 2012). The variation trends of the FDZ width and fresh groundwater discharge possessed a well agreement, suggesting that the width of FDZ at the aquifer-sea interface can be used as an indicator of fresh groundwater discharge, even in an unstable regime, to provide a basis for field monitoring. The salt mass in the USP also fluctuated over time, and the fluctuation trend was opposite to those of the FDZ width and fresh groundwater discharge with a time delay. There was a causal relationship between the USP salt mass, the movement of salt fingers, and the FDZ width. During the period of 0–a, the USP salt mass increased with an increased gravity, thus providing the potential for salt-fingering flow. This period corresponded to the development stage of salt fingers in Figure 4. The finger development compressed the space between the middle-tide mark and the low-tide mark, which led to a decrease in the width of FDZ. After the moment a, salt finger movement was in the separation stage, and the USP salt mass reduced. The separation of salt finger further compressed the FDZ region, and the width of FDZ decreased. The finger was located in the middle between the USP and SW (Figure 5B1) at the time b, and the width of FDZ was minimal. After the moment b, the finger continued to move toward

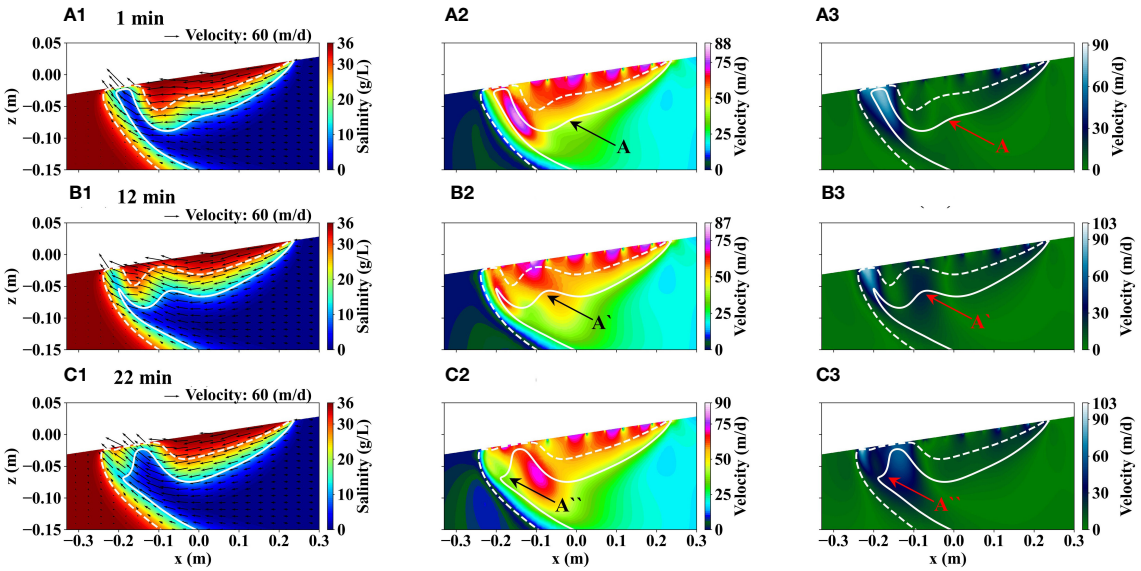

FIGURE 5
Salinity distribution and groundwater flow field in the intertidal zone during salt-fingering flow. The middle and right panels indicate the scalar magnitude of the horizontal and vertical components of flow velocity, respectively.

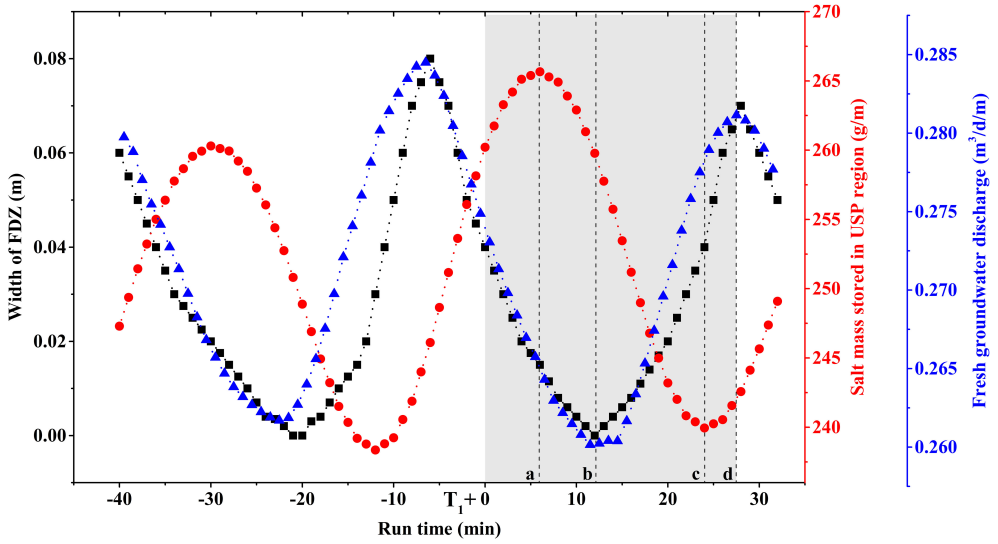

FIGURE 6
Temporal variation of the USP salt mass (including separated salt fingers), the width of FDZ at the aquifer-sea interface, and the flux of fresh groundwater discharge during salt-fingering flow. The shaded part is the corresponding time in Figures 3, 4.

the SW, and the FDZ region between the finger and the USP increased, resulting in an increase in the width of FDZ at the aquifer-sea interface. The salt finger began to enter the mergence stage (Figure 5C1) at the moment c, and the USP salt mass was minimal. After that, the total salt mass of the USP rose as the salt mass of the main part of the USP increased (laying the foundation for the development of the next salt finger). At the moment d, the salt finger disappeared in the intertidal zone, and the width of FDZ was maximum. After the d moment, the expansion of USP associated with an increase in salt mass provided a potential for the next finger, which caused the FDZ space to be compressed and decreased the width of FDZ at the aquifer-sea interface again.

3.2 Effect of fixed subsurface inflow

The changes in subsurface freshwater inflow can break the balance between tidal forces and inland hydraulic gradients, and thus induce the expansion or constriction of the USP in the intertidal zone, altering the potential for salt-fingering flow (Fang et al., 2021). Figure 7 shows the temporal data of the movement trajectory and speed of salt finger under an increased freshwater influx in case F2. The trajectories of the finger tip and middle are indicated by B and B', respectively. For comparison, the trajectory under a small freshwater influx in case F1 as shown in Figure 3B is also presented and represented by A and A'. As shown in Figure 7A, the vertical infiltration depth of the finger decreased with an increase in fixed freshwater inflows, due to the reduced potential of salt-fingering flow. This led to a shrinkage of the movement range of salt fingers in the intertidal zone under an increased freshwater influx condition, and the location where the finger disappeared at the aquifer-sea interface was far from the low-tide mark. In addition, the period of salt finger movement was 20 min in case F2, which is also less than 28 min in case F1 with a small freshwater inflow.

The variation trend of the movement speed of salt finger in case F2 (Figure 7B) was basically consistent with that in case F1 with a small freshwater inflow as shown in Figure 4. However, there were also some differences in the movement speed under different freshwater inflows. The horizontal speed of the salt finger was about 9.5 m/d at the separation stage, which was greater than 8.1 m/d in case F1. The maximum value of the vertical speed was 8.5 m/d, faster than the result of 6 m/d in case F1. In the vertical direction, the continuous upward movement of the finger was accompanied by a negative speed. The average results of groundwater dynamics in the intertidal zone under different freshwater inflows are listed in Table 2. As inland freshwater influxes increased, the mean width of FDZ and the mean flux of fresh groundwater discharge increased, and the mean salt mass of USP decreased. Since the freshwater velocity in the FDZ region near the low-tide mark was facing upward and seaward, the increased freshwater discharge not only limited the downward infiltration of the salt finger, but also accelerated the horizontal and vertical movement of the salt finger to disappear in the low-tide mark. So, in Table 2, the average speed of the finger tip and middle in case F2 increased compared to the results in case F1 with a small freshwater inflow. In general, increased freshwater inflows compressed the active space of the salt finger, accelerated its movement speed, and ultimately led to a decrease in the duration time in the intertidal zone. These findings highlighted the significant impact of fixed freshwater inflows on the movement characteristics (trajectory, speed, and residence time) of salt fingers. In real-world aquifers, both tidal amplitudes and inland freshwater inputs vary instantaneously over time, which continues to change the hydrodynamic conditions of the intertidal zone and the potential of subsequent salt-fingering flow. Under these transient hydrodynamic conditions, the movement characteristics

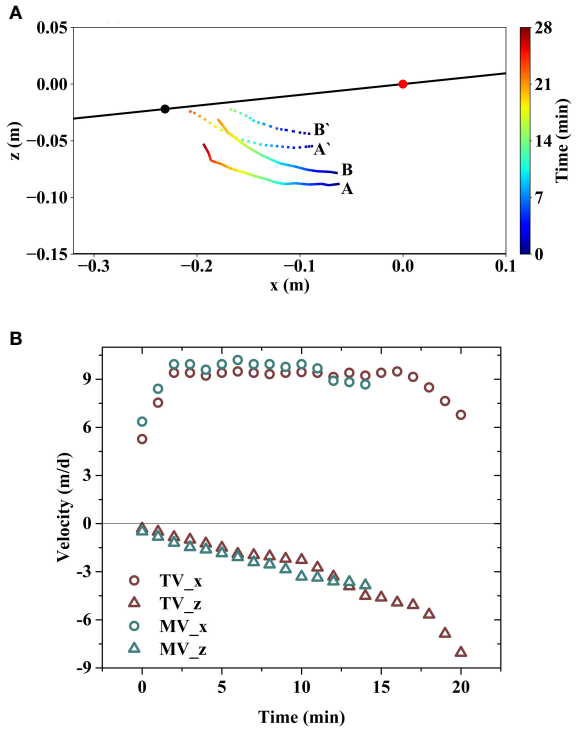

FIGURE 7
Movement trajectory **(A)** and speed **(B)** of salt finger under an increased freshwater influx of 0.296 m^3/d/m. The trajectories of the finger tip and middle are indicated by B and B′, respectively. For comparison, the trajectory under a small freshwater influx of 0.271 m^3/d/m is also presented and represented by A and A′. The black and red circles indicate the low and middle tide marks, respectively.

of salt-fingering flow may differ from the above findings of the fixed cases.

3.3 Effect of seasonal subsurface inflow

Figure 8 measures the temporal results of the finger speed, width of FDZ at the aquifer-sea interface, fresh groundwater discharge, and USP salt mass under the condition of seasonal subsurface inflow. The seasonal influx varied between 0.323–0.271 m^3/d/m with a period of 365 min, and it should be noted that the USP regime was stable when the freshwater inflow was fixed at 0.323 m^3/d/m. As shown in Figure 8B, the evolution trend of the horizontal and vertical speeds of salt fingers in an individual finger cycle was basically consistent with that in the fixed cases. The duration time of salt finger movement in an individual cycle was relatively short, with an average value of 17.49 min. Except for the complete salt finger movement at the time of 250 min, the mergence stage was absent for other finger cycles. That is, before reaching the SW, the salt finger had already flowed out of the intertidal zone. The variation in the width of FDZ is also shown in Figure 8B. Consistent with the results of the fixed cases (Figure 6), the time of salt finger movement was around the time when the width of FDZ was minimal. The evolution trend of the width of FDZ was consistent with that of fresh groundwater discharge and opposite to that of the USP salt mass with a certain delay (Figure 8C).

During the circulation of the variation in the USP salt mass and the width of FDZ, not every cycle possessed a salt-fingering flow as shown in Figure 8. For example, there was no salt finger movement at 60 min. In addition, the duration time of salt-fingering flow was also inconsistent in the cycles where salt finger occurred. For example, the duration time was 27 min at the run time of about 250 min, while the duration time was 9 min at the run time of about 210 min. This indicated that the intensity of salt-fingering flow varied over time under the condition of seasonal freshwater inflow.

In addition to gravity induced by the density difference, Fang et al. (2022b) found that the fluctuations of USP interface caused by seasonal freshwater inflow could generate interface perturbation and thus triggered the onset of salt-fingering flow. The effect of interface perturbation has been confirmed and identified as a critical driver in other free- and mixed-convection systems (Schincariol et al., 1997; Simmons and Narayan, 1997). In this section, we quantified the interface perturbation in each cycle by measuring the maximum difference in the USP salt mass, e.g., the difference between the time a and c in Figure 6. Similarly, the responsive change in the width of FDZ in each cycle was measured by its maximum difference, as calculated between the time b and d in Figure 6. The quantitative results of the duration time of salt fingers, the maximum difference in the width of FDZ, and the maximum difference in the USP salt mass in each cycle over one 365 min seasonal influxes are presented in Figure 9. In the cycle where salt-fingering flow occurs, the differences in the FDZ width and the USP salt mass are highlighted by the red color. The differences in the FDZ width during the finger cycles were greater than those in the no finger cycles. As the duration of salt finger movement increased with the enhanced salt-fingering flow, the difference in the FDZ width increased. Thus, the difference in the FDZ width in the cycle can be termed as a positive response to the intensity of salt-fingering flow. The duration of salt-fingering flow was related to subsurface freshwater inflow and the difference in the USP salt mass. At the time of 24 min, the seasonal influx of 0.320 m^3/d/m was high with a strong resistance for salt-finger flow, and the fixed case with the same flux was stable for the intertidal environment. However, salt-fingering flow in the seasonal case was generated at this moment because of the powerful interface perturbation with the difference in the USP salt mass of 20 g/m

TABLE 2 Average results of groundwater dynamics in the intertidal zone under different freshwater inflows.

Case name	Width of FDZ (m)	Freh groundwater discharge (m^3/d/m)	Salt mass of USP (g/m)	TV_x (m/d)	TV_z (m/d)	MV_x (m/d)	MV_z (m/d)
Case F1	0.029	0.271	251	6.98	-1.78	7.31	-2.04
Case F2	0.034	0.292	225	8.83	-3.12	9.34	-3.85

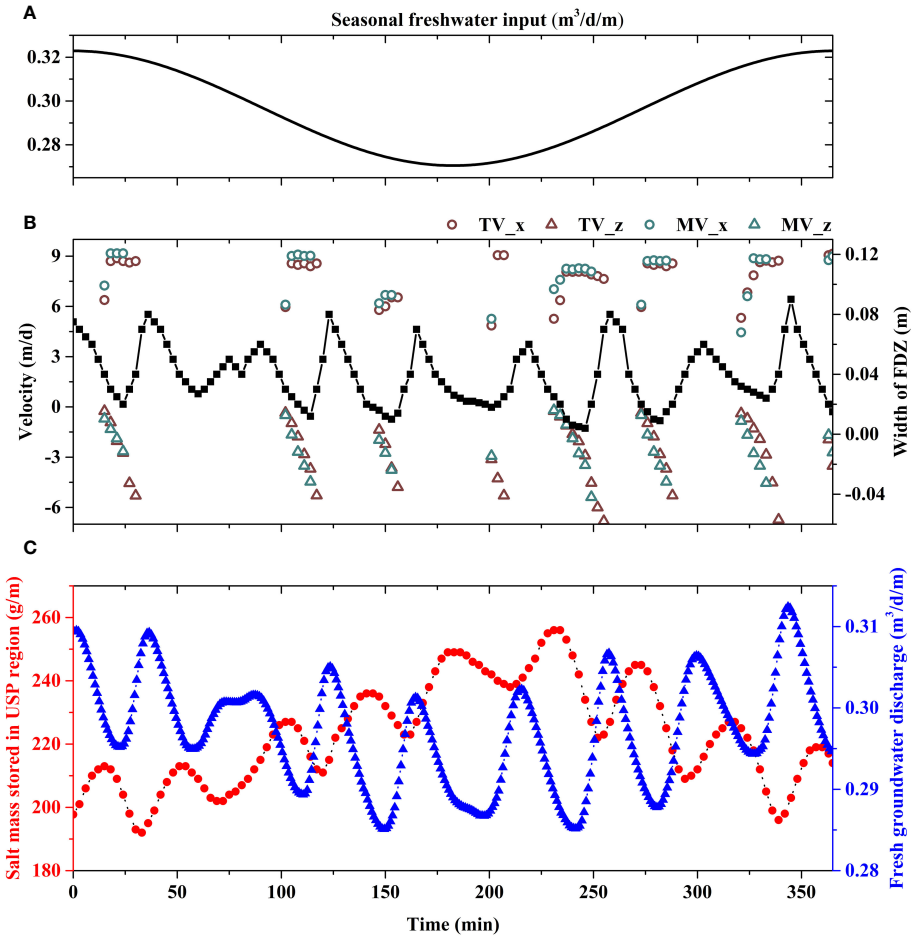

FIGURE 8
Temporal characteristics of the finger speed, width of FDZ at the aquifer-sea interface **(B)**, fresh groundwater discharge, and the USP salt mass **(C)** under the condition of seasonal subsurface inflow **(A)**. In **(A)**, the seasonal influx varies between 0.323–0.271 m^3/d/m with a period of 365 min.

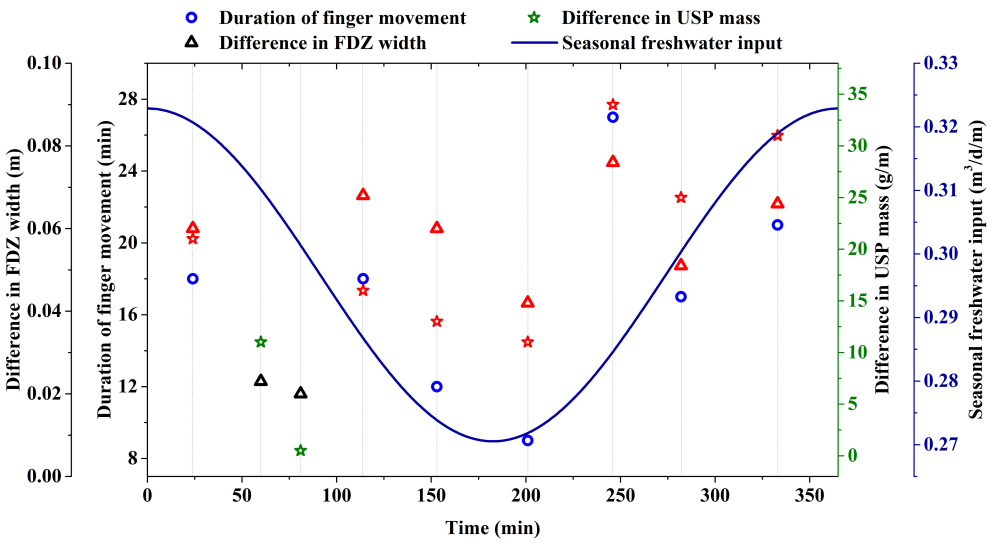

FIGURE 9
Quantitative results of the duration time of salt fingers, the maximum difference in the width of FDZ, and the maximum difference in the USP salt mass in each cycle over one 365 min seasonal influxes. In the cycle where salt-fingering flow occurs, the differences in the FDZ width and the USP salt mass are highlighted by the red color. The seasonal variation of subsurface freshwater inflow is indicated by a solid blue line, corresponding to the right coordinate.

(Figure 9). Although the seasonal influx was decreased with a decreasing resistance at the time of 60 min and 80 min, flow instability did not occur at these moments, due to a decreased in the difference in the USP salt mass illustrating a weak interface perturbation (Fang et al., 2022b). At the time of 200 min, notwithstanding the difference in the USP salt mass of 12 g/m was close to that at the time of 60 min, the reduction of seasonal influx associated with a decreasing resistance resulted in the onset of flow instability. The longest duration of salt fingers accompanied with the maximum intensity of flow instability was recorded at the time of 245 min due to the largest difference in the USP salt mass and a small seasonal influx, which led to a largest difference in the width of FDZ at the aquifer-sea interface.

Temporal changes in seasonal freshwater inflow can cause additional interface perturbation and affect the occurrence of salt-fingering flow. The period of seasonal freshwater inflow determines the variation frequency of interface perturbation, thus affecting the movement characteristics of salt fingers. Under the same fluctuation range, the period of seasonal influx increased from 365 min to 548 min and 730 min, and the comparisons of the movement speed of salt fingers and the duration time are shown in Figure 10. Figure 10A counts the mean and range of the finger speed in the horizontal and vertical directions. Under different periods, the mean and extreme values of the finger speed were basically the same. The mean duration of salt fingers decreased slightly with the increase of freshwater periods (Figure 10B). Because the reduced frequency of freshwater inflow led to a decrease in interface perturbation for the intertidal environment, resulting in a decrease in the intensity of salt-fingering flow (Fang et al., 2022b). This contributed to a reduce in the proportion of the duration time of salt finger movement to the freshwater period as the period increased.

3.4 Implications

Under the influence of salt-fingering flow, the FDZ in the intertidal zone and the discharge position at the aquifer-sea interface continue to change over time, which makes trouble for field monitoring of SGD. This study found that the variation trends of the FDZ width at the aquifer-sea interface and fresh SGD possessed a well agreement under the influence of salt-fingering flow (Figure 6). We suggested that the width of FDZ at the aquifer-sea interface can be used as an indicator of fresh SGD, even in an unstable regime, to provide a basis for field monitoring. Fang et al. (2021) reviewed the absence of field studies regarding salt-fingering flow and pointed out a critical reason that traditional monitoring strategies were not suitable for rapid changes in the intertidal salinity. Geophysical methods are fast and efficient, and can invert intertidal salinity evolutions by monitoring electromagnetic information (Huizer et al., 2017). In the sandy tidal flat of Shilaoren, Jiaozhou Bay, Zhang Y. et al. (2021; 2023) and Xing et al. (2023) capture the temporal movement of salt-fingering flow via electrical resistivity tomography. Therefore, for SGD field monitoring under the influence of salt-fingering flow, we can use geophysical methods to invert the intertidal salinity distribution, and then accurately capture the width and location of FDZ at the aquifer-sea interface, and finally estimate the temporal and spatial variation of fresh SGD.

The speed and duration of salt finger movement change significantly with external forces, which has important implications for field monitoring. The results in Figure 7 and Table 2 indicated that with the increase of subsurface freshwater inflow, the active space of salt fingers was compressed, and the movement speed increased, thus reducing the duration time of salt fingers in the intertidal zone. Field monitoring of salt-fingering flow is already difficult, but the weak flow instability with a fast movement speed and a short duration time due to increased subsurface inflow, may further increase the difficulty of field monitoring of salt-fingering flow. Therefore, increased caution must be taken in field measurements if a weak salt-fingering flow in the intertidal zone is expect under specific hydrogeological conditions.

Transient changes in the external forces of coastal aquifers, such as seasonal or daily seawater temperatures (Bhagat et al., 2021), spring-neap variability in tidal amplitude (Glaser et al., 2021), and seasonality in subsurface inflow or hydraulic gradient (Qu et al.,

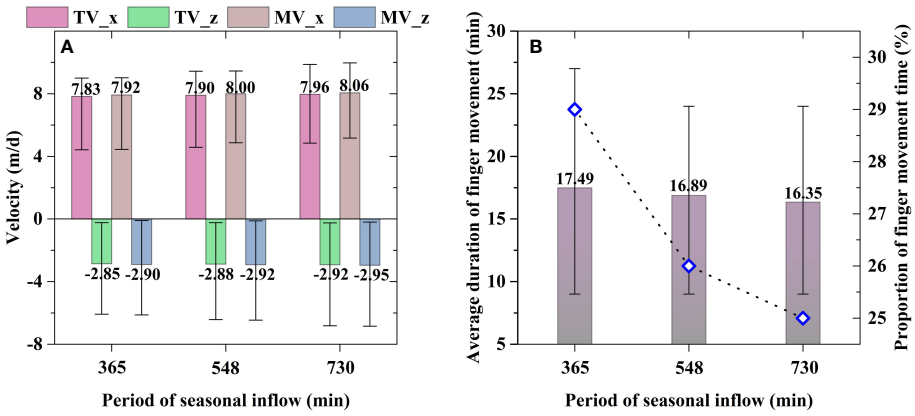

FIGURE 10
Comparisons of the movement speed **(A)** of salt fingers and the duration time **(B)** under different seasonal freshwater periods. In **(A)**, the mean and range (extremum values) of the finger speed in the horizontal and vertical directions are displayed. In **(B)**, the column chart corresponds to the left coordinate, and the scatter plot corresponds to the right coordinate.

2020), will generate a dynamic intertidal environment and induce the evolution of the USP associated with interface perturbation. Interface perturbation has been confirmed to be an important mechanism for the onset of free convection or mixing convection (Schincariol et al., 1997). Figures 8 and 9 show that under the fluctuation of seasonal freshwater inflow, salt-fingering flow not only occurs at the time of a low freshwater influx, but also generates when the freshwater influx is high. And the fixed case with the same high flux is stable for the intertidal environment. By measuring the interface perturbation by the maximum difference in the USP salt mass in each cycle, we found that the important reason for the formation of salt-fingering flow at a high freshwater inflow is the powerful interface perturbation with a large difference in the USP salt mass. The transient external forces accompanied with interface perturbation induced variable and complex movement features of salt fingers including speed and duration time (Figure 9), in contrast to the results under the condition of fixed external forces. Real-world aquifers usually subject to the combined influence of multiple external forces and possess a more complex intertidal environment, which may lead to more complex and variable movement characteristics of salt-fingering flow. Notwithstanding, this study found that the duration and proportion of salt-fingering flow decreased as the period of seasonal freshwater inflow increased due to the weak interface perturbation. This gives us some insight into the estimation of the movement characteristics of salt-fingering flow under multiple instantaneous forces.

The movement of salt fingers in the intertidal zone has an important impact on SGD and related solute transport. As shown in Figure 6, salt finger movement caused the responsive changes in the width of FDZ and fresh SGD fluxes. Terrigenous matter carried by fresh SGD and sea-derived matter delivered by salt SGD are mixed at the USP edge and experience biogeochemical reactions (Heiss et al., 2020). This mixing zone is also known as a subterranean estuary (Robinson et al., 2018). The movement speed and duration time of salt fingers determine the reaction time between terrigenous matter and sea-derived matter and thus affect the reaction rate of subterranean estuaries, which finally determines the chemical loads of land- and sea-derived matters discharged into the ocean. As shown in Figure 4, there is a long duration time and a wide active region as the flow instability is forceful. This is conducive to the reaction of subterranean estuaries, and the reaction position can be extended to the lower part of the aquifer with the enhancement of salt-fingering flow. However, when salt-fingering flow is weak (Figure 7), the finger moves with an increased speed and a compressed active space, and the duration time decreases, which is not conducive to the reaction of subterranean estuaries.

Real-world aquifers usually subject to the combined influence of multiple external forces (e.g., seasonal or daily seawater temperatures (Bhagat et al., 2021), spring-neap variability in tidal amplitude (Glaser et al., 2021), and seasonality in subsurface inflow or hydraulic gradient (Qu et al., 2020)) and possess a more complex intertidal environment, which may lead to more complex and variable movement characteristics of salt-fingering flow than presented in this study. Moreover, the complexity of coastal aquifers such as heterogeneity and anisotropy, is neglected. Greskowiak (2014) found that a high horizontal hydraulic conductivity favors ambient groundwater flow, thus inhibiting the generation of salt-fingering flow. While a high vertical hydraulic conductivity provides better conditions for a downward movement of the denser saline plume and supports fingering flow. The investigations in other instability systems (e.g., Elder problem) provide an insight into the critical effect of heterogeneity on flow instability, but there are no general conclusions for inhibition or support, which depends on the structure and variance of the permeability field. Thus, the complexity of coastal aquifers is highly likely to affect the onset of salt-finger flow and subsequent movement characteristics. Future studies are required to investigate the combined influence of multiple external forces and the complexity of coastal aquifers. Nevertheless, this study provides a useful assessment of groundwater dynamics in the intertidal zone during salt-fingering flow under the conditions with fixed and temporal external forces, which lays the foundation for gaining a better understanding of the potential implications of salt-fingering flow on SGD and related solute transports.

4 Conclusions

This study conducted laboratory-scale numerical simulations to investigate groundwater dynamics in the intertidal zone during salt-fingering flow. The movement features of salt fingers and the response laws of FDZ were carefully quantified. The key new findings are summarized as follows:

During salt-fingering flow, the finger was repeatedly generated and detached from the USP region, which included the process of the development, separation, and mergence. Horizontally, the finger moved toward the sea, and the finger speed first increased at the development stage, then remained unchanged at the separation stage, and finally decreased at the mergence stage. The movement speed of salt fingers was closely related to ambient freshwater flow in the FDZ. In the vertical direction, the finger first permeated downward with a decreasing speed, and then the upward discharge of fresh groundwater in the FDZ region with an increased flow velocity pushed the finger upwards with an increasing speed.

In contrast to the results in a stable USP regime, the width of FDZ at the aquifer-sea interface fluctuated over time, and the variation trends possessed a well agreement with the flux of fresh groundwater discharge. This suggested that the width of FDZ at the aquifer-sea interface can be used as an indicator of fresh groundwater discharge, even in an unstable regime, to provide a basis for field monitoring. There was a causal relationship between the USP salt mass, the movement of salt fingers, and the FDZ width at the aquifer-sea interface.

As fixed subsurface inflow increased, the movement range of salt finger was compressed in the intertidal zone, and the location where the finger disappeared at the aquifer-sea interface was far from the low-tide mark. The increased freshwater discharge not only limited the downward infiltration of salt fingers, but also accelerated the

horizontal and vertically upward movement of salt fingers. These ultimately led to a decrease in the duration time in the intertidal zone.

Temporal changes in seasonal freshwater inflow could cause additional interface perturbation and affected the occurrence of salt-fingering flow and subsequent movement characteristics. The intensity of salt-fingering flow varied over time under the condition of seasonal freshwater inflow. The duration time of salt finger movement in an individual cycle was relatively short, with an average value of 17.49 min less than that of 20–28 min in fixed cases. The difference in the FDZ width at the aquifer-sea interface in the cycle was identified as a positive response to the intensity of salt-fingering flow. The mean duration of salt fingers decreased slightly with the increase of seasonal freshwater periods due to a decrease in the interface perturbation for the intertidal environment.

Data availability statement

The original contributions presented in the study are included in the article/Supplementary Material. Further inquiries can be directed to the corresponding authors.

Author contributions

YF: Conceptualization, Investigation, Methodology, Validation, Writing – original draft, Writing – review & editing. JQ: Funding acquisition, Resources, Writing – review & editing, Conceptualization. LM: Supervision, Visualization, Writing – review & editing, Project administration. HW: Writing – review & editing, Conceptualization, Formal analysis, Investigation.

Funding

The author(s) declare financial support was received for the research, authorship, and/or publication of this article. This study was supported by the National Natural Science Foundation of China (41831289, 42302268), China Postdoctoral Science Foundation (2022M720979), and the Fundamental Research Funds for the Central Universities (JZ2023HGQB0166).

Conflict of interest

The authors declare that the research was conducted in the absence of any commercial or financial relationships that could be construed as a potential conflict of interest.

Publisher's note

Supplementary material

The Supplementary Material for this article can be found online at: https://www.frontiersin.org/articles/10.3389/fmars.2023.1319751/full#supplementary-material

References

Andrisoa, A., Lartaud, F., Rodellas, V., Neveu, I., and Stieglitz, T. C. (2019). Enhanced growth rates of the Mediterranean mussel in a coastal lagoon driven by groundwater inflow. *Front. Mar. Sci.* 6. doi: 10.3389/fmars.2019.00753

Bhagat, C., Khandekar, A., Singh, A., Mohapatra, P. K., and Kumar, M. (2021). Delineation of submarine groundwater discharge and seawater intrusion zones using anomalies in the field water quality parameters, groundwater level fluctuation and sea surface temperature along the Gujarat coast of India. *J. Environ. Manage.* 296, 113176. doi: 10.1016/j.jenvman.2021.113176

Diersch, H. R. G. (2014). *FEFLOW: Finite element modeling of flow, mass and heat transport in porous and fractured media* (Berlin Heidelberg:Springer Science & Business Media). doi: 10.1007/978-3-642-38739-5

Evans, T. B., and Wilson, A. M. (2017). Submarine groundwater discharge and solute transport under a transgressive barrier island. *J. Hydrol.* 547, 97–110. doi: 10.1016/j.jhydrol.2017.01.028

Fang, Y., Zheng, T., Guo, B., Zhan, H., Wang, H., Zheng, X., et al. (2022a). Transformation in the stability of tide-Induced upper saline plume driven by transient external forcing. *Water Resour. Res.* 58 (6), e2021WR031331. doi: 10.1029/2021WR031331

Fang, Y., Zheng, T., Wang, H., Zheng, X., and Walther, M. (2022b). Influence of dynamically stable-unstable flow on seawater intrusion and submarine groundwater discharge over tidal and seasonal cycles. *J. Geophys. Res.: Oceans* 127 (4), e2021JC018209. doi: 10.1029/2021JC018209

Fang, Y., Zheng, T., Zheng, X., Yang, H., Wang, H., and Walther, M. (2021). Influence of tide-induced unstable flow on seawater intrusion and submarine groundwater discharge. *Water Resour. Res.* 57, e2020WR029038. doi: 10.1029/2020WR029038

Geng, X., Michael, H. A., Boufadel, M. C., Molz, F. J., Gerges, F., and Lee, K. (2020). Heterogeneity affects intertidal flow topology in coastal beach aquifers. *Geophys. Res. Lett.* 47, e2020GL089612. doi: 10.1029/2020GL089612

Glaser, C., Frei, S., Massmann, G., and Gilfedder, B. S. (2021). Tidal creeks as hot-spots for hydrological exchange in a coastal landscape. *J. Hydrol.* 597, 126158. doi: 10.1016/j.jhydrol.2021.126158

Goswami, R. R., and Clement, T. P. (2007). Laboratory-scale investigation of saltwater intrusion dynamics. *Water Resour. Res.* 43 (4), W4411–W4418. doi: 10.1029/2006WR005151

Greskowiak, J. (2014). Tide-induced salt-fingering flow during submarine groundwater discharge. *Geophys. Res. Lett.* 41 (18), 6413–6419. doi: 10.1002/2014GL061184

Heiss, J. W., and Michael, H. A. (2014). Saltwater-freshwater mixing dynamics in a sandy beach aquifer over tidal, spring-neap, and seasonal cycles. *Water Resour. Res.* 50 (8), 6747–6766. doi: 10.1002/2014WR015574

Heiss, J. W., Michael, H. A., and Koneshloo, M. (2020). Denitrification hotspots in intertidal mixing zones linked to geologic heterogeneity. *Environ. Res. Lett.* 15 (8), 84015. doi: 10.1088/1748-9326/ab90a6

Heiss, J. W., Post, V. E. A., Laattoe, T., Russoniello, C. J., and Michael, H. A. (2017). Physical controls on biogeochemical processes in intertidal zones of beach aquifers. *Water Resour. Res.* 53 (1), 9225–9244. doi: 10.1002/2017WR021110

Huizer, S., Karaoulis, M. C., Oude Essink, G. H. P., and Bierkens, M. F. P. (2017). Monitoring and simulation of salinity changes in response to tide and storm surges in a sandy coastal aquifer system. *Water Resour. Res.* 53 (8), 6487–6509. doi: 10.1002/2016WR020339

Kim, K. H., Heiss, J. H., and Michael, H. (2022). Seasonal and spatial production patterns of dissolved inorganic carbon and total alkalinity in a shallow beach aquifer. *Front. Mar. Sci.* 9. doi: 10.3389/fmars.2022.856281

Kooi, H., Groen, J., and Leijnse, A. (2000). Modes of seawater intrusion during transgressions. *Water Resour. Res.* 36 (12), 3581–3589. doi: 10.1029/2000WR900243

Kuan, W. K., Jin, G., Xin, P., Robinson, C. E., Gibbes, B., and Li, L. (2012). Tidal influence on seawater intrusion in unconfined coastal aquifers. *Water Resour. Res.* 48 (2), 136–149. doi: 10.1029/2011WR010678

Kuan, W. K., Xin, P., Jin, G., Robinson, C. E., Gibbes, B., and Li, L. (2019). Combined effect of tides and varying inland groundwater input on flow and salinity distribution in unconfined coastal aquifers. *Water Resour. Res.* 55, 8864–8880. doi: 10.1029/2018WR024492

Kwon, E. Y., Kim, G., Primeau, F., Moore, W. S., Cho, H., Devries, T., et al. (2014). Global estimate of submarine groundwater discharge based on an observationally constrained radium isotope model. *Geophys. Res. Lett.* 41 (23), 8438–8444. doi: 10.1002/2014GL061574

Lebbe, L. (1981). The subterranean flow of fresh and salt water underneath the Western Belgium beach. *In Rapporter Och Meddelanden Sveriges Geologiska Undersökning* 27, 193–219.

Lu, C., and Werner, A. D. (2013). Timescales of seawater intrusion and retreat. *Adv. Water Resour.* 59, 39–51. doi: 10.1016/j.advwatres.2013.05.005

Nguyen, T. T. M., Yu, X., Pu, L., Xin, P., Zhang, C., Barry, D. A., et al. (2020). Effects of temperature on tidally influenced coastal unconfined aquifers. *Water Resour. Res.* 56 (4), e2019WR26660. doi: 10.1029/2019WR026660

Qu, W., Li, H., Wang, C., Zheng, C., Wang, X., and Zhang, Y. (2020). Numerical simulations of seasonally oscillated groundwater dynamics in coastal confined aquifers. *Groundwater* 58, 550–559. doi: 10.1111/gwat.12926

Robinson, C. E., Xin, P., Santos, I. R., Charette, M. A., Li, L., and Barry, D. A. (2018). Groundwater dynamics in subterranean estuaries of coastal unconfined aquifers: Controls on submarine groundwater discharge and chemical inputs to the ocean. *Adv. Water Resour.* 115, 315–331. doi: 10.1016/j.advwatres.2017.10.041

Rodellas, V., Garcia-Orellana, J., Masqué, P., Feldman, M., and Weinstein, Y. (2015). Submarine groundwater discharge as a major source of nutrients to the Mediterranean Sea. *Proc. Natl. Acad. Sci. United States America* 112 (13), 3926–3930. doi: 10.1073/pnas.1419049112

Röper, T., Greskowiak, J., and Massmann, G. (2015). Instabilities of submarine groundwater discharge under tidal forcing. *Limnol. Oceanogr.* 60 (1), 22–28. doi: 10.1002/lno.10005

Santos, I. R., Chen, X., Lecher, A. L., Sawyer, A. H., Moosdorf, N., Rodellas, V., et al. (2021). Submarine groundwater discharge impacts on coastal nutrient biogeochemistry. *Nat. Rev. Earth Environ.* 2, 307–323. doi: 10.1038/s43017-021-00152-0

Schincariol, R. A., Schwartz, F. W., and Mendoza, C. A. (1997). Instabilities in variable density flows: Stability and sensitivity analyses for homogeneous and heterogeneous media. *Water Resour. Res.* 33 (1), 31–41. doi: 10.1029/96WR02587

Shen, C., Zhang, C., Kong, J., Xin, P., Lu, C., Zhao, Z., et al. (2019). Solute transport influenced by unstable flow in beach aquifers. *Adv. Water Resour.* 125, 68–81. doi: 10.1016/j.advwatres.2019.01.009

Simmons, C. T., and Narayan, K. A. (1997). Mixed convection processes below a saline disposal basin. *J. Hydrol.* 194 (1), 263–285. doi: 10.1016/S0022-1694(96)03204-0

Starke, C., Ekau, W., and Moosdorf, N. (2020). Enhanced productivity and fish abundance at a submarine spring in a coastal lagoon on Tahiti, French Polynesia. *Front. Mar. Sci.* 6. doi: 10.3389/fmars.2019.00809

Van Genuchten, M. T. (1980). A closed-form equation for predicting the hydraulic conductivity of unsaturated Soils1. *Soil Sci. Soc. America J.* 44 (5), 892. doi: 10.2136/sssaj1980.03615995004400050002x

Wu, X., Xu, Z., Xu, Z., and Hu, B. X. (2023). Impact of connected conduit on pumping-induced seawater intrusion in a coastal karst aquifer. *Front. Mar. Sci.* 10. doi: 10.3389/fmars.2023.1277005

Xie, Y., Simmons, C. T., and Werner, A. D. (2011). Speed of free convective fingering in porous media. *Water Resour. Res.* 47 (11), W11501. doi: 10.1029/2011WR010555

Xie, Y., Simmons, C. T., Werner, A. D., and Diersch, H. G. (2012). Prediction and uncertainty of free convection phenomena in porous media. *Water Resour. Res.* 48 (2), W02535. doi: 10.1029/2011WR011346

Xin, P., Wang, S. S. J., Lu, C., Robinson, C. E., and Li, L. (2015). Nonlinear interactions of waves and tides in a subterranean estuary. *Geophys. Res. Lett.* 42 (7), 2277–2284. doi: 10.1002/2015GL063643

Xing, C., Zhang, Y., Guo, X., and Sun, J. (2023). Time series investigation of electrical resistivity tomography reveals the key drivers of tide and storm on groundwater discharge. *Estuarine Coast. Shelf Sci.* 282, 108225. doi: 10.1016/j.ecss.2023.108225

Yu, X., Xin, P., Wang, S. S. J., Shen, C., and Li, L. (2019). Effects of multi-constituent tides on a subterranean estuary. *Adv. Water Resour.* 124, 53–67. doi: 10.1016/j.advwatres.2018.12.006

Zhang, J., Lu, C., Shen, C., Zhang, C., Kong, J., and Li, L. (2021). Effects of a low-permeability layer on unstable flow pattern and land-sourced solute transport in coastal aquifers. *J. Hydrol.* 598, 126397. doi: 10.1016/j.jhydrol.2021.126397

Zhang, Y., Wu, J., Zhang, K., Guo, X., Xing, C., Li, N., et al. (2021). Analysis of seasonal differences in tidally influenced groundwater discharge processes in sandy tidal flats: A case study of Shilaoren Beach, Qingdao, China. *J. Hydrol.* 603, 127128. doi: 10.1016/j.jhydrol.2021.127128

Zhang, Y., Xing, C., Guo, X., Zheng, T., Zhang, K., Xiao, X., et al. (2023). Temporal and spatial distribution patterns of upper saline plumes and seawater-groundwater exchange under tidal effect. *J. Hydrol.* 625, 130042. doi: 10.1016/j.jhydrol.2023.130042

Zhang, B., Zheng, T., Zheng, X., and Walther, M. (2021). Utilization of pit lake on the cleaning process of residual saltwater in unconfined coastal aquifers. *Sci. Total Environ.* 770, 144670. doi: 10.1016/j.scitotenv.2020.144670

Zheng, T., Gao, M., Chang, Q., Zheng, X., and Walther, M. (2022). Dynamic desalination of intruding seawater after construction of cut-off walls in a coastal unconfined aquifer. *Front. Mar. Sci.* 9. doi: 10.3389/fmars.2022.857807

frontiers | Frontiers in Marine Science

TYPE Original Research
PUBLISHED 07 December 2023
DOI 10.3389/fmars.2023.1335064

OPEN ACCESS

EDITED BY
Chengji Shen,
Hohai University, China

REVIEWED BY
Gang Yang,
Nanjing University of Information Science and Technology, China
Yuwei Hu,
Chinese Academy of Sciences (CAS), China
Zhang Bo,
Shandong University of Science and Technology, China

*CORRESPONDENCE
Ye Ma
ye.mawater@outlook.com

RECEIVED 08 November 2023
ACCEPTED 24 November 2023
PUBLISHED 07 December 2023

CITATION
Wang Q, Ma Y, Cheng Z and Du Y (2023) Coastline changes under natural and anthropogenic drivers in a macro-tidal estuary between 2000-2020.
Front. Mar. Sci. 10:1335064.
doi: 10.3389/fmars.2023.1335064

Coastline changes under natural and anthropogenic drivers in a macro-tidal estuary between 2000-2020

Qian Wang[1], Ye Ma[1,2]*, Zhixin Cheng[1,2] and Yixiao Du[1]

[1]College of Environmental Science and Engineering, Dalian Maritime University, Dalian, Liaoning, China, [2]Centre for Ports and Maritime Safety, Dalian Maritime University, Dalian, Liaoning, China

Coastline changes in estuarine areas can result from a combination of natural processes such as erosion, sedimentation, and sea-level rise, as well as human activities, including urbanization and infrastructure development. These changes have the potential to affect the local environment, including submarine groundwater discharge, wetlands, and navigation routes. The Yalu River Estuary (YRE), situated on the border between China and North Korea, has been experiencing significant changes in its coastline over recent years. This study aims to investigate the coastline dynamics in the YRE from 2000 to 2020. The study employs Landsat 5/7/8 satellite data and proposes a modified Normalized Difference Water Index (NDWI) to accurately delineate the coast boundary, particularly in areas with extensive tidal flats like the YRE. The research findings indicate that from 2010 to 2020, significant changes occurred in the YRE shoreline, with erosion being the dominant trend. Human activities and alternations in hydrological conditions are important factors affecting the YRE coastline changes, contributing to the formation of distinctive spatiotemporal patterns. An extreme flooding event in the year 2010 also altered the inner estuarine coastline in the YRE, indicating the impact of strong natural drivers. Findings from this study provide a comprehensive understanding of the evolving coastal environment, considering natural and anthropogenic drivers, and highlight the importance of continuous monitoring in a region of ecological and geopolitical significance.

KEYWORDS

coastline, tidal estuary, satellite image, human impacts, image processing

1 Introduction

The coastline serves as a critical interface between land and the ocean, holding significant importance for both marine and terrestrial ecosystems, as well as human activities (Barbier et al., 2011). The study of coastline changes provides valuable insights into the dynamic interactions between the ocean and land, enabling the prediction of coastal erosion trends,

assessment of land degradation, and evaluation of the effectiveness of marine and coastal management strategies (Alesheikh et al., 2007). These changes are closely linked to natural phenomena such as climate change, sea-level rise, and river erosion, making coastline analysis an essential indicator of environmental transformations (Sánchez-Arcilla et al., 2016). Therefore, investigating coastline changes is crucial for the preservation of marine and coastal ecosystems, as well as the development of sustainable marine policies and management strategies.

Furthermore, human activities have exerted extensive influences on estuarine environments and coastlines. Various factors, including the overexploitation of river water resources, land development, and modifications to channels, have altered the sediment-carrying capacity of rivers, resulting in sedimentation and erosion in estuaries (Zhu et al., 2017; Xu et al., 2019). Additionally, activities such as port construction, coastal protection measures, and changes in coastal land use have significant impacts on coastlines, leading to coastal erosion, beach erosion, and ecosystem degradation (Turner et al., 1998). Along the entire coastal area of China, the most significant changes have occurred along the Bohai Sea coast. The proportion of artificial coastlines expanded from approximately 42.4% in 1990 to 81.5% in 2019 (Tian et al., 2020). Human activities have dominantly influenced the transport and the supply of sediment in coastal regions. This has led to the transformation of naturally meandering coastlines into straighter and more geometrically uniform artificial shorelines, resulting in a reduction of the overall length of these coastlines (Hapke et al., 2013).These anthropogenic activities pose potential threats to coastal populations, economies, and ecosystems. The anthropogenic activities on the changes of coastline could be a controlling factor for the development of the aquaculture industry, which can enhance food production and boost economic growth in coastal and rural communities. The natural irregular coastline is a crucial factor influencing water exchange between coastal regions and the open ocean, creating micro-environments with oceanographic conditions that sustain unique ecosystems for the local marine farming industry (Quiñones et al., 2019). Furthermore, anthropogenic activities, such as dredging, can disrupt the natural sediment balance along coastlines. Such changes can lead to coastal erosion, negatively impacting coastal infrastructure and potentially requiring costly mitigation measures, which could be involved with relatively high costs (Bianchini et al., 2019).

Two major methods have been widely used for coastline extraction (Muttitanon and Tripathi, 2005), with the regards of remote sensing image processing. The methods are the post-classification change detection approach and the direct spectral comparison approaches. The post-classification change detection approach involves comparing classified images from different time periods to identify and analyse land cover changes (Sahin et al., 2022). However, it is important to note that the accuracy of the data obtained through this approach is limited, and the accuracy generally depends on the precision of land cover classification in the study area, thereby resulting in larger deviations (Morgan and Hodgson, 2021). In contrast, the direct spectral comparison approach involves comparing the original data images through a series of algorithmic transformations to obtain comparative results (Zhang et al., 2013). Nevertheless, the direct spectral comparison approach is constrained by limitations such as lower spatial resolution and susceptibility to environmental factors, such as waves and tides. This precision could be even worse in areas with intensive tidal flats, a reliable method for coastline extraction in such area requires further exploration.

The Yalu River Estuary (YRE), a region of ecological and geopolitical significance on the China-North Korea border, has been subjected to substantial coastline changes over the years. The YRE features an irregular coastline, encompassing diverse landscapes, including underwater tidal ridges downstream, a delta plain in the estuary, and extensive tidal flats (Gao et al., 2012). Construction of upstream reservoirs has significantly decreased sediment supply and freshwater discharge, causing transformations in the river's West Branch, including its transition from a major waterway to a tidal inlet heavily impacted by siltation (Cheng et al., 2019). Large-scale reclamations have been conducted in the West Branch, accompanied by continuous dredging activities in Dandong Harbour's deep navigation channel (Cheng et al., 2020). While previous studies documented the coastline dynamics up to 2010 before the construction of the harbour, this research aims to bridge the gap by investigating coastline changes in the YRE over two decades from 2000 to 2020.

In this study, we investigate coastline changes in the YRE due to natural and human activities, therefore, this study focuses on the investigations of the coastline dynamics in the YRE from 2000 to 2020 using Landsat 5/7/8 satellite data. By including a modified Normalized Difference Water Index (NDWI), processing results can be more accurate to reflect the coastline condition in this estuary with complex tidal flats. Our findings provide a comprehensive understanding of the evolving coastal environment, considering natural and anthropogenic drivers, and highlight the importance of continuous monitoring in a region of ecological and geopolitical significance.

2 Methods

2.1 Study area

The Yalu River, originating from the Changbai Mountain in northeast China, flows between Dandong in the Liaoning Province of China and Sinuiju in North Korea, as shown in Figure 1. The Yalu River Estuary (YRE) is a vital coastal region that serves as a natural boundary between China and North Korea (Cheng et al., 2016). The area's coastline plays a crucial role in maintaining ecological balance and serving as a habitat for numerous species, and the YRE is a macro-tidal estuary with significant tidal variations. As reported by Bai et al. (2008), it exhibits an average tidal range of around 4.6 m, escalating to a maximum of approximately 6.7 m. The estuarine area displays a mix of tidal patterns. A consistent semi-diurnal tide is observed outside the estuary's entrance, while inside, the tide shifts to an irregular semi-diurnal pattern, influencing a tidal zone extending up to 54 km, as described by Yu et al. (2014). For areas with a macro-tidal range,

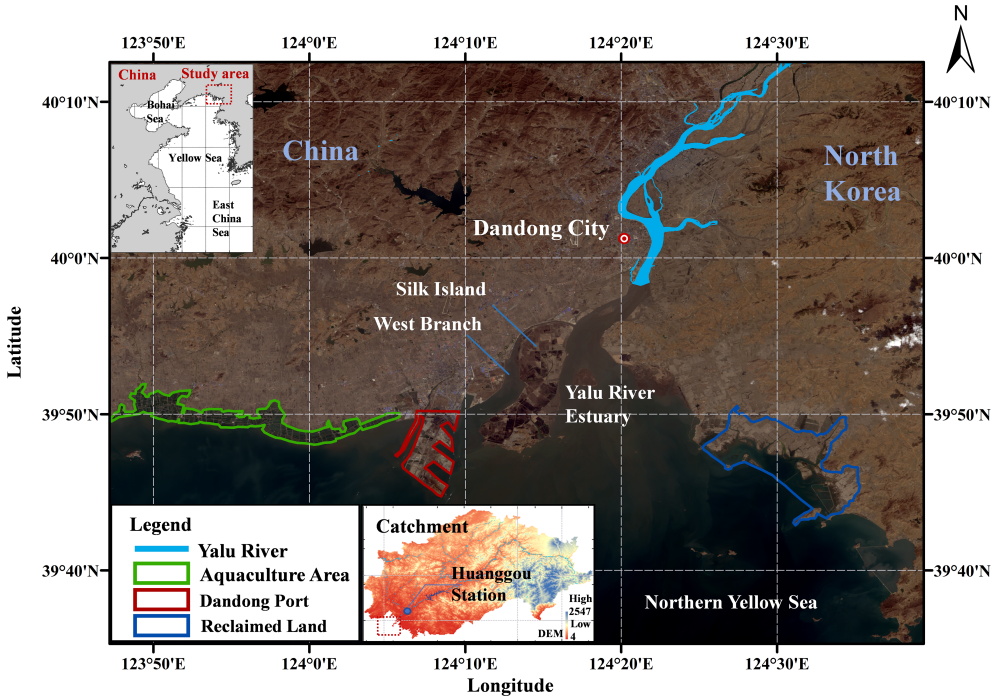

FIGURE 1
Satellite image of the study area in the Yalu River estuary, satellite image is from Landsat 8 OLI, and image was taken on April 10, 2020.

like the one in this study, the impact of tides on the coastline can lead to the increase of erosion or deposition. In turn, this macro-tide can significantly alter the coastline's shape. Furthermore, areas with smaller tidal ranges (micro tides: less than 2 meters, mesotides: 2-4 meters), wave action might play a more dominant role in shaping coastlines in these areas compared to macro-tidal regions. Due to strong coast erosion on the west bank of the river in China, the country has experienced significant land loss, resulting in a westward shift of the borderline from 1976 to 2010 (Li et al., 2012). To maintain the stability of this border, both the Chinese and North Korean governments have implemented various engineering projects, including dam construction and land reclamation.

The natural influences on coastline dynamics are profoundly affected by local hydrodynamic conditions, such as wave and current patterns, and particularly by the variations between high and low tides. Waves, particularly during high-energy events like storms, can erode beaches and dunes. Furthermore, the difference between high and low tides significantly influences the sediment movement and deposition along the coast. Coastline changes were corresponding with variations in the tidal range could reveal patterns of erosion and accretion. Large tide range can create extensive tidal flats, where areas that are periodically submerged and exposed, influencing sediment deposition and erosion patterns.

Thus, analysing coastline changes in this region is crucial for providing scientific guidance to both governments on this border-related issue.

The YRE region exhibits an irregular coastline with diverse landscapes, such as underwater tidal ridges downstream and a delta plain with a large-scale wetland in the estuary (Gao et al., 2012). Additionally, the region is distributed with extensive tidal flats. The construction of reservoirs upstream has led to a significant reduction in suspended sediment supply and freshwater discharge from the river (Shi et al., 2017). Specifically, the West Branch, which used to be the main waterway prior to these constructions, transformed into a tidal inlet and experienced substantial siltation thereafter. Extensive reclamation of tidal flats has occurred around Silk Island and Dandong Harbour in the West Branch, accompanied by continuous dredging in Dandong Harbour to maintain a deep navigation channel. These activities have altered the coastline and topography in the surrounding area, necessitating a comprehensive assessment of the associated impacts.

2.2 Satellite images

Satellite images from 2010 to 2020, applied in this study, were captured by the Landsat 5, 7, and 8 satellites, all of which are integral components of the United States NASA's Landsat program, the Landsat program has been providing images for nearly five decades (Roy et al., 2016). Specifically, Landsat 5 was equipped with a Multispectral Scanner and a Thematic Mapper, Landsat 7 featured an Enhanced Thematic Mapper Plus, and Landsat 8 was outfitted with an Operational Land Imager (OLI) and a Thermal Infrared Sensor (Zhu et al., 2016). Distinguished from other satellites, the Landsat series boasts several unique features: a sun-synchronous polar orbit, relatively low orbital altitude, rapid orbital cycles, multispectral sensor data acquisition, and imagery of varying resolutions. These attributes enable the Landsat satellites to provide high-quality, continuous, and global earth observation

data. Furthermore, the Landsat collections includes imagery that has undergone radiometric and geometric corrections (Dwyer et al., 2018), thus reducing some aspects of the processing requirement. We also processed images from 2000 to 2010 which have been documented in previous study (Li et al., 2012), to extend our analysis to a longer temporal coverage. Images of before and after flooding season in April and October were analysed every year. To achieve more accurate results, the selection of the satellite images was based on the following criteria: (1) lowest cloud coverage near the study area, (2) relatively closer date of the image acquisition for each year, and (3) similar tidal phase during the image acquisition.

In this study, we eventually utilized 45 satellite images obtained from the United States Geological Survey website (https://www.usgs.gov). In order to convert radiometric data to the above-water surface remote sensing reflectance data, the FLAASH atmospheric correction module from Environment for Visualizing Images (ENVI) was used to radiometric calibrate and atmospheric correct the obtained images. In term of the advanced image segmentation, eCognition 10.3 allows for the identification and delineation of different land cover features, including the coastline, by analysing spectral, spatial, and textural information from remote sensing images. Image segmentation is a crucial step in coastline analysis, as it allows for the accurate extraction of coastal boundaries (Dellepiane et al., 2004).

2.3 Modified normalized difference water index

When analysing the state of coastlines using remote sensing data, the primary objective is to extract the coastline within a specified timeframe, taking into account the factors such as tides to understand the coastline's variability and to identify the instantaneous waterline. The methodologies for automatically delineating the water's edge from remote sensing imagery are classified into edge detection, thresholding, and image classification techniques.

Recognizing the challenge of identifying the water boundary in areas with massive tidal flats, we introduced a modified Normalized Difference Water Index (NDWI). The conventional NDWI is based on the green and near-infrared bands, which can be less effective in regions with extensive tidal flats. In our research, we adopt a modified NDWI approach. Our modification incorporates additional bands or spectral indices to better differentiate between water and non-water surfaces in such areas. This methodology provides superior precision and resolution, enabling the detection of small-scale coastline changes.

In this study, modified NDWI utilizes the differences in reflectance between water and land in multi-spectral imagery to identify coastal areas (Bijeesh and Narasimhamurthy, 2020). Modified NDWI was refined by substituting NIR (0.76-0.90 μm) band in the original NDWI with the Short-Wave Infrared (SWIR1) band:

$$MNDWI = \frac{Green - SWIR1}{Green + SWIR1} \quad (1)$$

where the Green spectral band is 0.525 ~0.600 μm, and SWIR1 (1.560 ~1.660 μm) corresponds to the Short-Wave Infrared first band. Due to the similarity in the reflectance characteristics of water bodies and land cover, such as building area, in the NIR band and their significant differences in the SWIR1 band, the modified NDWI proves more effective in eliminating noise from tidal flat and building area.

In most cases, modified NDWI can better reveal the fine characteristics of water body by using SWIR1 band instead of NIR band used in NDWI, it can distinguish water bodies more easily and solve the problem that shadow noise is difficult to eliminate in water extraction. The previous studies have shown that modified NDWI is more suitable for enhancing water information than NDWI, and can extract water bodies more accurately (Du et al., 2014; Singh et al., 2015). In terms of accuracy, the Kappa coefficient of water extraction using modified NDWI was 0.0433 to 0.1348 higher than that using NDWI (Xu, 2006). Compared with NDWI, modified NDWI can better distinguish water from non-water from satellite images to extract coastline data.

2.4 Coastline change analysis workflow

By applying thresholding techniques to modified NDWI calculations, accurate coastline boundaries can be extracted from remote sensing images. Thereafter, the Digital Shoreline Analysis System (DSAS) was applied to analyse coastline positions over time. Coastline erosion or accretion rates could be calculated by the DSAS, which enables the assessment of the impact of erosion and siltation on coastal coastlines in coastal areas using remote sensing data (Quang et al., 2021). By overlaying different temporal datasets and employing spatial analysis tools, the coastal features over time along the coastline could be examined. The DSAS module consists of five steps: (1) coastline extraction; (2) baseline creation, where the baseline is created using a buffer method with the same curved shape as the nearest coastline; (3) generation of cross-shore profiles by defining intervals and orthogonally projecting the cross-shore profiles onto different-year coastlines after multiple adjustments; (4) calculation of the distance between the baseline and coastline; (5) calculation of coastline change rates. The End Point Rate (EPR) and Net Shoreline Movement (NSM) models are applied to calculate the rates using adjacent coastlines. EPR and NSM are essential tools for analysing coastline changes. EPR focuses on the rate of change over time, providing a temporal perspective, while NSM offers a spatial perspective by quantifying the total movement of the shoreline. In addition, NSM is used to measure long-term net coastline changes between 2000 and 2020, while EPR displays the annual rate of change during the mentioned period. Together, they offer a robust framework for understanding and managing coastal environments. The calculation method for EPR is as below:

$$E_{i,j} = \frac{d_j - d_i}{\Delta Y_{j,i}} \quad (2)$$

where $E_{i,j}$ represents the rate of change in the coastline endpoint along a certain baseline from one period to another; d_j is the distance from the coastline in the j period along line to the

baseline; *di* is the distance from the coastline in the *i* period along line to the baseline; and $\triangle Y_{j,i}$ is the difference in years between the *j* and *i* coastline periods. The workflow of the coastline change analysis in this study is demonstrated in Figure 2.

3 Results and discussion

3.1 Coastline changes under anthropogenic impacts

Our analysis of Landsat images revealed significant coastline changes in the YRE from 2010 to 2020. The changes were categorized into erosion and accretion, which were further correlated with environmental and anthropogenic factors. Human activities, such as land reclamation and construction of harbours, were identified as key contributors to coastline changes.

Coastal human structures can induce two primary phenomena: 1) modifications in pre-existing hydrodynamic conditions; and 2) a rapid seaward advancement of the coastline, resulting in significant changes to the coastline, a reduction in sea area, and a decrease in the amount of water accommodated by the tide. Engineering projects that intersect the tidal current at an angle can induce deflection of flow, altering the direction of the current, and may even create flows along the embankment that are nearly perpendicular to the original current direction. This is particularly pronounced when the velocity of the incoming tide exceeds that of the outgoing tide, leading to enhanced sediment accumulation and tidal flat siltation. Consequently, they alter the sedimentary balance affecting the shoreline, leading to coastal erosion and accretion.

Over the past decade, there has been an escalating trend in the utilization of the YRE's coastline, with a notable increase in the diversity of artificial coastline types (Figure 3). We extract the coastline in spring to eliminate the influence from the wet season. While some sections of the YRE's coastal dynamics exhibit subtle changes. However, there are notable spatial distribution changes in certain areas, which may be attributed primarily to the region's coastal composition, predominantly of bedrock and silt coastlines. The relative stability of bedrock sections is higher, whereas the silt coastlines exhibit less stability.

From 2010 to 2020, the Yalu River's coastline maps reveal a notable changing trend (Figure 4). Comparing the change pattern of the estuarine coastline from 2010 to 2014, a noticeable expansion of artificial coastlines is evident in the Donggang City area, with clear differences. Additionally, there is an increased presence of islands in the south-eastern region. During this period, the overall area of the YRE coastline increased, primarily due to the construction of coastal artificial structures. Since 2014, there has been a substantial increase in the extent of artificial coastlines in the YRE basin. These artificial constructs encompass various features such as aquaculture embankments, tidal barriers, salt fields, and port terminals. This transition highlights the diminishing spatial footprint of natural coastlines within the region. By comparing the spatiotemporal changes in the southern coastline segments between 2014 and 2020, it can be observed that the coastal area has also increased in size in 2020, mainly due to land reclamation projects, leading to an increase in land area. This is closely related to a series of local coastline protection policies and the implementation of various coastal land reclamation projects.

In general, the estuarine area has expanded in 2020, compared to 2010, but there is a certain degree of erosion observed in the area

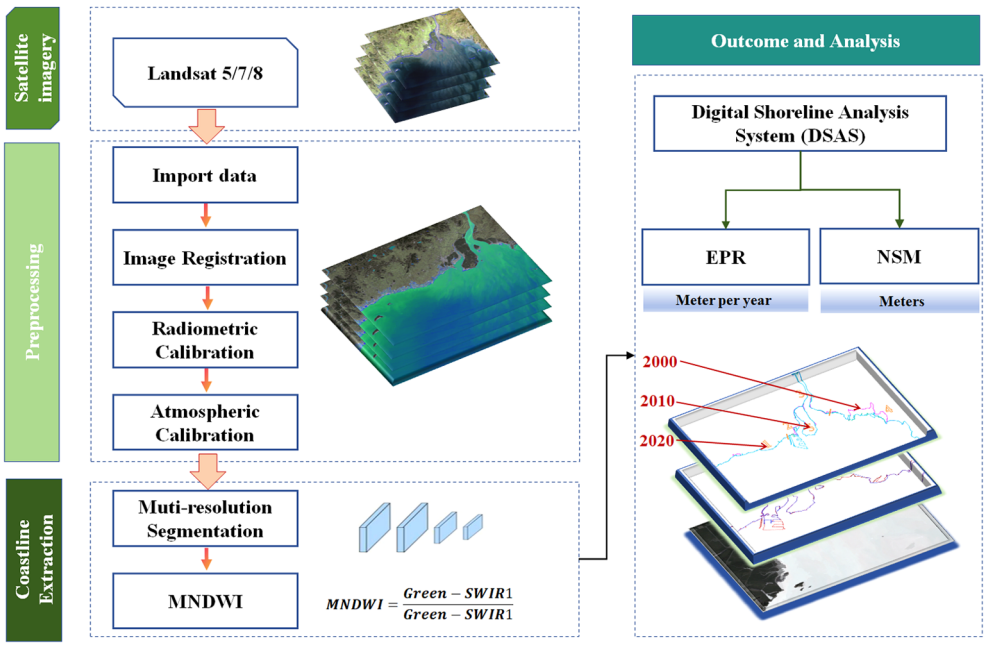

FIGURE 2
The applied methods for the extraction of coastline changes in this study.

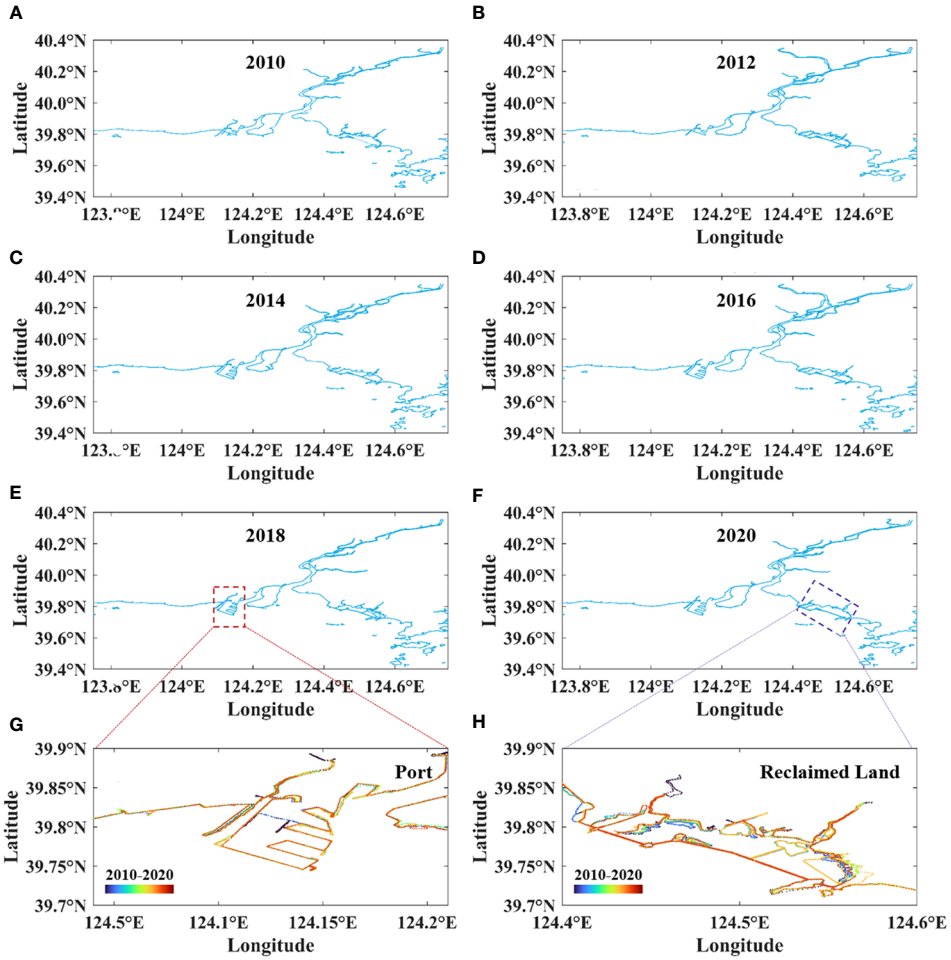

FIGURE 3
(A–F) the distribution of coastline from 2010 to 2020, **(G)** the coastline of port from 2010 to 2020, **(H)** the coastline of reclaimed land from 2010 to 2020.

near the mouth of the Yalu River, accompanied by a year-on-year reduction in the island areas at the estuarine mouth.

To elucidate the spatiotemporal characteristics of the YRE coastline changes more effectively, this study segmented the research area into five distinct sections: S1, S2, S3, S4, and S5 (Figure 5A). The coastline changing trends for each period are summarised in Table 1. Section S1 encompasses the western aquaculture sector of the YRE. Section S2 includes the Dandong port construction area. Section S3 is designated as the inner estuary region, and Section S4 constitutes the eastern bank of the YRE.

Between the years 2000 and 2010, the YRE coast exhibited spatial transformations, with the spatial distribution of the EPR depicted in Figure 5B. According to these results, during the decade of 2000-2010, there was a general trend of accretion along the YRE coastline. A breakdown by sector revealed that section S1 and S2 experienced modest accretion, with average NSM of 74.4 m and 335.62 m, respectively. The highest rate of accretion was noted in section S2 at 134.19 m per year, while the maximum erosion rate occurred in section S1 at 55.46 m per year. In section S3, coastal changes were relatively mild, but the overarching trend was still one of accretion. The most significant changes were recorded in section S4, which had a maximum accretion rate of 549.16 m per year, and an average NSM of 1205.45 m.

During the period from 2010 to 2020, the coastal areas of the YRE, particularly in section S1 and S2, exhibited patterns of sediment accumulation (Figure 5B). Section S1 maintained a relatively stable condition with only minor accretion observed. In contrast, section S2 underwent the most dramatic changes, with the highest accumulation rate recorded at 784.77 m per year and an average net coastline accretion amounting to 1071.88 m. Section S3 displayed a trend towards slight erosion overall, with the maximum erosion rate reaching 117.18 m per year and an average net erosion of the coastline being 74.24 m. Similarly, section S4 also experienced marginal erosion with the maximum erosion rate at 56.37 m per year and an average net coastline erosion totalling 21.04 m.

Between the years 2000 and 2020, the overall coastline of the YRE displayed a trend of accretion (Figure 5B). However, the temporal and spatial distribution of the EPR was heterogeneous.

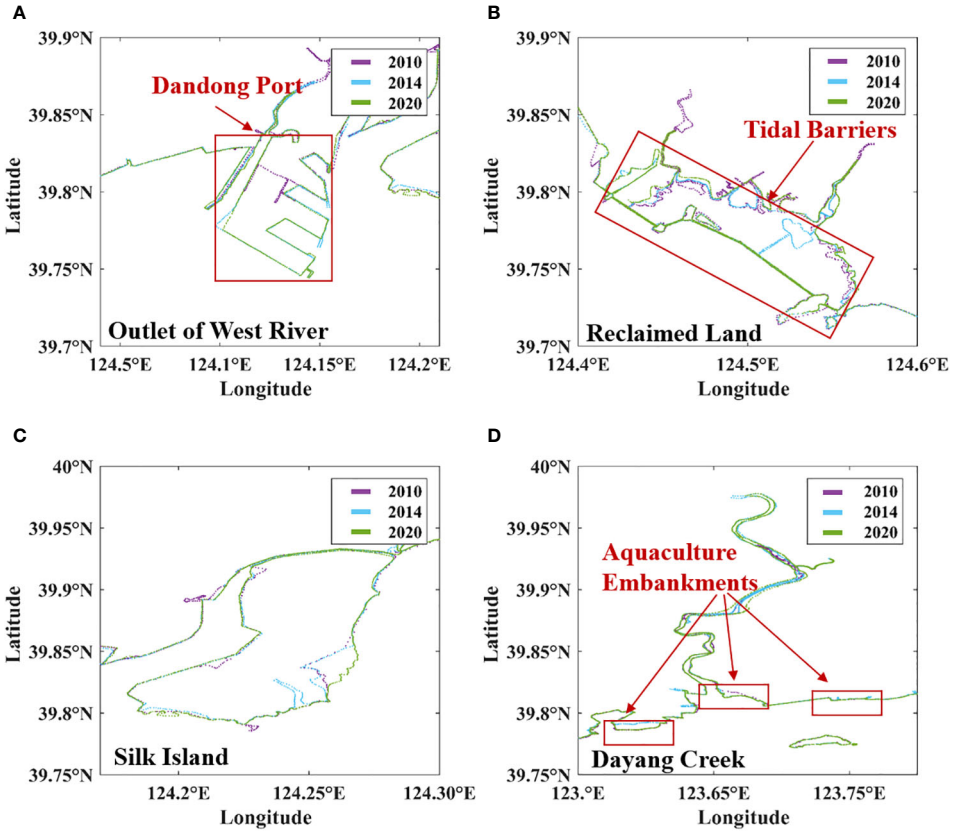

FIGURE 4
The changes of the coastline due to the anthropogenic activities in 2010, 2014 and 2020, **(A)** the local port area, **(B)** the reclaimed land region, **(C)** the silk island, and **(D)** the local Dayang creek.

With the comparison of all sections, S3 (the inner estuary) showed minor erosive tendencies, with the highest erosion rate being 57.05 m per year and an average net coastline erosion of 38.37 m. The other sections exhibited accretion, with particularly noticeable contributions to coastline growth from the construction activities in the local Port area (S2) and land reclamation in section S4. Moreover, S5 (the sandy island) experienced slight erosion throughout the 2000-2020 period, with the maximum erosion rate at 24.99 m per year and an average net coastline erosion amounting to 52.49 m.

The alterations in the length of the YRE coastline from 2000 to 2020 are summarised in Table 2. It is evident from the table that over the past two decades, the total coastline length across sections S1 to S4 has demonstrated an increasing trend, with an extension of approximately 59 km. This increment corresponds to a 22.6% surge, with an annual average growth rate of 2.95 km per annum. The most significant change occurred between 2010 and 2020, during which the coastline length expanded by 49.3 km. Examining the changes by section, during 2000-2020, the coastline of section S2 experienced a growth of 396.9% due to the construction activities in Dandong Port. Consequently, it is apparent that the primary contributor to the change in the YRE's coastline length during 2000-2020 was the increase in artificial coastline resulting from the development of local Port.

3.2 Impacts of natural processes on coastline change

In recent years, the occurrence of extreme weather has accelerated the coastline change of the estuarine region, with flooding events caused by extreme rainfall having a severe impact on the estuarine landscape (Cooper, 2002; Xie et al., 2018; Du et al., 2023). Even just one strong flooding can induce dramatic changes in the estuarine landscape (Dittmann et al., 2015; Ward et al., 2018).

In August 2010, the Yalu River basin experienced a severe flooding event (recurring every 50 years) caused by subtropical high pressure (Du et al., 2023). Intense rainfalls reached the catchment on 19th August 2010, resulting in a peak discharge of 12,800 m^3/s at Huanggou Hydrological Station (Figure 6), the Huanggou hydrological Station is in the lower reaches of the Yalu River, with a catchment area of 55,420 km^2. Analysing the monthly sediment transport, runoff, and precipitation data of the Yalu River reveals the following trends. In 2010, the river's sediment load reached its peak, coinciding with the highest monthly average precipitation. When examining the overall trend, the average runoff in 2010 reached its maximum in August, accompanied by the peak precipitation in the area. This indicates that, in 2010, precipitation was the predominant factor influencing river runoff in the region. The increase in precipitation contributed to the expansion of the YRE area. In 2013, despite relatively high rainfall, the

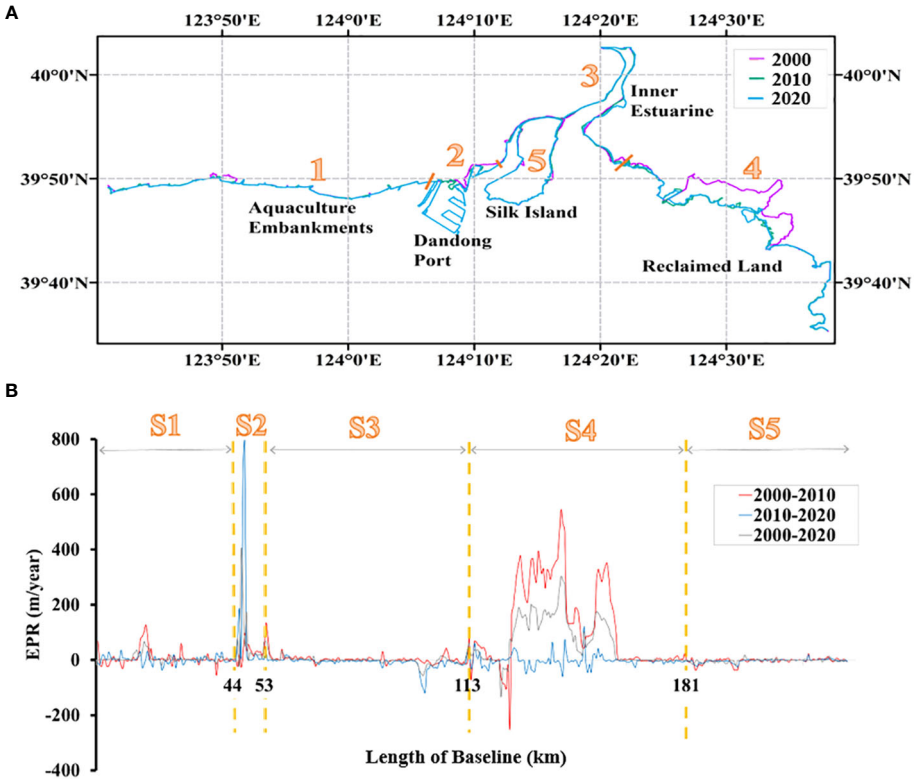

FIGURE 5
(A) the division of the coastline into 5 sections in YRE, and **(B)** the EPR for each section.

TABLE 1 The coastline summary of each section.

Time	Section	Variation length (km)	Average EPR ($m \cdot a^{-1}$)	Max Accumulation EPR ($m \cdot a^{-1}$)	Max Erosion EPR ($m \cdot a^{-1}$)	Average NSM (m)
2000 | 2010	S1	4.5	7.37	127.65	55.46	74.4
	S2	13	33.24	134.19	27.53	335.62
	S3	-1.6	2.47	80.38	22.6	24.94
	S4	-2.4	119.4	549.16	103.88	1205.45
	S5	-1	-2.63	22.79	37.72	-26.5
2010 | 2020	S1	-2.2	1.79	35.7	35.35	16.92
	S2	49.3	112.83	787.44	4.29	1071.88
	S3	2.1	-7.65	43.11	117.18	-72.24
	S4	-3.7	-2.33	122.35	56.37	-21.04
	S5	1	-2.58	17.63	20.8	-29.47
2000 | 2020	S1	2.3	5.06	65.41	19.56	98.89
	S2	62.3	68.51	395.4	14.84	1338.45
	S3	0.5	-1.96	60.81	57.05	-38.37
	S4	-6.1	65.63	302.58	134.25	1282.2
	S5	0	-2.44	19	24.99	-52.49

10.3389/fmars.2023.1335064

TABLE 2 The length of coastlines and growth rate of the sections from 2000 to 2020.

	S1-S4(km)	Growth Rate (%)	S2(km)	Growth Rate (%)	S5(km)	Growth Rate (%)
2000 | 2010	260.7 | 274.2	5.2	15.7 | 28.7	82.8	55.6 | 55.2	0
2010 | 2020	274.2 | 319.7	16.7	28.7 | 78	171.8	55.2 | 55.6	-0.7
2000 | 2020	260.7 | 319.7	22.6	15.7 | 78	396.9	| 55.6	0

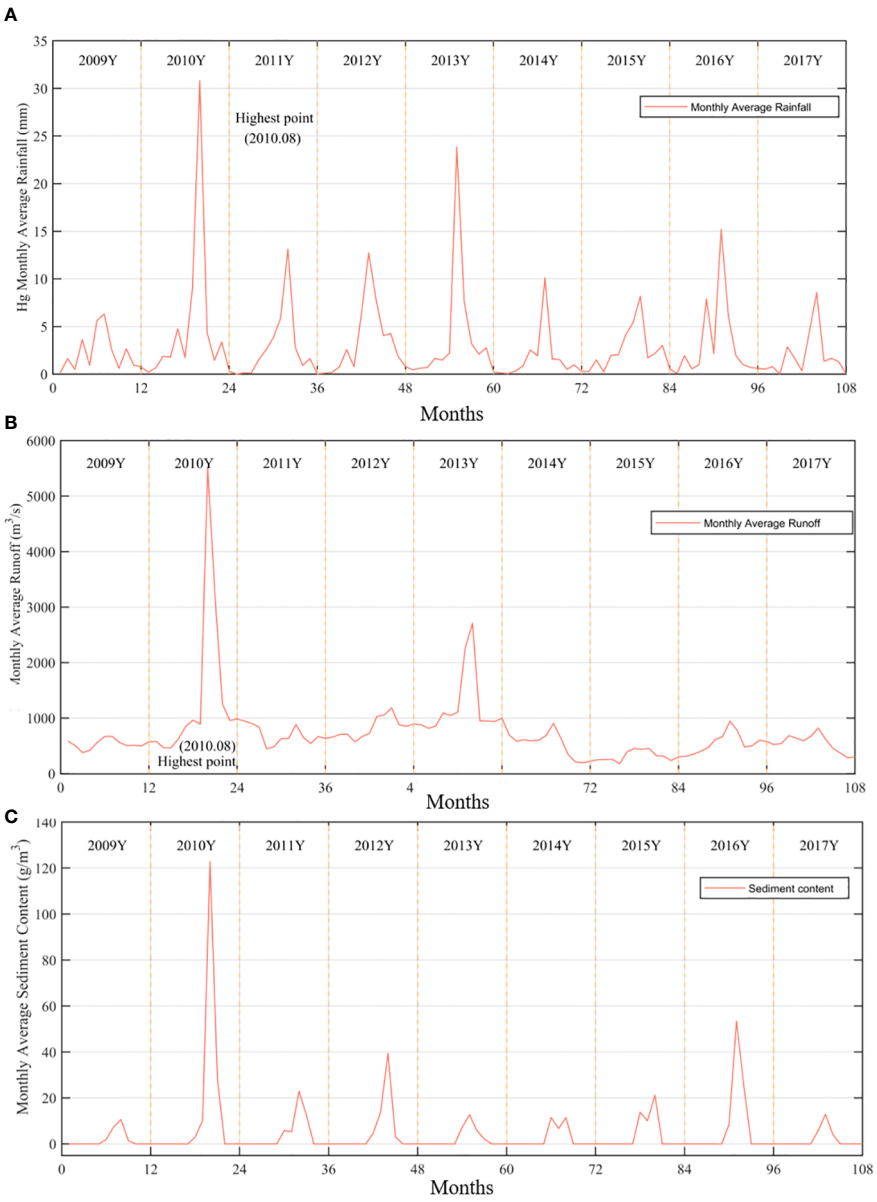

FIGURE 6
The monitoring data from 2009 to 2017, **(A)** the monthly average precipitation, **(B)** monthly average runoff, and **(C)** monthly average sediment discharge at the hydrological measurement station in the Yalu River basin.

sediment transport remained stable, leading to a minor peak in the YRE's runoff for that year. Estuarine sediments are mainly from two sources: terrigenous sediments discharged by rivers and flood events, and neritic sediments, including the local resuspended sediments from the seabed. Driven by extreme flooding caused by heavy rains in 2010, sediment content in YRE increased dramatically (Figure 6C), resulting in a significant expansion of the coastline in the fall of 2010. Flood events often carry significant amounts of sediments from inland areas to the coast. The volume, composition, and grain size of these sediments can vary greatly between events, directly influencing the nature of coastline changes. For instance, heavier sediment loads can lead to rapid buildup of the coastline, while finer sediments might be easily redistributed by tidal and wave actions, leading to more subtle changes. In areas with higher sediment deposition, this can lead to the formation of new landforms like sandbars or deltas, significantly altering the coastal landscape.

After the flood season, the runoff basin area of the Yalu River in 2010 autumn was significantly larger than that of 2010 spring. Compared to the previous year, the number of tributaries of the Yalu River increased slightly, which may be related to local precipitation. During the same period, the coastline area of the YRE is expected to increase, reflecting a certain trend of coastal accumulation, such as Silk Island and eastern bank of YRE. Land areas were slightly increased compared to the previous year, while the length of the estuary continued to expand (Figures 7A, B).

Furthermore, when comparing the spatial and temporal distribution characteristics of the YRE coastline in 2013 and 2010 during spring season, it can be observed that the pattern in the estuary region in 2013 is similar to that in 2010. From this, it can be inferred that the changes in the YRE are significant but overall in a dynamic balance. This may be related to local precipitation and sediment transport, as these two factors have interacted over the long term, resulting in cyclic changes in the size of the coastline segments in the region, with no significant overall trend.

Comparing seasonal variation in 2013 with the second highest runoff in the past decade, it is evident that in autumn 2013, the western river's basin area in this region increased (Figures 7C, D). From images of the following years, this pattern in the West Channel in this region remained stable, indicating that this change is persistent and stable, with distinct characteristics.

Furthermore, the distributions of coastline in spring for the year of 2010, 2012 and 2014 are illustrated in Figure 8. Comparative analysis can find that the area of the coastline has generally increased, and the increased coastline types are mainly artificial coastlines. In addition to the increase in artificial shorelines, there is also an increase in the estuary bank area caused by partial sediment accumulation at the estuary. This is usually related to the amount of sediment and rainfall in the area during the flood events. Changes in hydrological conditions and sediment load are significant factors in the YRE coastline changes. The YRE is a land-sea bidirectional

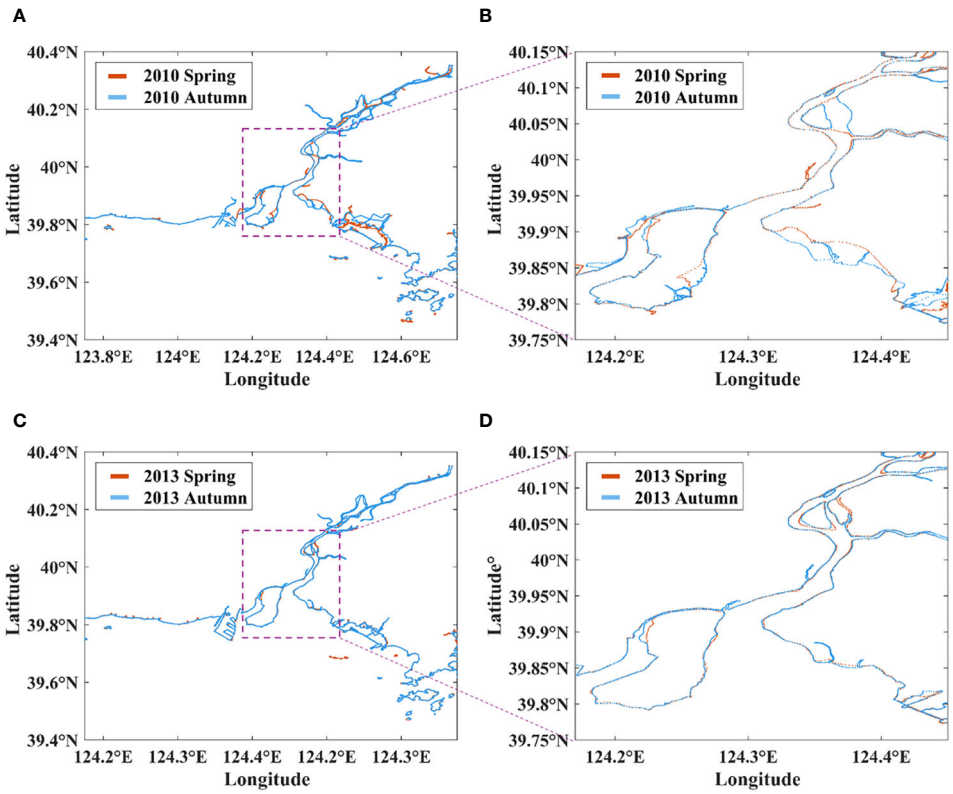

FIGURE 7
The distribution of coastline in spring and autumn for the year of 2010 and 2013, **(A)** overall shoreline of YRE in spring and autumn 2010, **(B)** partial shoreline of YRE in spring and autumn 2010, **(C)** overall shoreline of YRE in spring and autumn 2013, **(D)** partial shoreline of YRE in spring and autumn 2013.

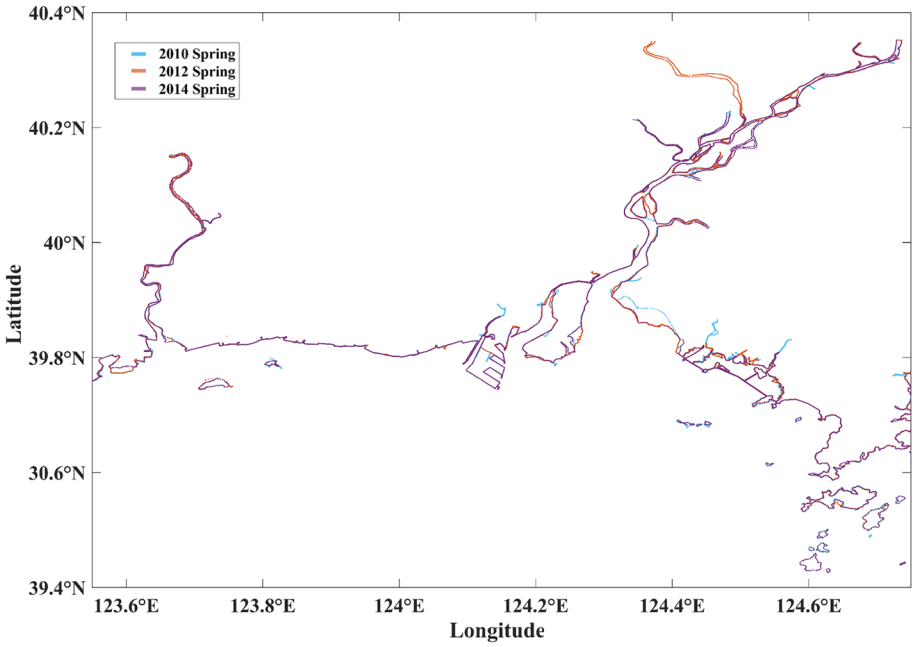

FIGURE 8
The coastline distribution in spring for the year of 2010, 2012 and 2014.

estuary type, with abundant terrestrial and marine sediments in the region. Under the influence of waves and tides, nearshore sediments will eventually accumulate on land or flow into the ocean with the tide, leading to coastline migration.

4 Conclusion

This study summarizes the causes of YRE coastline changes, mainly divided into anthropogenic and natural factors. On the anthropogenic side, the construction of aquaculture areas and embankments is the main project for artificial coastline construction and is a major influencing factor for coastline expansion. Due to the construction of a large number of artificial hydraulic structures, the morphology changes along the YRE have been greatly affected, with an increase of 22.6% from 2000 to 2020 for S1-S4. In addition, the prevalence of land reclamation in recent years is also an important factor restricting changes in the coastline. Regarding natural factors, the differences in hydrological conditions and sediment transport of the areas of aquaculture and embankments have led to inconsistent rates of coastal erosion.

This study shows that from 2010 to 2020, the YRE coastline changes were quite significant, indicating a shift from a phase of expansion to erosion. The YRE and its downstream channels eventually expanded towards both banks, with numerous riverbed islands forming. Analysis reveals that human activities and alternations in hydrological conditions are important factors affecting the YRE coastline changes, contributing to the formation of distinctive spatiotemporal patterns.

The findings highlight the complex interplay between natural and anthropogenic factors in shaping the coastal environment. The observed coastline changes in the YRE have significant implications for the region. Erosion can lead to loss of habitat and infrastructure damage, while accretion can impact navigational routes and submarine groundwater discharge. It is essential to balance economic development with environmental conservation to ensure the long-term sustainability of the estuary ecosystem. Future research should focus on predictive modelling and integrated coastal zone management to address the challenges posed by coastline changes in this unique estuarine ecosystem.

Data availability statement

The original contributions presented in the study are included in the article/supplementary material. Further inquiries can be directed to the corresponding author.

Author contributions

QW: Software, Validation, Writing – original draft. YM: Conceptualization, Data curation, Writing – review & editing. ZC: Funding acquisition, Methodology, Software, Visualization, Writing – review & editing. YD: Visualization, Writing – review & editing.

Funding

The author(s) declare financial support was received for the research, authorship, and/or publication of this article. This study

was funded by the National Key Research and Development Program of China (Grant No. 2021YFB2601100), the National Natural Science Foundation of China (Grant No. 52201309, 42276170, 42106158), and the Fundamental Research Funds for the Central Universities (Grant No. 3132023158).

Acknowledgments

The Landsat images utilized in this study were sourced from the United States Geological Survey (USGS) website. We would also acknowledge the support from Liaodong University for the great help in field observation.

Conflict of interest

The authors declare that the research was conducted in the absence of any commercial or financial relationships that could be construed as a potential conflict of interest.

Publisher's note

References

Alesheikh, A. A., Ghorbanali, A., and Nouri, N. (2007). Coastline change detection using remote sensing. *Int. J. Environ. Sci. Technol.* 4, 61–66. doi: 10.1007/BF03325962

Bai, F., Gao, J., Wang, Y., Cheng, Y., and Lin, T. (2008). Tidal characteristics at yalu river estuary. *Mar. Sci. Bull.* 27, 7–13.

Barbier, E. B., Hacker, S. D., Kennedy, C., Koch, E. W., Stier, A. C., and Silliman, B. R. (2011). The value of estuarine and coastal ecosystem services. *Ecol. Monogr.* 81 (2), 169–193. doi: 10.1890/10-1510.1

Bianchini, A., Cento, F., Guzzini, A., Pellegrini, M., and Saccani, C. (2019). Sediment management in coastal infrastructures: Techno-economic and environmental impact assessment of alternative technologies to dredging. *J. Environ. Manage.* 248, 109332. doi: 10.1016/j.jenvman.2019.109332

Bijeesh, T., and Narasimhamurthy, K. (2020). Surface water detection and delineation using remote sensing images: A review of methods and algorithms. *Sustain. Water Resour. Manage.* 6, 1–23. doi: 10.1007/s40899-020-00425-4

Cheng, Z., Jalon-Rójas, I., Wang, X. H., and Liu, Y. (2020). Impacts of land reclamation on sediment transport and sedimentary environment in a macro-tidal estuary. *Estuarine. Coast. Shelf. Sci.* 242, 106861. doi: 10.1016/j.ecss.2020.106861

Cheng, Z., Wang, X. H., Jalon-Rojas, I., and Liu, Y. (2019). Reconstruction of sedimentation changes under anthropogenic influence in a medium-scale estuary based on a decadal chronological framework. *Estuarine. Coast. Shelf. Sci.* 227, 106295. doi: 10.1016/j.ecss.2019.106295

Cheng, Z., Wang, X. H., Paull, D., and Gao, J. (2016). Application of the geostationary ocean color imager to mapping the diurnal and seasonal variability of surface suspended matter in a macro-tidal estuary. *Remote Sens.* 8 (3), 244. doi: 10.3390/rs8030244

Cooper, J. (2002). The role of extreme floods in estuary-coastal behaviour: contrasts between river-and tide-dominated microtidal estuaries. *Sediment. Geol.* 150 (1-2), 123–137. doi: 10.1016/S0037-0738(01)00271-8

Dellepiane, S., De Laurentiis, R., and Giordano, F. (2004). Coastline extraction from SAR images and a method for the evaluation of the coastline precision. *Pattern Recognition. Lett.* 25 (13), 1461–1470. doi: 10.1016/j.patrec.2004.05.022

Dittmann, S., Baring, R., Baggalley, S., Cantin, A., Earl, J., Gannon, R., et al. (2015). Drought and flood effects on macrobenthic communities in the estuary of Australia's largest river system. *Estuarine. Coast. Shelf. Sci.* 165, 36–51. doi: 10.1016/j.ecss.2015.08.023

Du, Y., Cheng, Z., and You, Z. (2023). Morphological changes in a macro-tidal estuary during extreme flooding events. *Front. Mar. Sci.* 9, 1112494. doi: 10.3389/fmars.2022.1112494

Du, Z., Li, W., Zhou, D., Tian, L., Ling, F., Wang, H., et al. (2014). Analysis of Landsat-8 OLI imagery for land surface water mapping. *Remote Sens. Lett.* 5, 672–681. doi: 10.1080/2150704X.2014.960606

Dwyer, J. L., Roy, D. P., Sauer, B., Jenkerson, C. B., Zhang, H. K., and Lymburner, L. (2018). Analysis ready data: enabling analysis of the landsat archive. *Remote Sens.* 10, 1363. doi: 10.3390/rs10091363

Gao, J.-h., Jun, L., Harry, W., Bai, F.-l., Cheng, Y., and Wang, Y.-p. (2012). Rapid changes of sediment dynamic processes in Yalu River Estuary under anthropogenic impacts. *Int. J. Sediment. Res.* 27 (1), 37–49. doi: 10.1016/S1001-6279(12)60014-6

Hapke, C. J., Kratzmann, M. G., and Himmelstoss, E. A. (2013). Geomorphic and human influence on large-scale coastal change. *Geomorphology* 199, 160–170. doi: 10.1016/j.geomorph.2012.11.025

Li, L., Zhang, J., Ma, Y., and Cui, X. (2012). Monitoring the coastline change in the Yalu River Estuary from 1976 to 2010 based on remote sensing images. *Bull. Surv. Mapp.* 386, 390.

Morgan, G. R., and Hodgson, M. E. (2021). A post-classification change detection model with confidences in high resolution multi-date sUAS imagery in coastal south carolina. *Int. J. Remote Sens.* 42 (11), 4309–4336. doi: 10.1080/01431161.2021.1890266

Muttitanon, W., and Tripathi, N. K. (2005). Land use/land cover changes in the coastal zone of Ban Don Bay, Thailand using Landsat 5 TM data. *Int. J. Remote Sens.* 26 (11), 2311–2323. doi: 10.1080/01431160512331326666

Quang, D. N., Ngan, V. H., Tam, H. S., Viet, N. T., Tinh, N. X., and Tanaka, H. (2021). Long-term shoreline evolution using dsas technique: a case study of Quang Nam province, Vietnam. *J. Mar. Sci. Eng.* 9, 10, 1124. doi: 10.3390/jmse9101124

Quiñones, R. A., Fuentes, M., Montes, R. M., Soto, D., and León-Muñoz, J. (2019). Environmental issues in Chilean salmon farming: a review. *Rev. Aquacult.* 11 (2), 375–402. doi: 10.1111/raq.12337

Roy, D. P., Zhang, H. K., Ju, J., Gomez-Dans, J. L., Lewis, P. E., Schaaf, C. B., et al. (2016). A general method to normalize Landsat reflectance data to nadir BRDF adjusted reflectance. *Remote Sens. Environ.* 176, 255–271. doi: 10.1016/j.rse.2016.01.023

Sahin, G., Cabuk, S. N., and Cetin, M. (2022). The change detection in coastal settlements using image processing techniques: a case study of Korfez. *Environ. Sci. pollut. Res.* 29 (10), 15172–15187. doi: 10.1007/s11356-021-16660-x

Sánchez-Arcilla, A., García-León, M., Gracia, V., Devoy, R., Stanica, A., and Gault, J. (2016). Managing coastal environments under climate change: Pathways to adaptation. *Sci. Total. Environ.* 572, 1336–1352. doi: 10.1016/j.scitotenv.2016.01.124

Shi, Y., Liu, Z., Gao, J., Yang, Y., and Wang, Y. (2017). The response of sedimentary record to catchment changes induced by human activities in the western intertidal flat of Yalu River Estuary, China. *Acta Oceanol. Sin.* 36, 54–63. doi: 10.1007/s13131-016-0941-7

Singh, K. V., Setia, R., Sahoo, S., Prasad, A., and Pateriya, B. (2015). Evaluation of NDWI and MNDWI for assessment of waterlogging by integrating digital elevation model and groundwater level. *Geocarto. Int.* 30, 650–661. doi: 10.1080/10106049.2014.965757

Tian, H., Xu, K., Goes, J. I., Liu, Q., and H.d.R. and Yang, M. (2020). Shoreline changes along the coast of mainland China—time to pause and reflect? *ISPRS. Int. J. Geo-Information.* 9 (10), 572. doi: 10.3390/ijgi9100572

Turner, R. K., Lorenzoni, I., Beaumont, N., Bateman, I. J., Langford, I. H., and McDonald, A. L. (1998). Coastal management for sustainable development: analysing environmental and socio-economic changes on the UK coast. *Geographical. J.* 164 (3), 269–281. doi: 10.2307/3060616

Ward, P. J., Couasnon, A., Eilander, D., Haigh, I. D., Hendry, A., Muis, S., et al. (2018). Dependence between high sea-level and high river discharge increases flood hazard in global deltas and estuaries. *Environ. Res. Lett.* 13 (8), 084012. doi: 10.1353/book.99575

Xie, D., Pan, C., Gao, S., and Wang, Z. B. (2018). Morphodynamics of the Qiantang Estuary, China: Controls of river flood events and tidal bores. *Mar. Geol.* 406, 27–33. doi: 10.1016/j.margeo.2018.09.003

Xu, H. (2006). Modification of normalised difference water index (NDWI) to enhance open water features in remotely sensed imagery. *Int. J. Remote Sens.* 27, 3025–3033. doi: 10.1080/01431160600589179

Xu, Y., Cheng, L., Zheng, J., Zhu, Y., Wu, Y., Shi, J., et al. (2019). Intensive anthropogenic influence on the morphological evolution of estuarine tidal channels. *J. Coast. Res.* 35 (6), 1237–1249. doi: 10.2112/JCOASTRES-D-18-00136.1

Yu, Q., Wang, Y., Gao, J., Gao, S., and Flemming, B. (2014). Turbidity maximum formation in a well-mixed macrotidal estuary: The role of tidal pumping. *J. Geophys. Res. Ocean.* 119, 7705–7724. doi: 10.1002/2014JC010228

Zhang, T., Yang, X., Hu, S., and Su, F. (2013). Extraction of coastline in aquaculture coast from multispectral remote sensing images: Object-based region growing integrating edge detection. *Remote Sens.* 5 (9), 4470–4487. doi: 10.3390/rs5094470

Zhu, Z., Fu, Y., Woodcock, C. E., Olofsson, P., Vogelmann, J. E., Holden, C., et al. (2016). Including land cover change in analysis of greenness trends using all available Landsat 5, 7, and 8 images: A case study from Guangzhou, China, (2000–2014). *Remote Sens. Environ.* 185, 243–257. doi: 10.1016/j.rse.2016.03.036

Zhu, Q., Wang, Y. P., Gao, S., Zhang, J., Li, M., Yang, Y., et al. (2017). Modeling morphological change in anthropogenically controlled estuaries. *Anthropocene* 17, 70–83. doi: 10.1016/j.ancene.2017.03.001

frontiers | Frontiers in Marine Science

TYPE Original Research
PUBLISHED 11 December 2023
DOI 10.3389/fmars.2023.1324273

OPEN ACCESS

EDITED BY
Chengji Shen,
Hohai University, China

REVIEWED BY
Qiang Chen,
Florida International University, United States
Junliang Gao,
Jiangsu University of Science and Technology, China
Seyed Masoud Mahmoudof,
Iranian National Institute for Oceanography and Atmospheric Science, Iran

*CORRESPONDENCE
Yanli He
heyanli0623@126.com
Hongfei Mao
maohongfei-gdou@qq.com

RECEIVED 19 October 2023
ACCEPTED 23 November 2023
PUBLISHED 11 December 2023

CITATION
Lin J, Hu L, He Y, Mao H, Wu G, Tian Z and Zhang D (2023) Verification of solitary wave numerical simulation and case study on interaction between solitary wave and semi-submerged structures based on SPH model.
Front. Mar. Sci. 10:1324273.
doi: 10.3389/fmars.2023.1324273

Verification of solitary wave numerical simulation and case study on interaction between solitary wave and semi-submerged structures based on SPH model

Jinbo Lin[1,2], Lili Hu[1], Yanli He[1]*, Hongfei Mao[1,2]*, Guanglin Wu[1], Zhenglin Tian[1] and Dandan Zhang[3]

[1]College of Ocean Engineering and Energy, Guangdong Ocean University, Zhanjiang, China, [2]Guangdong Provincial Key Laboratory of Intelligent Equipment for South China Sea Marine Ranching, Guangdong Ocean University, Zhanjiang, China, [3]Technical Center, Powerchina Hebei Electric Power Engineering CO., LTD., Shijiazhuang, China

Due to significant influence on the safety of marine structures, the interaction between extreme waves and structures is a crucial area of study in marine science. This paper focus on the verification of a solitary wave meshless SPH model and the application of the model on the interaction between solitary waves and semi-submersible structures. A solitary wave propagation model is established based on the SPH method combined with Rayleigh solitary wave theory, quintic kernel function, artificial viscosity, and Symplectic Method. The accuracy of the model is validated by comparing the calculated wave height with the theoretical value. The calculated results with relative particle spacing $H_0/d_0 \geq 20$ are in good agreement with the analytical solution. The simulated solitary wave is also quite stable with a maximum L_2 error 0.016. Therefore, the proposed SPH model can accurately simulate the propagation of the solitary waves. A case study on the interaction between solitary waves and semi-submersible platforms is conducted. The results show that the interaction between solitary waves and semi-submersible causes two double peaks with wave heights of 0.398 m and 0.410 m, respectively, induced by overtopping at the center of the platform. The wave transmission coefficient K_t is 0.880 due to that the solitary wave height reduces from 0.498 m to 0.438 m after the solitary wave propagates through the semi-submersible structure. In addition, the solitary wave induces significant vertical wave loads of the structure with a load amplitude of 0.688, while horizontal wave loads are relatively small with a load amplitude of 0.089. The solitary wave arrived the structure induces the upstream and downstream overtopping and forms a hydraulic jump leading to the complex flow field. The maximum velocity at the top and bottom of the structure is 2.2 m/s and 0.8 m/s respectively. Positive or negative vortex are formed at the bottom of the leading

edge, top and downstream of the structure with the maximum intensity 28 s^{-1} and -40 s^{-1}. In a word, the meshless SPH model can conveniently and accurately simulate the propagation of the solitary waves, and be applied to the investigation of the wave height, velocity, vorticity, wave load, and wave breaking of the interaction between solitary waves and structures in ocean engineering.

KEYWORDS

wave structure interaction, numerical simulation, solitary waves, semisubmersible structure, SPH

1 Introduction

The wave structure interactions are widely concerned in the marine science (Wang et al., 2011; Wang et al., 2013; Ding et al., 2020; Gao et al., 2020; Gao et al., 2021b; Gao et al., 2023; He et al., 2023) due to its significant effects on the safety and disaster prevention of marine and coastal engineering. For example, Sampath et al. (2016) simulated the large-scale solitary with incompressible SPH method. Rastgoftar et al. (2018) studied the drifted objects trajectory under tsunami waves based on an integrated numerical model. Mahmoudof and Azizpour (2020) established a linear formulation to estimate the wave reflection from plunging cliff coasts based on the field data. Mahmoudof et al. (2021, Mahmoudof and Hajivalie, 2021) analyzed the response of smooth submerged breakwaters triggered by irregular waves and the wave reflection from permeable rubble mound breakwater encountered with a bimodal wave regime based on experimental and field study. Especially, extreme waves such as tsunamis and typhoon waves have significant destructiveness due to its large wave heights, long wave lengths, and fast wave speed. The extreme waves acted on marine structures may cause the hydrodynamic loads of the structure to exceed its designed capacity resulting in huge damage or overturning accidents. These accidents not only induce huge loss of people's life and property but also serious marine pollution. Therefore, the hydrodynamic characteristics, wave loads, and dynamic responses of structure under extreme wave are always a hot topic in the ocean engineering. There are many type waves for extreme waves, such as solitary waves, focused waves, double solitary waves, N waves, and New Year waves. Researchers have conducted some research on waves. Ha et al. (2014) analyzed the climb around circular islands of solitary waves. Gao et al. (2020) investigated the harbor oscillations induced by focused transient wave groups by using FUNWAVE2.0. Wang et al. (2020) studied the secondary load cycle and inline forces on a vertical-mounted cylinder under New Year waves based on numerical simulation. Gao et al. (2021a) analyzed the hydrodynamic characteristics of transient harbor resonance triggered by double solitary waves with different wave parameters based on the fully nonlinear Boussinesq model. Among the various wave types of extreme waves, solitary waves have attracted widespread attention due to their similarity in wave characteristics with tsunamis, typhoon waves, and other extreme waves. In addition, solitary waves also can conveniently simulate extreme waves to analysis the interaction between extreme waves and ocean engineering structures due to the constant propagation speed, waveform invariance, vertical scaling ability, and strong nonlinear properties at large wave heights.

Researches on the characteristics of the solitary waves were widely conducted since the discovery of solitary waves in the 18th century. He J. H. et al. (2021) used theoretical analysis methods to study the solution properties of solitary waves propagating along non-smooth boundaries based on the fractal Korteweg de Vries (KdV) equation revealing that the peak value of solitary waves was weakly affected by non-smooth boundaries. Malek-Mohammadi and Testik (2015) proposed a new method for generating solitary waves with taking into account the evolutionary properties during wave generation by using a piston wave generator. The proposed method could generate more accurate solitary waves and had less attenuation during wave propagation by validating through wave tank experiments. Hunt-Raby et al. (2011) studied on the nearshore wave propagation, time variation of overtopping rate, and overtopping volume for the extreme wave overtopping of trapezoidal embankments through physical model experiments. Constantin et al. (2011) analyzed the pressure under solitary waves on a free water surface without swirling flow in a flat-bottomed water tank based on theoretical and experimental research. Xuan et al. (2013) used an improved wave generation method to generate two solitary waves with the same amplitude and peak separation distance in a wave tank, and analyzed the climbing characteristic of double solitary waves on a flat beach. Lo and Liu (2014) conducted solitary wave incident experiments in a wave tank, and studied the wave scattering of solitary waves propagating on a submerged horizontal plate. Chen et al. (2017) discussed the wave forces and wave run-up of solitary wave interaction with a group of vertical cylinders using a parallel particle-in-cell based incompressible flow solver PICIN. Ma et al. (2021) investigated the effects of water depths and wave heights on the free-surface oscillations within a harbor subjected to solitary waves through physical experiments combined with the wavelet-based bicoherence spectra technique.

Recently, numerical simulations are utilized to study solitary waves due to the low efficiency, high cost, and difficulty in getting rid of the influence of scale effect in physical model experiment.

Hsiao and Lin (2010); Wu et al. (2012), and Wu N. J. et al. (2014) investigated the solitary wave generation, propagation, interaction between solitary waves and submerged vertical obstacles, and the solitary waves overtopping characteristics of impermeable trapezoidal seawalls on a 1:20 inclined beach using a COBRAS (CORnell Breaking And Structure) numerical model based on finite point method. Tang et al. (2013); Zhang et al. (2015); Wu et al. (2016), and Higuera et al. (2018) numerically studied the generation of stable solitary by piston wave makers, swash flow dynamics generated by non-breaking solitary waves on steep slopes, influence of vegetation on solitary wave climbing on flat slopes, and influence of velocity on solitary wave motion using software such as OpenFOAM and Flow3D to solve the Reynolds averaged Navier Stokes (RANS) equation and shallow water equation based on finite volume methods combined with the k-epsilon turbulent closure and internal wave maker methods. Wu Y. T. et al. (2014) simulated the interaction between solitary waves and permeable breakwaters based on a three-dimensional large eddy simulation model, and conducted a study on the three-dimensional properties of wave flow through permeable breakwaters. Qu et al. (2017) used an internal wave source method based on a two-phase incompressible flow model combined with the volume of fluid (VOF) method to conduct numerical simulations of solitary wave climbing on shore and propagation on breakwaters. Wu and Hsiao (2018) generated stable and accurate solitary waves based on the Dirichlet boundary condition and internal mass source, and conducted numerical simulation on the propagation of solitary waves under constant water depth. Gao et al. (2019) investigated the transient resonance induced by solitary waves based on a fully nonlinear Boussinesq model. The effects of the offshore reef topography on the transient resonance induced are analyzed. Based on potential flow theory, Geng et al. (2021) used a parallel 3D boundary element method to calculate and simulate the interaction between incident solitary waves and a 3D submerged horizontal plate, and validated the model according to wave height, horizontal and vertical forces on the plate, and pitch moment.

The SPH model has unique advantages in dealing with large deformations and wave breaking due to the meshless nature. Therefore, some researchers have attempted to apply the SPH model to the investigation related to solitary wave at present (Li et al., 2012; Farhadi et al., 2016; He M. et al., 2021). Farahani and Dalrymple (2014) simulated the turbulent reverse horseshoe vortex structure caused by breaking solitary waves based on a 3D SPH model. Pan et al. (2015) analyzed the wave loads and motion responses of a tension leg platform under solitary waves based on a weakly compressible SPH method. Aristodemo et al. (2017) used weakly compressible SPH model to study the horizontal and vertical wave forces of an underwater horizontal cylinder under solitary waves, and proposed simple empirical formulas to calculate the hydrodynamic coefficients.

Although researchers have conducted research on the characteristics of solitary waves based on the SPH method, the capability of SPH method to simulate solitary waves in relevant studies has not been deeply validated considering different water depth and relative wave heights. This paper focuses on the verification of a solitary wave meshless SPH model and the application of the model on the interaction between solitary waves and semi-submersible structures. In this paper, a meshless numerical model of solitary waves, that could handle large deformation motion, wave surface fragmentation, and strong nonlinear waves, is established based on the SPH method combined with the Rayleigh solitary wave theory, quintic kernel function, artificial viscosity, and Symplectic Method. By comparing the calculated wave height results with the theoretical data and analyzing the stability of simulated solitary waves for a series test case with different water depths and relative wave heights, the accuracy of the SPH model in calculating solitary waves is thoroughly verified. Then, the validated model was used to simulate the interaction between solitary waves and semi-submersible platforms. The pattern of wave surface, wave load, and flow field were analyzed. Meanwhile, the application ability of the SPH model in the study of the interaction between solitary waves and ocean engineering structures was explored.

2 Methodology

2.1 Governing equations

The governing equations for viscous flow are made up with the Lagrangian continuity and momentum equation.

$$\frac{1}{\rho}\frac{D\rho}{Dt} + \nabla \cdot \boldsymbol{u} = 0 \tag{1}$$

$$\frac{D\boldsymbol{u}}{Dt} = -\frac{1}{\rho}\nabla P + \boldsymbol{g} + \boldsymbol{\Gamma} \tag{2}$$

where, u is the velocity vector, ρ is the density, P represents the pressure, Γ is the viscosity, g = (0, 0, -9.81) m/s^2 represents the gravitational acceleration.

The Lagrangian Navier-Stokes (N-S) equation can be obtained by desecrating the above two equations based on SPH method (Dalrymple and Rogers, 2006; Cunningham et al., 2014):

$$\frac{d\rho_i}{dt} = \sum_j m_j \boldsymbol{u}_{ij} \nabla_i W_{ij} \tag{3}$$

$$\frac{d\boldsymbol{u}_i}{dt} = -\sum_j m_j \left(\frac{P_i}{\rho_i^2} + \frac{P_j}{\rho_j^2} + \Gamma_{ij}\right) \nabla_i W_{ij} + g \tag{4}$$

where $u_{ij} = u_i - u_j$, is velocity difference between interpolation particle i and neighboring particle j. m represents particle mass. $W_{ij} = W(r_{ij}, h_s)$ represents kernel function, and $r_{ij} = r_i - r_j$ represents particle distance, h_s represents smooth length, and takes a value of 2.

To reduce density fluctuations in the continuity equation, a delta-SPH equation is adopted by introducing a correction term to the continuity equation (Crespo et al., 2015).

$$\frac{D\rho_i}{Dt} = \sum_{j=1}^{N} m_j \boldsymbol{u}_{ij} \cdot \nabla_i W_{ij} + 2\delta h_s \sum_{j=1}^{N} m_j \overline{c_{ab}} \left(\frac{\rho_i}{\rho_j} - 1\right) \frac{1}{\boldsymbol{r}_{ab}^2 + \eta^2} \cdot \nabla_i W_{ij} \tag{5}$$

where, $\eta^2 = 0.01h_s^2$, $\overline{c_{ab}} = (c_a + c_b)/2$, $\delta = 0.1$ represents a delta-SPH coefficient.

In this model, A quintic kernel function is adopted (Altomare et al., 2014; Saghatchi et al., 2014). The quintic kernel function provides a high-order interpolation characteristics to the calculation and maintain moderate computational complexity.

$$W(\boldsymbol{r}-\boldsymbol{r}',h)=W(R,\ h_s)=\alpha_d\left(1-\frac{R}{2}\right)^4(2R+1)\qquad 0\le R\le 2 \tag{6}$$

where, $\alpha_d=\frac{7}{4\pi h_s^2}$ for 2D model.

To maintain the explicit features and increase computational efficiency, a state equation is introduced and calculated instead of the pressure Poisson equation. Then the pressure is calculated according to particle density. The Tait equation of state (Canelas et al., 2015) is $P=B\left[(\rho/\rho_0)^{\gamma}-1\right]$, where $B=c_0^2\rho_0/\gamma$, $\rho_0=1000$ kg/m^3 represents the reference density, $\gamma=7$. $c_0=c(\rho_0)=\sqrt{(\partial P/\partial\rho)|\rho_0}$ is sound speed at reference density.

2.2 Viscous treatment

The artificial viscosity is widely used in SPH method due to its simple form and ability to prevent nonphysical penetration between approaching particles.

The artificial viscosity can be written as follows (Monaghan, 1992).

$$\Gamma_{ij}=\begin{cases}\frac{-\alpha\overline{c_{ij}}\mu_{ij}}{\overline{\rho_{ij}}} & \boldsymbol{v}_{ij}\cdot\boldsymbol{r}_{ij}<0\\ 0 & \boldsymbol{v}_{ij}\cdot\boldsymbol{r}_{ij}>0\end{cases} \tag{7}$$

$$\mu_{ij}=\frac{h_s\boldsymbol{v}_{ij}\cdot\boldsymbol{r}_{ij}}{r_{ij}^2+-0.01h_s^2} \tag{8}$$

where, $\alpha=0.01$ represents artificial viscosity coefficient. $\boldsymbol{r}_i$ and $\boldsymbol{v}_i$ represent position vector and the particle velocity, respectively. $\overline{c_{ij}}=0.5(c_i+c_j)$ is the average speed of sound.

2.3 Time integral

The equations are solved using the Symplectic method (Omidvar et al., 2012) which is time reversible without the influence of friction or viscosity and has explicit second-order accuracy. The variable time step method is used for the time step.

The equations of N-S and motion can be written as:

$$\begin{cases}\frac{d\boldsymbol{u}_i}{dt}=\boldsymbol{F}_i\\ \frac{d\rho_i}{dt}=D_i\\ \frac{d\boldsymbol{r}_i}{dt}=\boldsymbol{u}_i\end{cases} \tag{9}$$

A correction is introduced into the motion equation (Domínguez et al, 2011):

$$\frac{d\boldsymbol{r}_i}{dt}=\boldsymbol{u}_i+\epsilon\sum_{j=1}^{N}\frac{m_j}{\overline{\rho_{IJ}}}\boldsymbol{u}_{ji}W_{ij} \tag{10}$$

where, $\overline{\rho_{IJ}}=(\rho_i+\rho_j)/2$, $\epsilon=0.5$. This scheme can ensure that adjacent particles move at roughly the same speed avoiding particles with different speed getting too close.

The equation (9) is solved by the predictor–corrector algorithm (Gomez-Gesteira et al., 2012). Set $\boldsymbol{A}$ represents $\boldsymbol{u}$, $\boldsymbol{r}$, ρ respectively; $\boldsymbol{B}$ represents $\boldsymbol{F}$, $\boldsymbol{u}$, D. The predict step is:

$$\boldsymbol{A}_i^{n+1/2}=\boldsymbol{A}_i^n+(\Delta t\boldsymbol{B}_i^n)/2 \tag{11}$$

Then the pressure of half-time step calculated by the equation of state after those variables of half-time step are corrected.

$$\boldsymbol{A}_i^{n+1/2}=\boldsymbol{A}_i^n+(\Delta t\boldsymbol{B}_i^{n+1/2})/2 \tag{12}$$

Finally, next step variables calculated as:

$$\boldsymbol{A}_i^{n+1}=2\boldsymbol{A}_i^{n+1/2}-\boldsymbol{A}_i^n \tag{13}$$

Then, the pressure solved using the equation of state according to ρ_i^{n+1}.

CFL, force, and viscous diffusion should be considered for the time step Δtin SPH. A variable time step (Domínguez et al, 2011) can be calculated as follows:

$$\begin{aligned}\Delta t&=0.1\min(\Delta t_f,\ \Delta t_{cv});\ \Delta t_f=\frac{\min}{i}(\sqrt{h/|f_i|});\ \Delta t_{cv}\\&=\frac{\min}{i}\frac{h}{C_s+\frac{\max}{j}|hu_{ij}r_{ij}/(r_{ij}^2+\eta^2)|}\end{aligned} \tag{14}$$

2.4 Wave maker

The solitary waves are generated by a wave paddle according on the Rayleigh theory (Domínguez et al., 2019). The main assumption is the speed of the wave paddle is the same as horizontal average velocity of wave crest particles.

$$u(x_s,\ t)=\frac{dx_s}{dt} \tag{15}$$

where, $u(x_s, t)$ represents the average velocity in water depth of particles, x_s represents the wave paddle displacement.

$$u(x_s,\ t)=c_w\eta\frac{(x_s,\ t)}{d+\eta(x_s,\ t)} \tag{16}$$

where, d refers to water depth, c_w is wave speed, η refers to free surface.

The wave paddle displacement equation is obtained by combining equations (15) and (16) and integrating it.

$$x_s(t)=\frac{2H}{kd}\tanh[k(ct-x_s(t))] \tag{17}$$

where, k represents the edge coefficient. The edge coefficient describes the way that the free surface elevation tends toward the average wave surface at infinity. Then, the distribution of solitary waves expresses as follow.

$$\eta(x_s,\ t)=H\mathrm{sech}^2[k(ct-x_s)] \tag{18}$$

Above equation is an implicit equation that can be solved in several ways. Among these schemes, Rayleigh theory (Guizien and Barthélemy, 2002) has small amplitude loss during solitary wave propagation. According to Rayleigh theory, the theoretical surface elevation can be rewritten as:

$$\eta(x_s,\ t) = H\mathrm{sech}^2\left[k\left(c\left[t-\frac{T_f}{2}\right]+2\sqrt{\frac{H[H+d]}{3}}-x_s\right)\right] \quad (19)$$

where, $2\sqrt{H(H+d)/3}$ equals to the half wave paddle stroke. T_f is the solitary waves generation time. The parameters in the above equation can calculated according to follow equations:

$$c = \sqrt{g(H+d)} \quad (20)$$

$$T_f = \frac{2}{kc}\left(3.8+\frac{H}{d}\right) \quad (21)$$

$$x_s(t) = \frac{H}{k}\frac{\mathrm{tgh}\left(kc(t-T_f)\right)}{d+H\left[1-\mathrm{tgh}^2\left(kc(t-T_f)\right)\right]} \quad (22)$$

$$k = \sqrt{\frac{3H}{4d^2(H+d)}} \quad (23)$$

In the model, a dynamic boundary method (Crespo et al., 2007) is adopted to deal with the wall boundary. The dynamic boundary method is very suit to simulation with complex boundaries due to the simple implementation and low computational complexity.

23 Model validation

3.1 Model layout

To validate the model, a series of solitary wave test cases with initial water depths d_0 = 1.0 m, 2.0 m, 5.0 m, 10.0 m, and relative wave heights H_0/d_0 = 0.1, 0.3, and 0.5 are simulated. The calculated wave heights at six measurement point of every test case are compared with the theoretical data obtained from equation (19). The length of the numerical water tank is L_0/d_0 = 65. The height H/d_0 = 2.0. A schematic diagram showing a propagating solitary wave is depicted in Figure 1. The particle spacing is set to $H_0/\Delta x$ = 5, 10, 20, 40, and 80, respectively. The output time interval is 0.15 s, 0.15 s, 0.25 s, and 0.35 s with the total calculation time of 30 s, 30 s, 50 s, and 70 s for the test cases of 1.0 m, 2.0 m, 5.0 m, and 10.0 m water depth.

3.2 Qualitative comparison between the calculated results and analytical solutions

Figures 2-5 compare the wave heights between SPH results and exact solution at six measurement points x/H_0 = 2, 6, 10, 20, 30, and 50 corresponding figures (a), (b), (c), (d), (e), and (f). The lines with different color represent the calculation results of the model with relative particle spacing of $H_0/\Delta x$ = 5, 10, 20, 40, and 80, respectively. Some measuring points in Figures 2-5 experience the second and third rising of wave surface inducing the second and third wave peaks after the solitary wave passes through. The reason is the downstream boundary in the SPH model is a non-absorbing boundary. The solitary wave propagated downstream is reflected and reaches the measuring point resulting in the water level rising again. The propagation speed of solitary waves gradually slows down with the increasing water depth resulting in the arriving time of solitary waves gradually delays. The calculated solitary wave results are slightly affected by the water depth. As the water depth increases, a slight phase deviation between the calculation results and the analytical solution appears. The deviation slightly increases with the increase of water depth while the deviation is not significant.

For H_0/d_0 = 0.1, the calculation results of the wave heights for different relative particle spacing are not significantly different with a good agreement with the analytical solution. For H_0/d_0 = 0.3, the error of calculated wave heights is relatively large with the relative particle spacing $H_0/\Delta x < 20$ while the calculated results have little difference and are in good agreement with the analytical solution with $H_0/\Delta x \geq 20$. For the relative wave height 0.5, there is a significant difference in the numerical calculation results for different relative particle spacing. The calculated results also have a significant error with $H_0/\Delta x < 20$ while the calculated results are basically consistent and in good agreement with the analytical solution with $H_0/\Delta x \geq 20$.

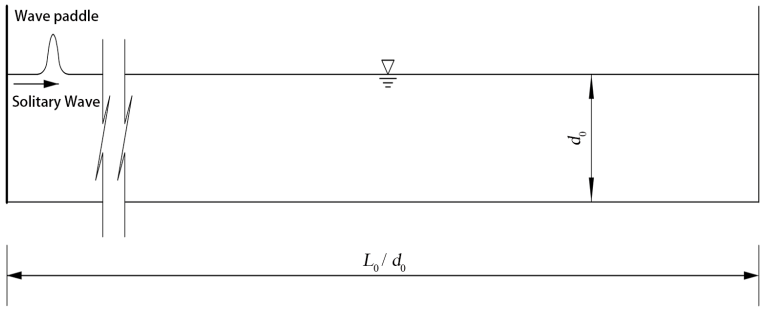

FIGURE 1
Layout of the validation model.

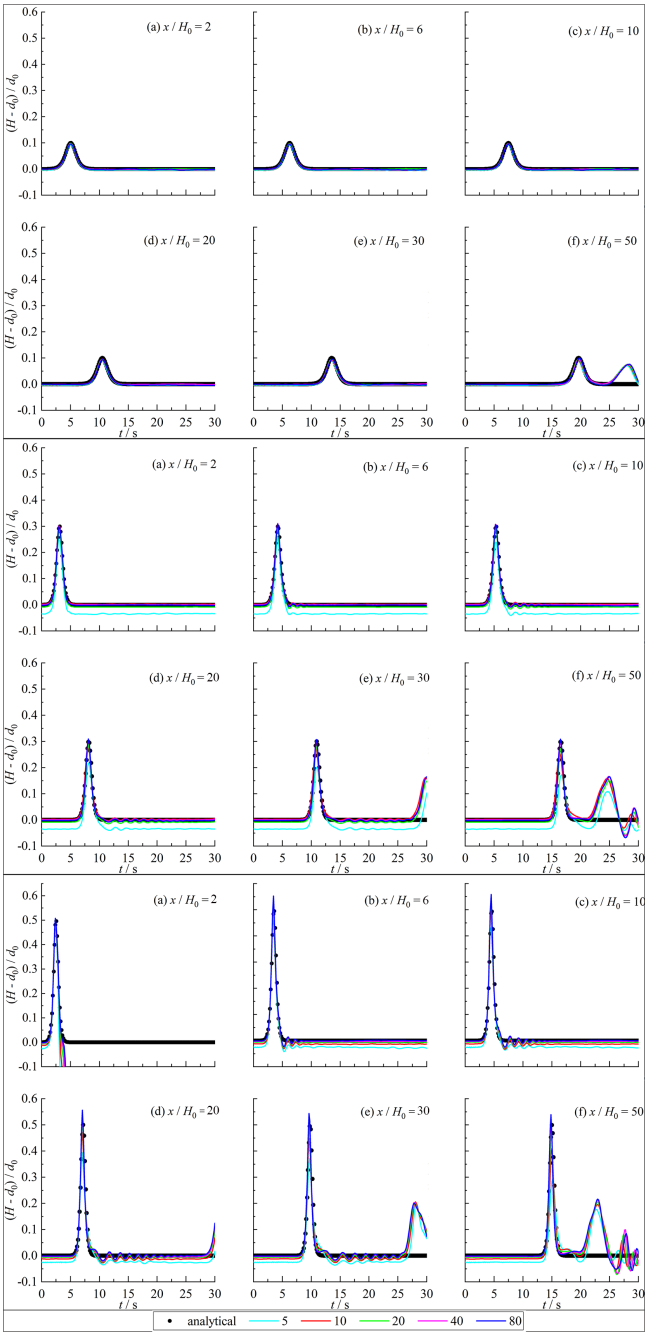

FIGURE 2
Comparison of the wave height between SPH results and exact solution for d_0 = 1.0 m.

The calculated solitary wave peaks with different relative particle spacing are not significantly different and in good agreement with the analytical solution with the small relative wave height (H_0/d_0 = 0.1). As the relative wave height increases (H_0/d_0 = 0.3, 0.5), the calculated solitary wave peaks with small relative particle spacing are underestimated with a rising error. In addition, the calculated wave peak results with different relative particle spacing values are not overestimated for the test cases with little relative wave heights (H_0/d_0 = 0.1 and 0.3) while the calculated wave peaks with large relative particle spacing ($H_0/\Delta x$ = 80) is higher than the analytical solution for the test cases with large relative wave height (H_0/d_0 = 0.5). The reason is that the larger relative particle spacing leads to a larger number of neighboring particles, which increases particle viscosity and ultimately leads to higher wave peaks. For the investigation of wave loads, dynamic responses, and mooring forces related to the marine engineering under the solitary waves, a most unfavorable conditions usually need to be considered. Therefore, the simulation of solitary waves based on the SPH model should take the relative particle spacing $H_0/\Delta x \geq 20$. At this condition, the calculation results are more accurate and more advantageous for engineering applications.

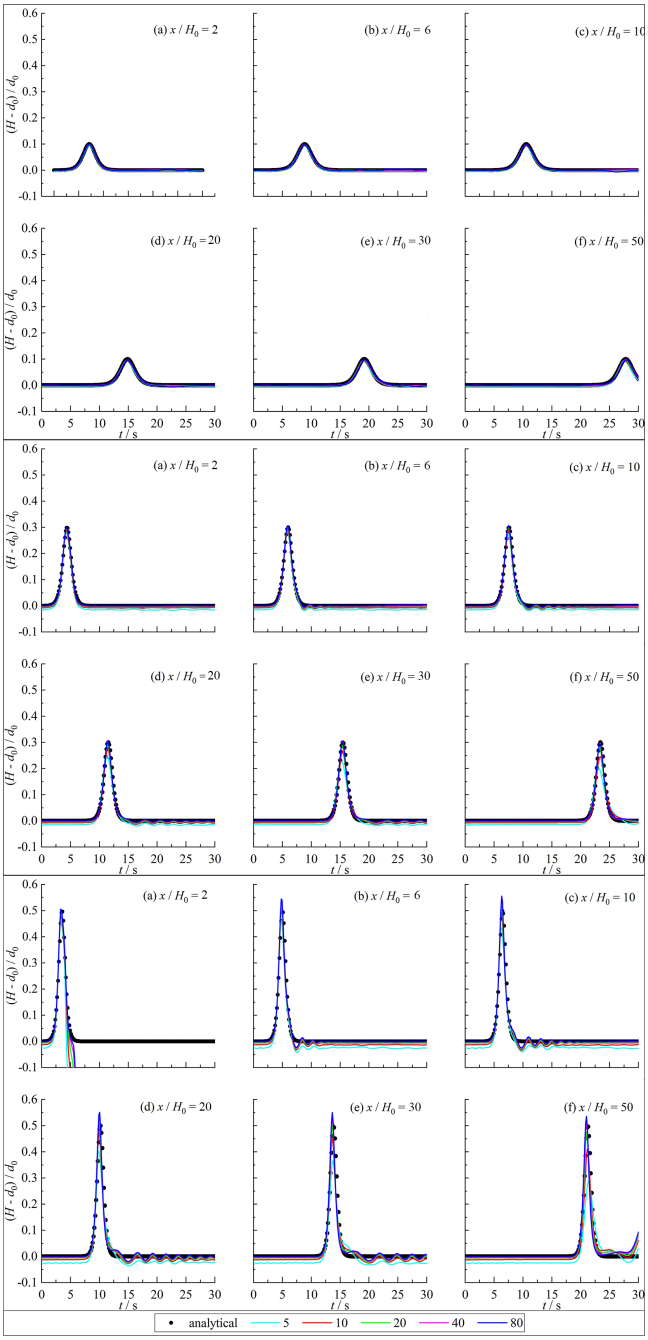

FIGURE 3
Comparison of the wave height between SPH results and exact solution for d_0 = 2.0 m.

3.3 Quantitative comparison between the calculated results and analytical solutions

To quantitatively analyze the calculation errors, Tables 1-4 provide the L_2 errors between the calculated wave heights of the SPH model and the analytical solution.

$$L_2 = \sqrt{\frac{1}{N}\sum_{t=0}^{N}\left(\frac{h_t^n - h_t^e}{h_t^e}\right)^2} \tag{24}$$

where h_t^n and h_t^e are the numerical result and the analytical solution at time t, respectively; N is the sample numbers.

The L_2 errors decreases and gradually stabilizes with the increase of relative particle spacing. The calculated results with different water depth indicate that the relative error is relatively large with a maximum value of 0.094 for $H_0/\Delta x = 5$. The calculation error is basically stable for $H_0/\Delta x \geq 20$. The minimum values of L_2 error for relative wave heights 0.1, 0.3, and 0.5 are 0.001, 0.002, and 0.007, respectively. The L_2 error gradually increases with the

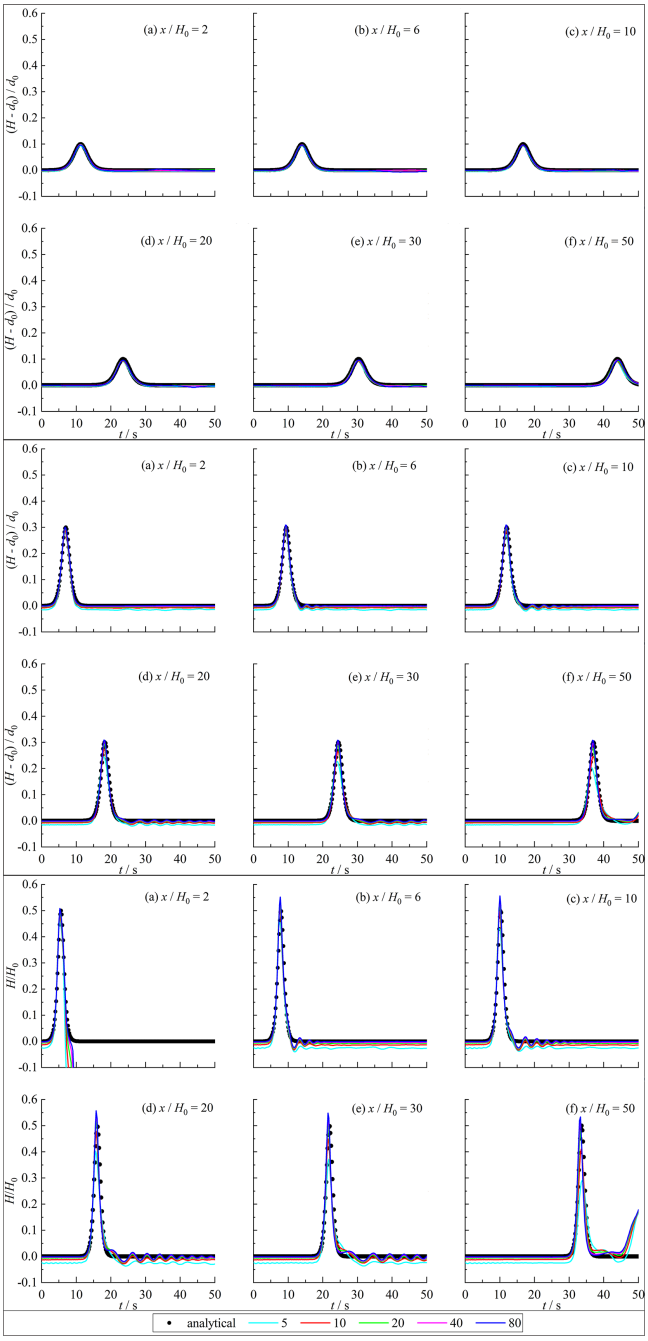

FIGURE 4
Comparison of the wave height between SPH results and exact solution for d_0 = 5.0 m.

increase of wave height. The calculation error for the model of H_0/d_0 = 0.1 is the smallest with a minimum value 0.001. The maximum error is reached for the model of H_0/d_0 = 0.5 with a maximum value of 0.093. For H_0/d_0 = 0.1, the water depth has little effect on the calculation error of the model. The calculation error of the SPH model with different water depth is basically the same with a maximum error 0.005 and a minimum error 0.001. For H_0/d_0 = 0.3, the calculation error of the model with 1 m water depth is highest with a maximum value 0.094 while the calculation error of the model with 2 m water depth is relatively small and gradually increases with the increase of water depth with a minimum error 0.002 and a maximum error 0.038. For H_0/d_0 = 0.5, the calculation error of the model with 1 m water depth is highest with a maximum value of 0.093 while the calculation error of the model with 2 m water depth is relatively small and gradually increases with the increase of water depth with a minimum error 0.007 and a maximum error 0.081. For H_0/d_0 = 0.1, the L_2 error gradually increases with the increase of measurement point distance, but the difference is not significant with a maximum difference 0.001 and a minimum difference 0. The L_2 error of the model for H_0/d_0 = 0.3 also gradually increases with the

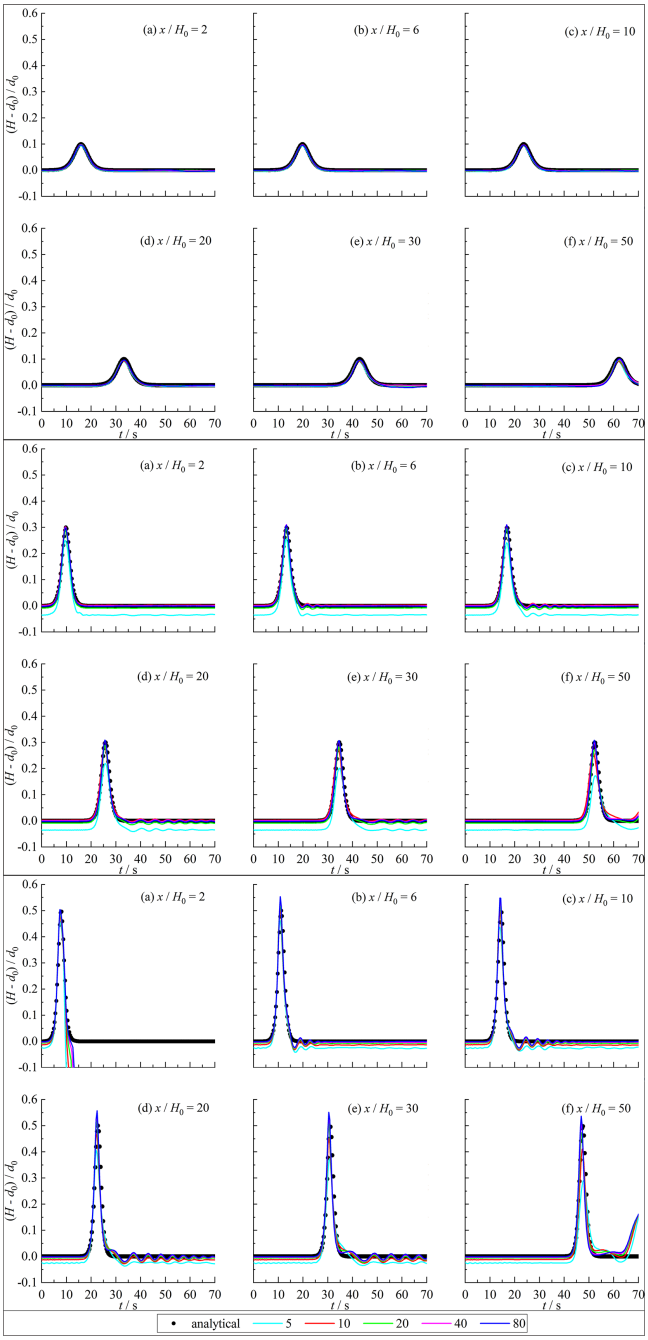

FIGURE 5
Comparison of the wave height between SPH results and exact solution for $d_{O\ =}$ 10.0 m.

increase of measurement point distance with a maximum difference 0.100 and a minimum difference 0. For $H_0/d_{0\ =}$ 0.5, the L_2 error of the calculated results also increases with the increase of measurement point distance with a maximum difference 0.016 and a minimum difference 0.

In summary, the model can accurately simulate the propagation of the solitary waves. The calculated results of the SPH model with the relative particle spacing greater than or equal to 20 is in good agreement with the analytical solution. Therefore, the relative particle spacing should be greater than or equal to 20 for the simulation of the solitary waves based on the SPH model. The error of the calculated results gradually increases with the increase of measurement point distance, but the change is not significant with a maximum difference 0.016 of the L_2 error. The influence of water depth on the L_2 error of the calculated results is relatively complex. The water depth has little effect on the calculation results with a small relative wave height. As the relative wave height increases, the calculation error with small water depth (1 m) is larger. The

10.3389/fmars.2023.1324273

TABLE 1 L_2 errors of the wave height for water depth 1 m.

H_0/d_0		0.1					0.3					0.5				
$H_0/\Delta x$		5	10	20	40	80	5	10	20	40	80	5	10	20	40	80
x/H_0	2	.005	.002	.001	.002	.002	.093	.086	.087	.086	.086	.098	.089	.087	.087	.086
	6	.005	.002	.001	.002	.002	.093	.086	.087	.086	.086	.091	.088	.087	.087	.087
	10	.005	.002	.001	.002	.002	.093	.086	.087	.086	.086	.090	.088	.088	.087	.087
	20	.005	.003	.002	.001	.004	.093	.086	.087	.086	.086	.091	.089	.088	.088	.088
	30	.005	.003	.002	.002	.002	.093	.087	.087	.086	.086	.091	.089	.088	.089	.089
	50	.005	.003	.002	.002	.003	.094	.087	.087	.086	.086	.093	.088	.088	.089	.090

calculation error with water depth greater than or equal to 2 m is smaller and slightly increases with water depth increase. The reason may be that the increase in water depth reduces the relative error.

3.4 Analysis of the attenuation of solitary wave peaks along the distance of measurement points

Figure 6 shows the calculated solitary wave peaks at different measurement points with a relative particle spacing of 20 under different water depths and relative wave heights. The error of calculated solitary wave peaks increases with the increase of relative wave height. The calculated wave peaks with the relative wave height 0.1 are in good agreement with the theoretical value while the wave peaks slightly decrease with the increase of the distance along the measuring point. The error of wave peaks with relative wave height 0.3 is slightly larger. The wave peaks first increase and then decrease with the distance along the measurement point increases. For the relative wave height 0.5, the error of wave peaks is large with that the peak values of the solitary wave also increase and then decrease with the distance along the measurement point increases. The peak value is the highest for $x/H_0 = 5$ and the peak value at the measurement points between 5 and 30 exceeds the analytical value. The calculated wave peaks do not vary significantly with water depth. The calculated results for water depths 1 m and 10 m differ largely from the theoretical values compared to the calculated results for water depths 2 m and 5 m. The errors of calculated wave peaks increase along the measurement points for the model of relative wave height 0.1 while the errors of calculated wave peak decrease and then increase for the model of relative wave heights 0.3 and 0.5 with the smallest error between $x/H_0 = 2$ - 5.

Table 5 gives the L_2 error of calculated solitary wave peaks for SPH model with different water depths and relative wave heights. The errors of the wave peaks gradually increase with the increase of relative wave height but the increasing value is not significant with a minimum L_2 error 0.033 and maximum L_2 error 0.052. The wave peaks calculated by the SPH model does not vary significantly with water depth. The L_2 errors for the model of water depths 1 m and 10 m are slightly larger with a maximum value 0.052 while it is smaller for the model of water depths 2 m and 5 m with a minimum value 0.033. The standard deviations of calculated solitary wave peaks are given in Table 6. The standard deviations increase with the increase of water depth and wave height, and reach the maximum at the model of water depth 10 m with relative wave height 0.5. The maximum standard deviation is 0.021 while the minimum value is 0.001.

In short, the calculated solitary wave peaks with small errors decrease along the measurement points distance. Meanwhile the solitary wave peaks are underestimated slightly for the model with small relative wave heights. As the relative wave heights increases, the calculated wave peaks show a trend of upward and then downward. The calculated results will overestimate the wave

TABLE 2 L_2 errors of the wave height for water depth 2 m.

H_0/d_0		0.1					0.3					0.5				
$H_0/\Delta x$		5	10	20	40	80	5	10	20	40	80	5	10	20	40	80
x/H_0	2	.005	.002	.001	.001	.002	.016	.008	.005	.003	.002	.080	.076	.074	.074	.073
	6	.005	.002	.001	.002	.002	.015	.009	.005	.004	.004	.078	.075	.074	.074	.074
	10	.005	.002	.002	.001	.003	.015	.009	.006	.005	.004	.078	.076	.075	.075	.075
	20	.005	.003	.002	.002	.003	.017	.009	.007	.005	.005	.078	.076	.076	.075	.075
	30	.005	.003	.002	.002	.003	.018	.009	.007	.005	.005	.079	.076	.076	.076	.076
	50	.006	.003	.002	.002	.002	.021	.011	.008	.005	.005	.081	.075	.075	.076	.077

TABLE 3 L_2 errors of the wave height for water depth 5 m.

H_0/d_0		0.1					0.3					0.5				
$H_0/\Delta x$		5	10	20	40	80	5	10	20	40	80	5	10	20	40	80
x/H_0	2	.005	.002	.001	.002	.002	.015	.008	.005	.003	.002	.033	.018	.011	.008	.007
	6	.005	.002	.001	.001	.003	.015	.009	.005	.004	.004	.028	.018	.013	.012	.011
	10	.005	.002	.001	.002	.002	.016	.009	.006	.004	.004	.028	.019	.016	.014	.014
	20	.005	.003	.002	.002	.003	.017	.009	.006	.005	.005	.029	.021	.018	.018	.018
	30	.005	.003	.002	.002	.003	.018	.009	.007	.005	.005	.030	.021	.019	.019	.020
	50	.006	.003	.002	.002	.003	.021	.011	.008	.006	.007	.034	.018	.017	.020	.023

peaks within a certain distance in the middle of the channel while the wave peaks will be underestimated at the beginning and end of the channel. The calculated wave peaks do not change significantly with water depth. The errors of the model with the large and small water depths are slightly larger than that the water depth is moderate. The maximum and minimum L_2 errors are 0.052 and 0.033, respectively. The errors of calculated wave peak along the measurement points gradually increase for the model with small relative wave height while the errors first decrease and then increase for the model with large relative wave height. The error is the smallest between x/H_0 = 2 - 5.

4 Case study on the interaction between the solitary waves and the semi-submerged structures

4.1 Model validation

A test case of solitary waves interaction with partially submerged rectangular obstacle is simulated to validate the model. The calculated wave heights are compared with the OpenFOAM results (Ma et al., 2019). The numerical flume is 2.0 m height and 100 m length. The initial water depth is 1.0 m. The wave height is 0.1 m. The rectangular structure is 5.0 m × 0.6 m with a center coordinate (32.5 m, 0.9 m). The particle spacing sets to 0.01 m. Figure 7 shows the comparing of wave height between the OpenFOAM results and SPH model at two points x = 1 m and 59 m. The phase and magnitude of the calculated wave height are in well agreement with the OpenFOAM results. The maximum absolute error is 0.004 m with relative error 0.4%.

4.2 Model layout

To analyze the characteristics of wave surface, velocity, vorticity, and wave loads of the interaction between solitary waves and semi-submersible structure, a 300 m × 10 m 2D rectangular numerical wave tank with a semi-submersible platform is adopted. The water depth is d_0 = 5.0 m. The size of the semi-submersible platform fixed above the still water surface is 5.0 m × 0.6 m with center coordinates (52.5 m, 0.9 m). The submerged height (distance from the bottom of the structure to the water surface) of the structure is 0.4 m. The model layout is shown in Figure 8. The relative wave height H_0/d_0 = 0.1. The relative particle spacing $H_0/\Delta x$ = 50.

4.3 Wave heights

Figure 9 shows the time history of the wave heights at the upstream (x = 35) and downstream (x = 60) measurement points of the structure. At t = 7 s, the solitary wave arrives the upstream measuring point inducing the wave height to rise. The wave height of upstream measuring point reaches maximum value 0.498 m at t = 15

TABLE 4 L_2 errors of the wave height for water depth 10 m.

H_0/d_0		0.1					0.3					0.5				
$H_0/\Delta x$		5	10	20	40	80	5	10	20	40	80	5	10	20	40	80
x/H_0	2	.005	.002	.001	.002	.002	.036	.004	.009	.003	.003	.033	.019	.011	.009	.008
	6	.005	.002	.001	.002	.002	.035	.005	.010	.004	.004	.028	.018	.014	.012	.012
	10	.005	.002	.001	.002	.002	.035	.006	.010	.004	.005	.028	.019	.016	.014	.015
	20	.005	.003	.002	.002	.002	.035	.008	.010	.005	.005	.029	.021	.019	.018	.018
	30	.005	.003	.002	.002	.004	.036	.010	.010	.006	.005	.029	.021	.020	.020	.021
	50	.006	.003	.002	.002	.004	.038	.014	.009	.007	.005	.034	.018	.017	.020	.024

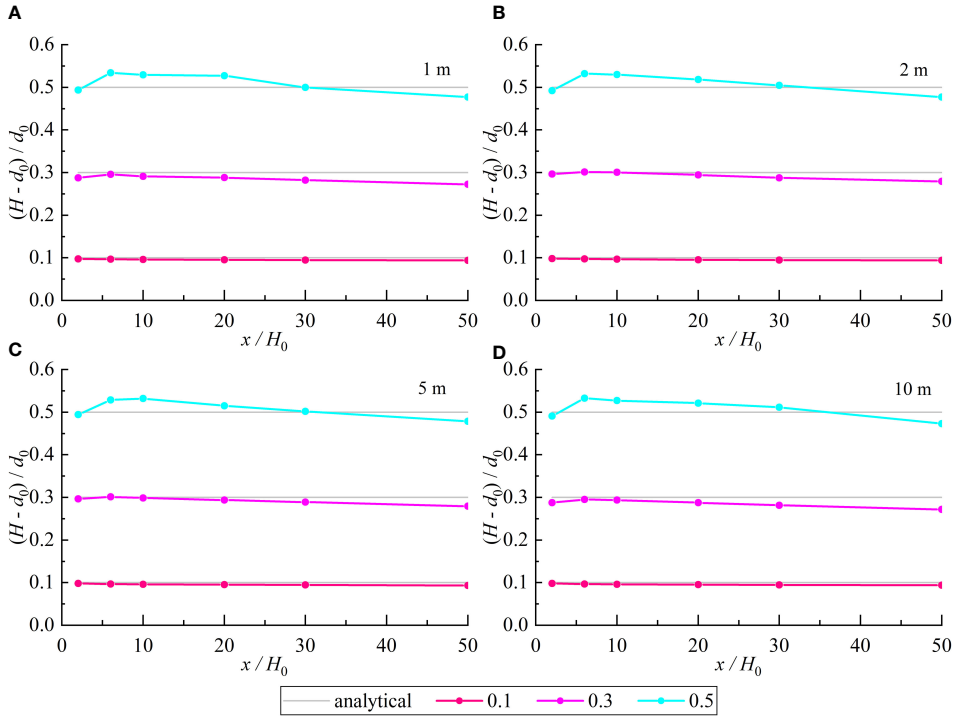

FIGURE 6
Solitary wave peak along the channel for water depth of 1 m, 2 m, 5 m, and 10 m **(A–D)**.

s. Then the solitary wave continues to propagate downstream through the upstream measuring point, and falls to form a wave surface oscillation. The oscillation gradually attenuates over time. At t = 10 s, the solitary wave crosses the structure and arrives the downstream measuring point inducing the wave height to rise. The solitary wave reaches the maximum value 0.438 m at t = 18 s. Then the wave continues to propagate downstream through the downstream measurement point, and drops with a gradually decaying wave surface oscillation.

Figure 10 gives the time history of the wave heights at the center of the semi-submersible platform x = 52.5 m. The initial wave height is -0.4 m of the platform bottom elevation due to the structure being submerged in water. At t = 16 s, the semi-submersible structure experiences overtopping. The solitary wave climbs to the top of the platform and arrives the measuring point inducing the wave surface to rapidly rise. The changes in wave surface are complex with two double peaks with a peak value of 0.398 m at t = 20 s and a maximum value 0.410 m at t = 33 s due to the fluctuation of the wave surface.

4.4 Wave loads

Figures 11 shows the time history of the horizontal and vertical wave loads coefficient C_x and C_z of the semi-submersible structures.

$$C_x = \frac{F_x}{\rho_0 g A}, \quad C_z = \frac{F_z}{\rho_0 g A} \tag{25}$$

where, A=0.6 m × 5 m is the area of the structure;F_x and F_z are the horizontal and vertical wave loads on structures. F_x and F_z are calculated by summing up the force of all the structure particles. The equations are:

$$\boldsymbol{F}_a = \frac{d\boldsymbol{u}_a}{dt} = -\sum_b m_b \left(\frac{P_b}{\rho_b^2} + \frac{P_a}{\rho_a^2} + \Pi_{ab} \right) \nabla_a W_{ab} + \boldsymbol{g} \tag{26}$$

TABLE 5 L_2 errors of solitary wave peak.

Water depth	Relative wave height		
	0.1	0.3	0.5
1 m	0.045	0.052	0.047
2 m	0.043	0.034	0.044
5 m	0.044	0.033	0.041
10 m	0.044	0.052	0.046

TABLE 6 Standard deviation of solitary wave peak.

Water depth	Relative wave height		
	0.1	0.3	0.5
1 m	0.001	0.007	0.001
2 m	0.001	0.008	0.020
5 m	0.002	0.007	0.019
10 m	0.001	0.008	0.021

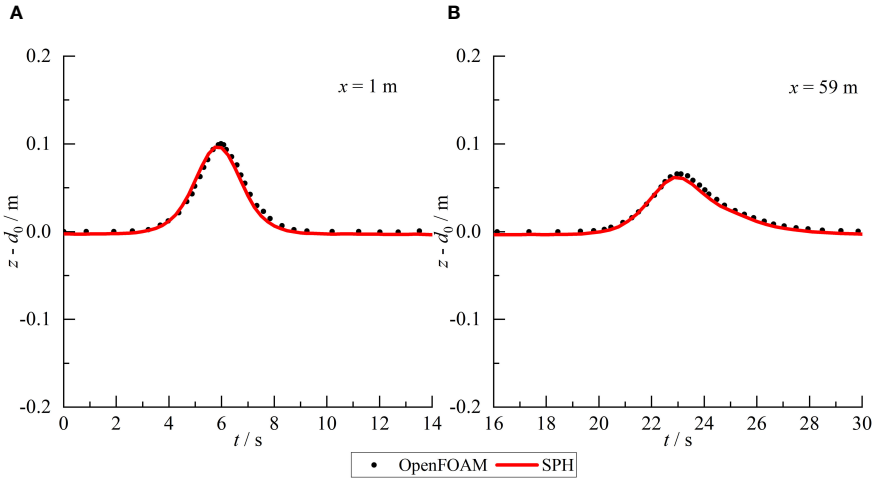

FIGURE 7
Comparison of the wave surface between SPH results and OpenFOAM results at position of x=1 m **(A)** and x =59 m **(B)**.

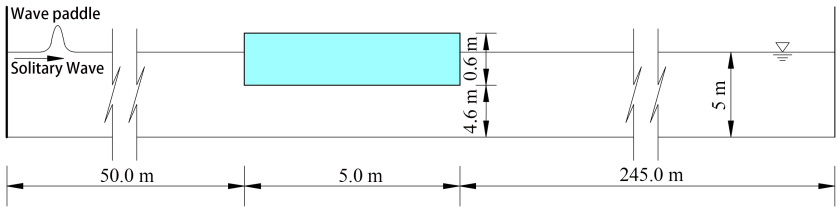

FIGURE 8
Schematic diagrams of the model.

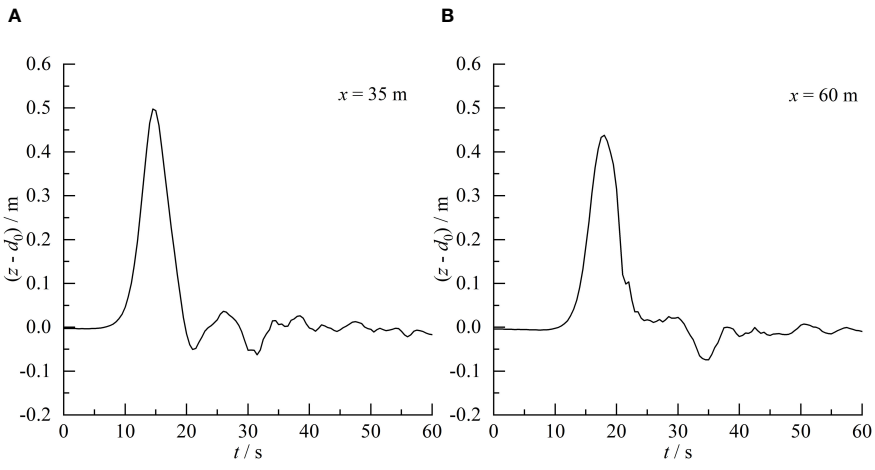

FIGURE 9
Time history of the wave height at position of x =35 m **(A)** and x=60 m **(B)**.

$$\boldsymbol{F} = m\sum \frac{d\boldsymbol{u}_a}{dt} \tag{27}$$

where, $F(F_x, F_z)$ is the total force acting on the structure. F_a is the force acting on arbitrary particle a that constitutes the structure.

At t = 10 s, the solitary wave arrives the semi-submersible platform resulting in a rapid increase in the horizontal force. The horizontal wave load reaches the maximum 0.066 at t = 16 s. The horizontal force on the platform rapidly decreased until it reaches the minimum -0.023 at t = 19 s. The horizontal wave load amplitude is 0.089. Then, the solitary wave passes through the structure and

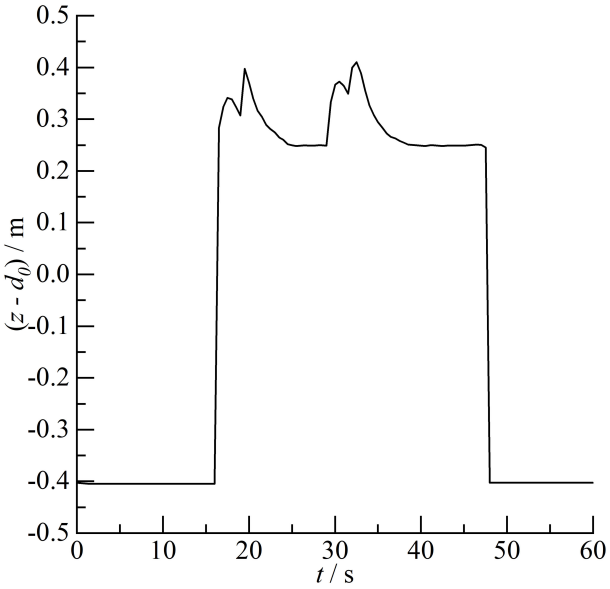

FIGURE 10
Time history of the wave height at the center of the structure.

continues to propagate downstream. The horizontal wave load also experiences an oscillation with a decreasing amplitude due to the wave surface oscillation induced by the interaction between the solitary waves and the platform. Similar to the horizontal wave loads, the solitary wave arrives the semi-submersible structure at t = 10 s inducing a rapid increase in the vertical wave loads. The vertical wave loads reach the maximum 0.635 at t = 16 s. The vertical forces rapidly decreases until it reaches the minimum -0.053 at t = 24 s. The vertical wave loads amplitude is 0.688. Similarly, the wave surface oscillation also causes an oscillation with a decreasing amplitude in the vertical wave loads due to the interaction between solitary waves and the structure. Obviously, the oscillation amplitude of the vertical wave loads is greater than the horizontal wave loads. In summary, both the horizontal and vertical wave loads on the semi-submersible platform exhibit positive and negative pressures with vertical and horizontal wave loads amplitudes 0.688 and 0.089, respectively. The vertical wave loads are significantly larger than the horizontal wave load. Therefore, the vertical forces on the platform should be the control stress for the structural design.

4.5 Velocity field

The velocity fields around the semi-submersible platform at six different instants are given in Figure 12. In Figure 12, u represents the velocity (m/s) in the x-axis direction. At t = 15 s, the solitary wave arrives the structure and climbs to the top of the structure inducing overtopping. Simultaneously, partial solitary waves pass through the bottom of the structure causing uplift of downstream wave surface. The velocity at the top of the structure is relatively high with a value 1.2 m/s while it is relatively small at the bottom of the structure with a value 0.5 m/s. The downstream wave surface rises and forms overtopping spreading upstream at t = 16 s. The upstream overtopping at the top of the structure increases. The velocity at the top and bottom of the structure increases to1.9 m/s and 0.7 m/s, respectively. Until t = 17.5 s, the solitary wave completely arrives the structure. The upstream wave surface begins to decline while the downstream wave surface continues to rise. The upstream and downstream overtopping approaches and collides to form a hydraulic jump. The velocity at the top and bottom of the structure reaches the maximum value 2.2 m/s and 0.8 m/s. At t = 18.5 s, the solitary wave passes through the structure causing the upstream wave surface to decrease continually and the downstream wave surface to rise continually. The hydraulic jump at the top of the structure develops and propagates upstream. The water at the top of the structure flows into the downstream lead to the decreasing of the overtopping. The velocity at the top and bottom of the structure decreases to 1.6 m/s and 0.7 m/s. Both the upstream and downstream wave surfaces drop at t = 19.5 s. Meanwhile, the overtopping continually flows into downstream flume leading to the declining of the wave surface on the top of the structure. The velocity continues to decrease. The maximum

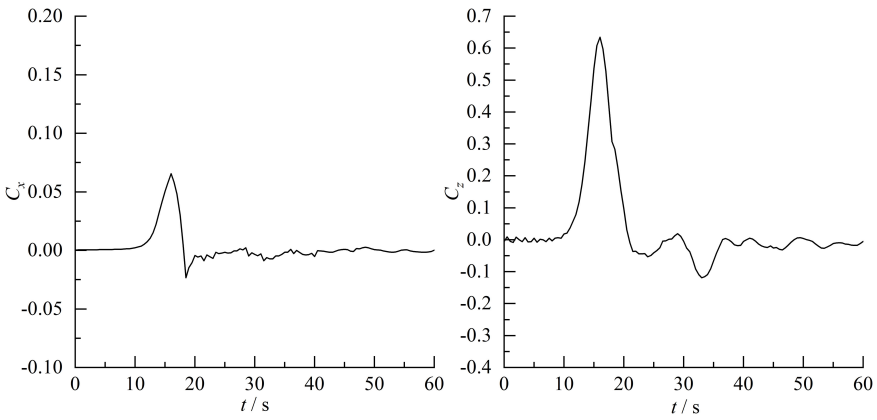

FIGURE 11
History of wave load coefficient of obstacle.

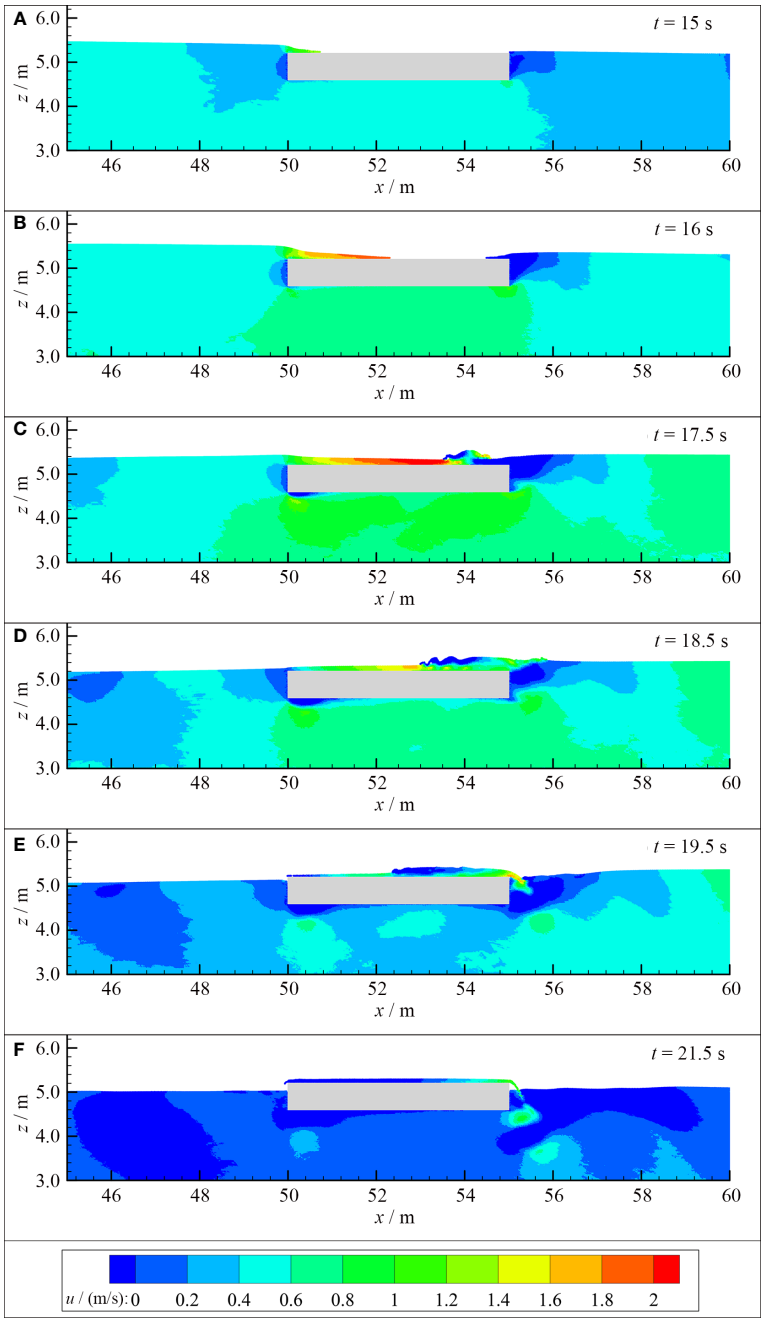

FIGURE 12
Velocity field of the interaction between solitary wave and semi-submersible platform at t= 15 s, 16 s, 17.5 s, 18.5 s, 19.5 s, and 21.5 s **(A–F)**.

velocity position is transferred to the upper right corner of the structure with a maximum value 1.8 m/s. Until t = 21.5 s, the solitary wave passes through the structure for a certain time. The wave surface around the structure reaches the initial wave surface 5 m again. The interaction between upstream and downstream overtopping is fully developed with only a thin layer of overtopping water continue to flow into the flume from the upstream and downstream of the structure. The velocity further decreases to 1.2 m/s.

4.6 Vorticity field

The vorticity field of the interaction between solitary wave and semi-submersible platform is given in Figure 13. *Vor Y* represents vorticity (s^{-1}) in Y direction. At t = 15 s, the solitary wave arrives the structure and generates a small overtopping. The vorticity appears at the four corners of the structure with positive vorticity in the upper left corner and negative vorticity in the rest. The vorticity at the four corners increases gradually at t = 16 s. Until t = 17.5 s, a

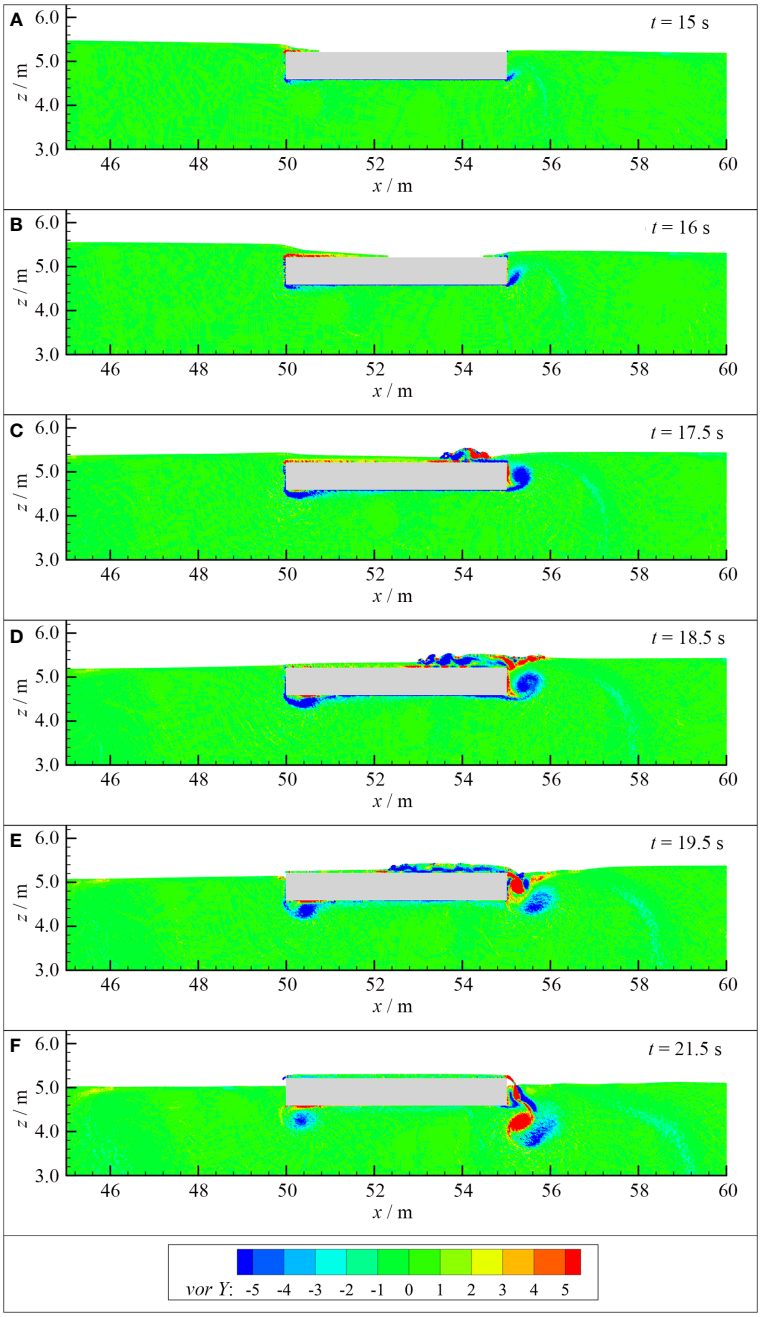

FIGURE 13
Vorticity field of the interaction between solitary wave and semi-submersible platform at t= 15 s, 16 s, 17.5 s, 18.5 s, 19.5 s, and 21.5 s **(A–F)**.

large counterclockwise vortex forms at the bottom of the structure leading edge with the maximum intensity -29 s^{-1}. The vortex intensity at the top of the leading edge of the structure gradually decreases. The vortex on the top of the structure is also complex due to the collision between upstream and downstream overtopping. Positive and negative vortices exist at the same time and change rapidly with the maximum intensity 26 s^{-1} and -33 s^{-1}, respectively. A large counter clockwise vortex appears downstream of the structure with the maximum intensity -8 s^{-1}. At t = 18.5 s, the anticlockwise vortex at the bottom of the structure leading edge increases and develops to the depth and downstream direction with the maximum intensity -14 s^{-1}. The vorticity on the top of the structure is further developed and becomes more complex. There are more positive and negative vortex structures and their mixing. The maximum intensity of positive and negative vortices is 16 s^{-1} and -40 s^{-1}. The counter clockwise vortex downstream of the structure develops with increasing area and moves away from the semi-submersible structure. The vortex intensity does not change significantly with the same maximum value -8 s^{-1}. The anti-clockwise vortex intensity at the bottom of the structure leading edge begins to weaken and continually develops to the depth and downstream direction with the intensity -10 s^{-1} at t = 19.5 s. The

intensity of the vortex on the top of the structure gradually weakens. The clockwise vortex disappears while only the counterclockwise vortex exists with the intensity -40 s^{-1}. The counter clockwise vortex area at the downstream of the structure continually increases with the decreased intensity -7 s^{-1}. Meanwhile, the clockwise vortex appears at the downstream of the structure near the wall with the maximum intensity 28 s^{-1}. Until t = 21.5 s, the intensity and range of the counterclockwise vortex at the bottom of the structure leading edge decrease rapidly with the maximum intensity -6 s^{-1}. The vortex on the top of the structure basically disappears. The scope of downstream vortex continues to increase. The intensity of clockwise vortex decreases while the intensity of counterclockwise vortex changes little. The maximum positive and negative vortex intensities are 16 s^{-1} and -7 s^{-1}, respectively. The vortex structure rapidly moves away from the structure toward the downstream and depth.

5 Conclusions

A meshless solitary waves model which can handle the large deformation and strong nonlinear waves is established based on the SPH method and Rayleigh solitary wave theory. The accuracy of the model is validated by analyzing the consistency between the calculated wave height results and theoretical data as well as the stability of simulated solitary waves. The calculated results of the SPH model with the relative particle spacing ≥ 20 are in good agreement with the analytical solution and has a good stability. The calculation error slightly increases with the increase of measurement point distance, but the change is not significant with a maximum L_2 error difference of 0.016. Therefore, the SPH model can accurately simulate the propagation of the solitary waves.

The results of the interaction between solitary waves and semi-submersible platforms indicate that an overtopping occurs leading to complex wave surface various and wave oscillation. Two double peaks appear at the central measuring point of the platform with maximum wave heights 0.398 m and 0.410 m, respectively. The maximum wave heights at the upstream and downstream measurement point reaches 0.498 m and 0.438 m, respectively. The wave transmission coefficient K_t = 0.880. The horizontal and vertical forces on the semi-submersible platform exhibit positive and negative pressures accompanying wave load amplitudes 0.688 and 0.089, respectively. The vertical load is significantly larger than the horizontal load, and the vertical forces on the platform should be the control stress for the structural design.

A hydraulic jump at the top of the structure is formed due to the interaction between the upstream and downstream overtopping inducing by the solitary waves. The maximum velocities at the top and bottom of the structure are 2.2 m/s and 0.8 m/s, respectively. A large counterclockwise vortex forms at the bottom of the structure leading edge with a maximum intensity -29 s^{-1}. Both positive and negative vorticity exist simultaneously and rapidly change with the maximum intensity 26 s^{-1} and -40 s^{-1} at the top of the structure due to the hydraulic jump. Downstream of the structure, a counterclockwise vortex first appears followed by a clockwise vortex with the maximum vortex intensity -8 s^{-1} and 28 s^{-1}, respectively.

Data availability statement

The raw data supporting the conclusions of this article will be made available by the authors, without undue reservation.

Author contributions

JL: Formal Analysis, Methodology, Writing – original draft. LH: Formal Analysis, Writing – original draft. YH: Resources, Visualization, Writing – review & editing. HM: Methodology, Visualization, Writing – review & editing. GW: Methodology, Supervision, Writing – review & editing. ZT: Investigation, Visualization, Writing – review & editing. DZ: Investigation, Visualization, Writing – review & editing.

Funding

The author(s) declare financial support was received for the research, authorship, and/or publication of this article. This work was financially supported by the National Natural Science Foundation of China (Grant No. 52001071); the Guangdong Basic and Applied Basic Research Foundation (Grant No. 2023A1515010890, 2022A1515240039); the Special Fund Competition Allocation Project of Guangdong Science and Technology Department (Grant No. 2021A05227); the Marine Youth Talent Innovation Project of Zhanjiang (Grant No. 2021E05009, 2021E05010); Non-funded Science and Technology Research Program Project of Zhanjiang (Grant No. 2021B01160, 2021B01416); the Doctor Initiate Projects of Guangdong Ocean University (No. 060302072103, R20068); Innovative Team for Structural Optimization of Ocean and Hydraulic Engineering(CXTD2023012).

Conflict of interest

Author DZ was employed by the company Powerchina Hebei Electric Power Engineering CO., LTD.

The remaining authors declare that the research was conducted in the absence of any commercial or financial relationships that could be construed as a potential conflict of interest.

Publisher's note

References

Altomare, C., Crespo, A. J. C., Rogers, B. D., Dominguez, J. M., Gironella, X., and Gómez-Gesteira, M. (2014). Numerical modelling of armour block sea breakwater with smoothed particle hydrodynamics. *Comput. Struct.* 130, 34–45. doi: 10.1016/j.compstruc.2013.10.011

Aristodemo, F., Tripepi, G., Meringolo, D. D., and Veltri, P. (2017). Solitary wave-induced forces on horizontal circular cylinders: Laboratory experiments and SPH simulations. *Coast. Eng.* 129, 17–35. doi: 10.1016/j.coastaleng.2017.08.011

Canelas, R. B., Domínguez, J. M., Crespo, A. J. C., Gomez-Gesteira, M., and Ferreira, R. M. L. (2015). A Smooth Particle Hydrodynamics discretization for the modelling of free surface flows and rigid body dynamics. *Int. J. Numer. Meth. Fluids.* 78, 581–593. doi: 10.1002/fld.4031

Chen, Q., Zang, J., Kelly, D. M., and Dimakopoulos, A. S. (2017). A 3-D numerical study of solitary wave interaction with vertical cylinders using a parallelised particle-in-cell solver. *J. Hydrodyn.* 29 (5), 790–799. doi: 10.1016/S1001-6058(16)60790-4

Constantin, A., Escher, J., and Hsu, H. C. (2011). Pressure beneath a solitary water wave: mathematical theory and experiments. *Arch. Ration. Mech. Anal.* 201 (1), 251–269. doi: 10.1007/s00205-011-0396-0

Crespo, A. J. C., Domínguez, J. M., Rogers, B. D., Gomez-Gesteira, M., Longshaw, S., Canelas, R., et al. (2015). DualSPHysics: Open-source parallel CFD solver based on Smoothed Particle Hydrodynamics (SPH). *Comput. Phys. Commun.* 187, 204–216. doi: 10.1016/j.cpc.2014.10.004

Crespo, A. J. C., Gómez-Gesteira, M., and Dalrymple, R. A. (2007). Boundary conditions generated by dynamic particles in SPH methods. *Comput. Mater. Con.* 5, 173–184.

Cunningham, L. S., Pringgana, G., and Rogers, B. D. (2014). Tsunami wave and structure interaction: an investigation with smoothed-particle hydrodynamics. *Proc. Inst. Civ. En-Eng.* 167, 126–138. doi: 10.1680/eacm.13.00028

Dalrymple, R. A., and Rogers, B. D. (2006). Numerical modeling of water waves with the SPH method. *Coast. Eng.* 53, 141–147. doi: 10.1016/j.coastaleng.2005.10.004

Ding, W., Ai, C., Jin, S., and Lin, J. (2020). Numerical investigation of an internal solitary wave interaction with horizontal cylinders. *Ocean Eng.* 208, 107430. doi: 10.1016/j.oceaneng.2020.107430

Domínguez, J. M., Altomare, C., Gonzalez-Cao, J., and LoMonaco, P. (2019). Towards a more complete tool for coastal engineering: solitary wave generation, propagation and breaking in an SPH-based model. *Coast. Eng. J.* 61, 15–40. doi: 10.1080/21664250.2018.1560682

Domínguez, J. M., Crespo, A. J. C., Gómez-Gesteira, M., and Marongiu, J. C. (2011). Neighbour lists in smoothed particle hydrodynamics. *Int. J. Numer. Meth. Fluids.* 67, 2026–2042. doi: 10.1002/fld.2481

Farahani, R. J., and Dalrymple, R. A. (2014). Three-dimensional reversed horseshoe vortex structures under broken solitary waves. *Coast. Eng.* 91, 261–279. doi: 10.1016/j.coastaleng.2014.06.006

Farhadi, A., Ershadi, H., Emdad, H., and Rad, E. G. (2016). Comparative study on the accuracy of solitary wave generations in an ISPH-based numerical wave flume. *Appl. Ocean Res.* 54, 115–136. doi: 10.1016/j.apor.2015.11.003

Gao, J., Ma, X., Chen, H., Zang, J., and Dong, G. (2021a). On hydrodynamic characteristics of transient harbor resonance excited by double solitary waves. *Ocean Eng.* 219, 108345. doi: 10.1016/j.oceaneng.2020.108345

Gao, J., Ma, X., Dong, G., Chen, H., Liu, Q., and Zang, J. (2021b). Investigation on the effects of Bragg reflection on harbor oscillations. *Coast. Eng.* 170, 103977. doi: 10.1016/j.coastaleng.2021.103977

Gao, J., Ma, X., Dong, G., Zang, Z., Ma, Y., and Zhou, L. (2019). Effects of offshore fringing reefs on the transient harbor resonance excited by solitary waves. *Ocean Eng.* 190, 106422. doi: 10.1016/j.oceaneng.2019.106422

Gao, J., Ma, X., Zang, J., Dong, G., Ma, X., Zhu, Y., et al. (2020). Numerical investigation of harbor oscillations induced by focused transient wave groups. *Coast. Eng.* 158, 103670. doi: 10.1016/j.coastaleng.2020.103670

Gao, J., Shi, H., Zang, J., and Liu, Y. (2023). Mechanism analysis on the mitigation of harbor resonance by periodic undulating topography. *Ocean Eng.* 281, 114923. doi: 10.1016/j.oceaneng.2023.114923

Geng, T., Liu, H., and Dias, F. (2021). Solitary-wave loads on a three-dimensional submerged horizontal plate: Numerical computations and comparison with experiments. *Phys. Fluids.* 33, 037129. doi: 10.1063/5.0043912

Gomez-Gesteira, M., Rogers, B. D., Crespo, A. J. C., Dalrymple, R. A., Narayanaswamy, M., and Dominguez, J. M. (2012). SPHysics – development of a free-surface fluid solver – Part 1: Theory and formulations. *Comput. Geosci.* 48, 289–299. doi: 10.1016/j.cageo.2012.02.029

Guizien, K., and Barthélemy, E. (2002). Accuracy of solitary wave generation by a piston wave maker. *J. Hydraul. Res.* 40, 321–331. doi: 10.1080/00221680209499946

Ha, T., Shim, J., Lin, P., and Cho, Y. (2014). Three-dimensional numerical simulation of solitary wave run-up using the IB method. *Coast. Eng.* 84, 38–55. doi: 10.1016/j.coastaleng.2013.11.003

He, M., Khayyer, A., Gao, X., Xu, W., and Liu, B. (2021). Theoretical method for generating solitary waves using plunger-type wavemakers and its Smoothed Particle Hydrodynamics validation. *Appl. Ocean Res.* 106, 102414. doi: 10.1016/j.apor.2020.102414

He, M., Liang, D. F., Ren, B., Li, J., and Shao, S. (2023). Wave interactions with multi-float structures: SPH model, experimental validation, and parametric study. *Coast. Eng.* 184, 104333. doi: 10.1016/j.coastaleng.2023.104333

He, J. H., Qie, N., and He, C. H. (2021). Solitary waves travelling along an unsmooth boundary. *Results Phys.* 24, 104104. doi: 10.1016/j.rinp.2021.104104

Higuera, P., Liu, P. L. F., Lin, C., Wong, W. Y., and Kao, M. J. (2018). Laboratory-scale swash flows generated by a non-breaking solitary wave on a steep slope. *J. Fluid Mech.* 847, 186–227. doi: 10.1017/jfm.2018.321

Hsiao, S. C., and Lin, T. C. (2010). Tsunami-like solitary waves impinging and overtopping an impermeable seawall: Experiment and RANS modeling. *Coast. Eng.* 57 (1), 1–18. doi: 10.1016/j.coastaleng.2009.08.004

Hunt-Raby, A. C., Borthwick, A. G. L., Stansby, P. K., and Taylor, P. H. (2011). Experimental measurement of focused wave group and solitary wave overtopping. *J. Hydraul. Res.* 49 (4), 450–464. doi: 10.1080/00221686.2010.542616

Li, J., Liu, H., Gong, K., and Tan, S. K. (2012). SPH modeling of solitary wave fissions over uneven bottoms. *Coast. Eng.* 60, 261–275. doi: 10.1016/j.coastaleng.2011.10.006

Lo, H. Y., and Liu, L. F. (2014). Solitary waves incident on a submerged horizontal plate. *J. Waterw. Port C-ASCE.* 140 (3), 04014009. doi: 10.1061/(ASCE)WW.1943-5460.0000236

Ma, X., Zheng, Z., Gao, J., Wu, H., Dong, Y., and Dong, G. (2021). Experimental investigation of transient harbor resonance induced by solitary waves. *Ocean Eng.* 230, 109044. doi: 10.1016/j.oceaneng.2021.109044

Ma, Y., Yuan, C., Ai, C., and Dong, G. (2019). Comparison between a non-hydrostatic model and OpenFOAM for 2D wave-structure interactions. *Ocean Eng.* 183, 419–425. doi: 10.1016/j.oceaneng.2019.05.002

Mahmoudof, S. M., and Azizpour, J. (2020). Field observation of wave reflection from plunging cliff coasts of chabahar. *Appl. Ocean Res.* 95, 102029. doi: 10.1016/j.apor.2019.102029

Mahmoudof, S. M., Eyhavand-Koohzadi, A., and Bagheri, M. (2021). Field study of wave reflection from permeable rubble mound breakwater of Chabahar Port. *Appl. Ocean Res.* 114, 102786. doi: 10.1016/j.apor.2021.102786

Mahmoudof, S. M., and Hajivalie, F. (2021). Experimental study of hydraulic response of smooth submerged breakwaters to irregular waves. *Oceanologia.* 05, 002. doi: 10.1016/j.oceano.2021.05.002

Malek-Mohammadi, S., and Testik, F. Y. (2015). New methodology for laboratory generation of solitary waves. *J. Waterw. Port C-ASCE.* 136 (5), 286–294. doi: 10.1061/(ASCE)WW.1943-5460.0000046

Monaghan, J. J. (1992). Smoothed particle hydrodynamics. *Annu. Rev. Astron. Astr.* 30, 543–574. doi: 10.1146/annurev.aa.30.090192.002551

Omidvar, P., Stansby, P. K., and Rogers, B. D. (2012). Wave body interaction in 2D using smoothed particle hydrodynamics (SPH) with variable particle mass. *Int. J. Numer. Meth. Fluids.* 68, 686–705. doi: 10.1002/fld.2528

Pan, K., IJzermans, R. H. A., Jones, B. D., Thyagarajan, A., wan Beest, B. W. H., and Williams, J. R. (2015). Application of the SPH method to solitary wave impact on an offshore platform. *Comp. Part. Mech.* 3, 155–166. doi: 10.1007/s40571-015-0069-0

Qu, K., Ren, X. Y., and Kraatz, S. (2017). Numerical investigation of tsunami-like wave hydrodynamic characteristics and its comparison with solitary wave. *Appl. Ocean Res.* 63, 36–48. doi: 10.1016/j.apor.2017.01.003

Rastgoftar, E., Jannat, M. R. A., and Banijamali, B. (2018). An integrated numerical method for simulation of drifted objects trajectory under real-world tsunami waves. *Appl. Ocean Res.* 73, 1–16. doi: 10.1016/j.apor.2018.01.013

Saghatchi, R., Ghazanfarian, J., and Gorji-Bandpy, M. (2014). Numerical simulation of water-entry and sedimentation of an elliptic cylinder using smoothed-particle hydrodynamics method. *J. Offshore Mech. Arct.* 136, 031801. doi: 10.1115/1.4026844

Sampath, R., Montanari, N., Akinci, N., Prescott, S., and Smith, C. (2016). Large-scale solitary wave simulation with implicit incompressible sph. *J. Ocean Eng. Mar. Energy.* 2, 313–329. doi: 10.1007/s40722-016-0060-8

Tang, J., Causon, D., Mingham, C., and Qian, L. (2013). Numerical study of vegetation damping effects on solitary wave run-up using the nonlinear shallow water equations. *Coast. Eng.* 75 (5), 21–28. doi: 10.1016/j.coastaleng.2013.01.002

Wang, G., Dong, G., Perlin, M., Ma, X., and Ma, Y. (2011). Numerical investigation of oscillations within a harbor of constant slope induced by seafloor movements. *Ocean Eng.* 38, 2151–2161. doi: 10.1016/j.oceaneng.2011.09.033

Wang, Y., Xu, F., and Zhang, Z. (2020). Numerical simulation of inline forces on a bottom-mounted circular cylinder under the action of a specific freak wave. *Front. Mar. Sci.* 7, 585240. doi: 10.3389/fmars.2020.585240

Wang, G., Zheng, J. H., Maa, J. P. Y., Zhang, J. S., and Tao, A. F. (2013). Numerical experiments on transverse oscillations induced by normal-incident waves in a rectangular harbor of constant slope. *Ocean Eng.* 57, 1–10. doi: 10.1016/j.oceaneng.2012.09.010

Wu, Y. T., and Hsiao, S. C. (2018). Generation of stable and accurate solitary waves in a viscous numerical wave tank. *Ocean Eng.* 167, 102–113. doi: 10.1016/j.oceaneng.2018.08.043

Wu, N. J., Hsiao, S. C., Chen, H. H., and Yang, R. Y. (2016). The study on solitary waves generated by a piston-type wave maker. *Ocean Eng.* 117, 114–129. doi: 10.1016/j.oceaneng.2016.03.020

Wu, Y. T., Hsiao, S. C., Huang, Z. C., and Hwang, K. S. (2012). Propagation of solitary waves over a bottom-mounted barrier. *Coast. Eng.* 62, 31–47. doi: 10.1016/j.coastaleng.2012.01.002

Wu, N. J., Tsay, T. K., and Chen, Y. Y. (2014). Generation of stable solitary waves by a piston-type wave maker. *Wave Motion* 51 (2), 240–255. doi: 10.1016/j.wavemoti.2013.07.005

Wu, Y. T., Yeh, C. L., and Hsiao, S. C. (2014). Three-dimensional numerical simulation on the interaction of solitary waves and porous breakwaters. *Coast Eng.* 85, 12–29. doi: 10.1016/j.coastaleng.2013.12.003

Xuan, R. T., Wu, W., and Liu, H. (2013). An experimental study on runup of two solitary waves on plane beaches. *J. Hydrodyn.* 25 (2), 317–320. doi: 10.1016/S1001-6058(13)60369-8

Zhang, J., Zheng, J., Jeng, D. S., and Guo, Y. (2015). Numerical simulation of solitary-wave propagation over a steady current. *J. Waterw. Port C-ASCE.* 141 (3), 04014041. doi: 10.1061/(ASCE)WW.1943-5460.0000281

frontiers | Frontiers in Marine Science

TYPE Original Research
PUBLISHED 04 January 2024
DOI 10.3389/fmars.2023.1324163

OPEN ACCESS

EDITED BY
Chengji Shen,
Hohai University, China

REVIEWED BY
Lei Guo,
Shandong University, China
Qiaona Guo,
Hohai University, China

*CORRESPONDENCE
Tengfei Fu
futengfei@fio.org.cn
Xiujun Guo
guojunqd@ouc.edu.cn

†These authors have contributed equally to this work and share first authorship

RECEIVED 19 October 2023
ACCEPTED 13 December 2023
PUBLISHED 04 January 2024

CITATION
Xiao X, Zhang Y, Fu T, Sun Z, Lei B, Li M and Guo X (2024) The two salinity peaks mode of marine salt supply to coastal underground brine during a single tidal cycle.
Front. Mar. Sci. 10:1324163.
doi: 10.3389/fmars.2023.1324163

The two salinity peaks mode of marine salt supply to coastal underground brine during a single tidal cycle

Xiaoteng Xiao[1,2†], Yufeng Zhang[1,2,3†], Tengfei Fu[4*], Zengbing Sun[3,5], Bingxiao Lei[3,5], Mingbo Li[3,5] and Xiujun Guo[1,2,3*]

[1]Key Laboratory of Shandong Province for Marine Environment and Geological Engineering, Ocean University of China, Qingdao, Shandong, China, [2]Key Lab of Marine Environment and Ecology, Ministry of Education, Ocean University of China, Qingdao, China, [3]Weifang Key Laboratory of Coastal Groundwater and Geological Environmental Protection and Restoration, Weifang, China, [4]Key Laboratory of Marine Geology and Metallogeny, First Institute of Oceanography, Ministry of Natural Resources, Qingdao, China, [5]Shandong Province No.4 Institute of Geological and Mineral Survey, Weifang, China

Seawater salt is constantly supplied from the marine environment to coastal underground brine deposits, meaning that brine has the potential for continuous extraction. There is currently a lack of information about the processes that drive the fluxes of seawater salt to underground brine deposits in tidal-driven brine mining areas. We chose the Yangkou salt field on the southern coast of Laizhou Bay, a brine mining area, as our study site. We monitored the spatial and temporal distribution of the underground brine reserve and the changes in water level and salinity in the mining area and adjacent tidal flats using electrical resistivity tomography and hydrogeological measurements. We monitored cross-sections along two survey lines and observed that the underground brine reserve receives a stable supply of seawater salt, and calculated that the rate of influx into the brine body in the mining area near the boundary of the precipitation funnel was 0.226–0.232 t/h. We calculated that a total salt flux of approximately 5.50 t enters the underground brine body every day through a 150 m long shoreline and a 1322.3 m^2 window, which is sufficient to sustain the daily extraction of one brine well. During tidal cycles, there are two peaks in the salinity of the water supplied to the underground brine reserve, which means that the brine supply is from at least two high-salinity salt sources in different tidal stages. The first salinity peak occurs during the initial stage of the rising tide after seawater inundates the tidal flat. At this time, seawater, which is a solution and carries a large amount of evaporated salt, is transported into the brine layer through highly permeable areas or biological channels and replenishes the brine in the mining area. The second salinity peak occurs

during the early stage of the falling tide. Influenced by hysteresis-driven tidal pumping, high-salinity brine from the lower intertidal zone is rapidly transported into the mining area, thereby increasing the salinity of the underground brine.

KEYWORDS

coastal underground brine, tidal effect, marine salt source, water and salt recharge process, electrical resistivity tomography (ERT)

1 Introduction

Coastal underground brine reserves constitute an important source of minerals for salt production and the extraction of bromine, iodine, and other chemical raw materials. These reserves are generally distributed in bay areas in semi-arid and arid climatic zones between 50° north and south worldwide (Sanford and Wood, 2001; Frank et al., 2009; Zhang, 2021) (Figure 1). The marine environment is the main source of salt for these coastal underground brine resources and, under the combined influence of ocean dynamics (density difference, tides, storm surges, etc.) and evaporation, shallow coastal underground brine reserves in extraction areas receive continuous supplies of water and salt supplies (Han, 1996; Boufadel, 2000; Robinson et al., 2007; Gonneea et al., 2013; Post et al., 2013; Sun et al., 2023).

The tidal flat represents a shallow coastal underground reserve of marine salt because of the evaporation that occurs (Han, 1996). Studies have shown that water and salt circulate between the seawater and shallow brine in mudflat areas with low-permeability surface sediments (10^{-7}–10^{-5} m/s) during tidal action, although the rate of water and salt exchange is low (Ma et al., 2015; Hou et al., 2016; Ma, 2016; Zhang, 2021). In some coastal salt marsh or tidal flat areas, there are areas of high-permeability sediments that serve as biological channels, and provide preferential pathways for rapid exchange between seawater and groundwater, and where the salt content of porewater in the sediment matrix increases near the channels (Harvey and Nuttle, 1995; Escapa et al., 2008; Xin et al., 2009; Wilson and Morris, 2012; Xiao et al., 2019). There is an exchange process between the evaporated salt on the tidal flat surface and the shallow brine in the mudflat. During the rising tide, evaporated salt dissolves in seawater and is transported to the shallow brine in the mudflat, where high-salinity brine participates in the groundwater-seawater cycle and is released through the tidal flat during the ebb tide (Del Pilar et al., 2015; Hou et al., 2016; Zhang, 2021; Sun et al., 2023).

High-salinity brine that is buried in the lower intertidal zone is another source of marine salt for shallow coastal underground brine reserves. Coastal underground brine reserves have two favorable characteristics that mean they can receive salt from the marine environment. First, as a result of historical frequent marine transgressions and regressions, most coastal aquifer systems have interlayers of fine-grained and coarse-grained sediments, and, of these, the coarse-grained sand layers serve as interconnected aquifers between the tidal flat and the extraction areas. Driven by the tide, groundwater and solutes are periodically transported from the tidal flat area to the extraction areas (Yi et al., 2012; Fu et al., 2020). Second, where coastal underground brine has been extracted over the long term, the groundwater level may be lower than the sea level in the extraction areas and depression cones may have formed (Han et al., 2014; Liu, 2018; Qi et al., 2019). The hydraulic gradient between the marine and groundwater environments may also increase in arid climate conditions and storm surge events (William et al., 2008; Yang et al., 2015; Xing et al., 2023). When the groundwater flow field is influenced by these conditions, the high-salinity brine buried in the lower intertidal zone can continuously supply the extraction areas.

The salt in the aquitard can be considered as the third type of salt source that can supply coastal underground brine reserves. The salt stored inside the aquitards can be replenished to its adjacent brine layer through diffusion (Li et al., 2021). During the marine invasion and regression, aquitards gradually form during the formation of coastal underground brine. The total amount of salt stored in the aquitards is enormous, with a large amount of high salinity ancient seawater stored inside. At the same time, it continuously captures salt from the flowing recharge water and evaporated salt dissolved and infiltrated on the surface of the tidal flats (Gao et al., 2016; Li et al., 2021). From the perspective of high salinity water reserves in aquitards, they have enormous potential to recharge underground brine in coastal mining areas. However, the permeability of aquitards is low (10^{-8}–10^{-10} m/s), and even if groundwater extraction increases its diffusion rate by hundreds of times, the rate of salt diffusion replenishing brine resources is still slow (Mongelli et al., 2013; Han et al., 2014; Larsen et al., 2017; Li et al., 2021). Therefore, during a short time scale (such as single or multiple tidal cycles), the release of salt from aquitards is very minimal, making it difficult to quickly and effectively replenish the underground brine resources in mining areas.

To sum up, although we have the theory of tidal flat halogenesis, information about the fate of evaporated salt on the tidal flat under tidal action, and various water-salt transport models that describe the processes in multiple tidally influenced coastal brine layers (Gao et al., 2016; Fu et al., 2020; Zhang, 2021), we do not have information about how the first two salt sources and tidal cycles influence the supply of salt to, and losses from, the shallow coastal groundwater in mining

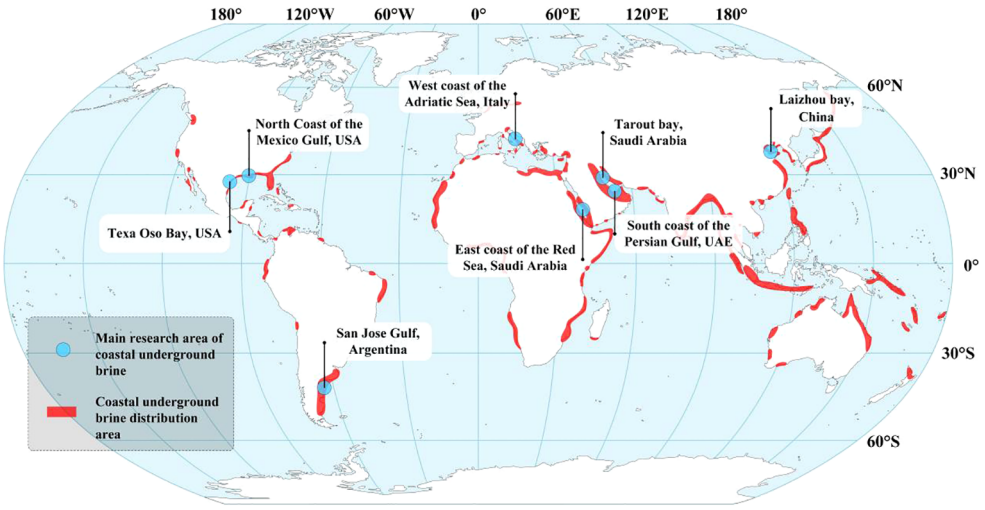

FIGURE 1
Distribution of the main worldwide coastal underground brine reserves and research areas (Sanford and Wood, 2001; Frank et al., 2009; Zhang, 2021).

areas. To describe the above process, we need information about how the groundwater salinity evolves and how it is distributed in the tidal flat and coastal brine mining area during the tidal cycle.

The combination of *in-situ* hydrological parameter observation and numerical simulation is one of the main methods for exploring hydrological processes and pore water salinity distribution in tidal flats and salt marshes (Xiao et al., 2019; Fang et al., 2021, 2022; Shen et al., 2022; Shen et al., 2023; Zheng et al., 2023). However, the above research methods can not accurately depict the groundwater salinity distribution at different tidal times in complex stratigraphic environments with high resolution. With the upgrading of hydrogeophysical monitoring instruments and the optimization of geophysical data interpretation methods, the Electrical resistivity tomography (ERT) is widely used to monitor and research groundwater hydrological processes in *in-situ* coastal zones. ERT survey results from different times can provide information about brackish water and seawater intrusion processes that can be analyzed and used to establish different types of coastal seawater-groundwater exchange models (Franco et al., 2009; Misonou et al., 2013; Fu et al., 2020; Zhang, 2021; Zhan et al., 2023; Zhang et al., 2023). Further, the Archie formula, Manning formula, and the salinity box model can be combined to support quantification of the groundwater discharge and salt flux in the tidal flat area (Zhang K. et al., 2021; Zhang Y. et al., 2021, 2023; Xing et al., 2023).

In this study, we monitored the resistivity profiles in the brine mining area and tidal flat area through the tidal cycle using ERT technology. We then combined the monitoring results for groundwater levels within the tidal cycle, salinity, and conductivity of the water in the brine mining wells, and analyzed the salt supply and loss processes in the shallow coastal groundwater in the chosen mining area.

2 Study area

The study area is on the southern coast of Laizhou Bay, in the northern part of Shandong Province, China. We did a survey that extended across the land-based brine extraction area and the tidal flat (Figure 2). The terrain on the land-based area is flat. The marine area consists of muddy sandy tidal flats that have a gentle slope of less than 3‰ and surface sediment that has a permeability coefficient of approximately 10^{-5} m/s. There are multiple brine extraction wells operating 24 hours per day on the land-based area.

The study area is characterized by irregular semidiurnal tides, and the average tidal range is approximately 0.9 m. The average flood tide duration is 6 h 22 min, and the average ebb tide duration is 6 h 6 min (Zhang, 2021).

Within the study area, there are three horizontal layers of brine. The upper and lower layers have low salinity, while the middle layer has high salinity (Zheng et al., 2014; Gao et al., 2016; Qi et al., 2019). These brine layers formed during the early Pleistocene period of the Cangzhou transgression, the late Pleistocene period of the Xianxian transgression, and the early Holocene period of the Huanghua transgression. The underground brine that formed during the Huanghua transgression is composed of groundwater brine that was deposited during the late Holocene. The total dissolved solids (TDS) of the brine ranges from 50 to 140 g/L (Gao et al., 2016).

The study area is on the marine-side boundary of the brine precipitation funnel. The observation results from June 2022 of 16 groundwater level observation logs in the Yangkou Salt Field and the surrounding area showed that (Figure 3A) the groundwater level rapidly decreased to −35 m over 7 km in a southwest direction from the research area. There is a significant hydraulic gradient between the nearshore research area and the inland extraction area, and groundwater from the tidal flat area continuously flows toward the landward side of the brine precipitation funnel. The two monitoring sections in this study were set up at an angle of approximately 36° with the groundwater flow direction. In July 2022, the groundwater levels at observation wells G1 and G2 in the extraction area were approximately −7.9 m and −5.2 m, respectively.

The stratigraphic information for geological borehole C within the research area (Figure 3A) shows that, from shallow to deep, the aquifer can be divided into a fine-grained sediment cover layer (top

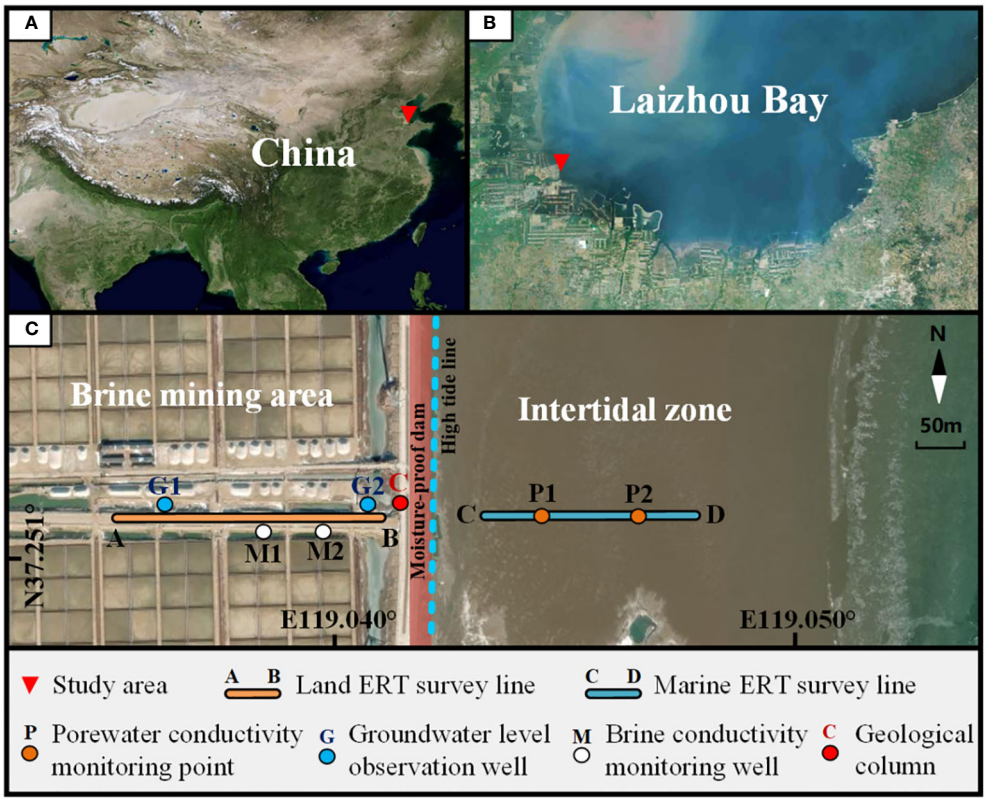

FIGURE 2
Map of the study area. **(A, B)** Location of the study area on the south coast of Laizhou Bay, East China. **(C)** The fieldwork layout in the brine mining area and the intertidal zone, including two ERT monitoring lines, two groundwater level observation wells, two brine sampling wells, one geological borehole, and two tidal flat pore water conductivity monitoring points.

layer), a phreatic brine aquifer layer that is about 14 m deep (middle layer), and a weakly permeable aquitard (bottom layer).

3 Materials and methods

3.1 Measurement of the conductivity and salinity of the seawater and underground brine

The seawater conductivity data were used to determine the electrical resistivity values within the seawater grid during the inversion of the ERT data, and to investigate the recharge relationship between the seawater and the subterranean brine. Seawater samples were collected from the endpoint of the marine ERT survey line and the conductivity of the samples was measured at the same time as the ERT measurements were taken. The brine conductivity and salinity data were used to validate the accuracy of the ERT inversion results and to calculate the salt flux of subterranean brine in the extraction area. Subterranean brine was extracted at M1 (150 m from point A) and M2 (225 m from point A) on the land ERT survey line (Figure 2C). The sampling depth was at a depth of approximately −10 m, and samples were collected for conductivity measurements over three consecutive tidal cycles. The conductivity of the water was measured with a water quality meter (AZ8362).

3.2 Porewater conductivity monitoring

The conductivity of the porewater in the intertidal sediments was measured at two points, at 530 m and 610 m, along the marine ERT survey line using a multi-parameter automatic monitor (Solinst LTC Levelogger Edge). The monitoring probe was wrapped with multiple layers of gauze to ensure it would not get blocked by sediment, and buried at a depth of 1 m. Data were collected every 0.5 h. This monitoring was done at the same time as the ERT monitoring.

3.3 Groundwater level monitoring

Two groundwater observation wells (G1 and G2) were installed along the land ERT survey line to measure the groundwater level (Figure 3B). The groundwater levels were measured at a time interval of 0.5 h using a steel tape water level meter with a resolution of 1 mm (Yingtianliang Company). Again, these measurements were done at the same time as the ERT survey.

3.4 ERT survey

The land ERT survey line (A–B) and marine ERT survey line (C–D) were along the vertical coastline (Figure 2). The monitoring results were analyzed to identify the salinity variations in the aquifer

10.3389/fmars.2023.1324163

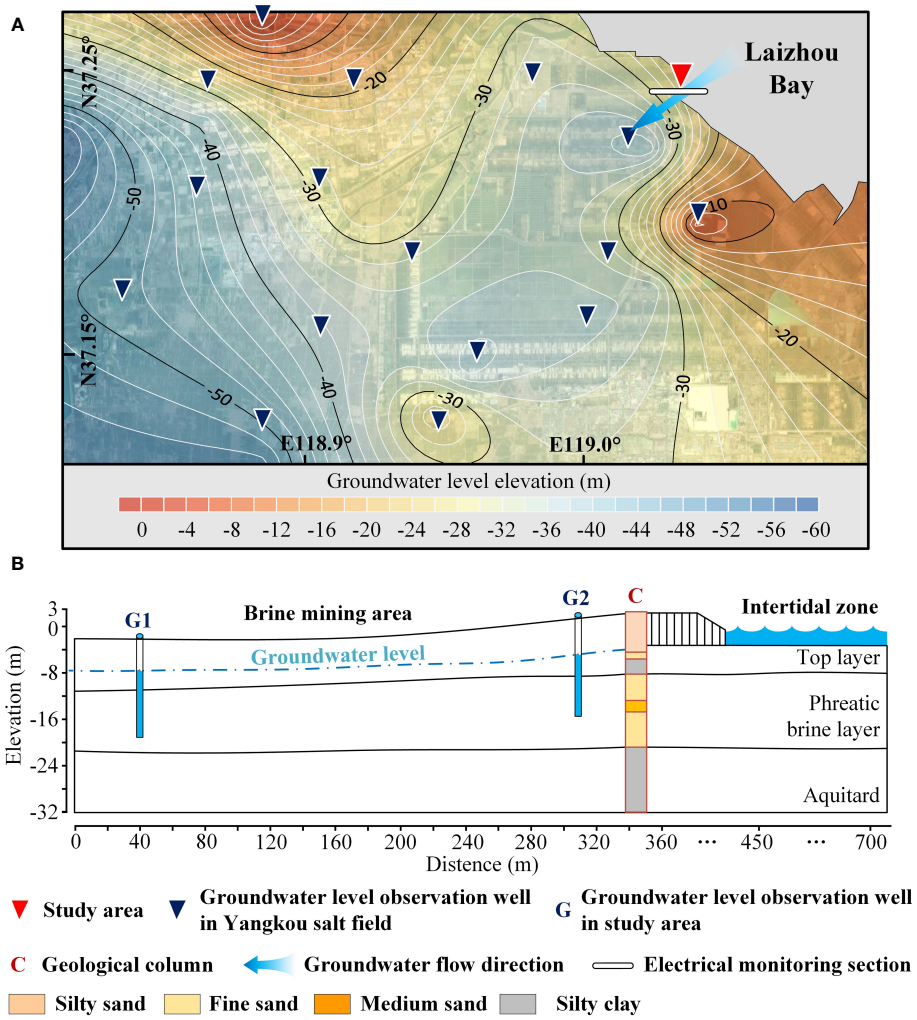

FIGURE 3
(A) The average groundwater level in the study area in June 2022. **(B)** Hydrogeological profile along the survey line in the study area.

between the marine area and the tidally influenced brine extraction areas. The land and marine ERT measurements were done simultaneously in July 2021.

3.4.1 Data acquisition

The ERT monitoring system (GEOPEN) used to monitor the land and marine areas consisted of an E60DN mainframe, a booster, and intelligent cables (with stainless steel electrodes). The terrestrial ERT monitoring system had cables with electrodes spaced at 5 m intervals. There were 64 electrodes altogether, and the total cable length was 315 m. The marine ERT monitoring system had cables with electrodes every 2.5 m. There were 100 electrodes, and the total cable length was 247.5 m.

The ERT measurements for the land and marine areas should have been taken at the bottom boundary of the subaqueous brine layer (elevation approximately −20 m). These measurements were taken with a Wenner-Schlumberger array; this equipment is widely used in coastal groundwater hydrological monitoring and is known for its large detection depth, high vertical resolution, and strong anti-interference ability (Hermans and Paepen, 2020; Wu et al., 2021). The array is powered by a 24V battery pack, and the user-defined maximum current is 1A and the power supply time is 1 s. The ERT measurements of the land and marine areas started synchronously, and the data acquisition took approximately 30 min.

The electrode layout methods proposed by Zhang Y. et al. (2021) and Xing et al. (2023) were consulted to find out how to prevent the electrode positions of the cables for the marine ERT monitoring from drifting under tidal influence. A 30-cm deep trench was excavated for the cables during low tide, three days before the monitoring work started, and the cables were placed in the trench and covered with sediment in situ.

The saturation of the sediment at 0, 80, 160, and 240 m deep where the electrodes of the marine ERT cable were located was measured at low tide. The saturation ranged from 97.1% to 99.8%. We concluded that the environment in which the electrodes of the marine ERT cable were placed was stable and that the sediment remained saturated during tidal cycles.

3.4.2 Data processing and inversion

The resistivity profile data were checked for quality and data points in the resistivity data that were more than three times greater or less than the adjacent data were removed. Less than 1% of the total resistivity data were removed in this process (Wu et al., 2021). The apparent resistivity values were converted to true resistivity values by time-lapse inversion. The ERT data were analyzed using the least squares method with RES2DINV software v.4.05.30 (Geotomo Inc.) (deGroot-Hedlin and Constable, 1990). The terrain elevation data and the corresponding seawater resistivity and sea level elevation data had to be combined before the resistivity data set was inverted. When calculating the inversion, RES2DINV performs terrain modeling, calculates the water layer thickness, establishes a simulation domain, and divides it into finite element grids. The resistivity between the beach surface and the sea level was calculated from the seawater resistivity. In this study, the seawater resistivity was based on the monitoring data.

The quality of the inversion result was evaluated by checking the Abs error (absolute error) between the measured and predicted apparent resistivity values. It is generally accepted that inversion results have more credibility when the absolute error is below 10%. However, an absolute error that is too low may lead to overfitting and data inconsistency (Dimova et al., 2012). Therefore, in this study, the absolute error was controlled at around 10%.

3.4.3 Inversion model appraisal

The depth-of-investigation (DOI) index is used to analyze the influence of inversion parameters on the model and evaluate the reliability of the inverted resistivity data (Oldenburg and Li, 1999; Paepen et al., 2020; Zhang Y. et al., 2021). The DOI index is calculated using Equation 1.

$$DOI = \frac{\left|\log R_{inv,1} - \log R_{inv,2}\right|}{2} \tag{1}$$

It is calculated based on two additional inversions ($R_{\mathrm{inv},1}$ and $R_{\mathrm{inv},2}$, which are inverted resistivities) using two reference models ($R_{\mathrm{app},1}$ and $R_{\mathrm{app},2}$) which are 0.1 and 10 times the average observed apparent resistivity of the datasets (Oldenburg and Li, 1999; Paepen et al., 2020; Zhang Y. et al., 2021).

3.4.4 Reliability analysis of inverted resistivity

The expected resistivity (R_p) of the sediments at the sampling or monitoring locations was calculated from the monitoring data for the conductivity of the submarine brine and of the porewater of tidal flat sediments. The numerical values and variations of R_p and the ERT inversion results (R_{inv}) were compared to verify the accuracy of the ERT inversion data.

Based on Archie's law (Archie, 1942) and the resistivity of the brine sample (R_w), the expected resistivity (R_p) of the sediments at the sampling points of the coastal mining area (M1, M2) can be calculated as follows:

$$R_p = \frac{a \cdot R_w}{\phi^m} \tag{2}$$

Where a is a tortuosity factor, m is a cementation factor, and ϕ is the porosity. The values of the porosity and rock electrical parameters were based on the results of testing the porosity of the sediment samples and empirical values of the electrical parameters for medium to fine sand layers (Jackson et al., 1978; Zhang et al., 2004; Zhang Y. et al., 2021). Here, ϕ=0.4, a=0.6, and m=1.4.

The resistivity of the sediments will be affected by a high clay content in the muddy tidal flat sediments because of the influence of the surface conductivity and pore fluid conductivity (Revil, 2013). The effects of the surface conductivity and R_w on the resistivity of the sediments can be separated with a modified version of Archie's law (Equation 3) that was proposed by Nguyen et al. (2009) and Shao et al. (2021). Therefore, the expected resistivity (R_p) of the sediments at the monitoring points (P1, P2) can be calculated based on R_w, as follows:

$$R_p = \frac{1}{(F' R_w)^{-1} + b} \tag{3}$$

Where F' represents the effective layer factor, and b represents the contribution of the surface conductivity to ρ, independent of the fluid conductivity. The parameters in Equation 3 were set based on the preliminary results from Zhang's (Zhang, 2021) study of the muddy tidal flats on the south coast of Laizhou Bay. F' was set to 2.5, and b was set to 0.335.

The resistivity data from four of the inversion calculation grids near the brine sampling points and two of the inversion calculation grids near the porewater conductivity monitoring points in the tidal flat sediments were extracted and their average values were calculated using the R_{inv} data extraction method of Zhang Y. et al. (2021) and Xing et al. (2023). The output from R_{inv} was then compared with the R_p calculated using Equations 2, 3 to determine the reliability of the ERT inversion results.

3.5 Calculation of the salt flux

The brine occurs in a water-bearing fine sand layer in the monitoring area, and its fluid movement follows Darcy's law. Therefore, the water flux passing through the monitoring section along the groundwater flow direction can be expressed by the basic flow equation and Darcy's law, as follows:

$$Q = A \sin\theta \times v \tag{4}$$

$$v = K \frac{\Delta h}{L \cos\theta} \tag{5}$$

Where Q is the flow rate (m^3/s), A is the underground brine flow area divided based on the ERT monitoring result (m^2), $A\sin\theta$ is the underground water flow area perpendicular to the flow direction, v is the flow velocity (m/s), and K is the permeability coefficient (m/s), which was taken as 1×10^{-4} m/s in this case (Guo, 2018; Chang, 2018). Δh is the hydraulic head difference (m) between G1 and G2, L is the length of the ERT monitoring section in the

brine extraction area (m), and θ is the angle between the flow field and the monitoring section (θ=36°).

By combining the Equations 4, 5 and salinity, density, and volume calculation equations (Equations 6–8), the salt flux passing through the monitoring section along the groundwater flow direction can be calculated using Equation 9, as follows:

$$S = \frac{m_s}{m_w} \tag{6}$$

$$m_w = \rho V \tag{7}$$

$$V = Q \times \Delta t \tag{8}$$

$$m_s = \frac{S \times \rho \times \Delta t \times A\sin\theta \times K \times \Delta h}{L\cos\theta} \tag{9}$$

Where S represents the salinity of the brine (g/kg), m_s represents the mass of salt (g), m_w represents the mass of brine (kg), and ρ represents the brine density (kg/m^3), which was assumed to be 1.08×10^3 (kg/m^3). V represents the brine volume (m^3) and Δt represents the time interval for sampling underground brine (s).

4 Results

4.1 Groundwater parameters

The water levels measured at the G1 and G2 groundwater monitoring wells followed a similar pattern (Figure 4). The groundwater level remained stable during the transition from low tide to high tide. The groundwater level increased slightly by less than 10 cm within 2 hours of the high tide. More than 2 hours after the high tide, the groundwater level started to decrease until the seawater receded, and the groundwater level returned to the pre-tidal level.

The salinity of the brine water followed a specific pattern during the three tidal cycles of the monitoring period (Figure 4). Within each tidal cycle, the salinity increased and decreased twice, producing two salinity peaks. The two salinity peaks occurred during the rising and falling tides of the same tidal cycle, at a time interval of approximately 5–7 hours (from low tide to low tide).

The conductivity was positively correlated with the salinity and reflected the changes in the seawater salinity. The seawater conductivity reached a peak after the seawater covered the tidal flat, but the conductivity of the seawater on the tidal flat decreased as the tide continued to rise. The conductivity values decreased until the seawater receded from the study area.

4.2 ERT inverted resistivity

4.2.1 Accuracy verification of the resistivity data

The R_p and R_{inv} values in the surface sediments of the tidal flats followed a similar pattern during the tidal cycle. The R_p and R_{inv} showed an overall decrease during the rising tide, and were lowest before the high tide. The R_p and R_{inv} then increased during the ebb tide (Figure 5A). The R_p and R_{inv} data for the brine mining area showed relatively little, but consistent, variation during the tidal process, which indicates that the underground brine area was relatively stable during the tidal cycle. During the flood tide, the R_p and R_{inv} values first decreased and then increased, and the resistivity values were lowest when the tidal flat was submerged by seawater. During the ebb tide, the R_p and R_{inv} values also decreased first and then increased, and the resistivity values were lowest after the high tide (Figure 5B). Overall, the R_p values showed less fluctuation than the R_{inv} values, but the values were generally close (Figures 5A, B). These results suggest that R_{inv} accurately reflects the variations in the porewater salinity.

4.2.2 Quality appraisal

A low DOI index is obtained when the resistivity structures in the model are driven by the data and not by the inversion process, which is influenced by the reference model (Paepen et al., 2020; Zhang et al., 2023). All cells with a DOI index greater than 0.2 were considered as

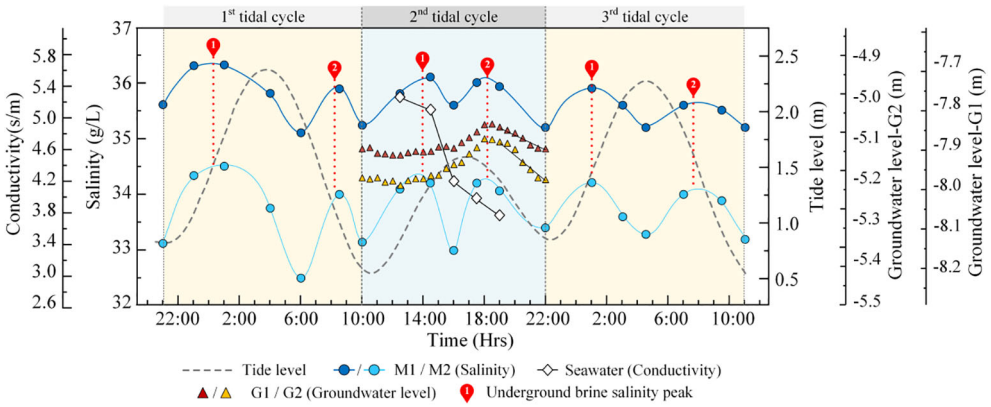

FIGURE 4
Underground brine salinity, groundwater level, and seawater conductivity in the mining area during tidal cycles (the blue area represents the ERT monitoring period, the 2nd tidal cycle).

10.3389/fmars.2023.1324163

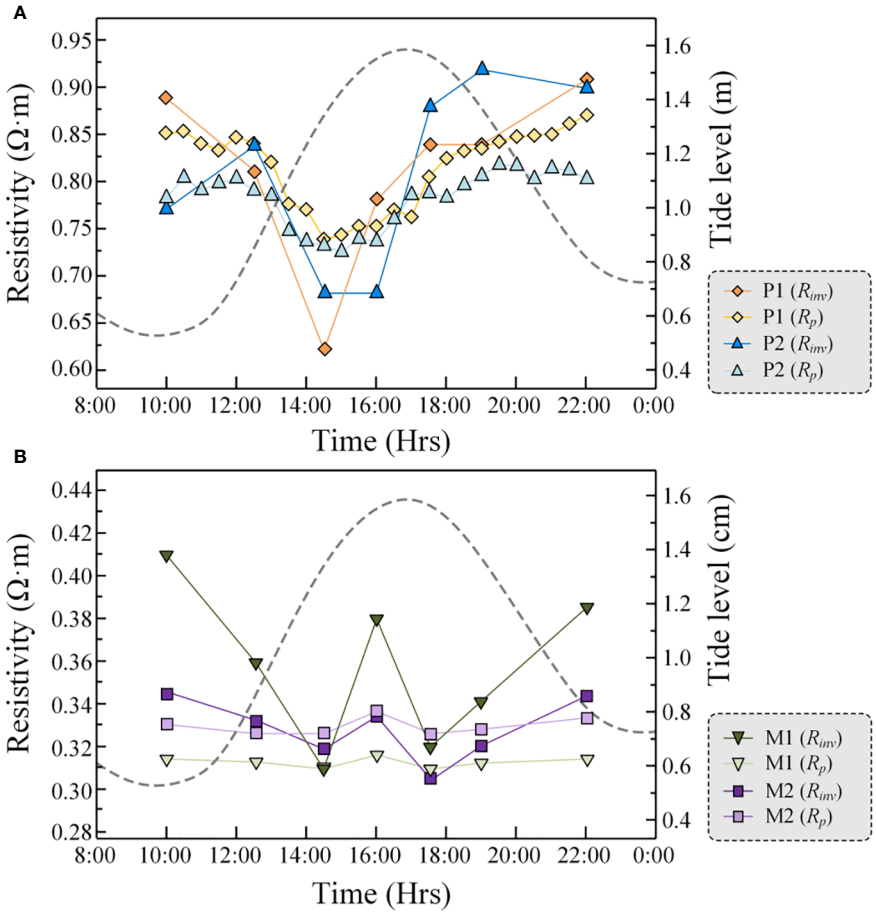

FIGURE 5
Changes in the expected resistivity and inverted resistivity in sediments in the tidal flat **(A)**/brine mining area **(B)** during the tidal cycle.

less reliable (Thompson et al., 2017). In this study, nearly all of the DOI index values of the ERT inverted result are less than 0.1. Only a small portion of the DOI index values of marine ERT inverted results in deep regions is between 0.1 and 0.15 (Figure 6). Therefore, all inversions are adequately sensitive to characterize the general sediment resistivity distribution in the studied area.

4.2.3 Variations in the inverted resistivity image during the tidal cycle

The average resistivity of the underground brine was 0.144 Ω·m. This value was substituted into Equation 2 and the expected resistivity of the brine zone was calculated as 0.32 Ω·m. This expected resistivity value was used as a standard to delineate the brine occurrence areas in the inversion resistivity profile. The top boundary of the brine body was generally consistent with the groundwater level. The distribution of the brine body remained relatively stable within the tidal cycle and occurred between -22 and -8 m, which was consistent with the distribution range of the brine layers from the geological column (Figures 3B, 7, 8).

The extent of the underground brine body followed two expansion and contraction cycles within the tidal cycle. During the rising tide, when the surface of the tidal flat was not covered by seawater (time a–b), the brine body in the mining area expanded, and the underground brine in the intertidal zone remained relatively stable. After the tidal flat was submerged in seawater (time c), the extent of the brine body in the mining area and the intertidal zone expanded significantly. During this stage, several anomalous low resistivity zones (< 0.8 Ω·m) that connected the tidal flat and the brine body appeared in the intertidal zone. During high tide (time d), the extent of the underground brine generally decreased, and most of the anomalous low resistivity zones that connected the brine body and the tidal flat in the intertidal zone disappeared. In the early stage of the ebb tide (time e), the underground brine body expanded again, and then shrunk during the subsequent ebb tide (time f–g). After the seawater receded from the tidal flat, the anomalous low resistivity zones connecting the brine body and the tidal flat in the intertidal zone completely disappeared (Figures 7, 8).

5 Discussion

5.1 Salt transport flux in the coastal brine mining areas during the tidal cycles

We calculated the amount of salt transport (m_s) and the transport rate (Rs) in the underground brine bodies at different

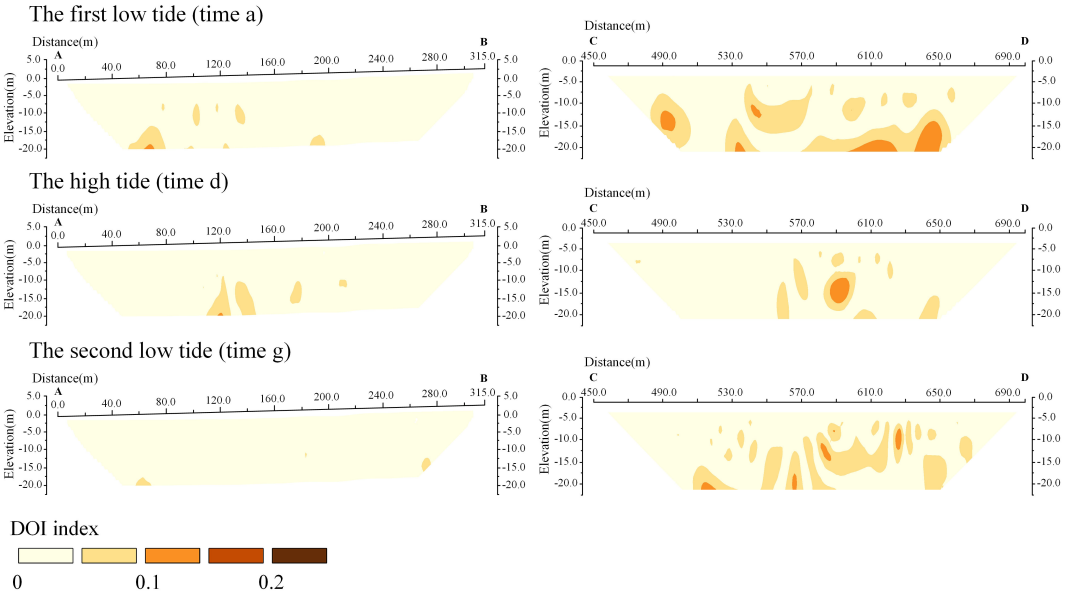

FIGURE 6
DOI index profiles for validating the effectiveness of inversion models. Here we only show the DOI index profiles of time a, d, and g, while the DOI index distribution patterns of other times are basically similar to the displayed profiles. **(A–D)** are the starting/ending points of land ERT survey line and marine ERT survey line respectively.

times during a single tidal cycle using Equation 9, the data for the extent of the brine body, and other results from the inversion of the ERT resistivity data (Figure 9; Table 1).

The coastal brine extraction area is at the marine boundary of the precipitation funnel (Figure 3A). The groundwater head difference between G1 and G2 (2.679–2.715 m) and the salinity of the underground brine (34.54–35.11 g/kg) did not fluctuate significantly as the tides fluctuated and when influenced by the large hydraulic gradient from the sea to the land, continuous brine extraction, and low permeability of the sandy tidal flats. This indicates that the underground brine in the coastal extraction area was constantly receiving a stable supply of salt from the marine environment. The results show that the salt was entering the brine body through the monitoring section at a rate of 0.226 −0.232 t/h, which means that the total salt flux entering the underground brine bodies over a vertical flow area of 1322.3 m^2 ($A\sin\theta$) was 2.75 t during a single tidal cycle or 5.50 t each day. The brine extraction wells in this area are pumped at a rate of

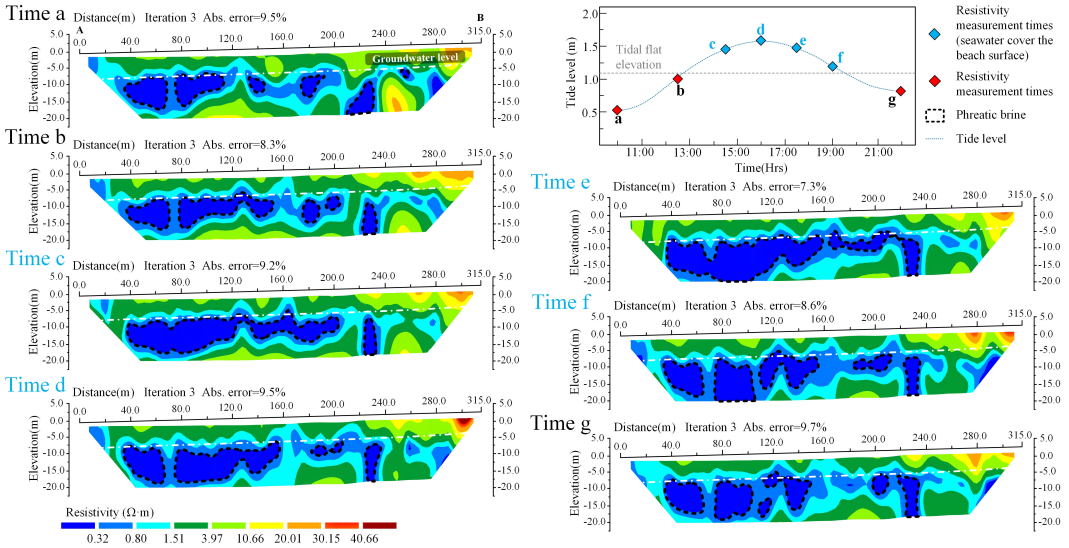

FIGURE 7
ERT inverted resistivity profiles during the tidal cycle in the brine mining area (AB line).

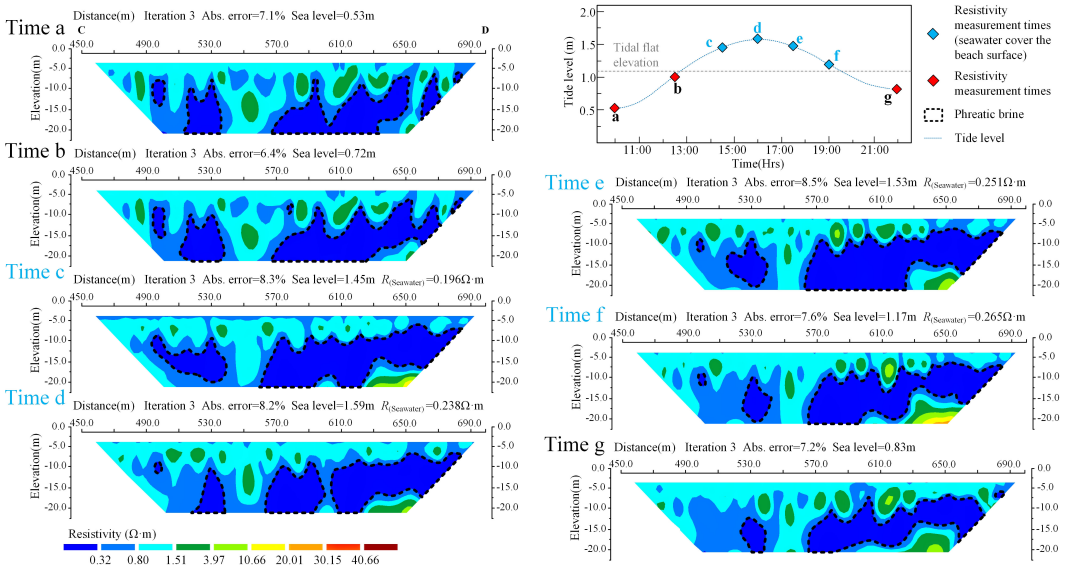

FIGURE 8
ERT Inverted resistivity profiles during the tidal cycle on the tidal flat (CD line).

approximately 5.5 m^3/h, which means that approximately 4.98 t of salt can be extracted per day. In an ideal scenario (assuming consistent tidal fluctuations and that the brine layer distribution in the monitored area remains the same), the daily salt supply replenished to the brine extraction zone along a 150 m ($L\sin\theta$) coastline can approximately sustain the extraction capacity of one brine well.

5.2 The salinity of the marine salt source supply to the coastal underground brine in the mining area

In the study area, water and salt from the marine environment continuously migrate into the underground brine layer in the extraction area under the combined influence of the seaward groundwater flow and tidal action. The rise and fall of *Rs* can reflect any changes in the water-salt migration state. The head difference (Δh) between G1 and G2 and the salinity (S) of the water replenishing the underground brine in the extraction area are the main factors that affect the water-salt migration rate (*Rs*) (Equation 9; Table 1). Although the ranges of the Δh and S values in the study area were small (Figure 10), these data can still indicate the water-salt migration state in the brine layer of the extraction area during different tidal stages.

In coastal aquifer systems, the groundwater salinity generally shows a single salinity peak with a time lag relative to the tides during the tidal cycles (Hou et al., 2016; Zhang et al., 2023). However, in this coastal brine extraction area, the groundwater salinity showed two salinity peaks. Fu et al. (2020) also observed two peaks in the groundwater salinity at northern Changyi Beach, which is also located on the southern coast of Laizhou Bay. This suggests that there are at least two pathways for salt transport from the marine environment to the coastal brine reserves in this region. There is also a stable pathway for salt loss in this area, i.e., the extraction of underground brine. Here, we combined the patterns of

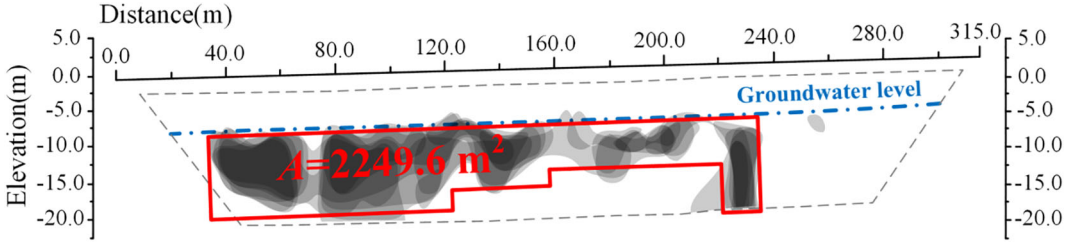

FIGURE 9
The distribution of the underground brine within the ERT monitoring profiles in the brine mining area. The gray shadow represents the extent of the underground brine at different tide times, which was divided using the ERT inverted resistivity profile data. The red box represents the range of the underground brine flow area that was involved in the calculation of the salt transport flux (A=2249.6 m^2).

10.3389/fmars.2023.1324163

TABLE 1 Calculation parameters and the results of the salinity transport flux.

Tidal stage	ρ (kg/m^3)	A (m2)	K (m/s)	L (m)	θ	Δh[a] (m)	Δt (s)	S[b] (g/kg)	m_s (t)	Rs[c] (t/h)
I	1080	2249.6	0.0001	260	36°	2.679	9000	34.54	0.566	0.226
II						2.693	7200	35.11	0.462	0.231
						2.702	5400	34.70	0.344	0.229
III						2.715	5400	34.66	0.345	0.230
						2.712	5400	35.05	0.349	0.232
IV						2.695	10800	34.72	0.686	0.229

a. Δh is the average hydraulic head difference during each Δt.
b. S is the average underground brine salinity measured in M1 and M2 during each Δt. (S is considered the salinity of the underground brine that supplies the mining area when calculating m_s).
c. Rs is the rate at which the coastal underground brine receives salt transport (a positive value means the coastal underground brine is being supplied by marine salt source).

the low-resistivity anomaly distribution in the ERT inversion resistivity profiles, and identified four stages in the marine salt supply, as follows:

Stage I (the early stage of the rising tide, when the seawater did not cover the beach surface). The underground brine in the extraction area is replenished from the lower part of the tidal flat (Del Pilar et al., 2015; Guo, 2018; Fu et al., 2020), and the salinity increases and the brine distribution range expands slightly on both the sea and land sides (Figures 4, 7, 8, 11A). During this stage, there is a time lag of several hours between the groundwater level and the tide (Gao et al., 2010; Su et al., 2018), and the rise in the tide does not cause changes in the groundwater levels of G1 and G2 (Figure 4). Δh stays the same, so the increase in S is the only factor that contributes to the increase in Rs (Figures 4, 10).

Stage II (during the rising tide, when the seawater covers the beach surface). In the early stage of stage II, the brine in the mining area is replenished from the lower part of the tidal flat and the high-salinity water infiltrating from the surface of the flat. The first salinity peak appears in the underground brine of the mining area (Figures 4, 10, 11B), and the extent of the brine area on the sea and land sides significantly expands (Figures 7, 8). The increase in Rs is caused by the increase in Δh and S. Because G2 is closer to the marine environment than G1, the groundwater level at G2 fluctuates slightly more than that at G1, which results in an increase in Δh (Figure 4). The value of S increases because of the dissolution of a large amount of evaporite salt after the tidal flat is submerged by seawater, and these high-salinity water bodies infiltrate into the aquifer system through bioactive channels or high-permeability sediment distribution zones near the coast (Del Pilar et al., 2015; Hou et al., 2016; Xiao et al., 2019). The ERT inversion resistivity profiles for the marine side show there are anomalous areas of low resistivity that connect the brine bodies and the tidal flat, which suggests that there are preferential pathways for high-salinity water replenishment (Figures 7, 8).

In the late part of stage II, a large amount of low-salinity seawater infiltrates from the surface of the flat, leading to a decrease in the salinity of the underground brine (Figures 4, 11B), and the extent of the brine on the sea and land sides decreases (Figures 7, 8). Although Δh continues to increase during this period, the rapid decrease in the seawater salinity

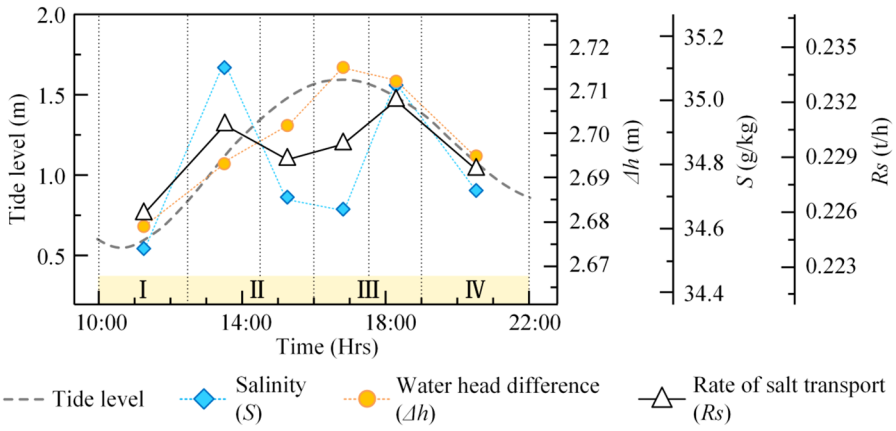

FIGURE 10
The relationship between the salinity, hydraulic head difference, and the salt transport rate. The yellow boxes show the four stages of salt transport during the tidal cycle (I–IV), namely, (I) the early stage of the rising tide, when the seawater did not cover the beach surface; (II) the rising tide, when the seawater covered the beach surface; (III) the early stage of the ebb tide, when seawater still covered the beach surface, and (IV) the ebb tide, when the seawater receded from the beach surface.

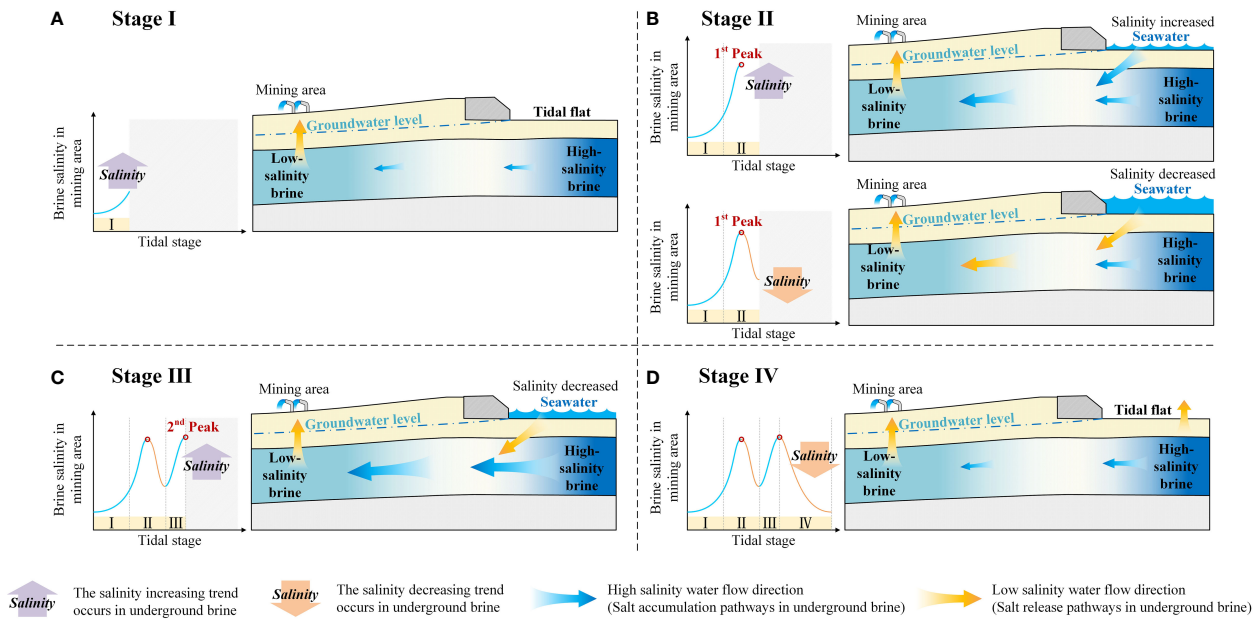

FIGURE 11
The two salinity peaks mode of marine salt source supplementing coastal underground brine during a single tidal cycle. **(A–D)** show the salt accumulation and pathways where underground brine is lost in mining areas during the tidal cycle (stages I–IV). The blue/yellow arrows represent the flow direction of water with different salinity that cause the accumulation/loss of salt in underground brine resources compared to the previous stage or the previous moment in the same stage.

leads to a significant reduction in *S*, and *Rs* shows an overall decrease (Figures 4, 7, 8, 10). The infiltration of low-salinity water through the flat restricts the amount of replenishment of high-salinity water from the lower part of the tidal flat to the brine mining area to some extent.

Stage III (the early stage of the ebb tide, when the seawater still covers the beach surface). A large amount of high-salinity water is transported from the sea to the land through the aquifer in a horizontal direction into the underground brine reserve in the mining area. The second salinity peak appears in the underground brine in the mining area (Figures 4, 10, 11C), and the extent of the brine expands again on the sea and land sides (Figures 7, 8). Because of the time lag, the pumping intensity of the tidal action peaks in this stage (Santos et al., 2011), and the groundwater levels at G1 and G2 and the head difference Δh all reached their peak values. The salinity *S* also reached its peak value synchronously. This means that a large amount of high-salinity water from the lower part of the tidal flat is transported into the underground brine in the mining area under the tidal driving force during this stage. The intruding low-salinity seawater no longer controls the salinity of the underground brine in the mining area.

Stage IV (during the ebb tide, when the seawater recedes from the beach surface). In this stage, the tidal action weakens and high-salinity groundwater is discharged to the beach (Hou, 2016; Guo, 2018; Zhang, 2021), leading to a synchronous decrease in Δh and *S*, and a decrease in *Rs* (Figures 4, 10). The intensity of the seawater supply from the marine to the brine in the mining area weakens, and the salinity of the underground brine in the mining area begins to decrease (Figure 4). The extent of the brine gradually narrows on both the sea and land (Figures 7, 8, 11D).

We also observed that *S* has more influence on *Rs* than Δh. First, during the tidal cycle, the pattern of fluctuations of *Rs* is more similar to pattern of the fluctuation of *S* than Δh. *Rs* and *S* have two peaks, which occur early in stage II and late in stage III. Second, from late in stage II until early in stage III, *S* decreases while Δh increases, leading to an overall decrease in *Rs*. This implies that the two salinity peaks in the underground brine extraction area depend on the salinity of the different salt sources during each tidal stage. Therefore, for two salinity peaks to occur during a single tidal cycle in the brine extraction area (1) there must be at least two salt sources for the brine extraction area, and (2) each source must have a high value at different stages in the tide.

When the brine extraction area is adjacent to areas with strong evaporation, such as salt marshes, tidal channels, high tide line areas, and areas with a distribution of high-salinity underground brine, condition (1) is satisfied. When there are localized high-permeability zones in muddy tidal flats and the tidal flats are long enough, condition (2) is satisfied. This is because the wide and gentle tidal flats exacerbate the time lag of the groundwater level fluctuations caused by tidal action (Gao et al., 2010; Su et al., 2018). The peaks in the horizontally transported flux of salt from the sea to the land in the shallow aquifer will occur several hours after the high tide. The rising tide can quickly submerge a large area of the tidal flats and transport large quantities of dissolved evaporated salt to the nearshore side through the flats. This flow can supply the underground brine reserve when it crosses high-permeability zones (Stahl et al., 2014; Xiao et al., 2019; Zhang, 2021; Zhang et al., 2023). The flux of salt transported to the extraction area through this pathway will peak earlier than the high tide.

6 Conclusions

The marine environment is the main source of salt for the underground brine reserves adjacent to tidal flats. In this study, ERT monitoring sections and hydrology monitoring holes were established in the *in-situ* coastal area to evaluate the salt flux and pattern of salt recharge from marine salt source to mining areas through coastal aquifers. Based on the monitoring results, we developed a new method to quantify the replenishment of salt from marine salt source through the coastal aquifer to the underground brine in the mining area; We also found that there are two tidal-driven salinity peaks in the salt supply for the underground brine reserve in the coastal mining area during a single tidal cycle. The main findings are as follows:

(1) The coastal brine exploitation area is located at the boundary of a precipitation funnel. The salinity of the underground brine and the pre-existing large hydraulic gradient from the sea to the land are not significantly affected by fluctuations in the tidal level. The underground brine reserve in the mining area consistently receives a stable supply of salt from the marine, at a rate of 0.226–0.232 t/h. The total salt flux entering the underground brine reserve via a 150 m long shoreline and a 1322.3 m^2 window flow is 5.50 t per day, which roughly equates to the daily extraction of one brine well.

(2) During a single tidal cycle, there were two salinity peaks in the supply to the underground brine reserve. For this to happen, there must be at least two sources supplying brine to the mining area, and the salinity of the different salt sources is high at different tidal stages. We observed that the first salinity peak occurred after the initial stage of the rising tide when the seawater inundated the tidal flat (Stage II early). During this stage, seawater dissolves and carries a large amount of evaporated salt and transports it to the brine layer through high-permeability zones or bioactive channels, ultimately supplying the mining area. Late in Stage II, the seawater salinity decreased and the salinity peak disappeared. The second salinity peak occurred during the early stage of the falling tide (Stage III). The flow of high-salinity brine in the lower part of the intertidal zone accelerated toward the mining area under the influence of the tidal pumping effect, but was subject to a time lag. During Stage IV, as the tidal action weakened, the intensity of the marine salt supply to the mining area decreased and the salinity peak disappeared.

Although the conclusions from this study will be a useful reference for related research on underground brine supplies and stores in coastal areas, further understanding of the hydrodynamic mechanism of the two salinity peaks mode will enable us to more accurately evaluate the replenishment of coastal underground brine resources by marine salt source. The research method used in this study could not identify the factors affecting the time interval between the two salinity peaks and their values. In the future, we can use the long period *in-situ* monitoring combined with numerical simulation methods to study the above problems.

Data availability statement

The original contributions presented in the study are included in the article/supplementary material. Further inquiries can be directed to the corresponding authors.

Author contributions

XX: Data curation, Formal analysis, Investigation, Methodology, Writing – original draft, Writing – review & editing. YZ: Data curation, Formal analysis, Investigation, Methodology, Writing – original draft, Writing – review & editing. TF: Funding acquisition, Investigation, Supervision, Writing – review & editing. ZS: Investigation, Methodology, Writing – review & editing. BL: Investigation, Methodology, Writing – review & editing. ML: Investigation, Methodology, Writing – review & editing. XG: Funding acquisition, Methodology, Supervision, Writing – review & editing.

Funding

The author(s) declare financial support was received for the research, authorship, and/or publication of this article. This study was financially supported by Open Fund of the 801 Institute of Hydrogeology and Engineering Geology (801KF2021–6). Key Scientific and Technological Research Project, Shandong Provincial Bureau of Geology & Mineral Resources (KY202206). The National Natural Science Foundation of China (41977234, 42276226, 42276223). Shandong Provincial Natural Science Foundation (ZR2022MD048). Key Research and Development Program of Shandong Province, China (2020JMRH0101). We also thanks the support of "Observation and Research Station of Seawater Intrusion and Soil Salinization, Laizhou Bay."

Conflict of interest

The authors declare that the research was conducted in the absence of any commercial or financial relationships that could be construed as a potential conflict of interest.

Publisher's note

References

Archie, G. E. (1942). The electrical resistivity log as an aid in determining some reservoir characteristics. *Trans. AIME* 146 (01), 54–62. doi: 10.2118/942054-G

Boufadel, M. C. (2000). A mechanistic study of nonlinear solute transport in a groundwater-surface water system Under steady state and transient hydraulic conditions. *Water Resour. Res.* 36 (9), 2549–2565. doi: 10.1029/2000WR900159

Chang, Y. (2018). *Quantitative study on seawater and groundwater exchange rate in muddy tidal flat in South Coast of Laizhou Bay, China*. M.S. Thesis (Beijing: China University of Geosciences).

deGroot-Hedlin, C., and Constable, S. (1990). Occam's inversion to generate smooth, two-dimensional models from magnetotelluric data. *Geophysics* 55 (12), 1613–1624. doi: 10.1190/1.1442813

Del Pilar, M., Carol, E., Hernández, M. A., and Bouza, P. J. (2015). Groundwater dynamic, temperature and salinity response to the tide in Patagonian marshes: Observations on a coastal wetland in San José Gulf, Argentina. *J. South Am. Earth Sci.* 62, 1–11. doi: 10.1016/j.jsames.2015.04.006

Dimova, N. T., Swarzenski, P. W., Dulaiova, H., and Glenn, C. R. (2012). Utilizing multichannel electrical resistivity methods to examine the dynamics of the fresh water-seawater interface in two Hawaiian groundwater systems. *J. Geophys. Res. Oceans* 117 (C2). doi: 10.1029/2011JC007509

Escapa, M., Perillo, G., and Iribarne, O. (2008). Sediment dynamics modulated by burrowing crab activities in contrasting sw Atlantic intertidal habitats. *Estuar. Coast. Shelf Sci.* 80 (3), 365–373. doi: 10.1016/j.ecss.2008.08.020

Fang, Y., Zheng, T., Wang, H., Zheng, X., and Walther, M. (2022). Influence of dynamically stable-unstable flow on seawater intrusion and submarine groundwater discharge over tidal and seasonal cycles. *J. Geophys. Res.: Oceans* 127, e2021JC018209. doi: 10.1029/2021JC018209

Fang, Y., Zheng, T., Zheng, X., Yang, H., Wang, H., and Walther, M. (2021). Influence of tide-induced unstable flow on seawater intrusion and submarine groundwater discharge. *Water Resour. Res.* (4 Pt.2), 57. doi: 10.1029/2020WR029038

Franco, R. D., Biella, G., Tosi, L., Teatini, P., Lozej, A., Chiozzotto, B., et al. (2009). Monitoring the saltwater intrusion by time lapse electrical resistivity tomography: The Chioggia test site (Venice Lagoon, Italy). *J. Appl. Geophys.* 69 (3-4), 117–130. doi: 10.1016/j.jappgeo.2009.08.004

Frank, V. W., van derGun, J., and Reckman, J. (2009). Global overview of saline groundwater occurrence and genesis (Report number: GP 2009-1). Utrecht IGRAC - U. N. *Int. Groundw. Resour. Assess. Cent*, 1–32.

Fu, T., Zhang, Y., Xu, X., Su, Q., and Guo, X. (2020). Assessment of submarine groundwater discharge in the intertidal zone of Laizhou Bay, China, using electrical resistivity tomography. *Estuar. Coast. Shelf Sci.* 245 (10), 106972. doi: 10.1016/j.ecss.2020.106972

Gao, M., Hou, G., and Guo, F. (2016). Conceptual model of underground brine formation in the silty coast of Laizhou bay, Bohai sea, China. *J. Coast. Res.* 74 (sp1), 157–165. doi: 10.2112/SI74-015.1

Gao, M., Ye, S., Shi, G., Yuan, H., Zhao, G., and Xue, Z. (2010). Oceanic tide-induced shallow groundwater regime fluctuations in coastal wetland. *Hydrogeol. Eng. Geol.* 37, 24–27. doi: 10.1016/S1876-3804(11)60004-9

Gonneea, M. E., Mulligan, A. E., and Charette, M. A. (2013). Climate-driven sea level anomalies modulate coastal groundwater dynamics and discharge. *Geophys. Res. Lett.* 40 (11), 2701–2706. doi: 10.1002/grl.50192

Guo, X. Q. (2018). Numerical simulation of Seawater-Groundwater exchange in QingXiang profile of Laizhou Bay, China. *China Univ. Geosci. (Beijing)*.

Han, Y. (1996). *Quaternary underground brine in the coastal areas of the northern China* (Science Press).

Han, D., Song, X., Currell, M., Yang, J., and Xiao, G. (2014). Chemical and isotopic constraints on evolution of groundwater salinization in the coastal plain aquifer of Laizhou Bay, China. *J. Hydrol.* 508 (2), 12–27. doi: 10.1016/j.jhydrol.2013.10.040

Harvey, J. W., and Nuttle, W. K. (1995). Fluxes of water and solute in a coastal wetland sediment. 2. effect of macropores on solute exchange with surface water. *J. Hydrol. (Amst)* 164, 109–125. doi: 10.1016/0022-1694(94)02562-P

Hermans, T., and Paepen, M. (2020). Combined inversion of land and marine electrical esistivity tomography for submarine groundwater discharge and saltwater intrusion characterization. *Geophys. Res. Lett.* 47, e2019GL085877. doi: 10.1029/2019GL085877

Hou, L. (2016). *Seawater-Groundwater exchange in a Silty Tidal Flat in the South Coast of Laizhou Bay,China* (Beijing: China University of Geosciences).

Hou, L., Li, H., Zheng, C., Ma, Q., Wang, C., Wang, X., et al. (2016). Seawater-groundwater exchange in a silty tidal flat in the south coast of Laizhou Bay, China. *J. Coast. Res.* 74, 136–148. doi: 10.2112/SI74-013.1

Jackson, P. D., Smith, D. T., and Stanford, P. N. (1978). Resistivity-porosity-particle shape relationships for marine sands. *Geophysics* 43 (6), 1250–1268. doi: 10.1190/1.1440891

Larsen, F., Tran, L. V., Hoang, H. V., Tran, L. T., Christiansen, A. V., and Pham, N. Q. (2017). Groundwater salinity influenced by holocene seawater trapped in incised valleys in the red river delta plain. *Nat. Geosci.* 10 (5), 376–381. doi: 10.1038/ngeo2938

Li, J., Gong, X., Liang, X., Liu, Y., Yang, J., Meng, X., et al. (2021). Salinity evolution of aquitard porewater associated with transgression and regression in the coastal plain of eastern china. *J. Hydrol.* 603, 127050. doi: 10.1016/j.jhydrol.2021.127050

Liu, S. (2018). *The evolution of ground-saline water and process mechanism of saline water intrusion in southern Laizhou Bay* (Wuhan: China University of Geosciences).

Ma, Q. (2016). *Quantifying seawater-groundwater exchange rates: case studies in muddy tidal flat and sandy beach in Laizhou Bay*. (Beijing: China University of Geosciences).

Ma, Q., Li, H., Wang, X., Wang, C., Wan, L., Wang, X., et al. (2015). Estimation of seawater–groundwater exchange rate: case study in a tidal flat with a large-scale seepage face (Laizhou Bay, China). *Hydrogeol. J.* 2 (23), 265–275. doi: 10.1007/s10040-014-1196-z

Misonou, T., Asaue, H., Yoshinaga, T., Matsukuma, Y., Koike, K., and Shimada, J. (2013). Hydrogeologic-structure and groundwater-movement imaging in tideland using electrical sounding resistivity: a case study on the Ariake Sea coast, southwest Japan. *Hydrogeol. J.* 21 (7), 1593–1603. doi: 10.1007/s10040-013-1022-z

Mongelli, G., Monni, S., Oggiano, G., Paternoster, M., and Sinisi, R. (2013). Tracing groundwater salinization processes in coastal aquifers: a hydrogeochemical and isotopic approach in na-cl brackish waters of north-western sardinia, italy. *Hydrol. Earth Syst. Sci.* 17 (7), 2917–2928. doi: 10.5194/hess-17-2917-2013

Nguyen, F., Kemna, A., Antonsson, A., Engesgaard, P., Kuras, O., Ogilvy, R., et al. (2009). Characterization of seawater intrusion using 2D electrical imaging. *Near Surf. Geophys.* 7 (1303), 377–390. doi: 10.3997/1873-0604.2009025

Oldenburg, D. W., and Li, Y. (1999). Estimating depth of investigation in DC resistivity and IP surveys. *Geophysics* 64 (2), 403–416. doi: 10.1190/1.1444545

Paepen, M., Hanssens, D., Smedt, P. D., Walraevens, K., and Hermans, T. (2020). Combining resistivity and frequency domain electromagnetic methods to investigate submarine groundwater discharge in the littoral zone. *Hydrol. Earth Sys. Sci.* 24 (7), 3539–3555. doi: 10.5194/hess-2019-540

Post, V. E. A., Vandenbohede, A., Werner, A. D., Maimun, and Teubner, M. D. (2013). Groundwater ages in coastal aquifers. *Adv. Water Resour.* 57 (7), 1–11. doi: 10.1016/j.advwatres.2013.03.011

Qi, H., Ma, C., He, Z., Hu, X., and Gao, L. (2019). Lithium and its isotopes as tracers of groundwater salinization: A study in the southern coastal plain of Laizhou Bay, China. *Sci. Total Environ.* 650 (2), 878–890. doi: 10.1016/j.scitotenv.2018.09.122

Revil, A. (2013). Effective conductivity and permittivity of unsaturated porous materials in the frequency range 1 mHz–1GHz. *Water Resour. Res.* 49 (1), 306–327. doi: 10.1029/2012WR012700

Robinson, C., Li, L., and Barry, D. A. (2007). Effect of tidal forcing on a subterranean estuary. *Adv. Water Resour.* 30 (4), 851–865. doi: 10.1016/j.advwatres.2006.07.006

Sanford, W. E., and Wood, W. W. (2001). Hydrology of the coastal sabkhas of Abu Dhabi, United Arab Emirates. *Hydrogeol. J.* 9 (4), 358–366. doi: 10.1007/s100400100137

Santos, I. R., Burnett, W. C., Misra, S., Suryaputra, I. G. N. A., Chanton, J. P., Dittmar, T., et al. (2011). Uranium and barium cycling in a salt wedge subterranean estuary: The influence of tidal pumping. *Chem. Geol.* 287 (1-2), 114–123. doi: 10.1016/j.chemgeo.2011.06.005

Shao, S., Guo, X., Gao, C., and Liu, H. (2021). Quantitative relationship between the resistivity distribution of the by-product plume and the hydrocarbon degradation in an aged hydrocarbon contaminated site. *J. Hydrol.* 596, 126112. doi: 10.1016/j.jhydrol.2021.126122

Shen, C., Fan, Y., Wang, X., Song, W., Li, L., and Lu, C. (2022). Effects of land reclamation on a subterranean estuary. *Water Resour. Res.* 58, e2022WR032164. doi: 10.1029/2022WR032164

Shen, C., Fan, Y., Zou, Y., Lu, C., Kong, J., Liu, Y., et al. (2023). Characterization of hypersaline zones in salt marshes. *Environ. Res. Letter.* 18 (2023), 044028. doi: 10.1088/1748-9326/acc418

Stahl, M. O., Tarek, M. H., Yeo, D. C. J., Badruzzaman, A. B. M., and Harvey, C. F. (2014). Crab burrows as conduits for groundwater-surface water exchange in Bangladesh, Geophys. *Res. Lett.* 41, 8342–8347. doi: 10.1002/2014GL061626

Su, Q., Xu, X., Chen, G., Fu, T., and Liu, W. (2018). Frequency and hysteresis of groundwater levels influenced by tides. *Ocean Dev. Manage.* 35 (10), 79–83. doi: 10.20016/j.cnki.hykfygl.2018.10.015

Sun, Q., Gao, M., Wen, Z., Hou, G., Dang, X., Liu, S., et al. (2023). Hydrochemical evolution processes of multiple-water quality interfaces (fresh/saline water, saline water/brine) on muddy coast under pumping conditions. *Sci. Total Environ.* 857, 159297. doi: 10.1016/j.scitotenv.2022.159297

Thompson, S. S., Kulessa, B., Benn, D. I., and Mertes, J. R. (2017). Anatomy of terminal moraine segments and implied lake stability on ngozumpa glacier, Nepal, from electrical resistivity tomography (ert). *Sci. Rep.* 7, 46766. doi: 10.1038/srep46766

William, P., Anderson,, and Lauer, R. M. (2008). The role of overwash in the evolution of mixing zone morphology within barrier islands. *Hydrogeol. J.* 16.8, 1483–1495. doi: 10.1007/s10040-008-0340-z

Wilson, A. M., and Morris, J. T. (2012). The influence of tidal forcing on groundwater flow and nutrient exchange in a salt marsh-dominated estuary. *Biogeochemistry* 108, 27–38. doi: 10.1007/s10533-010-9570-y

Wu, J., Guo, X., Xie, Y., Zhang, Z., Tang, H., Ma, Z., et al. (2021). Evolution of bubble-bearing areas in shallow fine-grained sediments during land reclamation with prefabricated vertical drain improvement. *Eng. Geol.* 280, 105630. doi: 10.1016/j.enggeo.2020.105630

Xiao, K., Wilson, A. M., Li, H., and Ryan, C. (2019). Crab burrows as preferential flow conduits for groundwater flow and transport in salt marshes: A modeling study. *Adv. Water Resour.* 132, 103408. doi: 10.1016/j.advwatres.2019.103408

Xin, P., Jin, G., Li, L., and Barry, D. A. (2009). Effects of crab burrows on pore water flows in salt marshes. *Adv. Water Resour.* 32 (3), 439–449. doi: 10.1016/j.advwatres.2008.12.008

Xing, C., Zhang, Y., Guo, X., and Sun, J. (2023). Time series investigation of electrical resistivity tomography reveals the key drivers of tide and storm on groundwater discharge. *Estuarine Coast. Shelf Sci.* 282, 108225. doi: 10.1016/j.ecss.2023.108225

Yang, J., Graf, T., and Ptak, T. (2015). Sea level rise and storm surge effects in a coastal heterogeneous aquifer: a 2D modelling study in northern Germany. *Grundwasser* 20 (1), 39–51. doi: 10.1007/s00767-014-0279-z

Yi, L., Yu, H., Ortiz, J. D., Xu, X., Chen, S., Ge, J., et al. (2012). Late Quaternary linkage of sedimentary records to three astronomical rhythms and the Asian monsoon, inferred from a coastal borehole in the south Bohai Sea, China. *Palaeogeogr. Palaeoclimatol. Palaeoecol.* 329, 101–117. doi: 10.1016/j.palaeo.2012.02.020

Zhan, L., Xin, P., Chen, J., Chen, X., and Li, L. (2023). Sustained upward groundwater discharge through salt marsh tidal creeks. *Limnol. Oceanogr. Lett.* doi: 10.1002/lol2.10359

Zhang, Y. (2021). *Study on the Process of Water and Salt Transport under Tidal Effects in Multi-layer Aquifers of Muddy Tidal Flats in the South Coast of Laizhou Bay* (Qingdao: Ocean University of China).

Zhang, K., Guo, X., Li, N., and Cui, X. (2021). Utilizing multichannel electrical resistivity methods to examine the contributions of submarine groundwater discharges. *Mar. Geores. Geotechnol.* 39 (7), 778–789. doi: 10.1080/1064119X.2020.1760971

Zhang, Z., Sun, J., Ma, J., and Hou, Y. (2004). *Effect of different value of a and m in Archie formula on water saturation* Vol. 6 (China: J. Univ. Petroleum).

Zhang, Y., Wu, J., Zhang, K., Guo, X., Xing, C., Li, N., et al. (2021). Analysis of seasonal differences in tidally influenced groundwater discharge processes in sandy tidal flats: A case study of Shilaoren Beach, Qingdao, China. *J. Hydrol.* 603, 127128. doi: 10.1016/j.jhydrol.2021.127128

Zhang, Y., Xing, C., Guo, X., Zheng, T., Zhang, K., Xiao, X., et al. (2023). Temporal and spatial distribution patterns of upper saline plumes and seawater-groundwater exchange under tidal effect. *J. Hydrol.* 625, 130042. doi: 10.1016/j.jhydrol.2023.130042

Zheng, T., Fang, Y., Gao, S., Zheng, X., Liu, T., and Luo, J. (2023). The impact of hydraulic conductivity anisotropy on the effectiveness of subsurface dam. *J. Hydrol.* 626, 130360. doi: 10.1016/j.jhydrol.2023.130360

Zheng, Y., Gao, M., Liu, S., and Wang, S. (2014). Distribution characteristics of subsurface brine resources on the southern coast of laizhou bay since late pleistocene. *Hydrogeol. Eng. Geol.* 41 (5), 11–18. doi: 10.16030/j.cnki.issn.1000-3665.2014.05.030

frontiers | Frontiers in Marine Science

TYPE Original Research
PUBLISHED 23 January 2024
DOI 10.3389/fmars.2024.1346275

OPEN ACCESS

EDITED BY
Chengji Shen,
Hohai University, China

REVIEWED BY
Lu Xia,
Shandong University of Science and Technology, China
Shanshan Li,
Qingdao Agricultural, China

*CORRESPONDENCE
Yudao Chen
cyd0056@vip.sina.com
Yuan Xia
xiayuan@glut.edu.cn

RECEIVED 29 November 2023
ACCEPTED 03 January 2024
PUBLISHED 23 January 2024

CITATION
Wang H, Zhang J, Chen Y, Xia Y, Jian P and Liang H (2024) Clogging risk of microplastics particles in porous media during artificial recharge: a laboratory experiment. *Front. Mar. Sci.* 11:1346275. doi: 10.3389/fmars.2024.1346275

Clogging risk of microplastics particles in porous media during artificial recharge: a laboratory experiment

Huan Wang[1,2,3], Junjie Zhang[1], Yudao Chen[1,2,3]*, Yuan Xia[1,2,3]*, Peng Jian[1] and Haozhi Liang[1]

[1]College of Environmental Science and Engineering, Guilin University of Technology, Guilin, China, [2]Guangxi Key Laboratory of Theory and Technology for Environmental Pollution Control, Guilin University of Technology, Guilin, China, [3]Collaborative Innovation Center for Water Pollution Control and Water Safety in Karst Area, Guilin University of Technology, Guilin, China

Management aquifer recharge (MAR) technology is widely applied to solve seawater intrusion caused by groundwater overexploitation in coastal areas. However, MAR creates an important pathway for microplastics (particle size< 5 mm) to enter groundwater. To explore the clogging potential of microplastics in aquifer media, a series of laboratory-scale column experiments were conducted in this study. The hydraulic conductivity of porous media and deposition amount of microplastics were investigated under different experimental conditions. In our study, most of the microplastics were intercepted in the sand column's surface layer. The difference of particle size in porous media greatly influence the clogging development. The hydraulic conductivity of the aquifer media decreased as the microplastic particle size decreased. When the particle size of microplastic was larger than 300 mm, most of the microplastics deposits on the surface of the porous media, forming a "microplastic accumulation layer". Microplastics are affected by particle size, flow shear stress and preferential flow during migration. The migration ability of microplastics increased significantly with the increase of hydraulic head difference and decreased with the increase of sand column depth. The bacteria microorganisms are projected to be a new biological control strategy in conjunction with MAR. The study of clogging risk of microplastics particles in porous media during artificial recharge provides novel and unique insights for the management and control of microplastic pollution in groundwater systems.

KEYWORDS

microplastics, groundwater artificial recharge, hydraulic conductivity, clogging risk, porous media

1 Introduction

Groundwater plays vital role in drinking, agricultural, domestic, and industrial uses worldwide (Aeschbach-Hertig and Gleeson, 2012; Gorelick and Zheng, 2015). Groundwater overexploitation cannot be neglected worldwide (Fang et al., 2022a); which leads to a series of environmental problems, such as seawater intrusion, soil salinization, ground subsidence, etc (Fang et al., 2022b). MAR technology can effectively control seawater intrusion by replenishing groundwater, and form an underground freshwater curtain in the coastal region to prevent further seawater intrusion. In addition, groundwater pollution is one of the environmental problems that cannot be neglected (Re, 2019). Major sources of groundwater pollution include agricultural runoff (Abdalla and Khalil, 2018), reuse of wastewater (Luo et al., 2014), biosolids (Gago et al., 2016), and industrial activities (Xu et al., 2021). Besides, groundwater can be contaminated by a wide variety of emerging pollutants related to anthropogenic activities (Lapworth et al., 2012; Hoellein et al., 2021; Bayabil et al., 2022; Khan, 2022) such as per- and poly-fluoroalkyl substances (PFASs) (Szabo et al., 2018; Hepburn et al., 2019) and pharmaceuticals (Sui et al., 2015). This prevents the beneficial use of groundwater resources and requires costly and technically challenging remediation (Smith et al., 2014).

Plastic products are widely used in human life and industry production due to their low cost, high ductility and stable properties (Paul-Pont et al., 2018; Murawski et al., 2022). Plastics can be classified into five types according to diameter: macroplastics (>25 mm), mesoplastics (1–25 mm), large microplastics (1–5 mm), small microplastics (1–1000 μm), and nanoplastics(<1 μm) (Eriksen et al., 2014; Dris et al., 2015; Alimi et al., 2018; Hanvey, 2023). Microplastics refer to fragments of plastic particles with size smaller than 5 mm (Chae et al., 2023; Leusch et al., 2023). As an emerging pollutant, microplastics have attracted great attention worldwide (Alimi et al., 2018) due to the large amount and wide distribution. From 1950 to 2017, global production of plastics increased from 1.5 million tons to 320 million tons and is expected to double within the next 20 years (Alimi et al., 2018; Wanner, 2021). However, case of the low recovery rate of plastics and difficult to decompose, it leads to serious environmental pollution. Microplastics are abundant in freshwater, marine and terrestrial environments, from beaches to the deepest part of the Mariana Trench (Cincinelli et al., 2021) and from cities to remote areas (Zhang et al., 2016), even in locations far from point sources such as Mount Everest (Napper et al., 2021). It is estimated that 71% of plastics produced globally were discarded and ended up in the environment (Geyer et al., 2017; Hohn et al., 2020). About 275 million metric tons of plastic trash from 192 coastal regions/nations entered the sea, totaling 4.8–12.7 million metric tons (Pirsaheb et al., 2020). In 2017-2018, 3.5 million tons of plastic were produced in Australia, with only 11% (38.5 thousand tons) of the plastics being recycled (Samandra, 2022). In recent years, the presence of microplastics in groundwater has been verified (Alnahdi et al., 2023). The maximum concentration of microplastics was 15.2 particles/L detected in karst aquifers in Illinois, USA (Panno et al., 2019). Microplastics (concentration of 0-7 microplastics/m^3) with a particle size of 50-150 μm were detected in groundwater in northern Germany (Mintenig et al., 2019). The average amount of microplastics detected across all sites in groundwater bores from Australia was 38 ± 8 microplastics/L (Samandra, 2022). Panno et al. (2019) proposed that microplastics are transported to karst groundwater through two potential ways: (1) Fractures and crevices in underlying aquifers in karst systems. (2) Groundwater contamination by septic systems and sinkholes in rural areas, leaky municipal sewage lines, and surface runoff. This confirms that hydrogeologic connections from the surface to the underlying aquifers provide a potential pathway for microplastics from the ground surface to groundwater.

In recent years, managed aquifer recharge (MAR) technology has been used in a large number of engineering applications to combat various environmental problems caused by groundwater overexploitation, such as seawater intrusion, which provides a potential pathway for microplastics to enter the groundwater environment (Wang H. et al., 2023; Wang et al., 2020). Some researchers have proposed that more studies are needed to investigate the presence of microplastics (MPs) in soils and groundwater. Microplastics possess stable carbon-hydrogen bonds. The chemical stability of microplastics and its resistance to degradation (Krueger et al., 2015; Geyer et al., 2017) make it face long degradation duration in natural environment. Long degradation duration and relatively large specific surface area of microplastics (Cole et al., 2011) allow it to easily adsorb some toxic substances, such as heavy metals (Ashton et al., 2010), endocrine disrupting chemicals (Ng and Obbard, 2006)and persistent organic pollutants (POPs) (Andrady, 2011; Guo et al., 2012). Some of the chemicals that microplastics contains are also threats to surrounding environment, such as plasticizers (Koelmans et al., 2019), bisphenol A (BPA), nonylphenol (NP), etc. Due to the small size, microplastics can be ingested by plants and animals; In fact, microplastic fragments have been commonly found in the intestines of fish (Tanaka and Takada, 2016), the digestive tracts of shellfish (Van Cauwenberghe and Janssen, 2014; Rochman et al., 2015), the feces of birds (Provencher et al., 2018), marine top predators such as whales (Nelms et al., 2018), and soil organisms, such as earthworms. Microplastics with small particle sizes are then likely to accumulate in organisms, causing physical damage such as ruptures in the gut and digestive tract (Yang X et al., 2022), abrasions and clogging (Guo et al., 2020). The ineligible harm of microplastic pollution to environment and organisms have attracted great attention.

Existing studies on microplastic contamination in the subsurface environment mainly focus on summarizing its sources and distribution, separation and detection methods, and ecotoxicity. Some researchers have paid attention to the impact of microplastics on saturation zone. For example, it has been reported that the penetration rate of microplastics in saturated sand increased as the particle size of polystyrene (PS) microplastics decreased from 2.0 mm to 0.8 mm (Dong, 2018). This indicates that the physicochemical properties of microplastics influence their ability of transport in porous media. The physical properties of porous media, such as particle size and non-homogeneity, also play an important role in the transport behavior of microplastics. Macroscopic inhomogeneity can cause preferential flow, enabling microplastics to be transported to deeper media. (Majdalani et al., 2008). Microscopic inhomogeneities, such as media surface roughness, can control the transport behavior of particles by affecting the forces between the media surface and particles (Li et al., 2019). The pore water flow rate in porous media is also an important factor affecting the deposition and release of microplastics on the

surface of aqueous media (Tong and Johnson, 2006). Research on the transport behavior of microplastics in porous media has increased significantly; however, the migration of microplastic particles in porous media mainly focuses on small particle sizes (Yan et al., 2020).There are still many physical and chemical factors that have not been taken into account, such as the particle size of porous media, the types of microplastic particles, as well as hydraulic condition, which require further research. There are still research gaps in microplastics migration and impact of microplastics on groundwater that need to be explored deeply. During artificial recharge process which was conducted to solve the problem of seawater intrusion, the transport behavior of microplastics from subsurface water to groundwater influenced by these factors lack of investigation.

In this study, the clogging risk of microplastics in aqueous media was investigated by a laboratory experiment, which simulate the artificial recharge process. The effects of different influencing factors, such as particle size (aqueous medium and microplastics) and hydrodynamic conditions, on the clogging of microplastics was explored in porous media during artificial recharge. The temporal and spatial variation of hydraulic conductivity influenced by particle size (aqueous media and microplastics) were investigated. The potential clogging risk of microplastics was evaluated. The preventive and controlled measures of microplastic clogging were proposed to guide MAR engineering applications.

2 Materials and methods

2.1 Experimental setup

The experimental device consisted of a column, water pump, waterhead constant device, water tank (including stirring device), and piezometer plate. The column was made of plexiglass with a height of 15 cm and an inner diameter of 4 cm. An overflow port was set 2 cm from the top of the column. Piezometer ports were placed at intervals of 3 cm along the column, numbered Y1, Y2, Y3, Y4, Y5 from top to bottom on the right side. Five sampling holes were set on the left side of the column at intervals of 3 cm and numbered A, B, C, D, E from top to bottom. The schematic diagram of the experimental device is presented in Figure 1.

2.2 Experiment material

Standard quartz sand (loss on ignition ≤ 0.40%, SiO_2 > 96%, Xiamen ISO Standard sand Co., Ltd, China) was used as porous media. The porous media was rinsed several times and soaked in 0.25 mol/L HCl for 12 h to remove metal impurities. The sand was rinsed with water to neutral pH and dried at 105 °C. After that, the sand was cauterized in a muffle furnace at 550 °C for 2 h to remove organic matter and sterilized by ultraviolet light before use. The simulated recharge water was prepared with PS microsphere (100 mg/L). PS microspheres was washed and dried at 25 °C before staining treatment with 1 μg/ml Nile Red-methanol solution.

2.3 Experimental operation

The amount of microplastic deposition on the aqueous media surface of the entire sand column was calculated using mass method. Sterilized sand samples were packed into the Plexiglas column according to the wet method with equal volume weight (1.63 g/cm^3). Sterile water was slowly passed from the bottom of the sand column to saturate the sand column for 24 h to remove any

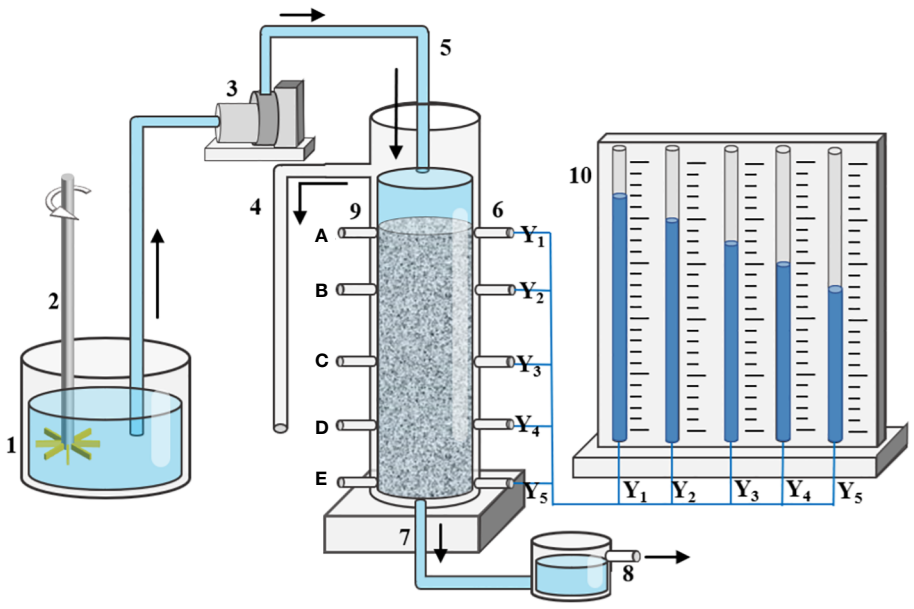

FIGURE 1
Schematic diagram of experimental setup.

remaining bubbles. Recharge water containing microplastics was introduced to the sand column from the top of the sand column. The values of the pressure plate and the flow rate at the outlet were recorded over time.

2.4 Experimental design

Column experiments were designed to simulate the process of artificial recharge in laboratory under conditions of continuous water supply. The influential factors, such as particle size of the aqueous media (AM) and microplastics (MP), and the hydrodynamic conditions (HC), were taken into consideration to investigate the clogging risk of microplastic particles. To minimize the possibility of accidental errors, our experiment was conducted in triplicate. The main groups and parameter designs were listed in Table 1.

2.5 Analytical methods

2.5.1 Hydraulic conductivity analysis

Hydraulic conductivity K was calculated according to Darcy's law, shown as Equation 1.

$$K = \frac{K4Q\Delta x}{\pi d^4 \Delta h} \quad (1)$$

Q is the flow rate at the outlet (m^3/d); "Δx" is the distance between any two pressure measuring tubes (m); "Δh" is the head difference between the two pressure measuring tubes (m); "d" is the inner diameter of the sand column (m).

In order to reflect the variation of the hydraulic conductivity of the sand column more intuitively, the relative hydraulic conductivity K' is introduced in this study (Equation 2).

$$K' = K_t / K_0 \quad (2)$$

Where K_0 is initial hydraulic conductivity of the sand layer (m/d); K_t is hydraulic conductivity of any sand layer at any moment (m/d). In this research, K' between 0-0.30 is considered as "significant clogging", K' between 0.30-0.80 is defined as "moderate clogging", and K' between 0.80-1.00 is regarded as "mild clogging".

2.5.2 Microplastic deposition amount

The amount of microplastic deposition on the aqueous media of the entire sand column was calculated using mass method. At the end of the experiment, the sand column was carefully placed horizontally and the wire mesh was removed. The sand sample was collected and dried until constant weight. The mass was recorded as m_0 (g).

The saturated NaCl solution was added to the sand samples and treated with an ultrasonic machine for 2 min. The sample was stirred with magnetic stirrer for 5 min. Then the microplastics was filtered repeatedly until the aqueous medium is clean. The constant weight of the sand sample is recorded as m_d (g). The amount of deposition S_S (g) is obtained using Equation 3.

$$S_s = m_0 - m_d \quad (3)$$

2.5.3 Fluorescence scanning microscope observation

Microplastics with diameter of 100 μm, 300 μm, and 500 μm were visualized by a fluorescence microscope (Panalytical Axios FAST, Freebo International Co., Ltd, Netherlands), as shown in Figure 2. Fluorescent particles in all fields of view are captured and photographed by a camera inside the fluorescence microscope. The size of the particles detected by the fluorescence microscope is calculated based on the square root of the particle area. The area was analyzed and measured using ImageJ software.

3 Results and discussion

3.1 Effect of medium size on hydraulic conductivity

Figure 3 describes the change in overall relative hydraulic conductivity (overall K') of entire sand column and the change in

TABLE 1 Main groups and parameter designs of recharge experiment.

Influential factors	Experimental group	Particle size of aqueous medium(mm)	Microplastic particle size(μm)	Hydraulic head difference (ΔH) (cm)
Aqueous Media particle (*AM*)	AM-F	<0.25(Fine sand)	100	5
	AM-M	0.25-0.50(Medium sand)		
	AM-C	0.50-1.00(Coarse sand)		
Microplastic particle (*MP*)	MP-100	0.25-0.50(Medium sand)	100	5
	MP-300		300	
	MP-500		500	
Hydraulic conditions (*HC*)	HC-5 HC-10 HC-15	0.25-0.50(Medium sand)	100	5
				10
				15

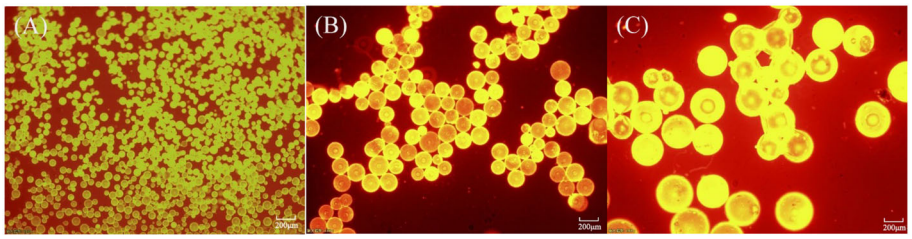

FIGURE 2
Fluorescence microscope(40X) images of 100μm **(A)**, 300μm **(B)**, 500μm **(C)** microplastics.

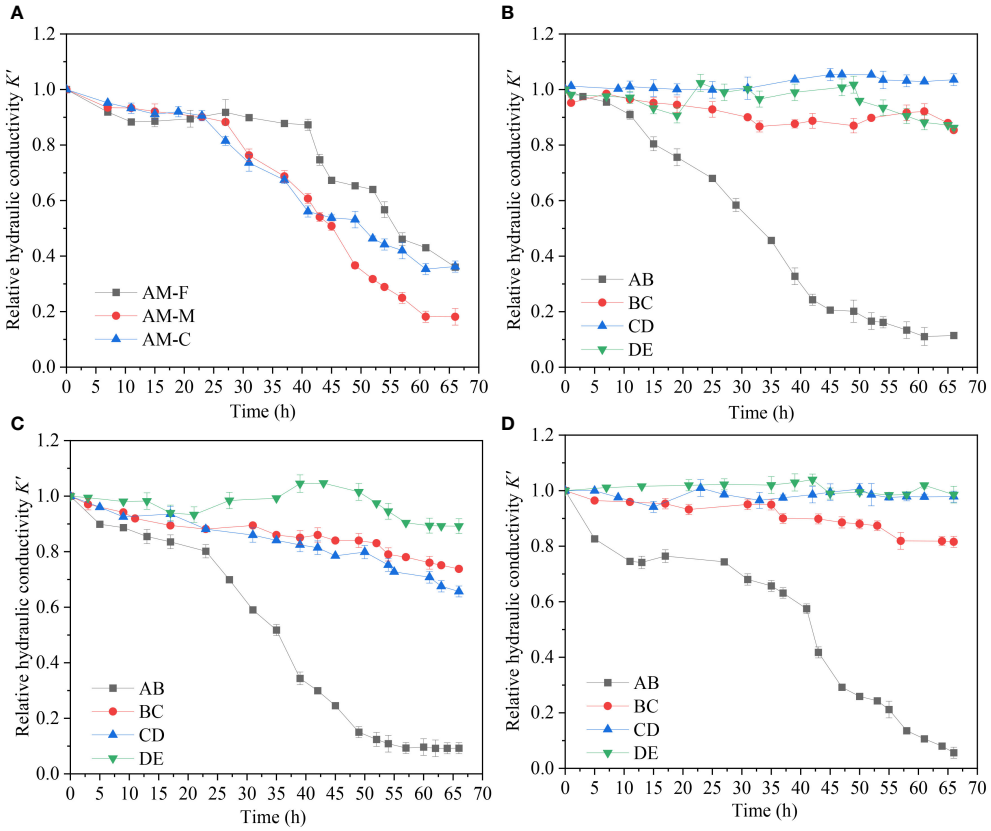

FIGURE 3
Spatial and temporal variation of hydraulic conductivity. **(A)** Overall hydraulic conductivity variation in experimental groups with different grain size **(B)** hydraulic conductivity variation of each seepage layer in coarse sand (AM-C) **(C)** hydraulic conductivity variation of each seepage layer of medium sand (AM-M) **(D)** hydraulic conductivity variation of each seepage layer of fine sand (AM-F).

relative hydraulic conductivity (*K'*) of each seepage layer over time during recharge (AB: 0-3 cm, BC: 3-6 cm, CD: 6-9 cm, DE: 9-12 cm). The overall *K'* in different experimental groups has different changing trends over time. Within the first 25 h, the overall *K'* of the sand column in AM groups changed similarly, all dropping to about 0.90. However, as the recharge continued, the differences of overall *K'* gradually became apparent. The overall *K'* values of sand column in AM-C and AM-M both decreased to around 0.60 at 40 h, which was more significant than that in AM-F (dropped to 0.90). After 66 h, the overall *K'* values in AM-C dropped to 0.36, which decreased by 63.8%, similar to that in AM-F which decreased by 64.0% with a value of 0.36. The overall *K'* values in AM-M decreased most significantly to 0.18, with a rate decreasing by 81.0%.

Figure 4 shows the relationship between the deposition amount of microplastics in AM groups and the overall *K'* after 66 h of recharge. It can be seen that the overall *K'* of the sand column in AM-M is lowest among AM groups, and the deposition amount is up to 6.00 g. The deposition amount in AM-F is 4.69 g, which is similar to that in AM-C group with a value of 4.67 g. The deposition amount of microplastics is closely related to the hydraulic conductivity of the sand column. Figures 3B-D shows the change of *K'* in each seepage layer for different particle size media in AM

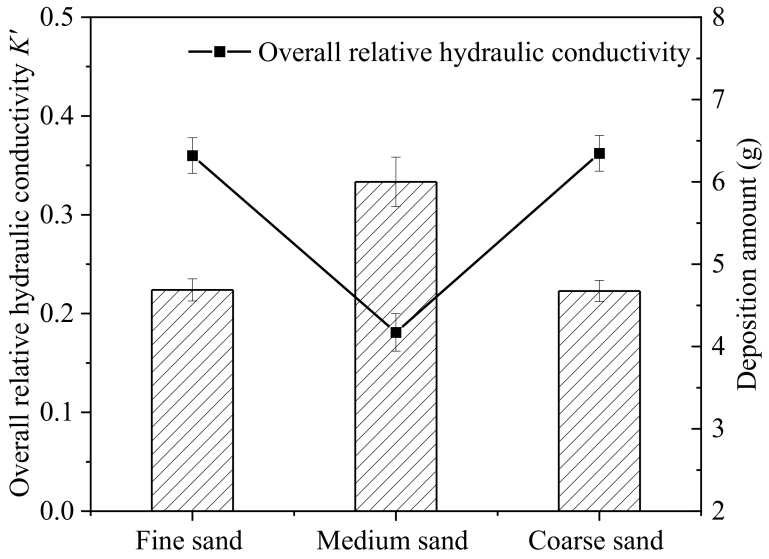

FIGURE 4
Relationship between the deposition amount of microplastics in different media grain size group and the overall relative hydraulic conductivity *K'* after end of recharge.

groups. The relative hydraulic conductivity of surface layers (AB layer) continues to decrease during the whole recharge process. This indicates that microplastics have a certain degree of deposition in the surface layer of the aqueous media, which caused the occurrence of clogging. However, the degree of surface clogging among these groups was obvious different. In this study, the clogging occurring in the surface layers (AB:0-3 cm) of the sand column was defined as the surface clogging, and the clogging occurred in other layers of the sand column (BC, CD, DE layers) was regarded as the internal clogging. This is consistent with others' studies. Huang (2021) observed that suspended particles mostly settle in the surface layer of the medium, causing more serious surface clogging than deep clogging in sand columns. Moreover, due to the different relative diameter ratios (dp/Dp) between suspended particles and porous media, the clogging degree of porous media in different layers and has difference in the same layer among three experimental groups. The relative diameter ratio of aqueous medium was larger in AM-C than that in the other two groups. When recharge process begins, microplastic particles migrate downward with water flow through larger pores in the medium, and a small part stays in the BC layer causing clogging. However, most of the microplastic particles migrate deeper into sand columns until DE layer and then migrate out of the sand columns. Among the AM groups, the pore throat diameter in AM-F group was the smallest, and the clogging of surface layer (AB layer) developed the fastest. The overall *K'* values of AM-F dropped to 0.88 within 10 h. However, there is a delayed drop trend of *K'* after 11 h and a continuous drop after 40 h due to accumulation of microplastics deposition in sand columns. Due to severe surface clogging in AM-F, most microplastic particles are trapped by AB layer and BC layer. The change of *K'* in deep layers (CD layer and DE layer) was not obvious in AM-F. The *K'* of each layer in AM-M exhibits a downward trend with varying degrees. It indicates that microplastic particles are intercepted and deposited in each seepage section of AM-M, which causes cake-filtration clogging on the surface layer and internal clogging inside sand columns. As a result, the most severe overall clogging development and the largest overall *K'* decrease of porous media occurred in AM-M.

Based on the results above, when recharge water contained with 100 μm microplastics particles (100 mg/L), medium size has greater impact on the microplastic transport and clogging behavior in porous media. The hydraulic conductivity in different experimental groups (AM-C, AM-M and AM-F) all showed a downward trend. However, the effect of different particle size of sand media on microplastic migration was obviously different. When the pore size of the coarse sand medium is larger, it is easier for microplastics to migrate through pore channels. However, the effect of particle size on microplastic migration was obviously different. The pore size of the coarse sand medium is larger, which is easier for microplastics to migrate through pore channels. Thus, the clogging development in AM-C is slower than the other two groups. The pore size of sand media in AM-F is smaller than that in the other two groups, forming a "cake-like" clogging on the surface of the medium. Under the combined action of gravity and hydrodynamics, the pressure on the particles continues to increase. When the pressure exceeds the limit that maintains the original stable equilibrium, the surface layer is compacted and microplastic particles are forced to migrate to deeper pore channels, resulting in periodic exacerbations of clogging. The overall clogging of the sand column also develops slowly in fine sand group. While the pore size of sand media in AM-M is moderate, part of the microplastics accumulated in the surface layer of the sand column to form surface clogging. Part of the microplastics penetrate into the deep sand column through medium pores and form internal clogging. Due to the development of internal-surface double clogging, clogging in AM-M is most severe.

3.2 Effect of microplastics particle size on hydraulic conductivity

To explore the influence of microplastic particle size on the hydraulic conductivity, the overall *K'* of the sand column and *K'* of different layers (AB: 0-3 cm, BC: 3-6 cm, CD: 6-9 cm, DE: 9-12 cm) with time are shown in Figure 5. According to Figure 5A, it was observed that particle size of microplastic has significant effect on the clogging of porous media. At the end of recharge, *K'* of the aqueous media is 0.18 and the final hydraulic conductivity decreases by 81.9% in MP-100. However, the overall *K'* fluctuates around 1.00 after 66 h of recharge in MP-300 and MP-500. It can be concluded that, microplastics with a particle size of 100 µm cause significant clogging, while microplastics with particle sizes of 300 µm and 500 µm hardly cause clogging. One possible explanation is that particles with smaller sizes have greater migration ability than the bigger ones. The migration distance of microplastics increases as the particle size decreases. When the particle size of microplastics increases to a certain extent, it is difficult for microplastics to penetrate into the porous medium. Thus, large amount of microplastics accumulates on the surface of the aqueous medium to form a "microplastic accumulation medium layer".

Figures 5B-D show that the surface layer (AB layer) is clogged when microplastic particle size is 100 µm. At the same time, microplastic particles migrate downward and are intercepted in BC and CD layers to form internal clogging. Therefore, there is a certain decrease in hydraulic conductivity of BC and CD layers. And *K'* of AB layer has a slight decrease under the 300 µm microplastic recharge, and the changes in *K'* of other seepage sections are not obvious over time. When recharging with 500 µm microplastics particle, hydraulic conductivity of porous media remains basically unchanged. The particle sizes of microplastics in our experimental groups are much larger compared to the size of porous media, which makes it difficult for microplastics to migrate into porous media and can only deposit on the surface layer of experimental sand column. After the end of recharge, the amount of microplastic particles deposited in the quartz sand column both reached about 7.5 g in MP-300 and MP-500. The deposition amount of microplastic particles in MP-100 was 5.8 g, which was less than that in MP-300 and MP-500. The quartz sand media acts as a filter, allowing water to pass through while larger microplastic particles trapped. This process contributes to the formation of the accumulation layer. Due to the restriction of particle size, a "microplastic accumulation layer" was formed on the surface layer of porous media. A new type of plastic material in the environment-plastic-rock complexes was formed when plastic debris irreversibly sorbs onto the quartz-dominated after historical flooding events (Wang L. et al., 2023). Due to the

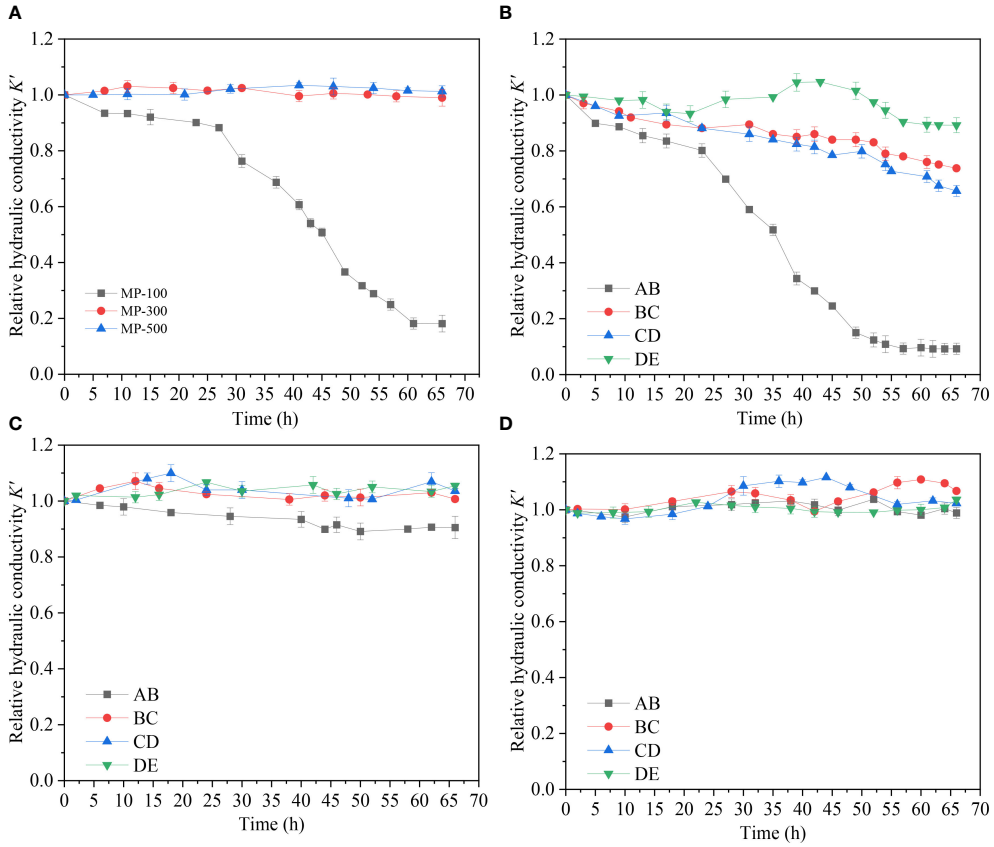

FIGURE 5
Spatial and temporal variation of hydraulic conductivity. **(A)** Overall hydraulic conductivity variation in experimental groups with different microplastics size **(B)** hydraulic conductivity variation of each seepage layer of 100 µm microplastics (MP-100) **(C)** hydraulic conductivity variation of each seepage layer of 300 µm microplastics (MP-300) **(D)** hydraulic conductivity variation of each seepage layer of 500 µm microplastics (MP-500).

limitation of experimental conditions, this plastic–rock complex was not observed in this study, but the effect of microplastic particles on particles in aqueous media can also be observed.

In Figure 6, although there is a large amount of 300 μm and 500 μm microplastic deposition, hydraulic conductivity does not decrease correspondingly. This also indicates that there are large amounts of microplastics deposition in MP-300 and MP-500. However, almost all of the microplastics deposit on surface layer of porous media to form "microplastic accumulation medium layer" without migrating into sand column through pore channels. Therefore, although there is a large amount deposition of microplastics in MP-300 and MP-500 groups, there are no decrease occurred in hydraulic conductivity, which is a very interesting phenomenon. In further studies, the complex interactions of physical adhesion, chemical binding and microbial colonization can be investigated during the development of "microplastic accumulation layer".

3.3 Effect of hydrodynamic conditions on the hydraulic conductivity

Under different hydraulic heads (ΔH=5 cm, 10 cm, 15 cm), effects of microplastics on the hydraulic conductivity were studied. The overall *K'* of the sand column and *K'* of different seepage layers (AB: 0-3 cm, BC: 3-6cm, CD: 6-9 cm, DE: 9-12 cm) were measured over time, as shown in Figure 7. It is shows that the overall *K'* of the sand column decreased over time under three different hydraulic conditions. At the end of recharge, the overall *K'* decreased most rapidly and significantly under HC-5, dropping to 18.0% of its initial value. The *K'* decreased by 22.0% to 0.78 under HC-10 and only decreased by 10.0% to 0.91 under HC-15, respectively. The effect of microplastic particles on the overall K' of sand column decreases with the increase of hydraulic heads. This trend is associated with the increased water flow velocity resulting from the increased hydraulic heads. Figures 7B-D show that the hydraulic conductivity of the surface layer (AB layer) decreased most significantly under all hydraulic conditions with the greatest decrease observed under HC-5. The *K'* in the surface layer (AB layer) of the sand column decreases to about 0.50 in group HC-10 and group HC-15. Microplastic particles have a substantial impact on the permeability of the surface layer of the aqueous media under the condition with different hydraulic heads. With higher hydraulic heads, microplastics do not cause clogging in the surface layer but instead migrate deeper into the sand column. The hydraulic conductivity of BC and CD layer all decreased to around 0.80 at the end of the experiment under HC-5. Under the condition of HC-10, *K'* decreased to around 0.90 in both in BC and CD layer. This indicates that microplastic particles exhibit higher deposition in BC and DE layer in the HC-5 group. This indicates that the *K'* of BC, CD, and DE layer under different hydraulic conditions has different change patterns, with a general trend of decreasing change as hydraulic head increases. This is closely related to the migration of microplastics in each layer of the sand column under different hydrodynamic conditions.

Combined with deposition amount shown in Figure 8, it was seen that microplastic deposition in the sand column was about four to five times higher under HC-5 than that under HC-10 or HC-15. Under lower hydraulic head conditions, the water flow velocity is relatively slow, resulting in a higher possibility of microplastic particles being trapped and deposited in the aqueous media. Under conditions with higher hydraulic heads, microplastics deposited less in the sand column because they had a greater migration ability due to higher flow rates. Besides that, during recharge process, microplastic particles did not have enough time to deposit in pore throats due to water shear forces and were forced to migrate downward until they exited the sand column. This effect

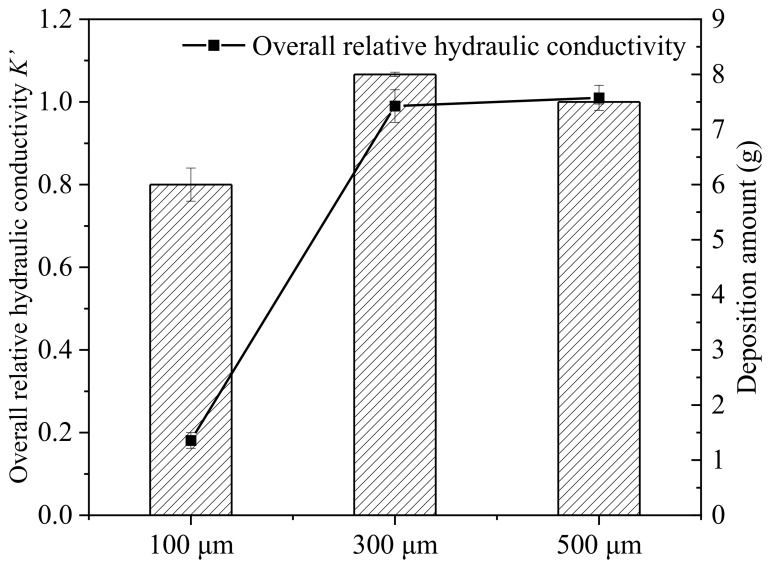

FIGURE 6
Relationship between the deposition amount of microplastics in different microplastics size group and the overall relative hydraulic conductivity *K'* after end of recharge.

10.3389/fmars.2024.1346275

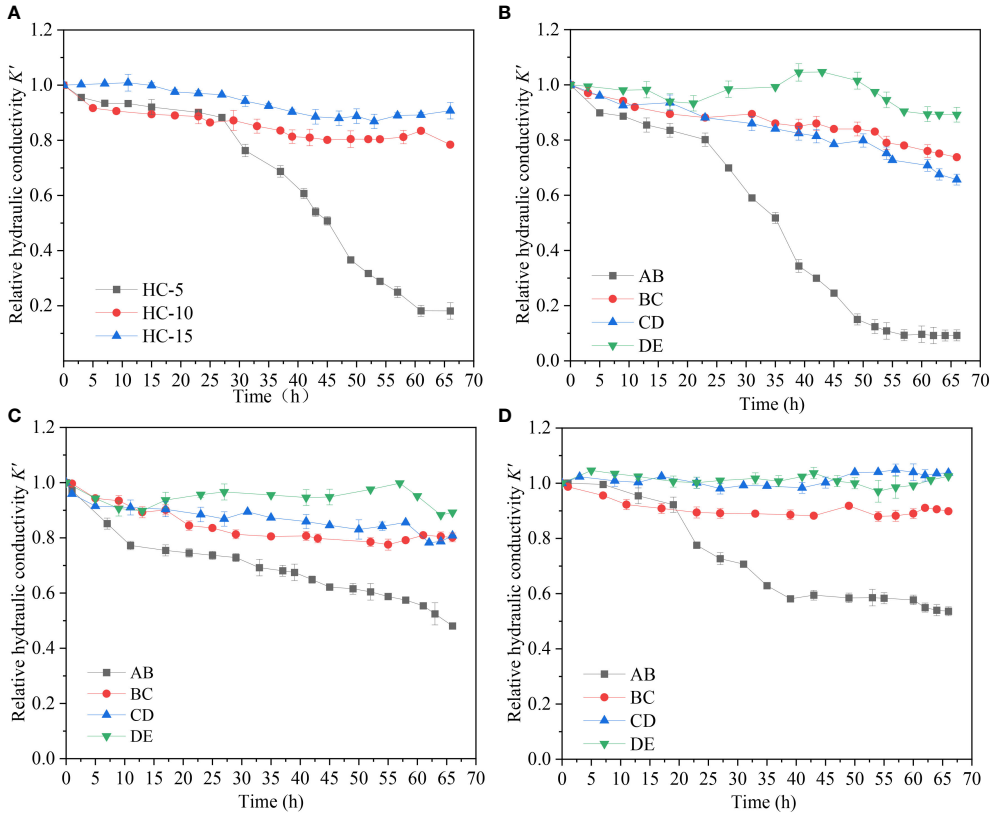

FIGURE 7
Spatial and temporal variation of hydraulic conductivity. **(A)** Overall hydraulic conductivity variation in experimental groups with different hydrodynamic conditions **(B)** hydraulic conductivity variation of each seepage layer of DH= 5cm (HC-5) (V) **(C)** hydraulic conductivity variation of each seepage layer of DH=10cm (HC-10) **(D)** hydraulic conductivity variation of each seepage layer of DH=15cm (HC-15).

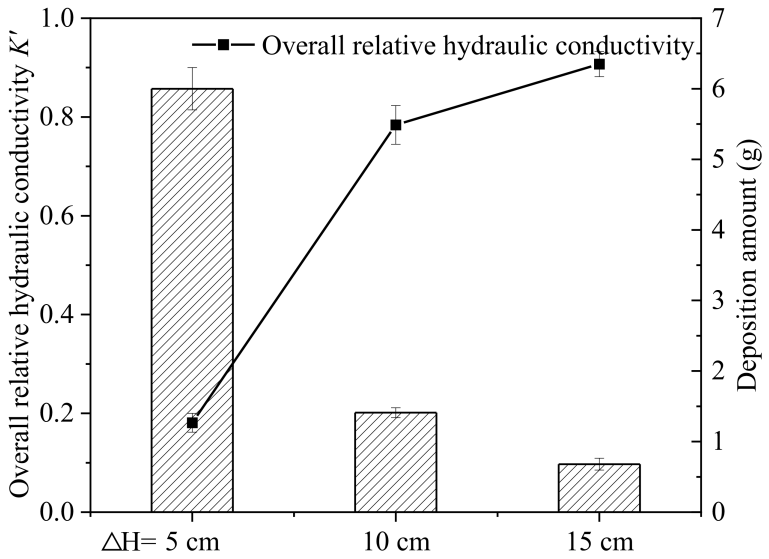

FIGURE 8
Relationship between the deposition amount of microplastics in different hydraulic head group and the overall relative hydraulic conductivity *K′* after end of recharge.

increases with increasing hydraulic head difference and decreases with increasing sand column depth.

3.4 Clogging mechanism analysis

Particle migration is influenced by many factors, such as particle properties, medium properties, hydraulic conditions, physicochemical property of water. Figure 9 shows the main mechanisms of microplastic particles settling along the water flow in our study. Microplastics have the characteristics of large specific surface area, long persistence and difficult degradation, which is significant different from traditional physical particles in water. (Wu P. et al., 2019; Maguire and Gardner, 2023; Yang H. et al., 2022). As typical organic synthetic polymer, microplastics have high hydrophobicity (Li et al., 2020). The properties of microplastics directly affect its deposition, migration and transformation of degradation (He et al., 2022). Due to the high hydrophobicity between microplastic particles, the double electric layer of microplastic particles is compressed and thinned under certain conditions, and the surface charge is shielded (Wang et al., 2022). As the electrostatic repulsion between particles decreases, it is easier for microplastic particles to undergo the coagulation (Wu J. et al., 2019). The coagulated microplastic agglomerates have larger particle size than the single one, which is not conducive to their transport in medium pores and increases the possibility of microplastic particle clogging (Jiang et al., 2022). The larger the medium particle size, the more conducive it is for microplastic particle to move out. Porous media with smaller particle sizes have smaller pore throats and permeability (He et al., 2023). This is well proved by the difference in hydraulic conductivity of aquifer medium among AM-F, AM-M and AM-C groups in this study. The interception of particles by the aqueous media plays a vital role during recharge process. Therefore, the migration and deposition processes of microplastics in porous media are a result of the interaction of media particle size, pore structure, and microplastic particle properties (Li and Prigiobbe, 2018; Li et al., 2023).

In our study, when the diameter of microplastic particles is larger than the pore diameter of the sand medium, the microplastic particles will collide with the pore wall and be filtered out. It caused a large amount of microplastic particles to deposit on the surface of porous medium and formed a “cake-like” clogging phenomenon and “microplastic accumulation layer”. Besides the interception effect, gravity deposition and bridging are also important effect influence the microplastic mitigation and deposition (Bydalek et al., 2023). Microplastic particles bridged with each other and accumulate in pores influenced by gravity and water flow. In addition, the flow rate of pore water in porous media is also an important factor affecting the deposition and release of microplastics on media surfaces. With increasing water flow, microplastics are subjected to stronger shear stress during migration process. This leads to shorter deposition time of microplastics and makes it more difficult to deposit on media surface (Li et al., 2023). In natural environment, differences in the

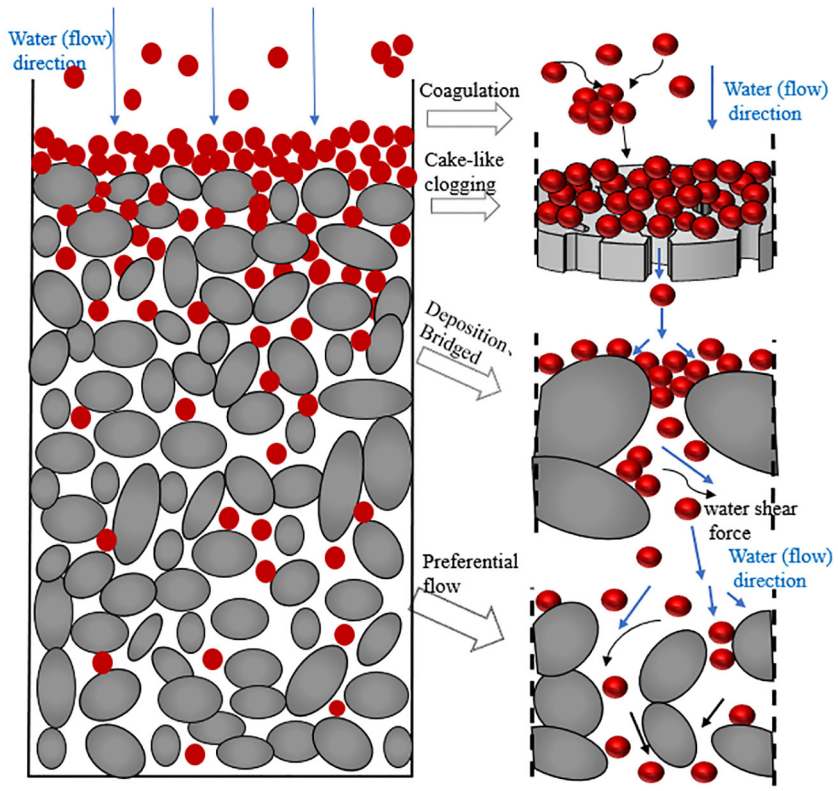

FIGURE 9
Schematic illustration of the microplastic clogging phenomenon in sand columns.

particle size of the media particles, the influence of animals and plants, and other factors create preferential channels through which water can pass through at a rapid rate (Bianchi et al., 2011).

Under preferential flow, water pass through the column with higher flow rate and may greatly influence the migration behavior of microplastics (Li and Prigiobbe, 2018). Thus, microplastics mainly migrate through preferential channels instead of being deposited throughout the porous medium uniformly. This preferential effect usually becomes more significant with increasing water flow. In our study, the particles in the aqueous medium mainly filter and deposit microplastic particles. However, in MP group, the large microplastic particles deposit on surface layer of porous media to form "microplastic accumulation medium layer" without migrating into sand column through pore channel; Under conditions with higher hydraulic heads, microplastic particles did not have enough time to deposit in pore throats due to shear forces and were forced to migrate downward until they exited the sand column. The deposition of microplastics in porous media is a complex process that takes into account multiple factors, such as microplastic particle characteristics, media characteristics, and hydrodynamic conditions (He et al., 2020). An intensive analysis of these mechanisms was beneficial for more accurately assess and the effective management of microplastics and provide a scientific basis for the development of more effective prevention and control strategies (Jiang et al., 2022).

3.5 Implications for microplastic risk and clogging control

In an effort to mitigate the clogging risk of microplastics in the management of artificial aquifers, a range of preventative and remedial approaches have been implemented in engineering practice. Although recharge water can be pretreated via sedimentation, coagulation, filtration, advanced oxidation, and disinfection prior to artificial recharge (Jeong et al., 2018), which lessens the clogging potential. These traditional pretreatment methods may be not applied well to microplastics. Similarly, rehabilitation methods include backwashing, surging, jetting, under-reaming, acidification, and biocide, which help restore the artificial recharge system may not function well in recharge system contained microplastics (Jeong et al., 2018). Due to the high chemical inertness and durability of microplastics, they are resistant to traditional biodegradation or chemical treatment, resulting in longer persistence and greater accumulation effects when clogging occurs with microplastics (Guo and Wang, 2019). Under certain hydrodynamic conditions, microplastic particles exhibit higher adsorption ability, lower density and stronger compressive than other particles, which facilitate clogging caused by microplastics to form larger aggregates, hinder their discharge from the aquifer, and alter the pore structure and permeability of the medium (Lim et al., 2022). Traditional treatments of media clogging have limited effectiveness in addressing clogging caused by microplastics. Clogging by microplastics not only compromises the technical feasibility and economic feasibility of MAR to solve seawater intrusion, but also poses potential risks to the environment and human health (Peng et al., 2017). For instance, microplastics may carry toxic or harmful substances or pathogens into aquatic environment, causing physiological or behavioral interference or damage to organisms (Pereao et al., 2020; Yang X. et al., 2022). These risks may be amplified over time. It has demonstrated that microplastics have transported into the aqueous media layer, forming a "plastid-rock complex" by interaction of physical adhesion, chemical binding and microbial colonization (Wang L et al., 2023). In this study, it is observed that the large plastic particles form a "microplastic accumulation layer" and affect the permeability of the aquifer medium.

Therefore, in-depth research and discussion on the clogging behavior of microplastics are needed during managed aquifer recharge (MAR). The generation and discharge of microplastics should be controlled from the source water. The monitoring and analysis of various types and sources of microplastics should be strengthened. The main sources and pathways should be identified and the effective emission reduction measures and policies should be formulated. This requires using more strict quality standards and more advanced treatment technologies. For example, certain microorganisms are verified to be able to degrade microplastic. Over 90 microorganisms, including bacteria and fungi, have been known to degrade petroleum-based plastics (Jumaah et al., 2017) mostly *in vitro* condition. *Galleria melonella* have been found capable of hydrolyzing polyethylene (PE) (Yang et al., 2014) such as *Bacillus* spp. (Sudhakar et al., 2008; Abrusci et al., 2013), *Rhodococcus* spp. (Bonhomme et al., 2003; Gilan et al., 2004; Fontanella et al., 2010), and *Pseudomonas* spp. (Rajandas et al., 2012). These microorganisms are expected to be combined with artificial aquifer management in the future to solve the problem of microplastic clogging as a new biological control method. At the same time, future research can focus on the migration behavior and clogging treatment of microplastics by disclosing the mechanism and estimating their influence and risk on MAR.

4 Conclusion

This study focuses on the transport behavior of microplastic particles and simulates the clogging of microplastics during artificial recharge by sand column experiments in laboratory. Most of the microplastics were intercepted in the sand column's surface layer. Internal clogging was more prevalent in the coarse sand group, while surface clogging was more prevalent in the fine sand group. Both types of clogging occurred in the medium sand. The hydraulic conductivity of the aqueous medium remains almost unaltered with a "microplastic accumulation medium layer" developed when the microplastic particle size are larger than 300 mm. The increase in water head difference increased the inflow velocity, which decreased the deposition period of microplastics on the medium's surface and hence enhanced their ability to migrate. This effect increases as the water head difference grows and reduces as the sand column depth increases. In MAR projects, to alleviate the problem of microplastic clogging in the future, bacteria microorganisms with the ability to degrade microplastics have broad application prospect in conjunction with artificial aquifer management. Further systematic and in-depth research is required to elucidate the extent and impact of different factors.

Data availability statement

The raw data supporting the conclusions of this article will be made available by the authors, without undue reservation.

Author contributions

HW: Conceptualization, Funding acquisition, Investigation, Writing – original draft. Writing – review & editing. JZ: Data curation, Validation, Writing – original draft. YC: Supervision, Writing – review & editing. YX: Validation, Writing – review & editing. PJ: Investigation, Methodology, Writing – review & editing. HL: Methodology, Writing – review & editing.

Funding

The author(s) declare financial support was received for the research, authorship, and/or publication of this article. This study was supported by the National Natural Science Foundation of China (42207064), Guangxi Science and Technology Planning Project (Grant No. GuiKe-AD 21220079), and the National Natural Science Foundation of Guangxi Province, China (Grant No. 2022GXNSFBA035577).

Conflict of interest

The authors declare that the research was conducted in the absence of any commercial or financial relationships that could be construed as a potential conflict of interest.

Publisher's note

All claims expressed in this article are solely those of the authors and do not necessarily represent those of their affiliated organizations, or those of the publisher, the editors and the reviewers. Any product that may be evaluated in this article, or claim that may be made by its manufacturer, is not guaranteed or endorsed by the publisher.

References

Abdalla, F., and Khalil, R. (2018). Potential effects of groundwater and surface water contamination in an urban area, Qus City, Upper Egypt. *J. Afr. Earth Sci.* 141, 164–178. doi: 10.1016/j.jafrearsci.2018.02.016

Abrusci, C., Pablos, J. L., Marín, I., Espí, E., Corrales, T., and Catalina, F. (2013). Comparative effect of metal stearates as pro-oxidant additives on bacterial biodegradation of thermal- and photo-degraded low density polyethylene mulching films. *Int. Biodeterior. Biodegrad. Biodeterior.* 83, 25–32. doi: 10.1016/j.ibiod.2013.04.002

Aeschbach-Hertig, W., and Gleeson, T. (2012). Regional strategies for the accelerating global problem of groundwater depletion. *Nat. Geosci.* 5, 853–861. doi: 10.1038/ngeo1617

Alimi, O. S., Budarz, J. F., Hernandez, L. M., and Tufenkji, N. (2018). Microplastics and nanoplastics in aquatic environments: aggregation, deposition, and enhanced contaminant transport. *Environ. Sci. Technol.* 52, 1704–1724. doi: 10.1021/acs.est.7b05559

Alnahdi, K. A., Alali, L. W., Suwaidan, M. K., and Akhtar, M. K. (2023). Engineering a microbiosphere to clean up the ocean – inspiration from the plastisphere. *Front. Mar. Sci.* 10. doi: 10.3389/fmars.2023.1017378

Andrady, A. L. (2011). Microplastics in the marine environment. *Mar. pollut. Bull.* 62, 1596–1605. doi: 10.1016/j.marpolbul.2011.05.030

Ashton, K., Holmes, L., and Turner, A. (2010). Association of metals with plastic production pellets in the marine environment. *Mar. pollut. Bull.* 60, 2050–2055. doi: 10.1016/j.marpolbul.2010.07.014

Bayabil, H. K., Teshome, F. T., and Li, Y. C. (2022). Emerging contaminants in soil and water. *Front. Environ. Sci.* 10. doi: 10.3389/fenvs.2022.873499

Bianchi, M., Zheng, C., Wilson, C., Tick, G. R., Liu, G., and Gorelick, S. M. (2011). Spatial connectivity in a highly heterogeneous aquifer: From cores to preferential flow paths. *Water Resour. Res.* 47, W05524. doi: 10.1029/2009WR008966

Bonhomme, S., Cuer, A., Delort, A. M., Lemaire, J., Sancelme, M., and Scott, G. (2003). Environmental biodegradation of polyethylene. *Polymer Degrad. Stabil.* 81, 441–452. doi: 10.1016/S0141-3910(03)00129-0

Bydalek, F., Ifayemi, D., Reynolds, L., Barden, R., Kasprzyk-Hordern, B., and Wenk, J. (2023). Microplastic dynamics in a free water surface constructed wetland. *Sci. Total Environ.* 858, 160113. doi: 10.1016/j.scitotenv.2022.160113

Chae, B., Oh, S., and Lee, D. G. (2023). Is 5 mm still a good upper size boundary for microplastics in aquatic environments? Perspectives on size distribution and toxicological effects. *Mar. pollut. Bull.* 196, 115591. doi: 10.1016/j.marpolbul.2023.115591

Cincinelli, A., Scopetani, C., Chelazzi, D., Martellini, T., Pogojeva, M., and Slobodnik, J. (2021). Microplastics in the black sea sediments. *Sci. Total Environ.* 760, 143898. doi: 10.1016/j.scitotenv.2020.143898

Cole, M., Lindeque, P., Halsband, C., and Galloway, T. S. (2011). Microplastics as contaminants in the marine environment: A review. Mar. *Mar. pollut. Bull.* 62, 2588–2597. doi: 10.1016/j.marpolbul.2011.09.025

Dong, Z. (2018). Size-dependent transport and retention of micron-sized plastic spheres in natural sand saturated with seawater. *Water Res.* 143, 518–526. doi: 10.1016/j.watres.2018.07.007

Dris, R., Imhof, H., Sanchez, W., Gasperi, J., Galgani, F., Tassin, B., et al. (2015). Beyond the ocean: contamination of freshwater ecosystems with (micro-)plastic particles. *Environ. Chem.* 12, 539. doi: 10.1071/EN14172

Eriksen, M., Lebreton, L. C. M., Carson, H. S., Thiel, M., Moore, C. J., Borerro, J. C., et al. (2014). Plastic Pollution in the World's Oceans: More than 5 Trillion Plastic Pieces Weighing over 250,000 Tons Afloat at Sea. *PloS One* 9, e111913. doi: 10.1371/journal.pone.0111913

Fang, Y., Zheng, T., Guo, B., Zhan, H., Wang, H., Zheng, X., et al. (2022a). Transformation in the stability of tide-induced upper saline plume driven by transient external forcing. *Water Resour. Res.* 58, e2021WR031331. doi: 10.1029/2021WR031331

Fang, Y., Zheng, T., Wang, H., Zheng, X., and Walther, M. (2022b). Influence of dynamically stable-unstable flow on seawater intrusion and submarine groundwater discharge over tidal and seasonal cycles. *J. Geophys. Res.: Oceans* 127, e2021JC018209. doi: 10.1029/2021JC018209

Fontanella, S., Bonhomme, S., Koutny, M., Husarova, L., Brusson, J.-M., Courdavault, J.-P., et al. (2010). Comparison of the biodegradability of various polyethylene films containing pro-oxidant additives. *Polymer Degrad. Stabil.* 95, 1011–1021. doi: 10.1016/j.polymdegradstab.2010.03.009

Gago, J., Galgani, F., Maes, T., and Thompson, R. C. (2016). Microplastics in seawater: recommendations from the marine strategy framework directive implementation process. *Front. Mar. Sci.* 3. doi: 10.3389/fmars.2016.00219

Geyer, R., Jambeck, J. R., and Law, K. L. (2017). Production, use, and fate of all plastics ever made. *Sci. Adv.* 3, e1700782. doi: 10.1126/sciadv.1700782

Gilan, I., Hadar, Y., and Sivan, A. (2004). Colonization, biofilm formation and biodegradation of polyethylene by a strain of Rhodococcus ruber. *Appl. Microbiol. Biotechnol.* 65, 97–104. doi: 10.1007/s00253-004-1584-8

Gorelick, S. M., and Zheng, C. (2015). Global change and the groundwater management challenge. *Water Resour. Res.* 51, 3031–3051. doi: 10.1002/2014WR016825

Guo, J.-J., Huang, X.-P., Xiang, L., Wang, Y.-Z., Li, Y.-W., Li, H., et al. (2020). Source, migration and toxicology of microplastics in soil. *Environ. Int.* 137, 105263. doi: 10.1016/j.envint.2019.105263

Guo, X., and Wang, J. (2019). The chemical behaviors of microplastics in marine environment: A review. *Mar. pollut. Bull.* 142, 1–14. doi: 10.1016/j.marpolbul.2019.03.019

Guo, X., Wang, X., Zhou, X., Kong, X., Tao, S., and Xing, B. (2012). Sorption of four hydrophobic organic compounds by three chemically distinct polymers: role of chemical and physical composition. *Environ. Sci. Technol.* 46, 7252–7259. doi: 10.1021/es301386z

Hanvey, I. (2023). Glass children: the lived experiences of siblings with a disability or chronic illness. *Pediatr. Pulmonol.* 58, S11–S12. doi: 10.1002/casp.2602

He, B., Wijesiri, B., Ayoko, G. A., Egodawatta, P., Rintoul, L., and Goonetilleke, A. (2020). Influential factors on microplastics occurrence in river sediments. *Science of The Total Environment* 738, 139901. doi: 10.1016/j.scitotenv.2020.139901

He, S., Jia, M., Xiang, Y., Song, B., Xiong, W., Cao, J., et al. (2022). Biofilm on microplastics in aqueous environment: Physicochemical properties and environmental implications. *J. Hazard. Mater.* 424, 127286. doi: 10.1016/j.jhazmat.2021.127286

He, H., Wu, T., Chen, Y.-F., and Yang, Z. (2023). A pore-scale investigation of microplastics migration and deposition during unsaturated flow in porous media. *Sci. Total Environ.* 858, 159934. doi: 10.1016/j.scitotenv.2022.159934

Hepburn, E., Madden, C., Szabo, D., Coggan, T. L., Clarke, B., and Currell, M. (2019). Contamination of groundwater with per- and polyfluoroalkyl substances (PFAS) from legacy landfills in an urban re-development precinct. *Environ. pollut.* 248, 101–113. doi: 10.1016/j.envpol.2019.02.018

Hoellein, T., Rovegno, C., Uhrin, A. V., Johnson, E., and Herring, C. (2021). Microplastics in invasive freshwater mussels (Dreissena sp.): spatiotemporal variation and occurrence with chemical contaminants. *Front. Mar. Sci.* 8. doi: 10.3389/fmars.2021.690401

Hohn, S., Acevedo-Trejos, E., Abrams, J. F., de Moura, J. F., Spranz, R., and Merico, A. (2020). The long-term legacy of plastic mass production. *Sci. Total Environ.* 746, 141115. doi: 10.1016/j.scitotenv.2020.141115

Huang, J. (2021). Microplastic pollution in soils and groundwater: Characteristics, analytical methods and impacts. *Chem. Eng. J.* 425, 131870. doi: 10.1016/j.cej.2021.131870

Jeong, H. Y., Jun, S.-C., Cheon, J.-Y., and Park, M. (2018). A review on clogging mechanisms and managements in aquifer storage and recovery (ASR) applications. *Geosci. J.* 22, 667–679. doi: 10.1007/s12303-017-0073-x

Jiang, Y., Zhou, S., Fei, J., Qin, Z., Yin, X., Sun, H., et al. (2022). Transport of different microplastics in porous media: Effect of the adhesion of surfactants on microplastics. *Water Res.* 215, 118262. doi: 10.1016/j.watres.2022.118262

Jumaah, O. S. (2017). Screening of Plastic Degrading Bacteria from Dumped Soil Area. *IOSR JESTFT* 11, 93–98. doi: 10.9790/2402-1105029398

Khan, S. (2022). Emerging contaminants of high concern for the environment: Current trends and future research. *Environ. Res.* 207, 112609. doi: 10.1016/j.envres.2021.112609

Koelmans, A. A., Mohamed Nor, N. H., Hermsen, E., Kooi, M., Mintenig, S. M., and De France, J. (2019). Microplastics in freshwaters and drinking water: Critical review and assessment of data quality. *Water Res.* 155, 410–422. doi: 10.1016/j.watres.2019.02.054

Krueger, M. C., Harms, H., and Schlosser, D. (2015). Prospects for microbiological solutions to environmental pollution with plastics. *Appl. Microbiol. Biotechnol.* 99, 8857–8874. doi: 10.1007/s00253-015-6879-4

Lapworth, D. J., Baran, N., Stuart, M. E., and Ward, R. S. (2012). Emerging organic contaminants in groundwater: A review of sources, fate and occurrence. *Environ. pollut.* 163, 287–303. doi: 10.1016/j.envpol.2011.12.034

Leusch, F., Lu, H.-C., Perera, K., Neale, P. A., and Ziajahromi, S. (2023). Analysis of the literature shows a remarkably consistent relationship between size and abundance of microplastics across different environmental matrices. *Environ. pollut.* 319, 120984. doi: 10.1016/j.envpol.2022.120984

Li, M., He, L., Hsieh, L., Rong, H., and Tong, M. (2023). Transport of plastic particles in natural porous media under freeze–thaw treatment: Effects of porous media property. *J. Hazard. Mater.* 442, 130084. doi: 10.1016/j.jhazmat.2022.130084

Li, Q., and Prigiobbe, V. (2018). Numerical simulations of the migration of fine particles through porous media. *Transp. Porous Med.* 122, 745–759. doi: 10.1007/s11242-018-1024-3

Li, J., Song, Y., and Cai, Y. (2020). Focus topics on microplastics in soil: Analytical methods, occurrence, transport, and ecological risks. *Environ. pollut.* 257, 113570. doi: 10.1016/j.envpol.2019.113570

Li, X., Xu, H., Gao, B., Sun, Y., Shi, X., and Wu, J. (2019). Transport of a PAH-degrading bacterium in saturated limestone media under various physicochemical conditions: Common and unexpected retention and remobilization behaviors. *J. Hazard. Mater.* 380, 120858. doi: 10.1016/j.jhazmat.2019.120858

Lim, C., Kim, N., Lee, J., and Yoon, Y. (2022). Potential of adsorption of diverse environmental contaminants onto microplastics. *Water* 14, 4086. doi: 10.3390/w14244086

Luo, Y., Guo, W., Ngo, H. H., Nghiem, L. D., Hai, F. I., Zhang, J., et al. (2014). A review on the occurrence of micropollutants in the aquatic environment and their fate and removal during wastewater treatment. *Sci. Total Environ.*, 473–474, 619–641. doi: 10.1016/j.scitotenv.2013.12.065

Maguire, L. W., and Gardner, C. M. (2023). Fate and transport of biological microcontaminants bound to microplastics in the soil environment. *Sci. Total Environ.* 892, 164439. doi: 10.1016/j.scitotenv.2023.164439

Majdalani, S., Michel, E., Di-Pietro, L., and Angulo-Jaramillo, R. (2008). Effects of wetting and drying cycles on in *situ* soil particle mobilization. *Eur. J. Soil Sci.* 59, 147–155. doi: 10.1111/j.1365-2389.2007.00964.x

Mintenig, S. M., Löder, M. G. J., Primpke, S., and Gerdts, G. (2019). Low numbers of microplastics detected in drinking water from ground water sources. *Sci. Total Environ.* 648, 631–635. doi: 10.1016/j.scitotenv.2018.08.178

Murawski, J., She, J., and Frishfelds, V. (2022). Modeling drift and fate of microplastics in the Baltic Sea. *Front. Mar. Sci.* 9. doi: 10.3389/fmars.2022.886295

Napper, I. E., Baroth, A., Barrett, A. C., Bhola, S., Chowdhury, G. W., Davies, B. F. R., et al. (2021). The abundance and characteristics of microplastics in surface water in the transboundary Ganges River. *Environ. pollut.* 274, 116348. doi: 10.1016/j.envpol.2020.116348

Nelms, S. E., Galloway, T. S., Godley, B. J., Jarvis, D. S., and Lindeque, P. K. (2018). Investigating microplastic trophic transfer in marine top predators. *Environ. pollut.* 238, 999–1007. doi: 10.1016/j.envpol.2018.02.016

Ng, K. L., and Obbard, J. P. (2006). Prevalence of microplastics in Singapore's coastal marine environment. *Mar. pollut. Bull.* 52, 761–767. doi: 10.1016/j.marpolbul.2005.11.017

Panno, S. V., Kelly, W. R., Scott, J., Zheng, W., McNeish, R. E., Holm, N., et al. (2019). Microplastic contamination in karst groundwater systems. *Groundwater* 57, 189–196. doi: 10.1111/gwat.12862

Paul-Pont, I., Tallec, K., Gonzalez-Fernandez, C., Lambert, C., Vincent, D., Mazurais, D., et al. (2018). Constraints and priorities for conducting experimental exposures of marine organisms to microplastics. *Front. Mar. Sci.* 5. doi: 10.3389/fmars.2018.00252

Peng, J., Wang, J., and Cai, L. (2017). Current understanding of microplastics in the environment: Occurrence, fate, risks, and what we should do. *Integrated Environ. Assess. Manage.* 13, 476–482. doi: 10.1002/ieam.1912

Pereao, O., Opeolu, B., and Fatoki, O. (2020). Microplastics in aquatic environment: characterization, ecotoxicological effect, implications for ecosystems and developments in South Africa. *Environ. Sci. pollut. Res.* 27, 22271–22291. doi: 10.1007/s11356-020-08688-2

Pirsaheb, M., Hossini, H., and Makhdoumi, P. (2020). Review of microplastic occurrence and toxicological effects in marine environment: Experimental evidence of inflammation. *Process Saf. Environ. Prot.* 142, 1–14. doi: 10.1016/j.psep.2020.05.050

Provencher, J. F., Vermaire, J. C., Avery-Gomm, S., Braune, B. M., and Mallory, M. L. (2018). Garbage in guano? Microplastic debris found in faecal precursors of seabirds known to ingest plastics. *Sci. Total Environ.* 644, 1477–1484. doi: 10.1016/j.scitotenv.2018.07.101

Rajandas, H., Parimannan, S., Sathasivam, K., Ravichandran, M., and Yin, L. S. (2012). A novel FTIR-ATR spectroscopy based technique for the estimation of low-density polyethylene biodegradation. *Polymer Testing* 31, 1094–1099. doi: 10.1016/j.polymertesting.2012.07.015

Re, V. (2019). Shedding light on the invisible: addressing the potential for groundwater contamination by plastic microfibers. *Hydrogeol. J.* 27, 2719–2727. doi: 10.1007/s10040-019-01998-x

Rochman, C. M., Tahir, A., Williams, S. L., Baxa, D. V., Lam, R., Miller, J. T., et al. (2015). Anthropogenic debris in seafood: Plastic debris and fibers from textiles in fish and bivalves sold for human consumption. *Sci. Rep.* 5, 14340. doi: 10.1038/srep14340

Samandra, S. (2022). Microplastic contamination of an unconfined groundwater aquifer in Victoria, Australia. *Sci. Total Environ.* 802, 149727. doi: 10.1016/j.scitotenv.2021.149727

Smith, B., Siegel, D., Neslund, C., and Carter, C. (2014). Organic contaminants in portland cements used in monitoring well construction. *Groundwater Monit. Remediation* 34, 102–111. doi: 10.1111/gwmr.12082

Sudhakar, M., Doble, M., Murthy, P. S., and Venkatesan, R. (2008). Marine microbe-mediated biodegradation of low- and high-density polyethylenes. *Int. Biodeterior. Biodegrad.* 61, 203–213. doi: 10.1016/j.ibiod.2007.07.011

Sui, Q., Wang, D., Zhao, W., Huang, J., Yu, G., Cao, X., et al. (2015). Pharmaceuticals and consumer products in four wastewater treatment plants in urban and suburb areas of Shanghai. *Environ. Sci. pollut. Res.* 22, 6086–6094. doi: 10.1007/s11356-014-3793-8

Szabo, D., Coggan, T. L., Robson, T. C., Currell, M., and Clarke, B. O. (2018). Investigating recycled water use as a diffuse source of per- and polyfluoroalkyl substances (PFASs) to groundwater in Melbourne, Australia. *Sci. Total Environ.* 644, 1409–1417. doi: 10.1016/j.scitotenv.2018.07.048

Tanaka, K., and Takada, H. (2016). Microplastic fragments and microbeads in digestive tracts of planktivorous fish from urban coastal waters. *Sci. Rep.* 6, 34351. doi: 10.1038/srep34351

Tong, M., and Johnson, W. P. (2006). Excess colloid retention in porous media as a function of colloid size, fluid velocity, and grain angularity. *Environ. Sci. Technol.* 40, 7725–7731. doi: 10.1021/es061201r

Van Cauwenberghe, L., and Janssen, C. R. (2014). Microplastics in bivalves cultured for human consumption. *Environ. pollut.* 193, 65–70. doi: 10.1016/j.envpol.2014.06.010

Wang, L., Bank, M. S., Rinklebe, J., and Hou, D. (2023). Plastic–rock complexes as hotspots for microplastic generation. *Environ. Sci. Technol.* 57, 7009–7017. doi: 10.1021/acs.est.3c00662

Wang, H., Xin, J., Zheng, X., Fang, Y., Zhao, M., and Zheng, T. (2023). Effect of biofilms on the clogging mechanisms of suspended particles in porous media during artificial recharge. *J. Hydrol.* 619, 129342. doi: 10.1016/j.jhydrol.2023.129342

Wang, H., Xin, J., Zheng, X., Li, M., Fang, Y., and Zheng, T. (2020). Clogging evolution in porous media under the coexistence of suspended particles and bacteria: Insights into the mechanisms and implications for groundwater recharge. *J. Hydrol.* 582, 124554. doi: 10.1016/j.jhydrol.2020.124554

Wang, Y., Xu, L., Chen, H., and Zhang, M. (2022). Retention and transport behavior of microplastic particles in water-saturated porous media. *Sci. Total Environ.* 808, 152154. doi: 10.1016/j.scitotenv.2021.152154

Wanner, P. (2021). Plastic in agricultural soils - A global risk for groundwater systems and drinking water supplies? - A review. *Chemosphere* 264, 128453. doi: 10.1016/j.chemosphere.2020.128453

Wu, P., Huang, J., Zheng, Y., Yang, Y., Zhang, Y., He, F., et al. (2019). Environmental occurrences, fate, and impacts of microplastics. *Ecotoxicol. Environ. Saf.* 184, 109612. doi: 10.1016/j.ecoenv.2019.109612

Wu, J., Jiang, R., Lin, W., and Ouyang, G. (2019). Effect of salinity and humic acid on the aggregation and toxicity of polystyrene nanoplastics with different functional groups and charges. *Environ. pollut.* 245, 836–843. doi: 10.1016/j.envpol.2018.11.055

Xu, Y., Gong, H., Chen, B., Zhang, Q., and Li, Z. (2021). Long-term and seasonal variation in groundwater storage in the North China Plain based on GRACE. *Int. J. Appl. Earth Observ. Geoinform.* 104, 102560. doi: 10.1016/j.jag.2021.102560

Yan, X., Yang, X., Tang, Z., Fu, J., Chen, F., Zhao, Y., et al. (2020). Downward transport of naturally-aged light microplastics in natural loamy sand and the implication to the dissemination of antibiotic resistance genes. *Environ. pollut.* 262, 114270. doi: 10.1016/j.envpol.2020.114270

Yang, X., Man, Y. B., Wong, M. H., Owen, R. B., and Chow, K. L. (2022). Environmental health impacts of microplastics exposure on structural organization levels in the human body. *Sci. Total Environ.* 825, 154025. doi: 10.1016/j.scitotenv.2022.154025

Yang, H., Yan, Y., Yu, Y., He, Y., Fu, B., and Wang, J. (2022). Distribution, sources, migration, influence and analytical methods of microplastics in soil ecosystems. Ecotox. *Ecotoxicol. Environ. Saf.* 243, 114009. doi: 10.1016/j.ecoenv.2022.114009

Yang, J., Yang, Y., Wu, W.-M., Zhao, J., and Jiang, L. (2014). Evidence of polyethylene biodegradation by bacterial strains from the guts of plastic-eating waxworms. *Environ. Sci. Technol.* 48, 13776–13784. doi: 10.1021/es504038a

Zhang, K., Su, J., Xiong, X., Wu, X., Wu, C., and Liu, J. (2016). Microplastic pollution of lakeshore sediments from remote lakes in Tibet plateau, China. *Environ. pollut.* 219, 450–455. doi: 10.1016/j.envpol.2016.05.048

frontiers | Frontiers in Marine Science

TYPE Original Research
PUBLISHED 11 April 2024
DOI 10.3389/fmars.2024.1385517

OPEN ACCESS

EDITED BY
Chengji Shen,
Hohai University, China

REVIEWED BY
Zhang Bo,
Shandong University of Science and Technology, China
Qingzhi Zhu,
Stony Brook University, United States
Kai Xiao,
Southern University of Science and Technology, China

*CORRESPONDENCE
Wenran Cao
wenran.cao@uqconnect.edu.au
Guanxi Yan
g.yan@uq.edu.au

RECEIVED 13 February 2024
ACCEPTED 26 March 2024
PUBLISHED 11 April 2024

CITATION
Cao W, Hofmann H, Yan G and Scheuermann A (2024) Porewater exchange and iron transformation in a coastal groundwater system: a field investigation, driving mechanisms analysis, and conceptual model.
Front. Mar. Sci. 11:1385517.
doi: 10.3389/fmars.2024.1385517

Porewater exchange and iron transformation in a coastal groundwater system: a field investigation, driving mechanisms analysis, and conceptual model

Wenran Cao[1]*, Harald Hofmann[2,3], Guanxi Yan[1]* and Alexander Scheuermann[1]

[1]School of Civil Engineering, University of Queensland, St. Lucia, QLD, Australia, [2]School of the Environment, University of Queensland, St. Lucia, QLD, Australia, [3]Environment, Commonwealth Scientific and Industrial Research Organisation (CSIRO), Dutton Park, QLD, Australia

The high concentration of dissolved iron (Fe) in coastal waters triggers Lyngbya blooms in the Moreton Bay region of Southeast Queensland, Australia. Previous studies have provided a restricted understanding of how land-derived Fe is transported and then transformed into other forms (e.g., Fe oxides) before its release into the ocean. Here, a field investigation was conducted at a sandy beach on the northern end of Deception Bay, Queensland, Australia, focusing on porewater exchange and Fe transformation. This study revealed that tides provided a significant mechanism for driving the groundwater-seawater mixing in the intertidal area. Such forcing formed an upper saline plume (USP) with high dissolved oxygen (DO), creating a dynamic reaction zone for Fe oxidation and precipitation beneath the USP. The spatial distribution of Fe oxides highlighted a substantial Fe content in the subsurface, providing concrete evidence for the transformation of Fe from an aqueous state to a solid form. It also exhibited a low-permeable area that served as a geochemical barrier, absorbing chemical components like phosphate. These findings can assist in constructing a more accurate transport model that couples physical and geochemical processes to quantify the mechanisms driving Fe transformation in coastal areas and further deepen our comprehension of the hydrogeochemical functionalities in land-ocean connectivity via groundwater.

KEYWORDS

coastal groundwater system, field investigation, groundwater-seawater mixing, Fe(II) and Fe(III), dissolved oxygen (DO), porewater and sediment

1 Introduction

In recent decades, there has been an increasing recognition that submarine groundwater discharge (SGD) is a significant pathway for transporting solutes from land to the ocean (Moore, 2003; Robinson et al., 2007; Xin et al., 2010; Liu et al., 2016; Shen et al., 2018; Russo et al., 2023). The movement of fresh groundwater from land to the ocean prevents seawater intrusion and creates two distinct zones in the intertidal area. One of those is the saltwater wedge (SW), traditionally recognized as the primary area where groundwater and seawater mix (Charette and Sholkovitz, 2002; Ullman et al., 2003; Miller and Ullman, 2004; Slomp and Van Cappellen, 2004; Zipperle and Reise, 2005); the other is the upper saline plume (USP), a surficial mixing zone characterized by high salinity (Robinson et al., 2006; Kroeger and Charette, 2008; Santos et al., 2009; Anwar et al., 2014). Between the SW and the USP, there is a confined freshwater discharge tube (FDT) that intersects the beach near the low tide (LT) mark. Around this FDT, geochemical conditions transit from a reduced, circumneutral pH freshwater to an oxygenated, higher pH seawater, which determines the chemical speciation and solubility of elements along the flow path.

Ferrous ions (i.e., Fe(II) or Fe^{2+}), as an element in groundwater owing to the abundance of iron-bearing minerals in Australia (Larrahondo and Burns, 2014), can undergo rapid oxidation to ferric ions (i.e., Fe(III) or Fe^{3+}) in the presence of dissolved oxygen (DO) in seawater (Viscarra Rossel et al., 2010). Compared to Fe(II), Fe(III) is less soluble and can precipitate as ferric oxyhydroxides (i.e., $Fe(OH)_3$) at the groundwater-seawater interface (Charette and Sholkovitz, 2002; Charette and Allen, 2006). Such precipitates in intertidal areas were observed by several field studies (Abal and Watkinson, 2000; Lloyd et al., 2009). Additional research indicated that the accumulation of these precipitates can act as a geochemical barrier retaining dissolved phosphate (PO_4^{3-}) within the coastal groundwater system (Charette and Sholkovitz, 2002; Spiteri et al., 2006; Lalonde et al., 2012; Linkhorst et al., 2017), thereby having a substantial impact on the regulation of subsurface chemical fluxes into the ocean. Thenceforth, the term “iron curtain” was proposed and has since gained widespread use to describe its environmental functionalities in coastal areas.

So far, SGD has been studied intensively with their response to continental processes (e.g., inland hydraulic heads) (Liu et al., 2016; Kuan et al., 2019; Mo et al., 2021) and oceanic oscillations (wave and tide particularly) (Li et al., 1999; Robinson et al., 2006; Xin et al., 2010; Shen et al., 2018). In contrast to the extensive numerical studies addressing coastal hydrogeological processes, limited research has been conducted on major ions and metals, and field-based studies on iron curtains are also scarce. However, major research efforts have been made to understand the geochemical zonation linked to iron (Fe) concentration and its speciation in the intertidal area (Gibbes et al., 2008; Roy et al., 2010; Porubsky et al., 2014; Reckhardt et al., 2015; Beck et al., 2016; Hanington et al., 2016; Paffrath et al., 2020). For instance, chemical analysis of porewater samples from an offshore site in North Stradbroke Island, Australia, revealed that dissolved Fe in groundwater primarily existed in the form of Fe(II); it also demonstrated the presence of high Fe(II) concentration compared to that in seawater (Gibbes et al., 2008). Furthermore, detailed measurements of Fe(II) concentrations obtained by incubating sediment cores from northern Deception Bay, Australia, provided evidence of Fe(II) efflux at the sediment-seawater interface (Hanington et al., 2016). Although these studies have delivered valuable insights into Fe in coastal areas, the understanding of subsurface processes remains incomplete because physical and geochemical processes are analyzed independently (Robinson et al., 2018). Henceforth, this results in a restricted comprehension of the spatial variations of the iron curtain and its impact on subsurface flow. In addition, the lack of field datasets poses challenges to the representativeness of model results. Therefore, there is still an urgent need for field data to improve the accuracy of numerical modeling.

In response to these research gaps, a field investigation was conducted at a sandy beach to explore both physical and geochemical processes in the intertidal area. This study aims to develop a conceptual model illustrating the transformation of Fe from an aqueous form to a solid phase in the coastal groundwater system. The research objectives are twofold: a) how geochemical conditions (e.g., pH and redox potential (Eh)) evolve from groundwater to seawater and influence the speciation and solubility of Fe in the intertidal area, and b) how Fe precipitates spatially vary along the groundwater-seawater interface to form a geochemical barrier that retains dissolved chemicals. This field-based study offered valuable datasets in assisting the comprehension of the geochemical transition from groundwater to seawater, and the conceptual model can help establish an effective procedure for accessing Fe transformation at the groundwater-seawater interface. In addition, this study contributes to an in-depth understanding of the evolution of coastal aquifers induced by these coupled processes and presents corresponding environmental functionalities in land-ocean connectivity through groundwater.

2 Field site

The field site (see Figure 1A) is a tidal beach with a mild slope ($\Delta h/\Delta L$ = 0.015) on the northern end of Deception Bay (27°5′3″S, 153°8′7″E, a part of Moreton Bay Region), Southeast Queensland, Australia. Moreton Bay is a sheltered coastal system protected by large sand islands (Moreton Island (Mulgumpin) and Stradbroke Island (Minjerribah)). The southern and western sides of Moreton Bay are strongly influenced by major river estuaries, which transport sediments into the bay, producing intertidal mudflats and mangrove swamps. The northern and eastern parts of the Bay have predominantly sandy beaches with occasional meadows. Based on the identification of probable freshwater features (rivers and creeks, but excluding rainfalls) in this region by incorporating field investigations with satellite maps, it is considered that the fresh groundwater is only from the northwest terrestrial environment (see Figure 1B).

This sandy beach was characterized by a subtidal and intertidal area that has been subjected to extensive and frequent Lygnbya blooms since the early 1990s (Albert et al., 2005). Up to the time of our field

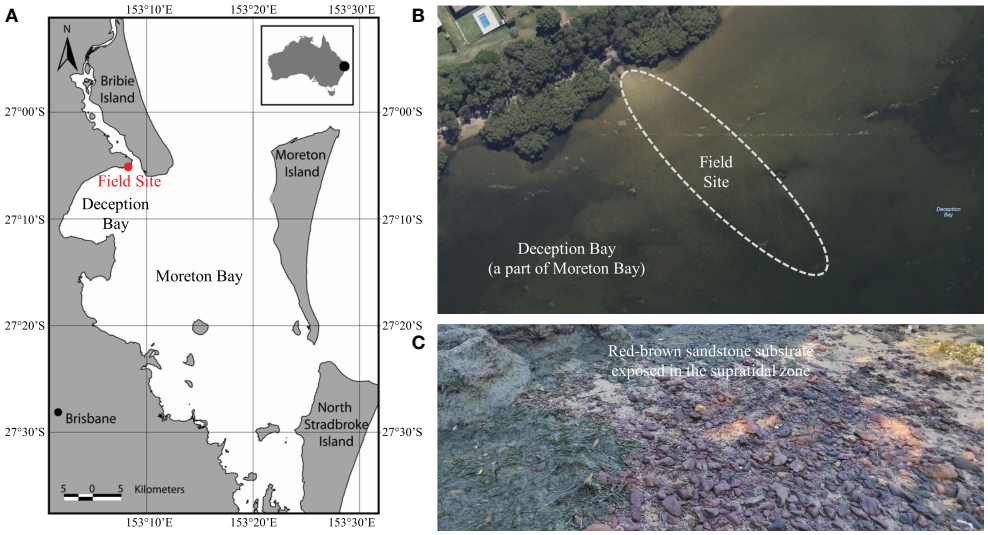

FIGURE 1
(A) Map of the field site in Sandstone Point, Southeast Queensland, Australia (adapted from Robinson et al., 2007). The field site is on the northern end of Deception Bay (27°5′3″S, 153°8′7″E), a part of the Moreton Bay Region protected by Moreton Island (Mulgumpin) and North Stradbroke Island (Minjerribah). **(B)** The sandy intertidal area of the field site with the nearby buildings and major vegetation; **(C)** Snapshot of red-brown sandstone substrate exposed in the supratidal zone of the field site, and the outcropping sediments were identified to contain Fe minerals in earlier studies.

investigation, more than 30 Lyngbya blooms had been observed by the ongoing *Lyngbya Monitoring Program* organized by the Queensland Government (Department of Environment, Science and Innovation, Queensland, Australia, 2013). The hypothesis that Lyngbya blooms can be exacerbated by the presence of Fe was proposed earlier (Hanington et al., 2016), and the outcropping sediments contain Fe minerals that were identified in earlier studies (Ahern et al., 2006a; Saeck et al., 2019). In addition, indurated Fe-rich sand crusts are exposed in proximity areas along the coastline (see Figure 1C), which supports the selection of this particular stretch of coast.

3 Field methodology

3.1 Monitoring system and equipment

The field investigation was conducted during spring tide in May 2021, and the field monitoring lasted five days from the 10th to the 14th of May 2021. It is widely accepted that the groundwater system, in this case, could be considered two-dimensional (2-D) under the Dupuit assumption for simplifying engineering-scale groundwater modeling (Liu et al., 2023). Additionally, it is assumed that there are minimal variations of the phreatic line (i.e., groundwater table) alongshore (Gibbes et al., 2007). Thus, a single cross-shore transect was selected from the landward of the high tide (HT) mark into the subtidal region in order to track groundwater processes in the intertidal area. Figure 2 shows a cross-shore transect that was 40 m in length and started from the HT mark. A field monitoring system was set up across the shoreline to take measurements, and all of the equipment was collectively placed in the intertidal area where there was a highly reactive area for porewater exchange. The exact position of the benchmark (BM) was identified using a GPS (Garmin Australasia Pty Ltd.), and the elevation was converted to the Australian Height Datum (AHD), which is the official vertical datum used in Australia. By following that, at the locations of equipment, their corresponding elevations in reference to the local BM were determined horizontally along this transect, using a self-leveling rotating laser (RL-H5A with a precision of ±1.5 mm, Topcon Positioning Systems Inc.).

Figure 2 illustrates the configuration of the monitoring system, which includes:

(1) The weather station, underpinned by a steel tripod, was electrically powered by a battery that was constantly recharged by a solar panel. It was also equipped with a remote-controlled datalogger, a weather-resistance camera, and a series of meteorological sensors, all of which were mounted on the tripod (see Figures 3A, B). Hence, the weather station could monitor the field conditions at a given interval, and the datalogger could record the datasets, which were subsequently sent to the internet-of-things (IoT) platform through a 3G/4G signal for instantaneous visualization

(2) The custom-made multi-level samplers (MLS, 2 m in length) were used to collect porewater samples to determine both physio-chemical variables and the chemical forms of dissolved Fe. As an improved design of those employed by Martin et al. (2003), each MLS comprises polyvinyl chloride (PVC) pipes (diameter of 50 mm, Holman Industries Pty Ltd.) with a threaded end and a pointed endcap, as well as ten sampling ports spaced at a spatial interval of 0.2 m along the pipe. They were installed at a 0.5 m offset to the piezometers at the site (see Figure 3A).

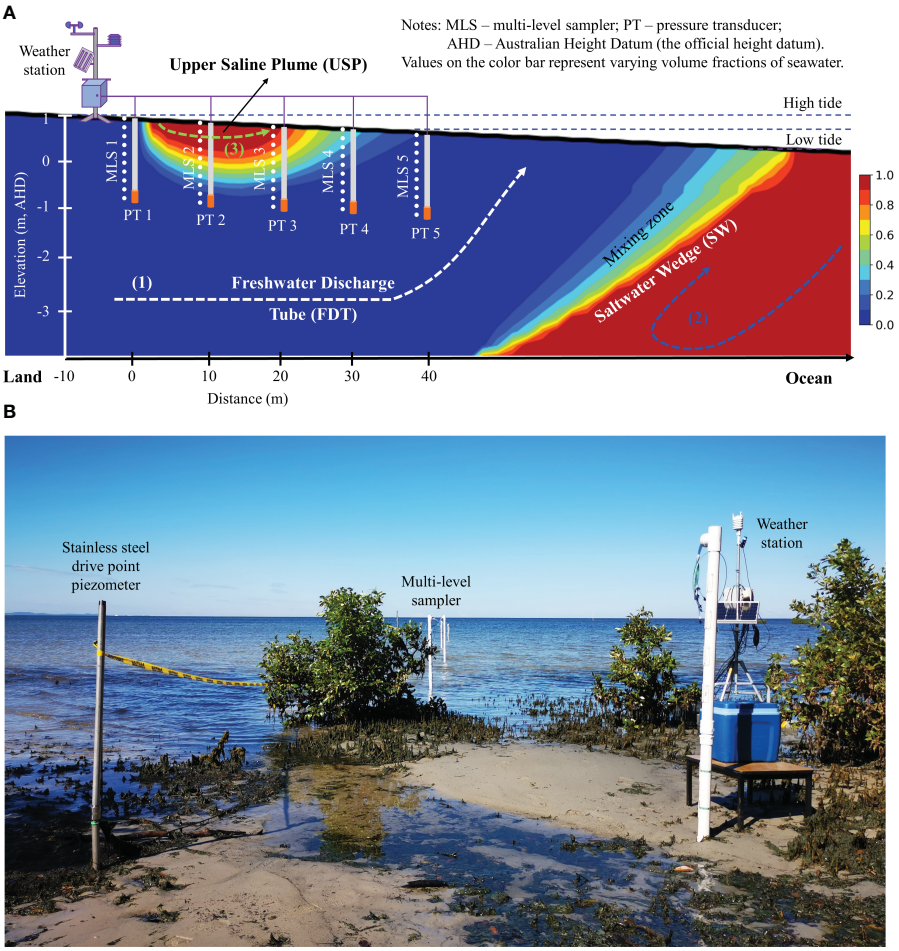

FIGURE 2
(A) Schematic diagram of field experimental setup in a coastal groundwater system. The bold black line is the beach profile. The horizontal direction represents the beach transect toward the ocean, and the vertical direction represents the elevation relative to the Australia Height Datum (AHD) which is the official height datum for Australia. As shown in the color bar, red indicates pure seawater with a volume fraction of 1.0, while blue represents pure fresh groundwater with a volume fraction of 0.0. In between the two is the mixing zone with varying volume fractions of seawater. The major processes in the intertidal area include (1) fresh groundwater discharge (shown as a white dashed line), (2) density-driven circulation (shown as a blue dashed line), and (3) tide-induced circulation (shown as a green dashed line). Between the saltwater wedge (SW) and the upper saline plume (USP), a freshwater discharge tube (FDT) intersects the beach. **(B)** Snapshot of field experimental setup along the beach transect in the intertidal area at Sandstone Point, Southeast Queensland, Australia. The field instruments included a solar-powered weather station, five multi-level samplers (MLS), and five drive point piezometers (equipped with pressure transducers (PT)) which were installed at 10-m intervals along the beach transect.

(3) An array of driving points of piezometers (equipped with PT, numbered PT1 to PT5 towards the ocean) was installed at 10 m intervals along this transect to record the temporal variations of the groundwater table driven by tidal fluctuations. As for borehole casing, several stainless steel standpipes (diameter of 25 mm, Solinst Inc.) were driven underground to the desired depth using a post driver. After casing those boreholes with stainless pipes, the bottom end of each pipe was covered by a screen within a length of 0.3 m. The sensors (AquaTROLL 200, In-Situ Inc.) in each borehole could instantaneously record the datasets of water level and pressure, electrical conductivity (EC), and temperature to the weather station at designated temporal intervals through a few data cables.

3.2 Field sampling and measurements

The porewater samples were collected using sampling ports at the MLS (see Figure 3A). As described in Figure 3B, the collected sample obtained from the spherical capture zone with a small radius (≈0.05 m) was representative of the porewater around the sampling port. The volume of each sample was limited to 120 mL to minimize the impact on the surrounding waters so that there was no cross-port interference and in-situ perturbation during porewater sampling. Figure 3C shows that porewater from each sampling port was extracted using a peristaltic pump (Geopump Series II, Geotech Environmental Equipment, Inc.) at a low flow rate of 60 mL/min and was rapidly transferred into a flow cell for a later determination of in-situ physio-chemical state variables (e.g.,

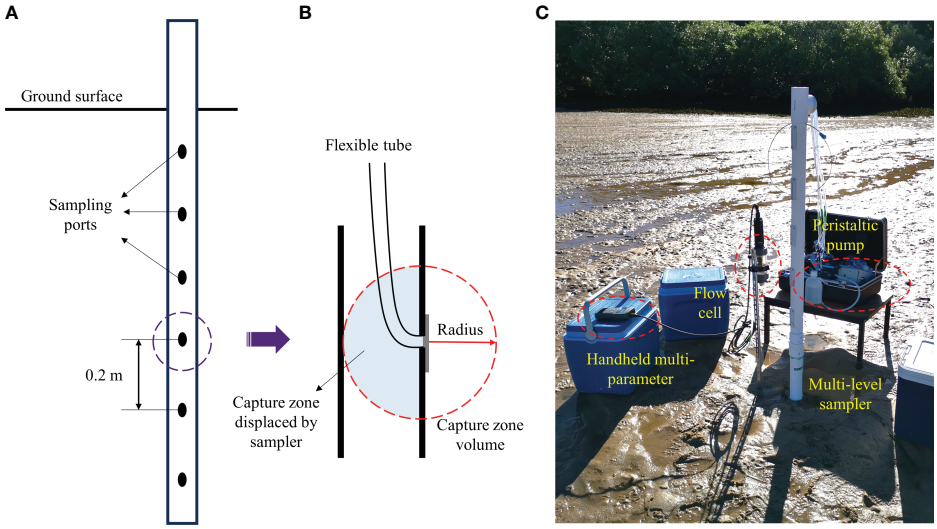

FIGURE 3
(A) Schematic diagram of MLS installed in the intertidal area. The sampling ports are spaced at a spatial interval of 0.2 m vertically. **(B)** Capture zone of each sampling port with a small radius of 0.05 m that limits the volume of porewater around the sampling port in order to prevent cross-port interference. **(C)** Snapshot of field sampling in the intertidal area. The porewater sampling procedure includes (1) extracting porewater with a peristaltic pump at a low flow rate; (2) transferring it into a flow cell for in-situ measurements using a handheld multi-parameter; (3) collecting the sample with a syringe and then transferring it into the sample bottle for storage.

salinity, DO, pH, and redox potential) using a portable probe (HI98194, Hanna Instruments, Inc.). The overflow collected by a syringe of 60 mL was thenceforth transferred into the high-density polyethylene (HDPE) plastic bottles through a sterile filter (filtering size = 0.45 μm). In order to stabilize the dissolved Fe in different chemical forms, the bottles were priorly acidified with hydrochloric acid (HCL), i.e., filling the container entirely. This step can effectively minimize any potential oxidation in storage during transport. Throughout the field investigation, porewater at each port was sampled twice per day, so it took 4–6 hours to reconstruct a complete profile by spatially interpolating the datasets collected from all ports. Although the spatial porewater measurements were not synchronized in terms of both equipment and operating procedure, all datasets were recorded within a single day, and this issue could be later resolved by temporal interpolation in the data post-analysis.

It was once suggested by Thamdrup et al. (1994) that porewater analysis is dependent on the collection of intact sediment cores where pore water samples are extracted, mainly when analysis of the solid phase is also undertaken (Gibbes et al., 2008). However, it was highly challenging to preserve the integrity of the sediment cores from the same location at different times. To provide an alternative resolution in this regard, additional sediments from ambient areas (within a diameter of 0.5 m) at each sampling location were manually retrieved underground using a hand auger in depths of 0.5 m and 1.0 m, respectively. Those sediments were directly transferred into glass containers to determine the content of Fe oxides. Moreover, when the intertidal area was exposed at low tides, the sediment core was collected by (1) pushing a plastic pipe (inner diameter 76 mm) vertically down into the sediment at the selected location; (2) carefully digging around the pipe with a spade or shovel to avoid excessive disturbance; (3) capping the pipe at the top to seal it completely at the maximum depth achievable; (4) slowly extracting the pipe from the sandy beach, and completely sealing the pipe at the bottom; (5) keeping it as upright as possible to minimize disturbance. As a result, three undisturbed sediment cores (two were Φ76 mm × L300 mm in burial depth, while one was Φ76 mm × L500 mm) were taken for additional analysis of the hydraulic and seepage properties.

3.3 Laboratory tests and analysis

The chemical analysis of those porewater samples was carried out in an environmental laboratory (ALS Ltd.). The concentration of total Fe in the sample was quantified using an inductively coupled plasma mass spectrometry (ICP-MS) (Agilent 7900, Agilent Technologies Pty Ltd.), while the specific concentration of Fe(II) was determined by a discrete analyzer which utilized ion selective electrodes (ISE) (Konelab Prime 60i, Thermo Fisher Scientific Inc.) The measured potential between each ISE and the reference electrode correlated with the natural logarithm of the ionic activity (as per the Nernst equation), which reflected changes across the ISE membrane/sample interface. Consequently, the concentration of Fe(III) was derived through a simple calculation employing the total Fe and dissolved Fe(II) values. Furthermore, the metals in sediments were extracted by an aqua regia digest (2 mL of 1:1 HNO_3 and 10 mL of 1:4 of HCl). The content of total Fe and total P was determined by an inductively coupled plasma -optic emission spectroscopy (ICP–OES) (Agilent 5110, Agilent Technologies Pty Ltd.) and a discrete analyzer (Konelab Prime 60i, Thermo Fisher Scientific Inc.), respectively.

Hydraulic conductivity (i.e., coefficient of permeability K in geomechanics) tests were conducted on sediment cores at the

Geomechanics Research Laboratory, School of Civil Engineering (SoCE) at the University of Queensland (UQ). The constant head method was utilized to measure the hydraulic conductivity by employing a Mariotte bottle to supply a constant hydraulic head at the boundary of the rigid-wall permeameter (ASTM D2434-68, 2006). In addition, the porosity of the in-situ sediment specimen was determined based on the theory of soil representative elementary volume (REV) in three-phase fractions (e.g., air, water, and solid); in order to achieve this, the specific gravity and dry density of in-situ specimen were measured separately using the gas pycnometer (ASTM D5550-23, 2023) and oven-drying methods (ASTM D7263-21, 2021). The particle size distribution (PSD) tests were performed on the sediment samples using the sieving method (ASTM D6913-17, 2021). The data obtained from porosity and effective particle size (d_{10}, d_{30}, and d_{60}), along with the Kozeny-Carman equation (see Equation 1), were used to estimate the hydraulic conductivity of the saturated sediment for comparison. It is crucial to repeat these tests at least three times and then take an average to eventually provide reliable hydraulic and seepage properties of the in-situ sediment specimens (Yan et al., 2022a, 2022b).

$$K = \frac{1}{C}\frac{\rho g}{\mu}\frac{n^3}{(1-n)^2}d^2 \quad (1)$$

where C is the shape factor (C = 180–270 for granular soil, such as sand), ρ is the water density (kg/m^3), g is the gravitational acceleration (m/s^2), μ is the water viscosity (Pa•s), n is porosity, d is the effective diameter (m), equivalent to the spatial mean diameter of pore hydraulic conduits (i.e., effective seepage flow paths).

4 Results and discussion

4.1 Tide-induced circulation and porewater exchange

Tidal data was collected from the gauge located at Scarborough Boat Harbour in northernmost Redcliffe, Queensland, Australia, which is approximately 10 km away from the studied site. The dataset covered a semi-diurnal tide from the 10th to the 14th of May 2021.

Figure 4 shows the field measurements in 2021 that occurred during spring tide. At HT, the water levels reached as high as 1.20 m, whereas they dropped to −0.80 m at LT. The observed condition in the field revealed that the investigated transect was inundated during HT while it became exposed to the atmosphere during LT. Consequently, the tidal force acting upon the beach led to notable porewater exchange processes in the intertidal area. Specifically, the receding tide resulted in porewater drainage from the intertidal area, which was later replaced by seawater infiltration during the rising tide. This semi-diurnal pattern can lead to the fluctuation of porewater physio-chemical variables in response to the groundwater table variations in the measured timeline. Tidal-induced circulation can contribute significantly to salt and solute transport in the intertidal area, which facilitates the exchange of geochemical conditions between the intertidal area and coastal seawater. This exchange mechanism plays an important role in the transformation and distribution of Fe in the porewater and sediment.

4.2 Porewater chemistry and oxidizing conditions

The porewater sampling was conducted during the daytime of 13th May 2021, aiming to study the geochemical conditions linked to Fe speciation in the beach transect, specifically focusing on the intertidal area. The manual measurements of extracted porewater samples were conducted twice at an interval of c.a. 4 h: (i) during HT when the intertidal area was inundated and (ii) during LT when it was exposed to the ambient atmospheric condition. Throughout the sampling, the temperature of extracted porewater was in the range of 20.1 °C to 22.6 °C, which suggested a minor impact on water density and viscosity, as well as on major physio-chemical variables, such as salinity, pH, DO, and Eh. Figure 5 illustrates the

FIGURE 4
Tidal readings at Scarborough Boat Harbour in northernmost Redcliffe, Queensland, Australia, located around 10 km away from the field site. The dataset captured semi-diurnal tide cycles (ranging from −0.8 m to 1.2 m based on the Australian Height Datum (AHD), the official vertical datum for Australia) between 10 May and 14 May 2021 (Source: Maritime Safety Queensland, Australia).

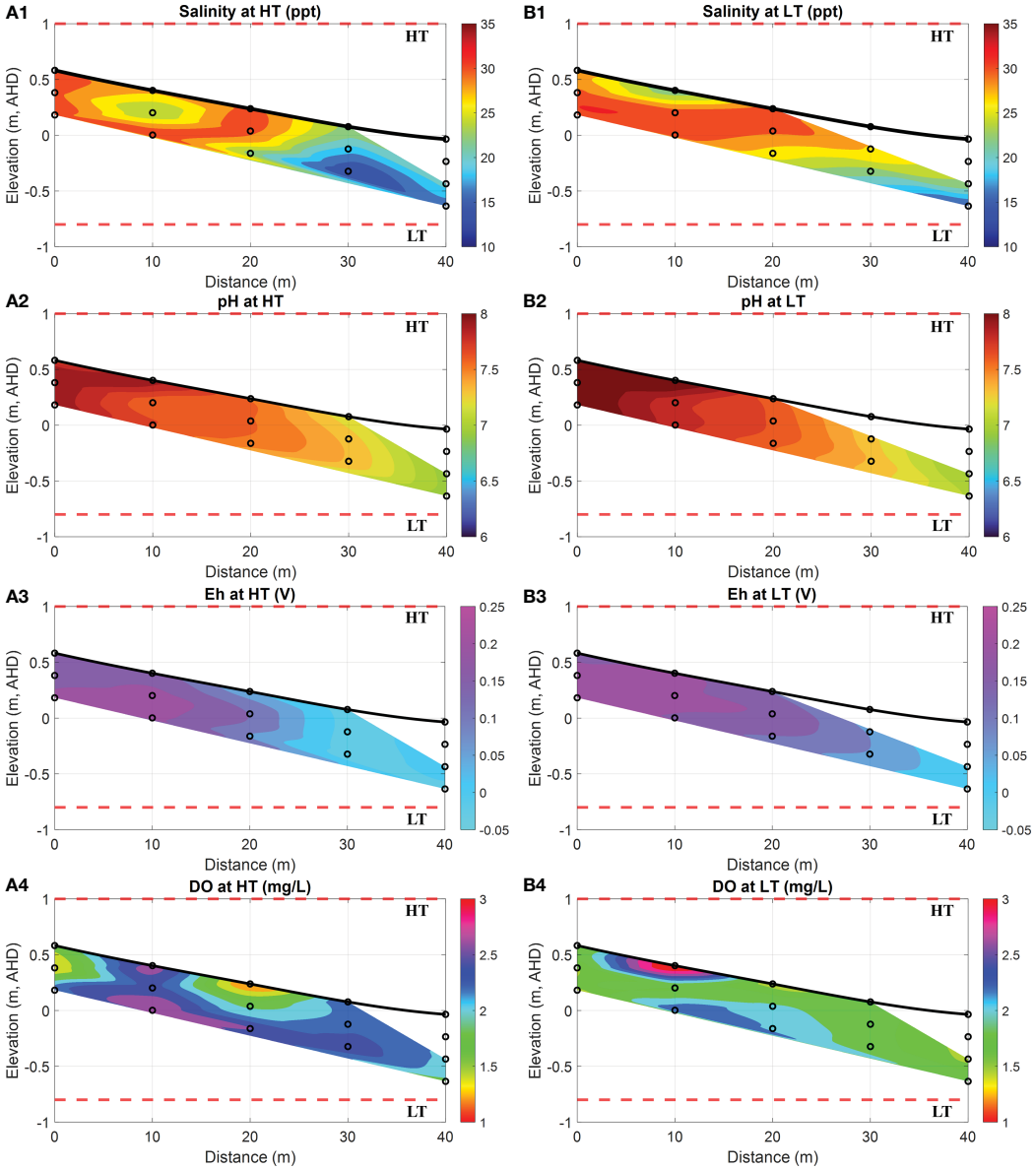

FIGURE 5
Spatial distribution of salinity, pH, Eh, and DO at HT and LT in the intertidal area. **(A1-A4)** show the salinity (in ppt, equivalent to g/kg), pH, Eh (in Volts) and DO (in mg/L) levels at HT, while **(B1-B4)** represent the salinity (in ppt, equivalent to g/kg), pH, Eh (in Volts) and DO (in mg/L) at LT. In addition, the bold black line is the beach profile, and the black circles represent the sampling points. The red dashed lines represent the HT and LT elevations in relation to the Australian Height Datum (AHD) which is the official vertical datum for Australia. The horizontal represents the distance towards the ocean, and the vertical represents the elevation relative to AHD.

spatial distribution of salinity, pH, Eh, and DO at HT and LT in the intertidal area. These data are essential for investigating major physio-geochemical mechanisms influencing the transformation of dissolved Fe(II) in the coastal groundwater system.

During both HT and LT, the porewater samples collected between the horizontal locations of 0 m and 20 m exhibited relatively high salinity, i.e., 31 ppt (a maximum value in orange areas of Figures 5A1, B1), along with a high pH value of 8.0 (a maximum value in dark red areas of Figures 5A2, B2). These findings suggested the presence of seawater in the submarine unconfined aquifer. Previous field observations also supported the existence of a USP due to tidal forces (Robinson et al., 2006, 2018). The tide-induced circulation maintained a surficial mixing zone with high salinity near the surface water infiltration area, consequently raising the pH value in the upper intertidal area. On the contrary, porewater samples collected from locations between 30 m and 40 m on the ocean side displayed relatively lower salinity at 15 ppt (a maximum value in blue areas of Figures 5A1, B1) and a moderate pH of 7.0 (a maximum value in green areas of Figures 5A2, B2), resembling the characteristics of fresh groundwater. Previous studies conducted near this site suggested that significant quantities of terrestrial fresh groundwater seep through soil profiles at depth and potentially are released into the offshore area of Deception Bay (Albert et al., 2005). Both the former

study and our field observations demonstrated that terrestrial groundwater was being transported to the adjacent intertidal area in the specific section of the transect along the beach.

Furthermore, DO measurements (see purple areas in Figures 5A4, B4) revealed a stripping zone with a high concentration of oxygen that reached up to 3.1 mg/L. This DO-rich seawater infiltrated into the intertidal transect due to tidal forcing. Consequently, a significant amount of DO entered the surface water infiltration zone, and thereby, it led to the high content of DO extending into the USP. However, the DO in this zone could be rapidly depleted through oxidation processes. As a result, the extent of the area with a relatively high content of DO exhibited dynamic variations over tidal cycles, which were attributed to the residence time of seawater circulation during the spring-neap tide (Robinson et al., 2007). Moreover, Eh is a parameter used to describe the tendency of a chemical species to either undergo reduction by accepting electrons or oxidation by donating electrons (Reddy, 2000). Its value of >0.1 V indicates oxic environments (Scholz, 2019). As shown in Figures 5A3, B3, the high values of Eh ranging from 0.1 V to 0.25 V between the horizontal locations of 0 m and 20 m indicated a strong oxidizing environment for redox-sensitive Fe(II), consistent with the pattern observed for DO (see purple areas in Figures 5A4, B4). Specifically, the oxidizing conditions were prominent at the seawater infiltration point from 0 m to 20 m, where a higher content of DO was observed. Meanwhile, the receding Eh (see cyan areas in Figures 5A3, B3) was observed at the groundwater discharging point between the horizontal locations of 30 m and 40 m.

More importantly, in contrast to the high concentrations of DO (see Figure 6A4) observed at high tides, Figure 6B4 demonstrated an exceptionally high DO concentration in porewater near the sediment surface. This phenomenon may be attributed to a combination of factors, including the short residence time of USP and air intrusion during desaturation periods. Considering the porewater sampling duration of 4–6 hours, air intrusion could become available at low tides when the intertidal area was exposed to the ambient environment. This exposure allowed air to infiltrate into the sediment, particularly into the surface layers where pore spaces were more accessible. As air infiltrated, oxygen from the atmosphere slowly dissolved into the porewater, which resulted in elevated levels of DO near the sediment–atmosphere interface. However, a high salinity observed between the distances of 5~15 m (see Figure 5A1) indicated the possible residence of USP and tidal influences on oxygen penetration, which may also contribute to the high DO levels observed in deeper sediment layers at the same location, as illustrated in Figure 5B4.

4.3 Fe transformation and phosphate removal

Further chemical analysis on porewater samples was carried out in the laboratory to determine the concentrations of dissolved Fe(II) and Fe(III) as well as PO_4^{3-}. As a result, Figure 6 illustrates the distribution of Fe(II), Fe(III) and PO_4^{3-} at HT and LT on 13th May 2021. In contrast to the low concentrations of PO_4^{3-}, the results at

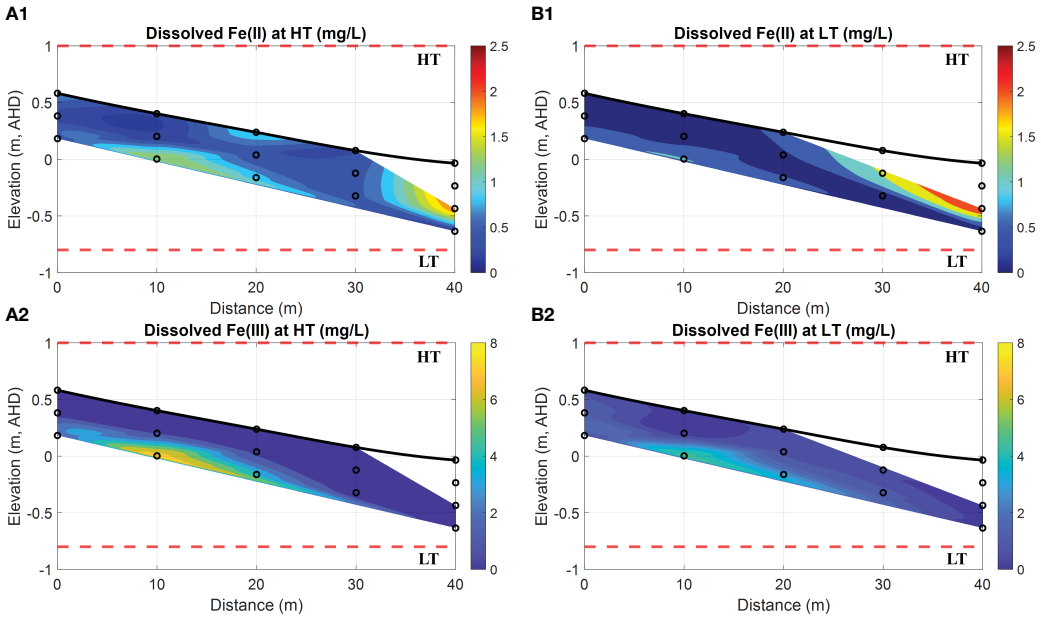

FIGURE 6
Spatial distribution of dissolved Fe(II) and Fe(III) at HT and LT in the intertidal area. **(A1,A2)** show the dissolved Fe(II) and Fe(III) (both in mg/L) at HT, respectively, while **(B1, B2)** represent the dissolved Fe(II) and Fe(III) (both in mg/L) at LT, respectively. In addition, the bold black line is the beach profile, and the black circles represent the sampling points. The red dashed lines represent the HT and LT elevations in relation to the Australian Height Datum (AHD) which is the official vertical datum for Australia. The horizontal represents the distance towards the ocean, and the vertical represents the elevation relative to AHD.

both HT and LT indicate that the porewater contains a substantial amount of Fe(II) in a range of 0.08~2.52 mg/L. However, a significant concentration of Fe(II) peaking at 1.99 mg/L or 2.52 mg/L was only observed in a restricted region at a distance of 40 m (see red area in Figures 6A1, B1).

Based on the chemical analysis of porewater samples taken between the horizontal locations of 0 m and 20 m, there was a presence of relatively low Fe(II) concentrations (with a maximum value of 1.01 mg/L, see cyan areas in Figures 6A1, B1) in the upper intertidal area, while high concentrations of dissolved Fe(III) (>5.0 mg/L, see yellow areas in Figures 6A2, B2) were observed in the same region. Upon comparing these patterns with the DO concentrations in Figures 5A4, B4, it is evident that the majority of Fe(II) had been oxidized to Fe(III) due to the strong oxidization at the bottom interface of the USP. In contrast, at the horizontal locations between 30 m and 40 m, relatively high concentrations of dissolved Fe(II) (within 0.8~1.8 mg/L, see red areas in Figures 6A1, B1) coincided with the environment characterized by lower values of DO and Eh at the exit of fresh SGD. Our field investigation, combined with previous studies on other sites near the current (Hanington et al., 2016), further supported the notion of benthic Fe released into Deception Bay through SGD. Moreover, by comparing Figures 6A2, B2, it was observed that the oxidation process from Fe (II) to Fe(III) during HT could be more significant than during LT. The reason is that tidal circulation provided more DO to the USP, which thereby facilitated the Fe(II) oxidation at the groundwater-seawater interface.

Furthermore, high concentrations of Fe(III) (up to 4.6 mg/L in a specific location) observed in porewater may contradict the conventional understanding of its limited solubility in aquatic environments. The discrepancy can be explained by the possible biogeochemical processes that are prevalent in anaerobic environments such as marine sediments and groundwater systems (Spiteri et al., 2008; McAllister et al., 2015; Sukekava et al., 2024). Due to possible microbial activities in aquatic settings, precipitated Fe oxides could undergo dissolution and re-precipitation, which allows them to alternate between ferrous and ferric states. Specifically, Fe-reducing bacteria can reduce Fe(III) within Fe oxides to more mobile and soluble Fe(II), while Fe-oxidizing bacteria transform Fe(II) into insoluble Fe(III) which then precipitates as solid-phase Fe oxides (Luef et al., 2013; Kügler et al., 2019; Baker et al., 2023). Consequently, such biogeochemical processes can profoundly influence the stability and remobilization of Fe oxides, which in turn influence the concentration and distribution of dissolved Fe(II) and Fe(III) in natural field conditions. Although Fe remobilization is beyond the scope of this study, the field investigation holds promise for further advancements in subsequent studies.

Figure 7 exhibits a consistently low concentration of dissolved PO_4^{3-} in porewater. Nevertheless, the PO_4^{3-} concentration observed between the horizontal locations of 0 m and 30 m (see cyan areas in Figures 7A, B) was less significant than that from 30 m to 40 m (see magenta areas in Figures 7A, B), referred to as the exit of fresh SGD (see blue areas in Figures 5A1, B1). This discrepancy implies a substantial decrease in phosphate concentration as the fresh groundwater moves through the FDT, as illustrated in Figure 2A, attributed to the presence of Fe oxides in the sediment. The subsequent analysis of sediment can provide evidence that Fe oxides can serve as a sink for dissolved PO_4^{3-} in this intertidal area.

4.4 Sediment chemistry and spatial heterogeneities

Based on the laboratory tests conducted at UQ, the physical properties, including seepage and hydraulic properties, of coastal sediment specimens are presented in Table 1. The results indicate that the sediment specimens can be classified as SP, which stands for poor-graded quartz sand, based on the unified soil classification system (USCS). Besides, these specimens contained a fine content (<0.075 mm) of 0.1%, according to the PSD test.

In addition, Figure 8 shows a 2-D cross-sectional beach transect that illustrates the spatial distribution of Fe oxides and phosphorous-containing compounds within the sediment.

Figure 8A shows three distinct regions (named Region #1, #2, and #3 in order) with intensive Fe that can be identified. Specifically, Region #1 was located at 0 m, closer to the ground in the upper

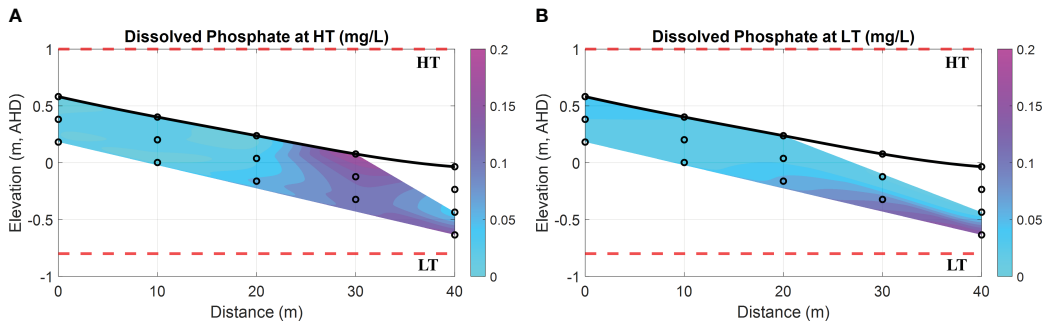

FIGURE 7
Spatial distribution of dissolved phosphate (PO_4^{3-}) at HT and LT in the intertidal area. **(A)** dissolved PO_4^{3-} (in mg/L) at HT; **(B)** dissolved PO_4^{3-} (in mg/L) at LT. In addition, the bold black line is the beach profile, and the black circles represent the sampling points. The red dashed lines represent the HT and LT elevations in relation to the Australian Height Datum (AHD) which is the official vertical datum for Australia. The horizontal represents the distance towards the ocean, and the vertical represents the elevation relative to AHD.

TABLE 1 Specification of coastal sediment specimens.

Category	Description	Value
Quartz sand	Dry density, $\rho_{d,max}$ (g/cm^3)	1.63
	Dry density, $\rho_{d,min}$ (g/cm^3)	1.59
	Porosity responding to dry density, n (-)	0.33~0.35
	Effective particle size, d_{10} (mm)	0.21
	Effective particle size, d_{30} (mm)	0.31
	Effective particle size, d_{60} (mm)	0.42
	Coefficient of uniformity, C_u	2.00
	Coefficient of curvature, C_c	1.09
	Estimated coefficient of permeability, K ($\times 10^{-4}$ m/s)	1.81~2.29 [a]

[a] Some values in this range were estimated by the Kozeny-Carman equation (see Equation 1).

intertidal area, whereas Region #2 was at 10 m with a depth of 1 m beneath the surface. Both regions exhibited substantial Fe, reaching up to 5220 mg/kg and 5830 mg/kg, respectively. Furthermore, Region #3 was suited at 40 m towards the ocean, and the total Fe peaked at 6520 mg/kg. Consequently, the spatial distribution of Fe along these regions displayed a strip-like pattern extending from the land to the ocean, corresponding to the bottom interface of the USP as shown in Figures 6A1, B1. This phenomenon can be attributed to the precipitation of Fe at the groundwater-seawater interface, a consequence of the subsurface mixing of Fe(II)-rich groundwater and DO-rich seawater. Through this mechanism, precipitated Fe can accumulate over time in the intertidal area, and this particular zone is commonly referred to as the iron curtain. It is important to acknowledge that the formation of an iron curtain is considerably more complex in the natural coastal environment and requires tens of thousands of years due to slow reaction kinetics. For example, the oxidative precipitation of Fe(II) exhibits a rate constant of 6.4×10^{-2} mmol^{-1}s^{-1} (Anwar et al., 2014).

Although several aspects, such as the aging process (Houben, 2003) and reduction process by microbial activities (Sevinç Şengör et al., 2007), were beyond the scope and capacities within the time scale of this investigation, the notable discrepancy in the concentrations of dissolved Fe(II) (up to 2.52 mg/L) and Fe(III) (up to 4.6 mg/L) was observed in local porewater samples when compared to their nanomolar levels conventionally found in aquatic settings. Such difference could be induced by possible biogeochemical processes, particularly when highly reactive Fe oxides were present in marine sediments. Previous studies have demonstrated that biogeochemical processes are prevalent in anaerobic environments (Spiteri et al., 2008; McAllister et al., 2015). In addition to pH-Eh conditions, two significant scenarios can influence the transformation, mobilization, and distribution of Fe speciation in groundwater systems. First, microorganisms play an important role in mediating Fe speciation through biological processes (Alotaibi et al., 2015; Wu et al., 2019). Microbial oxidation reactions, facilitated by Fe-oxidizing bacteria, transform Fe(II) to Fe (III) and promote the precipitation of Fe oxides in aerobic settings, whereas microbial reduction processes, driven by Fe-reducing bacteria, convert Fe(III) to Fe(II) and facilitate the remobilization of Fe oxides under anaerobic conditions (Luef et al., 2013; Baker et al., 2023). Second, Fe ions can form complexes with various ligands, including organic matter, humic substances, and inorganic ligands, which alter the solubility, stability, and reactivity of Fe speciation (Zhou et al., 2015; Sukekava et al., 2024). For example, organic ligands can enhance the solubility of Fe(III) by forming soluble Fe-organic complexes (Kügler et al., 2019). As a result, the combined effects of these factors determine the mobility and availability of Fe speciation in porewater and sediments within natural field settings.

With a specific surface area ranging from 530 m^2/g to 710 m^2/g (Hiemstra et al., 2019), ferrihydrite has a high capacity for adsorbing dissolved PO_4^{3-}. This characteristic results in the co-precipitation of Fe oxides and phosphorous-containing compounds (Chambers and Odum, 1990; Cornell and Schwertmann, 2003; Van Der Grift et al., 2016). Hence, the formation of Fe oxides can be regarded as a mechanism for sinking dissolved PO_4^{3-} in sandy sediment. In Figure 8B, high P content was observed in the intertidal sediment,

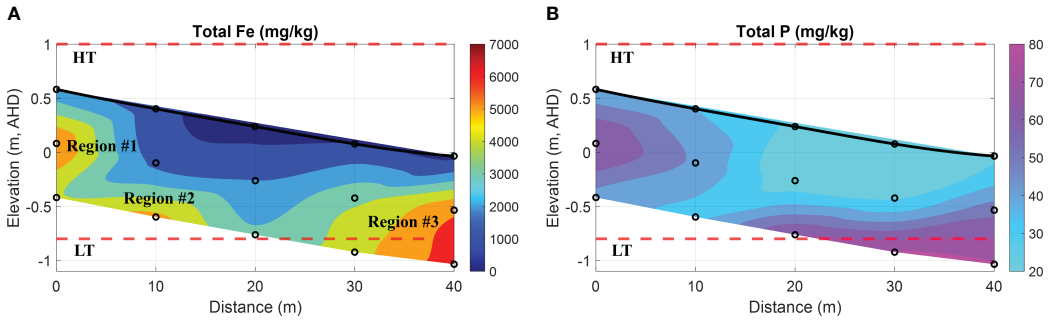

FIGURE 8
Spatial distribution of total Fe and P in the intertidal sediments. **(A)** total Fe oxides (represented as Fe in mg/kg); **(B)** total phosphorous-containing compounds (represented as P in mg/kg). In addition, the bold black line is the beach profile, and the black circles represent the sampling points. The red dashed lines represent the HT and LT elevations in relation to the Australian Height Datum (AHD) which is the official vertical datum for Australia. The horizontal represents the distance along the transect, and the vertical represents the elevation relative to AHD.

and the spatial distribution of total P in the field was consistent with that of total Fe in comparison with Figure 8A. The finding provides additional evidence to support the linear correlation between Fe oxides and P contents in the coastal bay, as investigated by (Charette and Sholkovitz, 2002; Testa et al., 2002). Furthermore, the analysis of seepage properties (e.g., hydraulic conductivity *K*) at various depths revealed that the *K* value at 1 m depth was averaged at 9.64×10^{-6} m/s, whereas the surface sediment had an estimated value of $(1.81\sim2.29) \times 10^{-4}$ m/s (see Table 1). The disparity between both was apparent, with a magnitude difference of up to two orders. According to the studies by (Carter and Bentley, 1991), the range of *K* values for poorly graded sands with little fines is typically between 5.35×10^{-5} m/s to 2.55×10^{-4} m/s. Therefore, the variation of *K* observed in the coastal sediment collected from two different depths can be attributed to the process of Fe precipitation or co-precipitation, rather than natural consolidation of beach sands. It is anticipated that this process will indefinitely continue unless a self-limiting mechanism is taken into account, such as the complete clogging of pore space. This would lead to the obstruction of porewater exchange, consequently influencing the evolution of the coastal groundwater system. However, it is beyond the scope of this investigation due to the time scale.

4.5 Sources of Fe and mobilization of Subterranean Fe

While Fe is the fourth most abundant element in the earth's crust (LePan and Venditti, 2021), the concentration of dissolved Fe (II) is typically very low (nanomolar-to-subnanomolar range) due to rapid oxidation to Fe(III) in oxygenated seawater with a pH > 7.0 (Fitzsimmons and Conway, 2023). Consequently, Fe(III) is more predominant than Fe(II), albeit still relatively low in concentration due to its low solubility in water bodies (Zhang et al., 2022). As shown in Figure 6A1, the transient peak of Fe(II) concentration at the groundwater-seawater interface reached 2.52 mg/L, which was eleven times higher than the value of 0.23 mg/L (data on 27 August 2018) observed in the borehole groundwater at a depth of 19.8 m in South Bribie Island, Queensland, Australia. Thus, the elevated concentration of Fe(II) in porewater is likely derived from a dissolved form of Fe(II) linked to local groundwater systems.

According to earlier studies, Sandstone Point is situated on a coastal plain with the underlying Landsborough Sandstone, characterized by quartz sand and consisting of Fe-rich minerals (Cox and Preda, 2005; Ahern et al., 2006b). Moreover, the intertidal area off Sandstone Point was subject to sampling in 2000. The report indicated that the soil was acidic (pH = 4.6~5.2) below a depth of 0.2 m and strongly acidic (pH< 3.4) at depths of 1~1.2 m (Albert et al., 2005; Ahern et al., 2006a). These findings suggest the presence of acid sulfate soils (ASS), which are omnipresent in the coastal areas of Queensland. When these soils are hydromechanically perturbated (e.g., agriculture and construction), the sulfides are exposed to air and react with oxygen to form sulfuric acid. This process leads to the decomposition of iron-bearing minerals (Manson et al., 2003), subsequently resulting in the release of iron ions into groundwater systems through rainwater infiltration and drainage systems (Larrahondo and Burns, 2014). As a result, surface soil samples (at depths of 0.2~0.3 m) exhibited low-to-moderate content of extractable Fe (up to 91 mg/kg), and elevated concentration of dissolved Fe(II) was identified in the groundwater, reaching up to 1.6 mg/L. This implies that significant volumes of fresh groundwater transport through the soil profiles at depth, transporting chemical solutes (including dissolved Fe(II)) to the adjacent intertidal area in Deception Bay, Queensland, Australia (Albert et al., 2005). The benthic release of Fe(II) was further validated through additional field and laboratory studies (Ahern et al., 2006a; Hanington et al., 2016; O'Neil and Dennison, 2016). Additionally, as emphasized in Section 4.4, biogeochemical mechanisms, particularly microbial reduction processes driven by Fe-reducing bacteria, may potentially convert Fe(III) to Fe(II) under anaerobic conditions, thereby facilitating the remobilization of Fe oxides in marine sediments. Its coupling with changes in pH and redox (i.e., Eh) conditions may ultimately determine the spatial distribution and concentration of Fe (II) in its dissolved form. This straightforward analysis indicates that a relatively high concentration of dissolved Fe(II) (see Figure 6A1) can likely be observed in porewater at the site under appropriate redox conditions.

In terms of geochemistry, the mixing of fresh groundwater and circulated seawater dominates the geochemical conditions along the flow path (see Figure 9). So biogeochemical zonations are created, and these zonations significantly affect the transformation, mobility, and removal of chemicals through the FDT. With respect to this field investigation, the mixing of Fe(II)-rich groundwater with oxygenated seawater in the intertidal area has been observed to induce the precipitation of Fe oxides at the groundwater-seawater interface beneath the USP. The accumulation of these minerals forms a less well-defined geochemical barrier, commonly referred to as an iron curtain, which has the capacity to retain dissolved chemicals such as phosphate. While this process can be viewed as a self-regulation mechanism affecting the ecology of coastal waters, specifically the nitrogen to phosphorus ratios (i.e., N/P), the discharge of freshwater with elevated Fe(II) could transport a substantial amount of bio-available Fe, which has the potential to stimulate the growth of Lyngbya. This influx of Fe(II) via SGD may represent a factor that has not received sufficient attention but contributes to the occurrence of Lyngbya blooms in the nearshore. To better address this concern, a more comprehensive field setup and an extended period of groundwater monitoring are required, and they need to incorporate reaction kinetics and site-specific information on major dissolved and solid-phase Fe, as well as the growth of Lyngbya.

5 Summary and prospects

The previous studies on the intertidal area primarily focused on groundwater flow and salt transport in an unconfined aquifer, with little emphasis on the transformation of redox-sensitive Fe(II) and the coupling between physical process (e.g., tide) and geochemical process (e.g., oxidative precipitation) along the seepage flow path.

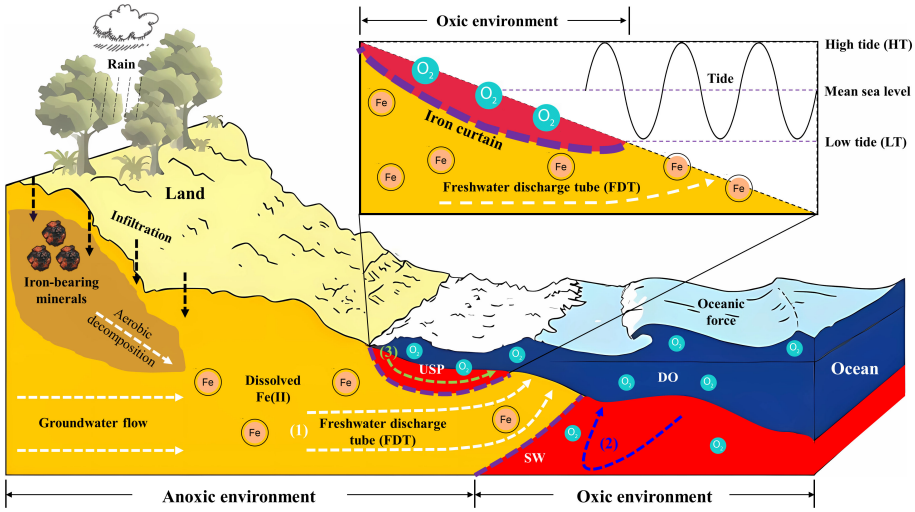

FIGURE 9
Conceptual model illustrating the hydrological and geochemical processes in the intertidal area. The delineated areas indicate distinct zones in the coastal environment: the orange area signifies the aquifer zone dominated by fresh groundwater, while the red area shows the seawater intrusion driven by oceanic oscillations such as tides. Within the intertidal area, three major processes include (1) fresh groundwater discharge (depicted by a white dashed line), (2) density-driven circulation (illustrated by a blue dashed line), and (3) tide-induced circulation (represented by a green dashed line). Between the saltwater wedge (SW) and the upper saline plume (USP), a freshwater discharge tube (FDT) intersects the beach. Moreover, the decomposition and dissolution of Fe-bearing minerals can lead to the release of Fe ions into groundwater systems (e.g., facilitated by rainwater infiltration as seen in a black dashed line). Fe(II)-rich groundwater can be oxidized by DO-rich seawater, and precipitate Fe oxides at the groundwater-seawater interface. The accumulation of these minerals can generate the iron curtain which acts as a geochemical barrier (shown by purple dashed lines) in the coastal aquifer system.

This study investigated the dynamics of porewater exchange and Fe speciation by conducting groundwater monitoring and sampling in a coastal bay. The field datasets provided concrete evidence of the subsurface mixing between fresh groundwater and oxygenated seawater, as well as the Fe transformation from an aqueous form to a solid phase at the groundwater-seawater interface beneath the USP. The findings also demonstrated the occurrence of an iron curtain that was observed to adsorb dissolved phosphate within the mixing zone of USP. Based on these field outcomes and corresponding implications, the research contributions can be summarized as follows:

A comprehensive field investigation demonstrated a geochemical transition from groundwater to seawater in the intertidal area. This area was characterized by the tide-induced circulating seawater and the discharge of fresh groundwater beneath. The dynamic process of groundwater-seawater mixing created a USP, a highly reactive zone that determined the speciation and solubility of Fe transporting through the FDT. Consequently, a substantial increase in DO concentration was observed, which created a localized hotspot with increased Eh. This indicated an oxidizing environment for Fe(II)-rich groundwater beneath and led to the oxidative precipitation of Fe(II) at the groundwater-seawater interface. Therefore, the sediment analysis revealed a spatial distribution of precipitated Fe with a strip-like pattern along this interface from land to the ocean. These regions with intensive accumulation of Fe oxides can be referred to as the iron curtain, acting as a geochemical barrier to retain dissolved phosphate by changing the seepage properties of coastal sediment. The field results indicated that the characterization of pH, DO, Eh and PO_4^{3-} profiles can be utilized as a practical approach to investigating and positioning the presence of iron curtains in the coastal area.

Furthermore, upon the geological settings and earlier studies conducted at Sandstone Point, Queensland, Australia, a conceptual model was developed to illustrate the origin of dissolved Fe and its mobilization associated with groundwater flow in the intertidal area. As described in Figure 9, the aerobic decomposition of iron-bearing minerals resulted in the release of iron ions into groundwater systems through infiltration. Subsequently, significant volumes of fresh groundwater delivered these dissolved ions to the adjacent intertidal area of the coastal bay. This process resulted in a notable concentration of dissolved Fe(II), and a peak value of 2.5 mg/L was observed in porewater at our site (see red areas Figures 6A1, B1), which was several orders of magnitude higher than that in seawater. In addition, the benthic release of additional Fe(II) could have the potential to stimulate the growth of Lyngbya in water bodies, and it is a factor that has received insufficient attention but contributes to the occurrence of Lyngbya blooms in the nearshore of Deception Bay, Queensland, Australia. Further investigations are still needed to better address the link between Fe and Lyngbya.

In summary, this study presents significant advancements in refining a conceptual model that explores the mobilization and transformation of Fe associated with coupled physical and geochemical processes due to groundwater-seawater mixing. Comprehending these processes provides valuable insights into the effect of tide-induced circulation on the speciation of redox-sensitive chemicals and the evolution of coastal aquifers. Although Fe minerals and microbial activities are very complex, introducing some uncertainties into flow and transport processes that were not

included in this research, the field outcomes establish a useful database and a unique opportunity to unravel the mechanism driving the formation of iron curtains and their environmental functionalities. In the long term, further investigations based on this study will contribute to more accurate predictions of future conditions, leveraging current seepage and geochemical features. This, in turn, will facilitate the development of improved strategies for sustainable management of coastal and marine ecosystems.

Data availability statement

The original contributions presented in the study are included in the article/Supplementary Material. Further inquiries can be directed to the corresponding authors.

Author contributions

WC: Conceptualization, Data curation, Formal analysis, Investigation, Methodology, Visualization, Writing – original draft, Writing – review & editing. HH: Methodology, Project administration, Resources, Supervision, Writing – review & editing. GY: Writing – review & editing. AS: Project administration, Supervision, Writing – review & editing.

Funding

The author(s) declare that financial support was received for the research, authorship, and/or publication of this article. This study was funded by the Australian Research Council through its Discovery Project (grant number: DP190103782).

Acknowledgments

The field monitoring design benefited from the original ideas of Professor Ling Li at Westlake University, and the collection of field data was assisted by Dr Chenming Zhang and Mr Zicheng Zhao at the University of Queensland. The authors thank the Queensland Government, the School of Civil Engineering and the School of the Environment at the University of Queensland for their support, and also appreciate the reviewers and editor for constructive comments on this paper.

Conflict of interest

The authors declare that the research was conducted in the absence of any commercial or financial relationships that could be construed as a potential conflict of interest.

Publisher's note

Supplementary material

The Supplementary Material for this article can be found online at: https://www.frontiersin.org/articles/10.3389/fmars.2024.1385517/full#supplementary-material

References

Abal, E., and Watkinson, A. (2000). *Investigation of Causes and Management of Lyngbya Blooms in SEQ*. PASSCON 2000 Pumicestone Passage and Deception Bay Catchment Conference, Brisbane, QLD Australia.

Ahern, K. S., O'Neil, J. M., Udy, J. W., and Albert, S. (2006a). Effects of iron additions on filament growth and productivity of the cyanobacterium Lyngbya majuscula. *Mar. Freshw. Res.* 57, 167. doi: 10.1071/MF05022

Ahern, K. S., Udy, J. W., and Pointon, S. M. (2006b). Investigating the potential for groundwater from different vegetation, soil and landuses to stimulate blooms of the cyanobacterium, Lyngbya majuscula, in coastal waters. *Mar. Freshw. Res.* 57, 177. doi: 10.1071/MF05115

Albert, S., O'Neil, J. M., Udy, J. W., Ahern, K. S., O'Sullivan, C. M., and Dennison, W. C. (2005). Blooms of the cyanobacterium Lyngbya majuscula in coastal Queensland, Australia: disparate sites, common factors. *Mar. pollut. Bull.* 51, 428–437. doi: 10.1016/j.marpolbul.2004.10.016

Alotaibi, M. D., Patterson, B. M., McKinley, A. J., Reeder, A. Y., Furness, A. J., and Donn, M. J. (2015). Fate of benzotriazole and 5-methylbenzotriazole in recycled water recharged into an anaerobic aquifer: Column studies. *Water Res.* 70, 184–195. doi: 10.1016/j.watres.2014.11.040

Anwar, N., Robinson, C., and Barry, D. A. (2014). Influence of tides and waves on the fate of nutrients in a nearshore aquifer: Numerical simulations. *Adv. Water Resour.* 73, 203–213. doi: 10.1016/j.advwatres.2014.08.015

ASTM D2434-68 (2006). *Test Method for Permeability of Granular Soils (Constant Head)*. ASTM International, West Conshohocken, PA, USA. doi: 10.1520/D2434-68R06

ASTM D5550-23 (2023). *Test Method for Specific Gravity of Soil Solids by Gas Pycnometer*. ASTM International, West Conshohocken, PA, USA. doi: 10.1520/D5550-23

ASTM D6913-17 (2021). *Test Methods for Particle-Size Distribution (Gradation) of Soils Using Sieve Analysis*. ASTM International, West Conshohocken, PA, USA. doi: 10.1520/D6913_D6913M-17

ASTM D7263-21 (2021). Test methods for laboratory determination of density (Unit weight) of soil specimens. *ASTM Int.* ASTM International, West Conshohocken, PA, USA. doi: 10.1520/D7263-21

Baker, I. R., Matzen, S. L., Schuler, C. J., Toner, B. M., and Girguis, P. R. (2023). Aerobic iron-oxidizing bacteria secrete metabolites that markedly impede abiotic iron oxidation. *PNAS Nexus* 2, pgad421. doi: 10.1093/pnasnexus/pgad421

Beck, A. J., Kellum, A. A., Luek, J. L., and Cochran, M. A. (2016). Chemical flux associated with spatially and temporally variable submarine groundwater discharge, and chemical modification in the subterranean estuary at gloucester point, VA (USA). *Estuaries Coasts* 39, 1–12. doi: 10.1007/s12237-015-9972-0

Carter, M., and Bentley, S. P. (1991). *Correlations of Soil Properties* (London: Pentech Press Publishers).

Chambers, R. M., and Odum, W. E. (1990). Porewater oxidation, dissolved phosphate and the iron curtain: Iron-phosphorus relations in tidal freshwater marshes. *Biogeochemistry* 10, 37–52. doi: 10.1007/BF00000891

Charette, M. A., and Allen, M. C. (2006). Precision ground water sampling in coastal aquifers using a direct-push, shielded-screen well-point system. *Groundwater Monit. Remediation* 26, 87–93. doi: 10.1111/j.1745-6592.2006.00076.x

Charette, M. A., and Sholkovitz, E. R. (2002). Oxidative precipitation of groundwater-derived ferrous iron in the subterranean estuary of a coastal bay. *Geophys. Res. Lett.* 29, 85-1-85–4. doi: 10.1029/2001GL014512

Cornell, R., and Schwertmann, U. (2003) *The Iron Oxides: Structure, Properties, Reactions, Occurrences and Uses*. Weinheim, Germany: Wiley-VCH Verlag GmbH & Co. KGaA. doi: 10.1002/3527602097

Cox, M. E., and Preda, M. (2005). Trace metal distribution within marine and estuarine sediments of western moreton bay, queensland, Australia: relation to land use and setting. *Geographical Res.* 43, 173–193. doi: 10.1111/j.1745-5871.2005.00312.x

Department of Environment, Science and Innovation, Queensland. (2013). *Lyngbya Monitoring Program, WetlandInfo website*, accessed 3 April 2024. Available at: https://wetlandinfo.des.qld.gov.au/wetlands/assessment/monitoring/current-and-future-monitoring/lyngbya-monitoring-program.html.

Fitzsimmons, J. N., and Conway, T. M. (2023). Novel insights into marine iron biogeochemistry from iron isotopes. *Annu. Rev. Mar. Sci.* 15, 383–406. doi: 10.1146/annurev-marine-032822-103431

Gibbes, B., Robinson, C., Carey, H., Li, L., and Lockington, D. (2008). Tidally driven pore water exchange in offshore intertidal sandbanks: Part I. Field measurements. *Estuarine Coast. Shelf Sci.* 79, 121–132. doi: 10.1016/j.ecss.2008.03.021

Gibbes, B., Robinson, C., Li, L., and Lockington, D. (2007). Measurement of hydrodynamics and pore water chemistry in intertidal groundwater systems. *J. Coast. Res.* 884–894.

Hanington, P., Rose, A., and Johnstone, R. (2016). The potential of benthic iron and phosphorus fluxes to support the growth of a bloom forming toxic cyanobacterium Lyngbya majuscula, Moreton Bay, Australia. *Mar. Freshw. Res.* 67, 1918. doi: 10.1071/MF15219

Hiemstra, T., Mendez, J. C., and Li, J. (2019). Evolution of the reactive surface area of ferrihydrite: time, pH, and temperature dependency of growth by Ostwald ripening. *Environ. Sci.: Nano* 6, 820–833. doi: 10.1039/C8EN01198B

Houben, G. J. (2003). Iron oxide incrustations in wells. Part 1: genesis, mineralogy and geochemistry. *Appl. Geochemistry* 18, 927–939. doi: 10.1016/S0883-2927(02)00242-1

Kroeger, K. D., and Charette, M. A. (2008). Nitrogen biogeochemistry of submarine groundwater discharge. *Limnol. Oceanogr* 53, 1025–1039. doi: 10.4319/lo.2008.53.3.1025

Kuan, W. K., Xin, P., Jin, G., Robinson, C. E., Gibbes, B., and Li, L. (2019). Combined effect of tides and varying inland groundwater input on flow and salinity distribution in unconfined coastal aquifers. *Water Resour. Res.* 55, 8864–8880. doi: 10.1029/2018WR024492

Kügler, S., Cooper, R. E., Wegner, C.-E., Mohr, J. F., Wichard, T., and Küsel, K. (2019). Iron-organic matter complexes accelerate microbial iron cycling in an iron-rich fen. *Sci. Total Environ.* 646, 972–988. doi: 10.1016/j.scitotenv.2018.07.258

Lalonde, K., Mucci, A., Ouellet, A., and Gélinas, Y. (2012). Preservation of organic matter in sediments promoted by iron. *Nature* 483, 198–200. doi: 10.1038/nature10855

Larrahondo, J. M., and Burns, S. E. (2014). Laboratory-prepared iron oxide coatings on sands: surface characterization and strength parameters. *J. Geotech. Geoenviron. Eng.* 140, 04013052. doi: 10.1061/(ASCE)GT.1943-5606.0001068

LePan, N., and Venditti, B. (2021) *Visualizing the Abundance of Elements in the Earth's Crust* (Elements Newsletter). Available at: https://elements.visualcapitalist.com/elements-in-the-earths-crust-abundance/.

Li, L., Barry, D. A., Stagnitti, F., and Parlange, J. Y. (1999). Submarine groundwater discharge and associated chemical input to a coastal sea. *Water Resour. Res.* 35, 3253–3259. doi: 10.1029/1999WR900189

Linkhorst, A., Dittmar, T., and Waska, H. (2017). Molecular fractionation of dissolved organic matter in a shallow subterranean estuary: the role of the iron curtain. *Environ. Sci. Technol.* 51, 1312–1320. doi: 10.1021/acs.est.6b03608

Liu, Y., Jiao, J. J., and Luo, X. (2016). Effects of inland water level oscillation on groundwater dynamics and land-sourced solute transport in a coastal aquifer. *Coast. Eng.* 114, 347–360. doi: 10.1016/j.coastaleng.2016.04.021

Liu, B., Yan, G., Ma, Y., and Scheuermann, A. (2023). Measurement of in-situ flow rate in borehole by heat pulse flowmeter: field-case study and reflection. *Geosciences* 13, 146. doi: 10.3390/geosciences13050146

Lloyd, R. R., Provis, J. L., and van Deventer, J. S. J. (2009). Microscopy and microanalysis of inorganic polymer cements. 1: remnant fly ash particles. *J. Mater Sci.* 44, 608–619. doi: 10.1007/s10853-008-3077-0

Luef, B., Fakra, S. C., Csencsits, R., Wrighton, K. C., Williams, K. H., Wilkins, M. J., et al. (2013). Iron-reducing bacteria accumulate ferric oxyhydroxide nanoparticle aggregates that may support planktonic growth. *ISME J.* 7, 338–350. doi: 10.1038/ismej.2012.103

Manson, F. J., Loneragan, N. R., and Phinn, S. R. (2003). Spatial and temporal variation in distribution of mangroves in Moreton Bay, subtropical Australia: a comparison of pattern metrics and change detection analyses based on aerial photographs. *Estuarine Coast. Shelf Sci.* 57, 653–666. doi: 10.1016/S0272-7714(02)00405-5

Martin, J. B., Hartl, K. M., Corbett, D. R., Swarzenski, P. W., and Cable, J. E. (2003). A multi-level pore-water sampler for permeable sediments. *J. Sedimentary Res.* 73, 128–132. doi: 10.1306/070802730128

McAllister, S. M., Barnett, J. M., Heiss, J. W., Findlay, A. J., MacDonald, D. J., Dow, C. L., et al. (2015). Dynamic hydrologic and biogeochemical processes drive microbially enhanced iron and sulfur cycling within the intertidal mixing zone of a beach aquifer: Fe and S cycling in a beach aquifer. *Limnol. Oceanogr.* 60, 329–345. doi: 10.1002/lno.10029

Miller, D. C., and Ullman, W. J. (2004). Ecological consequences of ground water discharge to Delaware Bay, United States. *Ground Water* 42, 959–970. doi: 10.1111/j.1745-6584.2004.tb02635.x

Mo, Y., Jin, G., Zhang, C., Xu, J., Tang, H., Shen, C., et al. (2021). Combined effect of inland groundwater input and tides on flow and salinization in the coastal reservoir and adjacent aquifer. *J. Hydrology* 600, 126575. doi: 10.1016/j.jhydrol.2021.126575

Moore, W. S. (2003). Sources and fluxes of submarine groundwater discharge delineated by radium isotopes. *Biogeochemistry* 66, 75–93. doi: 10.1023/B:BIOG.0000006065.77764.a0

O'Neil, J. M., and Dennison, W. C. (2016). "Discerning the Causes of Toxic Cyanobacteria (Lyngbya majuscula) Blooms in Moreton Bay, Australia," in *Aquatic Microbial Ecology and Biogeochemistry: A Dual Perspective*. Eds. P. M. Glibert and T. M. Kana (Springer International Publishing, Cham), 261–272. doi: 10.1007/978-3-319-30259-1_21

Paffrath, R., Pahnke, K., Behrens, M. K., Reckhardt, A., Ehlert, C., Schnetger, B., et al. (2020). Rare earth element behavior in a sandy subterranean estuary of the southern North Sea. *Front. Mar. Sci.* 7. doi: 10.3389/fmars.2020.00424

Porubsky, W. P., Weston, N. B., Moore, W. S., Ruppel, C., and Joye, S. B. (2014). Dynamics of submarine groundwater discharge and associated fluxes of dissolved nutrients, carbon, and trace gases to the coastal zone (Okatee River estuary, South Carolina). *Geochimica Cosmochimica Acta* 131, 81–97. doi: 10.1016/j.gca.2013.12.030

Reckhardt, A., Beck, M., Seidel, M., Riedel, T., Wehrmann, A., Bartholomä, A., et al. (2015). Carbon, nutrient and trace metal cycling in sandy sediments: A comparison of high-energy beaches and backbarrier tidal flats. *Estuarine Coast. Shelf Sci.* 159, 1–14. doi: 10.1016/j.ecss.2015.03.025

Reddy, K. (2000). Nitrate removal from groundwater using catalytic reduction. *Water Res.* 34, 995–1001. doi: 10.1016/S0043-1354(99)00227-4

Robinson, C., Gibbes, B., Carey, H., and Li, L. (2007). Salt-freshwater dynamics in a subterranean estuary over a spring-neap tidal cycle. *J. Geophys. Res.* 112, C09007. doi: 10.1029/2006JC003888

Robinson, C., Gibbes, B., and Li, L. (2006). Driving mechanisms for groundwater flow and salt transport in a subterranean estuary. *Geophys. Res. Lett.* 33, L03402. doi: 10.1029/2005GL025247

Robinson, C. E., Xin, P., Santos, I. R., Charette, M. A., Li, L., and Barry, D. A. (2018). Groundwater dynamics in subterranean estuaries of coastal unconfined aquifers: Controls on submarine groundwater discharge and chemical inputs to the ocean. *Adv. Water Resour.* 115, 315–331. doi: 10.1016/j.advwatres.2017.10.041

Roy, M., Martin, J. B., Cherrier, J., Cable, J. E., and Smith, C. G. (2010). Influence of sea level rise on iron diagenesis in an east Florida subterranean estuary. *Geochimica Cosmochimica Acta* 74, 5560–5573. doi: 10.1016/j.gca.2010.07.007

Russo, A. A., Boutt, D. F., Munk, L. A., and Jenckes, J. (2023). Contribution of fresh submarine groundwater discharge to the gulf of Alaska. *Water Resour. Res.* 59, e2023WR034912. doi: 10.1029/2023WR034912

Saeck, E., Grinham, A., Coates-Marnane, J., McAlister, T., and Burford, M. (2019). Primary producers in Moreton Bay: Phytoplankton, benthic microalgae and filamentous cyanobacteria. In Tibbetts, I. R., Rothlisberg, P. C., Neil, D. T., Hoburg, T. A., Brewer, D. T., and Arthington, A. H. (Editors). *Moreton Bay Quandamooka & Catchment: Past, present, and future*. The Moreton Bay Foundation (pp. 187-210). Brisbane, Australia. Available at: https://moretonbayfoundation.org/.

Santos, I. R., Burnett, W. C., Dittmar, T., Suryaputra, I. G. N. A., and Chanton, J. (2009). Tidal pumping drives nutrient and dissolved organic matter dynamics in a Gulf of Mexico subterranean estuary. *Geochimica Cosmochimica Acta* 73, 1325–1339. doi: 10.1016/j.gca.2008.11.029

Scholz, M. (2019). "Dye Wastewater Treatment by Vertical-Flow Constructed Wetlands," in *Sustainable Water Treatment* (Elsevier), 191–213. doi: 10.1016/B978-0-12-816246-0.00008-2

Sevinç Şengör, S., Spycher, N. F., Ginn, T. R., Sani, R. K., and Peyton, B. (2007). Biogeochemical reactive–diffusive transport of heavy metals in Lake Coeur d'Alene sediments. *Appl. Geochemistry* 22, 2569–2594. doi: 10.1016/j.apgeochem.2007.06.011

Shen, C., Zhang, C., Xin, P., Kong, J., and Li, L. (2018). Salt dynamics in coastal marshes: formation of hypersaline zones. *Water Resour. Res.* 54, 3259–3276. doi: 10.1029/2017WR022021

Slomp, C. P., and Van Cappellen, P. (2004). Nutrient inputs to the coastal ocean through submarine groundwater discharge: Controls and potential impact. *J. Hydrology* 295, 64–86. doi: 10.1016/j.jhydrol.2004.02.018

Spiteri, C., Regnier, P., Slomp, C. P., and Charette, M. A. (2006). pH-Dependent iron oxide precipitation in a subterranean estuary. *J. Geochemical Explor.* 88, 399–403. doi: 10.1016/j.gexplo.2005.08.084

Spiteri, C., Slomp, C. P., Tuncay, K., and Meile, C. (2008). Modeling biogeochemical processes in subterranean estuaries: Effect of flow dynamics and redox conditions on submarine groundwater discharge of nutrients: Biochemistry of subterranean estuaries. *Water Resour. Res.* 44, W02430. doi: 10.1029/2007WR006071

Sukekava, C. F., Downes, J., Filella, M., Vilanova, B., and Laglera, L. M. (2024). Ligand exchange provides new insight into the role of humic substances in the marine iron cycle. *Geochimica Cosmochimica Acta* 366, 17–30. doi: 10.1016/j.gca.2023.12.007

Testa, J. M., Charette, M. A., Sholkovitz, E. R., Allen, M. C., Rago, A., and Herbold, C. W. (2002). Dissolved iron cycling in the subterranean estuary of a coastal bay: waquoit bay, massachusetts. *Biol. Bull.* 203, 255–256. doi: 10.2307/1543427

Thamdrup, B., Finster, K., Fossing, H., Hansen, J. W., and Jørgensen, B. B. (1994). Thiosulfate and sulfite distributions in porewater of marine sediments related to manganese, iron, and sulfur geochemistry. *Geochimica Cosmochimica Acta* 58, 67–73. doi: 10.1016/0016-7037(94)90446-4

Ullman, W. J., Chang, B., Miller, D. C., and Madsen, J. A. (2003). Groundwater mixing, nutrient diagenesis, and discharges across a sandy beachface, Cape Henlopen, Delaware (USA). *Estuarine Coast. Shelf Sci.* 57, 539–552. doi: 10.1016/S0272-7714(02)00398-0

Van Der Grift, B., Behrends, T., Osté, L. A., Schot, P. P., Wassen, M. J., and Griffioen, J. (2016). Fe hydroxyphosphate precipitation and Fe(II) oxidation kinetics upon aeration of Fe(II) and phosphate-containing synthetic and natural solutions. *Geochimica Cosmochimica Acta* 186, 71–90. doi: 10.1016/j.gca.2016.04.035

Viscarra Rossel, R. A., Bui, E. N., de Caritat, P., and McKenzie, N. J. (2010). Mapping iron oxides and the color of Australian soil using visible–near-infrared reflectance spectra. *J. Geophys. Res.* 115, F04031. doi: 10.1029/2009JF001645

Wu, Z., Wang, S., and Ji, N. (2019). Distribution character of localized iron microniche in lake sediment microzone revealed by chemical image. *Environ. Sci. pollut. Res.* 26, 35704–35716. doi: 10.1007/s11356-019-06219-2

Xin, P., Robinson, C., Li, L., Barry, D. A., and Bakhtyar, R. (2010). Effects of wave forcing on a subterranean estuary. *Water Resour. Res.* 46, W12505. doi: 10.1029/2010WR009632

Yan, G., Ma, Y., Scheuermann, A., and Li, L. (2022a). The hydraulic properties of aquabeads considering forchheimer flow and local heterogeneity. *Geotech. Test. J.* 45, 20210234. doi: 10.1520/GTJ20210234

Yan, G., Shi, H., Ma, Y., Scheuermann, A., and Li, L. (2022b). Intrinsic permeabilities of transparent soil under various aqueous environmental conditions. *Géotechnique Lett.* 12, 225–231. doi: 10.1680/jgele.22.00049

Zhang, J., Zhu, X., Zhang, R., Ren, J., Wu, Y., Liu, S., et al. (2022). Dissolved fe in the east China sea under the influences of land sources and the boundary current with implications for global marginal seas. *Global Biogeochemical Cycles* 36, e2021GB006946. doi: 10.1029/2021GB006946

Zhou, S., Chen, S., Yuan, Y., and Lu, Q. (2015). Influence of humic acid complexation with metal ions on extracellular electron transfer activity. *Sci. Rep.* 5, 17067. doi: 10.1038/srep17067

Zipperle, A., and Reise, K. (2005). Freshwater springs on intertidal sand flats cause a switch in dominance among polychaete worms. *J. Sea Res.* 54, 143–150. doi: 10.1016/j.seares.2005.01.003

frontiers | Frontiers in Marine Science

TYPE Original Research
PUBLISHED 11 April 2024
DOI 10.3389/fmars.2024.1369869

OPEN ACCESS

EDITED BY
Tianyuan Zheng,
Ocean University of China, China

REVIEWED BY
Yunhai Fang,
Hefei University of Technology, China
Zhang Bo,
Shandong University of Science and Technology, China
Qinpeng Chang,
Ocean University of China, China

*CORRESPONDENCE
Jun Kong
kongjun999@126.com
Jun Wang
junw1997@163.com

RECEIVED 13 January 2024
ACCEPTED 04 March 2024
PUBLISHED 11 April 2024

CITATION
Gao C, Kong J, Wang J and Chen W (2024) Nitrate fate in coastal unconfined aquifers influenced by preferential flows. *Front. Mar. Sci.* 11:1369869. doi: 10.3389/fmars.2024.1369869

Nitrate fate in coastal unconfined aquifers influenced by preferential flows

Chao Gao[1,2], Jun Kong[1,2*], Jun Wang[1,2*] and Weilun Chen[1,2]

[1]Key Laboratory of Coastal Disaster and Protection (Hohai University), Ministry of Education, Nanjing, China, [2]State Key Laboratory of Hydrology, Water Resources and Hydraulic Engineering, Hohai University, Nanjing, China

This study examined the influence of preferential flow on pore water flows and marine nitrogen transport reaction in variable saturation and variable density coastal aquifers. The 2-D unconfined aquifer model established was based on the software COMSOL by coupling the dynamic and chemical processes together. The results showed that preferential flow affects groundwater flow and salinity distribution, leading to a more complicated mixing process. The preferential flow resulted in an increase in mixing zone area and the upper saline plume area of 10.33 and 2.62 m^2, respectively, a decrease in saltwater wedge area of 7.22 m^2, and an increase in nitrate (NO_3^-) removal efficiency from 7.9% to 8.97%. The NO_3^- removal efficiency increases progressively with the depth (*h*) and quantity (*n*) of preferential flows; however, it decreases after a certain quantity. Further quantitative analysis revealed an increase in the intensity of nitrification and dissolved oxygen inflow flux with preferential flow depth and quantity increase. This phenomenon usually occurs on coasts where biological caves are abundant. The results also offer significant implications for designing engineering measures to mitigate saltwater intrusion and are significant to prevent groundwater quality deterioration in coastal zones.

KEYWORDS

preferential flow, marine nitrogen, nitrification, denitrification, removal efficiency

1 Introduction

Groundwater is an important freshwater resource for industrial and agricultural purposes in coastal areas (Lu and Werner, 2013; Zhang et al., 2019). Nitrate pollution has deteriorated the quality of groundwater around the world due to an increase in human population and urban development (Anwar et al., 2014; Sun et al., 2021; Gao et al., 2024). Saltwater intrusion (SWI), as a global problem, seriously threatens freshwater resources and coastal productivity (Chang et al., 2019, 2020; Zheng et al., 2020, 2021, 2022; Chang et al., 2023, 2024). The NO_3^- concentration in drinking water derived from groundwater exceeds the standard permissible limit of 50 mg L^{-1} set by the World Health Organization (WHO) in most parts of the world (Kringel et al., 2016; Radfard et al., 2018). In China,

approximately 34.1% of groundwater resources are contaminated with NO_3^- (Zhang et al., 1996; Lu et al., 2019).

Groundwater flow and solute transport in aquifers under the tidal influence are very complex (Figure 1) (Robinson et al., 2007a; Fang et al., 2022a, b, 2023). Periodic tidal fluctuations can lead to the formation of two coexisting saltwater plumes in aquifers: (i) a saltwater wedge (SW) due to density-driven saltwater recirculation and (ii) an upper saline plume (USP) due to tide-driven saltwater recirculation (Robinson et al., 2007b; Kuan et al., 2019). Land-derived groundwater is generally transported between the SW and USP and discharged into the ocean near the low tide mark, which is an area where saltwater and freshwater mix between two different saltwater plumes. Several surveys have also reported a large number of macro-pores (such as crab burrows and invertebrate nests) in aquifers (Xin et al., 2009; Guimond et al., 2020; Xu et al., 2021; Pan et al., 2022; Xiao et al., 2022) and found that macro-pores are mainly concentrated in the upper supratidal zone and intertidal zone (Fanjul et al., 2008). The presence of crab holes and macro-pores increases the overall surface infiltration rate to a range of 0.1 to 1 m d^{-1}, which is one to two orders of magnitude higher than the matrix hydraulic conductivity (Hughes, 1998). They are well recognized to act as preferential flow paths and enhance the infiltration rate of surface water (Xiao et al., 2019), impact the distribution of salinity (Williams et al., 2014; Edith et al., 2015; Enrique et al., 2018), and change solute transport by increasing the connectivity of otherwise impermeable muddy soils (Xiao et al., 2019; Guimond et al., 2020), thus affecting biogeochemical processes in salt marshes (Xu et al., 2021; Pan et al., 2022; Xiao et al., 2022). Xin et al. (2009) studied a 3-D model simulated in the marsh with a two-layer soil configuration at the Chongming Dongtan wetland. Their results suggested that preferential flow can act as drains for the surrounding soil during the falling tide, which increases water exchange between marsh soils and tidal creeks. Xiao et al. (2019) constructed a model, and the results of their analysis suggested that preferential flow can promote soil permeability and facilitate solute transport in salt marshes. Additionally, preferential flow increases the connectivity between the soil surface and groundwater (Xu et al., 2021). It also intensifies the heterogeneity of the aquifer, leading to greater hydraulic conductivity (Kreyns et al., 2020). Although Gao et al. (2023) demonstrated that large pores increase USP and reduce SW, the mechanism is unclear. All combined, these studies confirmed that preferential flow or tidal-induced complex pore water flow and preferential flow have significant influences on solute transport. However, the effects of preferential flow distributed in the tidal zone on groundwater flow and solute transport in coastal unconfined aquifers under tidal conditions are not clear.

Saltwater transports a large quantity of dissolved oxygen (DO), NO_3^-, ammonium ion (NH_4^+), and dissolved organic carbon (DOC) into the aquifer. Several chemical reactions such as DOC degradation, aerobic respiration, nitrification (NH_4^+ transformation to NO_3^-), and denitrification (NO_3^- transformation to N_2) can take place (Meile et al., 2009; Sun et al., 2019). These processes are affected by tidal force, which can change the recycling rate and chemical composition of saltwater (Rocha, 2013; Zheng et al., 2020; Gao et al., 2022). Shuai et al. (2017) established a 2-D estuarine subsurface flow model based on the numerical model, assuming that DO, NO_3^-, NH_4^+, and DOC primarily originate from rivers. Nitrification occurs in the shallow layers, while denitrification occurs in the deeper anaerobic layers. These reactions, which are both controlled by redox conditions and DOC concentrations, play an important role in determining NO_3^- in the aquifer. Preferential flow can affect nitrification and denitrification reactions by directly or indirectly changing soil properties (Pan et al., 2022). These reactions are also influenced by

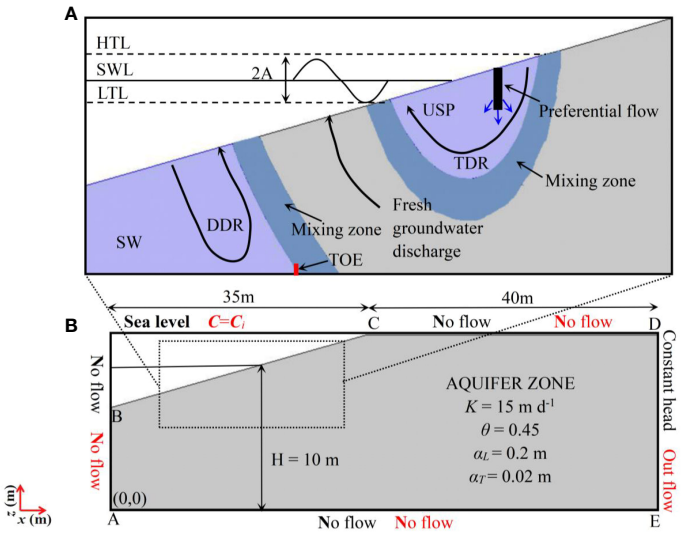

FIGURE 1
(A) Conceptual diagram of the seawater level, groundwater flow, and salinity distribution in a near-shore aquifer under tide action. Still water level (SWL), high tide level (HTL), low tide level (LTL), the black area is the preferential flow, the blue arrows indicate the direction of preferential flow. The upper saline plume (USP) formed by tide-driven recirculation (TDR), the saltwater wedge formed by density-driven recirculation (DDR), and the saltwater wedge toe (TOE) are shown. The freshwater–saltwater mixing zone associated with the saline plums are also depicted. **(B)** Numerical model domain, parameters, and boundary condition, the dashed box in **(B)** illustrates the area depicted in **(A)**.

the redox conditions, aeration, and particle composition of the solution (Xin et al., 2009). Xiao et al. (2019) conducted field observations and flow modeling to assess how crab burrows drive carbon exchange in an intertidal marsh in South Carolina. They found that the concentrations of dissolved inorganic and organic carbon in crab burrow pore water differ from that in the surrounding soil matrix, and the gas-phase concentrations of CO_2 in crab burrows were approximately six times greater than that in ambient air. These results suggested that crab burrows increase the reaction of carbon. Heiss (2020) evaluated the effect of deep whale burial on NO_3^- removal efficiencies in aquifers and found that organic carbon sources affected NO_3^- removal since DOC not only provided the reactant for denitrification but also provided an anaerobic environment (DOC oxidation). Cheng et al. (2020) investigated the effect of preferential flows on nitrification and denitrification in aquifers, and the results showed that preferential flows promoted sediment nitrification, and the degree of promotion was significant with the increase of density. Li et al. (2021) conducted laboratory experiments and found that crab burrows significantly affected the concentrations of NH_4^+ and NO_3^- and significantly promoted the nitrogen exchange flux at the sediment–water interface. It can be seen that the preferential flow not only effectively changes the pore water flow and solute transport rate but also increases the oxygen content of the aquifer and the contact area between the sediment and O_2, thus interfering with the reaction of NO_3^-.

So far, the effects of preferential flow distributed in the tidal zone under tidal conditions on pore water flow and nitrogen–sea source transport reaction in coastal unconfined aquifers remain unclear. In this study, numerical simulations were conducted to address the effects of preferential flow number and depth on the pore water flow, nitrification, and denitrification in sea sources under tidal action. The results might provide a theoretical reference for designing engineering measures to mitigate saltwater intrusion, groundwater quality management, and the ecological restoration of coastal zones.

2 Methods

The groundwater flow and solute transport reaction models are used to study the influence of preferential flow on salinity change, pore water flow, and nitrogen transport reaction in aquifers.

2.1 Groundwater flow and solute transport model

A 2-D coastal wetland model was developed to study the salinity change and solute transport of aquifers with variable saturation and density using the COMSOL finite element software. The simulation of flow with variable saturation and density was based on Richard's equation (Equation 1). Solute transport was based on the advection–dispersion–reaction equation (Equation 2) in porous media (Shuai et al., 2017):

$$\rho\left(S_eS+\frac{w_m}{\rho g}\right)\frac{\partial p}{\partial t}+\nabla\cdot\rho\left(\frac{-k_s}{\mu}k_r(\nabla P+\rho g\nabla Z)\right)=Q_m \quad (1)$$

$$\frac{\partial(\theta C_i)}{\partial t}+\nabla\cdot\rho(C_iu)=\nabla\cdot(D\nabla C_i)+R_i \quad (2)$$

where ρ is fluid density (kg m^{-3}), C_i is the concentration of species i (mM), P is the pressure (Pa), and Z is the elevation head (m). The value of k_s is the saturated hydraulic permeability (Equation 3), while k_r stands for the relative permeability (m s^{-1}) (Equation 4), u is the Darcy velocity (m s^{-1}), θ is the water content (-) (Equation 6), g is the acceleration of gravity (9.81m s^{-2}), Q_m in this equation represents a stress source term (kg m^{-3} s^{-1}), w_m is the specific moisture capacity (m^{-1}) (Equation 5), D is the hydrodynamic dispersion coefficient (m^2 s^{-1}), R_i is the reaction rate for species i (mM s^{-1}), S_e is the effective saturation (-) (Equations 7, 8), and S is water storage (P_a^{-1}). The constitutive relationship between relative permeability and pore pressure obeys the *van Genuchten* model (van Genuchten, 1980):

$$k_s=\frac{\mu K}{\rho g} \quad (3)$$

$$k_r=S_e^{0.5}(1-[1-S_e^{1/m}]^m)^2 \quad (4)$$

$$w_m=\frac{\alpha m}{1-m}(\theta_s-\theta_r)S_e^{1/m}[1-S_e^{1/m}]^m \quad (5)$$

$$\theta=\theta_r+S_e(\theta_s-\theta_r) \quad (6)$$

$$S_e=\frac{1}{(1+|\alpha P|^{n_i})^m} \quad (7)$$

$$m=1-\frac{1}{n_i} \quad (8)$$

where θ_s and θ_r is the saturated water content and relative water content (-), respectively. K is the hydraulic conductivity (m s^{-1}), where n_i, which is related to m in Equation 8, and a is the fitting parameter which describes the shape of both the moisture (m^{-1}) and relative permeability functions (-) obtained by *van Genuchten* (van Genuchten, 1980).

The model is a 2-D beach aquifer cross-section (Figure 1), where the left and bottom boundary (BAE) and the upper boundary (CD) are both set as no flow and zero solute flux boundaries (Xin et al., 2010; Shen et al., 2018). The right boundary (DE) is set as the inland boundary, while the ocean boundary (BC) is the permeable layer that is used to represent the interface between the beach surface and seawater or atmosphere and assigned a semi-pervious layer or seepage face boundary. The process is realized by the following formula (Equations 9–11):

$$-n\cdot\rho\frac{-k_s}{\mu}k_r(\nabla P+\rho g\nabla Z)=\rho R_b(H-H_b) \quad (9)$$

$$R_b=\frac{k_s}{L} \quad (10)$$

$$\begin{aligned} C &= C_{sea} && n \cdot u < 0 \\ -n \cdot D\nabla C &= 0 && n \cdot u \geq 0 \end{aligned} \quad (11)$$

where R_b is the conductance term (s^{-1}), defined as the ratio of the saturated hydraulic conductivity (k_s) with a coupling length scale (L, m). It was set at a high value allowing water to readily move in and out of the interface. H_b is the external head representing sea level (m), H is the total head (m), and C_{sea} is seawater salinity (ppt).

In order to deal with the boundary conditions reasonably, two conditions have been considered. When the aquifer is saturated and the external head (H_b) of the sea level is higher than the elevation head, the head difference is determined by the difference between the overlying seawater and the beach interface. However, if the total head (H) is higher than the sea level (H_b), and the pressure head is equal to or higher than the atmospheric pressure. The boundary is a seepage surface. If the value of R_b is 0 when the aquifer is unsaturated, the boundary is a no-flow boundary. The salinity is determined by the groundwater velocity at the node. If the velocity is inward (to the aquifer), the salinity is estimated by seawater salinity (C_{sea} = 35 ppt). If the groundwater flows from an aquifer, the zero concentration gradient was specified at the nodes. Previous studies have demonstrated that this modeling approach is useful in describing the water level movement and residence times within the transition zone (Xin et al., 2010; Shen et al., 2019).

A time-varying head ($H(t)$) Equation 12 was implemented at selected cells in this zone by:

$$H(t) = H_{msl} + A\sin(\omega t) \quad (12)$$

where $H(t)$ is tidal head (m), determined by time; H_{msl} is the mean sea level (10 m); A is tidal amplitude (0.5 m); $\omega = 2\pi/T$ is the angular frequency; and T is the tidal cycle (semi-diurnal tide, 12 h). These parameters were used in many studies (Anwar et al., 2014; Shuai et al., 2017).

The model domain represented a homogeneous and isotropic coastal aquifer with a thickness of 12 m and a sloping beach boundary (slope of 0.1; Figure 1), which was comparable to a typical sandy coastal aquifer system (Carsel and Parrish, 1988) with a hydraulic conductivity of 15 m d^{-1}, longitudinal dispersion coefficient (a_L) of 0.2 m, transverse dispersion coefficient (a_T) of 0.02 m (Anwar et al., 2014), and porosity of 0.45. Moreover, seawater salt concentration and density were set to 35 ppt (mass fraction) and 1,025 kg m^{-3}, respectively. The freshwater salt concentration of 0 ppt and a density of 1,000 kg m^{-3} (see Table 1) were both adopted from Robinson et al. (2014) and Shen et al. (2019).

The preferential flow had a width of 0.16 m and was assumed to be a homogeneous medium with high permeability and porosity (the permeability was 100 times higher than that of the matrix and the porosity was set as 1). This technology enabled simulations of the preferential flow rapid responses to tidal-water-level fluctuations without affecting the simulation results (Xin et al., 2009). Similar techniques and parameters have been used in groundwater models to simulate pore water flow and solute transport induced by macro-porosity (Xin et al., 2009; Xiao et al., 2019). The preferential flow was set upstream of the intertidal zone, and this was adopted from other studies where it was reported that preferential flow is mainly concentrated in the upper supratidal zone and intertidal zone (Fanjul et al., 2008; Ying, 2021).

For all simulations, the mesh density increased in the preferential flow zones and at the beach. The values for the Courant number and numerical Péclet number did not exceed 1 and 4, respectively, which satisfied the stability criterion and avoided numerical oscillation. During the simulation, a constant temperature was maintained, resulting in constant dynamic viscosity.

The simulation first conducted a no-preferential flow model under the tidal action. Subsequently, to investigate the influence of depth and quantity of preferential flow, we set different depths (2.3, 3.3, and 4.3 m) and quantities (from 1 to 3) of preferential flow conditions under the tide action (five groups of experiments were conducted). The specific parameters are listed in Table 2.

2.2 Solute reaction model

To study the transformation of marine nutrients, a reaction network of four reactive species was applied to the reaction model.

TABLE 1 Model parameters, boundary condition, and kinetic parameter.

Model parameters			
Parameter	Description	Value	Units
K	Hydraulic conductivity	15[a]	m d^{-1}
θ	Porosity	0.45	–
S_e	Residual saturation	0.1[a]	–
α_L	Transverse diffusion coefficient	0.2[a]	M
α_T	Longitudinal diffusion coefficient	0.02[a]	M
C_0	Seawater concentration	35[b,c]	kg m^{-3}
C_f	Freshwater concentration	0[b,c]	kg m^{-3}
ρ_s	Seawater density	1025[b,c]	kg m^{-3}
ρ_f	Freshwater density	1000[b,c]	kg m^{-3}
R_N	NO_3^- removal efficiency	–	%
Boundary condition			
NO_3^-	NO_3^- boundary concentration	0.25[a]	mM
NH_4^+	NH_4^+ boundary concentration	0.2[a]	mM
DO	DO boundary concentration	0.2[a]	mM
DOC	DOC boundary concentration	0.75[a]	mM
Kinetic parameter			
K_{fox}	Rate constant for oxidation of DOC	3.0×10^{-9}[d]	s^{-1}
K_{nitri}	Rate constant for nitrification	4.8×10^{-6}	mM^{-1} s^{-1}
K_{mO_2}	Limiting concentration of O_2	0.008[d]	mM
$K_{mNO_3^-}$	Limiting concentration of NO_3^-	0.001[d]	mM

Units for solutes are in mmol dm^{-3} pore water, denoted as mM, background concentrations are set to 0.
a, Anwar et al. (2014);
b, Robinson et al. (2014);
c, Shen et al. (2019);
d, Spiteri et al. (2008).

The model considered nitrification, denitrification, aerobic respiration, and DOC degradation.

The reaction model simulated the first-order reaction that required mixing for the inflow of DO, NO_3^-, NH_4^+, and DOC. The study omitted the production of NH_4^+ from DOC degradation and nitrification and only focused on the transformation of NO_3^- from marine-derived sources. The reactions and kinetic rate expressions are shown in Table 3. Kim et al. (2017) validated this reaction network by comparing the simulation results with field data from the Cape Shores beach adjacent to Delaware Bay.

Based on the studies of Bardini et al. (2012) and Spiteri et al. (2008), the parameters of the reactions are shown in Table 1. This study determined the influence of preferential flow under tide influence on the chemical transformations in a nearshore aquifer. The sensitivity analyses on the specific kinetic parameter values adopted were not performed, although these parameter values vary in different coastal settings. Similar to salt transport, the nutrient concentration was set along with the aquifer–ocean interface for the reactive solutes. The boundary conditions of the nutrients are presented in Figure 1, and the specific nutrient values are shown in Table 1. The TOE (the saltwater wedge toe) was used to evaluate the length of the saltwater wedge, and the NO_3^- removal efficiency (R_N) Equation 13 was quantified by:

$$R_N = \frac{\int_0^t \int_\Omega R_{NO_3^-} \theta d\Omega dt}{\int_0^t \int_l c_{0NO_3^-} f_b dl} \tag{13}$$

where Ω is the domain area, t is the tidal cycle time (12 h), f_b is the boundary flux, $R_{NO_3^-}$ is the rate of NO_3^- reaction, and l is the length of the boundary layer.

We performed four steps: (i) groundwater flow and salinity distributions for all cases at the static water level were run to steady state, (ii) the hydraulic gradient and salinity distributions obtained at the static water level were used as the initial conditions under tidal action, (iii) the salinity distributions obtained in step (ii) were used as the initial conditions for the chemical solute transport and were run to steady state; (iv) and the results of the previous step were run as the initial conditions for the reaction network until they stabilized. The simulations were run for 700 days to allow the reactive solutes to reach equilibrium.

3 Results

3.1 Model calibration

To verify the reliability of the model, we developed a numerical model consistent with the lab experiment of Xie et al. (2023), with an aquifer length of 4 m and width of 0.7 m and porosity of 0.45; the parameters a and n_i were set to 5.9 m^{-1} and 2.68, respectively, and the longitudinal dispersion coefficient (a_L) was 0.005 m and transverse dispersion coefficient (a_T) was 0.0005 m [for the specific parameters, please refer to Xie et al. (2023) for details]. We consider three case conditions: non-preferential flow, preferential flow at x = 0.8 m, z = 0.3 m, and preferential flow at x = 1.8 m, z = 0.3 m, and the preferential flow scales and parameter settings are also consistent with those of Xie et al. (2023).

From the experimental results in Xie et al. (2023) and numerical simulation results (Figure 2), the simulated results matched the experimental in all cases well (Figure 2). We can find that tidal forcing formed a USP and SW in the intertidal zone where saltwater infiltrated near the high tide mark and was discharged near the low tide mark. A fresh groundwater discharge zone (FDZ) separated the circulation cell from the lower interface located at the base of the beach. As expected, under the impact of preferential flow, when the preferential flow location is at x = 0.8 m, it has some effect on the salinity distribution and reduces the saltwater wedge deed extension. When the preferential flow location was at x =1.8 m, it has little effect on the salinity distribution, which is consistent with the salinity distribution pattern of the no-preferential flow condition.

The experimental and numerical results consistently demonstrated that the preferential flow could affect the salinity distribution in terrestrial environments, and the 2-D numerical model could be used to predict the water–salt exchange processes in aquifers.

3.2 Salinity and pore water flow

The salinity distribution under two different conditions is presented in Figure 3. Preferential flow modified the salinity distribution under tidal influence. The average salinity (average value of the whole aquifer) in the aquifer decreased from 7.21 to 7.03 ppt, while the TOE decreased from 24.2 to 23.09 m. Under the

TABLE 2 Model parameters and TOE and average salinity.

Case	Tide	Depth (m)	Quantity (n)	TOE (m)	Average salinity (ppt)
Case1 N-P	√	×	×	24.20	7.21
Case2 P-1	√	2.30	1	23.10	7.19
Case4 P-2	√	3.30	1	23.09	7.03
Case5 P-3	√	4.30	1	22.90	7.00
Case6 P-4	√	4.30	2	22.35	6.96
Case6 P-5	√	4.30	3	22.50	6.94

TABLE 3 Reaction and kinetic rate expressions.

	Reaction	Rate expression
DOC degradation[a]	$DOC \rightarrow CO_2$	Rate= K_{fox}[DOC]
Aerobic respiration[b]	$DOC+O_2 \rightarrow CO_2+H_2O$	If $[O_2] > Km_{O_2}$; Rate = K_{fox}[DOC] If $[O_2] < Km_{O_2}$; Rate = K_{fox}[DOC] $\frac{[O_2]}{Km_{O_2}}$
Nitrification[b]	$NH_4^+ + 2O_2 + 2HCO_3^- \rightarrow NO_3^- + 2CO_2 + 3H_2O$	Rate = $K_{nitri}[NH_4^+][O_2]$ If $[O_2] > Km_{O_2}$; Rate = 0
Denitrification[b]	$5DOC + 4NO_3^- + 4H^+ \rightarrow 5CO_2 + 7H_2O + 2N_2$	If $[O_2] < Km_{O_2}$ and $[NO_3^-] > KmNO_3^-$; Rate = K_{fox}[DOC](1- $\frac{[O_2]}{Km_{O_2}}$) If $[O_2] < Km_{O_2}$ and $[NO_3^-] < KmNO_3^-$; Rate = K_{fox}[DOC](1- $\frac{[O_2]}{Km_{O_2}}$) $\frac{[NO_3^-]}{KmNO_3^-}$

[a]Bardini et al. (2012).
[b]Spiteri et al. (2008).

tidal condition (Figure 3), the area of the mixing zone (MZA) (the area between 10% and 90% salinity contour) was 53.87 m^2, the area of USP (USPA) was 10.37 m^2, and the area of SW (SWA) was 156.0 m^2. However, under the preferential flow, the mixing zone and USP were increased, and SW was decreased, i.e., the MZA is 64.20 m^2, the USPA is 12.98 m^2, and the SWA is 148.79 m^2. This indicated that the preferential flow enhanced freshwater–saltwater mixing and USP (Figure 3E); the preferential flow weakened the length of SW in the aquifer and reduced the salinity.

To determine the effect of preferential flow on groundwater flow, saltwater circulation, and saltwater–freshwater exchange under tidal conditions, the travel time for specified particles in the aquifer was calculated [readers may refer to Xin et al. (2010) for more details]. Three particles were released both near the inland boundary and the beach surface (refer to Figure 3, Table 4 for the specific release location).

Under tidal action (Figure 3), a USP developed in the intertidal zone, with particles released from inland along the moving path of freshwater bypassing the USP and SW discharge to the sea. The deeper particles took longer than those in the shallow, e.g., the one starting from the shallow (x = 75 m, z = 9 m) took 257.1 d, while that from the deep inland (x = 75 m, z = 3 m) took 267.8 d (Figure 3), increasing by 4.2%. The difference in travel time among the three particles at the seaside varied dramatically as the particles released to the deeper beach moved further landward and took longer paths, e.g., the particle starting from x = 13 m, z = 8.8 m took 176.7 d, while that from x = 3 m, z = 7.42 m took 1,026.9 d (Figure 3, Table 4).

Preferential flow leads to pore water flow and an increase in USP. Therefore, the particles released from the inland shallow layer experienced USP resistance across the preferential flow, with the travel time increased slightly, e.g., it took 257.1 d for particles released from x = 75 m and z = 9 m and 258.2 d for preferential flow (Figure 3). The travel time of particles released from the beach was consistent with the travel time under non-preferential flow, decreasing with an increase in USP, e.g., the particle released from x = 3 m and z = 7.42 m needed 1,026.9 d with the non-preferential flow but only 908.4 d in the presence of preferential flow.

To further discuss the influence of preferential flow on groundwater flow and circulation, Figure 4 presents the velocity distribution of rising tide, high tide, falling tide, and low tide without and with preferential flow. Only the velocity distribution in the area of preferential flow is shown for comparison. As shown in Figure 4, the velocity distribution differed with the seawater level. When the tide rose, salt water flowed into the aquifer through the intersection of the tidal level and the aquifer. When the tide fell, the tidal water retreated, and the pore water flowed to the ocean (Figure 4). Under the preferential flow condition at the rising tide, a relatively large pore water velocity appeared and rapidly flowed into the aquifer, thereby providing a preferential gateway for the pore water. When the flood completely flowed over the marsh platform (t = 3 h), the saltwater level reached the maximum (10.5 m), and a sharp rise in the pore water velocity near the preferential flow model was observed [Figure 4—(2B)]. The direction of the pore water flow under preferential flow was vertically downward, and the magnitude increased considerably. This indicated that the over-topping water rapidly enters preferential flow and diffuses into the surrounding marsh soil. Furthermore, preferential flow enhances the mixing and dilution of saltwater–freshwater, thus reducing the salinity of groundwater and increasing the quality of drinking water.

3.3 Distribution of nutrients

The distributions of DO, NO_3^-, NH_4^+, and DOC under tidal [Figure 5—(1A), (2A), (3A), and (4A)] and preferential flow conditions [Figure 5—(1B), (2B), (3B), and (4B)] are presented in this section. There were differences in the distribution of nutrients. DO was mainly concentrated in the shallow layers of the aquifer and NO_3^- was in the shallow and medium layers of the aquifer (Note: we used shallow, middle, and deep zones to differentiate the characteristics of the distribution area of DO, NO_3^-, NH_4^+, and DOC. In this study, these three intervals are a relative region varying with the preferential flow, so we are only distinguishing between the same model) [Figure 5—(1A), (1B), (2A), and (2B)], while NH_4^+ [Figure 5—(3A) and (3B)] and DOC [Figure 5—(4A)

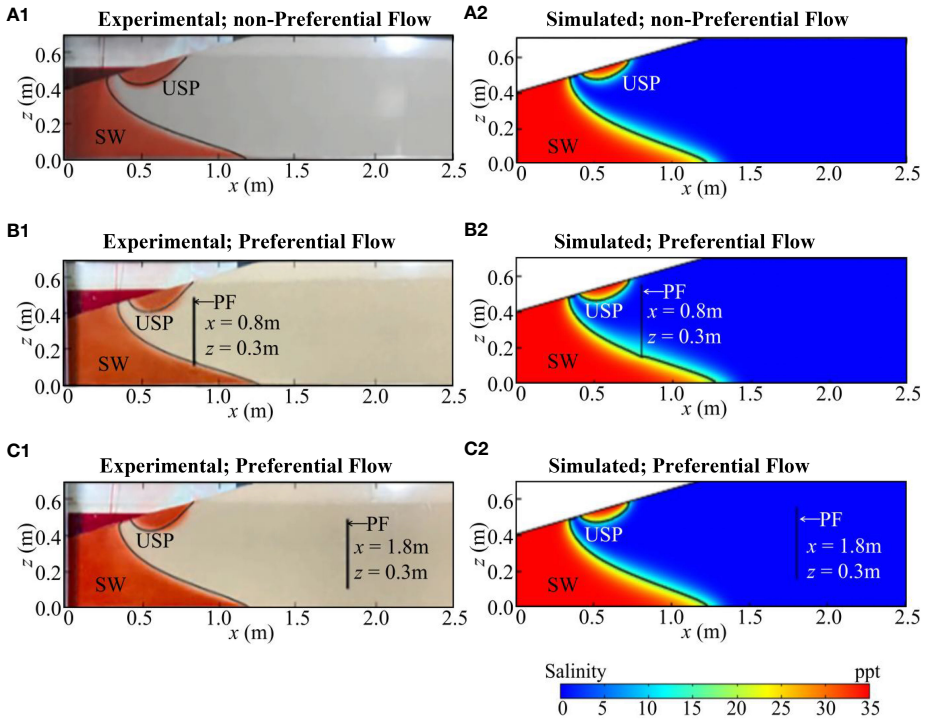

FIGURE 2
Experimental **(A1)**, **(B1)**, **(C1)** (Xie et al., 2023) and simulated **(A2)**, **(B2)**, **(C2)** results of non-preferential flow and preferential flow. The horizontal dotted lines is tidal range; in **(A1)**, **(B1)**, and **(C1)**, the solid black lines indicate the numerical results for 50% salinity contour isohalines by Xie et al. (2023), and in **(A2)**, **(B2)**, and **(C2)**, the solid black lines indicate 50% salinity contour isohalines based on COMSOL. PF is preferential flow.

and (4B)] were distributed in the entire aquifer with a relatively high concentration in the shallow layer and in the middle and shallow layers, respectively, e.g., the average concentration of DOC in the region z > 4 m is 0.058 mM larger than that at z< 4 m (0.025 mM), and the average concentration of NH_4^+ in the region z > 4 m is 0.012 mM larger than that at z< 4 m (0.011 mM). The nutrient concentration increased along preferential flow in the reaction process [Figure 5—(1B), (2B), (3B), and (4B)].

3.4 Reaction rate distribution

The reaction rate distributions of nitrification [Figure 6—(1A) and (1B)], denitrification [Figure 6—(2A) and (2B)], respiration [Figure 6—(3A) and (3B)], and DOC degradation [Figure 6—(4A) and (4B)] are described in this section.

Nitrification and respiration occurred primarily in the surface layers of the aquifer, while denitrification was dominant under the influence of anaerobic bacteria in the middle and deep layers where oxygen is depleted (Figure 6). DOC degradation occurred in the USP and SW of the whole aquifer under tidal action and preferential flow. However, the reaction rate in the middle and upper layers was relatively high [Figure 6—(4A) and (4B)], e.g., the average rate of DOC degradation in the region z > 4 m is 1.49×10^{-5} mM d^{-1} larger than that at z< 4 m (6.54×10^{-6} mM d^{-1}). Compared to the non-preferential flow condition, preferential flow resulted in the extension of nitrification, respiration, and DOC degradation along with the preferential flow in the reaction process. However, denitrification consistently took place in the deeper USP.

We quantitatively analyzed the NO_3^- removal efficiency (R_N). Under non-preferential flow condition, the R_N is 7.9%. When we insert the preferential flow, the NO_3^- removal efficiency (R_N) was modified, e.g., under the preferential flow action, the R_N is 8.97%. These results suggest that preferential flow increases the NO_3^- removal efficiency, thus decreasing the salinity distribution.

3.5 Sensitivity analysis

3.5.1 Preferential flow depth

The mixing zone and USP increased vertically with preferential flow depth, the retreat of SW, and the decrease in salinity in the aquifer with an increase in preferential flow depth (Figure 7), e.g., when the preferential flow depth was 2.3 m, MZA was 59.04 m^2, USP was 12.50 m^2, SW was 152.50 m^2, salinity was 7.19 ppt, and TOE was 23.10 m, and when the preferential flow depth was increased to 4.3 m, MZA was 69.11 m^2, USP was 13.01 m^2, SW was 147.22 m^2, salinity was 7.00 ppt, and TOE was 22.90 m (Figure 7).

The travel time of particles released from deep inland increased with preferential flow depth. With the persistent vertical increase of USP, the travel time and path of the particle passing the USP became longer, e.g., the particle released from x = 75 m and z = 3 m took 273 d and 280.6 d with depth that was 2.3 and 4.3 m, respectively. The travel time of the particle released from the beach was consistent with the previous section, decreasing with

10.3389/fmars.2024.1369869

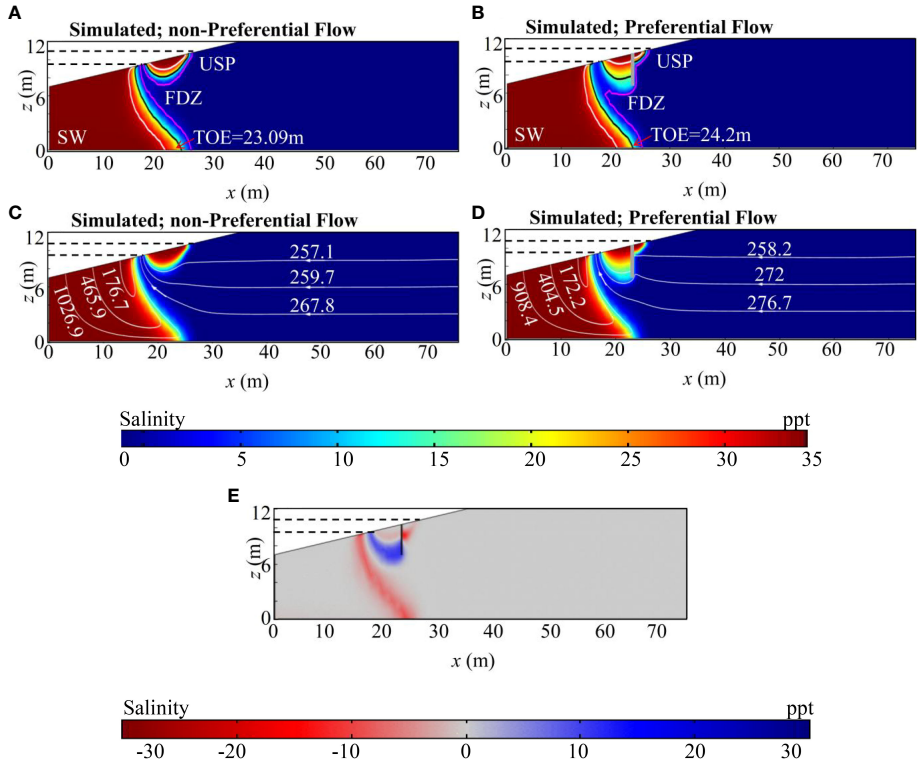

FIGURE 3
Simulation results: salinity distribution of tidal action in **(A, B)**, the pink, black, and white solid lines show the 10%, 50%, and 90% salinity contour, respectively. Saltwater wedge (SW), upper salinity plume (USP), saltwater wedge toe (TOE), and fresh water discharge area (FDZ). TOE is the intersection of 50% salinity contour and *x*-axis. The horizontal black dotted line shows the average sea level and tidal range. In **(C, D)**, the white solid line and data are particle path and travel time (unit: day). The particles start from the inland boundary and the beach, respectively. The gray vertical line indicates the preferential flow (h = 3.3 m). **(E)** Salinity difference graph (preferential flow - no preferential flow).

the preferential flow depth, e.g., the particle released from x = 3 m and z = 7.42 m took 1,007.6 d with depth that was 2.3 m, while under the preferential flow with depth at 4.3 m, it only required 927.1 d. This might be due to the retreat of SW with the change in preferential flow depth (Figure 8, Table 4).

The distribution of nutrients was consistent with the discussions in Sections 3.4 (Supplementary Figure S1). The significance of preferential flow depth on the distribution of nitrification, denitrification, respiration, and DOC degradation is shown in Supplementary Figure S2. All reactions were consistent with the discussions in Section 3.5. Nitrification and respiration consumption of deeper DO have their long residence time in the aquifer. Nitrification and respiration primarily occurred in the surface layers (Supplementary Figure S2). Denitrification was dominant in the middle and deep layers of the aquifer (Supplementary Figure S2), and DOC degradation occurred throughout the aquifer with a faster reaction rate in the middle and upper layers (Supplementary Figure S2). However, each reaction at the USP acted differently with preferential flow depth due to the rapid inflow of nutrients through the preferential flow, e.g., when the preferential flow depth was 2.3 m, the NO_3^- produced by nitrification was 3.184 g d^{-1}, and the NO_3^- removal efficiency was 8.72%. However, under a preferential flow depth of 4.3 m, the NO_3^- produced by nitrification was 3.298 g d^{-1}, and the NO_3^- removal efficiency was 9.04%.

3.5.2 Preferential flow quantity

The USP increased with preferential flow quantity, MZ increases and then decreases, SW decreases and then increases and decrease in salinity in the aquifer with an increase in preferential flow quantity (Figure 9), e.g., when the preferential

TABLE 4 Particle travel times and starting position.

Starting position (m)	No preferential Flow (*d*)	h = 2.3 m (*d*)	h = 3.3 m (*d*)	h = 4.3 m (*d*)	n = 2 (*d*)	n = 3 (*d*)
x = 3 m, z = 7.42 m	1,026.9	1,007.6	908.4	927.1	851.2	872.2
x = 8 m, z = 8.14 m	465.9	453.1	404.5	406.9	375.8	395.7
x = 13 m, z = 8.8 m	176.7	181.6	172.2	183	161.1	165.4
x = 75 m, z = 3 m	267.8	273	276.7	280.6	283.7	281.5
x = 75 m, z = 6 m	259.7	265.4	272	269.6	268.9	269.4
x = 75 m, z = 9 m	257.1	258.1	258.2	258.4	259.4	257.5

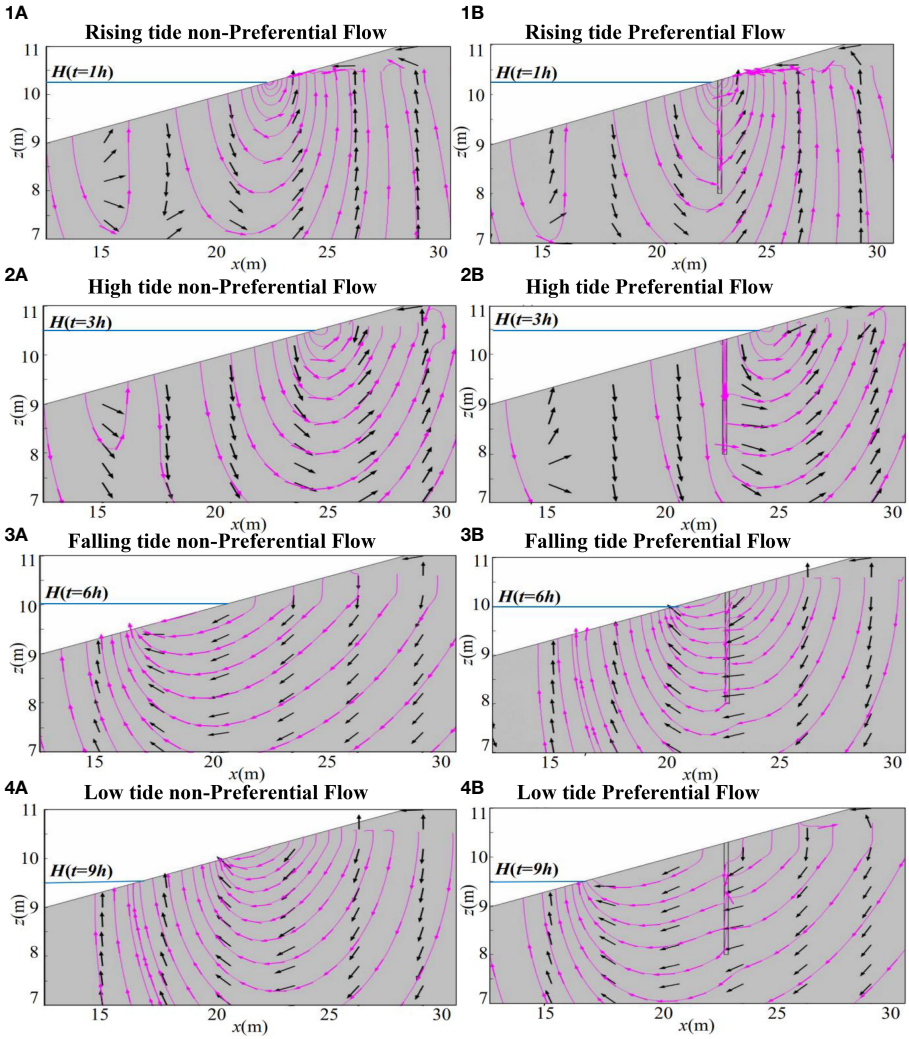

FIGURE 4
Simulation results: flow velocity at rising tide (t = 1 h), high tide (t = 3 h), falling tide (t = 6 h), and low tide (t = 9 h), **(1A)** - **(4A)**, **(1B)** - **(4B)** under without and with preferential flow, respectively. (Note: for comparison, only the velocity distribution in the area where the preferential flow).

flow was 1, MZA was 69.11 m^2, USP was 13.01 m^2, SW was 147.22 m^2, salinity was 7.00 ppt, and TOE was 22.9 m, and when the preferential flow quantity was increased to 3, MZA was 66.40 m^2, USP was 13.63 m^2, SW was 145.04 m^2, salinity was 6.94 ppt, and TOE was 22.50 m (Figure 9).

The travel time of particles released from deep inland increased with preferential flow quantity. With the persistent vertical increase of USP, the travel time and path of the particle passing the USP became longer, e.g., the particle released from x = 75 m and z = 3 m took 280.6 d and 281.5 d at n = 1 and n = 3, respectively. The travel time of the particle released from the beach was consistent with the previous section, decreasing with the preferential flow quantity, e.g., the particle released from x = 3 m and z = 7.42 m took 927.1 d with n that was 1, while under the preferential flow with n that was 3, it only required 872.2 d (Figure 10, Table 4).

The significance of preferential flow quantity on the distribution of nitrification, denitrification, respiration, and DOC degradation is shown in Supplementary Figure S3. Nitrification and respiration consumption of deeper DO have their long residence time in the aquifer. Nitrification and respiration primarily occurred in the surface layers (Supplementary Figures S3, S4), while denitrification was dominant in the middle and deep layers of the aquifer (Supplementary Figure S3), and DOC degradation occurred throughout the aquifer with a faster reaction rate in the middle and upper layers (Supplementary Figure S4). However, each reaction at the USP acted differently with preferential flow quantity due to the rapid inflow of nutrients through the preferential flow, e.g., when the preferential flow quantity was 1, the NO_3^- produced by nitrification was 3.298 g d^{-1}, and the NO_3^- removal efficiency was 9.03%; when the preferential flow quantity was 2, the NO_3^- produced by nitrification was 3.347 g d^{-1}, and the NO_3^- removal efficiency was 9.04%. However, under a preferential flow quantity that was 3, the NO_3^- produced by nitrification was 3.34 g d^{-1}, and the NO_3^- removal efficiency was 8.73%.

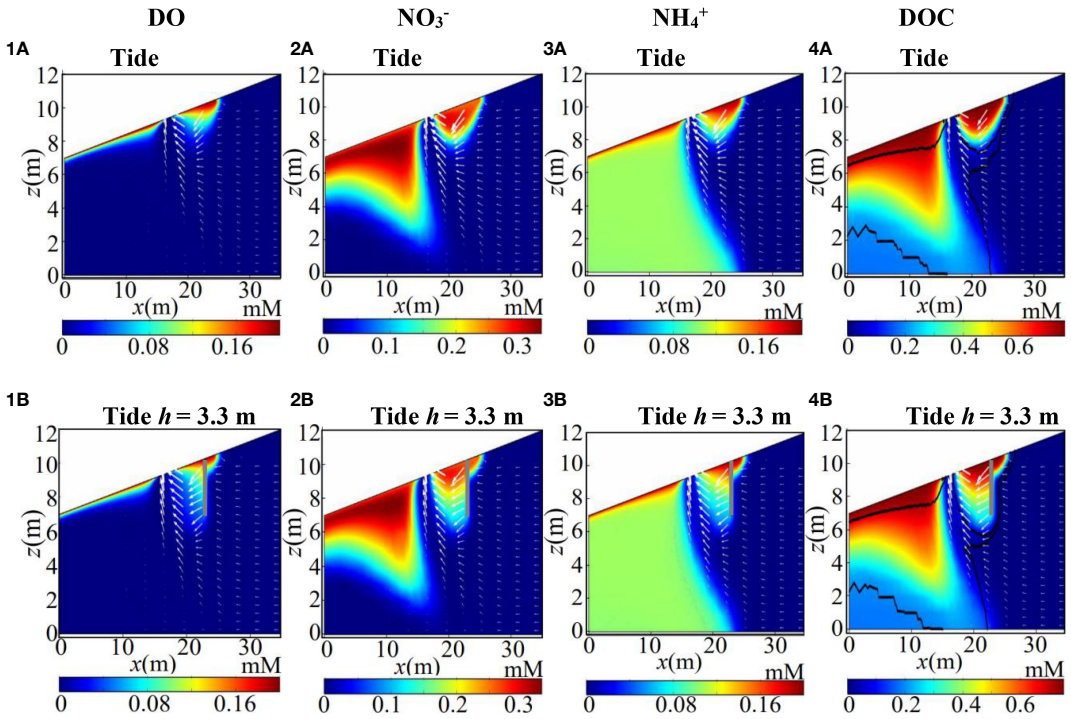

FIGURE 5
Simulation results: nutrient concentration distribution without preferential flow action **(A)** and with preferential flow action **(B)** (1), (2), (3), and (4) is DO, NO_3^-, NH_4^+, and DOC distribution after reaction, respectively. The black solid line is the isoline of denitrification, and the gray vertical line indicates the preferential flow; note that only the intertidal zone is shown.

4 Discussion

4.1 Implication of preferential flow on pore water flow

A USP promotes the retreat of SW under tidal action, which renders the SW closer to the ocean and limits saltwater intrusion. Preferential flow enhanced (Figure 3) this effect, driving SW further seaward, and this impact gradually increases with the depth of preferential flows (Figures 7, 9). These results are consistent with those of Gao et al. (2023), but they consider the under spring-neap tide action. The high hydraulic conductivity of the preferential flow increased the salt transport, resulting in a larger USP than the non-preferential flow; this could control SWI to some extent. Several previous studies have been performed to investigate saltwater–freshwater mixing dynamics—for example, Xie et al. (2023) investigated the effect of fracture characteristics on salinity distribution and groundwater flow through experiments and numerical simulations. They reported that the vertical fractures had a limited impact on most SWI properties. This seems to be different from our results. This is mainly due to the effect of fracture on SWI properties depending on their relative position to the saltwater. In our study, we focused on the longitudinal rift located inside the USP and connected to it. In addition, they noted that fractures can increase the mixing zone, which is consistent with our results. Preferential flow acted as a drain for the shallow layer during the falling tide and for a recharge well during the rising tide. This was the main reason for the increase in USPs and the decrease in the salinity of the aquifer. Additionally, Xiao et al. (2019) found that the salinity in crab burrows in the intertidal zone at high tide was slightly higher than in the soil matrix, e.g., the salinity of crab burrows reached 34 PSU and larger than the nearby soil matrix (33.4 PSU). This suggested that the presence of crab burrows can greatly enhance salt transport in salt marshes.

4.2 Implication of preferential flow on nitrification and denitrification

The nutrients from the sea were initially input in the numerical model with the salinity simultaneously. Nitrification primarily occurred in the surface layer (Figure 6, Supplementary Figures S2, S4) since nitrification, respiration consumption of deeper DO, and denitrification were dominant in the middle and deep layers of the aquifer (Figure 6, Supplementary Figures S2, S4). Shuai et al. (2017) had the same report, and they assumed that DO, NO_3^-, NH_4^+, and DOC primarily originate from rivers. They noted that nitrification occurs in the shallow layers, while denitrification occurs in the deeper anaerobic layers. In the presence of preferential flow, nitrification mainly occurred in the surface layer of the aquifer and extended along with the preferential flow (Figure 6, Supplementary Figures S2, S4). Nitrification and respiration consumption of deeper DO (Figure 5, Supplementary Figures S1, 3) and the preferential flow increase in the area of sediment air/

10.3389/fmars.2024.1369869

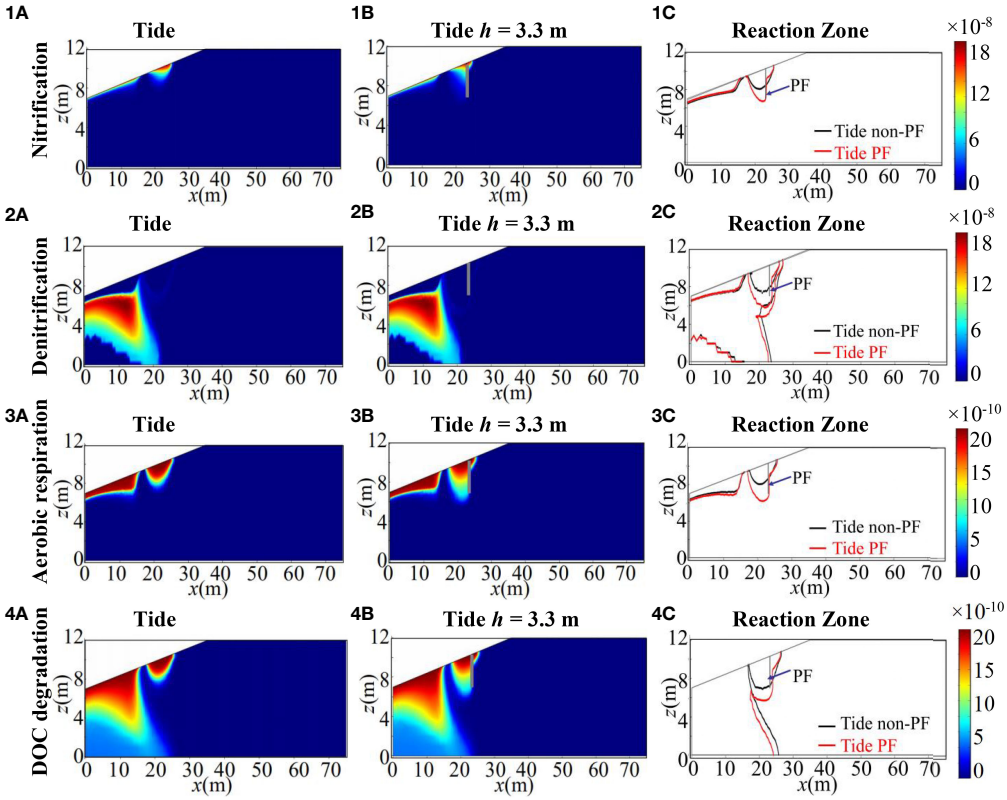

FIGURE 6
Simulation results: reaction distribution (mM s^{-1}). **(1C)–(4C)** is nitrification, denitrification, aerobic respiration, and DOC degradation reaction zone comparison under tidal and preferential flow. The gray vertical line indicates the preferential flow, PF is preferential flow.

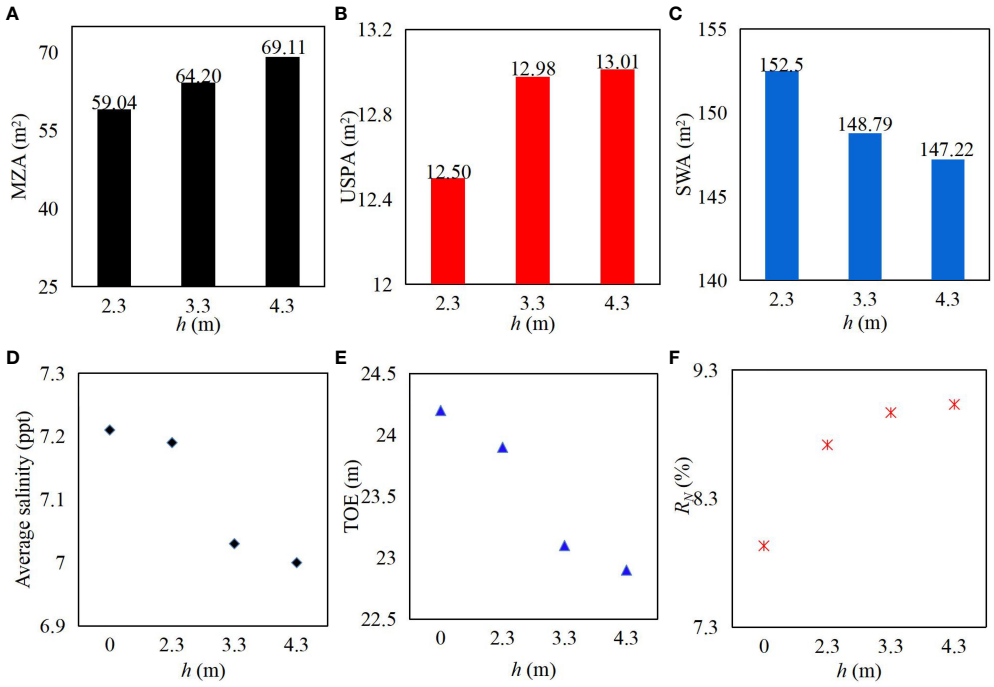

FIGURE 7
Simulation results: the mixing zone area (MZA) **(A)**, the USP area (USPA) **(B)**, the SW area (SWA) **(C)**, the salinity **(D)**, TOE **(E)**, and the NO_3^- removal rate (R_N) **(F)** with a different preferential flow depth.

10.3389/fmars.2024.1369869

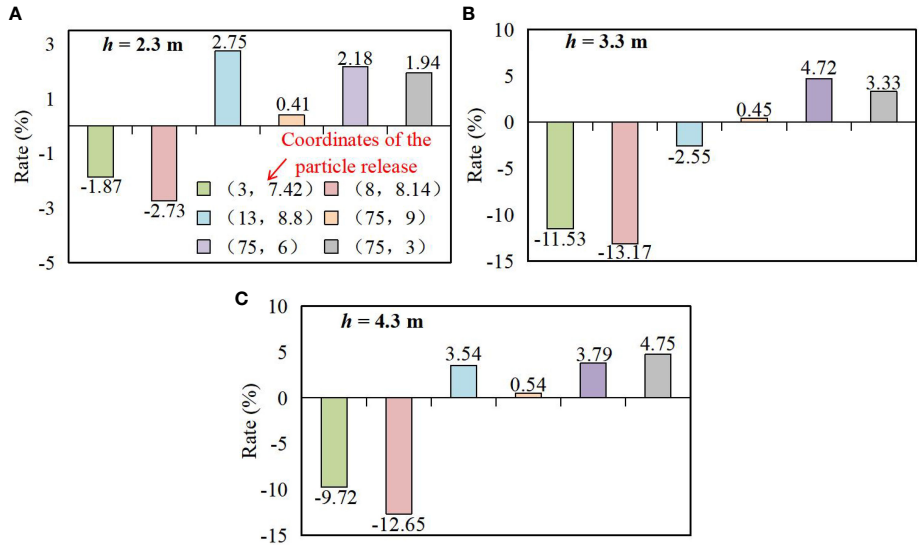

FIGURE 8
(A–C) Simulation results: rate of change in particle transport time. Positive values indicate an increase, while negative values indicate a decrease, and the colors and the data in parentheses are the coordinates of the particle release point.

water interface increased the exchange between surface water and groundwater and the concentration of DO in the aquifer. This resulted in the extension of nitrification and respiration along the preferential flow (Figure 6, Supplementary Figures S2, S4) and decreased the carbon stock of the sediment. Preferential flow increased the concentration of nutrients at the USP by dramatically enhancing nutrient transport and reducing SW as the USP pushed the SW seaward. However, total nitrification increased under preferential flow conditions and gradually increased with depth and amount of preferential flow; however, it decreases after a certain quantity.

In the presence of tidal action, the distribution of nutrients in the aquifer formed a USP and a SW. The travel and residence times were longer in the deeper layers of the aquifer for nutrients, nitrification,

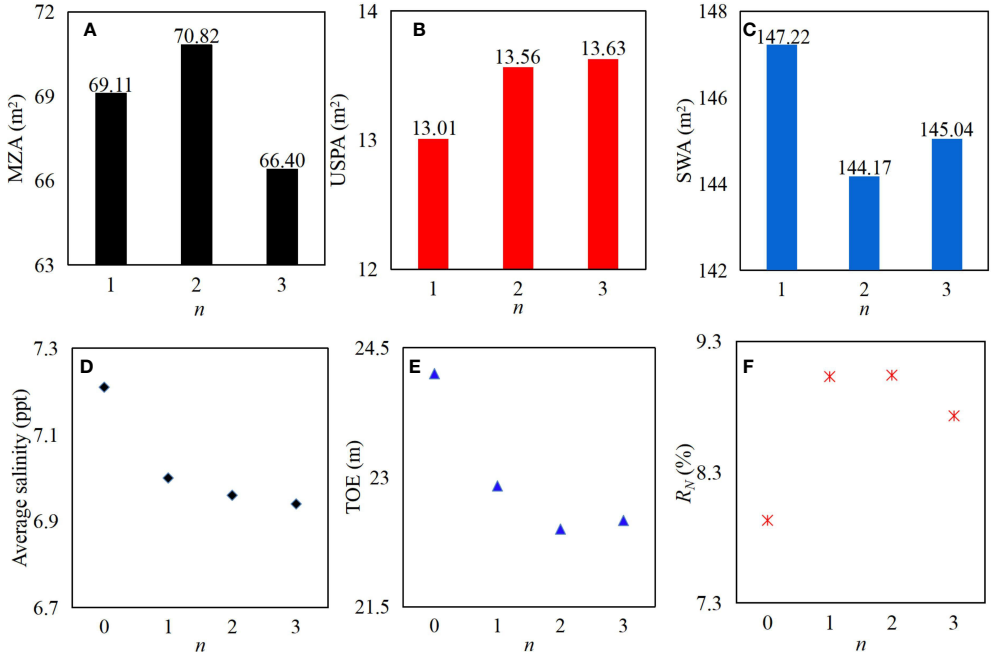

FIGURE 9
Simulation results: the mixing zone area (MZA) **(A)**, the USP area (MZA) **(B)**, the SW area (MZA) **(C)**, the salinity **(D)**, TOE **(E)**, and the NO_3^- removal rate **(F)** with a different number (*n*) of preferential flow.

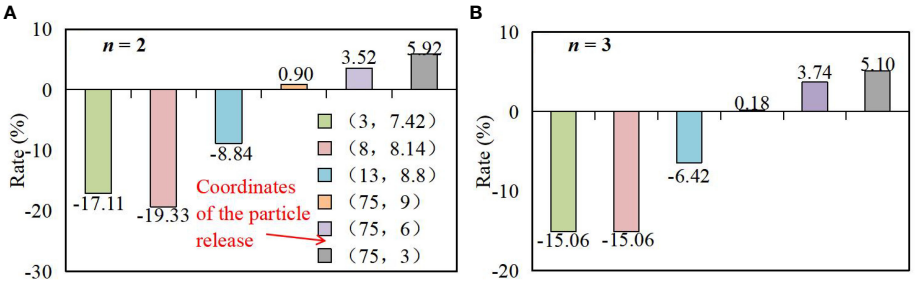

FIGURE 10
(A, B) Simulation results: rate of change in particle transport time. Positive values indicate an increase, while negative values indicate a decrease. The colors and the data in parentheses are the coordinates of the particle release point.

and respiration consumption of deeper DO (Figure 5, Supplementary Figures S1, S3), creating anaerobic conditions for denitrification. Subsequently, the NO_3^- produced was used up during denitrification, resulting in the reduction of NO_3^- in the deep layer (Figure 5—(2B), NO_3^- distribution). Denitrification occurred in the deeper USP as nitrification in the upper USP not only provided the reactant for denitrification but also offered an anaerobic environment. The NO_3^- removal efficiency increased compared to that in non-preferential flow, and this effect increases progressively with the depth and number of preferential flows; however, it decreases after a certain quantity. It can be observed that the existence of macro-porosity (such as crab burrows and invertebrate nests) facilitates the removal of NO_3^- from sea sources. Some previous studies demonstrated that denitrification also increased with the size of the mixing zone (Spiteri et al., 2008; Heiss et al., 2017; Gao et al., 2023). Heiss et al. (2017) reported that saltwater–freshwater mixing could promote denitrification in the intertidal zone.

In addition, Gao et al. (2023) investigated the effect of macropores on the salinity distribution and denitrification of the aquifer under spring-neap tide action. They pointed out that macropores can lead to NO_3^- removal efficiency increase. They investigated the reaction between DOC from the sea source and NO_3^- from the land source. In this study, we considered the relationship between DOC from the sea source and NO_3^-, which is the main reason for the difference, and it is also noteworthy that they also suggested that macropores can increase the mixing of saltwater and freshwater. This is consistent with our results. Thus, our study provides new insights into the relationship between macropores and salinity distribution and denitrification in the aquifers.

4.3 Knowledge gaps and research needs

This study elucidated the effect of preferential flow on salinity change and solute transformation under tidal conditions. It determined the importance of the depth and quantity of preferential flow, which guide the mitigation of saltwater intrusion and contaminant removal. However, the location and density (Fanjul et al., 2008; Ying, 2021) distribution of preferential flow should be further studied. The preferential flows are based on the actual and generalized, and the real aquifer preferential flow distribution pattern and specifications are extremely complex. Future research can focus on the real aquifer preferential flows on the saltwater intrusion characteristics as well as on the impact of solute transport transformation. Waves drive seawater recirculation (Anwar et al., 2014), and seasonal groundwater level drives groundwater fluctuations (Michael et al., 2005; Liu et al., 2016). This leads to the more complex nearshore mixing dynamics of freshwater and seawater, which, in turn, complicates NO_3^- transformation. In addition, other factors may also impact the biogeochemical processes in aquifers, including precipitation, evaporation, and long fluctuating tides (e.g., spring-neap tides), and sediment heterogeneity (Heiss and Hichael, 2014; Geng and Boufadel, 2017; Kreyns et al., 2020; Gao et al., 2023; Zheng et al., 2023), which need to be considered in the future work.

5 Conclusions

This study examined the combined effect of preferential flow and tide on pore water flow and marine nitrogen transport reaction in coastal aquifers. The following conclusions might be drawn:

(1) Under tidal action, preferential flow increases the hydraulic conductivity of the aquifer and accelerates the pore water flow and solute transport. The preferential flow results in the vertical increase of the USP and further retreat of SW. In the presence of preferential flow, the NO_3^- removal efficiency is increased.

(2) Nitrification mainly occurs in the surface layer of the aquifer, while denitrification dominates the middle and deep layers. The nitrification effect increases with the increase in the depth and quantity of preferential flow, and the NO_3^- removal efficiency increases progressively with the depth and number of preferential flows; however, it decreases after a certain quantity.

Data availability statement

The original contributions presented in the study are included in the article/Supplementary Material. Further inquiries can be directed to the corresponding authors. The model calibration experimental data used to produce Figure 2, A1, B1 and C1 are compiled from Xie et al. 2023.

Author contributions

CG: Conceptualization, Investigation, Methodology, Writing – original draft, Writing – review & editing. JK: Funding acquisition, Resources, Supervision, Visualization, Writing – review & editing. JW: Writing – review & editing. WC: Supervision, Writing – review & editing.

Funding

The author(s) declare financial support was received for the research, authorship, and/or publication of this article. This research was supported by the National Natural Science Foundation of China (51979095) and acknowledges the Postgraduate Research and Practice Innovation Program of Jiangsu Province (KYCX22_0658).

Conflict of interest

The authors declare that the research was conducted in the absence of any commercial or financial relationships that could be construed as a potential conflict of interest.

Publisher's note

Supplementary material

The Supplementary Material for this article can be found online at: https://www.frontiersin.org/articles/10.3389/fmars.2024.1369869/full#supplementary-material

References

Anwar, N., Robinson, C., and Barry, D. (2014). Influence of tides and waves on the fate of nutrients in a nearshore aquifer: numerical simulations. *Adv. Water Resour.* 73, 203–213. doi: 10.1016/j.advwatres.2014.08.015

Bardini, L., Boano, F., Cardenas, M., Revelli, R., and Ridolfi, L. (2012). Nutrient cycling in bed-form induced hyporheic zones. *Geochim. Cosmochim. Acta* 84, 47–61. doi: 10.1016/j.gca.2012.01.025

Carsel, R., and Parrish, R. (1988). Developing joint probability distributions of soil water retention characteristics. *Water Resour. Res.* 24, 755–769. doi: 10.1029/WR024i005p00755

Chang, Q., Zheng, T., Chen, Y., Zheng, X., and Walther, M. (2020). Investigation of the elevation of saltwater wedge due to subsurface dams. *Hydrol. Process* 34, 4251–4261. doi: 10.1002/hyp.v34.2210.1002/hyp.13863

Chang, Q., Zheng, T., Gao, C., Zheng, X., Lin, Y., Song, X., et al. (2024). Hydrodynamic behavior of freshwater-saltwater mixing zone in the context of subsurface physical barriers. *J. Environ. Manage.* 353, 120080. doi: 10.1016/j.jenvman.2024.120080

Chang, Q., Zheng, T., Zheng, X., Gao, C., Song, X., and Walther, M. (2023). Repulsion driven by groundwater level difference around cutoff walls on seawater intrusion in unconfined aquifers. *Sci. Total Environ.* 874, 162535. doi: 10.1016/j.scitotenv.2023.162535

Chang, Q., Zheng, T., Zheng, X., Zhang, B., Sun, Q., and Walther, M. (2019). Effect of subsurface dams on saltwater intrusion and fresh groundwater discharge. *J. Hydrol.* 576, 508–519. doi: 10.1016/j.jhydrol.2019.06.060

Cheng, H., Jiang, Z., Ma, X., and Wang, Y. (2020). Nitrogen dynamics in the mangrove sediments affected by crabs in the intertidal regions. *Ecotoxicology* 29, 669–675. doi: 10.1007/s10646-020-02212-5

Edith, A., Claudia, S., Lange, S., George, T., Pierre, L., and Li, J. (2015). Potential efficiency of riparian vegetated buffer strips in intercepting soluble compounds in the presence of subsurface preferential flows. *PloS One* 10, e0131840. doi: 10.1371/journal.pone.0131840

Enrique, O., Muoz-Carpena, R., Gao, B., and Fox, G. (2018). Riparian vadose zone PF: review of concepts, limitations, and perspectives. *Vadose Zone J.* 17, 1–20. doi: 10.2136/vzj2018.02.003

Fang, Y., Qian, J., Zheng, T., Zheng, X., and Walther, M. (2023). Submarine groundwater discharge in response to the construction of subsurface physical barriers in coastal aquifers. *J. Hydrol.* 617, 129010. doi: 10.1016/j.jhydrol.2022.129010

Fang, Y., Zheng, T., Wang, H., Guan, R., Zheng, X., and Walther, M. (2022b). Experimental and numerical evidence on the influence of tidal activity on the effectiveness of subsurface dams. *J. Hydrol.* 603, 127149. doi: 10.1016/j.jhydrol.2021.127149

Fang, Y., Zheng, T., Wang, H., Zheng, X., and Walther, M. (2022a). Nitrate transport behavior behind subsurface dams under varyinghydrological conditions. *Sci. Total Environ.* 838, 155903. doi: 10.1016/j.scitotenv.2022.155903

Fanjul, E., Grela, M., Canepuccia, A., and Iribarne, O. (2008). The southwest atlantic intertidal burrowing crab Neohelice granulata modifies nutrient loads of phreatic waters entering coastal area. *Estuar. Coast. Shelf Sci.* 79, 300–306. doi: 10.1016/j.ecss.2008.04.005

Gao, C., Kong, J., Zhou, L., Shen, C., and Wang, J. (2023). Macropores and burial of dissolved organic matter affect nitrate removal in intertidal aquifers. *J. Hydrol.* 617, 129011. doi: 10.1016/j.jhydrol.2022.129011

Gao, S., Zheng, T., Zhang, B., Fang, Y., and Zheng, X. (2024). Combined effects of aquifer heterogeneity and subsurface dam on nitrate contamination in coastal aquifers. *J. Environ. Manage.* 351, 119740. doi: 10.1016/j.jenvman.2023.119740

Gao, S., Zheng, T., Zheng, X., and Walther, M. (2022). Influence of layered heterogeneity on nitrate enrichment induced by cut-off walls in coastal aquifers. *J. Hydrol.* 609, 127722. doi: 10.1016/j.jhydrol.2022.127722

Geng, X., and Boufadel, M. C. (2017). The influence of evaporation and rainfall on supratidal groundwater dynamics and salinity structure in a sandy beach. *Water Resour. Res.* 53, 6218–6238. doi: 10.1002/2016WR020344

Guimond, J., Seyfferth, A., Moffett, K., and Michael, H. (2020). A physical-biogeochemical mechanism for negative feedback between marsh crabs and carbon storage. *Environ. Res. Lett.* 15, 034024. doi: 10.1088/1748-9326/ab60e2

Heiss, J. (2020). Whale burial and organic matter impacts on biogeochemical cycling in beach aquifers and leachate fluxes to the nearshore zone - sciencedirect. *J. Contam. Hydrol.* 233, 103656.1–16. doi: 10.1016/j.jconhyd.2020.103656

Heiss, J., and Hichael, H. (2014). Saltwater-freshwater mixing dynamics in a sandy beach aquifer over tidal, spring-neap, and seasonal cycles. *Water Resour. Res.* 50, 6747–6766. doi: 10.1002/2014WR015574

Heiss, J., Post, V., Laattoe, T., Russoniello, C., and Michael, H. (2017). Physical controls on biogeochemical processes in intertidal zones of beach aquifers. *Water Resour. Res.* 53, 9225–9244. doi: 10.1002/2017WR021110

Hughes, C. (1998). Characterisation of the hydrology of an estuarine wetland. *J. Hydrol.* 211, 34–49. doi: 10.1016/S0022-1694(98)00194-2

Kim, K., Heiss, J., Michael, H., Cai, W., Laattoe, T., and Post, V. (2017). Spatial patterns of groundwater biogeochemical reactivity in an intertidal beach aquifer. *J. Geophys. Res.: Biogeosci.* 122, 2548–2562. doi: 10.1002/2017JG003943

Kreyns, P., Geng, X., and Michael, H. (2020). The influence of connected heterogeneity on groundwater flow and salinity distributions in coastal volcanic aquifers. *J. Hydrol.* 586, 124863. doi: 10.1016/j.jhydrol.2020.124863

Kringel, R., Rechenburg, A., Kuitcha, D., Fouepe, A., and Fomo, M. (2016). Mass balance of nitrogen and potassium in urban groundwater in central Africa, Yaounde/Cameroon. *Sci. Total Environ.* 547, 382–395. doi: 10.1016/j.scitotenv.2015.12.090

Kuan, W., Xin, P., Jin, G., Robinson, C., Gibbes, B., and Li, L. (2019). Combined effect of tides and varying inland groundwater input on flow and salinity distribution in unconfined coastal aquifers. *Water Resour. Res.* 55, 8864–8880. doi: 10.1029/2018WR024492

Li, J., Hua, G., Liu, S., Liu, X., Huang, Y., and Shi, Y. (2021). Effects of crab disturbance on nitrogen migration and transformation in a coastal tidal flat wetland. *Environ. Sci. pollut. Res.* 28, 52345–52356. doi: 10.1007/s11356-021-14393-5

Liu, Y., Jiao, J., and Luo, X. (2016). Effects of inland water level oscillation on groundwater dynamics and land-sourced solute transport in a coastal aquifer. *Coast. Eng.* 114, 347–360. doi: 10.1016/j.coastaleng.2016.04.021

Lu, C., and Werner, A. (2013). Timescales of seawater intrusion and retreated. *Adv. Water Resour.* 59, 39–51. doi: 10.1016/j.advwatres.2013.05.005

Lu, J., Bai, Z., Velthof, G., Wu, Z., Chadwick, D., and Ma, L. (2019). Accumulation and leaching of nitrate in soils in wheat-maize production in China. *Agric. Water Manage.* 212, 407–415. doi: 10.1016/j.agwat.2018.08.039

Meile, C., Porubsky, W., Walker, R., and Payne, K. (2009). Natural attenuation of nitrogen loading from septic effluents: spatial and environmental controls. *Water Resour.* 44, 1399–1408. doi: 10.1016/j.watres.202009.11.019

Michael, H., Mulligan, A., and Harvey, C. (2005). Seasonal oscillations in water exchange between aquifers and the coastal ocean. *Nature* 436, 1145–1148. doi: 10.1038/nature03935

Pan, F., Xiao, K., Guo, Z., and Li, H. (2022). Effects of fiddler crab bioturbation on the geochemical migration and bioavailability of heavy metals in coastal wetlands. *J. Hazard. Mater.* 437, 129380. doi: 10.1016/j.jhazmat.2022.129380

Radfard, M., Rahmatinia, M., Tabatabaee, H., Solimani, H., Mahvi, A., and Azhdarpoor, A. (2018). Data on health risk assessment to the nitrate in drinking water of rural areas in the Khashcity, Iran. *Data Brief* 21, 1918–1923. doi: 10.1016/j.dib.2018.11.007

Robinson, C., Li, L., and Barry, D. (2007a). Effect of tidal forcing on a subterranean estuary. *Adv. Water Resour.* 30, 851–865. doi: 10.1016/j.advwatres.2006.07.006

Robinson, C., Li, L., and Prommer, H. (2007b). Tide-induced recirculation across the aquifer ocean interface. *Water Resour. Res.* 43. doi: 10.1029/2006WR005679

Robinson, C., Xin, P., Li, L., and Barry, D. (2014). Groundwater flow and salt transport in a subterranean estuary driven by intensified wave conditions. *Water Resour. Res.* 50, 165–181. doi: 10.1002/wrcr.v50.1

Rocha, L. (2013). Seasonal enhancement of submarine groundwater discharge (SGD)-derived nitrate loading into the Ria Formosa coastal lagoon assessed by 1-D modeling of benthic NO_3^-profiles. *Estuarine Coast. Shelf Sci.* 132, 56–64. doi: 10.1016/j.ecss.2012.04.015

Shen, C., Zhang, C., Kong, J., Xin, P., Lu, C., Zhao, Z., et al. (2019). Solute transport influenced by unstable flow in beach aquifers. *Adv. Water Resour.* 125, 68–81. doi: 10.1016/j.advwatres.2019.01.009

Shen, C., Zhang, C., Xin, P., Kong, J., and Li, L. (2018). Salt dynamics in coastal marshes: Formation of hypersaline zones. *Water Resour. Res.* 54, 3259–3276. doi: 10.1029/2017WR022021

Shuai, P., Cardenas, M., Knappett, P., Bennett, P., and Neilson, B. (2017). Denitrification in the banks of fluctuating rivers: the effects of river stage amplitude, sediment hydraulic conductivity and dispersivity, and ambient groundwater flow. *Water Resour. Res.* 53, 7951–7967. doi: 10.1002/2017WR020610

Spiteri, C., Slomp, C., Charette, M., Tuncay, K., and Meile, C. (2008). Flow and nutrient dynamics in a subterranean estuary (Waquoit Bay, MA, USA): Field data and reactive transport modeling. *Geochim. Cosmochim. Acta* 72, 3398–3412. doi: 10.1016/j.gca.2008.04.027

Sun, Q., Zheng, T., Zheng, X., Chang, Q., and Walther, M. (2019). Influence of a subsurface cutoff wall on nitrate contamination in an unconfined aquifer. *J. Hydrol.* 575, 234–243. doi: 10.1016/j.jhydrol.2019.05.030

Sun, Q., Zheng, T., Zheng, X., and Walther, M. (2021). Effects of physical barrier on seawater intrusion and nitrate accumulation in upstream aquifers. *J. Contam. Hydrol.* 243, 103913. doi: 10.1016/j.jconhyd.2021.103913

van Genuchten, M. (1980). A closed-form equation for predicting the hydraulic conductivity of unsaturated soils. *Soil Sci. Soc. America J.* 44, 892–898. doi: 10.2136/sssaj1980.03615995004400050002x

Williams, M., Buda, A., Elliott, H., Hamlett, J., Boyer, E., and Schmidt, J. (2014). Groundwater flow path dynamics and nitrogen transport potential in the riparian zone of an agricultural headwater catchment. *J. Hydrol.* 511, 870–879. doi: 10.1016/j.jhydrol.2014.02.033

Xiao, K., Pan, F., Santos, I., Zheng, Y., Zheng, C., Chen, N., et al. (2022). Crab bioturbation drives coupled iron-phosphate-sulfide cycling in mangrove and salt marsh soils. *Geoderma* 424, 115990. doi: 10.1016/j.geoderma.2022.115990

Xiao, K., Wilson, A., and Li, H. (2019). Crab burrows as preferential flow conduits for groundwater flow and transport in salt marshes: A modeling study. *Adv. Water Resour.* 132, 103408. doi: 10.1016/j.advwatres.2019.103408

Xie, Y., Wang, Y., Zhang, J., Ye, Y., Shen, C., Zeng, Y., et al. (2023). Seawater intrusion in fractured coastal aquifers influenced by tides: Laboratory and numerical investigations. *J. Hydrol.* 622, 129637. doi: 10.1016/j.jhydrol.2023.129637

Xin, P., Jin, G., Li, L., and Barry, D. (2009). Effects of crab burrows on pore water flows in salt marshes. *Adv. Water Resour.* 32, 439–449. doi: 10.1016/j.advwatres.2008.12.008

Xin, P., Robinson, C., Li, L., Barry, D., and Bakhtyar, R. (2010). Effects of wave forcing on a subterranean estuary. *Water Resour. Res.* 46, W12505. doi: 10.1029/2010WR009632

Xu, X., Xin, P., Zhou, T., and Xiao, K. (2021). Effect of macropores on pore-water flow and soil conditions in salt marshes subject to evaporation and tides. *Estuarine Coast. Shelf Sci.* 261, 107558. doi: 10.1016/j.ecss.2021.107558

Ying, Z. (2021). *Effect of macropores on water and salt exchange in coastal wetlands* (China: Hohai University, Master's thesis). 11p.

Zhang, W., Tian, Z., Zhang, N., and Li, X. (1996). Nitrate pollution of groundwater in northern China. *Agric. Ecosyst. Environ.* 59, 223–231. doi: 10.1016/0167-8809(96)01052-3

Zhang, B., Zheng, X., Zheng, T., Xin, J., Sui, S., and Zhang, D. (2019). The influence of slope collapse on water exchange between a pit lake and a heterogeneous aquifer. *Front. Environ. Sci. Eng.* 13, 9. doi: 10.1007/s11783-019-1104-9

Zheng, T., Gao, M., Chang, Q., Zheng, X., and Walther, M. (2022). Dynamic desalination of intruding seawater after construction of cut-off walls in a coastal unconfined aquifer. *Front. Mar. Sci.* 9. doi: 10.3389/fmars.2022.857807

Zheng, T., Yuan, F., Gao, S., Zheng, X., Liu, T., and Luo, J. (2023). The impact of hydraulic conductivity anisotropy on the effectiveness of subsurface dam. *J. Hydrol.* 626, 130360. doi: 10.1016/j.jhydrol.2023.130360

Zheng, T., Zheng, X., Chang, Q., and Zhan, H. (2021). Timescale and effectiveness of residual saltwater desalinization behind subsurface dams in an unconfined aquifer. *Water Resour. Res.* 57, e2020WR028493. doi: 10.1029/2020WR028493

Zheng, T., Zheng, X., Sun, Q., Wang, L., and Walther, M. (2020). Insights of variable permeability full-section wall for enhanced control of seawater intrusion and nitrate contamination in unconfined aquifers. *J. Hydrol.* 586, 124831. doi: 10.1016/j.jhydrol.2020.124831

frontiers | Frontiers in Marine Science

TYPE Original Research
PUBLISHED 16 May 2024
DOI 10.3389/fmars.2024.1413548

OPEN ACCESS

EDITED BY
Chengji Shen,
Hohai University, China

REVIEWED BY
Xiuqin Yang,
Nanjing University of Information Science and Technology, China
Peipeng Wu,
Jilin University, China

*CORRESPONDENCE
Yu Zhang
yuzhang@nhri.cn
Xiao Zhang
zxhhu1991@163.com

RECEIVED 07 April 2024
ACCEPTED 29 April 2024
PUBLISHED 16 May 2024

CITATION
Chen Y, Xu Y, Chen G, Zeng M, Zhang T, Zhang X and Zhang Y (2024) Analysis of influencing factors of seawater intrusion in the Yangtze River Estuary and control for water supply security.
Front. Mar. Sci. 11:1413548.
doi: 10.3389/fmars.2024.1413548

Analysis of influencing factors of seawater intrusion in the Yangtze River Estuary and control for water supply security

Yubin Chen[1,2], Yuni Xu[1,2], Guiya Chen[2,3], Ming Zeng[1,2], Tao Zhang[1,2], Xiao Zhang[1,2]* and Yu Zhang[4]*

[1]Bureau of Hydrology, Changjiang Water Resources Commission, Wuhan, China, [2]Innovation Team for Flood and Drought Disaster Prevention of Changjiang Water Resources Commission, Wuhan, China, [3]Changjiang Water Resources Commission, Wuhan, China, [4]Nanjing Hydraulic Research Institute, Nanjing, China

Seawater intrusion poses a significant threat to the water supply of coastal cities both presently and in the future. It is crucial to identify the controllable factors influencing seawater intrusion, both natural and anthropogenic, in order to ensure water supply security. This study examined seawater intrusion characteristics using monitoring data from 1994 to 2019. Factors such as daily flow rate, duration of intrusion, water quality, and tidal level were analyzed to establish correlations and identify the primary influencing factors in the Yangtze River Estuary. The findings reveal that seawater intrusion in this area is most prevalent from November to April, peaking in February and March. The key controllable factors affecting chloride levels at the intake are the daily flow rate at Datong Station and the tidal range at Xuliujing Station. Additionally, the study proposes control methods to safeguard water supply, including providing daily flow rate values for flushing seawater intrusion at Datong Station under different tidal ranges and intrusion durations. These research results provide valuable guidance for the emergency operation of the Three Gorges-centered reservoir group against seawater intrusion.

KEYWORDS

seawater intrusion, influencing factors, controllable factors, Yangtze River Estuary, water supply security

1 Introduction

Seawater intrusion usually occurs at the confluence of rivers and oceans. When the sea level at the river mouth is higher than the river level, seawater will flow into the river, and seawater intrusion will spread upstream along the river from the river mouth. The intrusion at the river mouth is mainly due to natural factors, but there are also human factors (Casillas-Trasvina et al., 2019; Xiao et al., 2021; Hu et al., 2024). The problem of seawater

intrusion at river mouths is a major issue affecting the construction of water sources for coastal cities at present and in the future (Liu et al., 2014; El-Jaat et al., 2018; Chen et al., 2019).

Tides and currents are the power source of the mixing of seawater and freshwater, caused by the gravitational forces of celestial bodies, and they have a crucial impact on seawater intrusion (Paiva and Schettini, 2021). The effects of tides and currents on seawater intrusion include: the convective transport of currents, turbulent mixing caused by tides, and the combined effect of tides and topography leading to tidal trapping and tidal transport (Li et al., 2022). Wind also has a significant impact on seawater intrusion (Tao et al., 2020). Different wind speeds and directions result in varying strengths of the rising and falling tides in the estuarine area, thus affecting seawater intrusion differently. Under the influence of different wind speeds and directions, the estuarine area can generate different horizontal circulations, which may have a certain impact on seawater intrusion in the estuarine area (Li et al., 2020). The decrease in upstream runoff during the dry season is also a major cause of seawater intrusion (He et al., 2018). Seawater backflow often occurs in the dry season of years with low upstream water flow. In addition, as a result of natural changes in river channels and human activities such as sand excavation and dredging of waterways, widespread riverbed incision in estuarine areas and deepening of major tidal channels occur, particularly during the dry season of large tides with low runoff (Li et al., 2023). The decrease in river flow and the relative increase in the action of tidal currents lead to increased seawater backflow. The rising sea level also promotes seawater backflow (Roy and Datta, 2018). Over the past 100 years, the global average sea level has been rising at a rate of 0.18 cm per year. With further global warming, the sea level is expected to rise more rapidly in the 21st century. It is predicted that the sea level will rise by 0.65 to 1 m in the 21st century (Boumis et al., 2023). By the year 2000, the sea level along the Chinese coast was rising at a rate of 0.25 cm per year. By 2030, the relative sea level rise range at the mouth of the Yangtze River will be 0.23 to 0.42 m, and it will rise by nearly 1 m in the 21st century, which will exacerbate seawater intrusion during the dry season (Zhou et al., 2022; Mu et al., 2024).

The Yangtze River Estuary is a densely populated and economically developed area in China, serving as the center for the country's economy, transportation, science and technology, industry, finance, trade, exhibitions, and shipping. With the development of the national economy and the rapid increase in population, the water supply in Shanghai is becoming increasingly strained. The seawater intrusion in the dry season every year seriously threatens the water intake of the Yangtze River source in Shanghai, leading to various water safety issues in production and daily life caused by seawater. This situation severely restricts the development and utilization of water resources in the Yangtze River Estuary and its economic development. The degree of seawater intrusion in the Yangtze River Estuary is closely related to factors such as the flow of the main stream of the Yangtze River, tides, wind stress, estuary morphology, and underwater topography, generally occurring from November to April during the dry season of winter and spring. During the dry season, the water supply reservoirs in the Yangtze River Estuary of Shanghai City are all threatened and affected by seawater intrusion for a certain period, with each intrusion generally lasting 5 to 7 days.

One of the more common and effective methods for preventing and resisting seawater intrusion is to adopt water diversion measures to "use freshwater to counter seawater" (Zhang et al., 2021). According to the overall layout of the comprehensive planning of the Yangtze River basin, a large number of key water control projects for the main and tributary rivers of the Yangtze River are being gradually implemented (Wang et al., 2022). As of 2019, more than 300 large reservoirs (with a total capacity of over 100 million cubic meters) have been built in the Yangtze River basin, with a total regulated capacity of over 180 billion cubic meters (Xu et al., 2023). Among them, there are 111 large reservoirs (above Yichang) in the upper reaches of the Yangtze River, with a total regulated capacity of over 80 billion cubic meters, continuously enhancing the regulation capacity of water resources in the Yangtze River basin (Wang et al., 2023). The development and regulation of water resources in the Yangtze River basin have already and will further impact the water resources situation and ecological environment in the Yangtze River Estuary (Chen et al., 2023). The impact of water resource regulation on the situation of seawater intrusion in the Yangtze River Estuary has become a widely concerned issue. Seawater intrusion is a major issue affecting the water supply of coastal cities at present and in the future. Identifying controllable key factors has important implications for ensuring water supply security. Therefore, based on monitoring data from 1994 to 2019, this study analyzed the characteristics of seawater intrusion. Factors such as daily average flow, duration of seawater intrusion, water quality, and tide level were selected to establish relevant relationships and identify the main controllable influencing factors of seawater intrusion in the Yangtze River Estuary. The results offer valuable guidance for emergency scheduling during seawater backflow in the reservoir group centered around the Three Gorges.

2 Study area

The Yangtze River Estuary is located in the Yangtze River Delta region, as shown in Figure 1. The tidal boundary of the Yangtze River Estuary is at Datong Station, which is 624 km away from the mouth of the river. Before the formation of the Xuliujing section during the 1950s to 1970s, the upper boundary of the estuarine section of the Yangtze River was generally considered to be at Jiangyin station. After the formation of the Xuliujing section, it is generally believed that the Xuliujing station is more reasonable as the upper boundary of the estuary section of the Yangtze River. The plan form of the estuary section of the Yangtze River is in the shape of a trumpet, with three levels of branching and four mouths entering the sea. The width of the river at the inlet of Xuliujing is 4.7 km. Below Xuliujing, Chongming Island divides the Yangtze River into its southern and northern branches. The mouth of the Yangtze River is a moderately tidal estuary, which is influenced by both the runoff of the Yangtze River and the ocean tides. There are numerous river channels on both sides of the river, making it a typical tidal plain river network area.

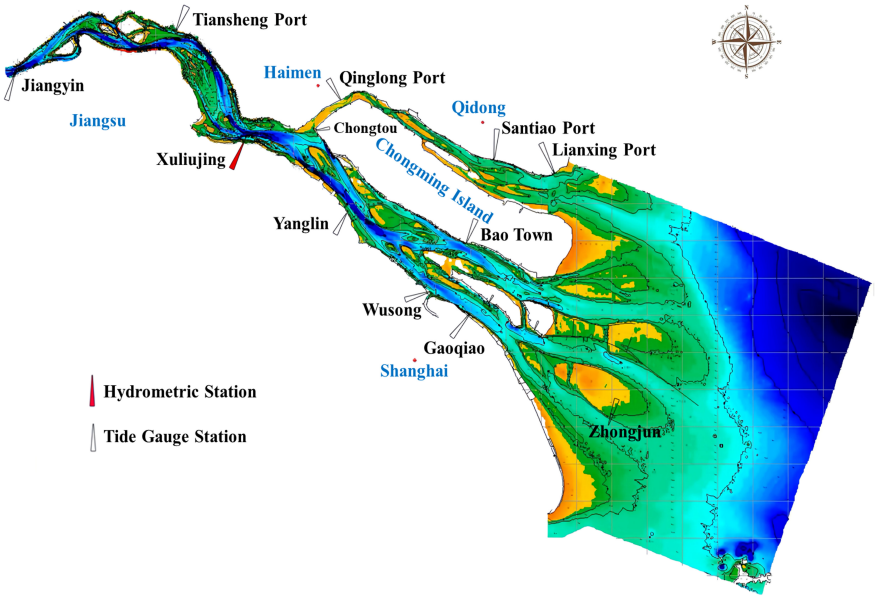

FIGURE 1
Map of study area.

3 Methods and data

3.1 Study object selection

In the usual sense, the Yangtze River Estuary refers to the estuary below Xuliujing, where the flow of Xuliujing represents the actual seaward flow. However, due to the back-and-forth flow at the Xuliujing station, its flow characteristics are difficult to describe. On the other hand, the Xuliujing station only started to have flow compilation data since 2005, with a short data sequence that does not match the long-term salinity measured data, making it difficult to establish a relevant relationship. Previous studies focused on the Datong station, establishing the relationship between the flow of Datong station and the salinity intrusion intensity of the estuary water source area. Some scholars also established the relationship between the flow of Datong station and the flow of Xuliujing station through investigations of the water diversion and drainage along the river. However, these works were carried out before 2005, without verified flow data of Xuliujing station (Chen et al., 2018; Mei et al., 2019). This study establishes the relationship between the flow of Datong station and the flow of Xuliujing station by collecting flow compilation data of Datong station and Xuliujing station in recent years, and simultaneously studies the response time of estuarine salinity to changes in upstream flow.

Analysis of the daily net flux of Xuliujing station and the daily flow of Datong Xuliujing station from January to December 2013 was conducted. The relationship between the daily net flux of Xuliujing and the flow of Datong in 2013 is shown in Figure 2. It can be observed from the figure that the daily flow of Datong changes relatively steadily, mainly influenced by tides, while the net flux shows larger daily fluctuations. However, overall, the difference in flow between Datong and Xuliujing station mostly falls within the range of ±5000 m^3/s.

The relationship between the monthly average flow of Datong station and Xuliujing station in 2013 is illustrated in Figure 3. It can be seen that during the dry season, the monthly net flux of Xuliujing is similar to the monthly flow of Datong. In most dry season months, the net flux of Xuliujing is slightly greater than the monthly flow of Datong. In months where the monthly net flux of Xuliujing is less than the monthly flow of Datong, the difference generally does not exceed 600 m^3/s.

The relationship between the monthly average net flux of Xuliujing and the monthly average flow of Datong from January to December 2013 is shown in Figure 4. It can be observed from the figure that the difference between the two is relatively small. Based on the above analysis, there is a good correlation between the flow at Datong station and the net flux at Xuliujing station at both daily and monthly levels. Therefore, using the flow at Datong station to replace the net flux at Xuliujing station is reasonable and feasible.

3.2 Influencing factors selection

3.2.1 Potential influencing factors

Potential factors affecting seawater intrusion at the Yangtze River Estuary include tides and tidal currents, wind, reduced upstream flow during the dry season, changes in the estuary and river channel topography, increasing water supply from the upstream areas within the basin, changes in the river channel bifurcation ratio, and rising sea levels.

3.2.1.1 Tides and tidal currents

Tides have a medium to small-scale periodic impact on the intrusion of seawater into the Yangtze River Estuary. The tidal regime in the Yangtze River Estuary is significantly influenced by

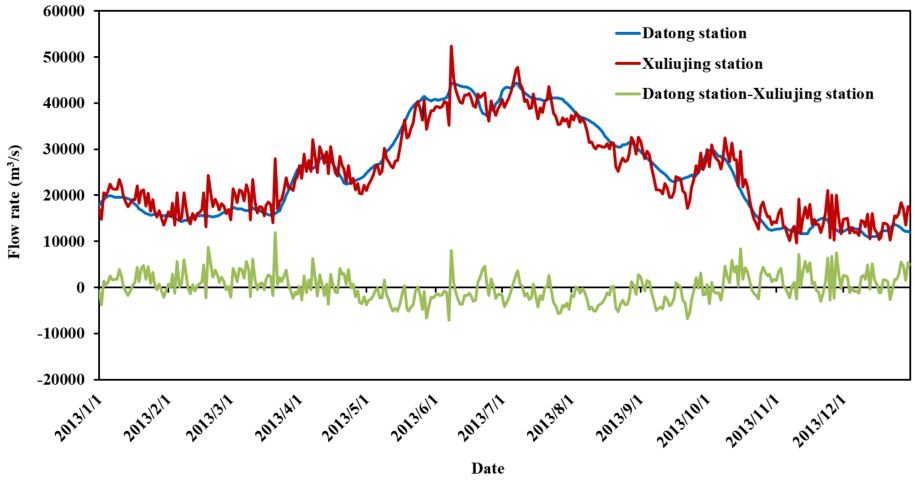

FIGURE 2
Relationship between the flow at Datong station and the net flux at Xuliujing station in 2013.

astronomical tides, exhibiting irregular semi-diurnal tidal characteristics as well as long-period characteristics such as spring and neap tides. The volume of inflowing tides in the estuary is enormous, reaching up to 266,000 m^3/s when the upstream flow is close to the annual average flow and the average tidal range is observed at the mouth. The intrusion of seawater into the Yangtze River Estuary corresponds to tidal patterns and also exhibits a pattern of spring and neap changes, with large and small tides occurring once each in a half-month period, leading to variations in daily average chloride concentrations (Biemond et al., 2023). Additionally, as the semi-diurnal tidal ebb and flow change over the course of a day, chloride concentrations in the Yangtze River Estuary also exhibit closely related concentration peaks and troughs.

3.2.1.2 Wind

Wind has a significant impact on the intrusion of seawater, with different wind speeds and directions affecting the strength of the tidal currents in the estuarine area, thereby influencing the intrusion of seawater into the estuary.

3.2.1.3 Decrease in upstream flow during the dry season

Previous studies have indicated a clear negative correlation between the chloride levels in the Yangtze River Estuary and the fluctuation of flow at the Datong station on the Yangtze River. During years with average or low flow in the dry season, seawater intrusion from the sea can reach as far as Wusong or even further upstream (Yin et al., 2018).

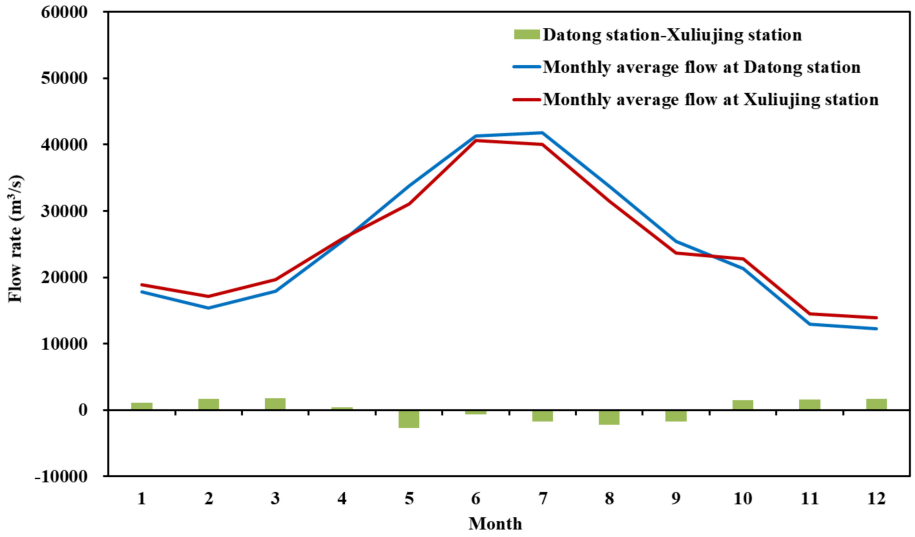

FIGURE 3
Comparison of the monthly average flow at Datong station and Xuliujing station in 2013.

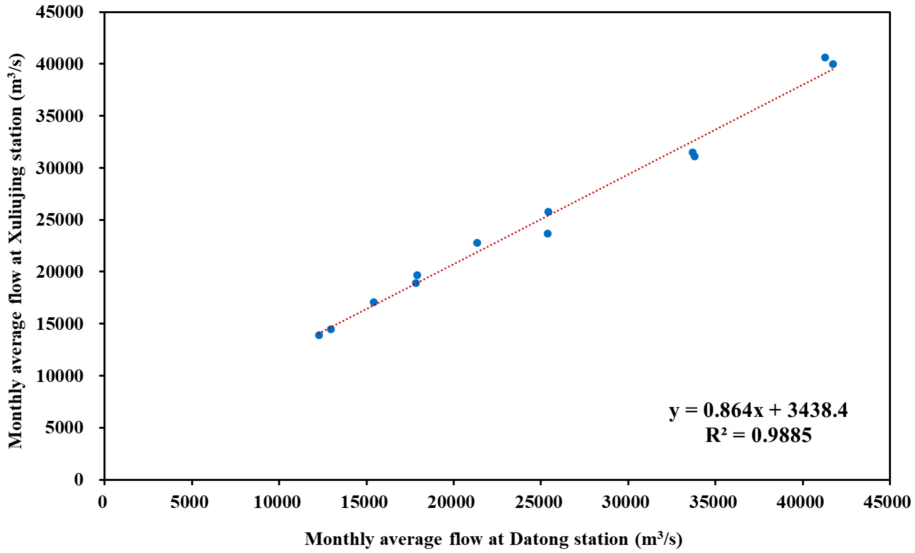

FIGURE 4
Relationship between the monthly average flow at Datong and the monthly average net flux at Xuliujing in 2013.

3.2.1.4 Changes in estuarine and river channel topography

The northern branch of the Yangtze River Estuary is dominated by the rising tide, and an important factor leading to the intrusion of seawater from the northern branch into the southern branch is the trumpet-shaped topography in the middle and lower reaches of the northern branch, which easily leads to the formation of tidal currents and large tidal ranges. As the rising tide in the northern branch strengthens and the high tide level in the northern branch exceeds that of the southern branch, the rising tide begins to intrude into the southern branch. This situation is more likely to occur during the large tides of the dry season with relatively low flow.

3.2.1.5 Increasing water supply in the upstream areas of the basin

With the growth of the economy and population, the water consumption in the entire basin has been continuously increasing. The total water consumption in the Yangtze River Basin has risen from 31.4 billion m^3 in 1949 to 132.5 billion m^3 in 1980, reaching 170.26 billion m^3 in 2003, and is projected to reach 221.9 billion m^3 by 2030. Considering the diversion of 41.3 billion m^3 of water from the South-to-North Water Diversion Project, the total water consumption will reach 263.2 billion m^3 (Cao et al., 2023). The increasing water consumption in the upstream areas of the basin has led to a reduction in water supply to the delta region, exacerbating the upstream intrusion of seawater in the delta region.

3.2.1.6 Changes in river channel bifurcation ratio

The bifurcation ratio of the river channels in the delta region has changed as a result of natural channel evolution and human activities such as sand mining and channel regulation. The bifurcation ratio of the northern branch of the Yangtze River Estuary has been decreasing year by year, with the northern branch's share of the total flow decreasing from 25% in 1915 to 7.6% in 1998. Since 1959, there has been a phenomenon of southward intrusion of water and sediment, with the bifurcation ratio remaining below 5% for a long period, and dropping to 1.3% after 1998. Due to the decrease in flow, the impact of tidal currents has relatively strengthened. In recent years, there has been a noticeable increase in the intrusion of seawater and tidal currents in the northern branch.

3.2.1.7 Sea level rise

By the year 2000, the sea level along the coast of China had been rising at a rate of 0.25 cm per year. By 2030, the relative sea level rise in the Yangtze River Estuary is projected to be between 0.23 and 0.42 meters, and is expected to increase by nearly 1 meter during the 21st century, exacerbating the intrusion of seawater during the dry season (Zhou et al., 2022; Boumis et al., 2023; Mu et al., 2024).

3.2.2 Basic characteristics of seawater intrusion in the Yangtze River Estuary

The estuary is affected by tides, oblique pressure effects, and mixing, resulting in the intrusion of seawaters from the sea into the inland areas, which is a common phenomenon in estuaries. However, in addition to the seawater intrusion from the downstream sea, the southern branch of the Yangtze River Estuary is also affected by the backflow of seawater from the northern branch, which is the most significant characteristic of seawater intrusion in the Yangtze River Estuary. The intrusion mode and the distribution of water sources and reservoirs in the Yangtze River Estuary are shown in Figure 5. The backflow of seawater from the northern branch into the southern branch is caused by the special terrain of the northern branch. The trumpet-shaped middle and lower reaches lead to a significant rise in water level during the flood tide, and even tidal bores occur in the upper Qinglong port channel, submerging large areas of tidal flats. The seawater enters the southern branch with the rising tide. During the ebb tide, as the water level drops, large areas of tidal flats in the upper reaches of the northern branch are exposed, making it difficult for the seawater that has entered the southern branch to return to the

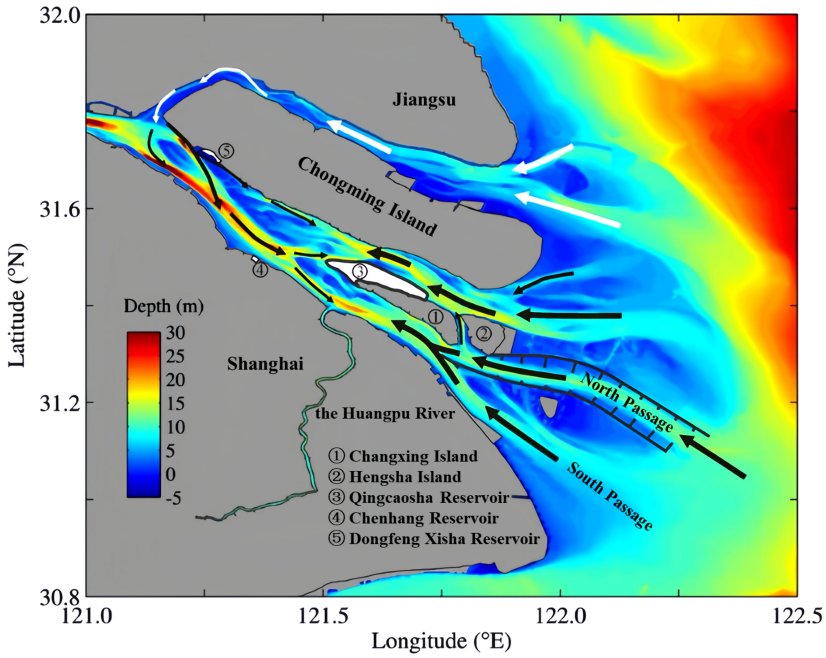

FIGURE 5
Schematic diagram of seawater intrusion and distribution of water sources and reservoirs in the Yangtze River Estuary.

northern branch with the receding tide. The majority of it flows downstream in the southern branch, affecting the water sources downstream. The upper reaches of the northern branch are shallow, and they almost form a right angle with the southern branch, allowing very little runoff to enter the northern branch, accounting for only 2–3% of the total runoff during the dry season. The low runoff is a significant factor contributing to the severe intrusion and backflow of seawater in the northern branch.

3.3 Analysis of multiple influencing factors

3.3.1 Statistical analysis and characteristics of seawater intrusion

Data from the Chenhang Reservoir intake from 1994 to 2019 were used to analyze the frequency, timing, and duration of seawater intrusion as indicators of the situation of seawater intrusion in the Yangtze River Estuary. According to the previous analysis, the flow rate at the Datong station represents the flow rate into the sea for analysis. The response time of the estuarine salinity to changes in the flow rate at the Datong station is approximately 3–5 days. Therefore, the average flow rate at the Datong station for the previous 4 days is taken as the flow rate into the sea at the time of seawater occurrence for analysis.

3.3.2 Analysis of multiple influencing factors

Based on the preliminary analysis of influencing factors, the relationship between the daily average flow rate at the Datong station from 1994 to 2014 and the duration of seawater intrusion was analyzed first. Then, the relationship between the highest chloride concentration during seawater intrusion and the duration of seawater intrusion was analyzed. The relationship between the average tidal range (the difference in water level between adjacent high and low tides within one tidal cycle, calculated as the arithmetic mean of the tidal range during each seawater period in this study, hereinafter referred to as tidal range) corresponding to the duration of seawater intrusion for each intrusion event was analyzed to explore the relationship between the tidal range and the duration of seawater intrusion. Finally, the interrelationship between the highest chloride concentration and the tidal range within different flow rate ranges, as well as the relationship between the chloride concentration and the flow rate within different tidal range ranges, were compared to identify the main influencing factors of seawater intrusion in the Yangtze River Estuary.

3.4 Control methods for ensuring water supply security

Most years in the water sources of the Yangtze River Estuary experience seawater intrusion. When short-term seawater intrusion occurs, it does not affect normal water supply due to water storage in the reservoir. Only when seawater intrusion is severe and exceeds the maximum water supply capacity of the reservoir does it pose a flood safety issue. Therefore, the water supply capacity of each water source in the Yangtze River Estuary needs to be considered, and the standard for critical flow rate needs to be determined.

Among the water sources in the Yangtze River Estuary in Shanghai, the design assurance rate of the Dongfengxisha Reservoir and Qingcaosha Reservoir is 97%-98%, with the typical design year being 1978–1979, and their assurance rate is higher than that of the Chenhang Reservoir at 92%, with the typical design year being 1986–1987, which is relatively dry compared to the typical

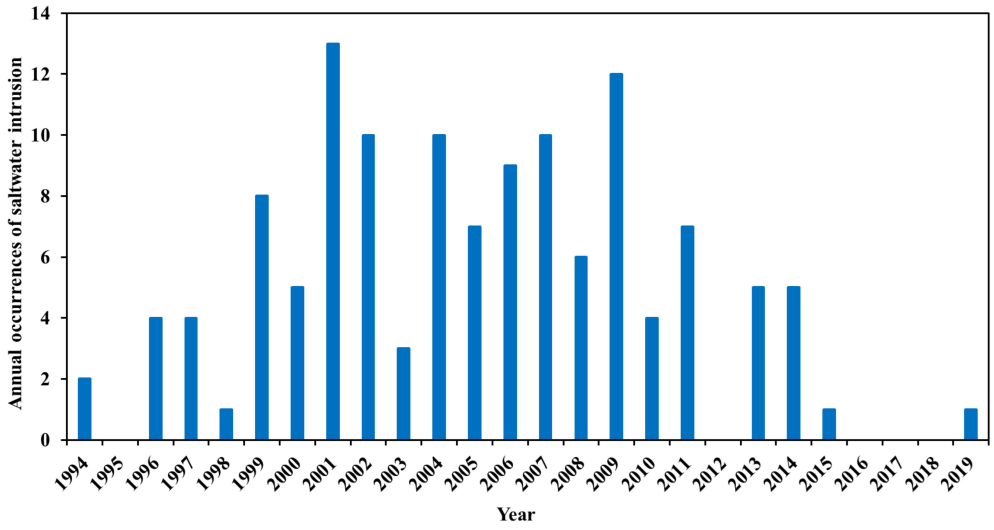

FIGURE 6
Annual occurrences of seawater intrusion from 1994 to 2019.

design year of the Chenhang Reservoir. When seawater intrusion is severe, the Chenhang Reservoir reaches its water supply limit first.

The effective storage capacity of the Chenhang Reservoir is 9.5 million m3, and the water supply scale during the seawater period is 1.4 million m^3/d. During periods of severe seawater intrusion, approximately 100,000 m^3 of water is transferred from the Baogang Reservoir to the Chenhang Reservoir daily. The water supply capacity of the Chenhang Reservoir is determined as $T_c = \frac{950}{140-10} \approx 7$d. Therefore, the average flow rate at the Datong station for 7 consecutive days, during which water intake at the Chenhang Reservoir should not be carried out, is defined as the critical flow rate for ensuring water supply security in Shanghai.

4 Results and discussion

4.1 Statistics and analysis of seawater intrusion

4.1.1 Statistics of seawater intrusion

The number of occurrences and duration of seawater intrusion at Chenhang Reservoir from 1994 to 2019 are shown in Figure 6 and Table 1. It can be observed that the number and duration of seawater intrusion during 2004–2014 were significantly higher and longer than those during 1994–2003. There were only 2 occurrences from 2015 to 2019, with one lasting for 6 days in 2015 and the other for 4 days in 2019. The average annual duration from 2004 to 2019 was less than that from 1994 to 2003.

Figure 7 shows the occurrences of seawater intrusion for each month from 1994 to 2019. The statistics indicate that seawater intrusion mainly occurred from November to April of the following year, with the most occurrences in January to April, particularly in February and March. A few occurrences happened in October and May, and very few occurred in August and September.

Figures 8 and 9 show the occurrences and average duration of seawater intrusion for each month from 1994 to 2003 and from 2004 to 2019, respectively. From Figure 8, it can be observed that, except for August, the occurrences of seawater intrusion from 2004 to 2019 were equal to or higher than those from 1994 to 2003. Similarly, Figure 9 indicates that, except for August, the duration of seawater intrusion from 2004 to 2019 was higher than that from 1994 to 2003. Based on the above statistical analysis, it is evident that the phenomenon of seawater intrusion has undergone certain changes after 2003.

TABLE 1 Occurrences and duration of seawater intrusion at Chenhang Reservoir.

Period	Occurrences	Total duration (days)	Average number of days per occurrence	Average number of days per year
1994–2003	50	318	6.36	31.8
2004–2014	75	483	6.44	43.91
2004–2019	77	493	6.4	30.8

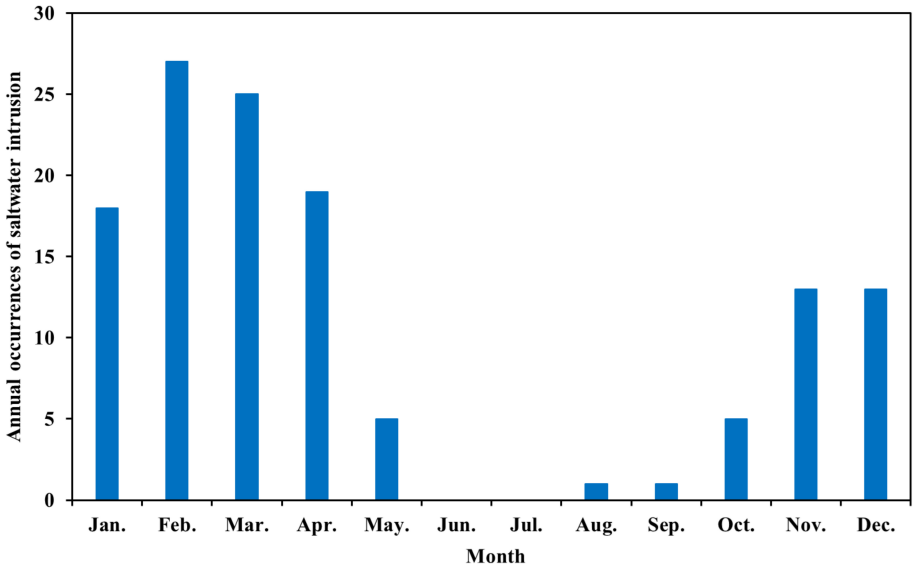

FIGURE 7
Occurrences of seawater intrusion for each month from 1994 to 2019.

4.1.2 Analysis of seawater intrusion characteristics

Based on the previous analysis, the flow at Datong station represents the inflow into the sea. The response time of estuarine salinity to changes in Datong flow is 3–5 days. In this study, the average flow of the previous 4 days at Datong station was taken as the inflow flow corresponding to the occurrence of seawater intrusion for analysis.

The impact of the flow of the Yangtze River on seawater intrusion is very complex. The strength of the seawater intrusion is not only related to the flow of the Yangtze River, but also closely related to the tidal intensity in the outer sea. From the relationship between chloride content and Datong flow, it is not a simple negative correlation between the two. Through the analysis of the daily average flow at Datong station and the highest chloride concentration, a trend is found that when the flow at Datong is greater than 25,000 m^3/s, there is rarely an exceedance of 250 mg/L in chloride concentration (as shown in Figure 10). This indicates that when the flow at Datong is less than 25,000 m^3/s, there may be a significant seawater intrusion.

4.2 Multiple influencing factor analysis

4.2.1 Correlation analysis between duration of seawater and daily average flow at Datong station

We first analyzed the correlation between the average daily flow at the Datong station and the duration of seawater intrusion. The

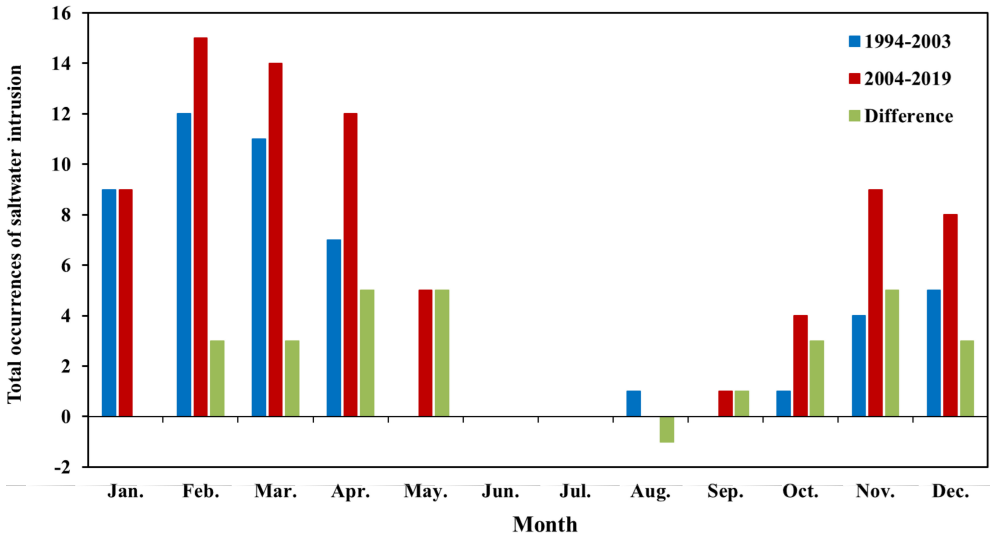

FIGURE 8
Total occurrences of seawater intrusion for each month from 1994 to 2003 and from 2004 to 2019.

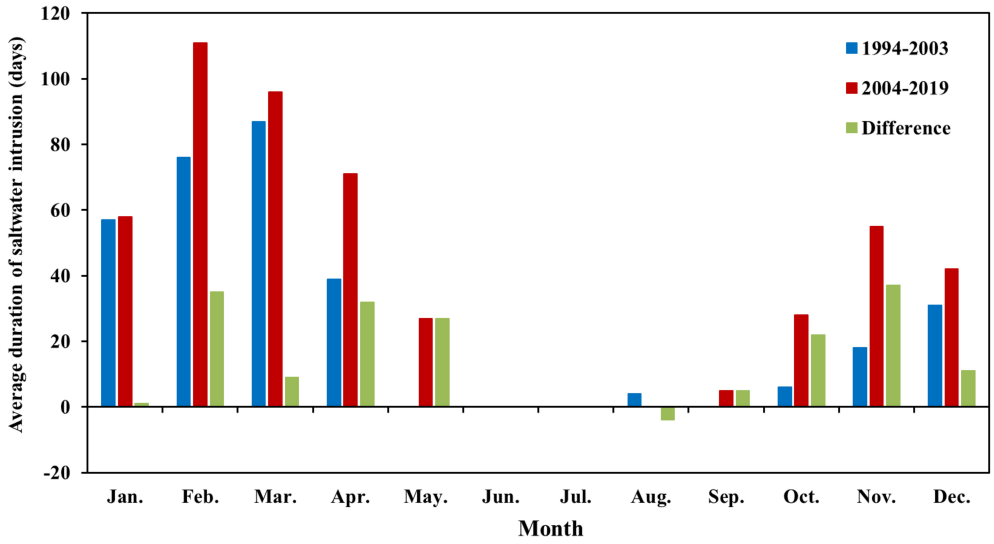

FIGURE 9
Average duration of seawater intrusion for each month from 1994 to 2003 and from 2004 to 2019.

statistics of 1994–2014 seawater intrusion duration corresponding to the first 4 days of Datong average daily flow are shown in Figure 11. It generally shows the trend that the smaller the average daily flow at Datong station corresponds to the longer duration of saltwater intrusion.

4.2.2 Correlation between duration of seawater intrusion and maximum chloride concentration

We further analyzed the correlation between the maximum chloride concentration during seawater intrusion and the duration of seawater intrusion. The duration of each seawater intrusion that occurred from 1994 to 2014 and the corresponding maximum chloride concentration during that seawater intrusion were visualized, as shown in Figure 12. The correlation generally shows a trend that the duration of seawater intrusion is longer as the maximum chloride concentration increases.

4.2.3 Influence of tidal range on the duration of seawater

To further understand the influencing factors of seawater intrusion, the mean tidal range corresponding to the duration within each seawater intrusion period from January 2004 to December 2019 was statistically analyzed (the tidal range is the difference in water level between adjacent high and low tide levels within a cycle, and this time the arithmetic mean was taken for each tidal range calculated during the seawater intrusion period). From

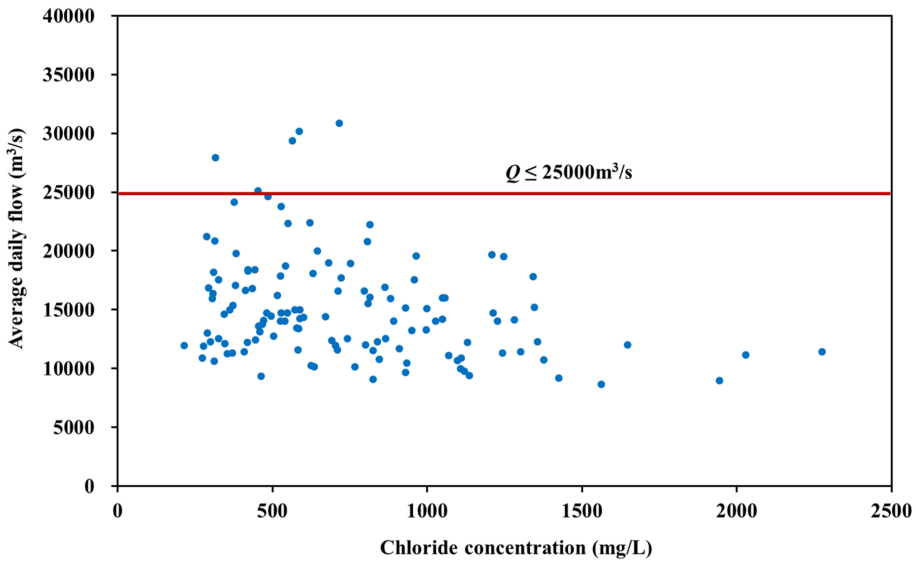

FIGURE 10
Relationship between maximum chloride concentration and average daily flow at Datong station during seawater intrusion.

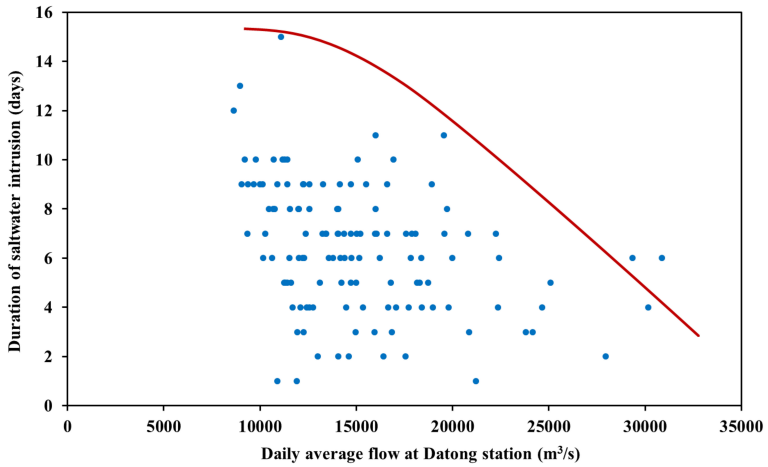

FIGURE 11
Correlation between duration of seawater intrusion and daily average flow at Datong station.

the relationship between tidal range and duration of seawater intrusion (Figure 13), it can be seen that the single-factor correlation between the duration of seawater intrusion and tidal range is not obvious. This is mainly because the duration of seawater intrusion is a result of the combined effect of flow and tidal range at the Datong station.

4.2.4 Correlation between chloride concentration in different flows and tidal ranges

The correlation between the maximum chloride concentration in different flows at Datong station and the tidal ranges at Xuliujing station is shown in Figure 14. It can be seen that when the flow rate of Datong is less than 15000 m^3/s, as long as the tidal range of Xuliujing is greater than 1.3 m, the exceeding of the chloride standard may occur. In the flow range of 15000~20000 m^3/s, when the tidal range at Xuliujing exceeds 1.5 m, chloride exceeding may occur. When the flow exceeds 20000 m^3/s and the tidal range at Xuliujing exceeds 2.0 m, chloride exceeding may occur. The effect of the Xuliujing tidal range on chlorinity is various for different ranges of flow at the Datong station, the lower the flow, the smaller the tidal range required for chlorinity exceedances to occur.

4.2.5 Correlation between chloride concentration in different tidal ranges and flows

The correlation between the maximum chloride concentration in different tidal ranges at Xuliujing station and the daily average flow at Datong is shown in Figure 15. It can be seen that when the tidal range at Xuliujing is less than 1.5 m, as long as the daily average flow at Datong is less than 15000 m^3/s, chloride exceeding may occur. When the tidal range at Xuliujing is between 1.5~2.0 m and the daily average flow at Datong is less than 20000 m^3/s, chloride exceeding may occur. When the tidal range at Xuliujing exceeds 2.0 m, as long as the daily average flow at Datong is less

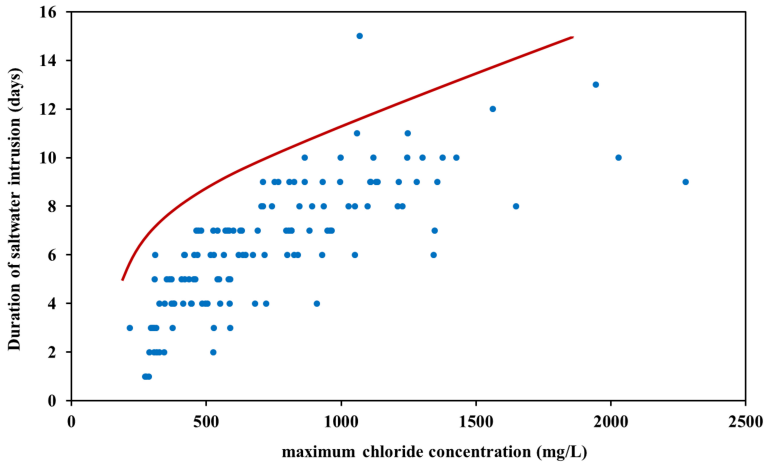

FIGURE 12
Correlation between duration of seawater intrusion and maximum chloride concentration.

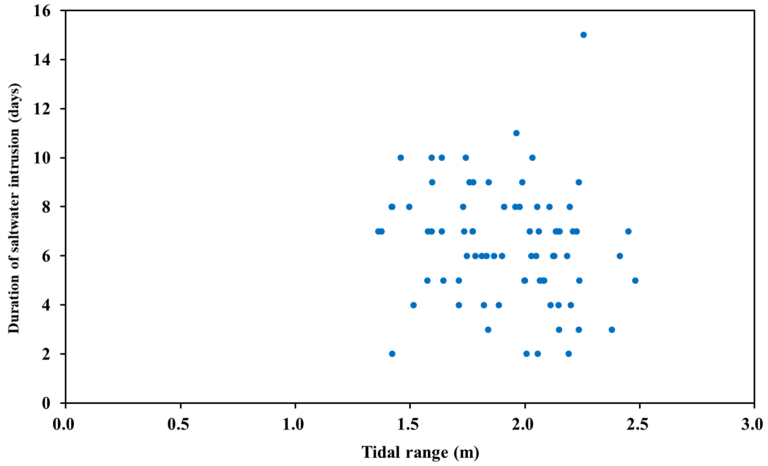

FIGURE 13
Correlation between tidal range and duration of seawater intrusion.

than 25000 m^3/s, chloride exceeding may occur. The influence of flow on chloride concentration is also various in different tidal range ranges, the larger the tidal range at Xuliujing, the larger the critical flow required for the occurrence of the maximum chloride concentration.

4.3 Control of water supply security

Based on the analysis from previous studies, it is known that the main influencing factors affecting the chlorine level at the water intake (causing seawater intrusion) are the daily flow at Datong station and the tidal range at Xuliujing station. We analyzed the data of seawater intrusion at the water intake of Chenhang Reservoir from 2004 to 2014, and examined the relationship between the duration of seawater intrusion, the corresponding average tidal range, and the daily average flow at Datong station in the 4 days prior to the occurrence of seawater intrusion, in order to determine the critical flow threshold under different durations and tidal ranges.

For safety considerations, this study takes the upper envelope of the daily average flow at Datong station for each point agency

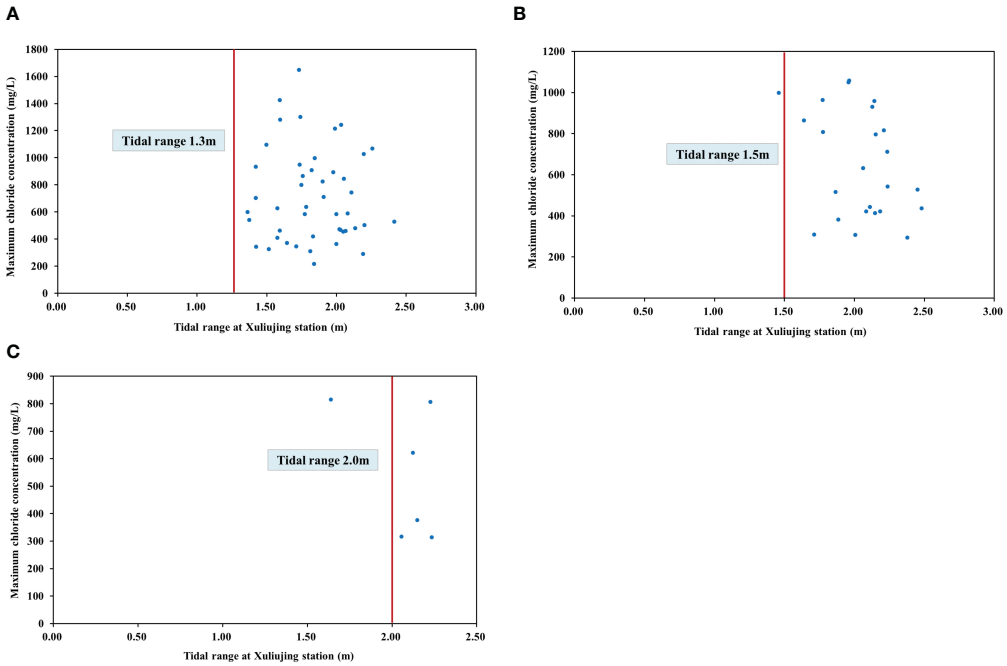

FIGURE 14
Correlation between chloride concentration in different flows at Datong and tidal ranges at Xuliujing: **(A)** Daily average flow at Datong less than 15000 m^3/s; **(B)** Daily average flow at Datong between 15000~20000 m^3/s; **(C)** Daily average flow at Datong larger than 20000 m^3/s.

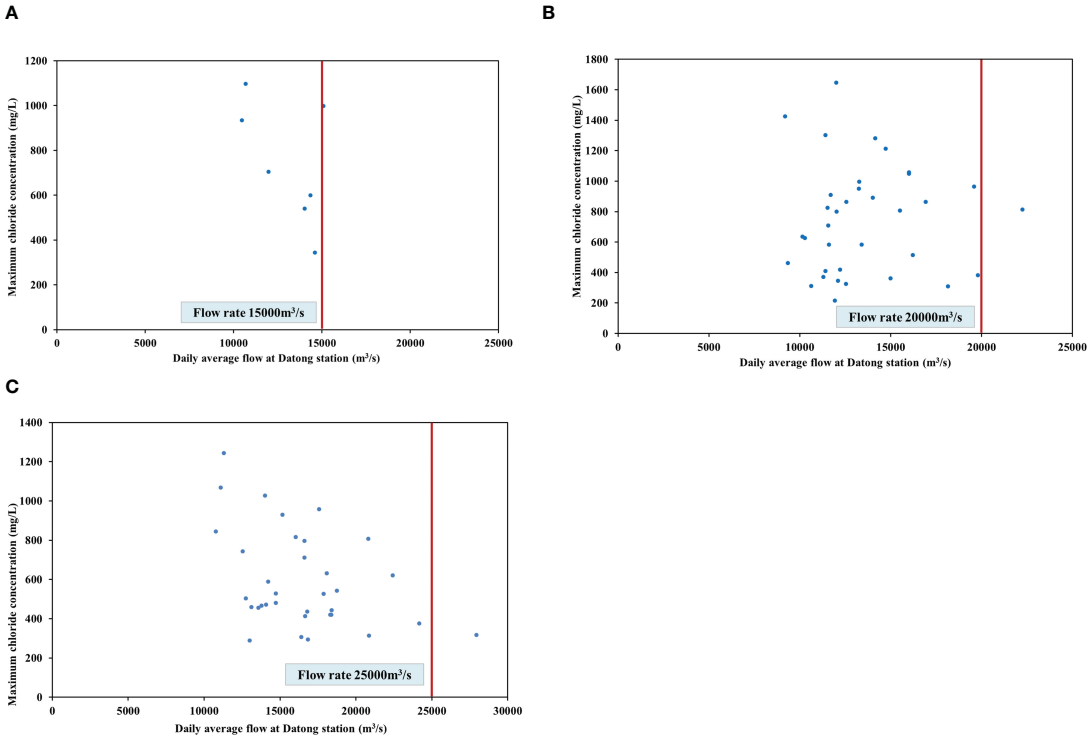

FIGURE 15
Correlation between chloride concentration in different tidal ranges at Xuliujing and daily average flows at Datong: **(A)** Tidal range less than 1.5 m; **(B)** Tidal range between 1.5~2.0 m; **(C)** Tidal range larger than 2.0 m.

(as shown in Figure 16) as the critical flow, which is a dynamic critical threshold. It can be observed from Figure 16 that, under the same duration, the greater the tidal range, the larger the daily flow.

Based on the upper envelope under the durations, the correlation between tidal range and daily flow at Datong station is fitted (as shown in Table 2). It is evident from the correlation that the fitting of each function is relatively good. Based on these correlations, the critical flow at Datong station under a certain standard of non-water intake days at Chenhang Reservoir (7 days) and a certain tidal range can be determined. It should be noted that the correlation obtained under a large number of samples for the duration of seawater intrusion is more reliable, while the correlation obtained under a small number of samples for the duration of seawater intrusion still needs to be confirmed.

Based on the statistical data from 2004 to 2014, the phenomenon of seawater intrusion with a duration of 11 days occurred only 2 times, with a duration of 12 days occurred only 1 time, with a duration of 13 days occurred only 1 time, with a duration of 14 days occurred 0 times, and with a duration of 15 days occurred only 1 time. There were no occurrences of seawater intrusion with a duration of more than 15 days. In summary, due to the small proportion of occurrences of seawater intrusion with a duration of 10 days or more (excluding 10 days) in the samples, no statistical analysis is conducted on the correlation between the tidal range and the daily flow at Datong station for seawater intrusion with a duration of 10 days or more.

It can be observed from the Table 3 that under different durations of seawater intrusion, the critical flow at Datong station corresponding to different tidal ranges at Xuliujing varies, further indicating the correlation between the critical flow at Datong station and the duration of seawater intrusion and the tidal range at Xuliujing.

5 Conclusions

The impact of natural and man-made factors on coastal cities due to seawater intrusion is significant. Identifying controllable key factors is essential for ensuring water supply security. This study selected factors such as daily flow, duration of seawater intrusion, water quality, and tidal level to establish correlations and identify the main influencing factors of seawater intrusion in the Yangtze River Estuary. Furthermore, control methods for safeguarding water supply security were proposed. The main conclusions are as follows:

(1) Seawater intrusion mainly occurs from November to April of the following year, with the highest frequency in the

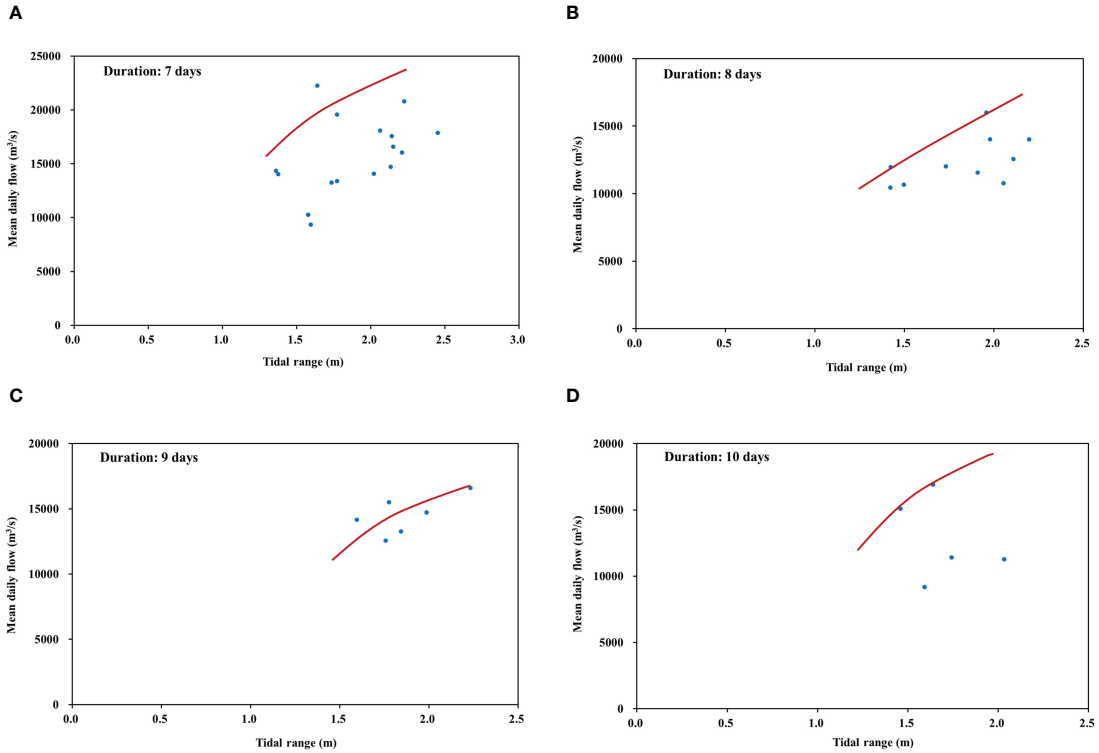

FIGURE 16
Correlation between tidal range and mean daily flow under different durations of seawater intrusion: **(A)** Duration 7 days; **(B)** Duration 8 days; **(C)** Duration 9 days; **(D)** Duration 10 days.

TABLE 2 Correlation between tidal range and daily flow at Datong station under different seawater intrusion durations.

Seawater intrusion duration	Correlation between tidal range and daily flow at Datong station
7 days	$y = 14411 \ln(x) + 9994.5$ $R^2 = 0.93$
8 days	$y = 14941 \ln(x) + 5965.2$ $R^2 = 0.93$
9 days	$y = 6877.6 \ln(x) + 11188$ $R^2 = 0.93$
10 days	$y = 14164 \ln(x) + 3741.8$ $R^2 = 0.97$

months of January to April, particularly in February and March. A few instances of seawater intrusion occur in October and May of the following year, and very few occur in August and September.

(2) By analyzing the important factors affecting the chlorine concentration at the intake (during seawater intrusion), such as the daily flow at Datong station and the tidal range at Xuliujing, the correlation between daily flow and tidal range under different durations of seawater intrusion was determined. The analysis revealed that under specific durations of seawater intrusion, the critical flow required to suppress the seawater increases with the tidal range. The research results provide guidance for emergency scheduling during seawater backflow in the reservoir group centered around the Three Gorges.

TABLE 3 Calculation table for tidal range and daily flow at Datong station under different seawater intrusion durations.

Daily flow at Datong station (m^3/s)		Tidal range (m)				
		1.5	1.7	2.0	2.2	2.5
Seawater intrusion duration	7 days	15838	17641	19983	21357	23199
	8 days	12522	14071	16083	17263	18845
	9 days	12267	13621	15378	16408	17790
	10 days	9485	11258	13560	14910	16720

Data availability statement

The original contributions presented in the study are included in the article/supplementary material. Further inquiries can be directed to the corresponding authors.

Author contributions

YC: Writing – original draft, Writing – review & editing. YX: Writing – original draft, Writing – review & editing. GC: Writing – original draft, Writing – review & editing. MZ: Writing – original draft, Writing – review & editing. TZ: Writing – original draft, Writing – review & editing. XZ: Writing – original draft, Writing – review & editing. YZ: Writing – original draft, Writing – review & editing.

Funding

The author(s) declare financial support was received for the research, authorship, and/or publication of this article. This work is supported by the National Key Research and Development Program 35 of China (Grant No. 2023YFC3206005, 2023YFC3206004); the National Natural Science Foundation of China (Grant No. 52209032). Technological Innovation and Application Development Key Project of Chongqing (Grant No. CSTB2022TIAD-KPX0132).

Conflict of interest

The authors declare that the research was conducted in the absence of any commercial or financial relationships that could be construed as a potential conflict of interest.

Publisher's note

References

Biemond, B., de Swart, H. E., and Dijkstra, H. A. (2023). Mechanisms of salt overspill at estuarine network junctions explained with an idealized model. *J. OF GEOPHYS. RESEARCH-OCEANS* 128, e2023JC019630. doi: 10.1029/2023JC019630

Boumis, G., Moftakhari, H. R., and Moradkhani, H. (2023). Coevolution of extreme sea levels and sea-level rise under global warming. *EARTHS Future* 11, e2023EF003649. doi: 10.1029/2023EF003649

Cao, M. L., Liu, W. F., Xu, B., Wang, L. C., Zhang, Y., and Zhang, Y. (2023). Multi-scenario optimization model for operation of inter-basin water transfer-supply systems considering cost-benefit relationships. *J. OF Water AND Climate Change* 14, 2872–2884. doi: 10.2166/wcc.2023.259

Casillas-Trasvina, A., Zhou, Y. X., Stigter, T. Y., Mussáa, F. E. F., and Juízo, D. (2019). Application of numerical models to assess multi-source seawater intrusion under natural and pumping conditions in the Great Maputo aquifer, Mozambique. *HYDROGEOL. J.* 27, 2973–2992. doi: 10.1007/s10040-019-02053-5

Chen, Q., Zhu, J. R., Lyu, H. H., and Chen, S. L. (2019). Determining critical river discharge as a means to provide water supply security to the Changjiang river estuary, China. *J. OF Coast. Res.* 35, 1087–1094. doi: 10.2112/JCOASTRES-D-18-00165.1

Chen, Y. B., Wang, M. L., Zhang, Y., Lu, Y., Xu, B., and Yu, L. (2023). Cascade hydropower system operation considering ecological flow based on different multi-objective genetic algorithms. *Water Resour. Manag.* 37, 3093–3110. doi: 10.1007/s11269-023-03491-3

Chen, Z. G., Wang, Z. X., Liu, Y. Y., and Wang, S. P. (2018). Estimating net discharge of the Yangtze River into the East China Sea. *Water SUPP.* 18, 1072–1080. doi: 10.2166/ws.2017.181

El-Jaat, M., Hulley, M., and Tétreault, M. (2018). Evaluation of the fast orthogonal search method for forecasting chloride levels in the Deltona groundwater supply (Florida, USA). *HYDROGEOL. J.* 26, 1809–1820. doi: 10.1007/s10040-017-1719-5

He, W., Zhang, J., Yu, X. D., Chen, S., and Luo, J. (2018). Effect of runoff variability and sea level on seawater intrusion: A case study of Nandu river estuary, China. *Water Resour. Res.* 54, 9919–9934. doi: 10.1029/2018WR023285

Hu, S. K., Deng, Z. H., Liu, B. J., Hu, M. C., Xu, B. Y., and Yu, X. (2024). Impact of tidal dynamics and typhoon-induced inundation on seawater intrusion in coastal farms. *Sci. OF THE TOTAL Environ.* 915, 170109. doi: 10.1016/j.scitotenv.2024.170109

Li, D., Liu, B. J., Lu, Y., and Fu, J. Y. (2023). Assessment of changes in severity of compound drought and seawater intrusion events based on a multi-index approach in Pearl River estuary. *HYDROL. PROCESSES* 37, e14986. doi: 10.1002/hyp.14986

Li, H. W., Yang, Q. S., Mo, S. H., Huang, J., Wang, S. M., Xie, R. Y., et al. (2022). Formation of turbidity maximum in the Modaomen estuary of the Pearl river, China: the roles of mouth bar. *J. OF GEOPHYS. RESEARCH-OCEANS* 127, e2022JC018766. doi: 10.1029/2022JC018766

Li, L. J., Zhu, J. R., Chant, R. J., Wang, C. N., and Pareja-Roman, L. F. (2020). Effect of dikes on seawater intrusion under various wind conditions in the Changjiang estuary. *J. OF GEOPHYS. RESEARCH-OCEANS* 125, e2019JC015685. doi: 10.1029/2019JC015685

Liu, B. J., Yan, S. L., Chen, X. H., Lian, Y. Q., and Xin, Y. B. (2014). Wavelet analysis of the dynamic characteristics of seawater intrusion - A case study in the Pearl River Estuary of China. *OCEAN Coast. Manage.* 95, 81–92. doi: 10.1016/j.ocecoaman.2014.03.027

Mei, X. F., Zhang, M., Dai, Z. J., Wei, W., and Li, W. H. (2019). Large addition of freshwater to the tidal reaches of the Yangtze (Changjiang) river. *ESTUARIES AND COASTS* 42, 629–640. doi: 10.1007/s12237-019-00518-0

Mu, D. P., Xu, T. H., and Yan, H. M. (2024). Sea level rise along China coast from 1950 to 2020. *Sci. CHINA-EARTH Sci.* 67 (3), 802–810 doi: 10.1007/s11430–023-1240-x

Paiva, B. P., and Schettini, C. A. F. (2021). Circulation and transport processes in a tidally forced salt-wedge estuary: The Sao Francisco river estuary, Northeast Brazil. *REGION. Stud. IN Mar. Sci.* 41, 101602. doi: 10.1016/j.rsma.2020.101602

Roy, D. K., and Datta, B. (2018). Influence of sea level rise on multiobjective management of seawater intrusion in coastal aquifers. *J. OF HYDROL. Eng.* 23, 04018035. doi: 10.1061/(ASCE)HE.1943-5584.0001680

Tao, Z. J., Chu, A., Chen, Y. P., Lu, S. Q., and Wang, B. (2020). Wind effect on the seawater intrusion in the Yangtze estuary. *J. OF Coast. Res.* 105, 42–46. doi: 10.2112/JCR-SI105-009.1

Wang, M. L., Zhang, Y., Lu, Y., Gao, L., and Wang, L. Z. (2023). Attribution analysis of streamflow changes based on large-scale hydrological modeling with uncertainties. *Water Resour. Manag.* 37, 713–730. doi: 10.1007/s11269-022-03396-7

Wang, M. L., Zhang, Y., Lu, Y., Wan, X. Y., Xu, B., and Yu, Y. (2022). Comparison of multi-objective genetic algorithms for optimization of cascade reservoir systems. *J. Water Clim. Change* 13, 4069–4086. doi: 10.2166/wcc.2022.290

Xiao, H., Tang, Y., Li, H. M., Zhang, L., Ngo-Duc, T., Chen, D. L., et al. (2021). Seawater intrusion into groundwater systems in the Mekong Delta and links to global change. *Adv. IN Climate Change Res.* 12, 342–352. doi: 10.1016/j.accre.2021.04.005

Xu, Y. S., Chen, Y. B., Ren, Y. F., Tang, Z. Y., Yang, X., and Zhang, Y. (2023). Attribution of streamflow changes considering spatial contributions and driver interactions based on hydrological modeling. *Water Resour. Manag.* 37, 1859–1877. doi: 10.1007/s11269-023-03459-3

Yin, K., Xu, S. D., and Huang, W. R. (2018). Estimating extreme sea levels in Yangtze Estuary by quadrature Joint Probability Optimal Sampling Method. *Coast. Eng.* 140, 331–341. doi: 10.1016/j.coastaleng.2018.08.007

Zhang, Y., Yu, L., Wu, S. Q., Wu, X. F., Dai, J. Y., Xue, W. Y., et al. (2021). A framework for adaptive control of multi-reservoir systems under changing environment. *J. Clean Prod.* 316, 128304. doi: 10.1016/j.jclepro.2021.128304

Zhou, D. X., Liu, Y., Feng, Y. K., Zhang, H. Y., Fu, Y. G., Liu, Y. X., et al. (2022). Absolute sea level changes along the coast of China from tide gauges, GNSS, and satellite altimetry. *J. OF GEOPHYS. RESEARCH-OCEANS* 127, e2022JC018994. doi: 10.1029/2022JC018994

frontiers | Frontiers in Marine Science

TYPE Original Research
PUBLISHED 21 May 2024
DOI 10.3389/fmars.2024.1382352

OPEN ACCESS

EDITED BY
Tianyuan Zheng,
Ocean University of China, China

REVIEWED BY
Zhang Bo,
Shandong University of Science and Technology, China
Yunhai Fang,
Hefei University of Technology, China
Zhongbo Wang,
Shantou University, China

*CORRESPONDENCE
Maosheng Gao
gaomsh66@sohu.com
Jianjun Jia
jjjia@sklec.ecnu.edu.cn

RECEIVED 05 February 2024
ACCEPTED 06 May 2024
PUBLISHED 21 May 2024

CITATION
Wang M, Jin B, Liu J, Gao M, Gao J and Jia J (2024) Genetic types and provenance indication of clastic amphibole in the South Yellow Sea. *Front. Mar. Sci.* 11:1382352. doi: 10.3389/fmars.2024.1382352

Genetic types and provenance indication of clastic amphibole in the South Yellow Sea

Mengyao Wang[1], Bingfu Jin[2], Jian Liu[1], Maosheng Gao[1]*, Jianhua Gao[3] and Jianjun Jia[4]*

[1]Qingdao Institute of Marine Geology, China Geological Survey, Qingdao, China, [2]School of Resources and Environmental Engineering, Ludong University, Yantai, China, [3]Ministry of Education Key Laboratory for Coast and Island Development, School of Geography and Ocean Science, Nanjing University, Nanjing, China, [4]State Key Laboratory of Estuarine and Coastal Research, East China Normal University, Shanghai, China

The main focus of studying sediment sources in marine areas is to determine the properties of clastic minerals originating from different rivers. Variations in the characteristics of clastic minerals occur due to differences in the types of source rocks within the watershed. Determining the source rock of clastic minerals in the marine area can improve the accuracy of provenance analysis. Electron probe microanalysis of 258 amphibole grains from six surface stations in the South Yellow Sea (SYS) was conducted to calculate the numerical and characteristic values of cations in the crystal structure. The results showed that amphibole in the SYS is mainly magnesiohornblende (52.2% ~ 81.4%) in the calcic amphibole subgroup, followed by tschermakite. The source rock types of amphibole are mainly different types of magmatic (ultrabasic, basic, and intermediate acidic) and metamorphic rocks. Amphibole derived from intermediate-acid intrusive rocks accounts for a large proportion (>40%). The genetic analysis of clastic amphibole in the SYS showed that most of the medium-acid invading amphibole belong to crust-mantle type, followed by mantle type. Most of the amphibole from metamorphic origins are of medium-low pressure type (± 80%). Combined with electron probe analysis of amphibole from the Huanghe River (the Yellow River, HH) and Changjiang River (the Yangtze River, CJ), the amphibole in the SYS exhibits characteristics inherited from these two rivers. The northern sea area has a strong resemblance to the sediments from the HH, while the southern area is more influenced by sediments supply from the CJ. The central area represents a mixed zone with a higher sediment supply from the HH. The clastic amphibole deduces the type of source rock in different watersheds, serving as a crucial link between the source rock, watershed, and marine area, providing a basis for provenance analysis.

KEYWORDS

sedimentary provenance, clastic amphibole, source rock, genesis of crystallization, South Yellow Sea

1 Introduction

Sediments transported by rivers rapidly accumulate in estuaries, then are resuspended into the sea by the action of waves and tides, and transported over long distances by water mass and circulation, with most of them settling in the shelf areas of marginal seas (Milliman and Meade, 1983; McKee et al., 2004). The western shelf area of the South Yellow Sea (SYS) is a convergence zone with a wide shelf and multiple terrestrial sediments. The sediments from the Huanghe River (HH), Changjiang River (CJ), and several other small and medium-sized rivers converge, resuspend, transport, and deposit in this area, making it a natural laboratory for studying marine sedimentary environments and terrestrial sediment characteristics.

Since the 1980s, significant progress has been made in the study of the differentiation and distribution of terrestrial sediments in the SYS shelf area (Qin, 1989; He, 2006). This includes analyzing the differences in sediment composition between the CJ and the HH based on heavy mineral assemblages and the proportion of clay minerals, as well as determining the distribution area of river-derived clay minerals in the sea (Soo-Chul et al., 2000; Han et al., 2022). By analyzing whole samples or fine-grained geochemical elements, various indices such as trace elements, rare earth elements, and their ratios have been identified to discriminate river-derived sediments in the SYS (Yang and Li, 2000; Yang and Youn, 2007; Zhou et al., 2015). Additionally, studies have found that parameters such as Ti, Cr/Th, Ti/Nb, and Zr/Nb in sediments can reliably identify the contributions of the CJ, the HH, and Korean rivers to the sediment composition in the Yellow Sea (Yang et al., 2003a, b). However, the high degree of mixing of different materials in whole samples or the influence of different mineral types at limited grain sizes may introduce uncertainties in source analysis.

With the advancement of provenance analysis, some heavy minerals have been found to reflect differences in source rock types and origins, providing a basis for determining specific material sources (Morton et al., 2005; Nie et al., 2010; Safonova et al., 2010; Krippner et al., 2016; Wang et al., 2018; Shang et al., 2021; Jin et al., 2022). Among them, the combination of geochronology and mineral geochemical elements of garnet can identify the sources of magmatic origin components, while monazite can be used to analyze the sources of metamorphic origin components (Guo et al., 2020). Zircon U-Pb ages can quantitatively analyze the contribution of the Huanghe River to the Changjiang River subaqueous delta (Shang et al., 2021). Yang et al. (2004) conducted a study on the chemical composition of magnetite in surface sediments in the eastern South China Sea, TiO_2-Al_2O_3-MgO genetic classification diagram method indicates that the magnetite in the sediments is mainly derived from intermediate-acidic and basic magmatic rocks. However, most of these individual minerals are accessory minerals and only exist in certain types of rocks, which may result in the loss of some source signals.

Amphibole, as one of the major rock-forming minerals, is widely distributed in sediments from rivers and marine areas worldwide (Carver et al., 1972; Yue et al., 2018; Fan et al., 2021). In addition, amphiboles in rivers at mid to high latitudes have low weathering degrees and show little variation in chemical elements. Amphiboles derived from different rocks under different diagenetic and mineralization conditions have specific compositions and structural characteristics, which can clearly reflect the differences in source rock types and sedimentary environments, providing a basis for provenance analysis (Liu, 1986; Zhao et al., 1993; Hawthorne et al., 2012; Jin et al., 2013; Fan et al., 2021). The Mg-(Na+K+Ca)-(Fe^{2+}+Fe^{3+}) ternary diagram can be used to differentiate the genetic types of amphiboles (Chen et al., 1988). The analysis of different rivers such as the Liaohe River, Yalu River, Huanghe River, Changjiang River, and Huaihe River, have provided a systematic study of the origin characteristics, crystallization temperature and pressure conditions, and geochemical features of amphiboles in mid-high latitude rivers in China (Jin et al., 2014; Wang, 2019; Fan et al., 2021). With the deepening of research on the source-to-sink system, further studies on the sedimentary clastic amphiboles in marginal seas and continental shelves are needed.

In this study, we analyze the source rock types and depositional environments of clastic minerals in the continental shelf area, tracing them back to the rock types in the watershed region for provenance identification. Using this approach, we conduct electron probe element analysis on clastic amphiboles in the SYS, classify the amphibole species, and match them with the characteristics of riverine amphiboles. This allows us to verify the backward tracing of riverine sediments from sink to source, connecting the watershed-continental shelf sediment transport system. This research has significant implications for understanding the evolution of this important source-sink system from rivers to the ocean.

2 Samples and methods

2.1 Samples

This study utilized surface sediment samples from the western South Yellow Sea. Six groups of sediment samples were collected from the SYS during the summer comprehensive cruise in 2014, as part of the Major Scientific Research Program of the Ministry of Science and Technology. DGPS positioning was used, the accuracy was about 1 m. The sediment samples were collected using a box corer with a sampling volume of about 2 kg for each sample, which was stored in self-sealing bags. The study area and sampling points are shown in Figure 1.

2.2 Methods

2.2.1 Clastic amphibole selection

Approximately 500 g of each surface sediment samples from the SYS were collected. Wet sieving was performed using sieves with apertures of 3Φ (0.125 mm) and 4Φ (0.063 mm). The sediment, which had been sieved to a grain size of 3Φ - 4Φ, was subsequently dried and its mass was measured. Following this, the resulting fine-grained clastic sand was subjected to a light-heavy mineral separation process using bromoform ($CHBr_3$), which has a density of 2.89 g/cm^3. The mineral separation lab was maintained at a constant temperature of 20°C, and the sediment was stirred three times with a glass rod at 15-minute intervals, combined with centrifugal force to allow heavy minerals to

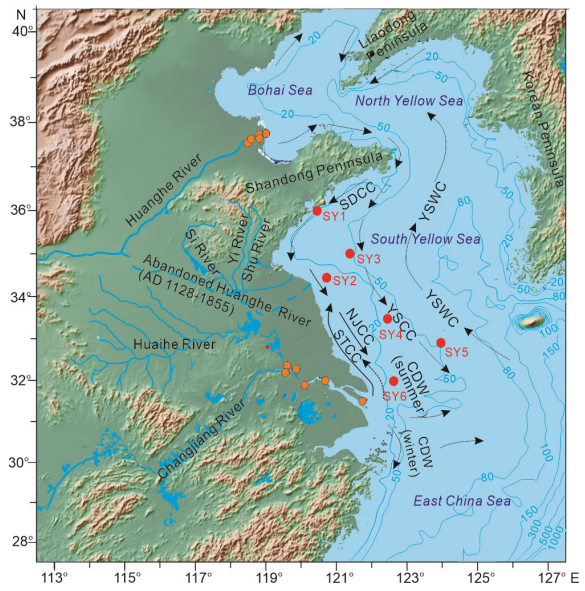

FIGURE 1
Location map showing the study area and sampling sites of sediments. The red dots in the figure were the sampling points of the surface samples of the South Yellow Sea in this paper. Yellow dots were watershed sampling points, and the data is from Wang, 2019; Fan et al., 2021. Circulation information cited in Qiao, 2011. SDCC, Shandong Coastal Current; YSWC, Yellow Sea Warm Current; YSCC, Yellow Sea Coastal Current; NJCC, North Jiangsu Coastal Current; STCC, Subei tide-induced coastal current; CDW, Changjiang Diluted Water.

settle. After 8 hours of settling, the floating and settled minerals were separated, washed with anhydrous ethanol, dried, and weighed to obtain the light and heavy mineral samples.

2 g of mineral samples were placed in diiodomethane (CH_2I_2, density of 3.32 g/cm^3) for amphibole flotation. The floated samples were rinsed by dimethyl sulfoxide, dried, and then examined under a stereomicroscope for the selection of amphibole mineral particles. In each sample group, 200 randomly selected amphibole particles were chosen, excluding those with severe alteration, weathering, or inclusions.

2.2.2 Amphibole electron microprobe elemental analysis

As a means of *in-situ* micro analysis, electron probe analysis can rapidly determine the elemental composition of solid sample surfaces (Reed, 1996). We conducted *in-situ* micro analysis on each amphibole grain to test for the content of main elements such as SiO_2, FeO, MgO, CaO, Al_2O_3, Na_2O, TiO_2, K_2O, MnO. Using 23 oxygen atoms as a reference, the cationic numerical values and characteristic values in the amphibole crystal structure formula were calculated to classify the amphibole, assign names, and determine the source rock type.

Each sample was randomly selected to obtain approximately 60 grains of amphibole for thin section preparation. The mineral grains were first mounted on double-sided adhesive tape and covered with a target mold coated with petroleum jelly. Epoxy resin and curing agent were poured into the mold and cured in a constant temperature oven (60°C) for 24 hours. The amphibole grains were then polished to expose a flat surface, approximately 1/3 or 1/2 of the grain, and coated with a carbon film about 20 nm thick. Subsequently, *in situ* geochemical analysis of the amphibole was conducted using the electron probe microanalyzer (JEOL JXA-8100) equipped with four spectrometers. The quantitative analysis of amphibole geochemical elements was performed under the following conditions: acceleration voltage of 15 kV, beam current of 10 nA, and beam spot diameter of 3 μm. The standard samples used were as follows: jadeite (Na), olivine (Mg), albite (Al, Si), orthoclase (K), diopside (Ca), rutile (Ti), rhodonite (Mn), and hematite (Fe). The aforementioned experiments were carried out at the Laboratory of Marine and Coastal Geology, Third Institute of Oceanography, Ministry of Natural Resources.

3 Results

3.1 Geochemical elements characteristics of amphiboles in the SYS

A total of 258 very fine sand-sized (3Φ - 4Φ) clastic amphibole grains from six stations in the surface sediments of the SYS were analyzed using an electron probe microanalyzer to determine the constant elements in each amphibole grain (Table 1). The clastic amphiboles in the South Yellow Sea have the highest SiO_2 content, with an average content exceeding 45% and a maximum value of 46.9%. The next highest element is FeO, with a content ranging from 14.6% to 16.3%, showing a decreasing trend from north to south. The average content of MgO and CaO in the SYS amphiboles is above 11%, with little difference between the two. The content of MgO increases from north to south, opposite to the trend of FeO.

TABLE 1 Average content of major elements in clastic amphibole in the surface of the South Yellow Sea (%).

Sample	SiO_2	FeO	MgO	CaO	Al_2O_3	Na_2O	TiO_2	K_2O	MnO
SY1	45.92	16.29	10.61	11.25	9.11	1.30	1.13	0.94	0.32
SY2	46.74	15.91	10.39	11.46	9.45	1.22	0.72	0.58	0.30
SY3	44.74	15.55	10.58	11.26	10.28	1.28	1.17	0.90	0.33
SY4	45.75	15.52	11.18	11.37	9.77	1.25	0.70	0.69	0.34
SY5	46.87	15.33	11.26	11.51	9.34	1.12	0.62	0.59	0.35
SY6	45.68	14.63	12.19	11.31	10.08	1.28	0.67	0.67	0.32

10.3389/fmars.2024.1382352

The average content of Al_2O_3 is around 9.7%, varying between 9.1% and 10.3%. The content of Na_2O shows little variation and is below 1.3%. The average content of TiO_2 and K_2O is relatively low, at 0.8% and 0.7% respectively, both less than 1%. The lowest content is MnO, ranging from 0.30% to 0.35%, with an average content of 0.33%. Overall, clastic amphiboles in the surface sediments of the SYS exhibit high silicon, high calcium, high iron and magnesium, and low sodium and potassium content in different locations.

3.2 Classification of amphibole species in the SYS

The charge arrangement and B-site cation types, recognized by the International Mineralogical Association (IMA), are used for the classification and naming of amphiboles (Hawthorne et al., 2012). The sum of B-site cations is $\Sigma B = {}^{B}Li + {}^{B}Na + {}^{B}\Sigma M^{2+} + {}^{B}Ca$, where ${}^{B}\Sigma M^{2+} = {}^{B}Mg + {}^{B}Fe^{2+} + {}^{B}Mn^{2+}$. It was found that among the 258 very fine sand-sized amphibole grains in the surface sediments of six stations in the South Yellow Sea, ${}^{B}(Ca + \Sigma M^{2+})/\Sigma B \geq 0.75$ and ${}^{B}Ca/\Sigma B \geq B\Sigma M^{2+}/\Sigma B$, indicating that they belong to the calcium amphibole subfamily.

To further classify the amphibole species, the cation values in the A-site and C-site of the amphibole crystal structure was used as a criterion, with the total charge written as: $A+ = {}^{A}(Na + K + 2Ca)$, $C+ = {}^{C}(Al + Fe^{3+} + 2Ti^{4+})$, where cations are expressed in apfu. The diagram uses ${}^{C}(Al + Fe^{3+} + 2Ti^{4+})$ apfu as the x-axis and ${}^{A}(Na + K + 2Ca)$ apfu as the y-axis, completing the nomenclature of amphibole species in the South Yellow Sea (Figure 2). Finally, the number of each amphibole species was counted to calculate their respective proportions.

The quantity and content of various amphibole in surface samples of the SYS were classified and analyzed. Among the samples, the content of magnesiohornblende was the highest, ranging from 52.2% to 81.4%, with the majority being above 70%. The average content of magnesiohornblende in the northern part of the SYS (SY1, SY2, SY3) was 70%, while in the southern part (SY4, SY5, SY6) it was 72%. The second most abundant amphibole was tschermakite with the highest content found in sample SY6 at 35.3%, and the lowest in sample SY1 at 18.4%. The average percentage of tschermakite in surface sediments of the South Yellow Sea was 23.4%, showing an increasing trend from north to south. Additionally, a certain amount of pargasite was found in the samples, with the highest content of 21.7% in SY3, and an average of around 3% in SY1, SY4, and SY5. Furthermore, SY1 also contains 4.1% of tremolite.

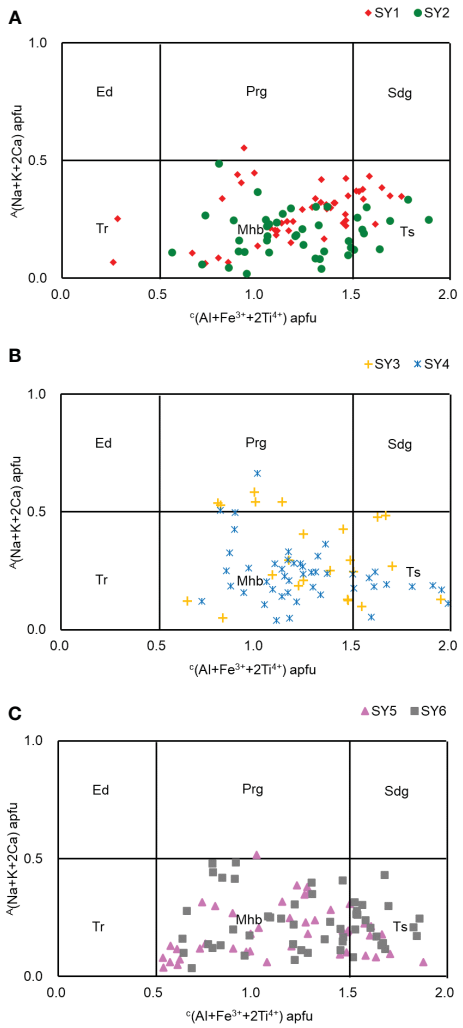

FIGURE 2
Classification of clastic amphibole in the surface sediments of the South Yellow Sea (referenced from Hawthorne et al., 2012). Ed, Edenite; Prg, Pargasite; Sdg, Sadanagaite; Tr, Tremolite; Mhb, Magnesiohornblende; Ts, Tschermakite. **(A–C)** represent the different classification of amphibole from different sites in the South Yellow Sea.

3.3 Source rock types indicated by amphibole in the SYS

In amphibole, Ti and Si are generally present in the form of tetravalent cations in the T and C sites, which are constant elements in amphibolite. Ti is greatly influenced by changes in crystallization temperature, with higher temperatures in crystal formation and geological processes resulting in higher Ti content. The Si content in amphibolite varies in different magma types, including ultrabasic, basic, intermediate, acidic or alkaline igneous rocks, as well as different metamorphic rocks (Chen et al., 1988). Therefore, the Si-Ti variation diagram can clearly reflect the source rock genesis type of amphibolite.

Projecting the Si and Ti cation counts of amphibole in the surface samples of the SYS onto a scatter plot of amphibole genesis (Figure 3). The majority of amphiboles in surface samples from the South Yellow Sea are derived from medium-acidic intrusive rocks and metamorphic rocks, with a small portion originating from ultrabasic-basic magmatite and retrogressive metamorphic or metasomatic rocks, and a few amphiboles derived from volcanic rocks. In terms of details, the proportions of different rock types indicated by amphiboles vary in different regions of the SYS. For example, SY1 from the northern part of the SYS, the content of amphiboles in medium-acidic intrusive rocks is 28.3%, and the proportion of metamorphic clastic amphiboles is around 24%. SY3 from the northern part of the estuary of the Huanghe

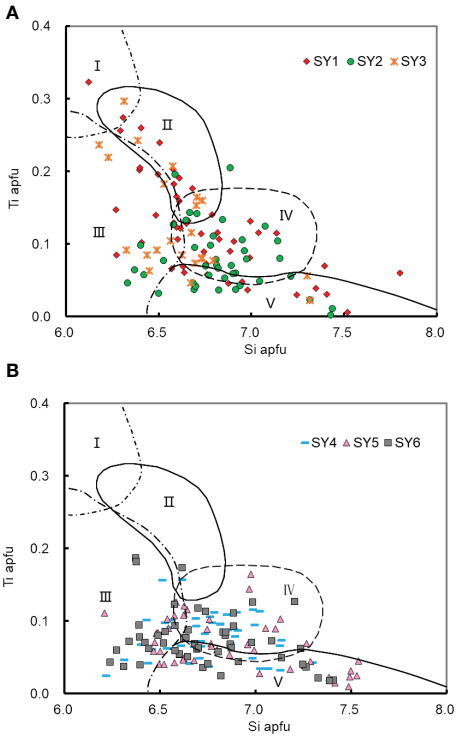

FIGURE 3
Si-Ti variation diagram and genetic classification of amphiboles in surface sediments of the South Yellow Sea (referenced from Chen et al., 1988). I = Magmatic amphiboles in volcanic rocks; II = Magmatic amphiboles in ultrabasic-basic rocks; III = Amphiboles in metamorphic rocks; IV = Amphiboles of magmatic genesis in mid-acid intrusive rocks; V = Amphiboles of retrogressive metamorphic or metasomatic genesis, **(A, B)** represent the different genetic types of surface samples from different sites in the South Yellow Sea.

River, which has similar characteristics to SY1, has a content of metamorphic and medium-acidic intrusive amphiboles of 32%; both samples have a few amphiboles falling into Class I, which belong to volcanic amphiboles in volcanic rocks. The content of amphiboles of different origins in samples SY2 and SY4 is similar, with amphiboles in medium-acidic intrusive rocks exceeding 50%. In comparison, SY2 has more retrogressive metamorphic or metasomatic genesis amphiboles than SY4. SY5 and SY6 are located in the southeastern and southern parts of the SYS, respectively. The content of amphiboles in medium-acidic intrusive rocks is around 43%, with the rest being metamorphic amphiboles; both samples have very little content of ultrabasic-basic volcanic rock amphiboles.

4 Discussion

4.1 Genetic analysis of clastic amphibole in SYS

4.1.1 Genesis of magmatic amphibole

In the surface sediments of different stations in the South Yellow Sea, 120 medium-acid intrusive amphiboles were projected onto a Ca-Fe^{2+}+Fe^{3+}-Mg ternary diagram, and divided into different magma source types (Figure 4). Among them, the crust-mantle hybrid amphiboles accounted for 80% in samples SY1 and SY2, with amphibole species being magnesiohornblende and edenite; the mantle-derived amphibole accounted for 20%, all of which were magnesiohornblende species in the calcium amphibole subfamily. Similarly, in SY3 located in the northern sea area of the study area, the proportion of crust-mantle hybrid amphibole was 77.8%, mostly edenite and magnesiohornblende; the mantle-derived amphibole accounted for 22.2%, and the amphibole species belonged to magnesiohornblende. SY4 and SY5 located in the southern part of the western shelf area of the SYS, the magma source types of medium-acid intrusive amphiboles were similar, with the proportions of crust-mantle hybrid amphiboles being 88.5% and 88.2% respectively, and the proportions of mantle-derived amphiboles being less than 12% in both samples. SY6 was located in the offshore area near the estuary of the CJ with the proportion of crust-mantle hybrid amphiboles from medium-acid intrusive magma sources being 87%, and the proportion of mantle-derived amphiboles being 13%. In summary, the medium-acid intrusive clastic amphiboles in different stations in the SYS are mostly crust-mantle hybrid amphiboles, followed by mantle-derived amphiboles, and no crust -derived amphiboles were found. The proportion of mantle-derived amphiboles in the northern part of the western shelf area of the SYS is higher than that in the southern part, with an average difference of about 10%.

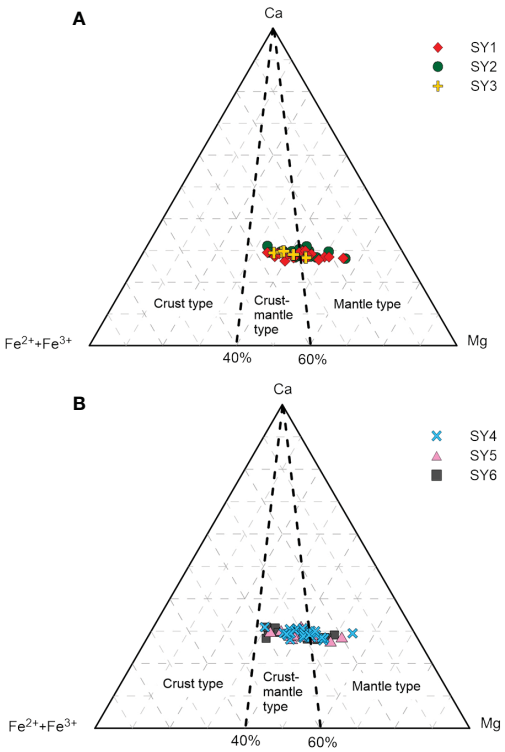

FIGURE 4
Magmatic source species of acidic intrusion type igneous amphibole in the surface sediments of the South Yellow Sea (referenced from Xue, 1991). **(A, B)** represent the magma source types of surface samples from different sites in the South Yellow Sea.

4.1.2 Genesis of metamorphic amphibole

During metamorphism, high content of ^{IV}Al in amphibole indicates a strong isomorphism with Si, representing a higher temperature during mineral formation; high content of ^{VI}Al indicates greater pressure during mineral formation (Xue, 1991). By projecting the metamorphic amphiboles (70 particles) into a diagram showing the relationship between ^{VI}Al-Si regional metamorphic pressure (Figure 5), it can be observed that most of the surface metamorphic amphiboles in the SYS have pressures below 500 mPa, indicating a medium to low-pressure metamorphic origin. A small amount of amphiboles belong to a high-pressure metamorphic origin. Specifically, all the metamorphic amphiboles in sample SY1 are of low-pressure origin, while sample SY3 has the highest proportion of high-pressure metamorphic amphiboles, accounting for 33%. Amphiboles of high-pressure metamorphic origin in samples SY4 and SY6 rank second, accounting for 25% and 23.5% respectively. The content of high-pressure metamorphic amphiboles in SY2 and SY5 is 16.7% and 15.4% respectively, showing a trend of lower content of nearshore high-pressure metamorphic amphiboles overall.

4.2 Significance of the provenance of amphibole in the SYS

4.2.1 Identification of seaward stream sediments

The electron probe element analysis of clastic amphibole from the Huanghe River and Changjiang River has been systematically studied. There are differences in the FeO and MgO contents of amphibole from the Changjiang and Huanghe rivers. The FeO and MgO contents in amphibole from the CJ are 14.4% and 12%, respectively, while those from the HH are 16.1% and 10.6%, respectively (Jin et al., 2013; Wang, 2019; Fan et al., 2021). When projecting the amphibole from different stations in the South Yellow Sea onto a FeO-MgO scatter plot (Figure 6A), distinct zones are observed for amphibole from the CJ and HH. The samples from stations (SY1, SY2, and SY3) in the northwestern part of the South Yellow Sea are closer to the HH, while the SY6 sample in the southern research area of the Yellow Sea is located near the CJ, indicating a greater influence from the CJ in this region. The SY4 and SY5 samples are located between the CJ and HH, indicating a combined influence from both rivers. Among them, the SY4 sample tends to be more influenced by the Huanghe River, while the SY5 sample is more influenced by the CJ.

The clastic amphibole in the HH and CJ originates from different types of magmatic and metamorphic rocks. By analyzing the proportions of source rock types indicated by clastic amphibole at the estuaries of the CJ and HH, it is found that the content of clastic amphibole of metamorphic origin in the CJ is slightly higher than that in the HH, accounting for 56.9% and 45.4% respectively. The Huanghe River, on the other hand, is characterized by a higher content of clastic amphibole of magmatic origin, accounting for over 54% (Figure 6B). Regarding the content of source rock types indicated by clastic amphibole in different stations in the SYS, samples from SY1, SY2, and SY3 located in the northern part of the western shelf area of the SYS are closer to the characteristic composition of the HH source rock types. The amphibole in these samples are mostly columnar and short columnar, appearing in dark green, grass green, and occasionally brown colors, with subangular shapes and some subrounded shapes, exhibiting similarities to the characteristics of amphibole s in Huanghe River sediments, indicating a significant influence from the HH.

The sediment of the HH is influenced by the Shandong Coastal Current (SDCC), flowing eastward from the northern part of the

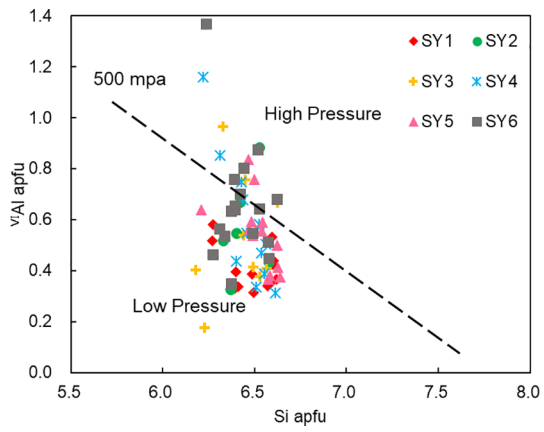

FIGURE 5
Illustration of the metamorphic genesis of amphibole ^{VI}Al-Si in the surface of the South Yellow Sea (referenced from Johnson and Rutherford, 1989).

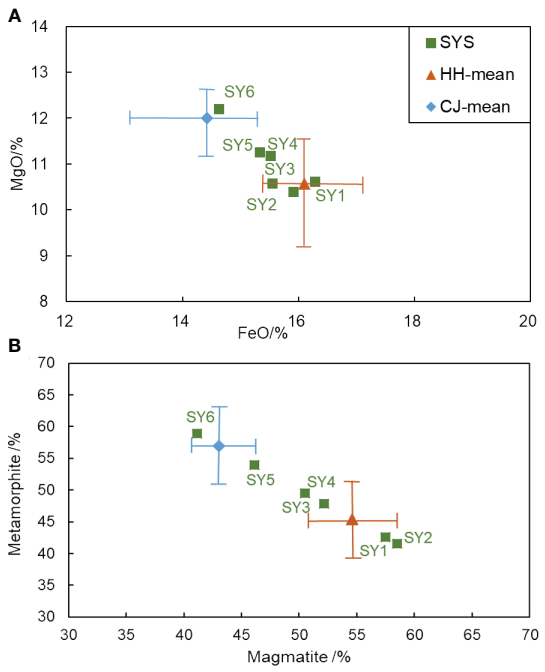

FIGURE 6
Scatterplot of provenance identification of amphibole in the South Yellow Sea (SYS). **(A)**, FeO-MgO content; **(B)**, proportion of source rock types. Average value of Huanghe River (HH-mean) and Changjiang River (CJ-mean) referenced from Jin et al., 2013; Wang, 2019; Fan et al., 2021.

Shandong Peninsula along the Bohai Bay and turning south at Chengshan Head, entering the SYS; then flowing southward along the Subei tide-induced coastal current (STCC), with the front reaching as far as near 30°N (Qin et al., 2018). The central region of the SYS is influenced by both the HH and the CJ. In sample SY4, the average proportions of clastic amphibole of magmatic and metamorphic genesis are 50.5% and 49.4% respectively, with a larger contribution from the HH. In sample SY5, the average proportions of clastic amphibole of magmatic and metamorphic genesis are 46.1% and 53.9% respectively, indicating a larger contribution from the CJ.

SY6 shows similar characteristics to the CJ in terms of the proportions of source rock types of clastic amphibole, with a higher proportion of clastic amphibole of metamorphic origin than magmatic origin, indicating that the southern sea area of the SYS is mainly supplied by the CJ. Furthermore, in SY6 sample, the amphiboles are predominantly columnar, green in color with some light green, and a relatively higher proportion of brown amphiboles. They exhibit poor roundness, subangular shapes, low degree of weathering, and are more similar to the characteristics of amphibole particles in the CJ sediments. The sediment entering the SYS from the CJ mainly undergoes long-distance transportation under the influence of the Changjiang Diluted Water (CDW), Subei tide-induced coastal current (STCC), and the Yellow Sea Warm Current (YSWC) (Qiao, 2011). The northward expansion of these water masses is significantly influenced by the wind field, with the East Asian monsoon playing an important role in the material entering the SYS from the CJ (Hori, 2001).

In summary, the northwestern part of the South Yellow Sea shelf area (SY1, SY2, and SY3) is influenced by the sediments from the HH, while the southern sea area (SY6) is mainly supplied by the CJ. The central part of the study area (SY4) is a mixed zone of sediments from the HH and CJ, with a slightly higher supply of sediments from the HH. In the southeastern part (SY5), the supply of sediments from the CJ is slightly higher than that from the HH. Furthermore, both the HH and the CJ contain calcic amphiboles, mainly consisting of magnesiohornblende. These amphiboles are predominantly derived from medium-acid intrusive rocks, followed by metamorphic rocks and retrograde or metasomatic rocks. The amphiboles derived from medium-acid plutonic rocks are mostly of crust-mantle origin, followed by mantle origin. Most of the metamorphic-derived amphiboles belong to the medium-low pressure metamorphic type (Fan et al., 2021). The above characteristics of amphiboles in rivers are reflected in the SYS. Therefore, the types and genetic characteristics of amphiboles are well inherited from rivers to the sea, making them a "powerful tool" for provenance analysis.

4.2.2 Tracing of source rock types

Tracing the bedrock and sediment types in the areas where the HH and CJ (Figure 7). The main source of sediment in the HH comes from the Loess Plateau in the middle reaches of the river, which covers about 2/3 of the total area of the Huanghe River basin (Wu et al., 2020). The sediment consists mainly of thick loess deposits, ranging from 100 to 200 meters in thickness, with some

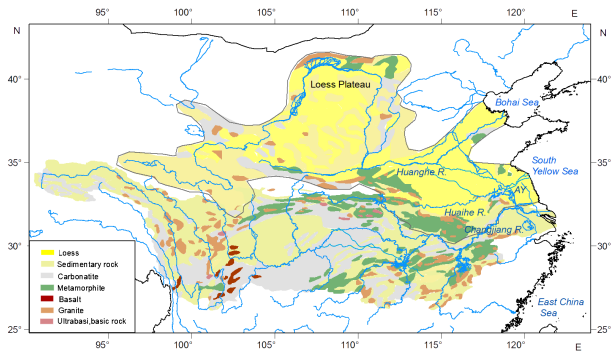

FIGURE 7
Geological map of the Changjiang, Huanghe - Huaihe rivers basin. Modified from Liu and Wang, 2002.

Triassic and Cretaceous sandstone debris. The grain size and mineral composition of the HH sediment largely inherit the characteristics of the loess. The majority of the amphiboles in the river also originate from the loess, which in turn originated from the Gobi Desert and surrounding orogenic belts in western China, where Paleozoic granitic rocks and pre-Cambrian metamorphic rocks (mainly gneiss) are widely developed (Liu, 1985). In addition, the magmatic rocks in the HH basin are fully developed, and granite is widely exposed, while there are also some metamorphic rocks, limestone and clastic rocks (Zhai, 2012). This results in a diverse range of amphibole types and complex origins in the HH, making it a representative of the mineral composition of the crust in the mid-latitude Asian continent.

In the Changjiang River basin sedimentary rocks, metamorphic rocks and magmatic rocks are exposed, and the tributaries flow through various geological structural zones, and the different layers are well-developed in different areas, resulting in a complex and diverse range of rock types (Ministry of Water Resources, 1999). In the upper reaches of the CJ, the prominent rock formations are the Emei Mountain basalt and the Neogene granite. Other exposed rock formations include carbonate rocks, metamorphic sandstone, red clastic rocks, and potassium-rich granite (Hou et al., 1999). In the middle reaches of river, the main rock types are metamorphic rocks and Early Paleozoic medium-acid intrusive rocks. Quaternary loose sediments and lacustrine sedimentary rocks are widely distributed, with fewer occurrences of carbonate rocks and sporadic occurrences of ultrabasic-basic rocks (Yang and Li, 1999). In the lower reaches of the CJ, the dominant rock type is Quaternary loose sediments, with a small amount of Cretaceous medium-acid intrusive rocks and acidic magmatic rocks (Chen et al., 2001). The sediment in the CJ mainly originates from the middle and upper reaches, where basic volcanic rocks and calcium-magnesium carbonate are widely distributed in the upper reaches, and the middle reaches are characterized by abundant medium-acid intrusive rocks and metamorphic rocks (Vezzoli et al., 2016). These areas are also associated with extensive magmatic activity, hydrothermal activity, and metamorphism, which are the main causes of the development of amphiboles in the CJ. The clastic amphiboles in the HH and CJ estuaries inherit the characteristics of their source rocks,

and can be used as geochemical trace element indicators to further determine the contribution and diffusion range of riverine sediments in the marine area.

4.3 Follow-up research

The South Yellow Sea is a region where multiple sources of sediments converge. It is influenced not only by the Huanghe and Changjiang rivers, but also by medium and small - sized rivers, residual sediments, offshore or coastal erosion materials, atmospheric transport, and even cosmic dust. Among these, cosmic dust can be ignored due to its negligible proportion. Meanwhile, there is a lack of suitable end-member samples for atmospheric transport, submarine residual sediments, and coastal erosion materials, making it difficult to identify end-member sources. In addition, the sediments from the open ocean in the SYS are mostly biogenic siliceous and calcareous clay.

The South Yellow Sea is influenced by multiple small and medium-sized rivers such as the abandoned Huanghe River, Huaihe River, and peninsula rivers (Liaodong Peninsula, Shandong Peninsula, Korean Peninsula). The abandoned Huanghe River, formed by historical channel changes of the Huanghe River, has sediment characteristics similar to the Huanghe River. The sediment transport of the Huaihe River is only 7.2 Mt yr^{-1}, with 70% of the sediment entering the Changjiang River and flowing into the sea (Liu et al., 2008). The peninsula rivers have short flow paths and steep gradients, and their sediment supply to the sea is mainly composed of fine sand, making them one of the main sources of coarse-grained sediment in the marginal sea area. Especially in the Shandong Peninsula, which extends deep into the Yellow Sea, the small and medium-sized rivers have long-term stability in delivering land-derived clastic sediments to the sea. Compared to the vast river basins composed of numerous tributaries of major rivers, the Shandong Peninsula has a smaller drainage area, lower complexity of lithology, and relatively uniform natural conditions such as climate and hydrodynamics, making it more suitable for the analysis of end-member characteristics under limited boundary conditions.

Future research can focus on analyzing the content of multiple grain-size heavy minerals and extracting the characteristic identification of amphibole elements that are unique to the small and medium-sized rivers in the Shandong Peninsula. This will help establish a heavy mineral-amphibole provenance tracer system and a mathematical model for quantitative estimation, deepening our understanding of the impact and contribution of the Shandong Peninsula as a source of sediment on the Yellow Sea shelf.

5 Conclusions

(1) Through electron probe testing of the major elements of amphiboles in the SYS, it was found that clastic amphiboles have a general characteristic of high Si and Ca content, high Fe and Mg content, and low Na and K content. The clastic amphiboles belong to the calcic amphibole subfamily, predominantly consisting of magnesiohornblende with a content exceeding 70%. Tschermakite exhibits the second highest abundance, while tremolite and pargasite are present in varying quantities.

(2) Most of the amphibole in the SYS originates from medium-acidic intrusive rocks and metamorphic rocks. Among them, the amphibole in medium-acidic intrusive rocks is mostly mantle-crust type, followed by mantle type, and a few are derived from crustal sources. The amphibole of metamorphic origin is mostly formed under pressures below 500 mPa, belonging to medium-low pressure metamorphic processes.

(3) The genesis characteristics of amphibole in the SYS were compared with those of the HH and CJ, the source rock types in these two river-basins were traced, which confirmed that the main source of the study area sediments are from these two rivers. The western shelf area of the SYS is influenced by different river, forming distinct zones. The northern sea area is influenced by the HH, while the southern sea area is mainly supplied by the CJ. The central area is a mixed zone of HH and CJ, with slightly higher supply from the HH. In the southeastern area, the supply of CJ is slightly higher than that of the HH.

(4) The amphibole inherits different source rock types from various river basins, establishing a common link between the source rocks, watersheds, and marine sediments, making it a powerful tool for terrestrial-marine provenance analysis. Future research should also consider other sediment sources, such as the supply from medium and small-sized rivers in the Shandong Peninsula, in order to deepen and expand the study on the influence and contribution of multiple sources of material in the marine area.

Data availability statement

The raw data supporting the conclusions of this article will be made available by the authors, without undue reservation.

Author contributions

MW: Data curation, Writing – original draft. BJ: Conceptualization, Methodology, Writing – review & editing. JL: Validation, Writing – review & editing. MG: Funding acquisition, Supervision, Writing – review & editing. JG: Resources, Supervision, Writing – review & editing. JJ: Funding acquisition, Writing – review & editing.

Funding

The author(s) declare financial support was received for the research, authorship, and/or publication of this article. This work was financially supported by the National Natural Science Foundation of China (Grant No. U2106203; No. 41977173; No. 41330964; No. 41876092), the National Geological Survey Project of China Geology Survey (No. DD20221775), Qingdao Postdoctoral Applied Research Project (QDBSH20240102122) and the China-ASEAN maritime cooperation fund (Cooperative researches on the

marine geo-environments and geo-hazards in the Yangtze River and the Red River deltas).

Conflict of interest

The authors declare that the research was conducted in the absence of any commercial or financial relationships that could be construed as a potential conflict of interest.

Publisher's note

References

Carver, R., Douglas, L., and Yoshiki, S. (1972). Procedures in sedimentary petrology. *Soil Sci.* 114, 500. doi: 10.1097/00010694-197212000-00027

Chen, G. Y., Sun, D. S., and Yin, H. A. (1988). *Genetic mineralogy and prospecting mineralogy* (Chongqing: Chongqing Press).

Chen, Z. Y., Li, J. F., Shen, H. T., and Wang, Z. H. (2001). Yangtze River of China: historical analysis of discharge variability and sediment flux. *Geomorphology* 41, 77–91. doi: 10.1016/S0169-555X(01)00106-4

Fan, S., Jin, B. F., Yue, W., Dang, L. L., Wang, M. Y., and Kong, Q. X. (2021). Type and genesis of amphibole in the Huanghe River and Changjiang River estuaries and significance of its provenance. *Geosci J.* 25, 575–587. doi: 10.1007/s12303-020-0061-4

Guo, R. H., Hu, X. M., Garzanti, E., Lai, W., and Mark, C. (2020). How faithfully do the geochronological and geochemical signatures of clastic zircon, titanite, rutile and monazite record magmatic and metamorphic events? A case study from the Himalaya and Tibet. *Earth-Sci. Rev.* 201, 103082. doi: 10.1016/j.earscirev.2020.103082

Han, Z. Z., Wang, Y. B., Sun, Y. G., Ai, L. N., Wu, X., and Yang, Y. P. (2022). Composition of minerals in surface sediments of the Yellow Sea and their provenance. *Mar. Geol. Frontiers* 38, 10–19.

Hawthorne, F. C., Oberti, R., Harlow, G. E., Maresch, W. V., Martin, R. F., Schumacher, J. C., et al. (2012). IMA report: Nomenclature of the amphibole supergroup. *Am. Mineralogist* 97, 2031–2048. doi: 10.2138/am.2012.4276

He, Q. X. (2006). *Chinese marine sedimentary geology* (Beijing: China Ocean Press).

Hori, K. (2001). Sedimentary facies and Holocene progradation rates of the Changjiang (Yangtze) delta, China. *Geomorphology* 41, 233–248. doi: 10.1016/S0169-555X(01)00119-2

Hou, Z. Q., Wang, Y. L., Xia, L. Q., Li, H. Y., and Guo, L. J. (1999). Emei large igneous province: Characteristics and origin. *Geological review* 45, 885–891.

Jin, B. F., Dang, L. L., Kong, Q. X., Wang, M. Y., Yue, W., and Fan, S. M. (2022). Comparison of geochemical characteristics of lithophile elements of amphibole: identification of estuarine sediment provenance, Huanghe and Changjiang rivers. *Acta Sedimentologica Sinica* 40, 149–165.

Jin, B. F., Yue, W., and Wang, K. S. (2013). The Crystallochemistry characteristics and genetic analysis of amphibole in the sediments of the Huanghe River. *Acta Oceanologica Sinica* 35, 131–143.

Jin, B. F., Yue, W., and Wang, K. S. (2014). Chemical composition of clastic amphibole in the sedimental of the Huanghe River, Liao River and Yalu River, and its implication for sediment provenance. *Acta Oceanologica Sinica* 36, 11–21.

Johnson, M. C., and Rutherford, M. (1989). Experimental calibration of the aluminum-in-hornblende geobarometer with applicable to Long Valley Caldera (California) volcanic rocks. *Geol* 17, 837–841. doi: 10.1130/0091-7613(1989)017<0837:ECOTAI>2.3.CO;2

Krippner, A., Meinhold, G., Morton, A. C., Schönig, J., and von Eynatten, H. (2016). Heavy minerals and garnet geochemistry of stream sediments and bedrocks from the Almklovdalen area, Western Gneiss Region, SW Norway: Implications for provenance analysis. *Sediment Geol.* 336, 96–105. doi: 10.1016/j.sedgeo.2015.09.009

Liu, D. S. (1985). *Loess and environment* (Beijing: Science press).

Liu, J. H. (1986). *Genetic classification of hornblendes and its application.* (Changchun: Journal of Changchun Institute of Geology). 1, 41–48.

Liu, C., He, Y., and Zhang, Y. (2008). Trends analysis of the water and sediment loads of the main rivers in China using water-sediment diagram. *Adv. Water Sci.* 19, 317–324.

Liu, X. Y., and Wang, Q. (2002). *Geological atlas of China* (Geological Publishing House).

McKee, B. A., Aller, R., Allison, M. A., Bianchi, T., and Kineke, G. (2004). Transport and transformation of dissolved and particulate materials on continental margins influenced by major rivers: benthic boundary layer and seabed processes. *Cont. Shelf Res.* 24, 899–926. doi: 10.1016/j.csr.2004.02.009

Milliman, J. D., and Meade, R. H. (1983). World-wide delivery of river sediment to the oceans. *J. Geol.* 91, 1–21. doi: 10.1086/628741

Ministry of Water Resources and Changjiang River Water Resources Commission (1999). *Atlas of the Changjiang River Basin* (Beijing: China Cartographic Publishing House).

Morton, A. C., Whitham, A. G., and Fanning, C. M. (2005). Provenance of Late Cretaceous to Paleocene submarine fan sandstones in the Norwegian Sea: Integration of heavy mineral, mineral chemical and zircon age data. *Sediment Geol.* 182, 3–28. doi: 10.1016/j.sedgeo.2005.08.007

Nie, J. S., Song, Y. G., King, J. W., and Egli, R. (2010). Consistent grain size distribution of pedogenic maghemite of surface soils and Miocene loessic soils on the Chinese Loess Plateau. *J. Quaternary Sci.: Published Quaternary Res. Assoc.* 25, 261–266. doi: 10.1002/jqs.1304

Qiao, F. L. (2011). *Chinese regional oceanography - physical oceanography* (Beijing: China Ocean Press).

Qin, Y. S. (1989). *Geology of the Yellow Sea* (Beijing: China Ocean Press).

Qin, Y. C., Xue, C., and Jiang, X. (2018). Tidal current-dominated depositional environments in the central-northern Yellow Sea as revealed by heavy-mineral and grain-size dispersals. *Mar. Geol.* 398, 59–72. doi: 10.1016/j.margeo.2018.01.004

Reed, S. J. (1996). *Electron Microprobe analysis and scanning microscopy in geology* (Cambridge: Cambridge University Press), 165–197.

Safonova, I., Maruyama, S., Hirata, T., Kon, Y., and Rino, S. (2010). LA-ICP-MS U-Pb ages of clastic zircons from Russia largest rivers: Implications for major granitoid events in Eurasia and global episodes of supercontinent formation. *J. Geodynamics* 50, 134–153. doi: 10.1016/j.jog.2010.02.008

Shang, Y., Nian, X. M., Zhang, W. G., and Wang, F. (2021). Yellow River's contribution to the building of Yangtze delta during the last 500 years - evidence from clastic zircon U-Pb geochronology. *Geophys. Res. Lett.* 48, 1–10. doi: 10.1029/2020GL091896

Soo-Chul, P., Hyun-Hee, L., Hyuk-Soo, H., and Gwang-Hoon, L. (2000). Evolution of late Quaternary mud deposits and recent sediment budget in the southeastern Yellow Sea. *Mar. Geol.* 170, 271–288. doi: 10.1016/S0025-3227(00)00099-2

Vezzoli, G., Garzanti, E., Limonta, M., Ando, S., and Yang, S. Y. (2016). Erosion patterns in the Changjiang (Yangtze River) catchment revealed by bulk-sample versus single-mineral provenance budgets. *Geomorphology* 261, 177–192. doi: 10.1016/j.geomorph.2016.02.031

Wang, M. Y. (2019). *Study on characteristics of main clastic minerals in modern sediments of the Hongze Lake reach in the Huaihe River* (Yantai: Ludong University).

Wang, Z. B., Yang, S. Y., Mei, X., and Lu, K. (2018). clastic garnet chemistry of the Changjiang (Yangtze River) sediments and their provenance implication. *J. Tongji Univ. (Natural Science)* 46, 1455–1472.

Wu, X., Wang, H. J., Bi, N. S., Saito, Y., Xu, J. P., Zhang, Y., et al. (2020). Climate and human battle for dominance over the Yellow River's sediment discharge: From the Mid-Holocene to the Anthropocene. *Mar. Geol.* 425, 106188. doi: 10.1016/j.margeo.2020.106188

Xue, J. (1991). *Genetic mineralogy* (Wuhan: China University of Geosciences Press).

Yang, S. Y., Jung, H. S., Lim, D. I., and Li, C. X. (2003a). A review on the provenance discrimination of sediments in the Yellow Sea. *Earth-Sci. Rev.* 63, 93–120. doi: 10.1016/S0012-8252(03)00033-3

Yang, S. Y., and Li, C. (1999). Element composition and tracer function of modern surface sediments from the Yangtze and Yellow rivers. *Prog. Natural Sci.* 9, 930–937.

Yang, S. Y., and Li, C. Y. (2000). Elemental composition in the sediments of the Yangtze and the Yellow Rivers and their tracing implication. *Prog. Natural Sci.: Materials Int.* 10, 616–618.

Yang, S. Y., Li, C. X., Hoi-Soo, J., Dong-Il, L. M., and Man-Sik, C. (2003b). Geochemistry of trace elements in Chinese and Korean river sediments. *Mar. geol. Quaternary geol.* 23, 6.

Yang, Q. H., Lin, Z. H., Zhang, F. Y., and Zhou, H. Y. (2004). Mineral characteristics of hornblende and magnetite in surface sediments in the east of the South China Sea and their genesis. *Mar. geol. Quaternary geol.* 24, 29–35.

Yang, S. Y., and Youn, J. S. (2007). Geochemical compositions and provenance discrimination of the central south Yellow Sea sediments. *Mar. Geol.* 243, 229–241. doi: 10.1016/j.margeo.2007.05.001

Yue, W., Jin, B. F., and Zhao, B. C. (2018). Transparent heavy minerals and magnetite geochemical composition of the Yangtze River sediments: Implication for provenance evolution of the Yangtze Delta. *Sediment Geol* 364, 42–52. doi: 10.1016/j.sedgeo.2017.12.006

Zhai, M. G. (2012). Evolution of the north China craton and early plate tectonics. *Acta Geographica Sinica* 86, 1335–1349.

Zhao, S. Y., Bian, Q. J., and Yan, W. Q. (1993). *Crystallography and mineralogy* (Beijing: Higher Education Press).

Zhou, X., Li, A., Jiang, F., and Lu, J. (2015). Effects of grain size distribution on mineralogical and chemical compositions: a case study from size-fractional sediments of the Huanghe (Yellow River) and Changjiang (Yangtze River). *Geological J.* 17, 23–46. doi: 10.1002/gj.2546

frontiers | Frontiers in Marine Science

TYPE Original Research
PUBLISHED 11 July 2024
DOI 10.3389/fmars.2024.1412052

OPEN ACCESS

EDITED BY
Chengji Shen,
Hohai University, China

REVIEWED BY
Yunhai Fang,
Hefei University of Technology, China
Zhang Bo,
Shandong University of Science and Technology, China
Qiguo Sun,
Jiangsu University of Science and Technology, China
Zenhom Salem,
Tanta University, Egypt
Venkatramanan Senapathi,
National College, Tiruchirappalli, India

*CORRESPONDENCE
Xilai Zheng
zhxilai@ouc.edu.cn

RECEIVED 04 April 2024
ACCEPTED 27 June 2024
PUBLISHED 11 July 2024

CITATION
Chang Q, Gao C, Zheng X, Lin Y and Song X (2024) A novel subsurface adjustable dam for preventing active seawater intrusion in coastal aquifers.
Front. Mar. Sci. 11:1412052.
doi: 10.3389/fmars.2024.1412052

A novel subsurface adjustable dam for preventing active seawater intrusion in coastal aquifers

Qinpeng Chang[1,2], Chenchen Gao[1,3], Xilai Zheng[1,3]*, Yucheng Lin[1,3] and Xiaoran Song[4]

[1]College of Environmental Science and Engineering, Ocean University of China, Qingdao, China, [2]College of Marine Geosciences, Ocean University of China, Qingdao, China, [3]Key Laboratory of Marine Environment and Ecological Education, Ministry of Education, Ocean University of China, Qingdao, China, [4]Personnel Office, Qingdao Hydrological Center, Qingdao, Shandong, China

Subsurface physical barriers are widely used to prevent seawater intrusion in the world. After the construction of physical barriers, the residual saltwater is trapped upstream the barriers. Traditional physical barriers, including cutoff walls and subsurface dams, are fixed in structure and fail in prohibiting active seawater intrusion. In this work, a novel subsurface adjustable dam, composed of dam bodies and sluice gates, was designed to prevent active seawater intrusion and store groundwater flexibly according to seasonal variations in precipitation. We set three-dimensional field-scale numerical simulations to compare the control effects of adjustable dams, cutoff walls, and subsurface dams. The results revealed that the traditional subsurface physical barriers could mitigate the velocity of active seawater intrusion but were inadequate in completely preventing the intrusion process. Furthermore, although the traditional physical barriers temporarily alleviate the residual saltwater during the wet periods, the saltwater wedge would subsequently invade during next dry periods. Thus, the salt mass in the aquifer of traditional physical barriers scenarios exhibited a gradual annual increase. In contrast, the novel subsurface adjustable dam demonstrated the ability to prevent active seawater intrusion and remove the residual saltwater. During the dry periods, characterized by low precipitation recharge, the sluice gates were closed to obstruct the path of active seawater intrusion. Conversely, during the wet periods with abundant precipitation, the sluice gates were opened, facilitating the gradual removal of the residual saltwater. The flexible adjustment mechanism of subsurface adjustable dams resulted in a annual decrease in both the seawater intrusion length and the salt mass in the entire aquifer. These findings underscore the efficacy of the subsurface adjustable dam as a measure for preventing active seawater intrusion and simultaneously eliminating the residual saltwater.

KEYWORDS

active seawater intrusion, coastal aquifer, cutoff wall, subsurface dam, adjustable dam

1 Introduction

The exacerbating impacts of excessive groundwater extraction and rising sea levels have intensified seawater intrusion (SWI) in coastal aquifers, posing significant threats to groundwater quality (Lu et al., 2013; LeRoux et al., 2023). The implementation of subsurface physical barriers has emerged as an effective countermeasure to mitigate SWI and safeguard groundwater resources (Kong et al., 2023). Furthermore, the subsurface physical barriers can serve as groundwater reservoirs which augments fresh groundwater storage (Ishida et al., 2011). Thus, subsurface physical barriers have gained widespread adoption in coastal regions globally, including China, Japan, India, the Middle East, and South America (Zheng et al., 2020; Chang et al., 2023).

Traditional subsurface physical barriers fall into three primary categories: cutoff walls, subsurface dams, and full-section physical barriers (Kaleris and Ziogas, 2013). Subsurface dams impede the lower portion of the aquifer while maintaining an upper opening for discharge. Conversely, cutoff walls are constructed in the upper portion of the aquifer, leaving a lower opening for discharge. Luyun et al. (2011) demonstrated that the efficacy of cutoff walls in preventing SWI was comparable to that of recharge wells. Chang et al. (Chang et al., 2019, 2020) introduced the concept of minimum effective height for subsurface dams in SWI prevention, and attributed the upward movement of the saltwater wedge to the obstruction caused by subsurface dams. Subsequently, Chang et al. (Chang et al., 2021, 2022) investigated the mechanism of cutoff walls in SWI prevention and proposed optimization strategies. Shen et al. (2020) analyzed the impact of tidal forces and cutoff walls on groundwater flow and salinity distribution in coastal aquifers, revealing that tidal influence enhances the effectiveness of cutoff walls in SWI mitigation. Zheng et al. (Zheng et al., 2021, 2022) examined the dynamic desalination process of the residual saltwater trapped upstream the subsurface dams and cutoff walls. They suggested that the desalination time for subsurface dams can be protracted for decades, while that for cutoff walls is typically several years. Furthermore, Yin et al. (2023) proposed combining saltwater discharge or freshwater recharge to expedite the desalination of the residual saltwater upstream subsurface dams. On the other hand, field investigations of groundwater quality have indicated that the implementation of subsurface physical barriers can lead to the accumulation of land-based pollutants (Kang and Xu, 2017). Fang et al. (2021) and Sun et al. (2019) employed indoor experiments and numerical simulations to elucidate the mechanism of nitrate accumulation induced by cutoff walls and subsurface dams. Recently, a novel mixed physical barrier, integrating a cutoff wall and a subsurface dam, has been developed to enhance SWI prevention and facilitate the removal of the residual saltwater (Abdoulhalik and Ahmed, 2017; Gao et al., 2021).

Previous research on subsurface physical barriers has predominantly focused on passive seawater intrusion (SWI), where the inland groundwater level exceeds the seawater level (Gao et al., 2022; Wang et al., 2023). However, in numerous coastal regions experiencing excessive groundwater extraction, the inland groundwater level falls below sea level during the dry periods, leading to active SWI (Badaruddin et al., 2017). Unfortunately, none of the existing subsurface physical barriers, including cutoff walls, subsurface dams, or mixed barriers, can effectively prevent active SWI due to their bottom or top apertures for groundwater discharge. Thus, previous studies on traditional physical barriers have been limited to passive SWI. The impermeable full-section physical barrier, which completely obstructs the seepage path, has the potential to prevent active SWI. However, it may result in the accumulation of land-based contaminants in inland aquifers (Ishida et al., 2011; Kang and Xu, 2017). Moreover, the residual saltwater upstream of subsurface dams can persist for decades due to the obstruction, raising concerns about chronic saltwater contamination (Zheng et al., 2021; Chang et al., 2024). As a result, the impermeable full-section physical barrier has been gradually abandoned by researchers and designers.

Unlike the subsurface dam and cutoff wall, the subsurface permeable reactive barrier employs vertical openings to facilitate the flow of contaminant plumes through the reactive media (Figure 1A) (Blowes et al., 2000). Similarly, gated storm surge barriers, designed to mitigate coastal flood hazards during extreme storms, incorporate vertical auxiliary lift gates that are only closed during coastal flooding events (Figure 1B) (Orton et al., 2023). Inspired by the designs of subsurface permeable reactive barriers and gated storm surge barriers, we propose a novel subsurface adjustable dam consisting of high underground dam bodies and adjustable vertical sluice gates (Figure 2). The sluice

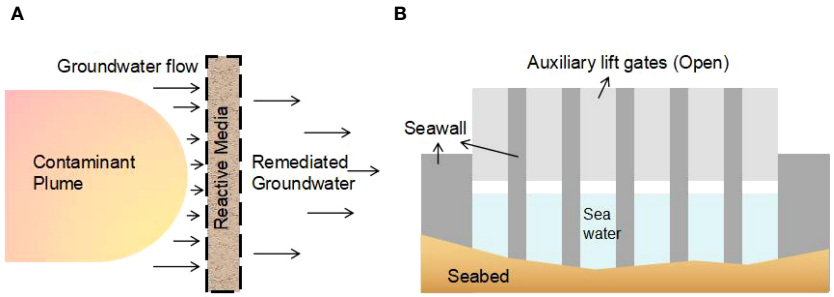

FIGURE 1
Schematics of **(A)** the overhead view of the subsurface permeable reactive barrier and **(B)** the elevation view of the storm surge barrier which includes auxiliary lift gates.

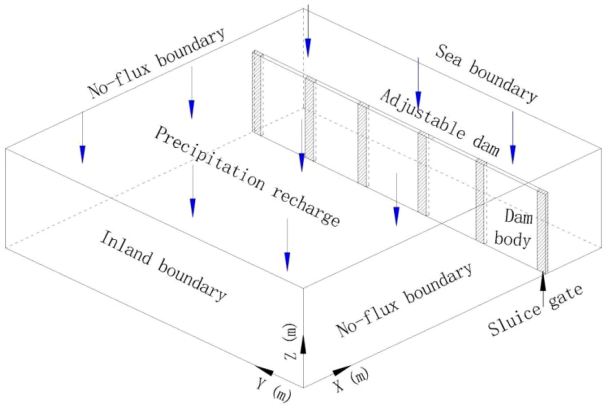

FIGURE 2
Schematic diagram of the conceptual model.

gates are integrated within the dam bodies, mimicking the structure of storm surge barriers with auxiliary lift gates (Figure 1B). Groundwater discharge is controlled by the sluice openings, which can be opened or closed in response to dynamic variations in precipitation. During the dry periods, the sluice gates are closed to conserve groundwater resources and prevent active SWI. Conversely, during the wet periods, the sluice gates can be opened to discharge the residual saltwater upstream the dam seawards. This novel subsurface adjustable dam enables flexible desalination of coastal aquifers during the wet periods and effective prevention of active SWI during the dry periods on an annual basis.

2 Methods

SEAWAT has been widely used to simulate the seawater intrusion process (Guo and Langevin, 2002). A three-dimensional hypothetical model domain (Figure 2) was used to represent the coastal unconfined aquifer (1000 m × 1000 m × 10 m). The aquifer was assumed to be horizontal, homogeneous, and isotropic. The field-scale model domain was discretized into 10 m × 10 m × 1 m elements. Dirichlet boundary conditions were applied to both the inland and seawater boundaries, with constant heads of 8 m and 9 m, to create the condition of active seawater intrusion. Constant concentrations of 35 g/L and 0 g/L were assigned to the sea and inland boundaries, respectively. The top boundary was defined as a Neumann boundary, with the precipitation recharge. No-flow boundary conditions were applied to all other boundaries. Constant monthly precipitation was used each year (Figure 3), and precipitation recharge into the aquifer was calculated using an infiltration coefficient of 0.33. The wet period was defined as July and August, when precipitation was significantly higher, while the dry period was defined as September to next June. For simplicity, evaporation was neglected.

The aquifer properties and solute transport parameters were adopted from previous seawater intrusion studies (e.g., Lu and Luo, 2010; Chang et al., 2022). The aquifer hydraulic conductivity (K_f) was set to 6E-4 m/s, the effective porosity (θ) was 0.3, and the molecular diffusion coefficient was 1E-9 m^2/s. The longitudinal dispersivity (α_L) was set to 5 m, and the transverse dispersivity (α_T) was 1/10 of α_L (Shoemaker, 2004). The dispersivity satisfied the Péclet number requirement ($Pe \approx \frac{\Delta L}{a_L} < 4$) to ensure numerical stability (Voss and Souza, 1987). The structure of the subsurface adjustable dam is illustrated in Figure 2. The adjustable dam, composed of underground dam bodies and sluice gates, is positioned 100 m from the sea boundary. The adjustable dam has a thickness of 1 m, a height equal to the sea level (9 m), and a hydraulic conductivity of 1E-9 m/s. The sluice gates have a length of 10 m, and six gates are evenly spaced within the dam bodies. The sluice gates are opened during the wet period (July and August) and closed during the dry period (September- next June) (Figure 3). All symbols used in the study are summarized in Table 1.

A set of field-scale scenarios were utilized to compare the effects of the SWI (no-barrier), cutoff wall (9 m depth), and subsurface dam (8 m and 9 m height), adjustable subsurface dam (9 m height) scenarios. The length, thickness, position, and hydraulic conductivity of the cutoff wall and subsurface dams were identical to those of the adjustable dam. The simulation period was four years and eight months, with a time step of one day. The simulation period was divided into two phases. In the first phase, seawater intrusion was allowed to occur for 18 months without any physical barriers. The simulated hydraulic head and salinity distribution at the end of the first phase (18th month) were then used as the initial conditions for the second phase. In the second phase, the physical barriers were assumed to be instantaneously installed, and the simulation continued for an additional 38 months.

The toe length of the saltwater wedge (*TL*) and the salt mass in the entire aquifer (*M*) were usually used as evaluation indices of seawater intrusion (Lu et al., 2009; Chang et al., 2023). The *TL* was defined as the distance between the 10% isohaline and the seawater boundary along the aquifer base, and it served as a measure of the extent of seawater intrusion. The *M*, on the other hand, was used to quantify the salinization extent of coastal aquifers.

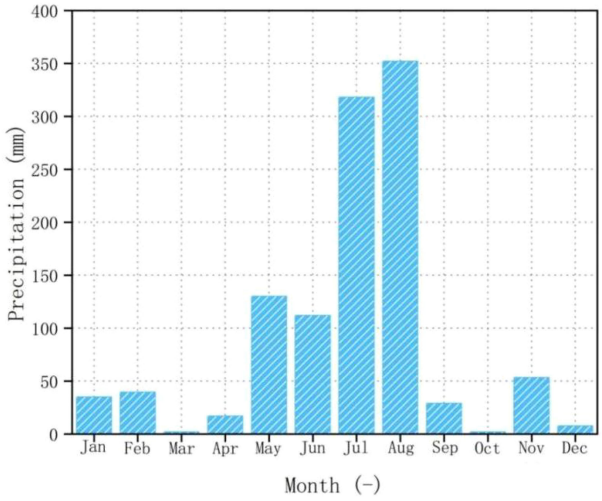

FIGURE 3
Monthly precipitation each year in the numerical simulation.

3 Results and discussion

3.1 Control effects of traditional subsurface physical barriers

Figure 4 presents the three-dimensional salinity distribution in the SWI and traditional subsurface physical barriers scenarios, and Figure 5 shows the corresponding cross-sectional views of the dynamic salinity distribution. In Figure 4, the semi-transparent gray region represents freshwater, while the non-transparent region represents saltwater, with its color transitioning from red to blue. The blue non-transparent surface corresponds to the 10% seawater salinity contour. Figure 6 records the dynamic variation in the toe length of the saltwater wedge (*TL*) in different scenarios. As shown in Figure 4A, the seawater has intruded inland in the first phase, and the *TL* at 18 months is 158.6 m. These simulated hydraulic head and salinity distributions are then used as the initial conditions for all subsequent simulations in the second phase. In the SWI scenario, the saltwater wedge toe temporarily retreats during July and August due to increased precipitation recharge (Figure 5A), resulting in a decrease in *TL* to 144.5 m at the end of the 2nd August (20th month). Subsequently, *TL* in the SWI scenario gradually increases to 317.2 m at the end of the 5th August (56th month). The dynamic variation of *TL* in the SWI scenario serves as a benchmark for evaluating the control effects of various subsurface physical barriers.

TABLE 1 List of symbols.

c_f	freshwater concentration [ML^{-3}]
c_s	saltwater concentration [ML^{-3}]
D	molecular diffusion coefficient [L^2T^{-1}]
h_f	freshwater level [L]
h_s	seawater level [L]
K_f	hydraulic conductivity [LT^{-1}]
M	salt mass in the entire aquifer [M]
TL	toe length of the saltwater wedge [L]
α_L	longitudinal dispersivity [L]
α_T	transverse dispersivity [L]
ρ_f	freshwater density [ML^{-3}]
ρ_s	seawater density [ML^{-3}]

The subsurface physical barriers were assumed to be instantaneously constructed 100 m from the sea boundary at the 18th month. Following the installation of the three traditional subsurface physical barriers, the front of the saltwater wedge was trapped upstream the physical barriers, which was known as the residual saltwater (Zheng et al., 2021). Figures 5B-D show that the saltwater continues to intrude inland, indicating that the traditional physical barriers are ineffective in preventing active seawater intrusion. In the 9 m-depth cutoff wall scenario, the toe length of the saltwater wedge (*TL*) briefly decreases below 100 km (at the barrier location) in the 21st and 22nd months (Figure 6), indicating a temporary clean-up of the residual saltwater upstream the wall. However, *TL* resumes its gradual increase after the 22nd month, except for temporary and slight retreats during the wet periods (July and August each year). In the 8 m-height subsurface dam scenario, *TL* retreats gradually to 124 m from the 19th to 21st months, followed by a growth during the next dry period and an again retreat during the subsequent wet period (Figure 6). The difference in *TL* between the 9 m-depth cutoff wall and 8 m-height subsurface dam scenarios decreases year by year, eventually becoming negligible at the 56th month. At the 56th month, *TL* is 257.4 m (9 m-depth cutoff wall) and 240.7 m (8 m-height subsurface dam), respectively. This suggests that the 8 m-height subsurface dam and 9 m-depth cutoff wall are equally ineffective against active SWI. The 9 m-height subsurface dam, which extends to the same height as the sea level, demonstrates a significantly improved ability to mitigate active SWI compared to the cutoff wall and lower subsurface dam (Figure 4). *TL* decreases from 158.6 m to 134.8 m (19th-22nd month) and then mildly

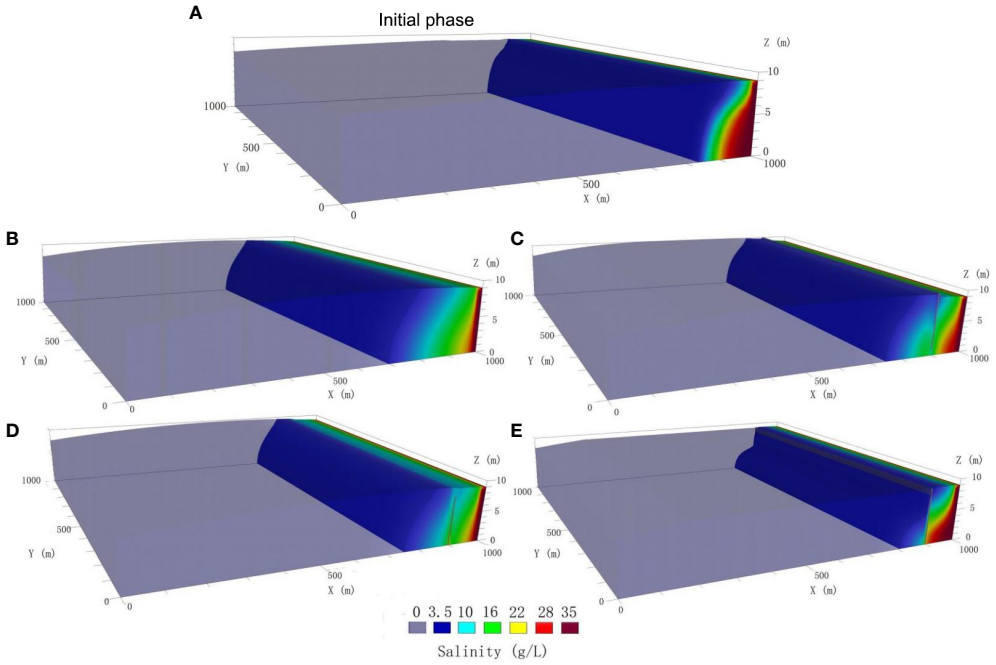

FIGURE 4
Three-dimensional salinity distribution **(A)** at 18th month (June, 2nd year, dry period) and at 56th month (August, 5th year, wet period) in the scenarios of **(B)** SWI, **(C)** cutoff wall (9 m-depth), **(D)** subsurface dam (8 m-height), **(E)** subsurface dam (9 m-height). The gray blocks represent the subsurface physical barriers.

increases monotonically over time. At the 56th month, *TL* is 195.2 m (9 m-height subsurface dam), which is considerably shorter than that of the other scenarios in Figure 6. This indicates that even a subsurface dam as high as the sea level is insufficient to prevent active SWI, although it substantially reduces the rate of seawater intrusion (Figure 5D). In conclusion, the traditional subsurface physical barriers can mitigate the velocity of active seawater intrusion, but they are ultimately unable to prevent it.

3.2 Control effects of the subsurface adjustable dam

The subsurface adjustable dam (9 m height) was also assumed to be installed instantaneously at 18th month, 100 m from the sea boundary. The sluice gates were configured to be open during the wet periods (July and August) and closed during the dry periods (September-next June). Figure 7 presents cross-sectional views of the dynamic salinity distribution in the adjustable dam scenario. The toe length of the saltwater wedge (*TL*) varies at different locations along the adjustable dam. The longest *TL* is observed at the middle of the dam body (Figure 7A), while the shortest *TL* is located at the middle of the sluice gate (Figure 7B). Figure 8 illustrates the three-dimensional salinity distribution in the subsurface adjustable dam scenario at the 54th and 56th months. When precipitation recharge is minimal during the dry period, the sluice gates are closed, effectively blocking the path of active seawater intrusion and confining the residual saltwater upstream the dam (Figure 8A). Conversely, during the wet period when precipitation increases significantly, the sluice gates are opened to discharge inland groundwater (Figure 8B). The upstream residual saltwater is also transported seawards through the sluice gate openings. As shown in Figure 7B, the upstream residual saltwater at the middle of the sluice gates is gradually removed over time, meanwhile the upstream residual saltwater at the middle of the dam bodies is also significantly reduced (Figure 7A).

Figure 9 illustrates the dynamic variation in the toe length of the saltwater wedge (*TL*) in the subsurface adjustable dam scenario at the middle of the dam body and the sluice gate. As shown in Figure 9, the *TL* at both the dam body and the sluice gate increases during the dry periods (September-next June). During the wet periods (July and August), the opening of the sluice gates accelerates groundwater discharge, enhancing the desalination process near the sluice gates and causing a more pronounced retreat of the saltwater wedge. Notably, the *TL* at the middle of the sluice gate declines more significantly than that at the middle of the dam body during each wet period. Furthermore, the *TL* at the middle of the sluice gate decreases to 86.7 m at the 31st month, indicating that the upstream residual saltwater has been completely removed. Subsequently, the saltwater wedge toe at the sluice gate never exceeds the dam location again. In contrast, the upstream residual saltwater at the middle of the dam body is cleared more gradually (Figure 7A). The fluctuation range of the *TL* at the middle of the dam body is less pronounced than that at the sluice gate (Figure 9), and the *TL* at the middle of the dam body never exceeds its initial value. Thus, the saltwater wedge at any location has receded each year since the installation of the adjustable dam, demonstrating the effectiveness of the dam in preventing active seawater intrusion.

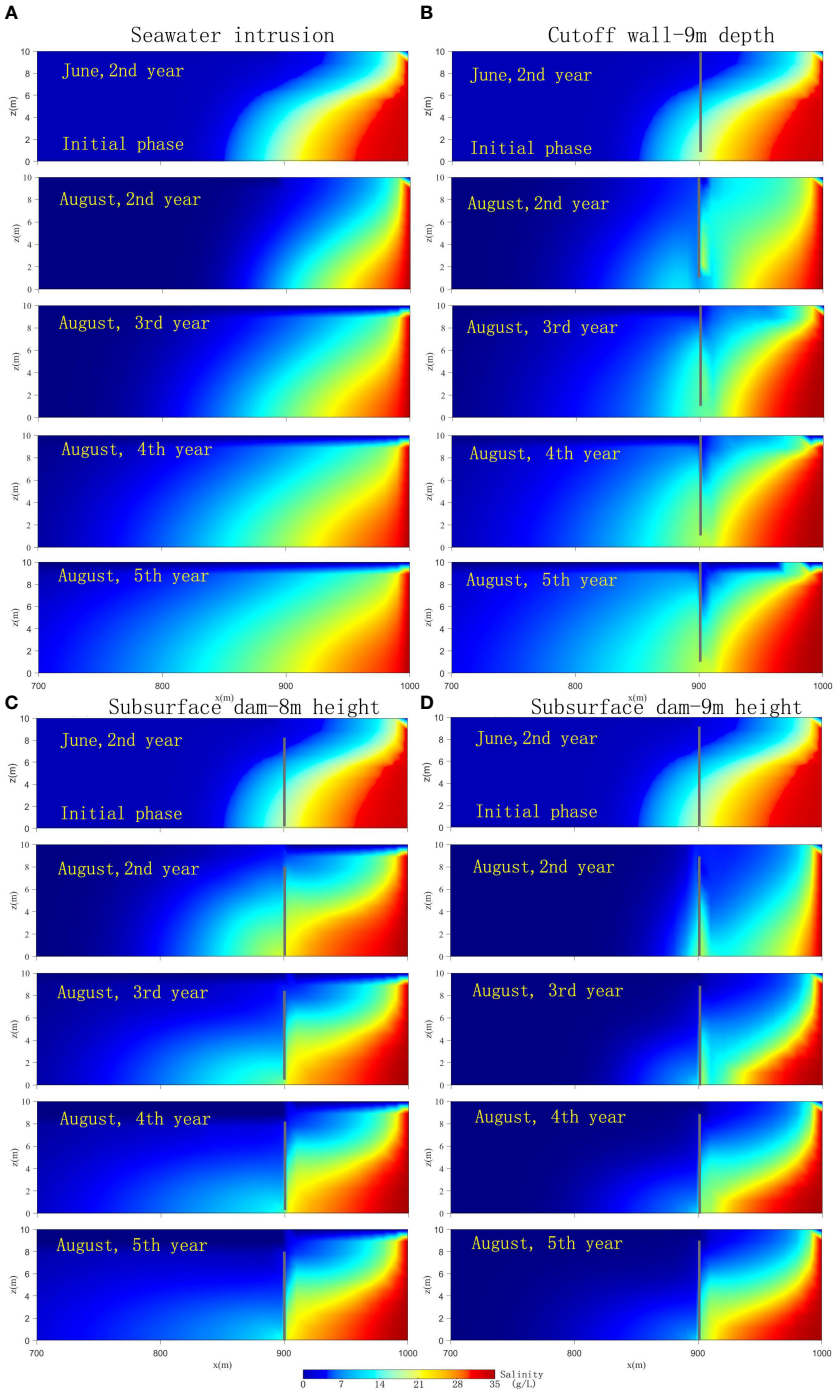

FIGURE 5
Cross-section of the dynamic salinity distribution in the **(A)** SWI, **(B)** cutoff wall (9 m-depth), **(C)** subsurface dam (8 m-height), and **(D)** subsurface dam (9 m-height) scenarios on an annual basis.

3.3 Groundwater desalination in different physical barriers scenarios

Figure 10 presents the salt mass in the entire aquifer (*M*) for all SWI and physical barriers scenarios. Notably, *M* peaks before the beginning of July each year in all scenarios. This is because the saltwater wedge keeps intruding during the dry periods (September-next June). However, *M* decreases during July and August due to the increased precipitation recharge, then reaching its lowest value at the end of August. Subsequently, as the precipitation recharge decreases again, seawater intrusion resumes, leading to an increase in *M*.

Compared to the SWI scenario, all the subsurface physical barriers could reduce the salt mass (*M*) to varying degrees throughout the simulation period. However, the overall trend of *M* in the SWI, cutoff wall, and subsurface dam scenarios

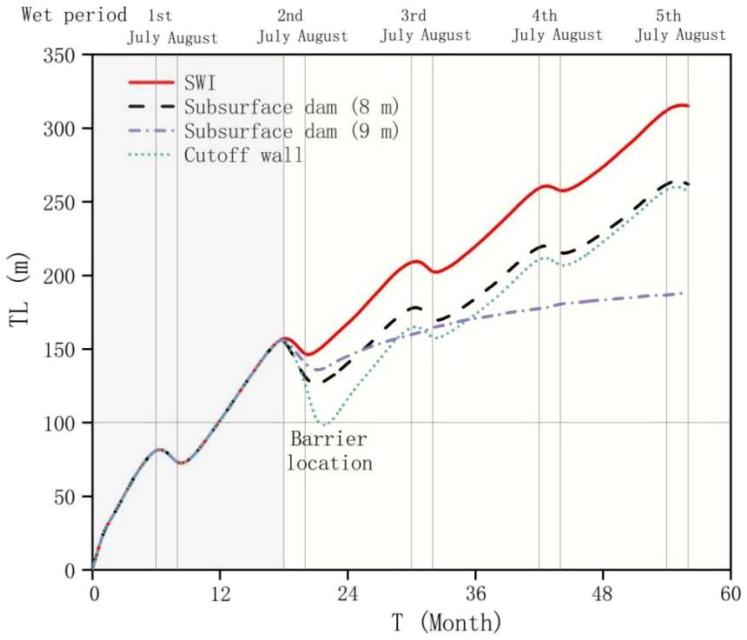

FIGURE 6
Dynamic variation in the toe length of the saltwater wedge in the SWI, subsurface dams (8 m-height and 9 m-height), and cutoff wall (9 m-depth) scenarios. The gray region represents the period without subsurface barriers, and the light yellow region means the period after the construction of subsurface barriers.

increase each year, despite temporary decrease during the wet periods (July and August). The *M* values in the 9 m-depth cutoff wall and 8 m-height subsurface dam scenarios are similar and slightly lower than that in the SWI case. In contrast, *M* in the 9 m-height subsurface dam scenario increases mildly and is significantly lower than that in the SWI case. These results indicate that the traditional physical barriers temporarily reduce the saltwater during the wet periods, but this reduction is offset by increased seawater intrusion during the next dry periods. Conversely, the overall trend of *M* in the subsurface adjustable dam scenario gradually decreases each year. This is because the residual saltwater upstream the adjustable dam is gradually removed when the sluice gates are open during the wet periods, meanwhile the downstream saltwater is prevented from intruding inland during the dry periods by the closed sluice gates.

In summary, the traditional subsurface physical barriers (cutoff wall and subsurface dam) are ineffective in preventing active seawater intrusion and desalinating the residual saltwater. In contrast, the subsurface adjustable dam can not only prevent the seawater from intruding inland during the dry periods but also remove the residual saltwater trapped upstream the dam during the wet periods.

4 Discussion

In contrast to conventional subsurface physical barriers, researchers have explored novel techniques to prevent SWI, such as mixed physical barrier (Abdoulhalik and Ahmed, 2017), variable permeability full-section wall (Zheng et al., 2020), and geochemical cutoff wall (Laabidi and Bouhlila, 2021). However, these structures remained fixed and lacked the ability to prevent active SWI. Our proposed adjustable dam adopts a proactive approach to coastal groundwater management. Operators can dynamically control the opening and closing of sluice gates based on real-time precipitation data. This enables the storage of groundwater resources and the prevention of active SWI during the dry periods. Conversely, during the wet periods, operators can open the sluice gates to discharge upstream groundwater and remove the residual saltwater, thereby improving water quality. Thus, this innovative approach simultaneously addresses the challenges of active SWI and the residual saltwater upstream of dams in coastal aquifers.

The dam bodies of subsurface adjustable dam can be constructed via excavation or grouting, utilizing low-permeability materials such as clay or cement mortar (Molfetta and Sethi, 2006; Yang et al., 2022). The height of the dam bodies must exceed the sea level to effectively intercept active SWI. In our numerical simulations, we assumed a constant sea level for simplicity. However, in practical applications, the adjustable dam should be designed to withstand the highest local tide level. Trenches are excavated in advance, and the soil on both sides is supported by porous grids. The sluice gates are positioned between these porous grates. The design of the sluice gates can vary depending on hydrogeological conditions and may include steel, cement, or rubber materials. The gates can be raised or

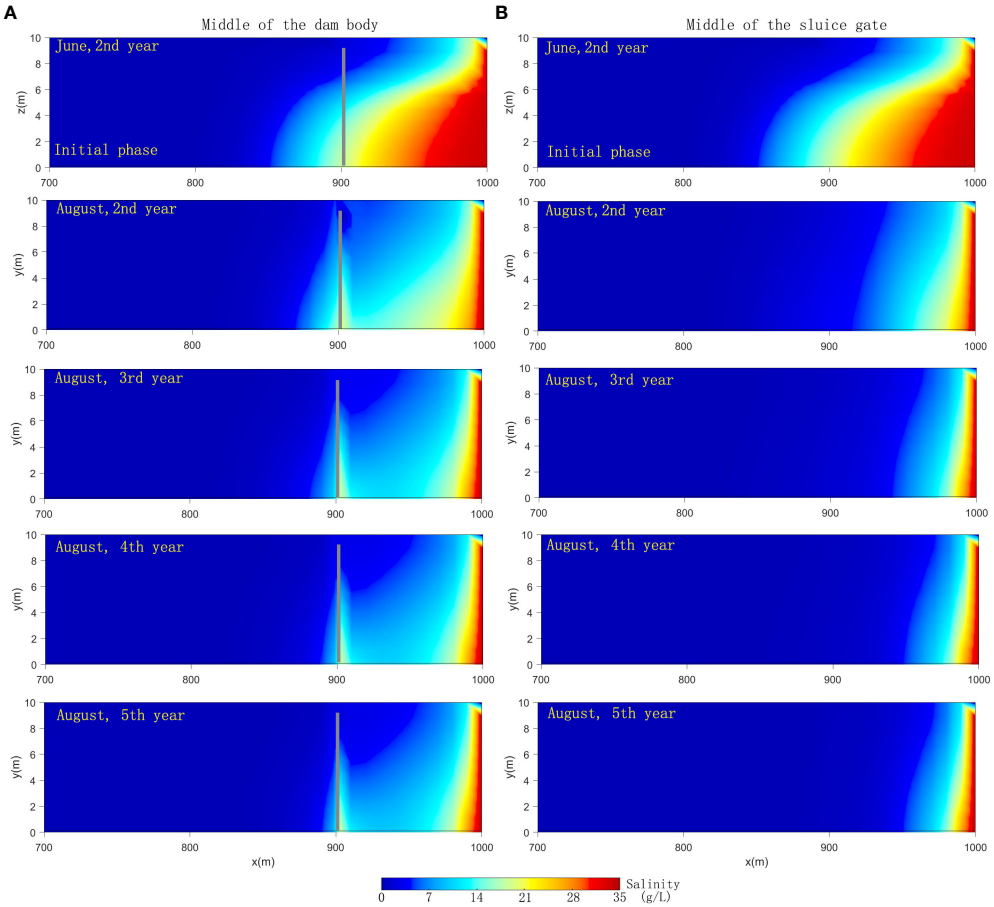

FIGURE 7
Cross-section of the salinity distribution at the **(A)** the middle of the dam body and **(B)** the middle of the sluice gate in the adjustable dam scenario on an annual basis.

lowered using a crane. Meanwhile the sluice gates can also be made into tank shapes which can lowered or raised by injecting or pumping water. Real-time monitoring of groundwater levels via monitoring wells allows for dynamic adjustment of the sluice gates based on precipitation and groundwater level variations. This enables flexible management of coastal groundwater resources, akin to the operation of surface reservoirs.

5 Summary and conclusion

The traditional subsurface physical barriers for preventing SWI, such as cutoff walls and subsurface dams, have fixed structures and cannot adapt to dynamic variations in precipitation. To address this limitation, we have designed a novel subsurface adjustable dam consisting of sluice gates and dam bodies. This innovative structure aims to prevent active seawater intrusion and desalinate the residual saltwater upstream the dam. To evaluate the effectiveness of the novel subsurface adjustable dam, we conducted a series of field-scale numerical simulations and compared its performance to those of traditional subsurface physical barriers. The key findings are summarized below.

1. Compared to the scenario without any subsurface physical barriers, all the subsurface physical barriers reduced the toe length of the saltwater wedge (*TL*) and the total salt mass within the aquifer (*M*) in varying degrees under the condition of active seawater intrusion. Among the traditional subsurface physical barriers, the 9 m-depth cutoff wall and the 8 m-height subsurface dam exhibited comparable control effects, although they were less effective than the 9 m-height subsurface dam (as high as the sea level). Notably, the novel subsurface adjustable dam demonstrated superior control on active seawater intrusion compared to all other traditional barrier types.
2. The traditional subsurface physical barriers could slow down active seawater intrusion process each year, while they failed in blocking active seawater intrusion completely. Meanwhile, although the traditional physical barriers could temporarily reduce the upstream residual saltwater in the wet period, the salt mass will increased more in the next dry period. Consequently, the overall salt mass in the cutoff wall and subsurface dam scenarios gradually increased on an annual basis, indicating that these traditional barriers lacked the capacity to desalinate the upstream residual saltwater.

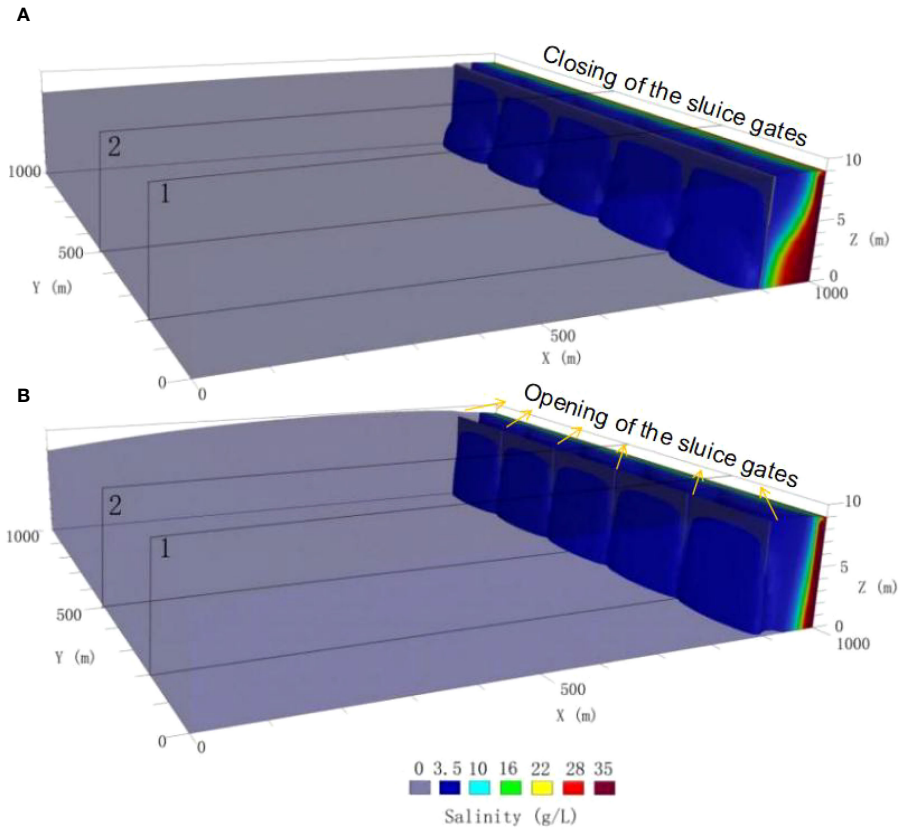

FIGURE 8
Three-dimensional salinity distribution in the adjustable dam scenario at the **(A)** 54th month (June, 5th year, dry period) and **(B)** 56th month (August, 5th year, wet period). The gray block represents the adjustable dam. The cross section 1 locates the middle of the sluice gate, and the cross section 2 locates the middle of the dam body.

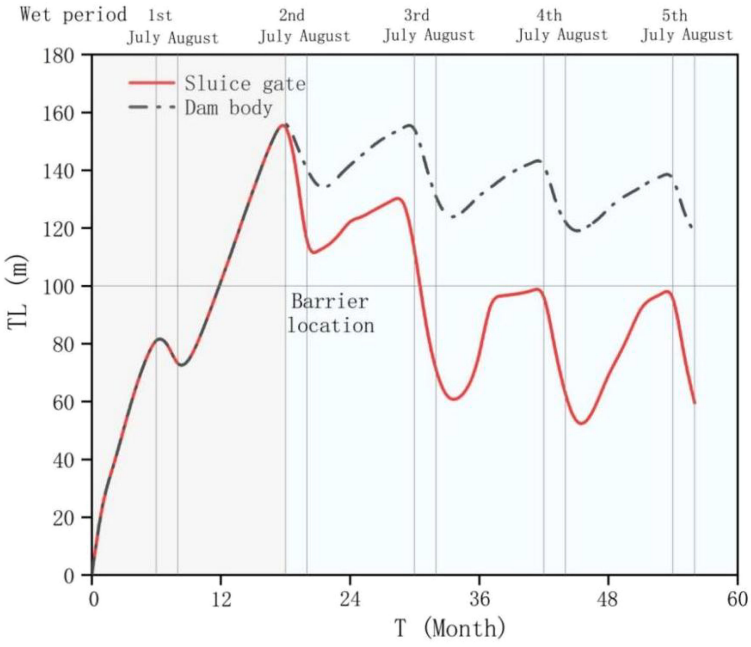

FIGURE 9
Dynamic variation in the toe length of the saltwater wedge in the subsurface adjustable dam scenario. The gray region represents the period without subsurface barriers, and the light blue region means the period after the construction of the adjustable dam.

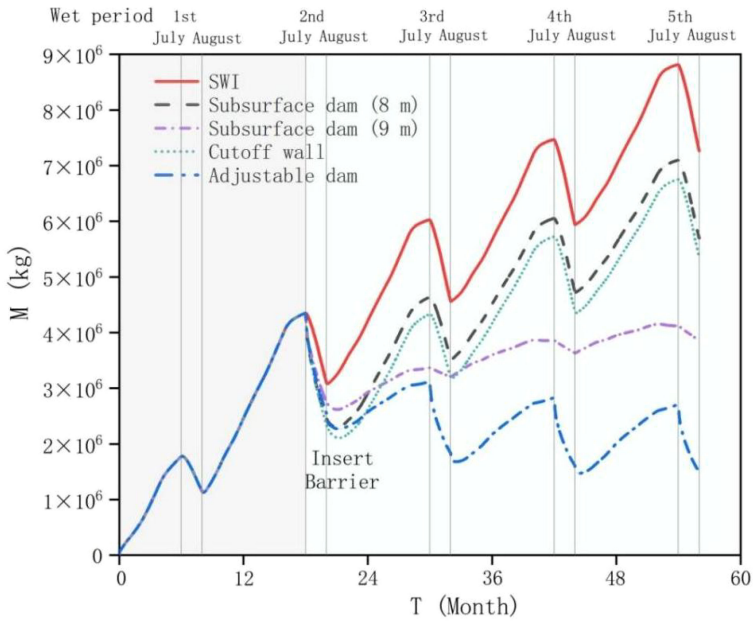

FIGURE 10
Dynamic variation of salt mass in the entire aquifer over time in different physical barriers scenarios. The gray region represents the period without subsurface barriers, and the light blue region means the period after the construction of subsurface barriers.

3. The novel subsurface adjustable dam could be dynamically regulated in response to the seasonal variation in precipitation. When the precipitation recharge was small during the dry period, the sluice gates were closed, then the path of active seawater intrusion was obstructed completely. During the wet period, the sluice gates were opened due to the large precipitation, the upstream residual saltwater was gradually removed through the opened sluice gates. Thus, both the toe length of saltwater wedge and the salt mass in the entire aquifer decreased each year attributing to the flexible adjustment ability of the novel dam. The above conclusion indicated that the subsurface adjustable dam was an effective measure which prevented active seawater intrusion and eliminated the upstream residual saltwater at the same time.

In this study, we have designed a novel adjustable dam and demonstrated its effectiveness in preventing active seawater intrusion and desalinating the upstream residual saltwater in coastal aquifers. Building on our prior studies (Chang et al., 2019, 2023), we have identified the hydraulic gradient as a pivotal determinant in the efficacy of physical barriers against seawater intrusion. The most unfavorable hydraulic gradient conditions are caused by the highest local tidal level and the lowest rainfall recharge. In the realm of field engineering, the design of physical barriers against seawater intrusion typically incorporates the highest recorded local tide level as a reference sea level. Thus, in this study, we assumed a constant sea level and seasonal variations in rainfall to simplify the numerical model.

Data availability statement

The original contributions presented in the study are included in the article/supplementary material. Further inquiries can be directed to the corresponding author.

Author contributions

QC: Conceptualization, Data curation, Formal analysis, Funding acquisition, Investigation, Methodology, Project administration, Resources, Software, Supervision, Validation, Visualization, Writing – original draft, Writing – review & editing. CG: Data curation, Investigation, Methodology, Validation, Visualization, Writing – original draft, Writing – review & editing. XZ: Conceptualization, Data curation, Formal analysis, Funding acquisition, Investigation, Methodology, Project administration, Resources, Software, Supervision, Validation, Visualization, Writing – original draft, Writing – review & editing. YL: Formal analysis, Investigation, Methodology, Visualization, Writing – original draft. XS: Methodology, Resources, Visualization, Writing – original draft.

Funding

The author(s) declare financial support was received for the research, authorship, and/or publication of this article. This work was supported by the National Natural Science Foundation of

China (No.42307069) and (No.42272282), the Shandong Provincial Natural Science Foundation (ZR2023QD019), the China Postdoctoral Science Foundation (2023T160609), the Postdoctoral Innovation Project of Shandong Province (SDCX-ZG-202203080), the Ecological Restoration Project of Qingdao (20220294), and the Fundamental Research Funds for the Central Universities (202461074).

Acknowledgments

We thank the editor and reviewers whose critical and constructive comments have helped us improve the quality of the manuscript greatly.

Conflict of interest

The authors declare that the research was conducted in the absence of any commercial or financial relationships that could be construed as a potential conflict of interest.

Publisher's note

References

Abdoulhalik, A., and Ahmed, A. A. (2017). The effectiveness of cutoff walls to control saltwater intrusion in multi-layered coastal aquifers: Experimental and numerical study. *J. Environ. Manage.* 199, 62–73. doi: 10.1016/j.jenvman.2017.05.040

Badaruddin, S., Werner, A. D., and Morgan, L. K. (2017). Characteristics of active seawater intrusion. *J. Hydrol.* 551, 632–647. doi: 10.1016/j.jhydrol.2017.04.031

Blowes, D. W., Ptacek, C. J., Benner, S. G., McRae, C. W. T., Bennett, T. A., and Puls, R. W. (2000). Treatment of inorganic contaminants using permeable reactive barriers. *J. Contam. Hydrol.* 45, 123–137. doi: 10.1016/S0169-7722(00)00122-4

Chang, Q., Zheng, T., Chen, Y., Zheng, X., and Walther, M. (2020). Investigation of the elevation of saltwater wedge due to subsurface dams. *Hydrol. Processes* 32, 4251–4261. doi: 10.1002/hyp.13863

Chang, Q., Zheng, T., Chen, Y., Zheng, X., and Walther, M. (2021). Influence of inland freshwater influx on the natural desalination of coastal aquifers with a cutoff wall. *Desalination* 499, 114863. doi: 10.1016/j.desal.2020.114863

Chang, Q., Zheng, T., Gao, C., Zheng, X., Lin, Y., Song, X., et al. (2024). Hydrodynamic behavior of freshwater-saltwater mixing zone in the context of subsurface physical barriers. *J. Environ. Manage.* 353, 120080. doi: 10.1016/j.jenvman.2024.120080

Chang, Q., Zheng, T., Gao, C., Zheng, X., and Walther, M. (2022). How to cope with downstream groundwater deterioration induced by cutoff walls in coastal aquifers. *J. Hydrol.* 610, 127804. doi: 10.1016/j.jhydrol.2022.127804

Chang, Q., Zheng, T., Zheng, X., Gao, C., Song, X., and Walther, M. (2023). Repulsion driven by groundwater level difference around cutoff walls on seawater intrusion in unconfined aquifers. *Sci. Total Environ.* 874, 162535. doi: 10.1016/j.scitotenv.2023.162535

Chang, Q., Zheng, T., Zheng, X., Zhang, B., Sun, Q., and Walther, M. (2019). Effect of subsurface dams on saltwater intrusion and fresh groundwater discharge. *J. Hydrol.* 576, 508–519. doi: 10.1016/j.jhydrol.2019.06.060

Fang, Y., Zheng, T., Wang, H., Guan, R., Zheng, X., and Walther, M. (2021). Experimental and numerical evidence on the influence of tidal activity on the effectiveness of subsurface dams. *J. Hydrol.*, 127149. doi: 10.1016/j.jhydrol.2021.127149

Gao, M., Zheng, T., Chang, Q., Zheng, X., and Walther, M. (2021). Effects of mixed physical barrier on residual saltwater removal and groundwater discharge in coastal aquifers. *Hydrol. Processes* 35, e14263. doi: 10.1002/hyp.14263

Gao, S., Zheng, T., Zheng, X., and Walther, M. (2022). Influence of layered heterogeneity on nitrate enrichment induced by cut-off walls in coastal aquifers. *J. Hydrol.* 609, 127722. doi: 10.1016/j.jhydrol.2022.127722

Guo, W., and Langevin, C. D. (2002). *User's Guide to SEAWAT: A Computer Program for Simulation of Three-Dimensional Variable-Density Groundwater Flow* (Tallahassee, Florida: US Geological Survey Techniques of Water Resources Investigations 6-A7). doi: 10.3133/ofr01434

Ishida, S., Tsuchihara, T., Yoshimoto, S., and Imaizumi, M. (2011). Sustainable use of groundwater with underground dams. *Japan Agric. Res. Q.* 45, 51–61. doi: 10.6090/jarq.45.51

Kaleris, V. K., and Ziogas, A. I. (2013). The effect of cutoff walls on saltwater intrusion and groundwater extraction in coastal aquifers. *J. Hydrol.* 476, 370–383. doi: 10.1016/j.jhydrol.2012.11.007

Kang, P., and Xu, S. (2017). The impact of an underground cut-off wall on nutrient dynamics in groundwater in the lower Wang River watershed, China. *Isotopes Environ. Health Stud.* 53, 36–53. doi: 10.1080/10256016.2016.1186670

Kong, J., Gao, C., Jiang, C., Wang, J., Gao, X., and Jing, L. (2023). Effect of the cutoff wall on the fate of nitrate in coastal unconfined aquifers under tidal action. *Front. Mar. Sci.* 10. doi: 10.3389/fmars.2023.1135072

Laabidi, E., and Bouhlila, R. (2021). A new technique of seawater intrusion control: development of geochemical cutoff wall. *Environ. Sci. Pollut. Res.* 28, 41794–41806. doi: 10.1007/s11356-021-13677-0

LeRoux, N. K., Frey, S. K., Lapen, D. R., Guimond, J. A., and Kurylyk, B. L. (2023). Mega-tidal and surface flooding controls on coastal groundwater and saltwater intrusion within agricultural dikelands. *Water Resour. Res.* 59, 1–21. doi: 10.1029/2023WR035054

Lu, C., Chen, Y., Zhang, C., and Luo, J. (2013). Steady-state freshwater-seawater mixing zone in stratified coastal aquifers. *J. Hydrol.* 505, 24–34. doi: 10.1016/j.jhydrol.2013.09.017

Lu, C., Kitanidis, P. K., and Luo, J. (2009). Effects of kinetic mass transfer and transient flow conditions on widening mixing zones in coastal aquifers. *Water Resour. Res.* 45, 1–17. doi: 10.1029/2008WR007643

Lu, C., and Luo, J. (2010). Dynamics of freshwater-seawater mixing zone development in dual-domain formations. *Water Resour. Res.* 46, 1–6. doi: 10.1029/2010WR009344

Luyun, R., Momii, K., and Nakagawa, K. (2011). Effects of recharge wells and flow barriers on seawater intrusion. *Ground Water* 49, 239–249. doi: 10.1111/gwat.2011.49.issue-2

Molfetta, A. D., and Sethi, R. (2006). Clamshell excavation of a permeable reactive barrier. *Environmental Geology.* 50, 361–369. doi: 10.1007/s00254-006-0215-3

Orton, P., Ralston, D., van Prooijen, B., Secor, D., Ganju, N., Chen, Z., et al. (2023). Increased utilization of storm surge barriers: A research agenda on estuary impacts. *Earth's Future* 11, e2022EF002991. doi: 10.1029/2022EF002991

Shen, Y., Xin, P., and Yu, X. (2020). Combined effect of cutoff wall and tides on groundwater flow and salinity distribution in coastal unconfined aquifers. *J. Hydrol.* 581, 124444. doi: 10.1016/j.jhydrol.2019.124444

Shoemaker, W. B. (2004). Important observations and parameters for a salt water intrusion model. *Ground Water* 42, 829–840. doi: 10.1111/j.1745-6584.2004.t01-2-.x

Sun, Q., Zheng, T., Zheng, X., Chang, Q., and Walther, M. (2019). Influence of a subsurface dam on nitrate contamination in an unconfined aquifer. *J. Hydrol.* 575, 234–243. doi: 10.1016/j.jhydrol.2019.05.030

Voss, C. I., and Souza, W. R. (1987). Variable density flow and solute transport simulation of regional aquifers containing a narrow freshwater-saltwater mixing zone. *Water Resour. Res.* 23, 1851–1866. doi: 10.1029/WR023i010p01851

Wang, J., Kong, J., Gao, C., and Zhou, L. (2023). Effect of mixed physical barrier on seawater intrusion and nitrate accumulation in coastal unconfined aquifers. *Environ. Sci. Pollut. Res.* 30, 105308–105328. doi: 10.1007/s11356-023-29637-9

Yang, Y. L., Reddy, K. R., Zhang, T., Fan, R. D., Fu, X. L., and Du, Y. J. (2022). Enhanced contaminant retardation by novel modified calcium bentonite backfill in slurry trench cutoff walls. *Construct. Build. Mater.* 320, 126285. doi: 10.1016/j.conbuildmat.2021.126285

Yin, J., Wang, N., Lu, C., Tsai, F. T. C., and Chen, H. (2023). Fast desalinization of residual saltwater using subsurface dams combined with saltwater discharge or freshwater recharge. *J. Hydrol.* 619, 129282. doi: 10.1016/j.jhydrol.2023.129282

Zheng, T., Gao, M., Chang, Q., Zheng, X., and Walther, M. (2022). Dynamic desalination of intruding seawater after construction of cut-off walls in a coastal unconfined aquifer. *Front. Mar. Sci.* 9. doi: 10.3389/fmars.2022.857807

Zheng, T., Zheng, X., Chang, Q., Zhan, H., and Walther, M. (2021). Timescale and effectiveness of residual saltwater desalinization behind subsurface dams in an unconfined aquifer. *Water Resour. Res.* 57, e2020WR028493. doi: 10.1029/2020WR028493

Zheng, T., Zheng, X., Sun, Q., Wang, L., and Walther, M. (2020). Insights of variable permeability full-section wall for enhanced control of seawater intrusion and nitrate contamination in unconfined aquifers. *J. Hydrol.* 586, 124831. doi: 10.1016/j.jhydrol.2020.124831

frontiers | Frontiers in Marine Science

TYPE Original Research
PUBLISHED 23 July 2024
DOI 10.3389/fmars.2024.1382206

OPEN ACCESS

EDITED BY
Marta Marcos,
University of the Balearic Islands, Spain

REVIEWED BY
Yuming Huang,
Chinese Academy of Sciences (CAS), China
Yunhai Fang,
Hefei University of Technology, China
Di Zhang,
Yellow River Conservancy Commission, China
Abu Reza Md. Towfiqul Islam,
Begum Rokeya University, Bangladesh

*CORRESPONDENCE
Qiaona Guo
guoqiaona2010@hhu.edu.cn

RECEIVED 05 February 2024
ACCEPTED 24 June 2024
PUBLISHED 23 July 2024

CITATION
Guo Q, Liu J, Zhu X and Dai Y (2024) Groundwater level fluctuation caused by tide and groundwater pumping in coastal multi-layer aquifer system.
Front. Mar. Sci. 11:1382206.
doi: 10.3389/fmars.2024.1382206

Groundwater level fluctuation caused by tide and groundwater pumping in coastal multi-layer aquifer system

Qiaona Guo[1*], Jinhui Liu[1], Xufen Zhu[1] and Yunfeng Dai[2]

[1]School of Earth Sciences and Engineering, Hohai University, Nanjing, China, [2]State Key Laboratory of Hydrology-Water Resources and Hydraulic Engineering, Nanjing Hydraulic Research Institute, Nanjing, China

This paper considered the groundwater head fluctuation induced by tide and pumping in the coastal multi-layered aquifer system. The multi-layered aquifer system comprises an unconfined aquifer, an upper confined aquifer, and a lower confined aquifer. An aquiclude exists between each two aquifers. All the layers terminate at the coastline. The new analytical solutions describing groundwater head variation in the coastal multi-confined aquifer system are derived. Superposition principle and image methods are used for the derivation of the analytical solutions. Analytical solutions of different situations of without considering pumping, of without considering tidal effect, and of *N*-layered confined aquifers are also derived. The impacts of the parameters of the initial phase shift of tide, pumping rate, position of the pumping well, storage coefficient, and transmissivity on the groundwater head fluctuation are discussed. The analytical solutions are applied with application examples in fitting field observations and parameter estimations. The estimated values of the hydraulic conductivities in the upper and lower confined aquifers are within the range of the values obtained from the field experiments. The fitted results of the analytical solutions capture the main characteristics of groundwater head fluctuation affected by the tide and groundwater pumping. The study of groundwater head fluctuation in the coastal zone is helpful to understand the mechanism of seawater intrusion under the influence of tide and groundwater pumping.

KEYWORDS

coastal zone, multi-layered aquifer system, tide fluctuation, groundwater pumping, analytical solution

1 Introduction

The coastal aquifer or inter-tidal zone is the interactive zone between the coastal zone and the land. The groundwater and seawater with all kinds of chemicals from land and sea interact with each other there. Due to the increasing exploitation of groundwater, global climate change, and pollutant discharge from the inland to sea, the coastal aquifer is in a fragile state (Debnath et al., 2015; Das et al., 2022; Yang et al., 2022). Typically, seawater intrusion leads to the increase of groundwater salinity, due to over-exploitation of groundwater in the coastal aquifer system (Werner et al., 2013; Lu et al., 2015; Guo et al., 2019; Yu and Michael, 2019). It causes a series of coastal ecological environment problems, which have brought great harm to the production, living, and economic development of coastal residents (Huizer et al., 2017; Jasechko et al., 2020; Peters et al., 2022). Therefore, it is very important to study the hydraulic connection between seawater and coastal aquifers.

The groundwater level in the coastal aquifer system fluctuates with the tide periodically. Many scholars in the field of hydrogeology have proposed a series of coastal aquifer models considering tidal effects, since Jacob (1950) derived the analytical solution of groundwater fluctuation under tidal effect in a single confined aquifer vertical to the coast (e.g., Li and Jiao, 2001a, Li and Jiao, 2001b, Li and Jiao, 2003; Chuang and Yeh, 2007; Guo et al., 2007; Hsieh et al., 2015; Ratner-Narovlansky et al., 2020). The aquifer is usually assumed to be a single homogeneous coastal aquifer (e.g., Cartwright et al., 2004) or multi-layered aquifer system (e.g., Guo et al., 2007; Xia et al., 2007; Chuang and Yeh, 2011; Bakker, 2019). For example, Zheng et al. (2022) have derived a horizontal two-dimensional analytical solution for the instantaneous water table within an unconfined coastal aquifer, accounting for the combined influences of rainfall recharge and tidal fluctuations. Luo et al. (2023) examined and considered interactions between the tide and sloping sea boundary and derived a new analytical solution to predict water table fluctuations in the coastal unconfined aquifer. During the above research process, the aquifer system may extend under the sea for a certain distance or an infinite distance and, sometimes, terminates at the coastline. Aquifers terminating at the coastline frequently appear in the writings of scholars who study coastal aquifers (e.g., Noorabadi et al., 2017; Guo et al., 2019; Zhu et al., 2023) and are widely distributed in coastal areas. However, multi-confined aquifers were seldom studied (e.g., Bresciani et al., 2015a, Bresciani et al., 2015b; Ratner-Narovlansky et al., 2020). For example, Ratner-Narovlansky et al. (2020) considered a multi-unit coastal aquifer, which consists of a superficial phreatic unit, underlain by two confined units. In above cases, the variation of groundwater table was investigated, which was affected by the tide. Generally speaking, the tide propagates farther in the confined aquifer than in the unconfined aquifer, because the storativity of the confined aquifer is lower than the specific yield of the unconfined aquifer (Zhang, 2021).

In addition to tidal fluctuations, groundwater exploitation is also the main factor causing the head variation in coastal aquifers. Nevertheless, there are few studies on the groundwater level fluctuations in coastal aquifer systems, considering tidal fluctuations and pumping. For example, Chapuis et al. (2006) obtained a closed-form solution of tide-induced head fluctuation considering pumping in a confined aquifer. Wang et al. (2014) derived analytical solutions of groundwater level variations in a coastal aquifer system including the unconfined aquifer, semi-permeable layer, and confined aquifer, considering the pumping and tidal effects. Zhou et al. (2017) applied numerical modeling considering the influences of pumping on tide-induced groundwater level fluctuations. Recently, Su et al. (2023) employed time series analysis techniques to assess the influences of brine water extraction, tidal fluctuations, and precipitation on the groundwater level in the Laizhou Bay region. The observed ocean water levels measured at tidal stations and groundwater levels are fitted to Jacob's analytical solution for aquifer parameter estimation in the Biscayne Aquifer by Rogers et al. (2023), Miami-Dade County, Florida (USA), which is a coastal, shallow, unconfined, and heterogeneous aquifer. In reality, the coastal aquifer system may have two or more confined aquifers in the vertical direction. With the continuous exploitation and utilization of groundwater resources, the groundwater level decreases in the shallow aquifer; therefore, the research on the groundwater resources in the deep aquifer is of great significance. However, the pumping in the multi-confined aquifers was rarely considered under the effect of tide in coastal zones.

Parameter estimation (PEST) and Pilot Point were used by Marshall et al. (2022) and Ackerer et al. (2023), respectively, for parametric inversion. The former inverts the model structure that best matches the measured data, and the latter estimates aquifer heterogeneity using Ghislain de Marsily based on Pilot Point. In comparison with traditional numerical model–based inversion methodologies such as PEST and Pilot Point, the application of analytical solutions for parameter inversion is more accurate for specific scenarios; however, this application of analytical solutions for parameter inversion remains less studied. An inversion method for hydraulic diffusivity has been provided by Li et al. (2022) based on the analytical solution for groundwater flow within a finite-length one-dimensional aquifer; based on the phreatic unsteady seepage model near the drainage ditches, Ren et al. (2022) used the method of solving the inverse problem of model to calculate the model parameters. This paper investigates the joint effects of tide and groundwater pumping in the coastal multi-layered aquifer system. The multi-layered aquifer system is composed of an unconfined aquifer, an upper confined aquifer, and a lower confined aquifer from top to bottom. There is an aquiclude between each two aquifers. A new analytical solution describing the groundwater level variation in the coastal multi-confined aquifer system is presented. The analytical solution is given to estimate the hydrogeological parameters considering both of the pumping and tidal effects in the confined aquifers. The study of water level fluctuation in the coastal multi-layer aquifer system is helpful to understand the mechanism of seawater intrusion under the influence of tide and groundwater pumping. It plays an important role in the maintenance of the ecological environment and the scientific development and utilization of groundwater resources in coastal areas.

2 Method

2.1 Mathematical model

A coastal multi-layer aquifer system is established, which is composed of an unconfined aquifer, an aquiclude, an upper confined aquifer, an aquiclude, and a lower confined aquifer from top to bottom (Figure 1). The assumptions of the model are as follows: (1) The coastline is a horizontal straight line, and all the layers are horizontal and extend inland infinitely. No flow boundary condition is used at the places sufficiently far from the coastline. (2) Each layer is homogeneous and isotropic, and the thickness of it is constant. All the layers terminate at the coastline. (3) The flow direction in the upper and lower confined aquifers is horizontal. (4) The seabed boundary of the multi-layered aquifer system is directly connected with seawater. (5) The multi-layered monitoring wells are arranged in the aquifer system, and there is constant flow pumping in the upper confined aquifer and the lower confined aquifer. (6) The density difference between seawater and freshwater is ignored, because the density difference between them has little impact on the fluctuation of groundwater level (Li and Chen, 1991).

The x-axis is perpendicular to the coastline and points to the land in a positive direction. The intersection of the x-axis with the coastline is the coordinate origin. The y-axis is parallel to the coastline and coincides with the coastline. The z-axis is taken to be vertical and positive upward. Based on the above assumptions, the governing equations and boundary conditions of groundwater flow in the upper confined aquifer are expressed as the following equations:

$$\boldsymbol{S_1}\frac{\partial \boldsymbol{H_1}}{\partial \boldsymbol{t}} = \boldsymbol{T_1}\left(\frac{\partial^2 \boldsymbol{H_1}}{\partial \boldsymbol{x}^2} + \frac{\partial^2 \boldsymbol{H_1}}{\partial \boldsymbol{y}^2}\right), \boldsymbol{t} > \boldsymbol{0}, \boldsymbol{x} > \boldsymbol{0} \tag{1}$$

$$\lim_{\boldsymbol{x}\to\infty}\frac{\partial \boldsymbol{H_1}}{\partial \boldsymbol{x}}(\boldsymbol{x},\boldsymbol{y},\boldsymbol{t}) = \lim_{\boldsymbol{y}\to\pm\infty}\frac{\partial \boldsymbol{H_1}}{\partial \boldsymbol{y}}(\boldsymbol{x},\boldsymbol{y},\boldsymbol{t}) = \boldsymbol{0} \tag{2}$$

$$\boldsymbol{H_1}(\boldsymbol{x},\boldsymbol{y},\boldsymbol{t})\big|_{\boldsymbol{x}=\boldsymbol{0}} = \boldsymbol{h_s}(\boldsymbol{t}) = \boldsymbol{A}\,\boldsymbol{cos}\,(\boldsymbol{\omega t} - \boldsymbol{\varphi}) \tag{3}$$

where $H_1(x, y, t)$, $\boldsymbol{S_1}$ and $\boldsymbol{T_1}$ represent the hydraulic head [L], storage coefficient [−], and transmissivity [L^2T^{-1}] of the upper confined aquifer; h_s is the hydraulic head of sea tide [L] at the time t [T]; **A**, ω *and* φ represent the tidal amplitude [L], the tidal angular velocity [T^{-1}], and the initial phase shift [−].

Ignoring the well storage effect of the pumping well, Darcy's law is applied, and the boundary conditions on the wall of well can be written as

$$\lim_{\boldsymbol{r_1}\to\boldsymbol{0}} \boldsymbol{r_1}\frac{\partial \boldsymbol{H_1}}{\partial \boldsymbol{r_1}} = \frac{\boldsymbol{Q}}{\boldsymbol{2\pi T_1}}, \quad \boldsymbol{t} > \boldsymbol{0} \tag{4a}$$

$$\boldsymbol{r_1} = \sqrt{(\boldsymbol{x}-\boldsymbol{d})^2 + \boldsymbol{y}^2}, \tag{4b}$$

where **Q** is the pumping rate of the well [L^3T^{-1}], **d** is the distance [L] between the center of the well and the coastline, and $\boldsymbol{r_1}$ is the horizontal distance [L] between any point in the aquifer and the pumping well.

The governing equations and boundary conditions of the initial head in the aquifer influenced by the tide before pumping can be expressed as follows:

$$\boldsymbol{S_1}\frac{\partial \boldsymbol{H_0}}{\partial \boldsymbol{t}} = \boldsymbol{T_1}\frac{\partial^2 \boldsymbol{H_0}}{\partial \boldsymbol{x}^2}, \boldsymbol{t} > \boldsymbol{0}, \boldsymbol{x} > \boldsymbol{0} \tag{5}$$

$$\lim_{\boldsymbol{x}\to\infty}\frac{\partial \boldsymbol{H_0}}{\partial \boldsymbol{x}}(\boldsymbol{x},\boldsymbol{t}) = \boldsymbol{0} \tag{6}$$

$$\boldsymbol{H_0}(\boldsymbol{x},\boldsymbol{t})\big|_{\boldsymbol{x}=\boldsymbol{0}} = \boldsymbol{h_s}(\boldsymbol{t}) = \boldsymbol{A}\,\boldsymbol{cos}\,(\boldsymbol{\omega t} - \boldsymbol{\varphi}) \tag{7}$$

where $\boldsymbol{H_0}$ is the initial groundwater head [L] of the upper confined aquifer under the influence of tide before pumping.

The lower confined aquifer is similar to the upper confined aquifer, therefore, the description of its governing equations and boundary conditions is ignored here.

2.2 Derivation of analytical solution

The solution of the mathematical models (Equations 5–7) is the analytical solution of groundwater level fluctuation in a confined aquifer given by Jacob (1950), which is under the boundary condition that the sea tide is a cosine function, namely, the initial condition of the mathematical model for the aquifer system can be expressed as follows:

$$\boldsymbol{H_0}(\boldsymbol{x},\boldsymbol{t}) = \boldsymbol{H_{Jacob}}(\boldsymbol{x},\boldsymbol{t}) = \boldsymbol{A}\boldsymbol{e}^{-\boldsymbol{a_c x}}\,\boldsymbol{cos}\,(\boldsymbol{\omega t} - \boldsymbol{a_c x} - \boldsymbol{\varphi}), \boldsymbol{x} \geq \boldsymbol{0} \tag{8}$$

where $a_c = \sqrt{\frac{\omega S_1}{2T_1}}$, which is an intermediate parameter. Therefore, one can have

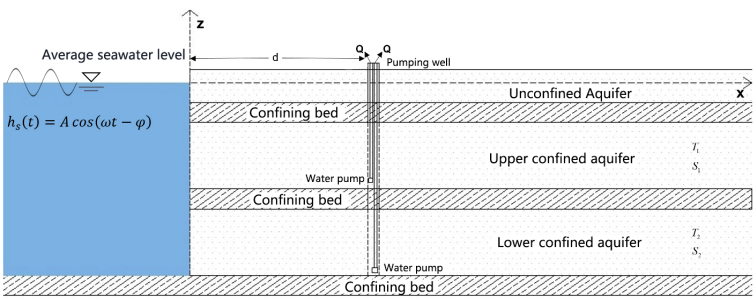

FIGURE 1
Schematic of pumping well in a multi-layered confined aquifer.

$$\boldsymbol{H_1(x,y,t)}\big|_{t=0} = \boldsymbol{H_{Jacob}(x,t)}\big|_{t=0} \tag{9}$$

In the traditional pumping test, the variation of hydraulic head is expressed by the drawdown, because the initial hydraulic head is a constant. However, the initial hydraulic head is not a constant under the effect of tide; therefore, H_1 is used to describe the variation of hydraulic head as shown in Equation 9. As the coastline is the recharge boundary of the aquifer system, according to the theory of image method, there is an imaginary injection well with a flow rate of **Q** at the symmetrical position **-d** relative to the pumping well.

According to the formula of well flow and superposition principle in the confined aquifer without leakage recharge, the analytical solution of Equations 1–3, 4a, 4b can be obtained as follows (detailed derivation process is shown in Appendix A):

$$\boldsymbol{H_1(x,y,t)} = \boldsymbol{H_{Jacob}(x,t)} + \frac{Q}{4\pi T_1}[\boldsymbol{W(u_2)} - \boldsymbol{W(u_1)}] \tag{10a}$$

where

$$\boldsymbol{W(u)} = \int_{u}^{\infty} \frac{e^{-y}}{y}\,dy \tag{10b}$$

$$\boldsymbol{u_1} = \frac{r_1^2 S_1}{4T_1 t},\ \boldsymbol{u_2} = \frac{r_2^2 S_1}{4T_1 t} \tag{10c}$$

$$\boldsymbol{r_2} = \sqrt{(x+d)^2 + y^2} \tag{10d}$$

where $\boldsymbol{W(u)}$ is a well function, $\boldsymbol{u_1}$ and $\boldsymbol{u_2}$ are the intermediate parameters, the expression of $\boldsymbol{r_1}$ is shown in Equation 4b, and $\boldsymbol{r_2}$ is the horizontal distance between any point in the aquifer and the fictitious injection well [L].

The groundwater flow governing equations, boundary conditions, and initial conditions in the lower confined aquifer are consistent with those in the upper confined aquifer. Therefore, the analytical solution of the equations can be directly obtained as follows:

$$H_2(x,y,t) = H_{Jacob}(x,t) + \frac{Q}{4\pi T_2}[W(u_2') - W(u_1')] \tag{11a}$$

$$u_1' = \frac{r_1^2 S_2}{4T_2 t}, \qquad u_2' = \frac{r_2^2 S_2}{4T_2 t} \tag{11b}$$

where u_1' *and* u_2' are the intermediate parameters; the expressions of $\boldsymbol{r_1}$ and $\boldsymbol{r_2}$ are shown in Equations 4b, 10d; $\boldsymbol{H_2}$, $\boldsymbol{S_2}$ and $\boldsymbol{T_2}$ represent the hydraulic head [L], storage coefficient [−], and transmissivity $[L^2T^{-1}]$ of the lower confined aquifer.

3 Discussion on analytical solution

3.1 Comparison of analytical solutions

In the coastal aquifer system without considering the leakage, the analytical solution of groundwater level fluctuation affected by tide is given by Jacob (1950), which is the analytical solution in a confined aquifer under the condition that the tide is a single cosine function (Hantush and Jacob, 1955).

When the pumping well is not considered or the pumping rate Q is equal to zero, the groundwater level fluctuation in the upper and lower confined aquifers satisfies the mathematical models (5) to (7). The solution of groundwater level fluctuation in the upper and lower confined aquifers is proposed by Jacob (1950). Namely Equation 12,

$$\boldsymbol{H_1(x,y,t)}\big|_{Q=0} = \boldsymbol{H_2(x,y,t)}\big|_{Q=0} = \boldsymbol{Ae^{-a_c x}\cos(\omega t - a_c x - \varphi)}$$
$$= \boldsymbol{H_{Jacob}(x,t)} \tag{12}$$

When the tidal effect is not considered or **A** = 0, the analytical solution of groundwater level fluctuation in the upper confined aquifer is written as follows:

$$H_1(x,y,t)|_{A=0} = \frac{Q}{4\pi T_1}[W(u_2) - W(u_1)] \tag{13}$$

where the expressions of $\boldsymbol{W(u)}$, $\boldsymbol{u_1}$, and $\boldsymbol{u_2}$ are shown in Equations 10b, c.

The analytical solution of groundwater level fluctuation in the lower confined aquifer is

$$H_2(x,y,t)|_{A=0} = \frac{Q}{4\pi T_2}[W(u_2') - W(u_1')] \tag{14}$$

where the expressions of $\boldsymbol{W(u)}$, u_1' *and* u_2' are shown in Equations 10b, 11b.

When the tidal effect is not considered or **A** = 0, according to the principle of image method, Equations 13, 14 can be obtained, because the sea is the recharge boundary of the aquifer system. The Theis well function $\boldsymbol{W(u)}$ and its related properties and assumptions have been studied and analyzed in detail (Fetter, 1994); therefore, it is not described here.

3.2 Analytical solution of N-layered confined aquifers

Based on the above model, consider a coastal multi-layered aquifer system consisting of the unconfined aquifer and N-layered confined aquifers from top to bottom (Figure 2). There is an aquiclude between each two confined layers, and other assumptions are consistent with those of the above basic model. Based on the above assumptions, the governing equation and boundary conditions of groundwater flow in the Nth confined aquifer are as follows:

$$\boldsymbol{S_n}\frac{\partial H_n}{\partial t} = \boldsymbol{T_n}\left(\frac{\partial^2 H_n}{\partial x^2} + \frac{\partial^2 H_n}{\partial y^2}\right), \boldsymbol{t > 0, x > 0} \tag{15}$$

$$\lim_{x\to\infty}\frac{\partial \boldsymbol{H_n}}{\partial \boldsymbol{x}}\boldsymbol{(x,y,t)} = \lim_{y\to\pm\infty}\frac{\partial \boldsymbol{H_n}}{\partial \boldsymbol{y}}\boldsymbol{(x,y,t)} = \boldsymbol{0} \tag{16}$$

$$\boldsymbol{H_n(x,y,t)}\big|_{x=0} = \boldsymbol{h_s(t)} = \boldsymbol{A\cos(\omega t - \varphi)} \tag{17}$$

where $H_n(x,y,t\ )$, S_n and T_n represent the hydraulic head [L], storage coefficient [−], and transmissivity $[L^2T^{-1}]$ of the Nth confined aquifer.

The well storage effect of the pumping well is ignored, and Darcy's law is applied. The boundary condition on the wall of well can be written as

10.3389/fmars.2024.1382206

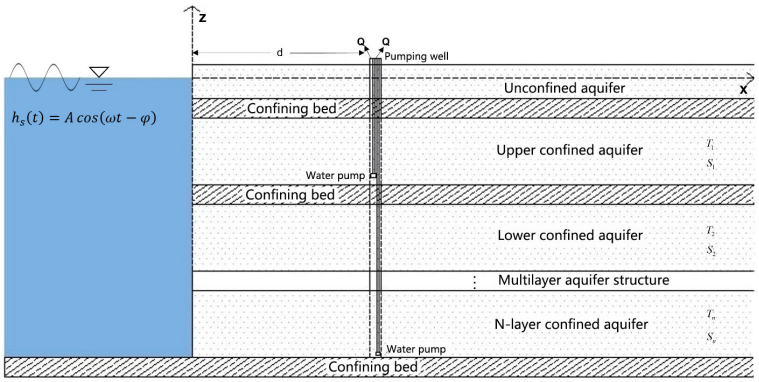

FIGURE 2
Schematic of pumping well in a N-layered confined aquifer.

$$\lim_{r_1 \to 0} r_1 \frac{\partial H_n}{\partial r_1} = \frac{Q}{2\pi T_n}, t > 0 \tag{18}$$

The governing equation and boundary conditions of initial head in the Nth confined aquifer under the tidal influence before pumping can be expressed as follows:

$$S_n \frac{\partial H_{n0}}{\partial t} = T_n \frac{\partial^2 H_{n0}}{\partial x^2}, t > 0, x > 0 \tag{19}$$

$$\lim_{x \to \infty} \frac{\partial H_{n0}}{\partial x}(x,t) = 0 \tag{20}$$

$$H_{n0}(x,t)|_{x=0} = h_s(t) = A\cos(\omega t - \varphi) \tag{21}$$

where H_{n0} is the initial groundwater head [L] of the Nth confined aquifer under the influence of tide before pumping.

The boundary conditions and initial conditions of groundwater head in the Nth confined aquifer are consistent with those of the upper confined aquifer; therefore, the analytical solution of the equations can be obtained directly

$$H_n(x,y,t) = H_{Jacob}(x,t) + \frac{Q}{4\pi T_n}[W(u_{n2}) - W(u_{n1})] \tag{22}$$

where

$$u_{n1} = \frac{r_1^2 S_n}{4T_n t}, u_{n2} = \frac{r_2^2 S_n}{4T_n t} \tag{23}$$

For the groundwater fluctuation in the coastal N-layered confined aquifer system under the effects of tide and pumping, the Equations 15–23 can be used to solve it.

3.3 Discussion on the impact of parameters

From the analytical solutions (10) and (11), it can be seen that the fluctuation of groundwater level under the effects of tide and well pumping is influenced by various parameters. It mainly includes parameters, which are tidal amplitude A $[L]$, initial phase shift φ [–], tidal angular velocity ω $[T^{-1}]$, the distance between the well center and coastline **d** [L], the pumping rate of well **Q** $[L^3T^{-1}]$, storage coefficient **S** [–], and transmissivity **T** $[L^2T^{-1}]$. The impact of the main parameters in the analytical solution is discussed. The values of parameters for different cases are listed in Table 1.

TABLE 1 Values of parameters for different cases.

Parameter	Case 1	Case 2	Case 3	Case 4	Case 5	Unit
A	1	1	1	1	1	m
φ	$\varphi_1 = 0 \varphi_2 = \pi/2 \varphi_3 = \pi \varphi_4 = 3\pi/2$	0	0	0	0	[–]
ω	$\pi/6$	$\pi/6$	$\pi/6$	$\pi/6$	$\pi/6$	h^{-1}
d	190	$d_1 = 180 d_2 = 240 d_3 = 300$	210	210	210	m
Q	600	600	$Q_1 = 40 Q_2 = 120 Q_3 = 360$	360	360	m^3/h
S	1.0×10^{-4}	1.0×10^{-4}	1.0×10^{-4}	$S_1 = 1.0 \times 10^{-4} S_2 = 3.0 \times 10^{-4} S_3 = 9.0 \times 10^{-4}$	1.0×10^{-4}	[–]
T	10	10	10	10	$T_1 = 10\ m^2/h$ $T_2 = 30\ m^2/h$ $T_3 = 90\ m^2/h$	m^2/h

10.3389/fmars.2024.1382206

Figure 3 shows how the groundwater head in the observation well located at $(x_0, y_0) = (200m, 0m)$ varies with time when the initial phase shift $\varphi = 0,\ \pi/2,\ \pi$, and $3\pi/2$ (*Case 1 in* Table 1). From Figure 3 one can see that the groundwater head in the observation well decreases dramatically during the initial pumping stage and then tends to be stabilized gradually with time. There is a significant difference in the initial drawdown corresponding to different initial phases during the early stage of pumping, based on the groundwater head variation from 0 h to 15 h. It indicates that the initial phase of tide affects the initial drawdown in the observation well during the pumping. The primary justification behind this is the direct correlation between tide phase and the establishment of the groundwater level during pumping operations. The groundwater head fluctuations corresponding to different initial phases exhibit a significant lag relationship, namely, the phase difference. Therefore, the observed data of groundwater head during the long-term pumping should be used to estimate the hydrogeological parameters. Otherwise, there may be significant errors if one uses the data of groundwater head fluctuation during the early pumping.

Figure 4 shows the variation of groundwater head with time in the observed well at the location x = 200 m when d = 180*m*, 240 *m and* 300*m*, respectively (*Case* 2 *in* Table 1). From Figure 4, one can see that the groundwater head in the observed well decreases rapidly within the initial 7 h of pumping. Then, it decreases gradually and stabilizes with time. The fluctuation of groundwater head in the aquifer exhibits periodic fluctuations, which is similar to tide. By comparing the three curves, it can be seen that the periodic fluctuation of groundwater head in the aquifer exhibits a lag phenomenon, as the distance from the pumping well to the coastline increases. The study further affirms that the influence of tidal fluctuations on groundwater levels decreases gradually from the coastal region to inland.

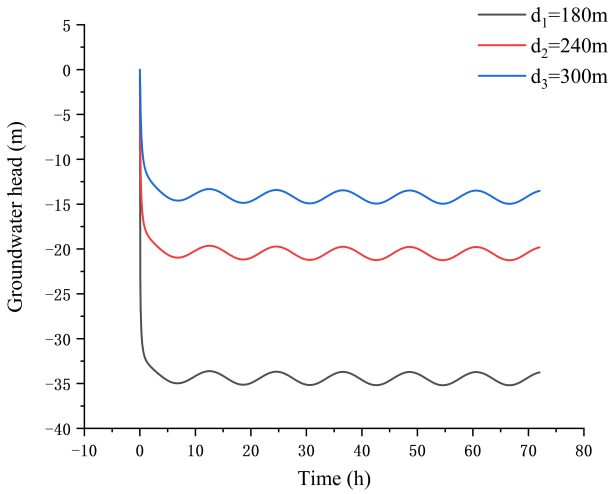

FIGURE 4
Changes of the groundwater head with time in an observed well located at x = 200 m during pumping for different values of the distance between the center of well and coastline.

Figure 5 shows the effects of pumping rate on the groundwater head fluctuation in the observed well at the location **x** = 290 m of the confined aquifer (*Case 3 in* Table 1). When the pumping rate Q_1 is $40m^3/h$, the groundwater head in the observed well drops about 2 m and then reaches a quasi–steady state. When the pumping rate Q_3 is $360m^3/h$, the groundwater head in the observed well drops about 7 m before reaching stability. It can be inferred that the pumping rate has a significant impact on the groundwater head in the observed well, and the high pumping flow rate causes an increase in the drawdown of the groundwater head. In the early stages of pumping, the groundwater head drops sharply due to the effect of pumping well. As the time increases, the groundwater head

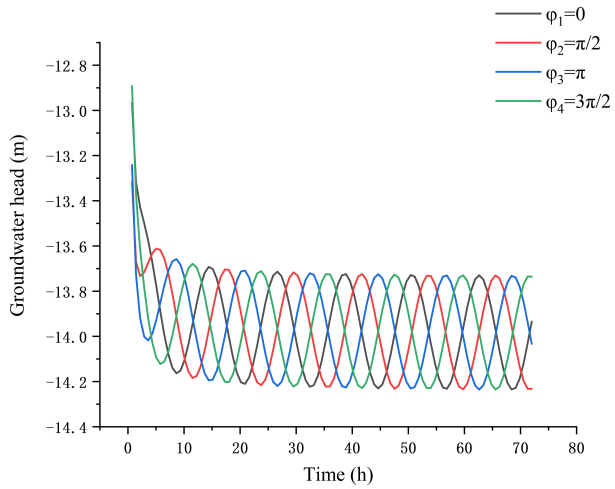

FIGURE 3
Changes of the groundwater head with time in the observation well located at (x0, y0) = (200 m, 0 m) during pumping for different values of the initial phase shifts.

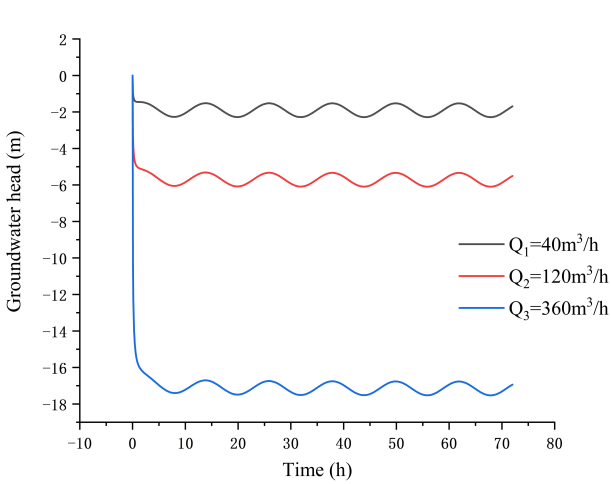

FIGURE 5
Variation of the groundwater head fluctuation in the observed well at the location x = 290 m of the confined aquifer for different values of pumping rate.

decreases rapidly in a short period of time, and, then, the decline rate decreases gradually. After 9 h, it can be seen that the fluctuation curve of the groundwater head shows the first obvious trough, and the groundwater head in the well stabilizes gradually, which presents a tidal fluctuation curve. By comparing the three curves, it can be found that as the pumping rate increases, the time for the groundwater level to reach a stable rate of decline increases. The aforementioned phenomenon is perceptible through the alteration of groundwater levels, which demonstrate that, as the amount of extraction increases, the difficulty in achieving and maintaining equilibrium also escalates.

Figure 6 shows how the groundwater head in the observation well located at **x** = 190 m changes with time for different values of storage coefficient (*Case 4 in* Table 1). From Figure 6, one can see that the groundwater head decreases gradually with time for different values of storage coefficient. The groundwater head tends to be stabilized at the time of 8 h, when the storage coefficient S_1 is 1.0×10^{-4}. The groundwater head gets a quasi–steady state at the time of 14 h, when the storage coefficient S_3 is 9.0×10^{-4}. However, the decreasing trend of groundwater head after reaching stability is more significant. It indicates that the water level decrease caused by the pumping becomes slowly, as the storage coefficient increases. The groundwater level fluctuation tends to be stabilized and shows a significant cosine fluctuation, when the storage coefficient is 1.0×10^{-4}. However, when the storage coefficient is 3.0×10^{-4}, it can be found that the amplitude of groundwater level fluctuation is significantly weaker than that of the water storage coefficient S_1 (1.0×10^{-4}). At the same time, the fluctuation of groundwater level is almost invisible, when the storage coefficient is 9.0×10^{-4}. It can be inferred that the storage coefficient affects the groundwater head significantly. As the storage coefficient increases, the fluctuation of groundwater level in the aquifer is less affected by the tidal fluctuations and shows a significant lag phenomenon.

Figure 7 shows how the groundwater head in the observation well located at **x** = 190 m changes with time for different values of transmissivity (*Case 5 in* Table 1). From Figure 7, one can see that the first time of a trough occurs in the groundwater head fluctuation curve is at 9 h, when the transmissivity is T_1(1.0×10^{-4} to 10). However, the first obvious trough appears at 7 h when the transmissivity is T_3(1.0×10^{-4} to 90). It indicates that the drawdown of groundwater head in the aquifer decreases as the transmissivity increases, and the periodic fluctuation of groundwater head shows a lag phenomenon. Comparing the three curves, it can be found that, when the values of transmissivity are T_1, T_2 (3.0×10^{-4} to 30 *and* T_3), the amplitude of periodic fluctuation is 0.5 m, 1 m, and 1.2 m, respectively. It indicates that the periodic fluctuation of groundwater head in the aquifer is affected by tides, as the transmissivity increases. The transmissivity of the confined aquifer reflects the sensitivity of the groundwater level to hydrodynamic factors such as pumping and tides within the aquifer.

Wang et al. (2014) also consider the analytical solutions of groundwater level fluctuations under tidal and pumping conditions, and it considers the leakage between the unconfined aquifer and confined aquifer. However, this study considers the analytical solutions of groundwater level fluctuations in multi-layer aquifer systems and neglects the leakage between layers. Wang et al. (2014) separately discussed the influence of factors such as tidal phase and pumping flow on water level fluctuations, and it was difficult to distinguish the tidal effect from the head drop caused by pumping when the pumping time is less than half a tidal cycle. Wang et al. (2014) discussed the parameters of the two factors separately but did not combine the tidal and pumping. In this study, the discussion focuses on the interaction between the tidal and pumping conditions and further studies the combined effect of tidal and pumping on groundwater level fluctuations.

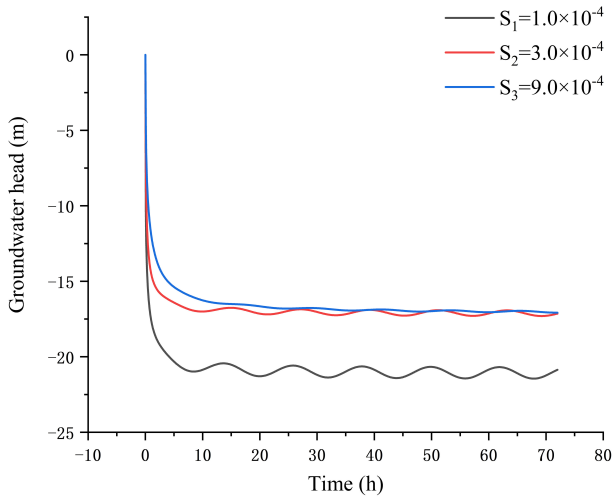

FIGURE 6
Variation of the groundwater head fluctuation in the observed well at the location x = 190 m of the confined aquifer for different values of storage coefficient.

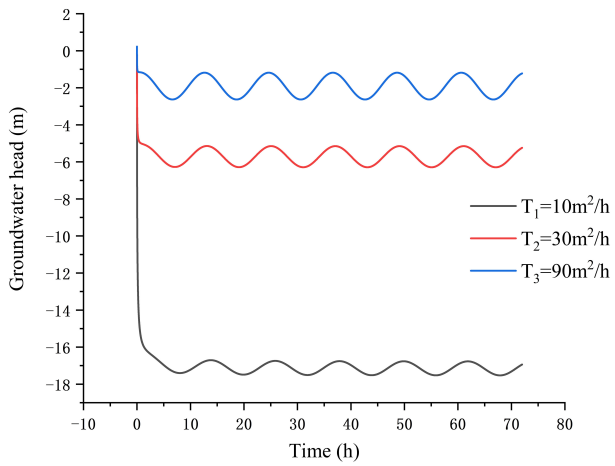

FIGURE 7
Variation of the groundwater head fluctuation in the observed well at the location x = 190 m of the confined aquifer for different values of transmissivity.

10.3389/fmars.2024.1382206

4 Practical application

4.1 Regional overview

The study area is located in Longkou City, Shandong Province, China, which is situated in the northwestern part of the Jiaodong Peninsula (between 120°13′ and 120°44′ E longitude and 37°27′ and 37°47′ N latitude; Figure 8). The total area of Longkou City is about 901 km^2. The maximum distance from north to south of Longkou is 37.43 km, and the maximum distance from east to west is 46.08 km, with a coastline of up to 68.4 km. The terrain and landform of Longkou City include the mountains, hills, and plains. The mountains are mainly located in the southeast of Longkou City, whereas the hills are located in the north of the southern part of the mountains. The plain area has formed three different types of landform due to its different genesis, including the coastal plain, the alluvial plain of mountain valley, and the alluvial plain in front of mountains. The exposed strata on the surface area are the Quaternary of the Cenozoic era, which mainly compose of sand, clay, and gravel. The research area has a semi-humid climate with significant seasonal changes, which is greatly affected by the monsoon. The average annual precipitation is 585.5 mm, which supplies the groundwater. The rivers are seasonal rivers in Longkou City, including the Huangshui River, Yongwen River, Beimanan River, Longkou North River, and Balisha River. The flow trend of groundwater is influenced by the terrain, which discharges into the Laizhou Bay from south to north. Longkou City is located in the warm temperate zone, with obvious characteristics of semi-humid monsoon land climate. It is heavily influenced by the monsoon and has four distinct seasons. There is less precipitation in spring, and the climate is dry, with the south wind as the main one; there is more rainfall in summer, with high and humid temperatures and more rainy weather; in autumn, the climate is dry and cool, with less rainfall; in winter, the temperature is low and the climate is cold, with the north wind as the main one. The average temperature for many years is 12.2°C, the maximum temperature is 38.3°C, the minimum temperature is −21.3°C, and the average evaporation for many years is 1479 mm. The average annual precipitation is 585.5 mm. Rainfall fluctuates greatly between years. There are significant differences in precipitation between seasons and regions. Rainfall in a year is most concentrated in July, August, and September. With the development of agriculture and industry, the demand for water such as farmland irrigation has increased, leading to high-intensity and unreasonable exploitation of groundwater in the area. As a result, the groundwater level in the coastal aquifer declines continuously in this area. In recent years, the problem of seawater intrusion in the region has been very serious. The measures were taken to prevent the seawater intrusion, and the area of seawater intrusion has gradually decreased.

According to the drilling data, the coastal aquifer system of Longkou western coast is composed of three permeable layers and two aquicludes between them. The three permeable layers include an unconfined aquifer, an upper confined aquifer, and a lower confined aquifer, as illustrated in Figure 9. The distance of four groups of boreholes from the coastline is 1.2 km, 2.1 km, 2.6 km, and 3.2 km sequentially, and each group of boreholes is distributed in three different aquifers (Dai et al., 2020). The geologic information of the coastal aquifer system is described from up to down sequence. Coarse and medium sand in the unconfined aquifer, sand and gravel in the upper confined aquifer, and coarse sand and gravel in the lower confined aquifer. The average thickness of the unconfined aquifer is about 3.30 m, the upper confined aquifer is about 4.00 m, and the lower confined aquifer is also about 4.00 m. Based on slug tests conducted at different depths of boreholes, the hydraulic conductivities of different aquifers were obtained, and they were about 2.93 m/h for the unconfined aquifer, from 1.47 m/h to 3.58 m/h

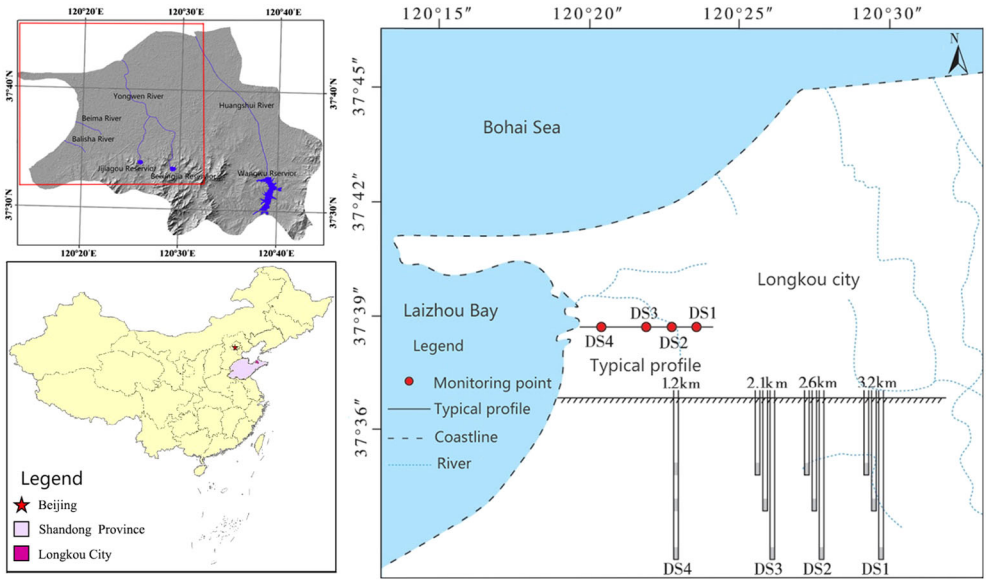

FIGURE 8
Distribution of monitoring wells in the seawater intrusion zone in Longkou City.

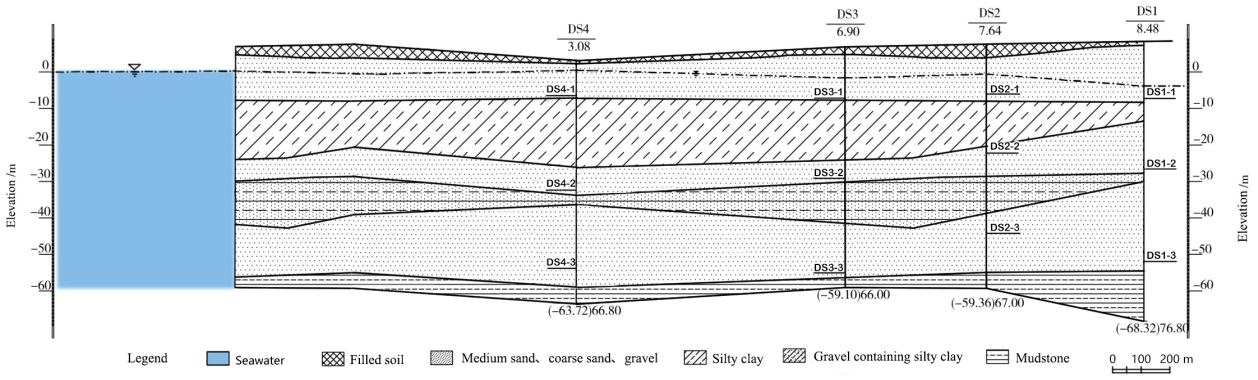

FIGURE 9
Generalizing the field test stratigraphic profile.

for the upper confined aquifer, and from 1.20 m/h to 5.22 m/h for the lower confined aquifer. The groundwater head and water quality in each borehole were monitored.

4.2 Example for parameter estimation

In order to verify the applicability of the analytical solution, the parameters in the analytical solution are assigned with reference to the actual situation (Table 2). The thickness and storage coefficient of the aquifer were determined by the oscillation test conducted by Dai et al. in the groundwater stratification monitoring well in the Longkou seawater intrusion area (Dai et al., 2020). The tidal amplitude A, initial phase shift φ and tidal angular velocity ω of tidal fluctuations are derived from the tidal prediction table of Longkou City when the monitoring well is working. The variation of the water level in the upper and lower confined aquifers are calculated within 60 h (2.5 cycles of sea tide). The value of the pumping rate of well Q is 400 m^3/h as shown in Table 2, and the pumping period is 60 h. The water level data in the four monitoring wells—DS3–2, DS4–2, DS3–3, and DS4–3—were selected to fit the analytical solution. Therefore, the inverse problem can be used to establish the corresponding solution method.

Let

$$\boldsymbol{\varphi_1(x,t)} = \frac{\partial H_1(x,y,t)}{\partial t}\ , \boldsymbol{t > 0, x > 0} \tag{24}$$

According to Equations 8, 10a–d, 24, one can obtain that

$$\boldsymbol{\varphi_1(x,t) = -\omega e^{-a_c x} sin(\omega t - a_c x - \varphi) + \frac{Q}{4\pi t K_1 M_1}} \left(\boldsymbol{e^{-\frac{(x+d)^2 S_1}{4tK_1M_1}} - e^{-\frac{(x-d)^2 S_1}{4tK_1M_1}}}\right), \boldsymbol{t > 0, x > 0} \tag{25}$$

when $\varphi_1(x,t)$ approaches zero, the change rate in groundwater head fluctuation of the upper confined aquifer is zero. It means that $\varphi_1(x,t)$ is equal to zero, when $H_1(x,y,t)$ reaches its extreme value.

Based on the measured curve of **H** relative to **t**, the extreme value $t_j[T]$ of the curve can be derived. Then, according to the values of parameters in Table 2, the hydraulic conductivity K_1 of the upper confined aquifer can be obtained based on Equation 25. The groundwater level within 60 h (2.5 tidal cycles) in the monitoring well DS2–2 was selected. The average value −1.78 m of it was taken as the initial head *of* H_{2-2}. Figure 10 shows the changes of the

TABLE 2 Values of the parameters.

Parameter	Value	Unit
A	1	m
ω	$\pi/12$	h^{-1}
φ	-3 $\pi/16$	[–]
d	1×10^4	m
Q	400	m^3/h
M_1	4	m
M_2	4	m
S_1	1.0×10^{-4}	[–]
S_2	0.9×10^{-5}	[–]

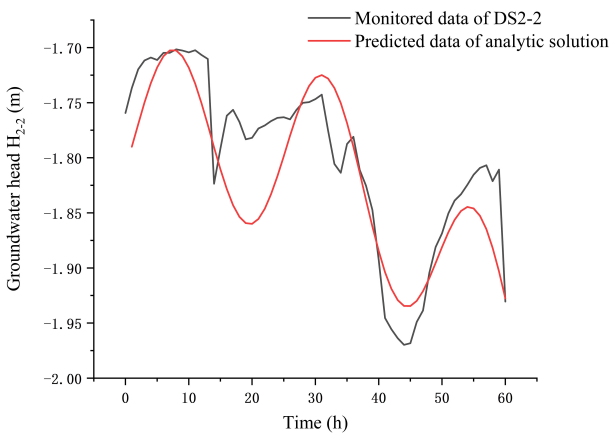

FIGURE 10
Comparison of the results of the analytical solution simulation with the monitoring data of well DS2–2.

observed H_{2-2} with time t in the well DS2–2. From Figure 10 one can see that the extreme values of t_{j2-2} are 8 h, 31 h, and 45 h. Therefore, the values of the hydraulic conductivity K_{2-2} of the upper confined aquifer are 3.07 m/h, 3.36 m/h, and 3.77 m/h, respectively, based on the Table 2 and Equation 25. The data collation is shown in DS2–2 of Table 3. The average value of K_{2-2} in the upper confined aquifer is 3.4 m/h, which is in the range from 1.47 m/h to 3.58 m/h as shown above. The calculated groundwater head based on the analytical solution (10) is shown in Figure 10, according to the hydraulic conductivity K_{2-2} and other parameters listed in Table 2. The mean square error (*MSE*) between the observed groundwater head and the predicted value calculated by the analytical solution (10) can be written as follows:

$$\boldsymbol{MSE} = \frac{1}{n}\sum_{i=1}^{n}(\boldsymbol{H_i} - \widehat{\boldsymbol{H_i}})^2, (\boldsymbol{n = 60}) \tag{26}$$

where H_i is the observed groundwater head and $\hat{H}_i$ is the predicted value calculated by the analytical solution (10). Therefore, MSE_{2-2} is 0.0018 based on Figure 10 and Equation 26.

The observed groundwater level within 60 h (2.5 sea tide cycles) in the monitoring well DS3–2 was chosen, and the average value of it was taken as the initial head, namely, H_{3-2} is equal to −4.83 m. Figure 11 shows the variation of the observed H_{3-2} with time t in the well DS3–2. From Figure 11, one can see that the extreme values of t_{j3-2} are 7 h, 19 h, 31 h, 42 h, and 55 h. Therefore, the values of the hydraulic conductivity K_{3-2} in the upper confined aquifer are 2.46 m/h, 2.46 m/h, 2.41 m/h, 3.42 m/h, and 2.22 m/h, respectively, based on Table 2 and Equation 25. The data collation is shown in DS3–2 of Table 3. The average value K_{3-2} of the hydraulic conductivity in the upper confined aquifer is 2.69 m/h, which is in the range between 1.47 m/h and 3.58 m/h. According to the average value of K_{3-2} and the other parameters assigned in Table 2, the calculated value H_{3-2} based on the analytical solution (10) is also plotted and shown in Figure 11. The mean square error MSE_{3-2} between the observed groundwater level and the predicted value in the monitoring well DS3–2 is 0.00052.

In fact, the fluctuation of seawater level is influenced by the spring-neap tides. Moreover, the layers between each two aquifers are relative aquicludes, and there maybe leakage recharge between layers. Therefore, the analytical solution under ideal conditions could not fully match the fluctuation of the groundwater level. Nevertheless, the fitted results of the analytical solution capture the main characteristics of the groundwater level affected by the tidal fluctuation and groundwater pumping as shown in Figures 10, 11. Based on the fitted curves of groundwater head in wells DS2–2 and

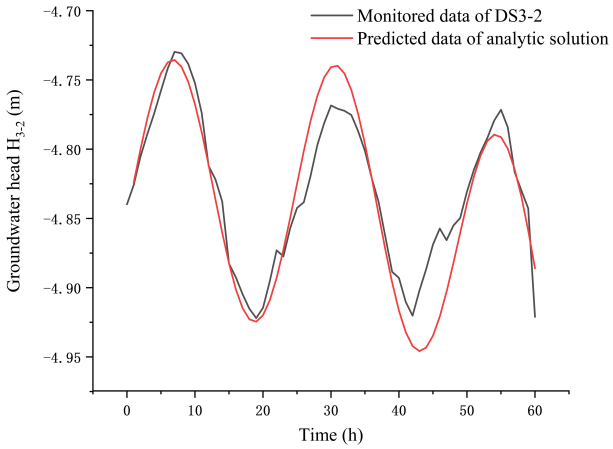

FIGURE 11
Comparison of the results of the analytical solution simulation with the monitoring data of well DS3–2.

DS3–2, one can observe a marked fluctuation in groundwater head in correlation with the tide, revealing a progressive decrease with increasing elapsed time. At the same time, the amplitude of groundwater level shows a decreasing trend. Comparing Figures 10, 11, it can be found that the decreasing trend of groundwater level in well DS2–2 is more obvious than that in well DS3–2. The reason is that the distance from the pumping well for well DS2–2 is closer than that of DS3–2. It indicates that the decreasing rate of groundwater head increases as the distance of observed well from the pumping well decreases.

Similarly, let

$$\boldsymbol{\varphi_2(x,t)} = \frac{\partial \boldsymbol{H_2(x,y,t)}}{\partial \boldsymbol{t}} \; \boldsymbol{t > 0, x > 0} \tag{27}$$

According to Equations 8, 10a–d, 27, one can obtain

$$\boldsymbol{\varphi_2(x,t)} = -\boldsymbol{\omega e^{-a_c x} sin(\omega t - a_c x - \varphi)} + \frac{\boldsymbol{Q}}{\boldsymbol{4\pi t K_2 M_2}} \left(\boldsymbol{e^{\frac{(x+d)^2 S_2}{4tK_2M_2}} - e^{\frac{(x-d)^2 S_2}{4tK_2M_2}}}\right), \boldsymbol{t > 0, x > 0} \tag{28}$$

when $\varphi_2(x,t)$ approaches zero, the change rate of groundwater head in the lower confined aquifer is 0. The value of $\varphi_2(x,t)$ is equal to zero, when $H_2(x,y,t)$ reaches its extreme value.

The observed groundwater level in the monitoring well DS3–3 within 60 h (2.5 sea tide cycles) was selected, and the average value was taken as the initial head H_{3-3} $(1.77m)$. Figure 12 reports the

TABLE 3 The data collation of parameter estimation.

Parameter	Unit	DS3–2	DS4–2	DS3–3	DS4–3
t_j	h	8, 31, 45	7, 19, 31, 42, 55	9, 21, 32, 42, 56	9, 33, 57
K	m/h	3.07, 3.36, 3.77	2.46, 2.46, 2.41, 3.42, 2.22	2.23, 1.85, 1.18, 3.99, 1.65	1.85, 1.84, 1.76
$\bar{K}$	m/h	3.4	2.69	2.18	1.82
MSE	-	0.0018	0.00052	0.00066	0.00036

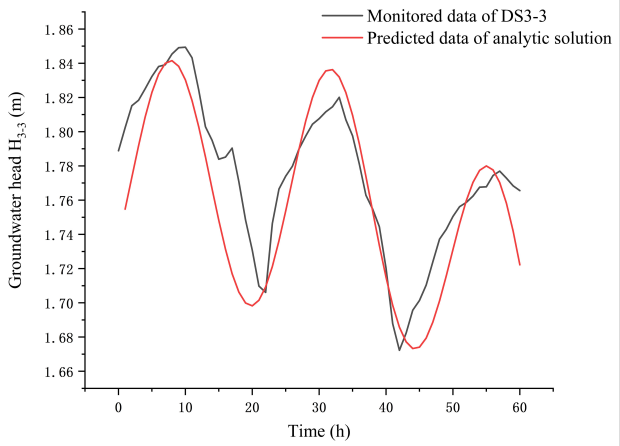

FIGURE 12
Comparison of the results of the analytical solution simulation with the monitoring data of well DS3–3.

variations of the observed groundwater level H_{3-3} with time in well DS3–3. It can be found that the extreme values of t_{j3-3} are 9 h, 21 h, 32 h, 42 h, and 56 h. Thus, the values of hydraulic conductivity K_{3-3} of the lower confined aquifer are 2.23 m/h, 1.85 m/h, 1.18 m/h, 3.99 m/h, and 1.65 m/h, respectively, based on the parameters in Table 2 and Equation 28. The data collation is shown in DS3–3 of Table 3. The average value of hydraulic conductivity K_{3-3} of the lower confined aquifer is 2.18 m/h, which is in the range between 1.20 m/h *and* 5.22 m/h as shown above. The calculated values of H_{3-3} based on the analytical solution (11) are also plotted in Figure 12, according to the hydraulic conductivity K_{3-3} and the other parameters listed in Table 2. The mean square error MSE_{3-3} between the observed values of the groundwater level and the predicted ones in the monitoring well DS3–2 is 0.00066.

The observed groundwater level in the monitoring well DS4–3 within 60 h (2.5 sea tide cycles) was selected, and the average value of groundwater head H_{4-3} was 1.88 m. Figure 13 shows the variations of the observed groundwater level H_{4-3} with time in well DS3–3. The observed extreme values of t_{j4-3} are 9 h, 33 h, and 57 h. The values of the hydraulic conductivity K_{4-3} of the lower confined aquifer are 1.85 m/h, 1.84 m/h, and 1.76 m/h, respectively, based on the parameters listed in Table 2 and Equation 28. The data collation is shown in DS4–2 of Table 3. The average value of the hydraulic conductivity K_{4-3} of the lower confined aquifer is 1.82m/h, which is in the range between 1.20m/h *and* 5.22m/h as shown above. The calculated groundwater level H_{4-3} based on the analytical solution (11) is also reported in Figure 13, according to the hydraulic conductivity K_{4-3} and other parameters listed in Table 2. The mean square error MSE_{4-3} between the observed values of groundwater head and the predicted ones in the monitoring well DS4–3 is 0.00036.

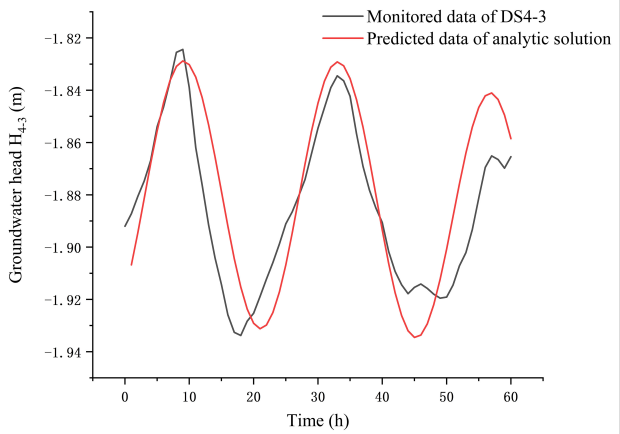

FIGURE 13
Comparison of the results of the analytical solution simulation with the monitoring data of well DS4–3.

Figures 12, 13 show the fitting curves between the measured groundwater level and the calculated one in the wells of the lower confined aquifer based on Equations 11a, b. In general, the calculated groundwater level in the lower confined aquifer fits well with the measured one. Similar to Figures 10–13 show that the groundwater level in the lower confined aquifer fluctuates with the tide, and the amplitude of it decreases gradually with groundwater pumping. At the same time, it can be observed that the decreasing trend of the groundwater level in well DS3–3 is more significant than that in well DS4–3, by comparing Figures 12, 13. It is mainly due to the fact that well DS3–3 is closer to the pumping well, which is influenced by the pumping significantly. The calculated groundwater level based on the analytical solution fits well with the observed one, which shows the main characteristics of groundwater fluctuation effected by the tide and groundwater pumping.

To sum up, the estimated values of the hydraulic conductivities in the upper and lower confined aquifers are within the range of the values obtained from the field experiments (Dai et al., 2020). The small error value of MSE for each case indicates a good fit between the calculated and observed groundwater head. It indicates that the method for calculating the hydraulic conductivity based on the analytical solutions (10) and (11) and Equations 25, 28 is reasonable and reliable.

5 Conclusions

This paper considered groundwater head fluctuation in the coastal multi-layered aquifer system caused by tide and groundwater exploitation. The multi-layered aquifer system is composed of an unconfined aquifer, an upper confined aquifer, and a lower confined aquifer from top to bottom. There is an aquiclude between each two aquifers. All the layers terminate at the coastline and extend infinitely toward the land. The new analytical solutions describing the groundwater head variation in the coastal multi-confined aquifer system are presented. Superposition principle and image methods are used for the derivation of the analytical solutions. Analytical solutions of different situations of without considering pumping, of without considering tidal effect, of N-layered confined aquifers are also discussed.

The fluctuation of groundwater head in the upper and lower confined aquifers under the effects of tide and well pumping is

influenced by the main parameters, including the initial phase shift of tide, pumping rate of well, position of the pumping well, storage coefficient, and transmissivity. The initial phase shift of tide has a significant impact on groundwater head, controlling the initial groundwater head and the magnitude and rate of groundwater head decline before pumping. As the distance from the pumping well to the coastline increases, the periodic fluctuation of the groundwater head exhibits a lag phenomenon during the pumping. The pumping rate influences the groundwater head, and the higher pumping rate causes decrease of groundwater head dramatically. As the storage coefficient increases, the fluctuation of groundwater head in the aquifer is less affected by the tide and shows a significant lag phenomenon. However, as the transmissivity increases, the periodic fluctuation of groundwater head in the aquifer is affected by the tide.

Our solutions are applied to analyze the observed groundwater head fluctuation caused by the tide and pumping in the wells, which situated in the coastal zone of Longkou City, Shandong Province, China. The method for calculating hydraulic conductivities based on the analytical solutions (10) and (11) and Equations 25, 28 is reasonable and reliable. The estimated values of hydraulic conductivities in the upper and lower confined aquifers are within the range of the values obtained from the field experiments. The smaller error value of MSE for each case indicates a good fit between the calculated groundwater head and observed one. The fitted results of the analytical solutions capture the main characteristics of groundwater head fluctuation affected by the tide and groundwater pumping. The study of groundwater head fluctuation in the coastal multi-layer aquifer system is helpful to understand the mechanism of seawater intrusion under the influence of tide and groundwater pumping.

The analytical solutions appear in aquifer systems where aquifers are separated by aquicludes, but aquifers may also be separated by aquitards, so further consideration should be given to leakage between aquifers based on analytical solutions. New analytical solutions applicable to aquifer systems where aquifers are separated by aquitards should be discussed in the future. Simplified aquifer systems often struggle to accurately accommodate the intricacies of complex geologic formations. To more accurately represent the consequences of the apparent mismatch between the actual geological environment and the simplified aquifer model, it is often useful to employ numerical simulations to clarify potential differences between analytical and numerical results or to develop more complex analytical or semi-analytical approaches in the future.

Data availability statement

The raw data supporting the conclusions of this article will be made available by the authors, without undue reservation.

Author contributions

QG: Writing – original draft. JL: Data curation, Investigation, Writing – original draft. XZ: Formal analysis, Writing – review & editing. YD: Investigation, Writing – review & editing.

Funding

The author(s) declare financial support was received for the research, authorship, and/or publication of this article. This work was supported by the National Natural Science Foundation of China (Grant No. 41772235).

Conflict of interest

The authors declare that the research was conducted in the absence of any commercial or financial relationships that could be construed as a potential conflict of interest.

Publisher's note

References

Ackerer, P., Carrera, J., and Delay, F. (2023). Identification of aquifer heterogeneity through inverse methods. *Comptes Rendus Geosci.* 355, 45–58. doi: 10.5802/crgeos.162

Bakker, M. (2019). Analytic solutions for tidal propagation in multilayer coastal aquifers. *Water Resour. Res.* 55, 3452–3464. doi: 10.1029/2019WR024757

Bresciani, E., Batelaan, O., Banks, E. W., Barnett, S. R., Batlle-Aguilar, J., Cook, P. G., et al. (2015a). *Assessment of Adelaide Plains Groundwater Resources: Summary Report* (Adelaide, South Australia: Goyder Institute for Water Research Technical Report Series No. 15/31).

Bresciani, E., Batelaan, O., Banks, E. W., Barnett, S. R., Batlle-Aguilar, J., Cook, P. G., et al. (2015b). *Assessment of Adelaide Plains Groundwater Resources: Appendices Part I – Field and Desktop Investigations* (Adelaide, South Australia: Goyder Institute for Water Research Technical Report Series No. 15/32).

Cartwright, N., Nielsen, P., and Li, L. (2004). Experimental observations of watertable waves in an unconfined aquifer with a sloping boundary. *Adv. Water Resour.* 27, 991–1004. doi: 10.1016/j.advwatres.2004.08.006

Chapuis, R. P., Belanger, C., and Chenaf, D. (2006). Pumping test in a confined aquifer under tidal influence. *Ground Water.* 44, 300–305. doi: 10.1111/j.1745-6584.2005.00139.x

Chuang, M. H., and Yeh, H. D. (2007). An analytical solution for the head distribution in a tidal leaky confined aquifer extending an infinite distance under the sea. *Adv. Water Resour.* 30 (3), 439–445. doi: 10.1016/j.advwatres.2006.05.011

Chuang, M. H., and Yeh, H. D. (2011). A generalized solution for groundwater head fluctuation in a tidal leaky aquifer system. *J. Earth Syst. Sci.* 120, 1055–1066. doi: 10.1007/s12040-011-0128-8

Dai, Y., Lin, J., Guo, Q., Sun, X., Chen, Y., and Liu, J. (2020). Experimental study on rapid evaluation of formation permeability in seawater intrusion area. *J. Hydraulic Engineering.* 10), 1234–1247. doi: 10.13243/j.cnki.slxb.20200108

Das, K., Debnath, P., Layek, M. K., Sarkar, S., Ghosal, S., Mishra, A. K., et al. (2022). Shallow and deep submarine groundwater discharge to a tropical sea: Implications to

coastal hydrodynamics and aquifer vulnerability. *J. Hydrol.* 605, 127335. doi: 10.1016/j.jhydrol.2021.127335

Debnath, P., Mukherjee, A., Singh, H. K., and Mondal, S. (2015). Delineating seasonal porewater displacement on a tidal Cat in the Bay of Bengal by thermal signature: Implications for submarine groundwater discharge. *J. Hydrol.* 29, 1185–1197. doi: 10.1016/j.jhydrol.2015.09.029

Fetter, C. W. (1994). *Applied Hydrogeology. 3rd ed.* (NJ, New York: Englewood Cliffs, Prentice Hall).

Guo, Q., Huang, J., Zhou, Z., and Wang, J. (2019). Experiment and numerical simulation of seawater intrusion under the influences of tidal fluctuation and groundwater exploitation in coastal multilayered aquifers. *Geofluids.* 2019, UNSP 2316271. doi: 10.1155/2019/2316271

Guo, Q., Li, H., Boufadel, M. C., Xia, Y., and Li, G. (2007). Tide-induced groundwater head fluctuation in coastal multi-layered aquifer systems with a submarine outlet-capping. *Adv. Water Resour.* 30, 1746–1755. doi: 10.1016/j.advwatres.2007.01.003

Hantush, M. S., and Jacob, C. E. (1955). Non-steady radial flow in an infinite leaky aquifer. *Transactions Am. Geophysical Union* 36, 95–100. doi: 10.1029/TR036i001p00095

Hsieh, P. C., Hsu, H. T., Liao, C. B., and Chiueh, P. T. (2015). Groundwater response to tidal fluctuation and rainfall in a coastal aquifer. *J. Hydrol.* 521, 132–140. doi: 10.1016/j.jhydrol.2014.11.069

Huizer, S., Karaoulis, M., Oude Essink, G., and Bierkens, M. (2017). Monitoring and simulation of salinity changes in response to tide and storm surges in a sandy coastal aquifer system. *Water Resour. Res.* 53, 6487–6509. doi: 10.1002/2016WR020339

Jacob, C. E. (1950). "Flow of groundwater," in *Engineering Hydraulics*. Ed. H. Rouse (John Wiley& Sons Inc, New York), 321–386.

Jasechko, S., Perrone, D., Seybold, H., Fan, Y., and Kirchner, J. W. (2020). Groundwater level observations in 250,000 coastal US wells reveal scope of potential seawater intrusion. *Nat. Commun.* 11, 1–9. doi: 10.1038/s41467-020-17038-2

Li, G. M., and Chen, C. X. (1991). Determining the length of confined aquifer roof extending under the sea by the tidal method. *J. Hydrol.* 123, 97–104. doi: 10.1016/0022-1694(91)90071-O

Li, H., and Jiao, J. J. (2001b). Tide-induced groundwater fluctuation in a coastal leaky confined aquifer system extending under the sea. *Water Resour. Res.* 37 (5), 1165–1171. doi: 10.1029/2000WR900296

Li, H., and Jiao, J. J. (2003). Tide-induced seawater-groundwater circulation in a multi-layered coastal leaky aquifer system. *J. Hydrol.* 274 (1-4), 211–224. doi: 10.1016/S002-1694(02)00413-4

Li, H. L., and Jiao, J. J. (2001a). Analytical studies of groundwater-head fluctuation in a coastal confined aquifer overlain by a leaky layer with storage. *Adv. Water Resour.* 24, 565–573. doi: 10.1016/S0309-1708(00)00074-9

Li, M. W., Zhou, Z. F., Huang, H. L., and Liao, J. X. (2022). Estimation of hydraulic diffusivity of a confined limestone aquifer at the Xiluodu Dam. *Geofluids.* 2022, 8732415. doi: 10.1155/2022/8732415

Lu, C., Xin, P., Li, L., and Luo, J. (2015). Steady state analytical solutions for pumping in a fully bounded rectangular aquifer. *Water Resour. Res.* 51, 8294–8302. doi: 10.1002/2015WR017019

Luo, Z. Y., Kong, J., and Barry, D. A. (2023). Watertable fluctuations in coastal unconfined aquifers with a sloping sea boundary: Vertical flow and dynamic effective porosity effects. *Adv. Water Resour.* 178, 104491. doi: 10.1016/j.advwatres.2023.104491

Marshall, S. K., Cook, P. G., Simmons, C. T., Konikow, L. F., and Dogramaci, S. (2022). An approach to include hydrogeologic barriers with unknown geometric properties in groundwater model inversions. *Water Rsources Resour.* 58, e2021WR031458. doi: 10.1029/2021WR031458

Noorabadi, S., Nazemi, A. H., Sadraddini, A. A., and Delirhasannia, R. (2017). Laboratory investigation of water extraction effects on saltwater wedge displacement. *Global J. Environ. Sci. Manage.* 3 (1), 21–32. doi: 10.22034/gjesm.2017.03.01.003

Peters, C. N., Kimsal, C., Frederiks, R. S., Paldor, A., McQuiggan, R., and Michael, H. A. (2022). Groundwater pumping causes salinization of coastal streams due to baseflow depletion: analytical framework and application to Savannah River,GA. *J. Hydrol.* 604, 127238. doi: 10.1016/j.jhydrol.2021.127238

Ratner-Narovlansky, Y., Weinstein, Y., and Yechieli, Y. (2020). Tidal fluctuations in a multiunit coastal aquifer. *J. Hydrol.* 580, 124222. doi: 10.1016/j.jhydrol.2019.124222

Ren, H. L., Tao, Y. Z., Lin, F., and Wei, T. (2022). Analytical solution and parameter inversion of transient seepage model of groundwater near ditch during drainage period. *J. Hydraulic Engineering.* 53, 117–125. (In chinese)

Rogers, M., Sukop, M. C., Obeysekera, J., and George, F. (2023). Aquifer parameter estimation using tide-induced water-table fluctuations in the Biscayne Aquifer, Miami-Dade County, Florida (USA). *Hydrogelogy J.* 31, 1031–1049. doi: 10.1007/s10040-023-02634-5

Su, Q., Yu, Y., Yang, L., Chen, B., Fu, T., Liu, W., et al. (2023). Study on the variation in coastal groundwater levels under high-intensity brine extraction conditions. *Sustainability.* 15, 16199. doi: 10.3390/su152316199

Wang, C., Li, H., Wan, L., Wang, X., and Jiang, X. (2014). Closed-form analytical solutions incorporating pumping and tidal effects in various coastal aquifer systems. *Adv. Water Res.* 69, 1–12. doi: 10.1016/j.advwatres.2014.03.003

Werner, A. D., Bakker, M., Post, V. E. A., Vandenbohede, A., Lu, C., Ataie-Ashtiani, B., et al. (2013). Seawater intrusion processes, investigation and management: recent advances and future challenges. *Adv. Water Re.* 51, 3–26. doi: 10.1016/j.advwatres.2012.03.004

Xia, Y., Li, H., Boufadel, M. C., Guo, Q., Li, G., and Magos, A. (2007). Tidal wave propagation in a coastal aquifer: Effects of leakages through its submarine outlet-capping and offshore roof. *J. Hydrol.* 337, 249–257. doi: 10.1016/j.jhydrol.2007.01.036

Yang, J., Shen, C. J., Xu, T., Xie, Y., and Lu, C. (2022). On the intrusion and recovery of ocean-sourced H-3 and C-14 in coastal aquifers considering ocean-surge inundation. *J. Hydrol.* 604, 127241. doi: 10.1016/j.jhydrol.2021.127241

Yu, X., and Michael, H. A. (2019). Mechanisms, configuration typology, and vulnerability of pumping-induced seawater intrusion in heterogeneous aquifers. *Adv. Water Res.* 128, 177–128. doi: 10.1016/j.advwatres.2019.04.013

Zhang, H. (2021). Characterization of a multi-layer karst aquifer through analysis of tidal fluctuation. *J. Hydrol.* 601, 126677. doi: 10.1016/j.jhydrol.2021.126677

Zheng, Y., Yang, M., and Liu, H. (2022). Horizontal two-dimensional groundwater-level fluctuations in response to the combined actions of tide and rainfall in an unconfined coastal aquifer. *Hydrogeol J.* 30, 2509–2518. doi: 10.1007/s10040-022-02564-8

Zhou, P., Qiao, X., and Li, X. (2017). Numerical modeling of the effects of pumping on tide-induced groundwater level fluctuation and on the accuracy of the aquifer's hydraulic parameters estimated via tidal method: a case study in donghai island, China. *J. Hydroinformatics.* 19, 607–619. doi: 10.2166/hydro.2017.089

Zhu, S. M., Zhou, Z. F., Werner, A. D., and Chen, Y. Q. (2023). Experimental analysis of intermittent pumping effects on seawater intrusion. *Water Resour. Res.* 59 (1), e2022WR032269. doi: 10.1029/2022WR032269

10.3389/fmars.2024.1382206

Appendix A. Derivation of the solution

The derivation process of the analytical solution for the initial and boundary value problems satisfied in the upper confined aquifer is as follows: $H_{Jacob}(x,t)$ satisfies the following equations

$$S_1\frac{\partial H_{Jacob}}{\partial t}=T_1\left(\frac{\partial^2 H_{Jacob}}{\partial x^2}+\frac{\partial^2 H_{Jacob}}{\partial y^2}\right),\ x>0,\ -\infty<y\langle+\infty,\ t\rangle 0 \quad \text{(A1)}$$

$$\lim_{x\to\infty}\frac{\partial H_{Jacob}}{\partial x}(x,t)=\lim_{y\to\pm\infty}\frac{\partial H_{Jacob}}{\partial y}(x,t)=0 \quad \text{(A2)}$$

$$H_{Jacob}(x,t)\big|_{x=0}=h_s(t)=A\cos(\omega t-\varphi) \quad \text{(A3)}$$

$$\lim_{r_1\to 0} r_1\frac{\partial H_{Jacob}}{\partial r_1}=0,\ t>0 \quad \text{(A4)}$$

The analytical solutions should meet the superposition principle, since the model (1)-(7) are linear equations.

Let

$$H_{Pump}(x,y,t)=H_1(x,y,t)-H_{Jacob}(x,t) \quad \text{(A5)}$$

Subtracting Equation A1, Equation A2, Equation A3, and Equation A4 from Equation 1, Equation 2, Equation 3, and Equation 4a, respectively, one can obtain that $H_{Pump}(x,y,t)$ satisfies the following equations

$$S_1\frac{\partial H_{Pump}}{\partial t}=T_1\left(\frac{\partial^2 H_{Pump}}{\partial x^2}+\frac{\partial^2 H_{Pump}}{\partial y^2}\right),\ x>0,\ -\infty<y\langle+\infty,\ t\rangle 0 \quad \text{(A6)}$$

$$\lim_{x\to\infty}\frac{\partial H_{Pump}}{\partial x}(x,y,t)=\lim_{y\to\pm\infty}\frac{\partial H_{Pump}}{\partial y}(x,y,t)=0 \quad \text{(A7)}$$

$$H_{Pump}(x,y,t)\big|_{x=0}=0 \quad \text{(A8)}$$

$$\lim_{r_1\to 0} r_1\frac{\partial H_{Pump}}{\partial r_1}=\frac{Q}{2\pi T_1},\ \ t>0 \quad \text{(A9)}$$

Note that the coastline is the recharge boundary of the aquifer system. According to the theory of image method, there is an imaginary injection well with a flow rate of **Q** at the symmetrical position **-d** relative to the pumping well. According to the complete well formula for a confined aquifer without overflow recharge and the superposition principle, the analytical solution of Equations (A6)- (A9) can be written

$$H_{Pump}(x,y,t)=\frac{Q}{4\pi T_1}[W(u_2)-W(u_1)] \quad \text{(A10)}$$

Substituting Equation A10 into Equation A5, one can obtain the solution Equation 10a.

The derivation principle of the analytical solution of the lower confined aquifer is the same as that of upper confined aquifer; therefore, the solution Equation 11a can be obtained.

frontiers | Frontiers in Marine Science

TYPE Original Research
PUBLISHED 08 August 2024
DOI 10.3389/fmars.2024.1411770

OPEN ACCESS

EDITED BY
Xiuyu Liang,
Southern University of Science and Technology, China

REVIEWED BY
Fei Gao,
Qingdao Institute of Marine Geology (QIMG), China
Li Li,
Zhejiang University, China

*CORRESPONDENCE
Guangxue Li
estuary@ouc.edu.cn

RECEIVED 04 April 2024
ACCEPTED 22 July 2024
PUBLISHED 08 August 2024

CITATION
Liu S, Li G, Liu S, Zhang L, Li M, Feng Q, Xing L, Yu D and Pan Y (2024) Impacts of sea ice on suspended sediment transport during heavy ice years in the Bohai Sea.
Front. Mar. Sci. 11:1411770.
doi: 10.3389/fmars.2024.1411770

Impacts of sea ice on suspended sediment transport during heavy ice years in the Bohai Sea

Siyu Liu[1,2], Guangxue Li[2,3]*, Shidong Liu[2,3], Lei Zhang[2], Mengqi Li[4], Qi Feng[2], Lvyang Xing[2], Di Yu[2] and Yufeng Pan[2]

[1]Academy of the Future Ocean, Ocean University of China, Qingdao, China, [2]College of Marine Geosciences, Ocean University of China, Qingdao, China, [3]Key Lab of Submarine Geosciences and Prospecting Techniques, MOE, Qingdao, China, [4]Research Institute of Petroleum Exploration and Development, PetroChina, Beijing, China

The Bohai Sea, known for being the lowest latitude seasonally frozen sea area in the world, experienced severe ice conditions with a 30-year recurrence period during the winter of 2009-2010. Water-sediment flux is a crucial parameter for water quality management in marine environment. Using a highly accurate three-dimensional hydrodynamic and sediment transport numerical model, the significant wave height (Hs), current velocity, suspended sediment concentration (SSC) and water-sediment flux in the Bohai Sea during ice-covered and ice-free conditions are compared. Our findings indicate that the current velocity and sediment resuspension decrease under the ice coverage, but increase at the edge of the ice. The net outflow tidal flux (TF) in winter under ice-free conditions accounts for 24.5% of the whole year. The net outflow TF increases by 32.7% during ice-covered conditions, primarily due to the pressure difference between high air pressure superimposing heavy sea ice in the northwest Bohai Sea and the low air pressure in Bohai Strait, resulting in increased ebb velocity and decreased flood velocity. The net outflow suspended sediment flux (SSF) during ice-free conditions in the winter is 2.32×10^9 kg, while SSF increases by 1.24 times during ice-covered conditions, leading to worse water quality in the outer sea. The decrease of TF in the southern part of the Bohai Strait and the reduction of suspended sediment concentration by nearly 15 mg/l lead to the significant decrease in SSF. This study has significance guiding value for understanding the source-sink sedimentation system and water quality research in East China Sea.

KEYWORDS

Bohai Sea, sea ice, water-sediment flux, sediment resuspension, pressure

Highlights

- The current velocity reduces by direct ice cover, but increases along ice edge.
- The area where the velocity increases during ebb tide is larger during ice cover.
- The net outflow water-sediment flux from the Bohai Sea increase under ice cover.
- The net outflow tidal flux increases by 32.7% due to the pressure difference.
- The net outflow suspended sediment flux increases by 1.24 times.

1 Introduction

The Bohai Sea, known for being the lowest latitude seasonally frozen sea area in the northern hemisphere (Wang et al., 2021; Li et al., 2024), freezes for approximately 3-4 months annually (Su and Wang, 2012). Sea ice poses threats to marine transportation safety, oil platform structural safety, offshore engineering operations, as well as aquaculture (Zhang and Li, 1999; Zhang et al., 2018; Zhou et al., 2023; Wang et al., 2024). Additionally, the Yellow River carries around 1.1 billion tons of sediment into the Bohai Sea each year (Milliman and Meade, 1983). The sediment accumulates near the Yellow River estuary in summer and is strongly resuspended in winter, subsequently transported to the open sea (Yang et al., 2011; Wang et al., 2014). In the marine environment, suspended sediment concentration (SSC) plays a vital role in water quality management and influences biogeochemical processes (Bilotta et al., 2012; Zhou et al., 2022). As an important link between the Yellow River and the open sea, the exchange of water and sediment in the Bohai Sea is especially crucial (Liu et al., 2024). At present, global climate change is experiencing peak fluctuations, making mid- and high-latitude bays more susceptible to extreme ice conditions (Xu et al., 2019). Therefore, investigating the impacts of sea ice on water-sediment flux and sediment transport during heavy ice winters in the Bohai Sea has significance guiding value for understanding the source-sink sedimentation system and water quality research in East China Sea.

Previous research on the impact of sea ice on hydrodynamic dynamics has predominantly focused on polar regions, and few studies have been carried out in seasonal frozen areas with frequent human activities, such as the Bohai Sea (Kug et al., 2015; Manson et al., 2016; Jiao et al., 2019). Sea ice reduced significant wave height (Hs) (Che et al., 2019; Zhang et al., 2020), and suppressed tidal amplitude (Zhang et al., 2019). The wave direction under the ice coverage changed compared to open water (Wahlgren et al., 2023). Researchers believed that due to ice coverage, the maximum surface current velocity decreased and lagged (Su et al., 2003), as well as the vertical distribution of current velocity changed from the traditional logarithmic type to the parabolic type (Jiang et al., 2020). Additionally, it was proposed that energy transferring from the open sea to the inner bay remains constant, albeit with reduction in vertical amplitude, causing energy to transform into horizontal flow along the coastal ice boundary (Liu et al., 2022). Most scholars asserted that sea ice inhibited sediment resuspension by limiting wave and current speed (Forest et al., 2008; Lannuzel et al., 2010; Murray et al., 2012; Bonsell and Dunton, 2018). Due to ice coverage, the SSC in Liaodong Bay was lower than that in Bohai Bay and Laizhou Bay (Xie et al., 2023). Sediment efflux was lowest at stations that were most recently ice-covered in the Pacific Arctic (Barrett et al., 2023). However, some scholars argued that ice mass interference increased seawater resistance and water body instability, thereby making it easier to trigger sediment resuspension (Peck et al., 2005; Giesbrecht et al., 2013).

Despite numerous researches on the impacts of sea ice on hydrodynamics and sediment resuspension, the water-sediment flux exchange between the Bohai Sea and the outer sea under ice coverage has not been fully investigated. In the winter of 2009-2010, severe ice conditions with a recurrence period of 30 years occurred in the Bohai Sea (Zhao et al., 2012). The thickness and extent of sea ice during this period were depicted in Figure 1. Using the MIKE three-dimensional hydrodynamic and sediment transport numerical model, the Hs, current velocity and SSC in the Bohai Sea were compared during both ice-covered and ice-free conditions from December 2009 to February 2010 to investigate the impacts of sea ice on the water-sediment flux.

2 Data and methods

2.1 Data sources

The field water level, current, wave height and SSC data were provided by the Acoustic Wave and Current instrument (AWAC) and Optical Back Scattering (OBS) installed at seabed-based observation station QD12 (119.1°E, 38.48°N, depth 5.5 m), located in western Laizhou Bay. The observation period was from 2 April 2009 to 7 April 2010. Sea ice thickness referred to the vertical distance from the ice surface to the ice bottom, while sea ice concentration represented the ratio of the sea ice coverage area to the total sea area (Lu et al., 2004; Ren et al., 2022). These parameters are fundamental for characterizing sea ice. The sea ice thickness and concentration data in the Bohai Sea used in this model from December 2009 to February 2010 were obtained from previous studies (Zhang and Tang, 2010; Zhang et al., 2019). The near-shore sea ice concentration was 0.55 in Bohai Bay and Laizhou Bay, 0.6 in Liaodong Bay, and 0.5 far offshore in the three bays. The near-shore sea ice thickness was 30 cm in Bohai Bay and Laizhou Bay, 55 cm in Liaodong Bay, and 20 cm far offshore in the three bays.

2.2 Model description

The MIKE 3 hydrodynamic and sediment transport model, developed by the Danish Hydraulic Institute (DHI), was employed in this study. MIKE is widely recommended and applied commercial numerical simulation system in the international marine engineering field (Warren and Bach, 1992; DHI, 2012), predominantly in applications within ports, rivers, lakes, estuaries, coastal regions, and oceans. Its triangular grid offers precise simulation of intricate and

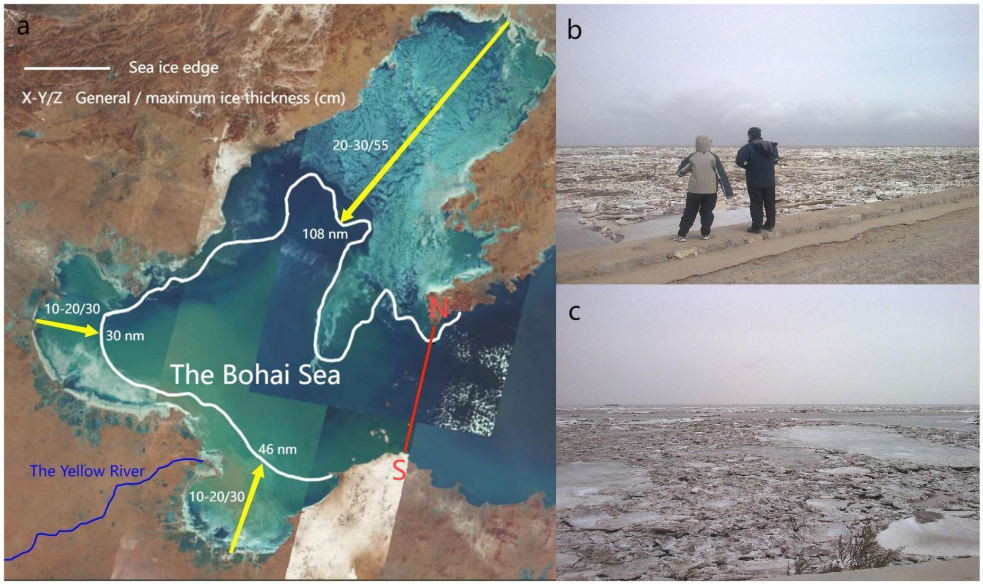

FIGURE 1
Sea ice extent and thickness of the Bohai Sea in February 2010. **(A)** Sea ice extent and thickness of the Bohai Sea from Landsat remote sensing images in February 2010. The red line is the Bohai Strait section. **(B, C)** The photos of sea ice on the west bank of Laizhou Bay in January 2010.

irregular coastlines, distinctly excelling in extensive areas and long-time numerical simulations. The accuracy of simulating wave, tide, current and sediment transport was validated extensively (Wang et al., 2017; Liu et al., 2018; Liu et al., 2024).

The Hydrodynamic Module is based on the three-dimensional incompressible Reynolds-averaged Navier-Stokes equations and adopts Boussinesq approximation and hydrostatic assumption (DHI, 2012). The local continuity equation is written as Formula 1:

$$\frac{\partial u}{\partial x}+\frac{\partial v}{\partial y}+\frac{\partial w}{\partial z}=S \tag{1}$$

The motion equations in the x and y direction are written as Formulas 2 and 3:

$$\begin{aligned}&\frac{\partial u}{\partial t}+\frac{\partial u^2}{\partial x}+\frac{\partial vu}{\partial y}+\frac{\partial wu}{\partial z}\\&=fv-g\frac{\partial \zeta}{\partial x}-\frac{1}{\rho_0}\frac{\partial p_a}{\partial x}-\frac{g}{\rho_0}\int_z^{\zeta}\frac{\partial \rho}{\partial x}dz-\frac{1}{\rho_0 h}\\&\left(\frac{\partial S_{xx}}{\partial x}+\frac{\partial S_{xy}}{\partial y}\right)+F_u+\frac{\partial}{\partial z}\left(v_t\frac{\partial u}{\partial z}\right)+u_sS\end{aligned} \tag{2}$$

$$\begin{aligned}&\frac{\partial v}{\partial t}+\frac{\partial v^2}{\partial y}+\frac{\partial uv}{\partial x}+\frac{\partial wv}{\partial z}\\&=-fu-g\frac{\partial \zeta}{\partial y}-\frac{1}{\rho_0}\frac{\partial p_a}{\partial y}-\frac{g}{\rho_0}\int_z^{\zeta}\frac{\partial \rho}{\partial y}dz-\frac{1}{\rho_0 h}\left(\frac{\partial S_{yx}}{\partial x}+\frac{\partial S_{yy}}{\partial y}\right)\\&+F_v+\frac{\partial}{\partial z}\left(v_t\frac{\partial v}{\partial z}\right)+v_sS\end{aligned} \tag{3}$$

Where t is the time, x, y, and z are the Cartesian coordinates, ζ is the surface elevation; d is the still water depth, $h=\zeta+d$ is the total water depth, u, v, and w are the velocity components in x, y and z directions, f is the Coriolis parameter ($f=2\Omega sin\theta$), where Ω is the earth rotational angular velocity and θ is the latitude, g is the gravity acceleration, ρ is the seawater density, ρ_0 is the reference seawater density, S_{xx}, S_{xy}, S_{yx}, and S_{yy} are components of the radiation stress tensor, v_t is the vertical turbulent viscosity, p_a is the atmospheric pressure, S is the magnitude of the discharge due to point sources, and (u_s, v_s) is the velocity by which the water is discharged into the ambient water (DHI, 2012). The horizontal stress terms are described using a gradient-stress relation (DHI, 2012), which is simplified to Formulas 4 and 5:

$$F_u=\frac{\partial}{\partial x}\left(2A\frac{\partial u}{\partial x}\right)+\frac{\partial}{\partial y}\left(A\left(\frac{\partial u}{\partial y}+\frac{\partial v}{\partial x}\right)\right) \tag{4}$$

$$F_v=\frac{\partial}{\partial x}\left(2A\left(\frac{\partial u}{\partial y}+\frac{\partial v}{\partial x}\right)\right)+\frac{\partial}{\partial y}\left(2A\frac{\partial v}{\partial y}\right) \tag{5}$$

where A is horizontal eddy viscosity.

Based on the conservation equation of wave action, MIKE SW uses the wave action density spectrum ($N(\sigma,\theta)$) to describe waves. The independent variables of the model are relative wave frequency (σ) and wave direction (θ). The relationship between wave action density and wave energy spectrum density ($E(\sigma,\theta)$) is written as Formula 6:

$$N(\sigma,\theta)=E(\sigma,\theta)/\sigma \tag{6}$$

Where σ is the relative frequency and θ is the wave direction.

2.3 Model configuration

The calculation area of the model encompassed the entire Bohai Sea, covering 37°-41°N and 117.5°-122.5°E, with an opening boundary at 121.9°E. The model was horizontally divided into

17,075 triangular grids, and vertically divided into 7 sigma layers with the surface and bottom layer encrypted. The land boundary was derived from 2009 Landsat satellite images and partially smoothed. Water depth was determined through a combination of electronic chart depth and measured depth. The boundary water level conditions were obtained from TPXO8 tidal data set (https://www.tpxo.net/global) with a spatial resolution of 1/30°. Monthly runoff and sediment discharge data of the Yellow River was from the Yellow River Sediment Bulletin (http://yrcc.gov.cn/gzfw/nsgb/index.html). The sediments distribution in the Bohai Sea was determined according to Li (2005). Since temperature and salinity had little influence on this study, the water temperature and salinity field are taken as constants (Li et al., 2001). Atmospheric forcing field data were provided by the European Centre for Medium-Range Weather Forecasts Reanalysis v5 (ERA5), including wind and mean sea level pressure, with a temporal resolution of 1 hr and a spatial resolution of 0.25°. The models under ice-covered and ice-free conditions utilized identical shoreline, water depth, wind field, runoff and opening boundary. The sole disparity lied in the sea ice conditions to study the impacts of sea ice on hydrodynamics (current and wave) and sediment resuspension.

2.4 Model verification

The model performance was assessed quantificationally by four indices: mean absolute error (*MAE*), root mean square error (*RMSE*), correlation coefficient (*R*), and prediction skill (*Skill*) (Liu et al., 2024). RMSE indicated the average deviation between model results and observation data, while Skill demonstrated the consistency index between model results and observed data (Liu et al., 2024). A Skill value of 1 indicated complete consistency between the model prediction and the measured data (Liu et al., 2024). According to Willmott (1981), the calculation formulas were as Formulas 7, 8 and 9.

$$MAE = \frac{1}{N}\sum_{k=1}^{N}|X_{modi} - X_{obsi}| \tag{7}$$

$$RMSE = \sqrt{\frac{1}{N}\sum_{k=1}^{N}(X_{modi} - X_{obsi})^2} \tag{8}$$

$$Skill = 1 - \frac{\sum_{k=1}^{N}|X_{modi} - X_{obsi}|^2}{\sum_{k=1}^{N}(|X_{modi} - \bar{X}_{obs}| + |X_{obsi} - \bar{X}_{obs}|)^2} \tag{9}$$

Where X_{mod} and X_{obs} were model and observation data, respectively, X_{obs} represented the average observation data, i was the instant, N was the sample size. Harmonic analysis was conducted on the tidal data over one-year period (Pawlowicz et al., 2002), revealing that the amplitude and phase of M_2, S_2, O_1 and K_1 tidal constituents were in good agreement with measured in the Bohai Sea (Figures 2A–C). The data on current velocity and direction, water level and Hs under sea ice coverage were also well-verified (Figures 2D–I). The regularity and magnitude of bottom SSC corresponded well with the observed data (Figure 2J). Table 1 presented the error calculation of each element. The model utilized in this study is capable of simulating the actual hydrodynamic environment in the Bohai Sea and holds potential for future research applications.

2.5 Calculation of water-sediment flux and wave-current induced shear stress

The annual tidal flux (TF) and suspended sediment flux (SSF) were calculated according to Formulas 10 and 11 (Liu et al., 2024).

$$TF = \iint_s \underset{u}{\rightarrow}\underset{n}{\rightarrow} d_s \tag{10}$$

$$SSF = \iint_s \underset{u}{\rightarrow}\underset{n}{\rightarrow} c d_s \tag{11}$$

Where, $\underset{u}{\rightarrow}$ was the velocity vector of one point in a section, $\underset{n}{\rightarrow}$ was the normal vector of the section, d_s was the area of the micro-element, c was the SSC on the micro-element. The direction of TF and SSF in the Bohai Strait was positive to the east and negative to the west. For the Bohai Strait, inflow was considered negative and outflow was positive (Figure 1A).

Currents and waves play a pivotal role controlling sediment resuspension (MacVean and Lacy, 2014), and bottom shear stress is crucial for predicting SSC (Heath et al., 2016). The current-induced shear stress (τ_c) was calculated by Formulas 12 and 13 (Soulsby, 1997):

$$U(z) = (u_\star/\kappa)\ln(z/z_0) \tag{12}$$

$$\tau_c = \rho u_\star^{\,2} \tag{13}$$

$U(z)$ is the average velocity (m/s) of the sampling period above the seabed z (m), $u_\star$ is the friction velocity (m/s), κ is the Carmen constant (0.4), ρ is the seawater density (1025 kg/m^3), and z_0 is the roughness length of the seabed ($z_0 = k_s/30$, where $k_s = 2.5D_{50}$ is the Nikuradse particle roughness and D_{50} is the median grain size of the sediment) (Li, 2005).

According to linear wave theory, the amplitude of the wave orbit velocity U_w and the major axis radius of near-bottom wave orbit A_w calculated by Formulas 14 and 15 (Shi et al., 2014):

$$U_w = \frac{\pi H_{rms}}{T\sinh(2\pi d/L)} \tag{14}$$

$$A_w = U_w T/2\pi \tag{15}$$

H_{rms} is the root mean square wave height (m) [$=Hs/\sqrt{2}$, Hs is the significant wave height (m)], T is the wave period (s), d is the water depth (m), and L is the wavelength (m), calculated by Formula 16 (Li and Amos, 2001; Wiberg and Sherwood, 2008):

$$L = gT^2\tanh(2\pi d/L)/2\pi \tag{16}$$

The orbital motion of waves increases the bed shear stress. Herein, wave-induced shear stress (τ_w) is calculated by Formula 17 (Soulsby, 1997):

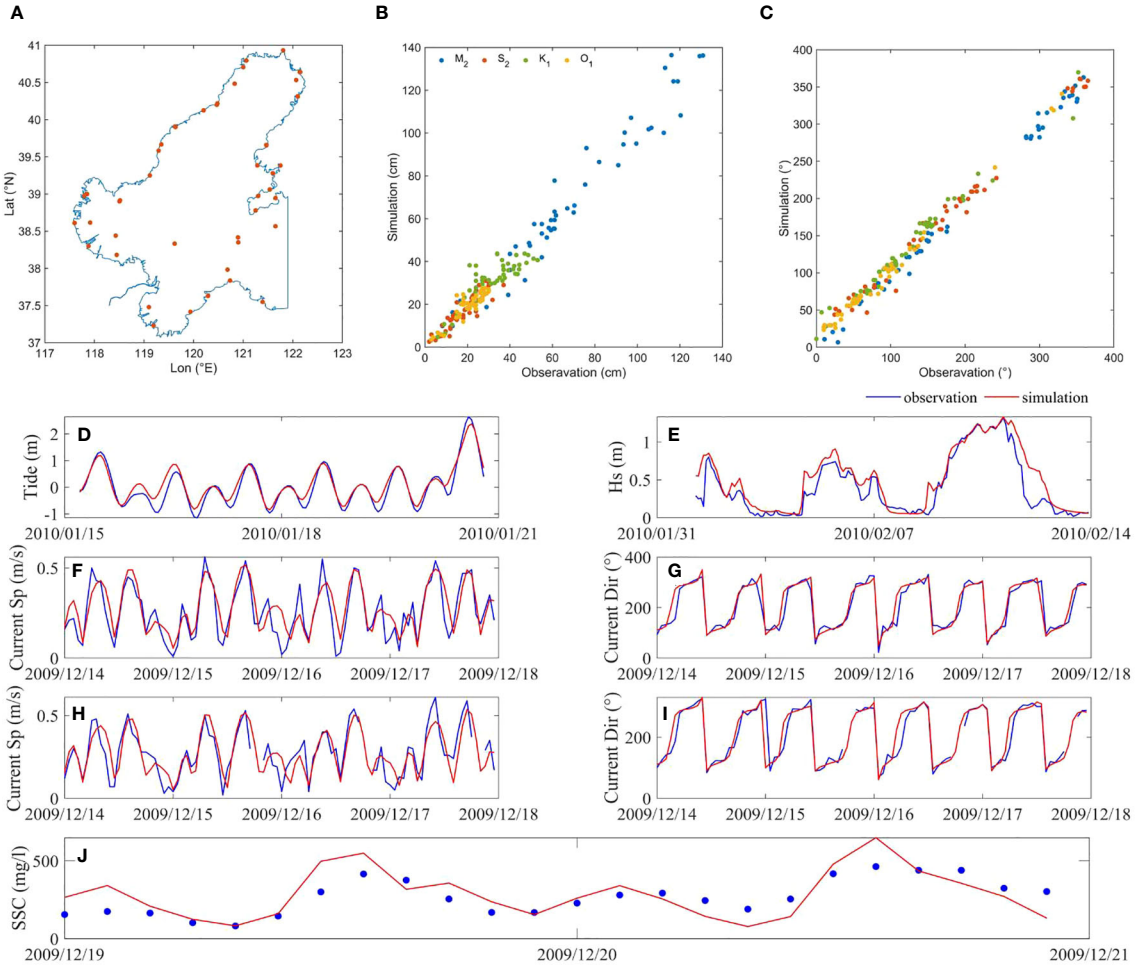

FIGURE 2
Comparison between model data and observation data. **(A)** The location of the tide stations. **(B)** Amplitude of M_2, S_2, O_1 and K_1 tidal constituents. **(C)** Phase of M_2, S_2, O_1 and K_1 tidal constituents. **(D)** Comparison of tide under ice coverage. **(E)** Comparison of Hs under ice coverage. **(F)** Comparison of bottom current velocity under ice coverage. **(G)** Comparison of bottom current direction under ice coverage. **(H)** Comparison of surface current velocity under ice coverage. **(I)** Comparison of surface current direction under ice coverage. **(J)** Comparison of bottom SSC.

$$\tau_w = \frac{1}{2}\rho f_w U_w{}^2 \tag{17}$$

ρ is the seawater density (1025 kg/m^3) and f_w is the wave friction coefficient related to the wave Reynolds number Re_w [$Re_w = A_w U_w/\nu$, where ν is the seawater kinematic viscosity coefficient (10^{-6} m^2/s)].

$$Re_w \le 10^5,\ f_w = 2Re_w^{-0.5};$$

$$Re_w > 10^5,\ f_w = 0.0521Re_w^{-0.187};$$

The wave-current induced shear stress (τ_{cw}) is calculated by Formulas 18 and 19 (Soulsby, 1995):

$$\tau_{cw} = [(\tau_m + \tau_m|cos\varphi|)^2 + (\tau_w sin\varphi|)^2]^{1/2} \tag{18}$$

$$\tau_m = \tau_c[1 + 1.2(\tau_w/(\tau_c + \tau_w))^{3.2}] \tag{19}$$

τ_m is the average shear stress under the action of waves and currents, and φ is the propagation angle of the waves and currents.

3 Results

3.1 Hydrodynamics and sediment resuspension variation

The sea ice coverage in Bohai Bay, Laizhou Bay, and Liaodong Bay has led to varying reductions in Hs and current velocity. The Hs decreased in the northeastern Liaodong Bay, with a maximum of nearly 1 m (Figures 3A, B). The friction of sea ice caused a reduction in surface velocity by over 6 cm/s and bottom velocity by over 2 cm/s in all three bays (Figures 3C–E). The central part of Bohai Sea and the Bohai Strait, not directly covered by sea ice, experienced current velocity fluctuations of within 2 cm/s. However, in the west of Dalian, current velocity increased significantly staying below 6 cm/s, most likely due to its proximity the ice edge.

Additionally, SSC decreased in most areas of the Bohai Sea under ice coverage, with the decreasing range of SSC increasing from surface to bottom (Figures 3F–H). Under ice coverage, SSC reduced by over 100 mg/l in the west of Bohai Bay, the north of

TABLE 1 Error calculation of elements.

Elements		MAE	RMSE	R	Skill
M_2	Amplitude (cm)	6.17	8.02	0.98	0.99
	Phase (°)	7.57	9.95	1.00	1.00
S_2	Amplitude (cm)	2.77	3.62	0.91	0.95
	Phase (°)	10.06	12.66	0.99	1.00
K_1	Amplitude (cm)	4.85	6.13	0.84	0.91
	Phase (°)	13.58	16.03	0.99	0.99
O_1	Amplitude (cm)	2.54	3.23	0.90	0.94
	Phase (°)	8.17	9.33	1.00	1.00
Tide (m)		0.12	0.16	0.98	0.98
Hs (m)		0.11	0.17	0.93	0.95
Current	Bottom speed (m/s)	0.07	0.09	0.83	0.88
	Surface speed (m/s)	0.07	0.08	0.81	0.90
	Bottom direction (°)	11.18	13.67	0.99	0.99
	Surface direction (°)	9.25	11.93	0.99	1.00
Bottom SSC (kg/m^3)		0.08	0.10	0.76	0.84

Liaodong Bay and near the Yellow River Estuary. On the other hand, SSC in the central of Bohai Sea and near Bohai Strait either increased or decreased in the range of 10 mg/l. The disturbance to the bottom sediment caused by increased current velocity at the ice edge in the west of Dalian led to a significant increase in bottom SSC (Figure 3F). The variations in surface SSC were showed in Figure 3H, with a decrease by more than 100 mg/l in the northern Liaodong Bay, 10-100 mg/l near the Yellow River Delta and southwestern Bohai Bay, and minor fluctuations in most other areas.

Bottom shear stress played a crucial role in sediment erosion, sedimentation, and resuspension. The interaction of waves, currents, and their coupling effects were key contributors to sediment resuspension. Through the analysis of τ_w, τ_c, and τ_{cw} under ice-covered and ice-free conditions, it was observed that the τ_w diminished in the Bohai Sea, with reduction of about 0.2 Pa near the coastline (Figure 4A). The τ_c decreased in all three bays, with the most significant decrease in the northern Liaodong Bay, up to 0.2 Pa, while τ_c increased approximately 0.04 Pa in the northern part of Bohai Strait (Figure 4B). The τ_{cw} notably decreased in the three bays, particularly in the shallow coastal waters (Figure 4C), causing a significant decrease in bottom SSC during ice-covered conditions (Figure 3D). Conversely, the τ_{cw} amplified in the northern Bohai Strait, leading to an increase in bottom SSC (Figure 3D).

3.2 Impacts of sea ice on TF

Under ice-free conditions, the outflow and inflow TF of the Bohai Strait (the red line in Figure 1A) during the entire winter (from December 2009 to February 2010) were 5.541×10^{12} m^3 and 5.492×10^{12} m^3, respectively, indicating a net outflow TF of 4.9×10^{10} m^3. The peak TF value was in the northern part of the Bohai Strait section (Figures 5C, D). Under ice-covered conditions, the outflow TF from the Bohai Strait in winter was 5.544×10^{12} m^3, which was 3×10^9 m^3 higher than that without ice. The inflow tidal flux was 5.479×10^{12} m^3, decreased by 1.3×10^{10} m^3 compared with the ice-free conditions (Figures 5A, B). Under ice-covered conditions, the net outflow TF from the Bohai Sea in winter was 6.5×10^{10} m^3, an increase of 32.7% compared with the ice-free conditions (Figures 5E, F). In the case of ice coverage, the outflow TF increased, while the inflow TF decreased.

3.3 Impacts of sea ice on SSF

Under ice-free conditions, the outflow and inflow SSF in the Bohai Strait in winter were 3.960×10^{10} kg and 3.728×10^{10} kg, respectively, showing the net outflow SSF of 2.32×10^9 kg. The highest value of SSF was in the southern part of the Bohai Strait section (the northern part of Shandong Peninsula; Figures 6C, D). Under ice-covered conditions, the outflow SSF from the Bohai Strait in winter was 3.489×10^{10} kg, which was 4.71×10^9 kg lower than under ice-free conditions, accounting for 11.9%. The inflow SSF was 2.970×10^{10} kg, reduced by 7.58×10^9 kg, accounting for 20.3% compared to the ice-free conditions (Figures 6A, B). Under ice-covered conditions, the net SSF in the Bohai Sea during winter was 5.19×10^9 kg, which was 1.24 times higher than that in the absence of ice (Figures 6E, F). Although both the inflow and outflow SSF were reduced under ice coverage, the inflow was even less, leading to a significant increase in the net outflow SSF from the Bohai Strait under ice coverage.

4 Discussion

4.1 Sea surface pressure

Under ice coverage, the current velocity decreased by more than 30 cm/s during rapid flood and ebb tides in the northern Liaodong Bay, but increased by over 5 cm/s at the edge of sea ice (Figures 7A–D). Liu et al. (1993) observed an along-ice-edge jet in polar regions, attributing it to reduced wave energy due to sea ice coverage, with energy being transferred to the sea ice and the underlying seawater. Dai et al. (2019) suggested that the rapid decrease in wave energy resulted in the interaction between the waves and sea ice occurring only near the marginal ice zone, leading to the jet formation. Additionally, observations in the Bohai Sea revealed that decreased wave height and tidal amplitude under ice coverage caused energy conversion into horizontal flow along the ice edge, leading to higher velocities (Liu et al., 2022).

Although the current velocity increased at the edge of sea ice, the area of increasing current velocity was large at the rapid ebb moment, including the northern area of Bohai Strait, while the area of increasing current velocity at the rapid flood moment was comparatively limited (Figures 7A–D). Figure 7E depicted the vertical current velocity profile at the edge of the sea ice during

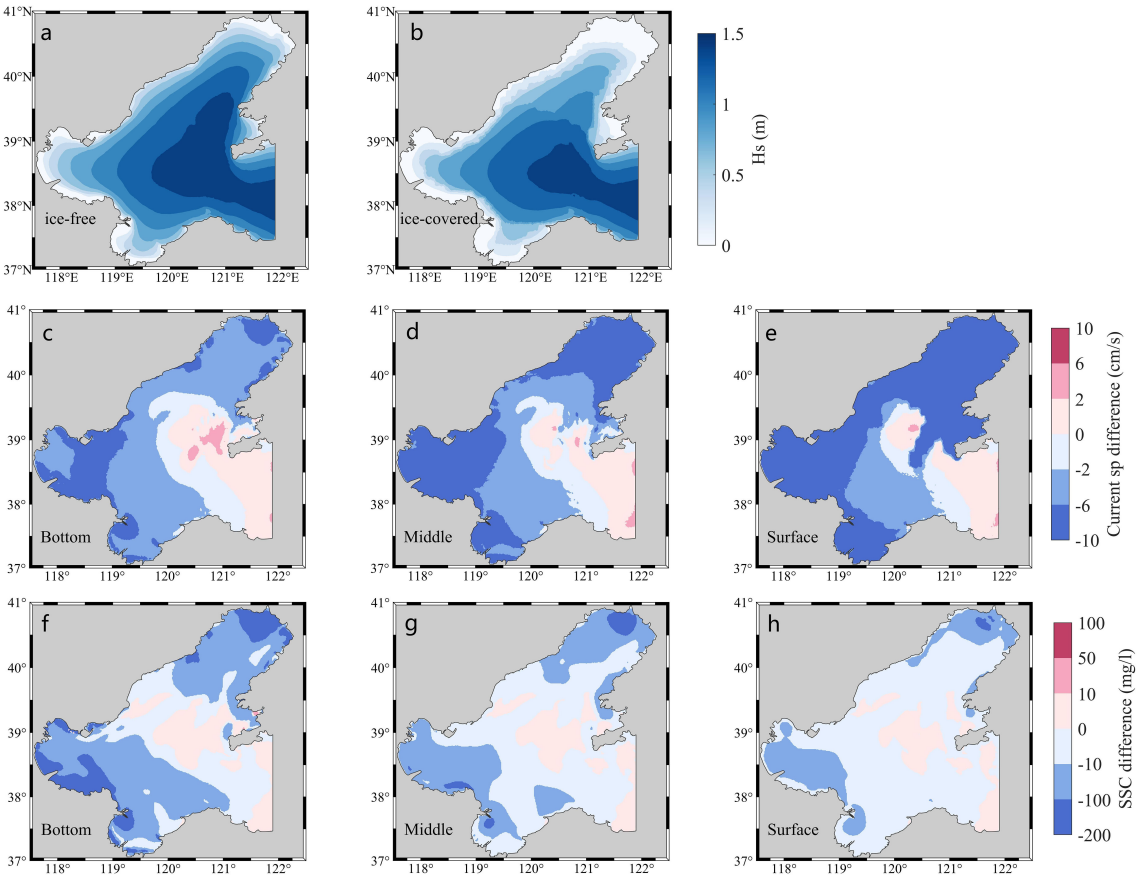

FIGURE 3
Comparison of significant wave height (Hs), current velocity and SSC in the Bohai Sea during winter (ice-covered minus ice-free). **(A)** Hs during ice-free condition. **(B)** Hs during ice-covered condition. **(C)** Bottom current velocity difference. **(D)** Middle current velocity difference. **(E)** Surface current velocity difference. **(F)** Bottom SSC difference. **(G)** Middle SSC difference. **(H)** Surface SSC difference.

the rapid flood and ebb. The current velocity from the bottom to the surface increased under ice-free conditions. However, under ice-covered conditions, the surface and bottom current velocity was lower due to friction, and the middle current velocity was largest. During the rapid ebb, the current velocity under ice-covered conditions exceeded that under ice-free conditions. Conversely, during the rapid flood, it was the opposite.

Section 3.2 revealed that sea ice coverage enhanced the outflow TF and lessened the inflow TF in the Bohai Sea. Comparison of mean sea level pressure data downloaded by ERA5 from December 2009 to February 2010 revealed a gradual pressure decrease from northwest to southeast (Figure 7F). During the ebb tide, the high pressure in Liaodong Bay combined with the pressure of heavy sea ice on the water body resulted in a pressure disparity between Liaodong Bay and the Bohai Strait, accelerating the current velocity in the north of the Bohai Strait, thereby increasing the outflow TF from the Bohai Sea. Conversely, during the flood tide, sea ice coverage impeded water from entering the Bohai Sea, thus diminishing the inflow TF into the Bohai Sea.

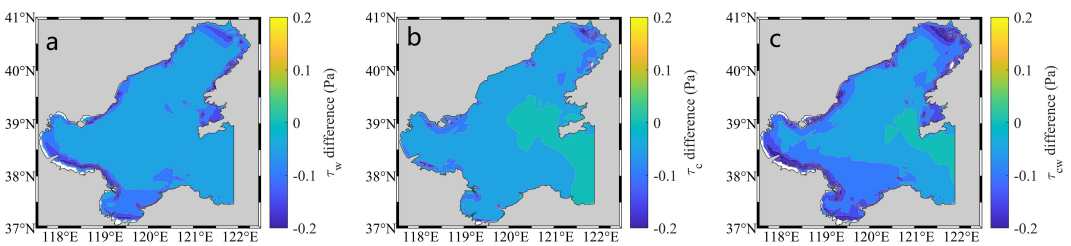

FIGURE 4
Comparison of shear stress in the Bohai Sea during winter (ice-covered minus ice-free). **(A)** Wave-induced shear stress (τ_w). **(B)** Current-induced shear stress (τ_c). **(C)** Wave-current induced shear stress (τ_{cw}).

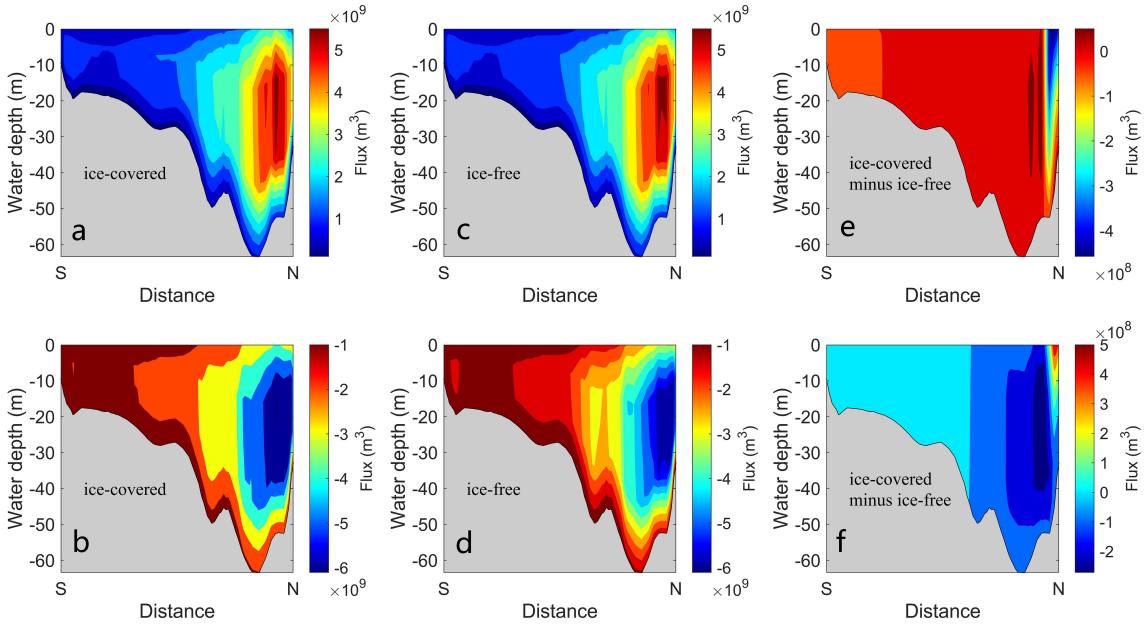

FIGURE 5
The net outflow and inflow TF under both ice-covered and ice-free conditions during winter in the Bohai Strait. **(A)** The outflow TF under ice-covered condition. **(B)** The outflow TF under ice-free condition. **(C)** The outflow TF difference (ice-covered minus ice-free). **(D)** The inflow TF under ice-covered condition. **(E)** The inflow TF under ice-free condition. **(F)** The inflow TF difference (ice-covered minus ice-free). The section orientation was shown in Figure 1A.

4.2 Current velocity and SSC

During winter, the average current velocity in the Bohai Strait was 0.37 m/s under ice-covered conditions and 0.38 m/s under ice-free conditions (Figures 8A, B). The current velocity in the northern part of the Bohai Strait (LaoTieshan waterway) was larger, averaging nearly 0.8 m/s, whereas the current velocity in the southernmost part was smaller, averaging approximately 0.5 m/s, which was similar as previous research (Jiang et al., 2019). In the northernmost part of the Bohai Strait, current velocity decreased

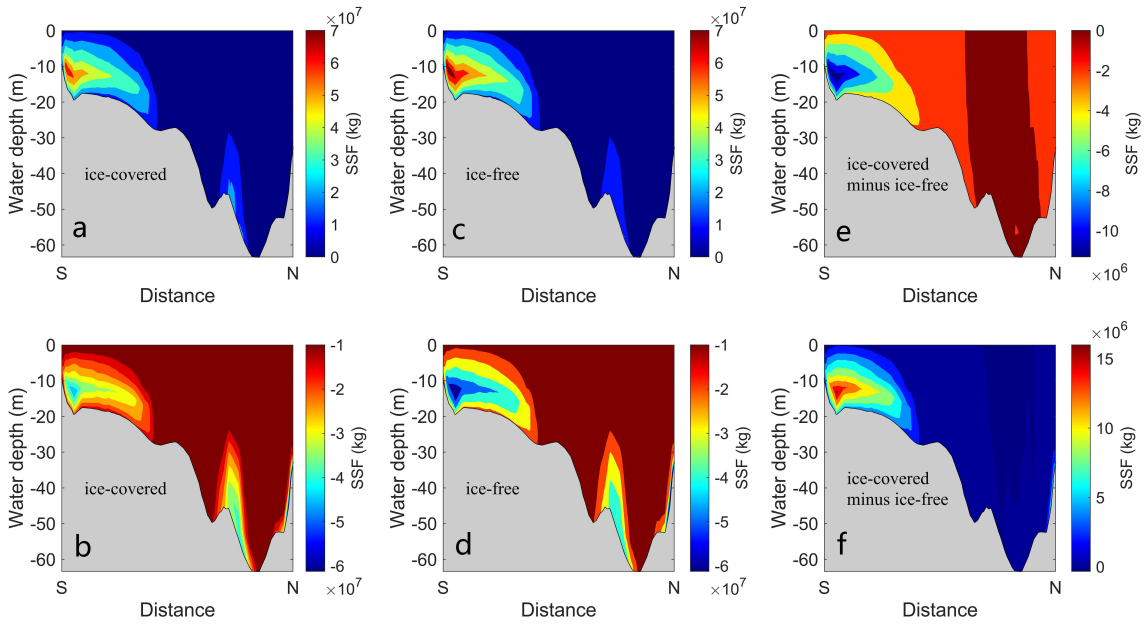

FIGURE 6
The net outflow and inflow SSF under both ice-covered and ice-free conditions during winter in the Bohai Strait. **(A)** The outflow SSF under ice-covered condition. **(B)** The outflow SSF under ice-free condition. **(C)** The outflow SSF difference (ice-covered minus ice-free). **(D)** The inflow SSF under ice-covered condition. **(E)** The inflow SSF under ice-free condition. **(F)** The inflow SSF difference (ice-covered minus ice-free).

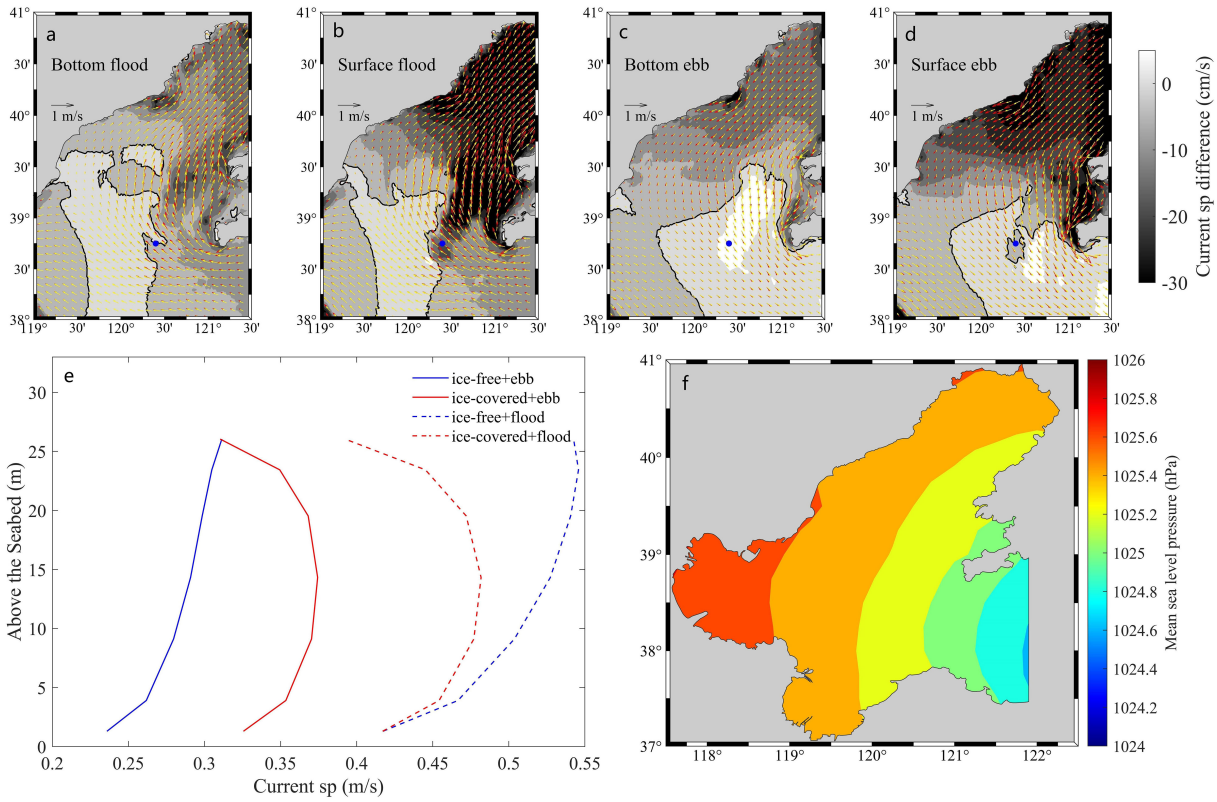

FIGURE 7
Comparison of bottom and surface current velocity and pressure in the northern Bohai Sea in winter. **(A)** Comparison of bottom current velocity at the rapid flood moment (ice-covered minus ice-free). The red arrow was the ice-free condition and the yellow arrow was the ice-covered condition. The black line served as the boundary between ice-covered and ice-free regions, equal to 0. **(B)** Comparison of surface current velocity at the rapid flood moment (ice-covered minus ice-free). **(C)** Comparison of bottom current velocity at the rapid ebb moment (ice-covered minus ice-free). **(D)** Comparison of surface current velocity at the rapid ebb moment (ice-covered minus ice-free). **(E)** The current velocity profile of a single point under ice-free and ice-covered conditions at the rapid flood and ebb moment. The point was located at the blue dot in **(A–D)**. **(F)** Mean sea level pressure in the Bohai Sea from December 2009 to February 2010.

due to substantial ice cover friction (Figure 8C). Conversely, in the northern sea ice margin area, current velocity slightly increased due to the effects of pressure. In the southern part of the Bohai Strait, the shallow water depth was affected by the surface sea ice, leading to a decrease in velocity.

During winter, the average SSC in the Bohai Strait was 13.1 mg/l under ice-covered conditions and 15.2 mg/l under ice-free conditions (Figures 8D, E). In the southern part of the Bohai Strait (the north coast of the Shandong Peninsula), SSC was high, and the ice coverage reduced current velocity, thereby lowering the SSC to a maximum of nearly 15 mg/l (Figure 8F). Additionally, Yu (2012) supported that the high SSC near the north coast of Shandong Peninsula in winter was due to the strong wind waves and coastal currents in winter. Under ice-covered conditions, the reduction of SSF into the Bohai Sea by 20.3% was attributed to the decrease in inflow TF superimposing the decrease in SSC. In the northern part of the Bohai Strait, outflow TF increased, while SSC was low and changed minimally. On the other hand, in the southern part, the outflow TF decreased slightly, but the higher SSC decreased significantly. Ultimately, the outflow SSF from the entire Bohai Strait decreased by 11.9%, as opposed to increasing like the TF.

4.3 Annual water-sediment flux

The annual (March 2009 to February 2010) outflow TF from the Bohai Strait was 2.21×10^{13} m^3 (Figure 9A), under ice-free conditions in winter representing approximately 25.1% of the total year (Figure 10A). Simultaneously, the annual inflow TF was 2.19×10^{13} m^3 (Figure 9B), also under ice-free conditions in winter accounting for about 25.1% (Figure 10A). The annual net outflow TF from Bohai Sea was 2×10^{11} m^3; during ice-free winters, the net outflow was 4.9×10^{10} m^3, making up 24.5% of the annual total, whereas during winters with ice coverage, the net outflow TF was 6.5×10^{10} m^3, accounting for 32.5% of the annual total (Figure 10A).

During the whole year, the outflow SSF from the Bohai Strait was 1.17×10^{11} kg (Figure 9C), under ice-free conditions in winter accounting for about 33.8% and under ice-covered conditions for about 29.8% (Figure 10B). The annual inflow SSF was 1.22×10^{11} kg (Figure 9D), under ice-free conditions in winter accounting for about 30.6% and under ice-covered conditions for about 24.3% (Figure 10B). The annual net inflow SSF to the Bohai Sea was 5×10^{9} kg. In winter, the net outflow SSF from the Bohai Sea was 2.32×10^{9} kg under ice-free conditions and 5.19×10^{9} kg under ice-covered conditions (Figure 10B).

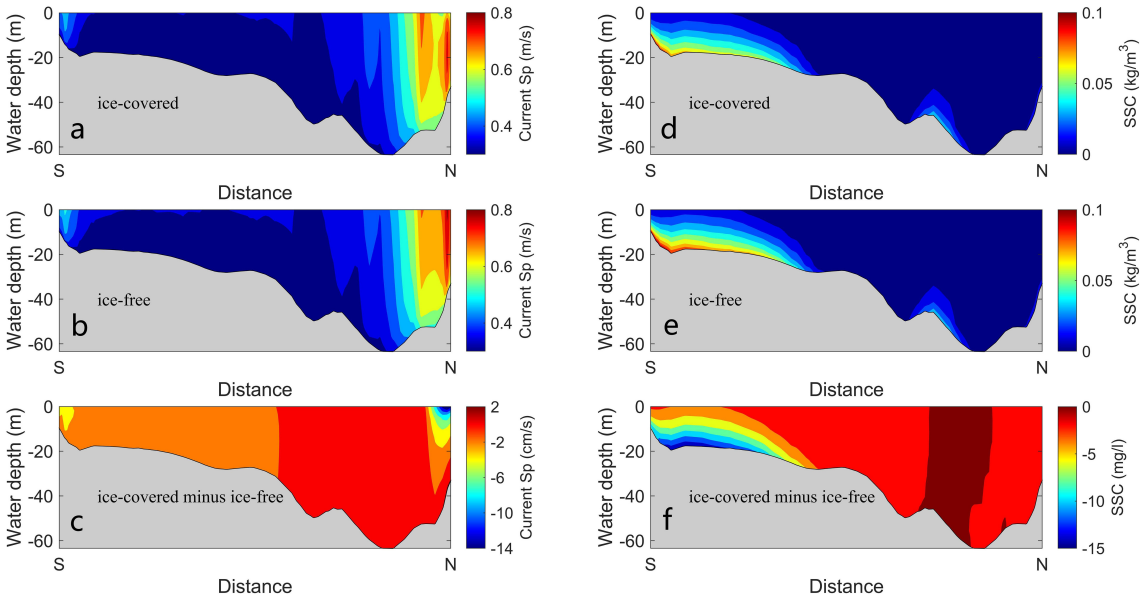

FIGURE 8
Comparison of current velocity and SSC in the Bohai Strait during winter. **(A)** The current velocity under ice-covered conditions. **(B)** The current velocity under ice-free conditions. **(C)** The current velocity difference (ice-covered minus ice-free). **(D)** The SSC under ice-covered conditions. **(E)** The SSC under ice-free conditions. **(F)** The SSC difference (ice-covered minus ice-free).

Strong gale processes may induce significant wind-driven compensation flow and water exchange phenomena in the Bohai Sea (Wan et al., 2015a). In a year with consistent wind speed and tidal current velocity, the inflow and outflow TF and SSF during winter (92 days) accounted for 24.7% of the annual cycle (365 days). Numerical simulation results showed that under ice-free conditions, the inflow and outflow TF during winter contributed to 25.1% of the entire year. Moreover, the inflow and outflow SSF during winter under ice-free conditions contributed to 33.8% and 30.6% of the entire year, respectively. These findings indicated a slightly stronger water exchange capacity, sediment resuspension and diffusion in winter, primarily attributed to the winter gale processes (Wan et al., 2015b).

5 Conclusions

The paper established a high-precision MIKE 3D hydrodynamic and sediment transport numerical model in the Bohai Sea, along with a demonstration of its reliability through comparison with observation data. The changes in current velocity, SSC, and water-sediment flux in the Bohai Sea under both ice-free and ice-covered conditions was fully investigated.

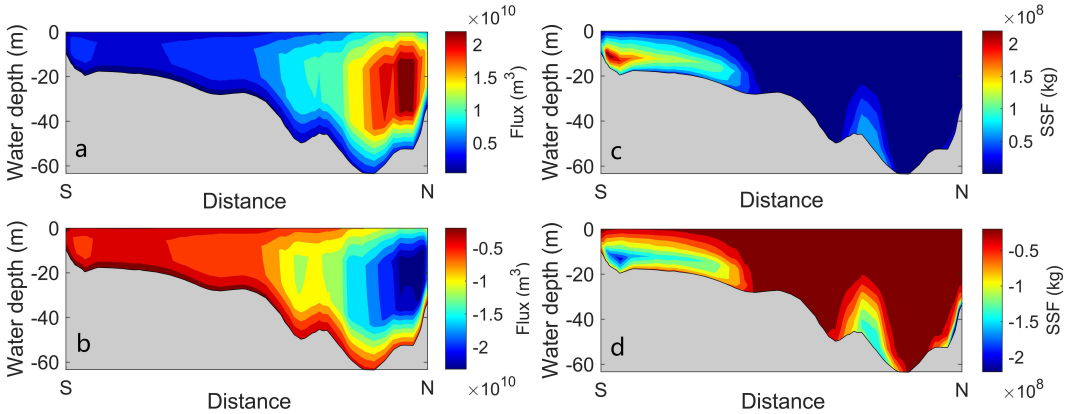

FIGURE 9
Annual inflow and outflow TF and SSF in the Bohai Strait. **(A)** Outflow TF. **(B)** Inflow TF. **(C)** Outflow SSF. **(D)** Inflow SSF.

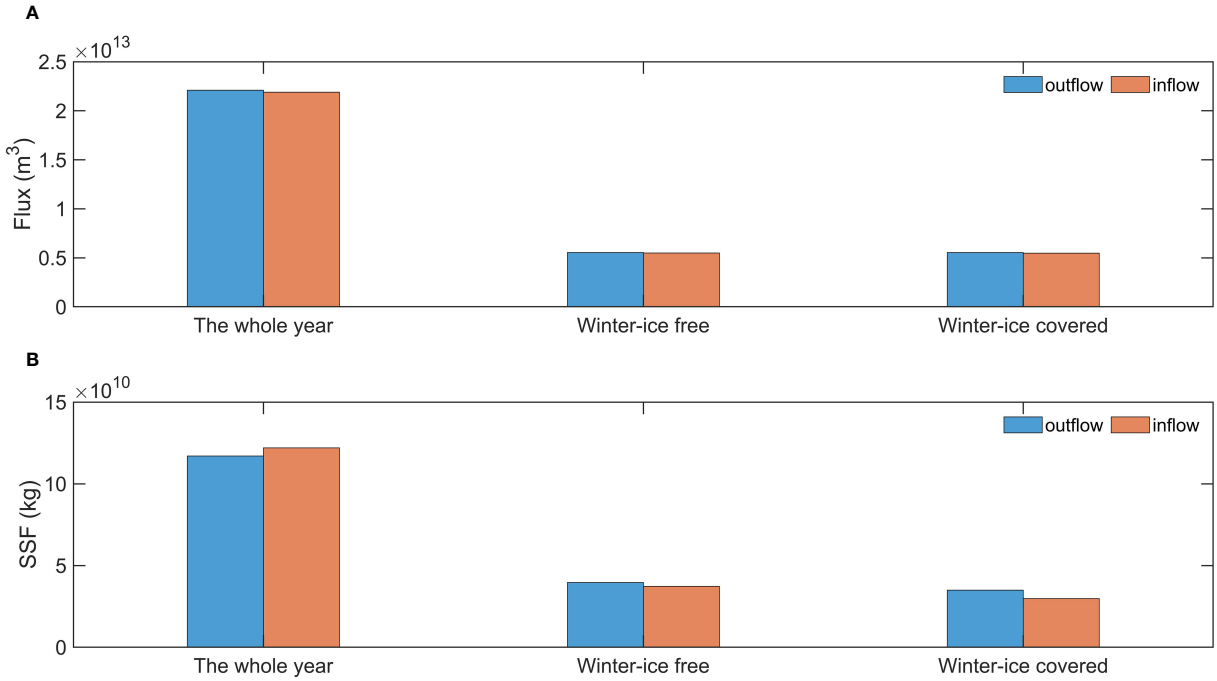

FIGURE 10
Statistical diagram of inflow and outflow water-sediment fluxes in the Bohai Strait throughout the whole year, under ice-free and ice-covered conditions. **(A)** TF. **(B)** SSF.

Furthermore, this study analyzed the response mechanism of suspended sediment transport to sea ice in the Bohai Sea during heavy ice years.

(1) Sea ice coverage inhibited the Hs, current velocity and sediment resuspension in the three bays of Bohai Sea, leading to varying degrees of decrease in Hs, current velocity and SSC. However, the current velocity increased at the edge of ice, intensifying disturbance to the bottom sediment. Additionally, under ice coverage, the current velocity in the middle layer was high, while it was low in the bottom and surface layer. Conversely, under ice-free conditions, the current velocity increased from the bottom to the surface.

(2) Under ice coverage, the inflow TF in the Bohai Sea decreased and the outflow TF increased. The net outflow TF in winter was 6.5×10^{10} m^3, which was 32.7% higher than that without ice. During the ebb tide, the high pressure in Liaodong Bay and the pressure of heavy sea ice on the water body resulted in a pressure disparity between Liaodong Bay and the Bohai Strait, leading to the acceleration of current velocity and the larger outflow TF from the Bohai Sea. During flood tide, sea ice coverage made it difficult for water to enter the Bohai Sea, so the inflow TF decreased. The annual net outflow TF from the Bohai Sea was 2×10^{11} m^3, under ice-free conditions in winter accounting for about 24.5% and under ice-covered conditions for about 32.5%.

(3) The average SSC in the Bohai Strait was 13.1 mg/l under ice-covered conditions and 15.2 mg/l under ice-free conditions. Under ice coverage, the decrease of SSF into Bohai Sea was attributed to the reduction of inflow TF and SSC, resulting in the inflow SSF decreasing by 20.3%. Despite an increase in outflow TF from the northern part of the Bohai Strait, the low and stable SSC led to minimal change. Conversely, the outflow TF in the southern part of the Bohai Strait decreased, significantly reducing the SSC by nearly 15 mg/l. Overall, the outflow SSF from the Bohai Sea decreased by 11.9%, unlike the TF. The annual net inflow SSF to the Bohai Sea was 5×10^9 kg, while in winter net outflow SSF was 5.19×10^9 kg under ice-covered conditions, which was 1.24 times higher than that under ice-free conditions.

Data availability statement

The numerical modeling data were generated by the MIKE 3D Hydrodynamic and mud transport module by the Danish Hydraulic Institute (DHI, 2012) (https://www.mikepoweredbydhi.com/). Field measurement data at BH02 station used in this paper are provided by College of Marine Geosciences, Ocean University of China (https://doi.org/10.6084/m9.figshare.23691366.v1). The model data used in this paper are available online (https://doi.org/10.6084/m9.figshare.25218113).

Author contributions

SYL: Formal analysis, Methodology, Software, Writing – original draft, Writing – review & editing. GL: Conceptualization, Formal analysis, Funding acquisition, Software, Supervision, Writing – review & editing. SDL: Formal analysis, Methodology,

Software, Writing – original draft. LZ: Data curation, Writing – original draft. ML: Methodology, Software, Writing – original draft. QF: Data curation, Methodology, Writing – original draft. LX: Conceptualization, Investigation, Writing – original draft. DY: Investigation, Methodology, Writing – original draft. YP: Formal analysis, Methodology, Writing – original draft.

Funding

The author(s) declare financial support was received for the research, authorship, and/or publication of this article. This study was jointly supported by the National Natural Science Foundation of China (grants 42121005), and Taishan Scholars Project (GXLI). Any users of the materials are required to clearly acknowledge the support of Ocean University of China.

Conflict of interest

Author ML was employed by PetroChina company.

The remaining authors declare that the research was conducted in the absence of any commercial or financial relationships that could be construed as a potential conflict of interest.

Publisher's note

References

Barrett, L., Vlahos, P., Hammond, D., and Mason, R. (2023). Sediment-water fluxes of inorganic carbon and nutrients in the Pacific Arctic during the sea ice melt season. *Continental Shelf Res.* 268, 105116. doi: 10.1016/j.csr.2023.105116

Bilotta, G., Burnside, N., Cheek, L., Dunbar, M., Grove, M., Harrison, C., et al. (2012). Developing environment-specific water quality guidelines for suspended particulate matter. *Water Res.* 46, 2324–2332. doi: 10.1016/j.watres.2012.01.055

Bonsell, C., and Dunton, K. (2018). Long-term patterns of benthic irradiance and kelp production in the central Beaufort sea reveal implications of warming for Arctic inner shelves. *Prog. Oceanography* 162, 160–170. doi: 10.1016/j.pocean.2018.02.016

Che, Y., Li, J., Guan, C., Lian, X., and Wu, K. (2019). Surface wave simulation during winter with sea ice in the bohai sea. *J. Oceanol. Limnol.* 37, 1857–1867. doi: 10.1016/j.oceaneng.2018.06.062

Dai, H., McWilliams, J., and Liang, J. (2019). Wave-driven currents in a marginal ice zone. *Ocean Model.* 134, 1–17. doi: 10.1016/j.ocemod.2018.11.006

DHI (2012). *MIKE 21 & MIKE 3 flow model FM. Hydrodynamic and Transport module scientific documentation, Release 2012* (Denmark: Danish Hydraulic Institute).

Forest, A., Sampei, M., Makabe, R., Sasaki, H., Barber, D., Gratton, Y., et al. (2008). The annual cycle of particulate organic carbon export in Franklin Bay (Canadian Arctic): Environmental control and food web implications. *J. Geophysical Research: Oceans* 113, C03S99. doi: 10.1029/2008JC004782

Giesbrecht, T., Sim, N., Orians, K. J., and Cullen, J. (2013). The distribution of dissolved and total dissolvable aluminum in the Beaufort Sea and Canada Basin region of the Arctic Ocean. *J. Geophysical Research: Oceans* 118, 6824–6837. doi: 10.1002/2013JC009202

Heath, M., Sabatino, A., Serpetti, N., Mccaig, C., and Murray, R. (2016). Modelling the sensitivity of suspended sediment profiles to tidal current and wave conditions. *Ocean Coast. Manage.* 147, 49–66. doi: 10.1016/j.ocecoaman.2016.10.018

Jiang, M., Pang, C., Liu, Z., and Jiang, J. (2020). mpact of sea ice on the hydrodynamics and suspended sediment concentration in the coastal waters of Qinhuangdao, China. *Water* 12 (2), 611. doi: 10.3390/w12020611

Jiang, S., Wang, N., Cheng, H., and Yin, Y. (2019). The study on hydrodynamic distribution characteristics of the bohai strait. *Periodical Ocean Univ. China* 49, 66–73. doi: 10.16441/j.cnki.hdxb.20190032

Jiao, C., Zhang, W., and Dong, S. (2019). Statistical Prediction for Annual Start Date and Duration of Sea ice Coverage at Qinhuangdao Observation Station. *J. Ocean Univ. China* 18, 1265–1272. doi: 10.1007/s11802-019-4060-x

Kug, J., Jeong, J., Jang, Y., Kim, B., Folland, C., Min, S., et al. (2015). Two distinct influences of Arctic warming on cold winters over North America and East Asia. *Nat. Geosci.* 8, 759–762. doi: 10.1038/ngeo2517

Lannuzel, D., Schoemann, V., Jong, J., Pasquer, B., Merwe, P., Masson, F., et al. (2010). Distribution of dissolved iron in Antarctic sea ice: Spatial, seasonal, and inter-annual variability. *J. Geophysical Research: Biogeosciences* 115, G03022. doi: 10.1029/2009JG001031

Li, G. (2005). *Study of Sedimentary Environment in the East China Sea* (Beijing: Science press).

Li, M., and Amos, C. (2001). Sedtrans96: the upgraded and better calibrated sediment-transport model for continental shelves. *Comput. Geosciences* 27, 619–645. doi: 10.1016/S0098-3004(00)00120-5

Li, G., Jiao, Y., Chen, X., Zhao, Y., Li, R., Guo, D., et al. (2024). Investigation of the recent ice characteristics in the Bohai sea in the winters of 2005–2022 using multi-source data. *Water* 16, 290. doi: 10.3390/w16020290

Li, G., Tang, Z., Yue, S., Zhuang, K., and Wei, H. (2001). Sedimentation in the shear front off the Yellow River mouth. *Continental Shelf Res.* 21, 607–625. doi: 10.1016/S0278-4343(00)00097-2

Liu, A., Häkkinen, S., and Peng, C. (1993).). Wave effects on ocean-ice interaction in the marginal ice zone. *J. Geophysical Res. Atmospheres* 98, 10025–10036. doi: 10.1029/93JC00653

Liu, S., Li, G., Liu, S., Xing, L., Pan, Y., and Yu, D. (2024). Impacts of reclamation on hydrodynamic and suspended sediment transport in the Bohai Sea. *J. Geophysical Research: Oceans* 129, e2023JC020570. doi: 10.1029/2023JC020570

Liu, S., Liu, S., Li, G., Zhang, S., Xu, J., Zhang, L., et al. (2022). Impacts of sea ice on marine dynamics in western Laizhou Bay, Bohai Sea. *Estuar. Coast. Shelf Sci.* 275, 105116. doi: 10.1016/j.ecss.2022.107958

Liu, S., Qiao, L., Li, G., Shi, J., Huang, L., Yao, Z., et al. (2018). Variation in the current shear front and its potential effect on sediment transport over the inner shelf of the East China Sea in winter. *J. Geophysical Research: Oceans* 123, 8264–8283. doi: 10.1029/2018JC014241

Lu, P., Li, Z., Dong, X., Zhang, Z., and Chen, S. (2004). Sea ice thickness and concentration analysis methods in arctic based on remote sensing images. *Chin. J. Polar Res.* 4, 317–323. doi: 10.1007/BF02873097

MacVean, L., and Lacy, J. R. (2014). Interactions between waves, sediment, and turbulence on a shallow estuarine mud flat. *J. Geophysical Research: Oceans* 119, 1534–1553. doi: 10.1002/2013JC009477

Manson, G., Davidson-Arnott, R., and Ollerhead, J. (2016). Attenuation of wave energy by nearshore sea ice: Prince edward Island, Canada. *J. Geophysical Research: Oceans* 318 (2), 253–263. doi: 10.2112/JCOASTRES-D-14-00207.1

Milliman, J., and Meade, R. (1983). World-wide delivery of river sediment to the oceans. *J. Geology* 91, 1–21. doi: 10.1086/628741

Murray, K., Miller, M., and Bowser, S. (2012). Depositional processes beneath coastal multi-year sea ice. *Sedimentology* 60 (2), 391–410. doi: 10.1111/j.1365-3091.2012.01345.x

Pawlowicz, R., Beardsley, B., and Lentz, S. (2002). Classical tidal harmonic analysis including error estimates in MATLAB using T_TIDE. *Comput. Geosciences* 28, 929–937. doi: 10.1016/S0098-3004(02)00013-4

Peck, L., Barnes, D., and Willmott, J. (2005). Responses to extreme seasonality in food supply: Diet plasticity in Antarctic brachiopods. *Mar. Biol.* 147, 453–463. doi: 10.1007/s00227-005-1591-z

Ren, Y., Li, X., and Zhang, W. (2022). A data-driven deep learning model for weekly sea ice concentration prediction of the Pan-Arctic during the melting season. *IEEE Trans. Geosci. Remote Sens.* 60, 1–19. doi: 10.1109/TGRS.2022.3177600

Shi, B., Yang, S., Wang, Y., Yu, Q., and Li, M. (2014). Intratidal erosion and deposition rates inferred from field observations of hydrodynamic and sedimentary processes: a case study of a mudflat–saltmarsh transition at the yangtze delta front. *Continental Shelf Res.* 90, 109–116. doi: 10.1016/j.csr.2014.01.019

Soulsby, R. (1995). Bed shear stresses due to combined waves and currents. In *Advances in Coastal Morphodynamics*, 4–23.

Soulsby, R. (1997). *Dynamics of Marine Sands (HR Wallingford Titles): A Manual for Practical Applications* (New York: Thomas Telford Publications).

Su, H., and Wang, Y. (2012). Using MODIS data to estimate sea ice thickness in the Bohai Sea (China) in the 2009–2010 winter. *J. Geophysical Research: Oceans* 117, C10018. doi: 10.1029/2012JC008251

Su, J., Wu, H., Knuth, M. A., and Gao, G. (2003). Modeling dynamic interaction of ice-ocean in the bohai sea. *J. Glaciol. Geocryol.* S2), 292–298.

Wahlgren, S., Thomson, J., Biddle, L., and Swart, S. (2023). Direct observations of wave-sea ice interactions in the Antarctic marginal ice zone. *J. Geophysical Research: Oceans* 128, e2023JC019948. doi: 10.1029/2023JC019948

Wan, K., Bao, X., Wang, Y., Wan, X., Li, H., and Liu, K. (2015a). Barotropic current oscillations coupled with the drawdown in Yellow and Bohai Sea. *Chin. J. Oceanology Limnology* 33, 272–281. doi: 10.1007/s00343-015-4056-3

Wan, X., Ma, Q., and Ma, W. (2015b). The effect of high frequency strong winds on winter circulation andWater exchange in the bohai sea by ROMS. *Periodical Ocean Univ. China* 4, 1–8. doi: 10.16441/j.cnki.hdxb.20140146

Wang, N., Li, G., Qiao, L., Shi, J., Dong, P., Xu, J., et al. (2017). Long-term evolution in the location, propagation, and magnitude of the tidal shear front off the Yellow River Mouth. *Continental Shelf Res.* 137, 1–12. doi: 10.1016/j.csr.2017.01.020

Wang, X., Liu, J., and Liu, H. (2024). Seasonal variability of arctic mid-level clouds and the relationships with sea ice from 2003 to 2022: a satellite perspective. *Remote Sens.* 16, 202. doi: 10.3390/rs16010202

Wang, A., Tang, M., Zhao, Q., Liu, Y., Li, B., Shi, Y., et al. (2021). Analysis of sea ice parameters for the design of an offshore wind farm in the Bohai Sea. *Ocean Eng.* 239, 109902. doi: 10.1016/j.oceaneng.2021.109902

Wang, H., Wang, A., Bi, N., Zeng, X., and Xiao, H. (2014). Seasonal distribution of suspended sediment in the Bohai Sea, China. *Continental Shelf Res.* 90, 17–32. doi: 10.1016/j.csr.2014.03.006

Warren, I., and Bach, H. (1992). MIKE 21: A modelling system for estuaries, coastal waters and seas. *Environ. Software* 7, 229–240. doi: 10.1016/0266-9838(92)90006-P

Wiberg, P., and Sherwood, C. (2008). Calculating wave-generated bottom orbital velocities from surface-wave parameters. *Comput. Geosciences* 34, 1243–1262. doi: 10.1016/j.cageo.2008.02.010

Willmott, C. (1981). On the validation of models. *Phys. Geogr.* 2, 184–194.

Xie, J., Feng, X., Chen, H., and Yin, B. (2023). Study on the mechanisms of interannual variation in suspended sediment concentration in the bohai sea based on GOCI. *J. Sea Res.* 195, 102416. doi: 10.1016/j.seares.2023.102416

Xu, N., Yuan, S., and Yan, Q. (2019). Sea ice in the Bohai Sea and its impact on marine ecological environment. *Environment Projection* (07), 20–25. doi: 10.14026/j.cnki.0253-9705.2019.07.005

Yang, Z., Ji, Y., Bi, N., Lei, K., and Wang, H. (2011). Sediment transport off the Huanghe (Yellow River) delta and in the adjacent Bohai Sea in winter and seasonal comparison. *Estuarine Coast. Shelf Sci.* 93, 173–181. doi: 10.1016/j.ecss.2010.06.005

Yu, J. (2012). *Seasonal variation and distribution of suspended sediment in the yellow sea* (Qingdao: Ocean University).

Zhang, Q., and Li, B. (1999). A comparative study on the characteristics of winter ice conditions between Bohai Sea in 1998/99 and other years. *Marrine Forecasts* 02, 80–87. doi: CNKI:SUN:HYYB.0.1999-01-006

Zhang, N., Li, S., Wu, Y., Wang, K., Zhang, Q., You, Z., et al. (2020). Effects of sea ice on wave energy flux distribution in the Bohai Sea. *Renew. Energy* 162, 2330–2343. doi: 10.1016/j.renene.2020.10.036

Zhang, N., Ma, Y., and Zhang, Q. (2018). Prediction of sea ice evolution in Liaodong Bay based on a back-propagation neural network model. *Cold Regions Sci. Technol.* 145, 65–75. doi: 10.1016/j.coldregions.2017.10.002

Zhang, Q., and Tang, M. (2010). "Analysis of the causes of a 30-year ice situation in Bohai Sea," in *The 26th Annual Meeting of the Chinese Geophysical Society*, 452–453. Beijing: National Marine Environmental Forecasting Center.

Zhang, N., Wang, J., Wu, Y., Wang, K., Zhang, Q., Wu, S., et al. (2019). A modelling study of ice effect on tidal damping in the Bohai Sea. *Ocean Eng.* 173, 748–760. doi: 10.1016/j.oceaneng.2019.01.049

Zhao, J., Bu, Q., and Liu, C. (2012). Genetic analysis of Sea ice in the Bohai Sea in January 2010. *Tianjin Sci. Technol.* 39, 68–70. doi: 10.14099/j.cnki.tjkj.2012.03.038

Zhou, S., Meijers, A., Meredith, M., Abrahamsen, E., Holland, P., Silvano, A., et al. (2023). Slowdown of Antarctic Bottom Water export driven by climatic wind and sea-ice changes. *Nat. Climate Change* 13, 701–709. doi: 10.1038/s41558-023-01695-4

Zhou, Y., Yu, D., Cheng, W., Gai, Y., Yao, H., Yang, L., et al. (2022). Monitoring multi-temporal and spatial variations of water transparency in the Jiaozhou Bay using GOCI data. *Mar. pollut. Bull.* 180, 113815. doi: 10.1016/j.marpolbul.2022.113815

Frontiers in Marine Science

Explores ocean-based solutions for emerging global challenges

The third most-cited marine and freshwater biology journal, advancing our understanding of marine systems and addressing global challenges including overfishing, pollution, and climate change.

Discover the latest Research Topics

See more →

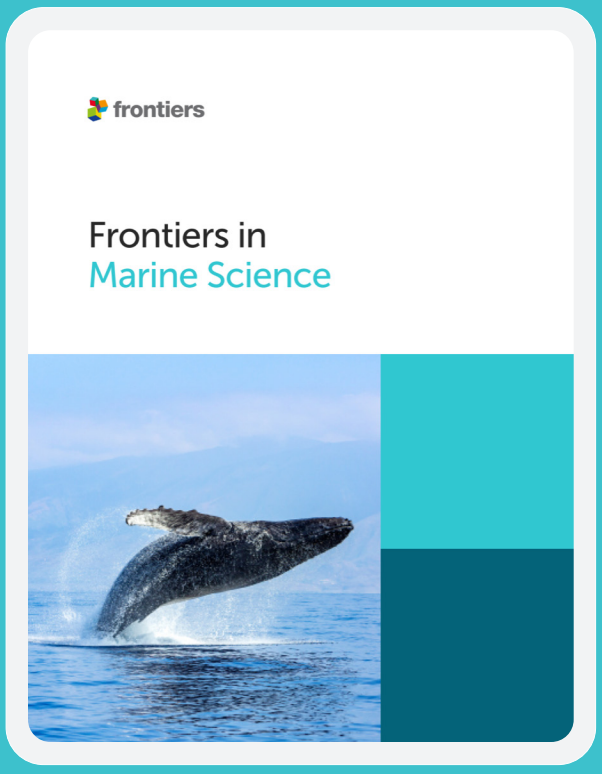

Frontiers

Avenue du Tribunal-Fédéral 34
1005 Lausanne, Switzerland
frontiersin.org

Contact us

+41 (0)21 510 17 00
frontiersin.org/about/contact